Rapport d'Habilitation à Diriger des Recherches
Université Pierre et Marie Curie
Spécialité : Mécanique

présenté par
Florent Ravelet

Etude expérimentale d'écoulements internes turbulents monophasiques et multiphasiques.

Soutenue le 20 novembre 2013 devant le jury composé de :

Georges Gérolymos :	président
Georges Descombes :	rapporteur
Souad Harmand :	rapporteur
Innocent Mutabazi :	rapporteur
Bérengère Dubrulle	
Farid Bakir	

Laboratoire DynFluid, Arts et Métiers ParisTech

à *Colette*

Remerciements

Je tiens tout d'abord à remercier chaleureusement les membres du jury pour m'avoir fait l'honneur d'évaluer ces travaux et pour les échanges que nous avons eu à cette occasion. J'espère que ceux-ci seront fructueux et en tout cas, ils me guideront dans un avenir proche.

La préparation de cet exercice s'est faite dans le cadre du laboratoire DynFluid, dont je remercie la directrice Paola Cinnella ainsi que le chef du groupe "turbomachines" Farid Bakir pour la liberté avec laquelle nous pouvons travailler et orienter nos travaux, tout en bénéficiant du soutien du laboratoire. Je tiens également à remercier l'ensemble des membres du laboratoire avec qui j'ai pu avoir des discussions diverses et variées et plus particulièrement ceux qui ont apporté des réponses à mes questions d'"ordre numérique", autour des instabilités, à propos d'équation d'Euler des turbomachines et d'"élévation de pression statique ? ou totale ?",…

Je suis redevable à l'ensemble des personnes avec qui j'ai pu collaborer ou dont j'ai pu profiter de la bienveillante direction et de l'expérience, au[1] premier chef Arnaud Chiffaudel et François Daviaud, René Delfos, Frédéric Risso puis Farid Bakir, ainsi que Thomas Loiseleux, Marc Rabaud, Louis Marié, Bérengère Dubrulle, Jacques Léorat, Jean-François Pinton, Philippe Odier, Mickaël Bourgoin, Catherine Colin, Christophe Sarraf, Robert Rey, Sofiane Khelladi et Ricardo Noguera, Brice Saint-Michel, …

De même, je tiens à remercier les élèves et étudiants en thèse que j'ai encadré, avec parfois un réel plaisir. Les résultats présentés ici doivent beaucoup en particulier à Arnaud Guet et Jérémie Pallacci, Jean-Renan de Céa et Charles Vallet, Antoine Lemaire, Pierre-Arthur Ratié, Hussain Nouri, Juan Wang, Amélie Danlos,…

Un travail à dominante expérimentale serait impossible sans un support technique de qualité. Un grand merci à Vincent Padilla et Marc Moulin, ainsi qu'à Joop Bode et Cor Gerritsen, Jean-Pierre Escafit, Marc Moulin et Josselin Mistigres.

Merci enfin aux amis et à la famille, à mes petits loups et à Edith qui m'a battu de 6 mois et trois jours pour l'accouchement.

---

[1] (x)

Table des matières

Introduction

1 Organisation du mémoire

Ce mémoire présente une synthèse de mes travaux de recherche effectués depuis ma soutenance de thèse en septembre 2005. L'ensemble s'articule autour de problèmes touchant aux ***écoulements turbulents***, tant ***monophasiques*** que ***multiphasiques*** abordés principalement d'un point de vue ***expérimental***. Les problèmes traités sont tout autant d'ordre ***fondamental*** que plus ***appliqué***. Cette présentation est organisée autour de 3 axes :

1. les instabilités et bifurcations en écoulements turbulents monophasiques ;
2. l'étude des écoulements dans les machines tournantes et leur conception ;
3. la dynamique et les instabilités en écoulements diphasiques.

Ces 3 axes ont en commun un certain nombre de traits, comme la caractérisation au moyen d'outils expérimentaux conçus à dessein, l'analyse des données obtenues (signaux temporels ou champs de vitesse LDV/PIV) au moyen du développement d'outils de post-traitement (analyse d'image) et enfin l'intérêt porté aux phénomènes instationnaires et dynamiques.

La première partie du mémoire consiste en une présentation synthétique de mes activités d'enseignement et de recherche. La seconde partie constitue une présentation détaillée de travaux et des perspectives associées, selon les 3 axes identifiés. Enfin, la troisième partie est un receuil des publications les plus significatives se rattachant à chacun de ces 3 axes.

2 Resumé du parcours scientifique

Ce résumé de mon parcours est aussi l'occasion de présenter l'ensemble des personnes avec qui j'ai eu la chance de travailler et de leur rendre hommage.

Découverte

Au cours de mes études d'ingénieur à l'ENSTA, j'ai eu l'occasion de découvrir puis d'approfondir la mécanique et la physique des fluides. En deuxième année, je me suis notamment dirigé vers un parcours approfondissant les problèmes d'instabilité, de chaos et de turbulence. J'ai eu la chance d'effectuer un stage de deux mois au FAST (Paris XI) sous la direction de T. Loiseleux, portant sur la formation de dunes sous-marines (Doppler *et al.* (2007)).

Après cette découverte de la recherche expérimentale, j'ai alors suivi, parallèlement à la formation « Architecture Navale et Génie Maritime » de troisième année de l'ENSTA, le DEA de mécanique de Paris VI, poursuivant l'étude des systèmes dynamiques, du non-linéaire et de la turbulence. Mon stage de DEA s'est effectué au Service de Physique de l'État Condensé du CEA-Saclay, sous la direction d'A. Chiffaudel et F. Daviaud, en prélude à ma thèse de doctorat.

Thèse de doctorat

Ma thèse de doctorat (Ravelet, 2005) porte d'une part sur l'étude des grandes échelles et de leurs fluctuations dans un écoulement turbulent fermé entre deux disques contrarotatifs munis de pales (écoulement de type « von Kármán – inertiel » : Douady *et al.* (1991); Cadot *et al.* (1997)). Ce travail constitue d'autre part une contribution au développement d'une expérience de magnétohydrodynamique en sodium liquide visant à observer l'effet dynamo (collaboration VKS regroupant les CEA Saclay et Cadarache, et les ENS Paris et Lyon[1]).

Nous avons ainsi mis en évidence et étudié principalement au moyen de mesures de couple une « bifurcation globale » de l'écoulement turbulent, caractérisée par la coexistence d'états moyens

---

[1] `http://perso.ens-lyon.fr/nicolas.plihon/VKS/index.php`

brisant les symétries du système et par des transitions avec hystérésis (Ravelet *et al.*, 2004) et observée uniquement pour des écoulements pleinement turbulents (Ravelet *et al.*, 2008b).

A partir de mesures par LDV[2] du champ de vitesse moyen et de simulations numériques avec un code de dynamo cinématique, nous avons alors cherché à optimiser la forme des pales en vue de l'obtention de l'effet dynamo (Ravelet *et al.*, 2005). En collaboration avec Stefani *et al.* (2006), nous avons mené des simulations complémentaires sur l'effet des conditions aux limites qui ont conduit au choix d'un matériau de forte perméabilité magnétique pour les impulseurs. J'ai enfin participé à un ensemble de campagnes sur l'expérience de dynamo en sodium liquide VKS2 jusqu'en 2008. Cette expérience est la première au monde à avoir mis en évidence la génération d'un champ magnétique en écoulement fortement turbulent (Monchaux *et al.*, 2007), à la dynamique riche, incluant des renversements aléatoires (Monchaux *et al.*, 2009).

Post-doctorat, TU-Delft

De 2005 à 2007, au "Laboratory for Aero & Hydrodynamics" de l'Université Technologique de Delft (Pays-Bas), je me suis intéressé au problème de la dispersion de deux liquides non miscibles en écoulement turbulent en collaboration avec R. Delfos et J. Westerweel.

J'ai développé un dispositif de Taylor-Couette, où le fluide est cisaillé entre deux cylindres coaxiaux indépendants (Andereck *et al.*, 1986), permettant une exploration des régimes *pleinement turbulents* et des transitions entre ces régimes.

En écoulement monophasique turbulent, une transition entre régimes dominés par la rotation et régimes dominés par le cisaillement est mise en relief (Ravelet *et al.*, 2010), depuis confirmée par notamment Paoletti & Lathrop (2011). Ces régimes sont caractérisés par des mesures PIV[3] stéréoscopiques. Concernant les études de dispersion (écoulement multiphasique eau / huile), ces études ont guidé le choix de la contrarotation comme régime d'intérêt. Les dispersions sont caractérisées par des mesures de LIF[4] avec adaptation des indices de réfraction des deux phases, et par des mesures de couples. Par rapport au cas monophasique, la puissance dissipée peut être multipliée par 2, avec présence de dynamiques très lentes dans le système (Ravelet *et al.*, 2007).

De façon annexe, nous avons fait profiter Rodriguez Pascual *et al.* (2009), d'un laboratoire voisin de l'Université de Delft, du savoir-faire acquis pour la mesure stéréoscopique du champ de vitesse dans ce type de géométrie afin d'étudier les transferts thermiques dans un dispositif servant à l'étude de la cristalisation eutectique.

Post-doctorat, IMFT

Suite à cette première expérience en écoulements multiphasiques, j'ai travaillé de 2007 à 2008 à l'Institut de Mécanique des Fluides de Toulouse avec F. Risso et C. Colin autour du problème de la rupture d'une inclusion dans un champ turbulent.

J'ai construit un dispositif expérimental dans lequel une bulle d'air est immobilisée dans un écoulement d'eau dont on ajuste indépendamment le niveau de turbulence et le mouvement moyen. A partir de trois vues perpendiculaires obtenues au moyen de caméras rapides, j'ai mis au point un algorithme de reconstruction d'un objet tridimensionnel dont nous étudions la dynamique de déformation et de rupture. L'apport majeur de l'expérience par rapport à l'état de l'art (Miller & Scriven (1968); Risso & Fabre (1998); Risso (2000)) est la prise en compte de la déformation déterministe due au mouvement moyen. L'importance du glissement et de

---

[2] Laser Doppler Velocimetry.

[3] Particle Image Velocimetry

[4] Light Induced Fluoresecence.

la prédéformation a tendance à imposer un mode de rupture par allongement dans un plan perpendiculaire à la gravité et à inhiber les effets de la turbulence sur la dynamique de rupture (Ravelet *et al.*, 2011a).

Les outils développés pour la caractérisation des modes propres d'oscillations ont également été utilisés dans le cas d'études sur la rupture de gouttes en présence de tensio-actifs menées par Abi Chebel *et al.* (2008, 2011), du Laboratoire de Génie Chimique.

Poste actuel, Arts et Metiers-ParisTech

J'ai été recruté en tant que Maître de Conférences (section 60) en septembre 2008 au LEMFI, situé à Arts et Metiers-ParisTech, centre de Paris. Ce laboratoire dirigé alors par R. Rey a depuis fusionné au 1^er^ janvier 2010 avec le laboratoire SINUMEF pour former le laboratoire DynFluid, dirigé par P. Cinnella. Mes activités de recherches s'inscrivent dans les thématiques de l'équipe « Ecoulements Internes et Turbomachines[5] », sous la responsabilité de F. Bakir.

Mon intégration dans cette équipe dont le ***cœur d'expertise*** est la conception et l'analyse des écoulements dans les ***turbomachines*** correspond pour ma part à un ***changement de thématique***, et à une ***ouverture*** vers une recherche tournée vers l'application et en lien fort avec de nombreux partenaires industriels. Elle correspond également à une volonté du laboratoire de ***renforcer, renouveller et développer l'activité expérimentale***, en apportant une sensibilité aux ***phénomènes physiques*** et aux aspects ***dynamiques et instationnaires***.

Depuis 2008, nous avons ainsi acquis un ensemble de matériels pérennes et transposables d'un dispositif expérimental à un autre : caméra rapide et éclairage par plaque de LED, cartes d'acquisition et environnement LabView, microphones et amplificateur, ainsi qu'une LDV bi-composante à trois chemins optiques et une LDV mono-composante depuis le recrutement de C. Sarraf en 2011. En termes de développement de l'activité expérimentale, les réalisations suivantes ont été effectuées au cours de cette période :

- Une extension de la boucle d'essai hydraulique cavitante du laboratoire comprenant une veine d'essai de section rectangulaire précédée de dispositifs tranquiliseurs. Cette veine jouissant d'accès optiques et d'un écoulement en entrée homogène avec un taux de turbulence de l'ordre de 2% est dédiée aux études des instabilités en régime cavitant. L'extension du circuit comporte également un banc d'essai pour hélices axiales (Solis *et al.*, 2010) permettant des visualisations et des mesures par LDV / PIV.
- Une boucle hydraulique dédiée à l'étude du transport solide de grandes particules en conduite horizontale. Une installation verticale permettant d'étudier le transport de solides par air-lift est en phase finale de construction.
- Un banc d'essai pour l'étude des ventilateurs subsoniques en conduite, réalisé au cours de la thèse de Hussain Nouri (2012). Ce banc d'essai permet d'étudier les écoulements entre deux rotors dont on peut varier la distance et le rapport des vitesses de rotation.

Mon activité de recherche depuis mon recrutement a porté, avec des intensités différentes, sur l'ensemble des 3 axes précédemment identifiés.

Axe 1. J'ai ainsi, dans la continuité de mes travaux de thèse autour du projet VKS, entretenu une collaboration avec B. Dubrulle et F. Daviaud du CEA-Saclay. J'ai pu notamment apporter des compétences acquises depuis mon recrutement à DynFluid autour des écoulements dans les turbomachines et autour de la simulation numérique des écoulements (CFD[6]). Nous avons ainsi pu mettre en évidence numériquement la présence de vortex entre les pales des impulseurs, et

---

[5] `http://www.dynfluid.eu/fr/equipes/turbomachines`

[6] Computational Fluid Dynamics

estimer les tenseurs “α” et “β” associés[7], apportant un éclairage sur les mécanismes à l'origine de la dynamo dans VKS (Ravelet *et al.*, 2012).

Axe 2. Dans le cadre de l'axe 2 (écoulements dans les machines tournantes), nous avons effectué une étude sur l'effet de l'épaisseur des pales sur les performances et le niveau des fluctuations de pression (Sarraf *et al.*, 2011). Nous avons comparé deux ventilateurs ne différant que par l'épaisseur des pales. Nous travaillons actuellement avec C. Sarraf sur l'influence du blocage aval sur les performances de ces ventilateurs (Sarraf *et al.*, 2013).

J'ai également pris en charge un ***thème nouveau*** que je porte au sein de l'équipe, autour de la prise en compte des ***interactions entre les rotors*** pour la conception de machines axiales subsoniques ***contrarotatives***. Un premier système de rotors contrarotatifs a été conçu par une procédure développée dans le cadre de la thèse de Nouri (2012). Après une étude des performances globales et une validation de la méthode de conception (Nouri *et al.*, 2012), nous avons étudié plus particulièrement les écoulements dans la zone entre rotors (Nouri *et al.*, 2013) en variant la ***distance entre rotors*** et le ***rapport des vitesses*** de rotation. Le rendement est beaucoup plus élevé que pour une machine conventionnelle, avec une zone de haut rendements très étendue. La distance a de plus un effet relativement faible sur les performances, mais très important sur le niveau et le contenu spectral des fluctuations de vitesse et de pression. Aux faibles distances, des interactions non-linéaires entre les rotors sont mises en évidence.

Axe 3. J'ai notamment travaillé sur l'influence de rugosités organisées en paroi sur les instabilités de poches de cavitation, en collaboration avec O. Coutier-Delgosha (LML / ENSAM Lille) et A. Danlos en postdoctorat au laboratoire. Sur la partie divergente d'un obstacle de type “Venturi”, donnant lieu à des ***instabilités en régime cavitant*** (Callenaere *et al.*, 2001; Barre *et al.*, 2009), différentes plaques munies de stries longitudinales sont utilisées. Au moyen de mesures par LDV, de visualisations et de mesures de pressions pariétales, nous montrons que la géométrie des stries et en particulier leur profondeur modifie la dynamique des poches de cavitation, réduisant leur taille ou même faisant basculer d'un régime à poches pulsant à basse fréquence à un régime à poches coupées périodiquement par un jet rentrant (Danlos *et al.*, 2013b).

Enfin, j'ai de manière annexe, dans le cadre d'un projet avec Technip, commencé une activité autour du transport hydraulique de particules solides de grande dimension (diamètre ≥ 5 mm en tuyau de diamètre 100 mm) en tuyau horizontal (Ravelet *et al.*, 2013). Les mesures de perte de charge en fonction de la vitesse du mélange à différentes concentrations de transport sont comparées à des modèles semi-empiriques issus de la littérature (Newitt *et al.*, 1955), et à des modèles 1D basés sur les bilans intégraux de masse et de quantité de mouvement (Doron *et al.*, 1987). Ces travaux ouvrent une piste de recherche au laboratoire sur le transport solide, notamment le développement de méthodes de simulations basées sur une pénalisation des équations, avec S. Khelladi, dans le cadre de la thèse d'Ewen Maréchal (problématique de givrage du carburant).

Positionnement actuel

Mon activité de recherche se concentre aujourd'hui principalement autour des axes 2 et 3, notamment à travers l'encadrement de 4 thèses (J.-E. Méhal, 2008– ; J. Wang, 2012– ; J. Antoun-Labib, 2012– et B. Bugeat, 2013–) et le support d'A. Danlos, en post-doctorat de 2011 à 2013.

---

[7] “α” est un tenseur dépendant de l'hélicité des fluctuations de vitesse et est grossièrement un terme source pour l'effet dynamo, et “β” est un tenseur de résistivité basé sur le tenseur de Reynolds.

Première partie

Eléments biographiques

1 Curriculum Vitae

Florent Ravelet
Lab. DynFluid, Arts et Métiers ParisTech
151, bd de l'hôpital, 75013 Paris
courriel : florent.ravelet@ensam.eu
site : `http://florent.ravelet.free.fr`

né le 14 septembre 1979
marié
trois enfants

Maître de Conférences au laboratoire DynFluid - Arts et Metiers ParisTech

---

Postes Occupés

2007-2008 : Stage postdoctoral, Institut de Mécanique des Fluides de Toulouse.

2005-2007 : Stage postdoctoral, lab. AHD, TU-Delft, Pays-Bas.

Études et diplômes

2002 - 2005 : Thèse de doctorat au CEA-Saclay, école doctorale de l'Ecole Polytechnique, mention « très honorable avec félicitations ».
2001 - 2002 : DEA de mécanique des fluides de Paris VI, mention « très bien ».
Options : instabilités en écoulements ouverts, contrôle du chaos.

1999 - 2002 : Ingénieur de l'ENSTA.
Voie Systèmes Mécaniques et Chimiques.
Spécialisation en Génie Maritime et Architecture Navale.
Premier prix de l'AGM-ITA (projet de fin d'études).

Activités de Recherche

Recherche à dominante expérimentale autour de la caractérisation et de l'analyse des écoulements turbulents internes :

- Bifurcations et instabilités des grandes échelles des écoulements de von Kármán et de Taylor-Couette.
- Aérodynamique instationnaire dans les turbomachines subsoniques.
- Rupture de bulles soumises à un champ turbulent.
- Instabilités en écoulement cavitant.
- Transport solide hydraulique et par air-lift.

Activités Pédagogiques

Enseignements :

- Formation ENSAM 2$^{\text{è}}$ année :
  - « Technologie des réacteurs nucléaires », 50 h/semestre (CM, TD & TP), responsable de l'Unité (66 h/semestre).
  - « Machine et Systèmes Energétiques », 18 h/an (TD).
- Formation Ingénieur 2000 GE 2$^{\text{è}}$ année :
  - « Technologie des réacteurs nucléaires », 15 h/an (CM & TD).
  - « Turbines hydrauliques », 19 h/an (TD & TP).
  - « Turbomachines », 31 h/an (TD & TP).
- Formation Ingénieur 2000 GE 3$^{\text{è}}$ année :
  - « Ecoulements diphasiques en conduite », 20 h/an (CM, TD & TP).

- Formation ENSAM 3$^{\text{è}}$ année.
  - « Panorama sur les énergies », 6 h/an (CM), Expertise « Industrie Nucléaire ».
  - « Conception d'un ventilateur axial contrarotatif », 9 h/an (TP), Master Recherche « Ingénierie des Machines à Conversion d'Energie ».

Encadrement de stages :

- 2 stages de licence L3.
- 2 stages de master M1.
- 10 stages de master recherche M2.
- 19 projets de fin d'étude d'élèves-ingénieurs ENSAM.

Publications

21 articles publiés dans des revues à comité de lecture.

28 actes de conférences avec comité de lecture (9 nationales et 19 internationales).

Encadrement de Thèses

1. Hussain Nouri, co-encadré (70%) avec F. Bakir, soutenue le 18 décembre 2012, prix Valembois de la SHF, nomination au prix Bézier.
2. Jean-Elie Méhal, co-encadré (30%) avec O. Coutier-Delgosha et F. Bakir, 2008–.
3. Ewen Maréchal, co-encadré (20%) avec S. Khelladi et F. Bakir, 2011–.
4. Juan Wang, co-encadrée (70%) avec F. Bakir, 2012–.
5. Joseph Antoun-Labib, co-encadré (50%) avec F. Bakir et S. Kouidri, 2012–.
6. Benjamin Bugeat, co-encadré (70%) avec F. Bakir, 2013–.

Autres activités scientifiques

– Responsable du site Web de l'équipe « Ecoulements Internes & Turbomachines ». (`http://www.dynfluid.eu/fr/equipes/turbomachines`)

– Co-organisateur des séminaires du laboratoire DynFluid de 2009 à 2012.

– Activité de *referee* pour les revues suivantes :

- Colloids and Surfaces A : Physicochemical and Engineering Aspects : 1 article ;
- Experimental Thermal and Fluid Science : 2 articles ;
- Experiments in Fluids : 1 article ;
- International Journal of Multiphase Flow : 1 article ;
- Journal of Fluids Engineering : 2 articles ;
- Journal of Fluid Mechanics : 2 articles ;
- Journal of Turbulence : 1 article ;
- Proc. Inst. Mech. Eng., Part A, Journal of Power and Energy : 1 article ;
- Proc. Inst. Mech. Eng., Part C, Journal of Mech. Eng. Sci. : 6 articles ;
- Proc. Inst. Mech. Eng., Part D, Journal of Automobile Engineering : 1 article.

Contrats et collaborations

Anr e-Meca (Valeo, Satie, Tempo, DynFluid, IFPn, SKF), 2012-2015.

Anr INCA soumise (LEGI, DynFluid, ICUBE, IRENAV), 2013.

Anr SCALE en construction (Valeo, DynFluid, Tempo).

Responsable scientifique pour des contrats avec Technip, Lectra, Fapmo, JMS consulting, Valeo.

2 Activités pédagogiques et d'encadrement

2.1 Enseignement

J'enseigne depuis 2008 au centre de Paris de l'Ecole Nationale Supérieure des Arts et Métiers. Les étudiants concernés sont d'horizons variés. Il s'agit en effet d'une part d'étudiants suivant la filière « classique », recrutés sur concours après classes préparatoires, et d'autre part d'étudiants suivant la formation en alternance « Ingénieurs 2000 », spécialité « Génie des Procédés Energétiques ». J'interviens principalement dans trois domaines :

- Turbomachines (TD, TP, 77 h/an).
- Modélisation des écoulements diphasiques en conduite (CM, TD & TP, 20 h/an).
- Centrales nucléaires de production d'électricité (CM, TD & TP, 121 h/an).

Ce dernier domaine constitue le « fil rouge » du support que j'anime pour un module pluridisciplinaire consacré à l'optimisation d'un système énergétique . Mes interventions portent tout d'abord sur les principes généraux de fonctionnement du cœur d'une centrale nucléaire après une introduction à la physique nucléaire. Le cycle énergétique et ses différents éléments sont ensuite traités sous forme de travaux dirigés, autour d'une centrale de type P.W.R du palier 900 MWe. Les problèmes vibratoires sur un élément du système sont illustrés en travaux pratiques (analyse modale). Enfin, la part la plus importante est consacrée à un Bureau d'Etude (CAO, maillage et simulation numérique) autour de la thermohydraulique dans une cuve de réacteur.

Je m'attache ainsi à donner aux étudiants à la fois une vision d'ingénierie (lecture de plans, questions sur l'influence du type de moteur électrique employé dans les TD et TP en turbomachines, par exemple), mais également un ensemble de notions faisant appel au sens physique : similitude et intérêt des nombres adimensionnels, analogies (thermique / hydraulique / électrique), conservation et bilans globaux de masse, quantité de mouvement et énergie, existence du non-linéaire et possibilité de solutions multiples,...

Dans la mesure du possible, les cours s'appuient sur les activités de recherche du laboratoire. Ainsi, les travaux autour du transport solide (Ravelet *et al.*, 2011b, 2013) illustrent le cours sur la modélisation en multiphasique. De même, l'installation développée autour des ventilateurs contrarotatifs (Nouri *et al.*, 2013), et une installation de pompage vertical par air-lift sont des supports de TP et ont pu être réalisés dans le cadre de projets pédagogiques.

2.2 Encadrement de stages

Au cours de ma thèse, j'ai eu l'occasion d'encadrer différents stagiaires :

- A. Guet, Licence de Mécanique, Paris XI (1 mois) : "TRANSITION À LA TURBULENCE DANS L'ÉCOULEMENT DE VON KÁRMÁN."
- J. Palacci, Licence ENS-Lyon (2 mois) : "ETUDE D'APPENDICES MÉCANIQUES SUR LA BIFURCATION GLOBALE DANS L'ÉCOULEMENT DE VON KÁRMÁN."
- S. Louvard, Maîtrise de Mécanique Paris XI (3 mois) : "DIMENSIONNEMENT DE LA COUCHE AU REPOS POUR VKS2."
- L. Tang, Maîtrise de Mécanique Paris XI (3 mois) : "MESURES PAR PIV D'UN NIVEAU GLOBAL DE FLUCTUATIONS."

Depuis mon recrutement à l'ENSAM, j'ai également encadré plusieurs Projets d'Expertise [1] et stages du master Recherche (M2) « Ingénierie des Machines à Conversion d'Energie ». Certains de ces stages et projets sont issus d'un besoin exprimé par un partenaire. Pour d'autres, les élèves

---

[1] PJE. Il s'agit d'un projet pour élèves de 3$^{\text{ème}}$ année de la formation classique, d'une journée par semaine au premier semestre et à temps complet au second semestre.

effectuent leur stage en entreprise. Ces points sont précisés le cas échéant.

- 2008–2009
  - S. Grégoire & E. Daly (PJE) : "Conception d'un moyen expérimental d'étude de l'hydrodynamique instationnaire dans une pompe axiale : application à la réduction du bruit acoustique." Partenaires : Fapmo / DCNS.
  - A. Aflak & G. Charoy (PJE) : "Subsea Mining Flow Assurance for a gas lift process." Partenaire : Technip.
  - Y. Karime (M2) : "Comparaison du comportement de deux ventilateurs à pales fines et épaisses."
  - S. Chauvel (M2) : "Estudo das formas de fundo em banco de areiai de estuário raso." Universidade Federal de Pernambuco, Brésil.
    Second semestre à l'étranger.
- 2009–2010
  - J.-R. de Céa & C. Vallet (PJE) : "Experimental analyis of liquid-solid flow in horizontal, vertical and flexible pipes." Partenaire : Technip.
    Prix Garengeat du meilleur Projet d'Expertise.
  - S. Gire (PJE) : "Conception et réalisation d'une veine d'essais destinée à des mesures fines pour l'amélioration des modèles en écoulement fortement cavitant."
  - F. Charpentier (PJE) : "Conception de connexions vissées pour le chemisage métallique d'alvéoles de stockage de déchets radioactifs de haute activité."
    ANDRA *(second semestre en entreprise).*
  - A. Lemaire (PJE) : "Minerai des abysses : étude expérimentale du transport solide en horizontal." Partenaire : Technip.
    Publication associée : Ravelet et al. *(2011b).*
  - G. Combes (PJE) : "Analyse expérimentale d'une électro-pompe de circulation destinée à un système de propulsion nucléaire." Partenaires : Fapmo / DCNS.
  - X. Balloy (M2) : "Estudo das formas de fundo em banco de areiai de estuário raso." Universidade Federal de Pernambuco, Brésil.
    Second semestre à l'étranger.
  - M. Bouffanais (M2) : "Etude expérimentale de l'interaction hélice / échangeur."
    Partenaires : Fapmo / DCNS.
- 2010–2011
  - J. Jégourel (PJE) : "Conception d'un banc d'essai pour hélices contrarotatives."
  - S. Balducci & G. Veyre de Soras (PJE) : "Minerai des abysses. Transport en conduite horizontale et en S : étude expérimentale." Partenaire : Technip.
  - A. Pastor (PJE) : "Etude expérimentale de l'hydrodynamique instationnaire dans une pompe axiale de circulation."
  - D. Harter (PJE) : "Validation de méthodes de contrôle non destructif des réacteurs de 4ème génération."
    CEA-Saclay *(second semestre en entreprise).*
  - P.-A. Ratié (M2) : "Vers une compréhension de la dynamo dans VKS : simulations numériques de l'écoulement dans les turbines." Partenaire : CEA-Saclay.
    Publication associée : Ravelet et al. *(2012).*
  - M. Fardeau (M2) : "Influence de la rugosité sur le phénomène de cavitation."
- 2011–2012
  - E. Cabrera (PJE) : "Etude expérimentale d'une soufflante à rotors contrarotatifs."

  - J. Rey Rueda (PJE) : "Etudes expérimentales innovantes de profils pour réduire les frottements aérodynamiques – réduction des émissions de CO_2 dans la mobilité interurbaine." Partenaires : Arkema / JMS Consulting.
  - X. Galan Cruz (PJE) : "Electro-Mécanique Embarquée à Compacité Améliorée, Conception d'un banc d'essais."
    ANR e-Meca.
  - N. Legrand (PJE) : "Fournir les compétences nécessaires au développement de nouveaux projets nucléaires."
    Atlantic Technologies *(second semestre en entreprise).*
  - T. Delaplace (PJE) : "Characterization of large particle slurry flow in horizontal and S-shape pipes."
    Technip *(second semestre en entreprise).*
  - P.-L. Royer (M2) : "Etude expérimentale d'instabilités en régime cavitant dans un modèle épuré de turbomachine."
  - R. Ruiz (M2) : "Vers une compréhension de la dynamo dans VKS : simulations numériques de l'écoulement dans les turbines." Partenaire : CEA-Saclay.
- 2012–2013
  - Y. Pengcheng (PJE) : "Conception d'un banc d'essais pour l'étude de l'aérodynamique interne d'un moteur électrique rapide ultra-compact."
    ANR e-Meca.
  - A. K. Hamidou Souley (PJE) : "SCALE : Réduction de masse des systèmes de refroidissement embarqués, étude d'un ventilateur axial."
  - L. Brocard (PJE) : "Modélisation fonctionnelle d'un banc d'essai H/F."
    SNECMA *(second semestre en entreprise).*
  - A. Gimeno Sanz (M2) : "Etude des couples dans un écoulement de von Kármán turbulent." Partenaire : CEA-Saclay.
  - A. Sanz Fernandez (M2) : "Simulation numérique de l'écoulement dans l'entrefer d'une machine électrique rapide ultra-compacte."
    ANR e-Meca.

2.3 Encadrement de thèses de doctorat

Etude expérimentale de l'écoulement et de l'interaction entre deux rotors contrarotatifs subsoniques

Doctorant : Hussain Nouri, directeur : F. Bakir. Thèse débutée en octobre 2009, soutenue le 18/12/2012. Prix Valembois (SHF) et nomination au prix Bézier (Fondation Arts et Métiers).

Cette thèse porte sur l'étude des écoulements entre deux rotors contrarotatifs. L'enjeu de cette thèse est de mieux comprendre les mécanismes physiques des écoulements présents dans cette zone critique, afin de contribuer, d'un point de vue fondamental à l'amélioration de la connaissance des interactions possibles entre les rotors dans la perspective d'une modélisation plus fiable des sources de bruit ; et d'un point de vue applicatif à établir les lignes directrices de conceptions de plus grande efficacité énergétique et acoustique de ces machines. La démarche consiste tout d'abord en la conception d'un banc d'essai permettant de faire varier la distance axiale et le rapport des vitesses de rotation de deux rotors. Ce banc d'essai est prévu pour la mesure des performances globales d'une part, et des fluctuations de pression et de vitesse entre les rotors d'autre part. Un premier système contrarotatif a été conçu et caractérisé au cours de cette thèse, permettant une première validation de la méthode de conception, confirmant le grand intérêt pratique d'un tel système, et donnant des premiers indices d'un fort couplage entre rotors à faible distance.

Bilan : 3 articles publiés et 8 actes de conférences.

Analyse de l'influence de rugosités organisées sur les écoulements cavitants instationnaires

Doctorant : Jean-Elie Méhal, directeur : F. Bakir. Co-encadrement de la thèse par O. Coutier-Delgosha (LML) et A. Danlos, en post-doctorat de septembre 2011 à septembre 2013. Thèse débutée en octobre 2008, soutenance prévue en 2013.

Ce travail porte sur l'évaluation d'une méthode de contrôle passif des instabilités de poches de cavitation par l'utilisation de stries longitudinales en paroi. Une géométrie de type Venturi a été implémentée dans la veine de cavitation du laboratoire. Ce choix est motivé par la richesse de la dynamique des poches de cavitation naissant sur la partie divergente de cette forme géométrique somme toute simple. Il s'agit d'un cas largement documenté, servant de plus de cas de référence à de nombreux groupes développant des approches numériques originales. Les poches de cavitation peuvent en effet montrer deux comportements dynamiques différents : dans un cas, la poche pulse à très basse fréquence, et pour l'autre régime, la poche croît puis est périodiquement découpée selon un cycle relativement régulier. Nous avons étudié les effets de stries d'usinage longitudinales de diamètre, profondeur et longueur d'onde différentes sur la dynamique des poches, par visualisations au moyen de caméra rapide. Les effets sur la couche limite en régime non cavitants sont caractérisés par LDV. Les résultats montrent qu'il est possible de réduire la taille moyenne des poches et leur rapport de forme, ainsi que de supprimer la transition vers le régime cyclique.

Bilan : 1 article soumis, 1 acte de conférence.

Etude et modélisation des phénomènes de givrage dans les systèmes carburant de turboréacteurs

Doctorant : Ewen Maréchal, directeur : F. Bakir, encadrant principal : S. Khelladi. Thèse débutée en octobre 2011, soutenance prévue en septembre 2014. Financement CIFRE Snecma.

Ce travail porte sur l'étude et la modélisation des mécanismes de formation, transport et dépôt de glace dans les systèmes carburant. Le but principal est le développement d'un outil prédictif. Il s'agit d'effectuer des simulations numériques d'écoulements eau/carburant dans des conditions givrantes afin de comprendre le comportement de différents éléments du système moteur.

Ma contribution porte sur l'assistance à la mise au point d'un dispositif expérimental afin de valider les différents modèles développés. Parmi ceux-ci, une technique de pénalisation du tenseur de déformation est notamment choisie afin de traiter le transport des particules, et sera validée sur la boucle de transport solide du laboratoire.

Aérodynamique instationnaire d'un étage d'une turbomachine axiale subsonique

Doctorante : Juan Wang, directeur : F. Bakir. Thèse débutée en mars 2012, soutenance prévue en septembre 2014.

Cette thèse s'inscrit dans la continuité des études initiées lors de la thèse de H. Nouri. La démarche consiste à pousser plus avant l'étude de la configuration contrarotative de base, à la comparer notamment à un étage rotor / stator, puis à concevoir et essayer d'autres configurations de rotors contrarotatifs, en variant notamment la répartition du chargement entre rotors et des vitesses de rotations, afin d'explorer l'influence de ces paramètres de conception sur l'extension de la plage de fonctionnement.

Bilan : 2 actes de conférence.

Modélisation des écoulements transsoniques confinés entre un stator et un rotor ultra-rapide

Doctorant : Joseph Antoun-Labib, directeur : F. Bakir. Co-encadrant : S. Kouidri (LIMSI). Thèse débutée en octobre 2012, soutenance prévue en septembre 2015.

Cette thèse s'inscrit dans l'ANR e-MECA[2]. Le développement de machines électriques de forte puissance et de taille réduite suscite actuellement une forte demande notamment dans le secteur automobile. L'une des pistes envisagées est l'augmentation de la vitesse de rotation. Dans ces machines ultra-rapides, la vitesse périphérique atteint des valeurs de l'ordre de 250 $m.s^{-1}$. Les pertes aérodynamiques dans les jeux entre rotors et stators deviennent alors très importantes, de même que les problèmes de refroidissement. Si l'écoulement de Taylor-Couette entre deux cylindres infinis, concentriques et lisses est largement étudié et modélisé en écoulement incompressible, les écoulements rencontrés dans les applications envisagées sont des écoulements en régime transsonique, entre deux parois extrêmement proches (rapports de rayons$>$ 0.98) pouvant être texturées, avec éventuellement un flux axial imposé et des effets de confinement non négligeables. L'enjeu de cette thèse est de contribuer à définir une méthodologie rapide et efficace de modélisation des pertes et des écoulements dans ce type de machines. La démarche consiste à réaliser un banc d'essai dédié où seront étudiées expérimentalement diverses configurations (rotors lisses et texturés, effets des rapports d'aspects radiaux et longitudinaux, écoulements axiaux avec prérotation ou non simulant un ventilateur en amont...).

Etude et optimisation de nouveaux concepts de ventilateurs pour le refroidissement de machines électriques tournantes

Doctorant : Benjamin Bugeat, directeur : F. Bakir. Thèse débutée en mars 2013, soutenance prévue en mars 2016. Financement CIFRE Valéo.

Actuellement Valeo travaille sur de nouvelles machines électriques d'une dizaine de kilowatt entraînées par courroie et refroidies par air. Afin d'améliorer le refroidissement du rotor, on envisage d'utiliser un soufflage dans des canaux rotoriques. Une meilleure compréhension des écoulements, une analyse de paramètres géométriques influents et une optimisation des aubes des ventilateurs sont alors nécessaires. Plusieurs paramètres géométriques peuvent avoir une grande influence sur les performances aérauliques. Deux paramètres seront alors étudiés : la longueur du rotor et la section de passage des canaux rotoriques liée directement à la quantité de cuivre utilisée. Il s'agit alors de valider expérimentalement le débit d'air dans le rotor de même que le débit total dans cette machine possédant plusieurs entrées et sorties ainsi que des écoulements de recirculation. Les essais seront couplés à une étude numérique réalisée à l'aide de logiciel de CFD afin de mieux comprendre les écoulements.

---

[2] « electro-Mécanique Embarquée à Compacité Améliorée », partenaires Valéo, SKF et laboratoires Satie, DynFluid et Tempo.

3 Liste de Publications au 31 août 2013

Articles publiés - revues à comité de lecture

2004-2008

1. F. Ravelet, L. Marié, A. Chiffaudel and F. Daviaud. *Multistability and memory effect in a highly turbulent flow : Experimental evidence for a global bifurcation.* Phys. Rev. Lett. **93**, 164501 (2004).
2. F. Ravelet, A. Chiffaudel, F. Daviaud and J. Léorat. *Towards a von Kármán dynamo : numerical studies based on experimental flows.* Phys. Fluids **17**, 117104 (2005).
3. R. Monchaux, F. Ravelet, B. Dubrulle, A. Chiffaudel and F. Daviaud. *Properties of Steady States in Turbulent Axisymmetric Flows.* Phys. Rev. Lett. **96**, 124502 (2006).
4. F. Stefani, M. Xu, G. Gerbeth, F. Ravelet, A. Chiffaudel, F. Daviaud and J. Léorat. *Ambivalent effects of added layers on steady kinematic dynamos in cylindrical geometry : application to the VKS experiment.* Eur. J. Mech. B, **25**, 894 (2006).
5. R. Volk, F. Ravelet, R. Monchaux, M. Berhanu, A. Chiffaudel, F. Daviaud, Ph. Odier, J.-F. Pinton, S. Fauve, N. Mordant, and F. Pétrélis. *Transport of magnetic field by a turbulent flow of liquid sodium.* Phys. Rev. Lett. **97**, 074501 (2006).
6. R. Monchaux, M. Berhanu, M. Bourgoin, M. Moulin, Ph. Odier, J.-F. Pinton, R. Volk, S. Fauve, N. Mordant, F. Pétrélis, A. Chiffaudel, F. Daviaud, B. Dubrulle, C. Gasquet, L. Marié and F. Ravelet. *Generation of magnetic field by dynamo action in a turbulent flow of liquid sodium.* Phys. Rev. Lett. **98**, 044502 (2007).
7. M. Berhanu, R. Monchaux, S. Fauve, N. Mordant, F. Pétrélis, A. Chiffaudel, F. Daviaud, B. Dubrulle, L. Marié, F. Ravelet, M. Bourgoin, Ph. Odier, J.-F. Pinton and R. Volk. *Magnetic field reversals in an experimental turbulent dynamo.* Eur. Phys. Letters. **77**, 59001 (2007).
8. F. Ravelet, A. Chiffaudel and F. Daviaud. *Supercritical transition to turbulence in an inertially-driven von Kármán closed flow.* J. Fluid Mech. **601**, 339 (2008).
9. F. Ravelet, M. Berhanu, R. Monchaux, S. Aumaître, A. Chiffaudel, F. Daviaud, B. Dubrulle, M. Bourgoin, P. Odier, N. Plihon, J.-F. Pinton, R. Volk, S. Fauve, N. Mordant and F. Pétrélis. *Chaotic Dynamos Generated by a Turbulent Flow of Liquid Sodium.* Phys. Rev. Lett. **101**, 074502 (2008).

Sept. 2008 –

10. VKS Collaboration. *The VKS experiment : turbulent dynamical dynamos.* Comptes Rendus Physique **9**, 689 (2008).
11. M. Rodriguez Pascual, F. Ravelet, R. Delfos, J. J. Derksen and G. J. Witkamp. *Large eddy simulations and stereoscopic particle image velocimetry measurements in a scraped heat exchanger crystallizer geometry.* Chemical Engineering Science **64**, 2127 (2009).
12. VKS Collaboration. *The von Kármán Sodium experiment : Turbulent dynamical dynamos* Phys. Fluids **21**, 035108 (2009).
13. M. Berhanu, B. Gallet, R. Monchaux, M. Bourgoin, Ph. Odier, J.-F. Pinton, N. Plihon, R. Volk, S. Fauve, N. Mordant, F. Pétrélis, S. Aumaître, A. Chiffaudel, F. Daviaud, B. Dubrulle and F. Ravelet. *Bistability between a stationary and an oscillatory dynamo in a turbulent flow of liquid sodium* J. Fluid Mech. **641**, 217 (2009).

14. F. Ravelet, R. Delfos and J. Westerweel. *Influence of global rotation and Reynolds number on the large-scale features of a turbulent Taylor-Couette flow.* Phys. Fluids **22**, 055103 (2010).
15. C. Sarraf, H. Nouri, F. Ravelet and F. Bakir. *Experimental study of blade thickness effects on the overall and local performances of a Controlled Vortex Designed axial-flow fan.* Exp. Thermal Fluid Sci. **35**, 684 (2011).
16. F. Ravelet, C. Colin and F. Risso. *On the dynamics and breakup of a bubble rising in a turbulent flow.* Phys. Fluids **23**, 103301 (2011).
17. F. Ravelet, B. Dubrulle, F. Daviaud and P.-A. Ratié. *Kinematic Alpha Tensors and dynamo mechanisms in a von Kármán swirling flow.* Phys. Rev. Lett. **109**, 024503 (2012).
18. H. Nouri, F. Ravelet, F. Bakir, C. Sarraf, and R. Rey. *Design and Experimental Validation of a Ducted Counter-Rotating Axial-Flow Fans System.* J. Fluids Eng. **134**, 104504 (2012).
19. H. Nouri, A. Danlos, F. Ravelet, F. Bakir, and C. Sarraf. *Experimental study of the instationary flow between two ducted Counter-rotating rotors.* J. Eng. Gas Turb. Power **135**, 022601 (2013).
20. F. Ravelet, F. Bakir, S. Khelladi, and R. Rey. *Experimental study of hydraulic transport of large particles in horizontal pipes.* Exp. Thermal and Fluid Science **45**, 187 (2013).
21. A. Zaaraoui, F. Ravelet, F. Margnat, S. Khelladi. *High Accuracy Volume Flow Rate Measurement Using Vortex Counting.* Flow Meas. Inst. **33**, 138 (2013).

Articles soumis – revues à comité de lecture

1. B. Saint-Michel, B. Dubrulle, F. Ravelet, F. Daviaud. *Forcing-type-dependent stability of steady states in a turbulent swirling flow.* submitted to Phys. Rev. Letters, june 2013. `http://hal.archives-ouvertes.fr/hal-00773512`.
2. A. Danlos, J.-E. Mehal, F. Ravelet, O. Coutier-Delgosha, F. Bakir. *Study of the cavitating instability on a grooved Venturi profile.* submitted to J. Fluids Eng., april 2013. `http://hal.archives-ouvertes.fr/hal-00765996`.
3. V. Atim-Kokondji, S. Khelladi, F. Ravelet, F. Bakir and R. Yu. *Performance assessment of an horizontal air / water separator deflector with low volume fraction of air.* submitted to Int. J. Multiphase Flow, march 2013. `http://hal.archives-ouvertes.fr/hal-00804447`.

Conférences invitées

2004-2008

1. L. Marié, F. Ravelet and C. Sarraf, *Complex behaviour of the large-scale features of turbulent flows.* SIAM Conference on applications of dynamical systems, Snowbird (Etats-Unis), mai 2005.
2. F. Ravelet, A. Chiffaudel and F. Daviaud. *Bifurcation globale de l'écoulement de von Kármán turbulent : caractérisation et seuil d'apparition en nombre de Reynolds.* XVIIème Congrès Français de Mécanique (CFM2005), Troyes (France), 29 août-2 septembre 2005 (2005).

3. A. Chiffaudel, F. Ravelet, L. Marié and F. Daviaud. *Bifurcation turbulente et multistabilité d'un écoulement à très grand nombre de Reynolds.* Journée de Dynamique Non Linéaire, Marseille, 13 juin 2006.

Actes de conférences avec comité de lecture

2004-2008

1. F. Ravelet, A. Chiffaudel, F. Daviaud and L. Marié, *Collision de bifurcations globalement sous-critiques dans un écoulement de von Kármán fortement turbulent. In* Actes du Quatrième Colloque sur le chaos temporel et le chaos spatio-temporel, Rouen, 15-16 décembre 2003, pp 149 (2003).
2. F. Ravelet, A. Chiffaudel, F. Daviaud and L. Marié. *Bifurcation globale et effet mémoire dans un écoulement très turbulent. In* Septième rencontre du non-linéaire, Paris 11-12 mars 2004. Editeurs Y. Pomeau & R. Ribotta. Non Linéaire Publications, Orsay, pp 251–256 (2004).
3. F. Ravelet, A. Chiffaudel and F. Daviaud. *Bifurcation globale de l'écoulement de von Kármán turbulent : seuil de l'apparition du phénomène en nombre de Reynolds. In* Huitième rencontre du non-linéaire, Paris 9-11 mars 2005. Editeurs Y. Pomeau & R. Ribotta. Non Linéaire Publications, Orsay, pp 229 (2005).
4. F. Ravelet, A. Chiffaudel and F. Daviaud. *Bifurcation globale de l'écoulement de von Kármán turbulent : caractérisation et seuil d'apparition en nombre de Reynolds. In* Actes du XVIIème Congrès Français de Mécanique (CFM2005), Troyes (France), 29 août-2 Septembre 2005 (2005).
5. M. Berhanu, A. Chiffaudel, F. Daviaud, S. Fauve, R. Monchaux, N. Mordant, Ph. Odier, F. Ravelet, F. Pétrélis, J.-F. Pinton and R. Volk. *Observation de transport de champ magnétique dans un écoulement turbulent de sodium liquide. In* Neuvième rencontre du non-linéaire, Paris 8-10 mars 2006. Editeurs M. Lefranc, C. Letellier & L. Pastur. Non Linéaire Publications, Orsay, pp 25 (2006).
6. F. Ravelet, R. Delfos and J. Westerweel, *Experimental studies of liquid-liquid dispersion in a turbulent shear flow.* Proceedings of the 11th European Turbulence Conference (Porto, 25-28 June 2007).
7. F. Ravelet, R. Delfos and J. Westerweel, *Emergence of large scale secondary flow in a turbulent Taylor-Couette flow.* Proceedings of the Turbulence and Shear Flow Phenomena (Munich, 27-29 August 2007).
8. M. Rodriguez, F. Ravelet, R. Delfos and G. J. Witkamp, *Measurement of flow field and wall temperature distribution in a scraped heat exchanger crystallizer.* Proceedings of the 5th Eurotherm Conference (Eindhoven, 18-22 May 2008).
9. N. Abi Chebel, O. Masbernat, F. Risso, P. Guiraud, F. Ravelet, C. Dalmazzone and C. Noïk, *Imaging method for interface rheological characterization*, Proceedings of the 13th International Symposium on Flow Visualization (Nice, 1-4 July 2008).

Sept. 2008 –

10. M. Rodriguez, F. Ravelet, R. Delfos, J. J. Derksen and G. J. Witkamp, *Computational Fluid Dynamics and measurement of flow field and wall temperature distribution in a scraped heat exchanger crystallizer.* Proceedings of the 17th International Symposium on Industrial Crystallization (Maastricht, 14-17 September 2008).

11. R. Delfos, F. Ravelet and J. Westerweel, *Scaling of torque in turbulent Taylor-Couette flow with background rotation.* Proceedings of the 12th European Turbulence Conference, p. 629 (Marburg, 7-10 September 2009).
12. P.-P. Cortet, S. Atis, A. Chiffaudel, F. Daviaud, B. Dubrulle and F. Ravelet, *Experimental study of the von Kármán flow from* $Re = 10^2$ *to* 10^6 *: spontaneous symmetry breaking and turbulent bifurcations.* Proceedings of the 12th European Turbulence Conference, p. 59 (Marburg, 7-10 September 2009).
13. C. Sarraf, F. Ravelet, H. Nouri and F. Bakir, *Effects of blades Thickness on the Aerodynamical and Acoustical Performances of Axial Fans*, 7th International Conference on Heat Transfer, Fluid Mechanics and Thermodynamics, paper n^o 1428, 19-21 July 2010, Antalya, Turkey.
14. F. Ravelet, S. Khelladi, H. Nouri, F. Bakir, H. Kim, Y. Bae, Y. J. Moon, *Study of the Aerodynamics/Aeroacoustics of an Axial-Flow Fan : Experimental Validation of a LES/LPCE/Brinkman Penalization Method*, 16th AIAA/CEAS Aeroacoustics Conference, paper n^o AIAA 2010-3869, 7-9 June 2010, Stockholm, Sweden.
15. H. Nouri, F. Ravelet, C. Sarraf and F. Bakir, *Experimental study of the global and the local performances of thick blades axial-flow.* 3rd Joint US-European Fluids Engineering Summer Meeting, 22nd Symposium on Fluid Machinery, paper n^o FEDSM-ICNMM2010-30623, 1-5 August 2010, Montreal, Canada.
16. M. Solis, F. Ravelet, S. Khelladi and F. Bakir, *Experimental and numerical analysis of the flow inside a configuration including an axial pump and tubular exchanger.* 3rd Joint US-European Fluids Engineering Summer Meeting, 22nd Symposium on Fluid Machinery, paper n^o FEDSM-ICNMM2010-30723, 1-5 August 2010, Montreal, Canada.
17. H. Nouri, F. Ravelet, F. Bakir and C. Sarraf, *Experimental investigation on ducted counter-rotating axial flow fans.* Proceedings of ASME-JSME-KSME Joint Fluids Engineering Conference 2011, 23rd Symposium on Fluid Machinery, paper n^o AJK2011-22061, 24-29 July 2011, Hamamatsu, Japan.
18. F. Ravelet, H. Nouri, C. Sarraf and F. Bakir, *Experiments On The Design and Global Performances Of A Ducted Counter-rotating Axial-Flow Fans System.* Proceedings of the 10^{th} International Symposium on Experimental Computational Aerothermodynamics of Internal Flows, paper n^o ISAIF10-005, 4-7 July 2011, Brussels, Belgium.
19. H. Nouri, F. Ravelet, F. Bakir and C. Sarraf, *Experimental investigations on the design of a ducted counter-rotating axial-flow fans system.* 46^{th} Symposium of Applied Aerodynamics Aerodynamics of Rotating Bodies, paper n^o 23, March 28-30 2011, Orléans, France.
20. F. Ravelet, A. Lemaire and F. Bakir, *Etude expérimentale du transport hydraulique de grandes particules en conduite horizontale et en forme de S.* 20ème Congrès Français de Mécanique. Besançon, 29 août-2 septembre 2011, France.
21. H. Nouri, F. Ravelet, F. Bakir and C. Sarraf, *Experimental investigation on ducted counter-rotating axial flow fans.* 14th International Symposium on Transport Phenomena and Dynamics of Rotating Machinery, ISROMAC-14, paper n^o 1132, February 27th - March 2nd, 2012, Honolulu, HI, USA.
22. H. Nouri, F. Ravelet, F. Bakir and C. Sarraf, *Experimental investigation on ducted counter-rotating axial flow fans.* FAN2012, International Conference on Fan Noise, Technology and Numerical Methods, paper n^o 38, 18-20 april 2012, Senlis, France.

23. H. Kim, Y. Jo, I. H. Bai, Y. J. Moon, F. Ravelet, S. Khelladi and F. Bakir, *3D Computation of Axial-flow Fan Noise by LPCE - Brinkman Penalization Method.* FAN2012, International Conference on Fan Noise, Technology and Numerical Methods, paper n^o 50, 18-20 April 2012 Senlis, France.
24. A. Danlos, J.-E. Mehal, F. Ravelet and C. Sarraf, *Study of Passive Control of the cavitation instability on a venturi profile.* CAV2012, 8th International Symposium on Cavitation, paper n^o 240, 13-16 August 2012, Singapore.
25. J. Wang, F. Ravelet and F. Bakir, *Experimental comparison between a counter-rotating axial-flow fan and a conventional rotor-stator stage.* ETC2013, 10th European Turbomachinery Conference, 15-19 April 2013, Lappeenranta, Finland.
26. J. Wang, F. Ravelet, F. Bakir and C. Sarraf, *Influence de la répartition de la charge sur les performances d'une turbomachine axiale contrarotative.* 21ème Congrès Français de Mécanique. Bordeaux, 26-30 août 2013, France.
27. C. Sarraf, F. Ravelet and F. Bakir, *Étude expérimentale de l'influence du blocage aval sur les performances d'un ventilateur axial.* 21ème Congrès Français de Mécanique. Bordeaux, 26-30 août 2013, France.
28. A. Danlos, F. Ravelet and F. Bakir, *Etude numérique des gains de performances et de capacité d'aspiration apportés par un étage axial contrarotatif par rapport à une pompe mono-rotor.* 21ème Congrès Français de Mécanique. Bordeaux, 26-30 août 2013, France.

Communications à des congrès

2004-2008

1. L. Marié, F. Ravelet, A. Chiffaudel et F. Daviaud, *Bifurcation globale d'un écoulement turbulent.* 8èmes Journées de la Matière Condensée (JMC8), SFP, Marseille, 27 août 2002.
2. *Global bifurcation of the turbulent von Kármán flow.* Marburg-GIT-LadHyX PROCOPE Meeting, LadHyX-Ecole Polytechnique, Palaiseau, 13-14 novembre 2002.
3. F. Ravelet, L. Marié, A. Chiffaudel and F. Daviaud, *Collision de bifurcations sous-critiques dans un écoulement turbulent.* 23ème Rencontre de Physique Statistique, Paris, 23-24 janvier 2003.
4. F. Ravelet, L. Marié, F. Daviaud et A. Chiffaudel, *Bifurcation globale d'un écoulement de von Kármán turbulent.* GDR Turbulence, Grenoble, 27-28 janvier 2003.
5. F. Ravelet, L. Marié, F. Daviaud et A. Chiffaudel, *Collision de bifurcations sous-critiques dans un écoulement de von Kármán fortement turbulent.* Troisième Journée de Dynamique des Fluides sur le Plateau, Orsay, 24 avril 2003.
6. F. Ravelet, A. Chiffaudel and F. Daviaud. *Effects of a conducting shell surrounding a numerical von Kármán dynamo*, Mathematical Aspects of Natural Dynamos, Caramulo (Portugal), August 31 - September 6, 2003.
7. F. Ravelet, A. Chiffaudel, F. Daviaud and J. Léorat. *Optimization of the VKS experiment : design of an homogeneous fluid dynamo based on von Karman flow*, COST / GDR Dynamo Joint meeting, Paris (France), January 22-23, 2004.
8. F. Ravelet, A. Chiffaudel, F. Daviaud and J. Léorat. *Effet des conditions aux limites sur une dynamo cinématique de type von Kármán*, GDR Dynamo meeting, Nice (France), 4-5 mai, 2004.

9. F. Ravelet, A. Chiffaudel et F. Daviaud, *Bifurcation globale, effet mémoire et multistabilité dans un écoulement très turbulent.* 9èmes Journées de la Matière Condensée (JMC9), SFP, Nancy, 2 septembre 2004.
10. F. Ravelet, A. Chiffaudel et F. Daviaud, *La bifurcation globale de l'écoulement de von Kármán : effets du nombre de Reynolds.* Quatrième Journée de Dynamique des Fluides sur le Plateau, Orsay, 15 novembre 2004.
11. F. Ravelet, A. Chiffaudel, F. Daviaud and J. Léorat. *Towards a von Kármán dynamo : numerical studies based on experimental flows*, Perm Dynamo Days, Perm (Russie), 7-11 février, 2005.
12. F. Ravelet, R. Monchaux, F. Daviaud, A. Chiffaudel et B. Dubrulle. *Premiers résultats de l'expérience VKS2*, Sixième Journée de Dynamique des Fluides sur le Plateau, Universit'e de Paris-Sud, Orsay, 14 novembre 2005.
13. A. Chiffaudel, F. Ravelet, L. Marié and F. Daviaud. *Multistabilité et bifurcations globales dans un écoulement très turbulent. Expérience de laboratoire et observations géophysiques.* Séminaire à l'Ecole Normale Supérieure, Paris, 29 novembre 2005.
14. F. Ravelet, R. Volk, A. Chiffaudel, F. Daviaud, B. Dubrulle, S. Fauve, N. Mordant, Ph. Odier, F. Pétrélis and J.-F. Pinton. *Premiers résultats de l'expérience VKS2*, Réunion annuelle du GDR Dynamo, Lyon, 27-28 mars 2006.
15. F. Ravelet, A. Chiffaudel et F. Daviaud, *Transition à la turbulence dans un écoulement fermé de von Kármán, forcé inertiellement.* 10èmes Journées de la Matière Condensée (JMC10), SFP, Toulouse, 30 août 2006.
16. F. Ravelet, R. Delfos and J. Westerweel, *Experimental study of liquid-liquid dispersion in a turbulent shear-flow.* 10èmes Journées de la Matière Condensée (JMC10), SFP, Toulouse, 30 août 2006.
17. F. Ravelet, A. Chiffaudel and F. Daviaud, *Fluctuations à grande échelle dans un écoulement fermé de von Kármán, forcé inertiellement.* Réunion des GDR dynamo et turbulence, Nice, 6-10 novembre 2006.
18. F. Ravelet, R. Delfos and J. Westerweel, *Combined PIV-LIF measurements in a turbulent liquid-liquid Taylor Couette flow.* Annual Meeting of the APS Division of Fluid Dynamics, Tampa Bay, 19-21 novembre 2006.
19. F. Ravelet, A. Chiffaudel and F. Daviaud, *Transition à la turbulence dans l'écoulement de von Kármán symétrique.* Réunion du GDR turbulence, Lyon, 31 mars-2 avril 2008.

Sept. 2008 –

20. Y. J. Moon, H. KIM, Y. BAE, F. Ravelet, S. Khelladi, H. Nouri and F. Bakir, *Prediction of axial fan noise by linearized perturbed compressible equations with large eddy simulation.* The Joint 159^th Meeting of the Acoustical Society of America/Noise-Con 2010, 19-23 April 2010. Baltimore. J. Acoust. Soc. Am. Volume 127, Issue 3, pp. 1837-1837.
21. F. Ravelet, R. Campos-Amezcua, S. Khelladi, L. Bergerat, Z. Mazur-Czerwiec, R. Rey and F. Bakir, *Numerical analysis of unsteady cavitating flow in a 3D axial inducer.* SHF Conference on Cavitation and Hydraulic Machines 26 May to 27 May 2011. Lausanne, Switzerland .

Séminaires

1. *Experimental evidence for a global bifurcation in a highly turbulent von Kármán flow.* Matière et Systèmes Complexes, Université Paris 7, Paris, 1 mars 2005.
2. *Experimental evidence for a global bifurcation in a highly turbulent von Kármán flow.* Laboratory for aero and hydrodynamics, Delft University of Technology, Delft, Pays-Bas, 3 mars 2005.
3. *Multistabilité et bifurcations globales dans un écoulement très turbulent. Expérience de laboratoire et observations géophysiques.* Séminaire à l'Ecole Normale Supérieure, Paris, 29 novembre 2005.
4. *Multistabilité et bifurcations globales dans un écoulement très turbulent.* LEGI, Grenoble, 28 septembre 2006.
5. *Emergence of large scale secondary flow in a turbulent Taylor-Couette flow.* Komplexe Systeme (B. Eckhardt), Philipps Universität, Marburg, Allemagne, 06 septembre 2007.
6. *Effets du nombre de Reynolds et de la rotation globale sur la structure à grande échelle d'un écoulement de Taylor-Couette turbulent.* FAST, Orsay, 13 décembre 2007.
7. *La dynamique du champ magnétique terrestre reproduite au laboratoire : réalisation expérimentale de l'effet dynamo en écoulement turbulent.* IMFT, Toulouse, 9 janvier 2008.
8. *Effet de la mise en rotation sur la structure de l'écoulement secondaire à grande échelle dans un écoulement de Taylor-Couette turbulent.* ENSTA, Palaiseau, 13 février 2008.
9. *PIV stéréoscopique et tomographique dans un écoulement de Taylor-Couette Turbulent, transitions en fonction du rapport de rotation des cylindres.* Laboratoire Ondes et Milieux Complexes, UMR 6294 CNRS, Le Havre, 26 octobre 2012.
10. A. Danlos & F. Ravelet, *Dynamique de la poche de cavitation développée sur un profil de venturi rainuré.* ENSTA, Palaiseau, 20 mars 2013.

Autres publications

1. F. Ravelet. *Etude expérimentale de l'écoulement tourbillonnaire de von Kármán et application à l'effet dynamo.* Rapport de Stage de DEA, Université Paris 6 (2002).
2. F. Ravelet. *Bifurcations globales hydrodynamiques et magnétohydrodynamiques dans un écoulement de von Kármán turbulent.* Thèse de doctorat, Ecole doctorale de l'Ecole Polytechnique (2005).
3. F. Ravelet. *Réunion GDR Turbulence / GDR Dynamo Nice, 6 novembre - 9 novembre 2006. Rapport sur la session n°4. Rôle des grandes échelles ; instabilités en présence de bruit (bifurcations dans les milieux turbulents, dynamos à bas Pm).* `http://gdr-turbulence.pmmh.espci.fr/Nov2006/theme4.pdf`

Deuxième partie

Rapport scientifique

1 Axe 1 : Instabilités et bifurcations en écoulements turbulents monophasiques

Cet axe regroupe un ensemble de résultats expérimentaux et numériques portant sur des bifurcations susceptibles d'affecter un écoulement pleinement turbulent. Nous nous intéressons plus particulièrement à des transitions de la stucture à grande échelle sous l'influence des paramètres de contrôle, conduisant à de l'hystérésis ou à une dynamique non-triviale à grande échelle. Ce type de comportement est par exemple observé autour de cylindres, sur des ailes delta ou dans des divergents (Schewe, 1983; Goman *et al.*, 1985; Shtern & Hussain, 1999), en convection de Rayleigh-Bénard (Sreenivasan *et al.*, 2002) ou encore en Taylor-Couette à surface libre (Mujica & Lathrop, 2006). Ces comportements sont ici étudiés dans un premier temps pour un écoulement cisaillé entre deux disques munis de pales en eau et en métal liquide (§ 1.1), puis pour un écoulement cisaillé entre deux cylindres coaxiaux (§ 1.2).

1.1 Ecoulement de von Kármán inertiel (2002-2013)

Position du problème

Il s'agit de l'écoulement cisaillé produit dans un cylindre entre deux disques coaxiaux munis de pales. Ce dispositif, connu aussi dans la communauté de la turbulence sous le nom de “French washing-machine”, permet d'obtenir dans un faible volume un écoulement très fortement turbulent et a été intensément utilisé dans les années 1990 et 2000 dans le cadre d'études sur les propriétés statistiques des petites échelles de la turbulence.

Douady *et al.* (1991) ont ainsi mis en évidence et étudié des filaments de vorticité intenses et très intermittents connectés à des évènements de basse pression rares et intenses. Les fluctuations de pression ont notamment été étudiées par Fauve *et al.* (1993). Cet écoulement a aussi permis la mesure des fonctions de structures d'ordre élevé, et la mise en évidence de l'intermittence [1] (Zocchi *et al.*, 1994; Moisy *et al.*, 2001). Des études du point de vue lagrangien de la turbulence ont montré récemment des distributions d'accélération très intermittentes et des corrélations à longue portée pour la norme des accélérations, leur direction étant elle très vite oubliée (La Porta *et al.*, 2001).

Les travaux rapportés ici se concentrent quant-à eux tout d'abord sur les propriétés hydrodynamiques des grandes échelles de cet écoulement et sur les effets du mode de forçage, dans la lignée de travaux portant eux sur la statistique de grandeurs plus globales comme la puissance injectée (Labbé *et al.*, 1996; Cadot *et al.*, 1997; Titon & Cadot, 2003). L'accent est mis ici sur l'aspect temporel, en particulier pour la dynamique des grandes structures dans la couche de mélange entre les deux impulseurs. Dans un premier temps, nous nous intéressons à la transition à la turbulence, à la construction de la dynamique lente de la couche de mélange et à la façon dont l'écoulement devient sensible à la forme des pales lorsque l'écoulement est turbulent (p. 27). Nous montrons également la coexistence possible *en régime turbulent inertiel* d'états moyens différents et étudions les transitions entre ces états (p. 30). Puis, dans une expérience en sodium liquide, nous étudions la génération d'un champ magnétique par instabilité dynamo, et montrons différents régimes dynamiques pour le champ magnétique, incluant renversements aléatoires, ou bouffées intermittentes, selon la dissymétrie du forçage (p. 33). Nous présentons enfin une contribution à la compréhension des mécanismes générateurs de l'effet dynamo (p. 38).

---

[1] Au sens où l'invariance d'échelle dans une vision « autosimilaire »de la turbulence « à la Kolmogorov (1991a,b) » est brisée, l'activité turbulente étant de plus en plus localisée quand on observe des échelles de plus en plus petites.

Dispositifs expérimentaux

Expérience VKE

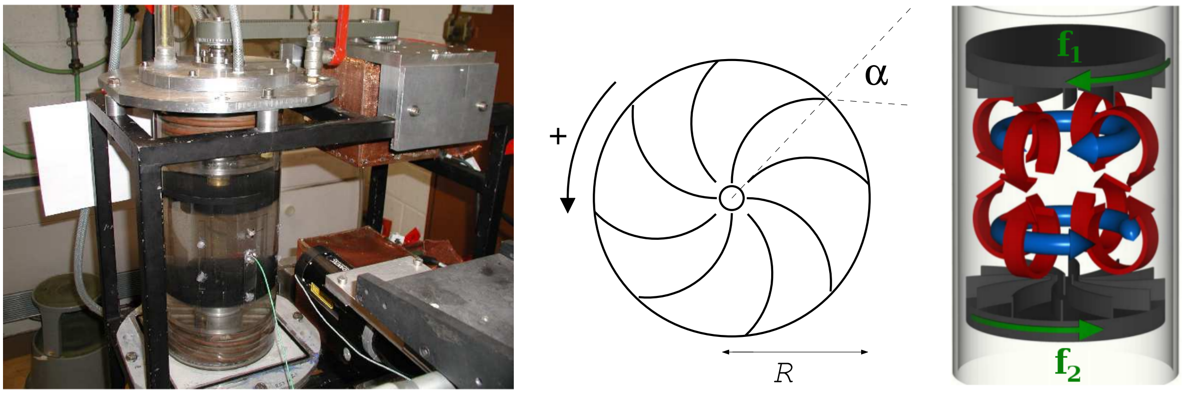

(a) (b) (c)

FIGURE 1 – *(a) Photographie du montage VKE. (b) Schéma d'un impulseur. Angle de sortie α : angle entre le rayon sur lequel s'appuie la pale et la tangente à la pale en bout de disque. (c) Phénoménologie de l'écoulement contrarotatif.*

Une photographie du montage expérimental VKE —pour « von Kármán Eau »— se trouve en Fig. 1a. Il se compose d'une cuve en plexiglas cylindrique d'axe vertical, de rayon intérieur $R_c = 100$ mm. Le rapport d'aspect de la zone d'écoulement est $H/R_c = 1.8$, avec H la distance séparant les deux disques coaxiaux, munis ou non de pales, appelés ci-après « impulseurs ». L'impulseur du haut est notée 1, celui du bas 2. La vitesse de rotation ou le couple fourni par chaque impulseur peuvent être contrôlés indépendamment. Par convention, les deux vitesses de rotations ont le même signe en contrarotation. On introduit $f = (f_1 + f_2)/2$ une fréquence de rotation réduite. Le nombre de Reynolds est défini comme $Re = 2\pi f R_c^2 \nu^{-1}$, avec ν la viscosité cinématique du fluide. Pour de l'eau, le nombre de Reynolds maximal est ainsi $Re = 1.2 \times 10^6$.

On définit l'opération de symétrie $\mathcal{R}_\pi$, rotation d'angle π autour de tout axe radial passant par le milieu de la cuve. Cette opération échange le rôle des impulseurs 1 et 2. Ces impulseurs sont des disques de rayon R, munis de 8 ou 16 pales en forme d'arcs de cercles tangents à un rayon au centre du disque. La courbure est caractérisée par l'angle de sortie α (voir Fig. 1b). Lorsque les pales sont courbées, les deux sens de rotation possibles ne sont plus équivalents. Nous les distinguons par le signe de l'angle α.

La phénoménologie de l'écoulement moyen est illustrée en Fig. 1c pour le cas de la contrarotation exacte. Chaque impulseur agit à la manière d'une roue de pompe centrifuge. Il entraîne le fluide situé près de lui en rotation, créant une composante de vitesse *toroïdale* (flèches bleues en Fig. 1c). Le fluide compris entre les pales est expulsé radialement par centrifugation, ce qui crée un pompage vers la roue au niveau de l'axe central. Le fluide éjecté recircule ensuite le long des parois du cylindre. Le champ de vitesse résultant formant des cellules de recirculation dans le plan (r,z) est qualifié de *poloïdal* (flèches rouges en Fig. 1c). L'écoulement moyen attendu est axisymétrique et, dans ce cas (contrarotation exacte), invariant par $\mathcal{R}_\pi$.

Expérience VKS

L'expérience VKS —pour « von Kármán Sodium »—, dont une photographie et un schéma se trouvent en Fig. 2, a pour but d'étudier la génération de champ magnétique par effet dynamo

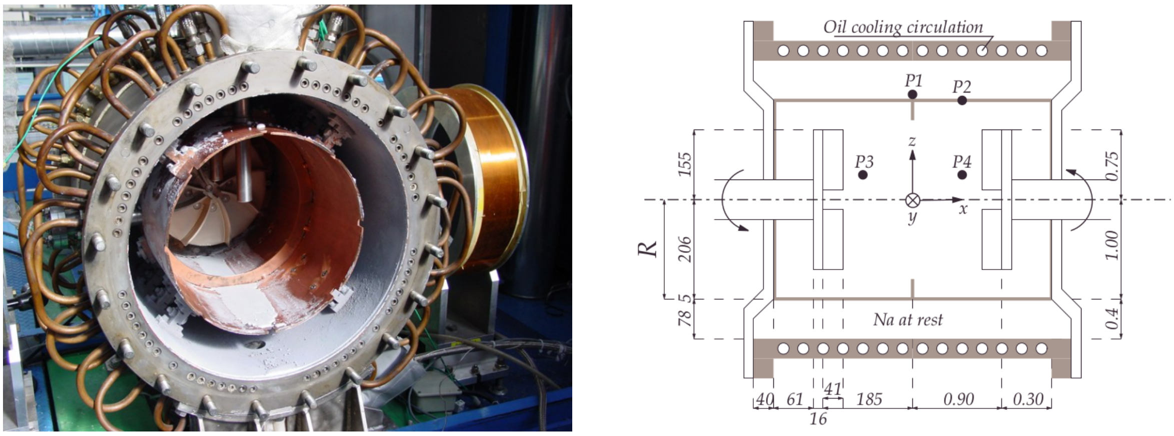

(a) (b)

Figure 2 – *(a) Photographie de l'intérieur de la cuve de l'expérience VKS. On distingue au fond un impulseur (TM73) en fer doux, ainsi que le cylindre interne en cuivre (chemise) muni de son anneau médian. (b) Schéma coté (figure d'A. Chiffaudel).*

dans un écoulement turbulent de sodium liquide. L'expérience est similaire à VKE à quelques détails près. Le dispositif se compose d'une cuve cylindrique en cuivre de diamètre intérieur 578 mm dans laquelle est inséré un cylindre en cuivre fin, de rayon intérieur $R_c = 206$ mm, afin d'avoir une couche de sodium au repos à l'extérieur du cylindre. L'écoulement est créé entre deux impulseurs distants de $H = 371$ mm. Le rapport d'aspect est ainsi identique dans VKS et VKE, avec un facteur d'échelle 2.06. Enfin, un anneau peut être inséré dans le plan médian.

Transition à la turbulence

L'étude décrite ici est motivée par l'existence d'une « bifurcation globale » de l'écoulement (Ravelet *et al.*, 2004), décrite en détails plus loin, observée *uniquement* à grand nombre de Reynolds ($Re \geqslant 10^4$) et pour des angles particuliers des pales des impulseurs (pour $\alpha \leqslant -57\,^\circ$, voir Ravelet, 2005). L'une des questions se posant alors est le rôle respectif des fluctuations turbulentes, de la forme des écoulements moyens et de sa modification en fonction du nombre de Reynolds sur le phénomène de multistabilité. Nous avons alors étudié l'évolution de différentes grandeurs globales, comme le couple C nécéssaire à maintenir une vitesse des impulseurs constante, et de paramètres locaux de l'écoulement comme les fluctuations de vitesse dans le plan médian, en fonction du nombre de Reynolds, depuis les régimes laminaires ($Re \simeq 10^2$) jusqu'aux régimes turbulents ($Re \geqslant 10^6$), et ceci pour deux impulseurs munis de pales d'angle $\alpha = \pm 72\,^\circ$ et pour des disques lisses. Cette étude est publiée dans Ravelet *et al.* (2008b). Dans cette partie, le forçage est $\mathcal{R}_\pi$ -symétrique[2] et se fait en imposant une vitesse de rotation constante.

A un nombre de Reynolds de l'ordre de 100, l'écoulement est laminaire, comme le confirment les visualisations présentées en Fig. 3a-b. L'écoulement est également stationnaire et respecte les symétries du problème (axisymétrie et suymétrie $\mathcal{R}_\pi$). En outre, il possède la phénoménologie décrite en Fig. 1c, les cellules de recirculation poloïdale étant visibles en Fig. 3a. Enfin, on note que les écoulements créés par les impulseurs munis de pales d'orientation $\pm 72\,^\circ$ sont visuellement identiques. Les couples nécéssaires à l'entrainement sont également égaux pour ces deux impulseurs, jusqu'à environ $Re \simeq 300$ (voir Fig. 4a). Le caractère laminaire est cohérent avec une dépendance en Re^{-1} du couple adimensionnel $K_p = C\left(\rho R_c^5 \left(2\pi f\right)^2\right)^{-1}$. Nous montrons également que les deux écoulements mesurés à $Re = 120$ sont semblables à un écoulement en-

---

[2] Autrement dit, on se limite dans cette étude au cas de la contrarotation parfaite.

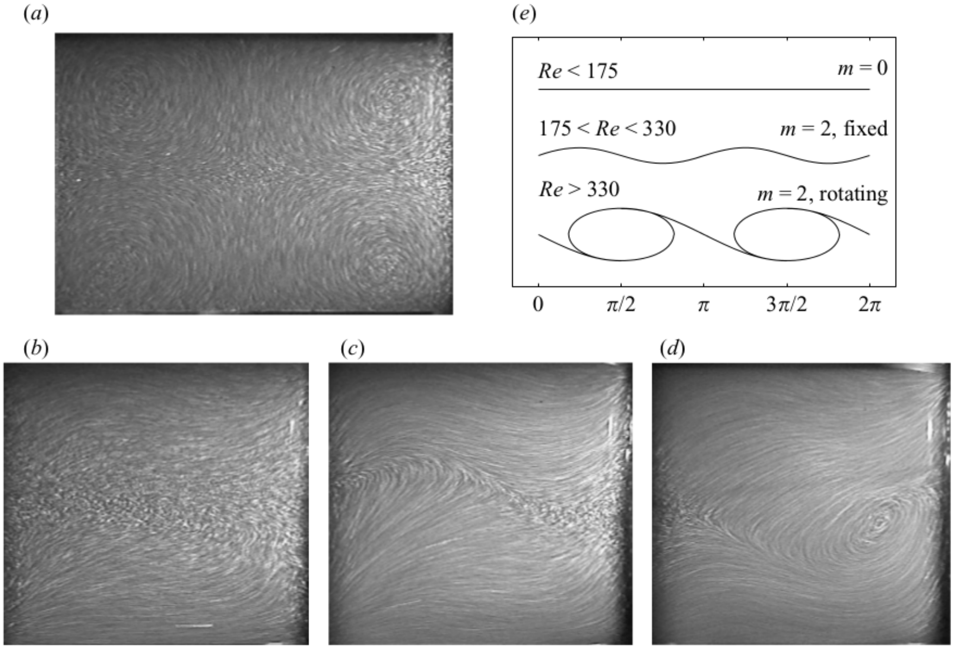

Figure *3 – Visualisation et schémas de l'écoulement laminaire pour les impulseurs d'angle* $\alpha = -72\ ^\circ$*. Images intégrées sur 1/25 s, traceurs : fines bulles d'air. Image prise sur une hauteur* $1.4R_c$ *(hauteur des pales* $0.2R_c$*. (a) Vue méridienne de l'écoulement à* $Re = 90$*. (b,c,d) Vues en proche paroi à* $Re = 90$*,* $Re = 185$ *et* $Re = 345$*. (e) Schémas de la couche de mélange.*

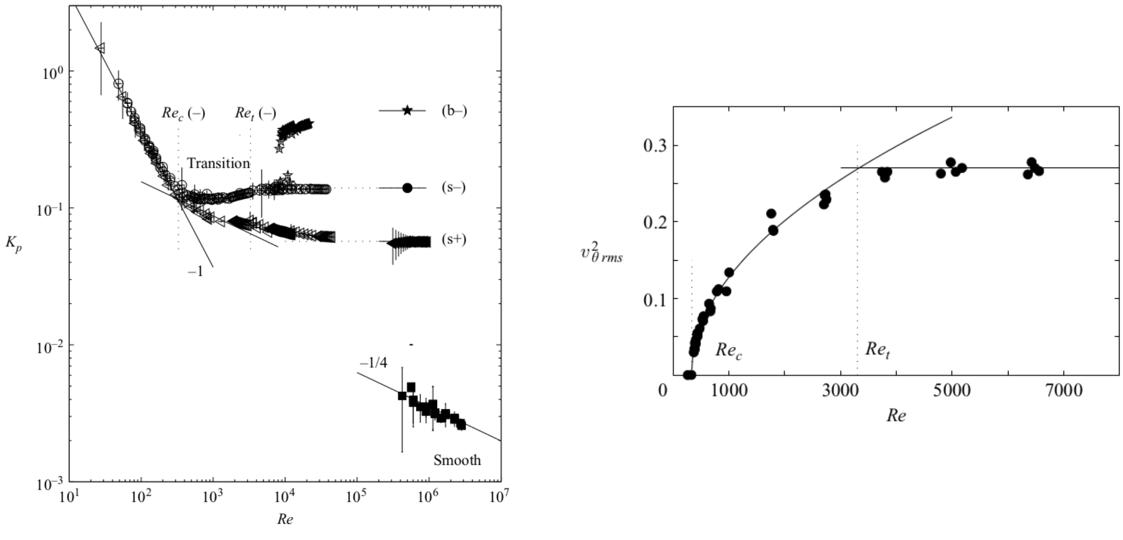

(a) (b)

Figure *4 – (a) Couple adimensionnel* K_p *en fonction de Re. Labels (s+) et (s-) : états* $\mathcal{R}_\pi$ *-symétriques, pales d'angles* $\alpha = 72\ ^\circ$ *et* $\alpha = -72\ ^\circ$*. Label (b-) : états brisant la symétrie* $\mathcal{R}_\pi$ *, impulseurs avec pales d'angle* $\alpha = -72\ ^\circ$*. Label (Smooth) : disques lisses. (b) Variance de la vitesse azimutale mesurée par LDV au niveau de la couche de mélange en fonction de Re pour les impulseurs* $\alpha = -72\ ^\circ$*, fit de la forme* $v^2_{\theta\, rms} = a \times (Re - Re_c)^{1/2}$*, avec* $Re_c = 328 \pm 8$*. L'intersection avec l'asymptote* $v^2_{\theta\, rms} \simeq 0.27$ *donne* $Re_t = 3.3 \times 10^3$*.*

tre disques lisses distants de $H = 1.4R_c$, au moyen d'une simulation numérique effectuée avec le code de Nore *et al.* (2003). Une explication est qu'à très bas Re, l'ordre de grandeur de la taille des couches limites dans l'expérience est en effet supérieure à la distance entre les disques et la paroi cylindrique ainsi qu'à la distance radiale entre deux pales successives. La première instabilité se produit à $Re = 175 \pm 5$ et conduit à une ondulation stationnaire de la couche de mélange, avec un nombre d'onde azimutal $m = 2$ (voir Fig. 3c), cohérent avec le cas de disques lisses en rapport d'aspect $H = 1.4R_c$ (Nore *et al.*, 2003).

La seconde instabilité se produit autour de $Re \simeq 300$ dans le sens négatif et correspond au développement d'une onde propagative (voir Fig. 3d). Les deux sens de rotation se distinguent alors (voir Fig. 4a) et le caractère inertiel de l'entrainement devient visible. La variance temporelle de la vitesse en un point de la couche de mélange permet de suivre la transition depuis la première dépendance temporelle jusqu'à la turbulence. L'évolution de cette quantité en fonction de Re est tracée en Fig. 4b pour les impulseurs munis de pales d'angle $\alpha = -72\,^\circ$. Cette courbe permet de définir deux seuils : l'un ($Re_c = 328 \pm 8$) correspondant à l'apparition de l'instationnarité, et l'autre ($Re_t \simeq 3300$) correspondant à une saturation de la variance.

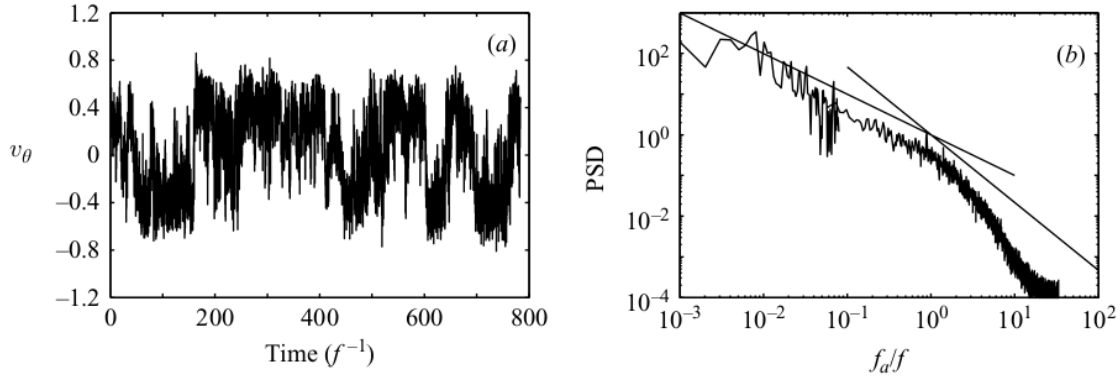

FIGURE 5 – *Signal de vitesse azimutale $v_\theta(t)$ mesurée par LDV au niveau de la couche de mélange pour les impulseurs $\alpha = -72\ ^\circ$ à $Re = 1.0 \times 10^3$ et densité spectrale de puissance.*

L'analyse des signaux de vitesse en un point de la couche de mélange, dont un exemple est fourni en Fig. 5, permet de mettre en évidence une dynamique temporelle très riche. On distingue en effet deux domaines de part et d'autre de la fréquence de rotation des impulseurs f. La partie haute fréquence semble cohérente avec une loi d'échelle en $-5/3$ et apparait progressivement pour $Re \geqslant 1000$. La partie basse fréquence est imputée à une dynamique chaotique des grandes structures de la couche de mélange et se construit progressivement : à $Re = 380$ il existe une fréquence bien définie de l'ordre de $1/300f$, puis le chaos apparait vers $Re \gtrsim 400$, et la bande spectrale entre $f/100$ et f se peuple alors progressivement pour $400 \geqslant Re \geqslant 1000$.

En régime turbulent, les deux sens de rotation se distinguent également par le fait que pour le sens négatif, le coefficient K_p devient indépendant de Re dès $Re \gtrsim 3300$. En revanche, pour le sens positif, il existe toujours une légère dépendance en Re, au moins jusqu'à $Re \simeq 10^5$. Le coefficient de couple à $Re > 10^5$ est environ 3 fois plus important pour le sens négatif que pour le sens négatif, et 100 fois plus important que pour des disques lisses. Enfin, la multistabilité de l'écoulement n'est observée que dans le sens négatif, et pour $Re \geqslant 10^4$.

Depuis ces travaux, une quantité globale caractérisant les fluctuations turbulentes obtenue à partir de mesures par PIV stéréoscopique a été introduite par Cortet *et al.* (2009). Cette quantité $\delta(t)$ généralise la variance utilisée ici, et correspond à la moyenne spatiale de l'énergie cinétique instantanée de l'écoulement, normalisée par l'énergie cinétique de l'écoulement moyen (en temps). Les résultats de Cortet *et al.* (2009) confirment l'établissement d'un régime où cette propriété statistique est indépendante de Re pour $1.25 \times 10^5 \leqslant Re \leqslant 5 \times 10^5$. La moyenne et l'écart-type de $\delta(t)$ mettent en évidence les différences entre impulseurs en termes d' « intensité globale turbulente », la valeur moyenne de δ et son écart-type étant environ 25% plus élevées pour les impulseurs tournant en sens négatif. Cortet *et al.* (2011), en étudiant la sensibilité de l'écoulement à de petites dissymétries du forçage, ont en outre montré l'existence d'une transition autour de $Re = 4 \times 10^4$ pour les impulseurs d'angle $\alpha = +72\,^\circ$ se traduisant par une divergence de cette sensibilité.

Multistabilité de l'écoulement moyen

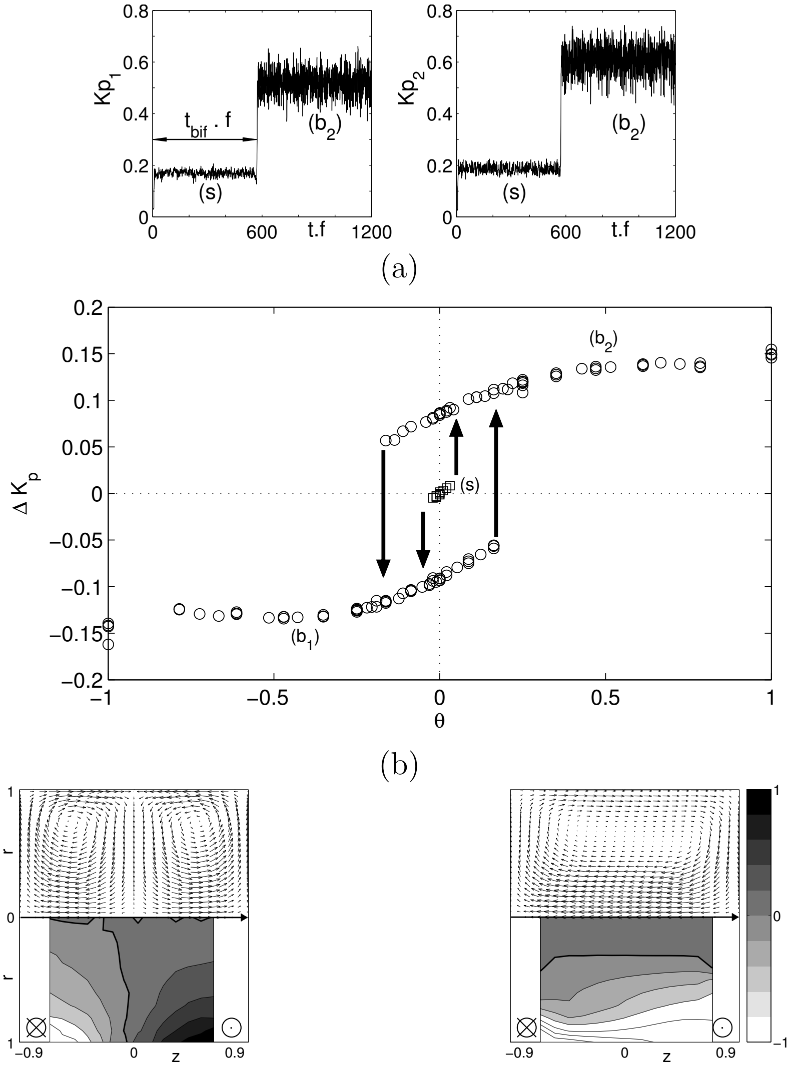

(a)

(b)

(c) (d)

FIGURE 6 – *(a) Signaux temporels des couples lors d'une bifurcation* $(s) \to (b_2)$*, pour* $\theta = 0.0204$ *et* $f = 4.08$ *Hz. (b) Différence des couples adimensionnels en fonction de* θ *pour* $2 \times 10^5 \leqslant Re \leqslant 8 \times 10^5$*. (c) Champ de vitesse moyen obtenu par LDV pour l'état* (s)*. (d) Champ de vitesse pour l'état* (b_1)*.*

A l'encontre du paradigme classique de la turbulence comme un processus ergodique où moyennes temporelles et moyennes sur un ensemble de réalisations sont confondues, *i.e.* où l'écoulement turbulent visite au cours du temps l'ensemble des configurations possibles, l'écoulement de von Kármán est susceptible de présenter, dans le cas d'impulseurs d'angle $\alpha = -72\,^\circ$ et à $Re \geqslant 10^4$, trois états moyens fort différents pour la même condition de forçage (Ravelet *et al.*, 2004). L'état obtenu dépend de la manière dont l'écoulement a été « préparé ».

Ce phénomène est illustré en Fig. 6. La dissymétrie relative du forçage est mesurée par le paramètre $\theta = \frac{f_2 - f_1}{f_2 + f_1}$. Pour $\theta = 0$, *i.e.* pour un forçage statistiquement $\mathcal{R}_\pi$ -symétrique, l'écoulement obtenu respecte en moyenne la symétrie $\mathcal{R}_\pi$ *lorsque les deux moteurs sont démarrés de manière synchrone.* Dans cet état noté (s), les couples sur les deux impulseurs sont égaux ($\Delta K_p = 0$, voir $\square$ en Fig. 6b) et l'écoulement moyen (voir Fig. 6c) présente la phénoménologie décrite en Fig. 1c. Lorsque les deux moteurs n'ont pas été démarrés en même temps, l'écoulement obtenu à $\theta = 0$ brise la symétrie $\mathcal{R}_\pi$: l'écoulement est constitué d'une seule cellule (voir Fig. 6d) et les couples ne sont plus égaux ($\Delta K_p \simeq \pm 0.1$, voir $\circ$ en Fig. 6b). L'un des deux impulseurs s'impose ; selon qu'il s'agisse de l'impulseur 1 ou 2, cet état est noté (b_1) ou (b_2), pour « bifurqué vers 1 ou 2 ».

Le diagramme de la figure 6b présente les domaines d'existence des états (s), (b_1) et (b_2) en fonction de la dissymétrie relative du forçage θ, pour $Re \geqslant 2 \times 10^5$. On voit ainsi apparaître un cycle d'hystérésis. L'état (s) n'est en outre jamais atteint à partir d'un état (b). Les signaux tracés en Fig. 6a montrent une transition de $(s) \to (b_2)$ observée après préparation d'un état (s) en $\theta = 0$, amené ensuite en $\theta = 0.0204$. La transition se produit au bout d'un temps dont la statistique est exponentielle, le temps caractéristique dépendant de $|\theta|$ et divergeant en $\theta = 0$ (Ravelet *et al.*, 2004). La branche (s) représentée en Fig. 6b est donc métastable, seul le point à $\theta = 0$ étant marginalement stable.

Les deux branches (b_1) et (b_2) se recouvrent et traversent l'axe $\theta = 0$: il existe donc des états « antinaturels » où, par exemple pour $\theta < 0$, on observe un état (b_2) bien que $f_2 < f_1$. On observe alors parfois lors des transitions de l'état antinaturel vers l'état naturel que le système passe un certain temps dans le voisinage d'un état « intermédiaire », comme le montre la Fig. 7.

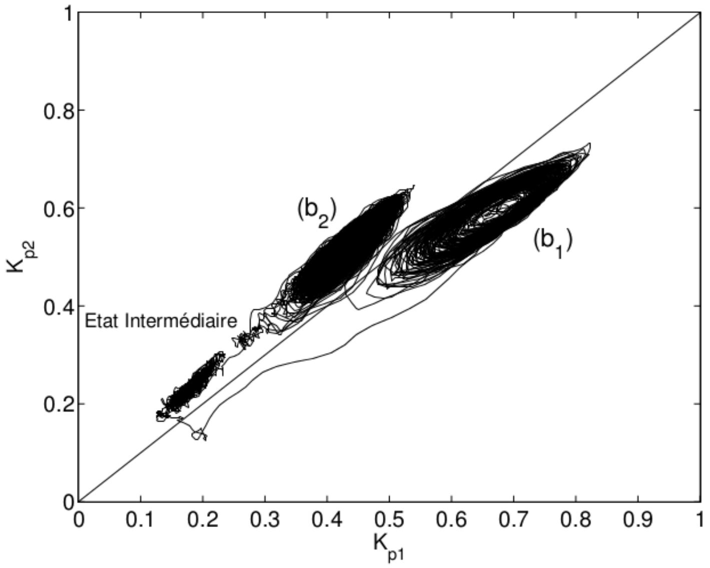

FIGURE 7 – *Exemple de transition* $(b_2) \to (b_1)$ *avec passage par un état intermédiaire.* $\theta = -0.116$, $Re = 2.2 \times 10^5$.

Dans le diagramme des états (Fig. 6b), on a donc une « zone interdite » lorsque la *vitesse* des impulseurs est imposée. En imposant les *couples* et plus particulièrement la *dissymétrie relative des couples* $\gamma = \frac{C_2-C_1}{C_2+C_1}$ dans cette zone, on observe différents régimes. Quelques résultats sont présentés dans les thèses de Marié (2003); Ravelet (2005). L'étude détaillée de la réponse du

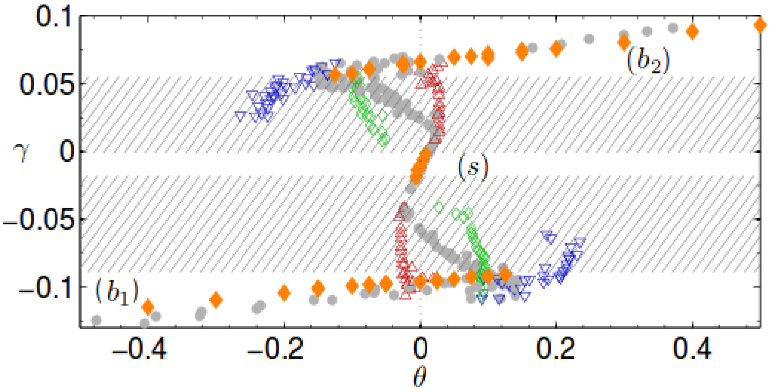

FIGURE 8 – *Diagramme de bifurcation regroupant les moyennes temporelles des dissymétries relatives de vitesse θ et de couple θ, à vitesse imposée (♦) et à couples imposés (●). Zone hachurée : zone interdite en vitesse imposée. Dans cette zone, à couple imposé, les branches $(\widetilde{s})$ (△), $(\widetilde{b_1})$ et $(\widetilde{b_2})$ (▽) prolongent les branches (s), (b_1) et (b_2). Les nouvelles branches $(\widetilde{i_1})$ et $(\widetilde{i_2})$ (◇) obtenues à γ imposé correspondent à des maxima locaux sur les densités de probabilité de θ. Figure extraite de Saint-Michel* et al. *(2013).*

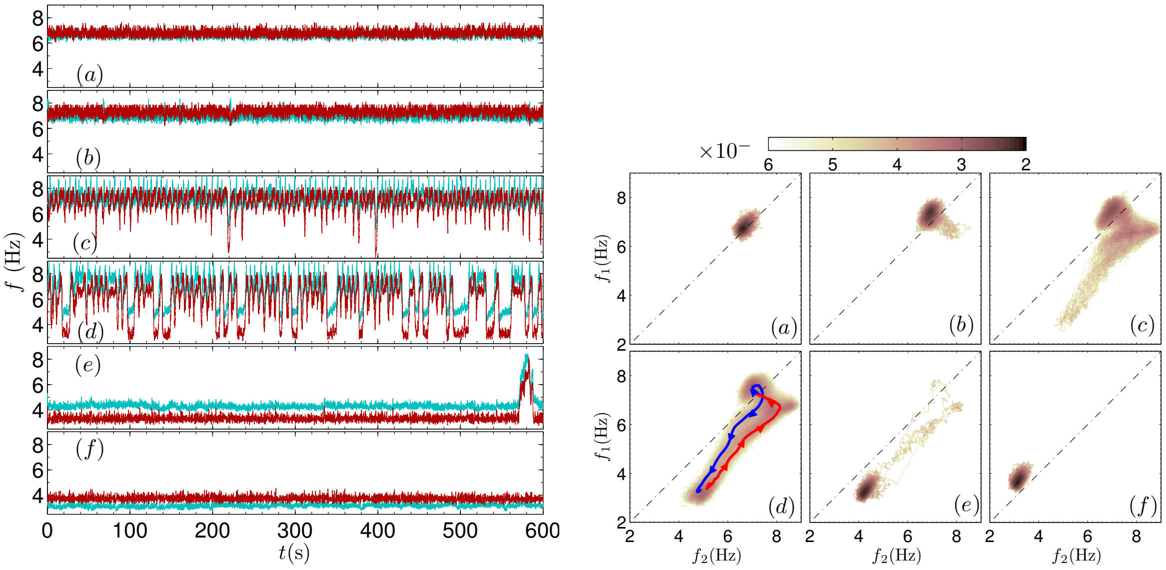

(A) (B)

FIGURE 9 – *Signaux temporels (A) et densités de probabilités jointes (B) des vitesses des impulseurs f_1 et f_2 pour différents γ. (a), $\gamma = -0.0164$: état rapide stationnaire $(\widetilde{s})$; (b), $\gamma = -0.0460$: début des excursions vers un état rapide intermédiaire $(\widetilde{i_1})$; (c), $\gamma = -0.0668$: oscillations irrégulières entre états rapides $(\widetilde{s})$ et $(\widetilde{i_1})$ avec début d'excursions vers un état lent $(\widetilde{b_1})$; (d), $\gamma = -0.0891$: régime de multi-stabilité des trois états ; (e), $\gamma = -0.0912$: état quasi-stationnaire lent $(\widetilde{b_1})$ avec un évènement vers un état rapide ; (f), $\gamma = -0.1049$: état stationnaire bifurqué (b_1). Figure extraite de Saint-Michel* et al. *(2013).*

système à ce mode de régulation constitue une grande partie de la thèse de B. Saint-Michel, en cours de rédaction, et est synthétisée dans Saint-Michel *et al.* (2013).

L'ensemble des points de fonctionnement du système est représenté en Fig. 8. Tout d'abord, on a bien une superposition des états stationnaires obtenus en commande en vitesse (♦) avec ceux obtenus en commande en couple (●) : on retrouve les branches (s), (b_1) et (b_2). Partant de $\gamma = 0$ et augmentant la dissymétrie relative des couples γ, la branche (s) se prolonge légèrement par des états stationnaires (exemple en Fig. 9a). Puis le système ne trouve plus d'états strictement stationnaires et transite aléatoirement entre différents états. Ce phénomène apparaît (voir exemple en Fig. 9b) au moment où la courbe $\theta = f(\gamma)$ présente un point d'inflexion, *i.e.* lorsqu'en moyenne on a une *réponse négative à une variation de dissymétrie* : $\frac{\partial \overline{\theta}}{\partial \overline{\gamma}} < 0$. La multi-stabilité est la plus criante en milieu de zone interdite (voir Fig. 9d). Trois états sont identifiés, que l'on pourra situer dans le plan $\{f_1 ; f_2\}$ de la Fig. 9 :

- un état $(\widetilde{s})$, où les impulseurs tournent rapidement, l'impulseur forçant le plus étant le plus rapide. Cet état prolonge la branche (s). Dans cet état, l'écoulement moyen présente deux cellules dissymétriques séparées par une ligne $v_\theta = 0$ plane de position $z = cte$ (voir Fig. 6c) ;
- un état $(\widetilde{b_{1,2}})$, où les impulseurs tournent lentement, l'impulseur forçant le plus étant en outre le plus lent ce qui rappelle l'état bifurqué *antinaturel*. Les branches $(\widetilde{b_{1,2}})$ prolongent d'ailleurs les branches antinaturelles $(b_{1,2})$. Dans cet état, l'écoulement moyen présente une seule cellule avec une ligne $v_\theta = 0$ en $r = cte$ (voir Fig. 6d) ;
- un état « intermédiaire » $(\widetilde{i_{1,2}})$. On pourrait le qualifier d'état « symétrique antinaturel » : les deux impulseurs tournent rapidement, l'impulseur forçant le plus étant cette fois le plus lent. Dans cet état, l'écoulement moyen présente deux cellules dissymétriques séparées par une ligne $v_\theta = 0$ de forme incurvée. Cette branche se raccorde à la branche antinaturelle (b) là où elle semble perdre sa stabilité lors des expériences à vitesse imposée. L'état intermédiaire observé lors de la transition (à vitesse imposée) de la Fig. 7 a le caractère « symétrique antinaturel » d'un état $(\widetilde{i_2})$.

Bien que le système soit très turbulent, ces observations sont interprétables en termes de systèmes dynamiques à petit nombre de degrés de liberté, sous forme d'échanges de stabilités entre « modes ». On observe également de manière générale des distributions de temps de résidence dans les états métastables de type exponentielles, faisant songer au cas de taux d'échappements de puits de potentiels en présence de bruit ("Kramers' escape rate"). D'autres formes de multistabilité en régime turbulent sont observées pour d'autres impulseurs ou en présence d'appendices sur la cuve (Ravelet, 2005; Cortet *et al.*, 2011; de la Torre & Burguete, 2007), ce dernier exemple étant modélisé par Burguete & de la Torre (2009) par un système dynamique à quelques modes, bruité.

Régimes dynamiques du champ dynamo dans l'écoulement en sodium liquide

L'effet dynamo, à l'origine du champ magnétique de la terre ou du soleil, est une instabilité du champ magnétique dans un fluide conducteur en écoulement (Moffatt, 1978). Le paramètre de contrôle de cette instabilité est le nombre de Reynolds magnétique R_m, rapport entre les effets d'advection par le champ de vitesse et de diffusion du champ magnétique. Le nombre de Prandtl magnétique, rapport entre les échelles de dissipation du champ de vitesse et du champ magnétique est très faible pour les objets astrophysiques évoqués. Cette instabilité se produit donc *a priori* sur un écoulement turbulent. L'expérience VKS est le premier dispositif expérimental ayant généré une instabilité dynamo en écoulement peu contraint et fortement turbulent (Monchaux *et al.*, 2007). Outre cette génération d'un champ magnétique stationnaire en contrarotation exacte, au delà d'un seuil en R_m, par une bifurcation supercritique imparfaite, cette expérience montre aussi une grande variété de régimes dynamiques, obtenue en introduisant une dissymétrie θ dans l'entrainement. Cette dynamique est là aussi interprétable en termes de systèmes dynamiques de basse dimension (Ravelet *et al.*, 2008a; Monchaux *et al.*, 2009).

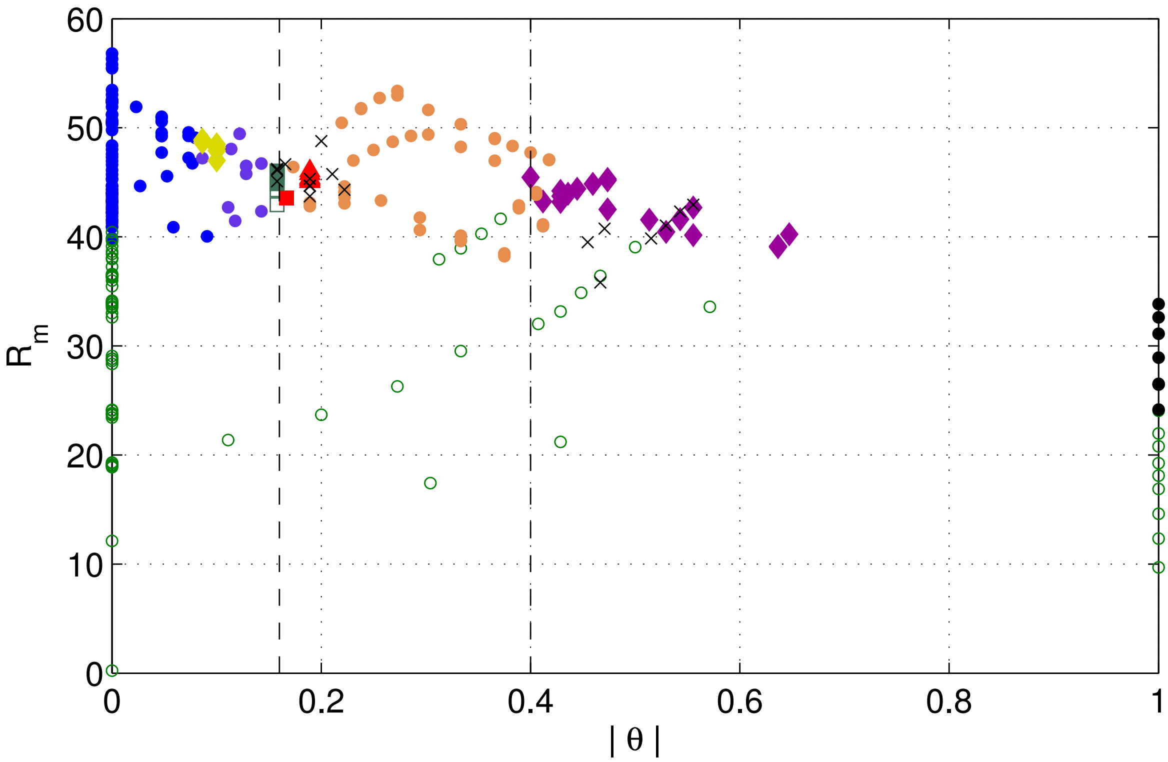

Figure *10 – Diagramme des régimes dynamo pour VKS avec chemise et anneau, dans le plan* $\{R_m\,;\,|\theta|\}$. *(○) : pas de dynamo ; (●) : dynamo stationnaire de type* 1*, champ fort (Monchaux* et al.*, 2007) ; (●) : dynamo stationnaire de type* 2*, champ fort ; (●) : dynamo stationnaire de type* 3*, champ fort, modulation à basse fréquence, avec comportement hystérétique ; (●) : dynamo stationnaire de type* 4*, champ faible ; (♦) : dynamos périodiques ;* × *: extinctions (Monchaux* et al.*, 2009). (♦) : cycles limites (basculements) ; (■) : renversements ; (□) : pseudo-renversements ; (■) : bouffées symétriques ; (▲) : bouffées asymétriques (Ravelet* et al.*, 2008a).*

Les résultats présentés ici se restreignent à la première configuration de l'expérience VKS dans laquelle l'effet dynamo a été observé, lors des campagnes VKS2g, VKS2h et VKS2i à laquelle j'ai participé. Dans cette configuration l'écoulement est généré entre deux impulseurs TM73 (dont la géométrie est issue de l'étude de Ravelet *et al.*, 2005) en fer doux. Les impulseurs d'angle $|\alpha| = 34\,^\circ$ tournent dans le sens positif. La cuve est munie de sa chemise en cuivre et d'un anneau dans le plan médian. Cet anneau suggéré au cours de ma thèse a pour effet « d'accrocher » la couche de mélange et de réduire l'intensité globale turbulente δ de 25% (Cortet *et al.*, 2009).

La figure 10 rassemble les différents régimes obtenus. Le nombre de Reynolds magnétique est défini ici[3] avec le rayon de la chemise R_c comme échelle de longueur, et avec la moyenne des vitesses périphériques de chaque impulseur comme échelle de vitesse. En contrarotation

---

[3] On attire l'attention du lecteur sur le fait que trois définitions de R_m ont été utilisées : une dans Ravelet *et al.* (2005); Monchaux *et al.* (2007, 2009), une autre dans Ravelet *et al.* (2008a) puis la présente à partir de Berhanu *et al.* (2010).

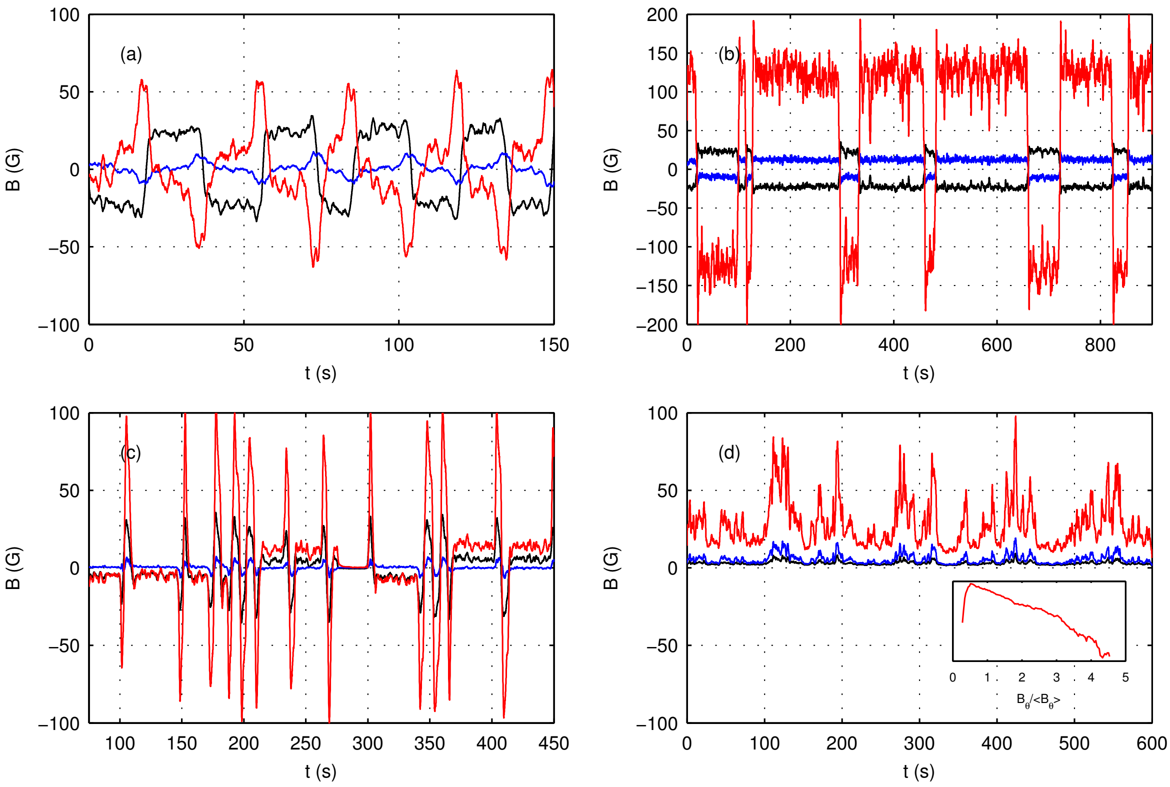

Figure *11 – Signaux temporels des trois composantes du champ magnétique (B_r, B_θ et B_z), filtrés passe-bas à 1 Hz montrant les différents régimes. (a) : Cycles limites (basculements), $\theta = 0.086$, $R_m = 49$, ♦ en Fig. 10. (b) : Renversements, $\theta = -0.158$, $R_m = 46$, ■ en Fig. 10. (c) : Bursts symétriques, $\theta = 0.167$, $R_m = 44$, ■ en Fig. 10. (d) : Bursts asymétriques, $\theta = 0.189$, $R_m = 45$, ▲ en Fig. 10, pdf de B_θ en encart. La sonde est en $r = R_c$, à égale distance des deux impulseurs ($z = 0$, point P1 de la Fig. 2b) pour (a), (c) et (d), et en $z = 0.53$ (point P2 de la Fig. 2b) pour (b).*

parfaite, le mode instable est un dipole axial stationnaire axisymétrique anti-$\mathcal{R}_\pi$ -symétrique, contrairement au mode le plus instable prévu en ne tenant compte que de l'action du champ de vitesse moyenné dans le temps, qui est un dipole transverse (mode azimutal $m = 1$) $\mathcal{R}_\pi$ -symétrique (Ravelet *et al.*, 2005).

La majorité des régimes dynamos correspondent à des champs magnétiques stationnaires ou à des oscillations périodiques. On observe également des régimes dynamiques variés, dans des zones restreintes correspondant à certaines plages ou valeurs de dissymétrie du forçage. Nous détaillons ici ces régimes, illustrés par des signaux temporels en Fig. 11 et par des coupes dans des espaces de phase en Fig. 12.

1. Pour $|\theta| \simeq 0.09$ et $47 \lesssim R_m \lesssim 49$: régimes de **basculements** quasiment périodiques.

   Partant de $\theta = 0$ et $R_{m,0} = 53$, on observe un champ magnétique stationnaire, s'identifiant à un dipole axial axisymétrique ($B_r = 0$ au point de mesure, nuage bleu en Fig. 12a). En augmentant θ et en ayant une variation de R_m telle que $R_m \simeq R_{m,0}/(1+|\theta|)$, la composante radiale augmente et la composante azimutale diminue (mode quadrupolaire axisymétrique en $\theta = 0.07$ avec $B_\theta = 0$, nuage rouge en Fig. 12a), puis en $\theta = 0.086$, on observe une bifurcation globale vers un cycle limite (voir signal en Fig. 11a), dont la trajectoire passe dans le plan $\{B_r\,;\,B_\theta\}$ par les points fixes correspondants aux régimes stationnaires

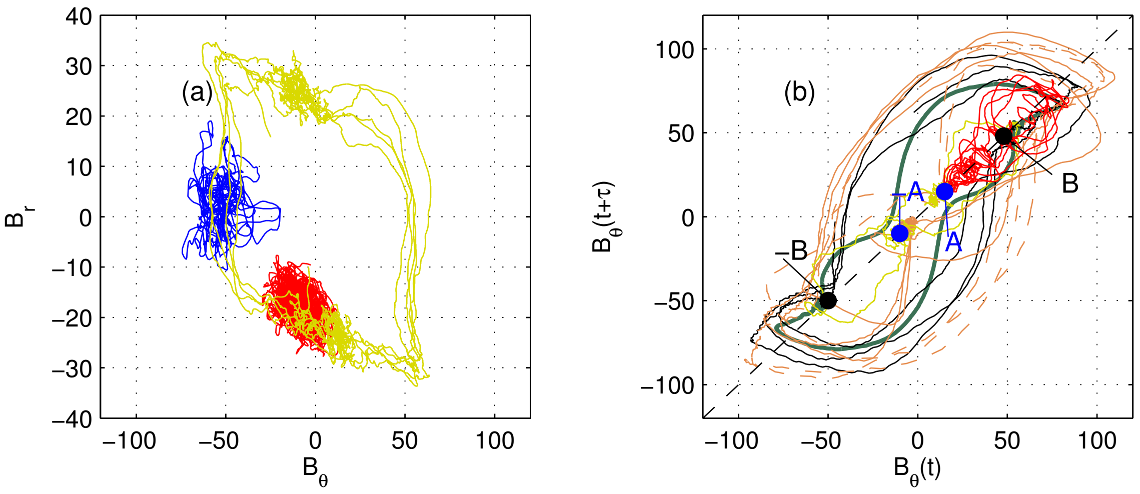

FIGURE *12 – (a) Coupe dans le plan* $\{B_\theta\,;\,B_r\}$. ***Mode stationnaire dipolaire***, $\theta = 0$, $R_m = 53$. ***Mode stationnaire quadrupolaire***, $\theta = 0.073$, $R_m = 49.5$. ***Cycles limites (basculements)***, $\theta = 0.086$, $R_m = 49$ *(b) Coupe dans l'espace des phases* $\{B_\theta(t)\,;\,B_\theta(t+\tau)\}$, *avec* $\tau = 1$ *s.* ***Renversements***, $\theta = -0.158$, $R_m = 46$, *signal multiplié par un facteur ad-hoc à cause de la position différente du point de mesure.* ***Pseudo-renversements***, $\theta = 0.158$, $R_m = 43$. ***Bursts symétriques***, $\theta = 0.167$, $R_m = 44$. *En trait plein, portion de signal* $-A \rightarrow -B \rightarrow B \rightarrow -A$ *(soit de* $t = 115$ *à* $t = 170$ *s en Fig. 11c) et en pointillés , portion de signal* $A \rightarrow B \rightarrow -B \rightarrow A$ *(soit de* $t = 350$ *à* $t = 450$ *s en Fig. 11c).* ***Bursts asymétriques***, $\theta = 0.189$, $R_m = 45$.

précédents et par les points images par la symétrie $\mathbf{B} \rightarrow -\mathbf{B}$ (voir trajectoire jaune en Fig. 12a).

2. Pour $|\theta| \simeq 0.16$ et $44.5 \lesssim R_m \lesssim 46$: régimes de **renversements** (voir signal en Fig. 11b). Les trois composantes du champ se renversent ensemble, *i.e.* au cours du renversement, les trois composantes changent de signe et la norme du champ magnétique s'annule. Les intervalles de temps entre renversements sont aléatoires et peuvent durer jusqu'à 10^2 temps de diffusion ohmique ($\simeq 1$ s ici), la durée d'un renversement étant de cet ordre de grandeur.

   La valeur de R_m modifie assez fortement la dynamique des renversements (voir Fig. 12b), et pour $43 \lesssim R_m \lesssim 44$, on a des « **pseudo-renversements** » où les trois composantes ne s'annulent plus en même temps et où les changements de polarité deviennent quasi-périodiques.

3. Pour $0.16 \lesssim |\theta| \lesssim 0.19$ et $43 \lesssim R_m \lesssim 46$: zone avec **coexistence de régimes** stationnaires de type 3, de bouffées (bursts) symétriques et asymétriques, et d'extinctions de la dynamo.

   Les **bouffées symétriques** (voir signal en Fig. 11c) sont obtenues à bas R_m en $\theta = 0.167$. Il ne s'agit pas de renversements dans la mesure où la norme du champ ne s'annule pas et où les trois composantes ne changent pas de signe ensemble. Le champ magnétique reste sur un état de faible amplitude quasi-stationnaire, avec $B_z \simeq B_\theta \simeq -8$ G, $B_r \simeq +0$ G, puis lors d'une bouffée va rejoindre rapidement un pic de grande amplitude $B_z \simeq -25$ G, $B_\theta \simeq -80$ G, $B_r \simeq -5$ G, suivi d'un pic opposé $B_z \simeq +25$ G, $B_\theta \simeq +80$ G, $B_r \simeq +5$ G, avant de revenir dans l'état quasi-stationnaire de départ (exemple de $t = 115$ à $t = 170$ s en Fig. 11c) ou dans l'état quasi-stationnaire opposé (exemple de $t = 310$ à $t = 375$ s en Fig. 11c, avec deux oscillations avant retour dans l'état quasi-stationnaire).

   Les **bouffées asymétriques** observées à $\theta = 0.189$ ne présentent pas de changements de signe des composantes du champ et se caractérisent par un état le plus probable tel que

$B_\theta \simeq 20$ G, avec des bouffées intermittentes jusqu'à $B_\theta \simeq 100$ G donnant une distribution de probabilité avec une queue exponentielle.

On a enfin un exemple d'extinction transitoire de la dynamo de $t = 280$ à $t = 300$ s en Fig. 11c.

Les trajectoires tracées dans une projection de basse dimension de l'espace des phases en Fig. 12 sont remarquablement robustes malgré le grand niveau de turbulence de l'écoulement.

- Dans le cas des basculements, on observe comme décrit plus haut un cycle limite (Fig. 12a), pouvant être lié à une bifurcation selle-nœud des modes dipolaires et quadrupolaires.
- Dans le cas des renversements (courbe verte épaisse en Fig. 12b), les états quasi-stationnaires sont les points $\pm B$. Lors d'un renversement, le système quitte par exemple B, ralentit près de A pour rejoindre $-B$ en le contournant, avec un over-shoot. Dans le cas des pseudo-renversements (courbe noire), les trajectoirs ne s'approchent plus des points $\pm A$.
- Les bursts asymétriques partent eux des points fixes instables $\pm A$ et empruntent des trajectoires robustes dans le plan, tournant autour des points $\pm B$ de manière plus complexe que pour les pseudo-renversements (voir traits pleins et pointillés).
- Les bursts symétriques sont des excursions chaotiques depuis le point fixe instable A.

Ces comportements variés peuvent s'expliquer par la compétition de deux modes dynamos correspondant aux deux points fixes A et B identifiés ici, dont la stabilité change sous de petites variations de l'asymétrie du forçage, et par l'effet des fluctuations turbulentes (Pétrélis *et al.*, 2009), ou bien par un modèle à trois modes : deux modes dynamos et un mode hydrodynamique (Gissinger, 2012). Les liens entre cette richesse de comportements et l'écoulement sous-jacent sont d'ailleurs une question ouverte. En effet, exposons les faits observés :

- Tout d'abord, l'écoulement moyenné en temps ne peut expliquer seul l'effet dynamo. Nous y revenons dans le paragraphe suivant.
- La présence de disques et de pales en fer doux est nécéssaire pour au moins un impulseur tournant (Boisson *et al.*, 2012).
- La valeur $|\theta| \simeq 0.16$ correspond à une zone de transition entre un écoulement à une cellule et un écoulement à deux cellules, avec une légère hystérésis, pour le montage TM73 en sens positif avec anneau (Cortet *et al.*, 2009).
- Dans le cas où l'anneau est retiré, les régimes obtenus sont assez différents (Berhanu *et al.*, 2010, voir Fig. 13) : on observe des renversements en $|\theta| \simeq 0.09$, là où l'écoulement présente la transition sans anneau, mais également vers $\theta = 0.21$, là où rien ne semble se produire de particulier dans l'écoulement.

On peut donc penser que les bifurcations hydrodynamiques ne sont pas nécéssaires aux changements de régimes magnétiques, mais qu'une corrélation peut exister, d'autant plus que la rétroaction du champ magnétique sur l'écoulement est inconnue et modifie certainement le forçage de l'écoulement avec les possibles conséquences que laissent supposer les observations de, entre autres, de la Torre & Burguete (2007); Ravelet *et al.* (2008b); Burguete & de la Torre (2009); Cortet *et al.* (2011); Saint-Michel *et al.* (2013). De plus, avec anneau, on a un effet dynamo aussi bien dans le sens de rotation positif des impulseurs que négatif, alors que sans anneau, l'effet dynamo ne se produit que dans le sens positif de rotation (Boisson *et al.*, 2012). Les détails de l'écoulement dans VKS ont donc un rôle à jouer dans l'origine de la dynamo et dans sa dynamique. Nous exposons au paragraphe suivant l'état de l'art sur la compréhension de l'origine de la dynamo VKS.

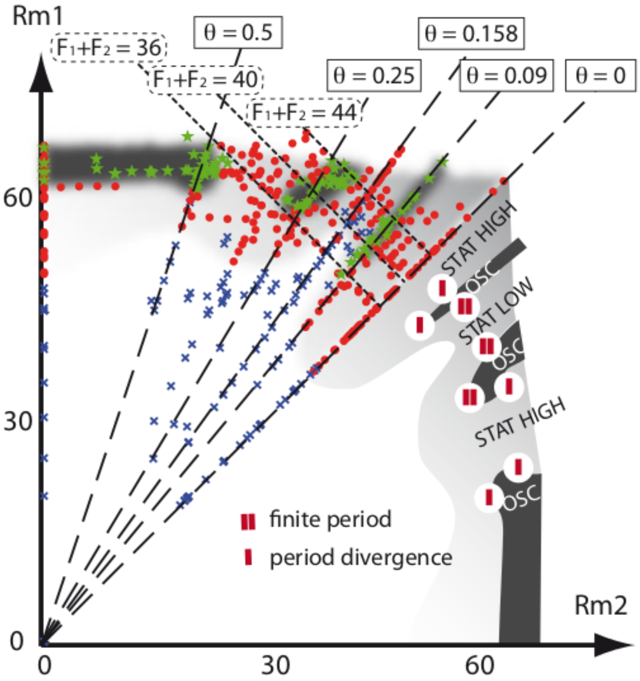

FIGURE *13 – Diagramme des régimes observés sans anneau, image extraite de Berhanu* et al. *(2010, figure 2).*

Mécanismes de la dynamo VKS

L'effet dynamo, c'est-à-dire la conversion d'énergie cinétique en énergie magnétique dans un fluide conducteur en écoulement, est un problème d'instabilité du champ magnétique, par le biais de mécanismes coopératifs d'induction (Verhille *et al.*, 2010a). En effet, un fluide conducteur en écoulement en présence d'un champ magnétique va générer un champ électromoteur induit. Celui-ci engendre des courants, eux-même à l'origine d'un champ magnétique induit. Si le champ ainsi généré est colinéaire au champ incident, on peut avoir une croissance de celui-ci. L'équation d'induction pour un fluide conducteur vérifiant la loi d'Ohm, dans le cadre de la mécanique classique, s'écrit :

$$\frac{\partial \vec{B}}{\partial t} = R_m\, \vec{\nabla} \times (\vec{v} \times \vec{B}) + \Delta \vec{B}$$

On est donc en présence d'un terme de diffusion $\Delta \vec{B}$ qui va tendre à dissiper le champ, et d'un terme en $\vec{\nabla} \times (\vec{v} \times \vec{B})$, dont l'importance relative est mesurée par R_m. Ce terme peut se décomposer en un terme d'advection et un terme d'étirement par les gradients de vitesse[4] Cette équation est linéaire en $\vec{B}$: la saturation de l'instabilité se produit par la rétroaction du champ magnétique sur l'écoulement (force de Laplace).

Cette instabilité ne peut avoir lieu d'une part que si l'écoulement a une vitesse suffisante (si le paramètre de contrôle R_m dépasse un certain seuil), mais surtout uniquement si l'écoulement possède une topologie adéquate permettant l'amplification du champ à partir d'une fluctuation de champ magnétique. Par exemple, une rotation différentielle permet d'induire un champ toroïdal à partir d'un champ poloïdal (effet Ω). L'hélicité du champ de vitesse moyen (effet Parker) ou un effet coopératif des petites échelles (effet α) permettent la création d'un champ poloïdal (toroïdal) à partir d'un champ toroïdal (poloïdal). Des gradients de conductivité ou de

---

[4] Notons que cette équation est similaire à celle de la vorticité en écoulement incompressible.

perméabilité peuvent également être mis en jeu comme l'ont montré Verhille *et al.* (2010a, voir également la revue des différents effets dans cet article de synthèse).

Les mécanismes à l'origine de l'effet dynamo dans l'expérience VKS ne sont pas encore définitivement compris. Il est clair, à cause des symétries du mode neutre engendré en contrarotation exacte, que l'écoulement moyenné en temps caractérisé par Ravelet *et al.* (2005) ne peut seul expliquer l'effet dynamo (Théorême de Cowling stipulant qu'un écoulement axisymétrique ne peut entretenir un champ magnétique axisymétrique, voir par exemple Moffatt, 1978).

Plusieurs pistes sont possibles pour identifier les mécanismes réellement à l'œuvre dans l'instabilité dynamo telle qu'observée expérimentalement dans VKS. Un effet Ω très efficace, du à la contrarotation, et permettant la conversion champ poloïdal → champ toroïdal semble bien être à l'œuvre (Bourgoin *et al.*, 2002). Le problème est l'identification d'un (ou plusieurs) mécanismes de conversion du champ toroïdal en champ poloïdal. On pourrait penser au caractère turbulent de l'écoulement et avoir un effet α à petite échelle, par exemple par un gradient de l'intensité turbulente. La présence des pales dans l'écoulement induit en outre des fluctuations de vitesse non-axisymétriques. Partant de ce constat, Pétrélis *et al.* (2007) supposent la présence de tourbillons organisés dans les pales, de nature hélicitaire, suffisamment « cohérent » (de temps de vie assez long) pour donner un effet Parker localisé.

Plusieurs études numériques récentes relatives à cette identification des mécanismes de la dynamo VKS ont ainsi été menées. Ainsi, sur la base d'un champ de vitesses synthétique, Gissinger (2009) montre qualitativement que l'ajout d'une composante de vitesse en $\exp(i(m\theta + \omega t))$[5] permet l'obtention d'un mode compatible avec l'observation. Laguerre *et al.* (2008) réalisent quant-à eux une simulation à partir du champ de vitesse moyenné en temps mesuré dans VKE, en ajoutant dans l'équation un terme ad-hoc de la forme $\vec{\nabla} \times \left(\alpha(\vec{B} \cdot \vec{e_\theta})\vec{e_\theta}\right)$. D'après ce résultat, le seuil observé serait obtenu avec une valeur $\alpha \simeq 2V$, V étant l'échelle de vitesse sur laquelle est bâtie le R_m, ici la vitesse périphérique des impulseurs. Cette valeur semble donc élevée. Enfin, en remarquant que la dynamo n'est observée expérimentalement que dans le cas où au moins un des impulseurs est en fer doux[6], de perméabilité magnétique relative $\mu_r \simeq 100$, Giesecke *et al.* (2010) étudient l'effet d'une distribution de μ_r en $\exp(i(m\theta + \omega t))$ et montrent qu'il est toujours nécessaire d'invoquer un effet α mais cette fois-ci d'un ou deux ordres de grandeurs plus faible.

Afin d'apporter des éléments de réponse sur la présence ou non de structures hélicitaires fortement cohérentes dans les canaux inter-aubages de nos impulseurs, nous avons mené des études combinant les approches expérimentales et numériques (Ravelet *et al.*, 2012). Le signal de vitesse azimutale tracé en Fig. 14 permet de confirmer la présence de recirculations entre les pales. Ce signal a été obtenu par mesure LDV pour des impulseurs TM80 à pales droites. En effet, dans ce cas la mesure est possible car l'angle entre deux pales (45 ˚) est de l'ordre de grandeur de l'angle entre les faisceaux lasers de notre LDV *dans l'eau* : $\mathrm{i_{eau}} = asin\left(sin(\mathrm{i_{LDV}}) n_{eau}^{-1}\right)$ avec $\mathrm{i_{LDV}} = 60$ ˚ l'angle entre faisceaux dans l'air et $n_{eau} \simeq 1.33$ l'indice optique de l'eau[7]. Les vitesses du fluide sont bien égales à la vitesse de la pale à sa proximité immédiate. Toutefois, entre deux pales la vitesse est réduite d'environ 30%.

Les simulations numériques ont été menées avec un solveur utilisant la méthode des volumes finis[8]. L'écoulement avec un seul impulseur tournant a été simulé en utilisant une approche stationnaire, avec plusieurs domaines considérés comme des référentiels stationnaires ou tour-

---

[5] $m = 8$ pales.

[6] Le choix d'un matériau de haute perméabilité avait initialement été fait pour « isoler magnétiquement » l'écoulement entre impulseurs de la zone derrière les disques suite aux travaux de Stefani *et al.* (2006).

[7] Voir détails sur les noms des impulseurs et les mesures par LDV dans Ravelet (2005)

[8] Fluent 6.3

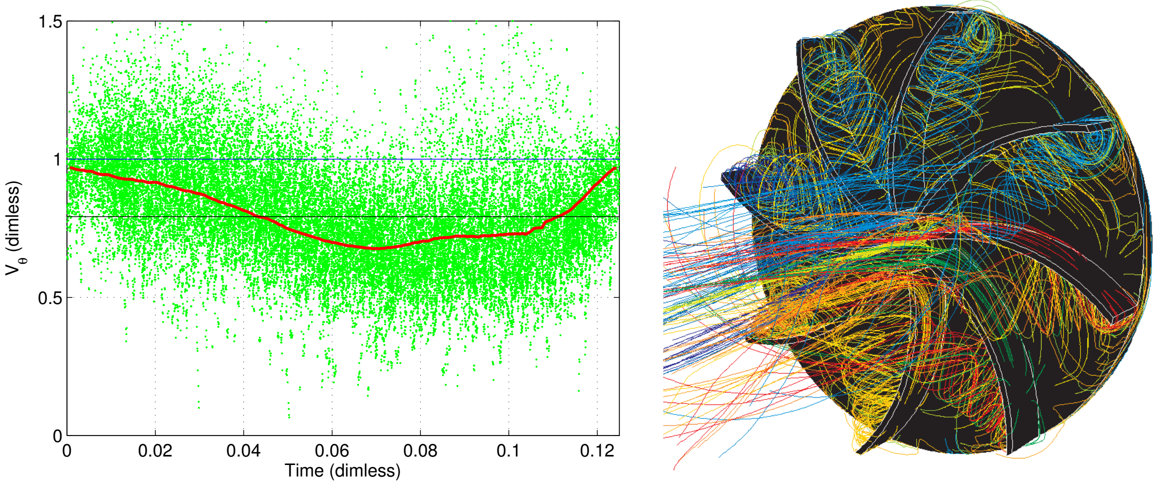

Figure 14 – *A gauche : signal temporel de la vitesse azimutale dans les pales synchronisé sur un passage de pale (environ* 2000 *passages au total). La vitesse est adimensionnée par la vitesse périphérique de l'ailetage et le temps par un tour d'impulseur. Points verts : mesures LDV. Courbe rouge : moyenne glissante. Courbe bleue : vitesse de l'ailetage. Courbe noire : vitesse moyenne sur un huitième de tour. A droite : structures en forme de vortex radiaux observées dans la simulation numérique.*

nant ("Multiple Reference Frames"). Plusieurs « phases » entre impulseurs ont été simulées puis moyennées, ce qui constitue une approche pseudo-instationnaire. La turbulence est modélisée par un modèle de type "Reynolds averaged Navier-Stokes" (RANS) : le modèle "Realizable $k-\epsilon$" (Pope, 2000). Le champ de vitesse moyen dans la zone entre impulseurs a été comparé entre la simulation et une mesure par PIV stéréoscopique[9], ainsi que les couples sur les impulseurs et la simulation n'apparaît pas dénuée de toute pertinence.

Les résultats de CFD sont alors utilisés pour tirer des informations qualitatives (voir Fig. 14, à droite) et quantitatives. Nous mesurons en particulier les différentes composantes du tenseur d'hélicité (moyenné en azimut) h et confirmons que la composante $h_{\theta\theta}$ est la plus importante dans l'impulseur tournant, et est de signe négatif comme proposé par Laguerre *et al.* (2008). Le tenseur α est proportionnel au tenseur hélicité h ; en prenant pour temps de corrélation de ces tourbillons un temps de passage de pale, on arrive à une borne $|\alpha| \leqslant 0.2V$. Cette valeur est donc un ordre de grandeur inférieure à la valeur censée expliquer la dynamo par un effet α localisé dans les impulseurs (Laguerre *et al.*, 2008), mais est aussi un ordre de grandeur supérieure à la valeur minimale requise avec prise en compte de la distribution spatiale inhomogène de perméabilité magnétique telle qu'annoncée par Giesecke *et al.* (2010).

En conclusion, l'écoulement à l'intérieur des canaux inter-aubages dans les impulseurs est capable de générer un effet α suffisamment intense pour produire un effet dynamo même si le couplage avec les conditions aux limites électriques (sauts de conductivité) et magnétique ($B_{r,\theta} = 0$ au niveau des disques, et / ou distribution inhomogène de perméabilité) n'est pas tranché. Cet effet α est de plus très localisé, ce qui semble aller dans le sens des résultats des dernières campagnes de mesures qui ont montré en étudiant des écoulements avec un seul impulseur en fer doux et un autre en inox que la dynamo en contrarotation pourrait être la somme de deux dynamos localisées près des disques et faiblement couplées par le champ de vitesse (Verhille *et al.*, 2010b; Boisson *et al.*, 2012).

---

[9] Voir détails sur le système PIV utilisé à Saclay dans Monchaux (2007)

1.2 Ecoulement de Taylor-Couette (2005-2010)

Position du problème

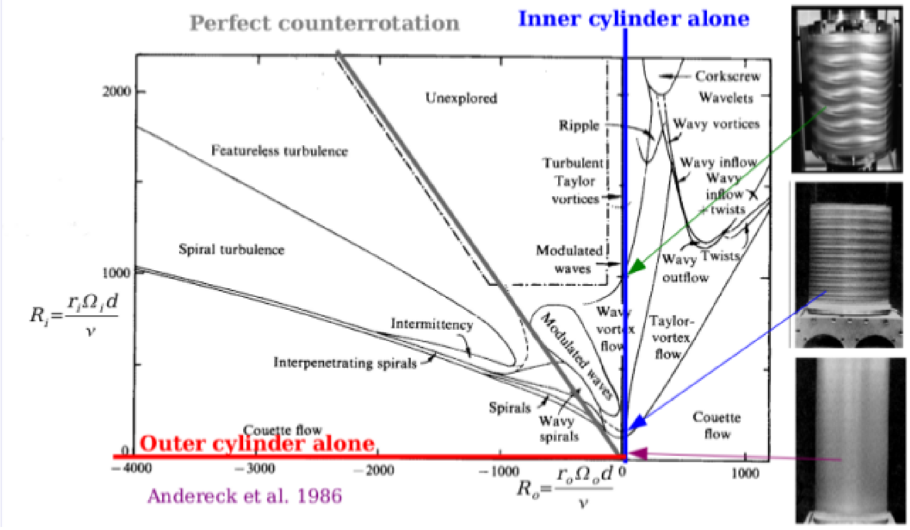

FIGURE 15 – *Carte des régimes extraite de Andereck* et al. *(1986). Les paramètres de contrôle sont les nombres de Reynolds* $R_i = r_i\omega_i d\nu^{-1}$ *et* $R_o = r_o\omega_o d\nu^{-1}$*, avec* $r_{i,o}$ *le rayon du cylindre intérieur (extérieur),* $\omega_{i,o}$ *leur vitesse angulaire,* $d = r_o - r_i$ *le "gap" ou « entrefer », et* ν *la viscosité cinématique du fluide. L'expérience est réalisée avec un rapport de rayons* $\eta = r_i/r_o = 0.883$*.*

L'écoulement de Taylor-Couette est l'écoulement produit entre deux cylindres coaxiaux tournants, de longueur infinie. Ce système est employé comme cas d'espèce des bifurcations hydrodynamiques et de la transition à la turbulence depuis les travaux de Taylor (1923) concernant la première bifurcation de l'écoulement laminaire vers un régime à rouleaux. Deux paramètres de contrôle indépendant —les vitesses angulaires de chaque cylindre— et deux paramètres géométriques —le rapport des rayons et le rapport d'aspect longitudinal— donnent lieu à une incroyable variété de régimes (Andereck *et al.*, 1986, voir la Fig. 15). A plus haut nombre de Reynolds, on pourrait s'attendre à une moindre dépendance de l'écoulement en ces paramètres (nombres de Reynolds ***et*** géométriques), or ce système est connu pour avoir des états turbulents présentant des inhomogénéités, sous formes de patchs, de spirales ou de bouffées (Coughlin & Marcus, 1996; Prigent *et al.*, 2002; Brauckmann & Eckhardt, 2013a).

Dans une perspective applicative, les propriétés de transport des écoulements turbulents sont une problématique capitale. Il s'agit également d'un point de vue fondamental d'un problème important, la difficulté étant le lien entre ce qui se passe près des parois et dans le volume de l'écoulement. L'écoulement de Taylor-Couette possède en outre une analogie forte avec l'écoulement de Rayleigh-Bénard (Dubrulle & Hersant, 2002; Eckhardt *et al.*, 2007; Grossmann & Lohse, 2011).

Le scaling des couples avec le nombre de Reynolds dans l'écoulement de Taylor-Couette a ainsi fait l'objet de nombreuses études, depuis les travaux de Wendt (1933) qui propose d'utiliser deux lois de puissances pures pour le couple mesuré en cylindre intérieur tournant seul, jusqu'à des $R_i = 10^5$ et pour $\eta = 0.68, 0.85, 0.93$ (voir définitions en Fig. 15). En revanche, les mesures de grande qualité de Lathrop *et al.* (1992); Lewis & Swinney (1999) en cylindre interne tournant seul jusqu'à $R_i = 10^6$ avec $\eta = 0.72$ montrent qu'il n'y a clairement pas de loi de puissance pure, mais une évolution continuelle de l'exposant local avec R_i, laissant supposer que les mécanismes de transport évoluent avec le nombre de Reynolds [10]. Or, pour de tels nombres de Reynolds, les structures de l'écoulement étaient encore relativement mal connues en 2005, de même que les lois d'échelles du couple dans les régimes *turbulents* où les deux cylindres tournent.

Dispositif expérimental

Le dispositif expérimental que nous avons conçu et réalisé avait donc comme objectif pour des écoulements turbulents avec deux cylindres tournant, d'une part de mesurer le couple, et d'autre part de réaliser des mesures de champs de vitesses.

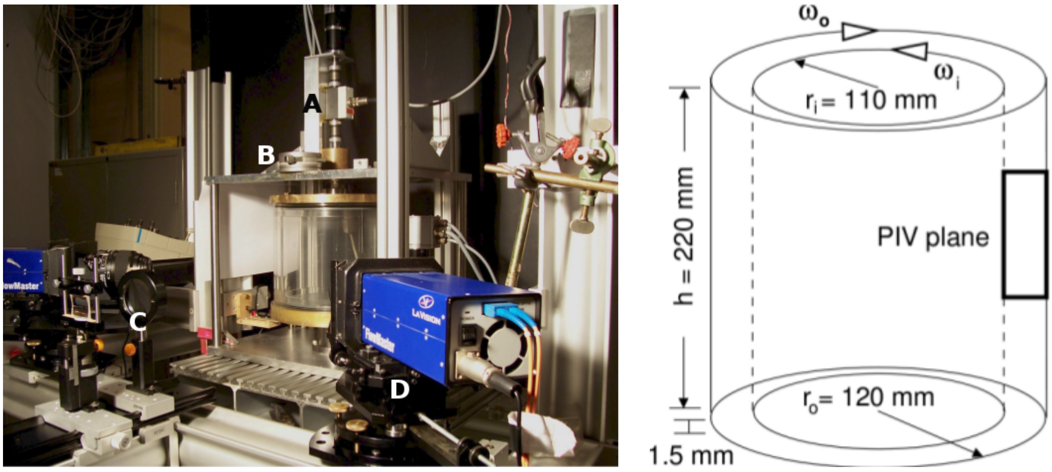

(a) (b)

FIGURE *16 – (a) Photographie du montage Taylor-Couette. On distingue le couplemètre A monté sur l'axe du cylindre interne, la platine micro-contrôle B pour la calibration, les lentilles C pour la création de la nappe laser et les caméras D montées sur Scheimpflug. (b) Dimensions du dispositif.*

Une photographie du dispositif avec les principales dimensions se trouve en Fig. 16. Le gap entre les deux cylindres est $d = r_o - r_i = 10$ mm, le rapport de rayons est $\eta = r_i/r_o = 0.917$ et le rapport d'aspect axial est $\Gamma = h/d = 22$. Le système est fermé et les couvercles tournent avec le cylindre externe. Les deux cylindres sont indépendants, entrainés par des moteurs sans balais, régulés en vitesse en boucle fermée, et pilotés avec un programme LABVIEW.

Le couple T sur le cylindre intérieur est mesuré par un couplemètre rotatif. Les mesures de vitesse sont faites au moyen d'un dispositif PIV stéréoscopique (Laser Nd :YAG, nappe laser d'épaisseur contrôlée, particules fluorescentes, logiciel DAVIS 7.2, voir Raffel *et al.* (2007) pour une présentation complète des différents éléments optiques et numériques d'une chaîne PIV).

La gamme de paramètres accessibles dans l'expérience est présentée en Fig. 17. Nous avons choisi d'utiliser un autre jeu de paramètres, plus pertinents à notre sens, proposés par Dubrulle *et al.* (2005) :

- Un nombre de Reynolds basé sur le cisaillement S (R_i et R_o sont signés)

$$Re_s = \frac{2|\eta R_o - R_i|}{1+\eta} = \frac{Sd^2}{\nu}$$

---

[10] au moins jusqu'à $R_i = 10^6$ dans ce rapport d'aspect

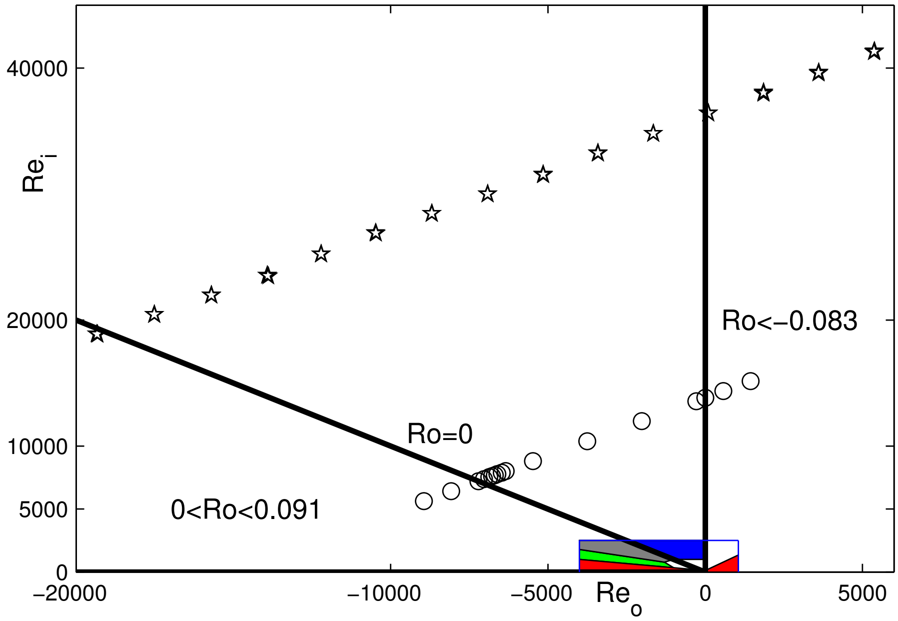

FIGURE *17 – Zone de l'espace des paramètres* $\{R_i\,; R_o\}$ *explorée. Axe vertical* $R_o = 0$ *:* $Ro = Ro_i = -0.083$*, Axe horizontal* $R_i = 0$ *:* $Ro = Ro_o = 0.091$*. Ligne* $R_i = -R_o$ *: contrarotation* $R_o = Ro_c = 0$*. (○) : Données PIV prises à* $Re_s = 1.4 \times 10^4$*. (⋆) : mesures à* $Re_s = 3.6 \times 10^4$*. En couleurs : espace des paramètres décrit par Andereck* et al. *(1986). En rouge : écoulement de Couette laminaire, en vert : "spiral turbulence", en gris : "featureless turbulence", en bleu : zone inexplorée.*

- Un nombre de rotation, rapport de la rotation moyenne au cisaillement (inverse d'un nombre de Rossby)

$$Ro = (1-\eta)\,\frac{R_i + R_o}{\eta R_o - R_i}$$

Ce nombre de rotation est positif (négatif) pour les écoulements cycloniques (anticycloniques), s'annule pour la contrarotation parfaite ($r_i\omega_i = -r_o\omega_o$) et vaut $Ro_i = \eta - 1$ pour $R_o = 0$ (cylindre extérieur fixe) et $Ro_o = (1-\eta)/\eta \simeq 0.091$ pour $R_i = 0$. Pour notre dispositif, avec $\eta = 0.917$, $Ro_i \simeq -0.083$ et $Ro_o \simeq 0.091$. D'autres choix sont possibles, notamment dans le cadre théorique de l'analogie avec la convection de Rayleigh-Bénard, le cisaillement est caractérisé par un nombre de Taylor qui, par rapport à notre nombre de Reynolds de cisaillement, prend la forme suivante (Eckhardt *et al.*, 2007; Grossmann & Lohse, 2011; Huisman *et al.*, 2012; Brauckmann & Eckhardt, 2013a,b) :

$$Ta = \frac{(1+\eta)^8}{256\eta^4} Re_s^2$$

Dans notre cas ($\eta = 0.917$), on a la relation $Ta = 1.01 Re_s^2$. Le second paramètre utilisé avec ce choix est simplement le rapport des vitesses angulaires $a = -\omega_o/\omega_i$: il est nul pour $R_o = 0$, infini pour $R_i = 0$ et vaut η en contrarotation parfaite.

Résultats

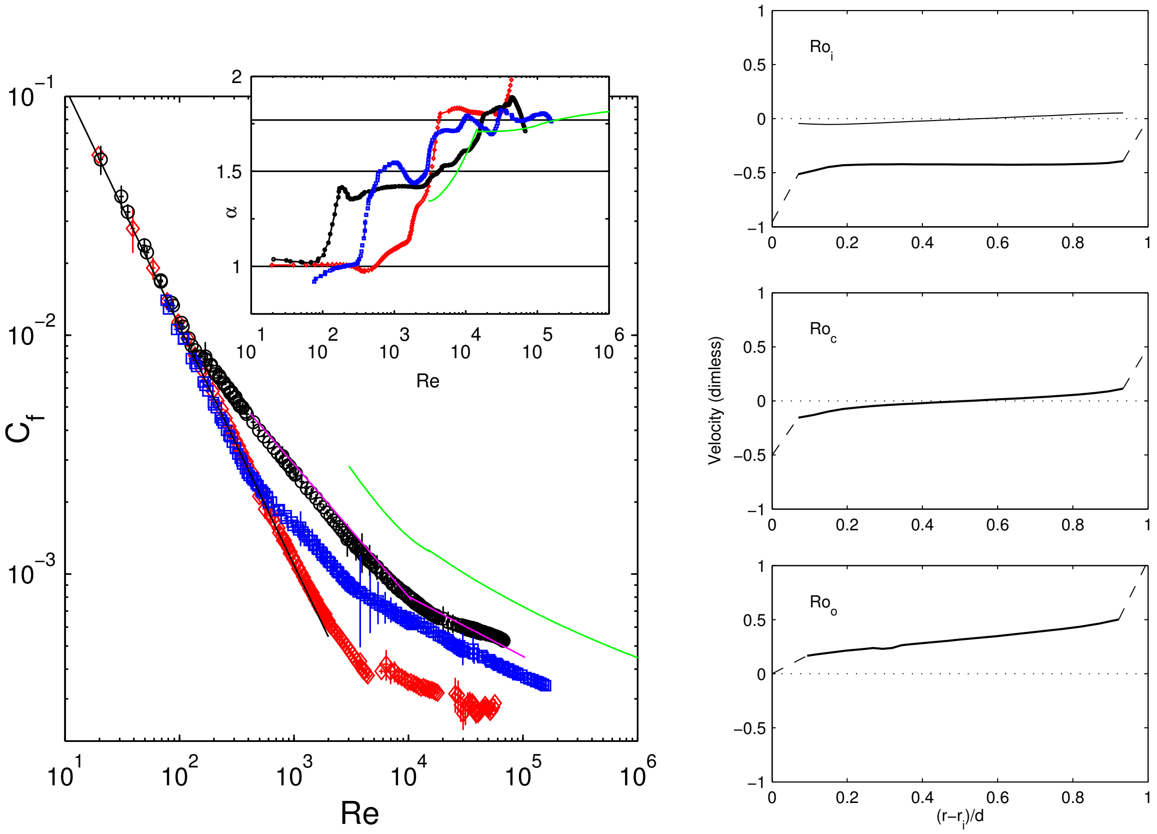

(a) (b)

Figure 18 – *(a) Coefficient de friction C_f en fonction de Re_s pour $Ro_i = \eta - 1$ (○), $Ro_c = 0$ (□) et $Ro_o = (1-\eta)/\eta$ (◇). Inset : exposant local α : $C_f \propto Re_s^{\alpha-2}$. Ligne verte : fit des données de Lewis & Swinney (1999) (eq. 3), pour Ro_i et $\eta = 0.724$. Ligne magenta : Racina & Kind (2006), eq. 10. Ligne noire : coefficient de friction laminaire $C_f = 1/(\eta Re_s)$. (b) Profils moyens de la vitesse azimutale à $Re_s = 1.4 \times 10^4$ pour trois nombres de rotation particuliers.*

Les résultats présentés ici ont été publiés dans Ravelet *et al.* (2010). Nous comparons en Fig. 18a l'évolution du coefficient de friction en fonction du nombre de Reynolds de cisaillement Re_s pour différents nombres de rotation Ro. Le coefficient de friction est défini par [11]

$$C_f = \frac{T}{2\pi\rho r_i^2 h(Sd)^2} = G\frac{(1-\eta)^2}{2\pi\eta^2}Re_s^{-2}$$

A bas Re_s, les trois courbes sont confondues et le coefficient de friction est bien celui prévu dans le cas d'un écoulement laminaire ($C_f \propto Re_s^{-1}$). Pour le cylindre interne seul (○), on a une première transition vers un écoulement à rouleaux de Taylor laminaires pour $Re_s \simeq 140$. Le coefficient de friction a alors une dépendance en $Re_s^{-1/2}$ (voir Inset en Fig. 18). Pour la contrarotation exacte (□), le seuil pour la première instabilité est en $Re_s \simeq 400$. Enfin, dans le cas du cylindre externe tournant seul (◇), l'écoulement est linéairement stable. On note une transition directe vers un écoulement turbulent à $4000 \lesssim Re_s \simeq 5000$.

---

[11] $G = T/(\rho h \nu^2)$ est un autre adimensionnement du couple, utilisé par notamment Lathrop *et al.* (1992).

Pour de plus grands nombres de Reynolds, l'écoulement en cylindre intérieur seul évolue progressivement vers un écoulement turbulent, l'exposant local —obtenu par dérivation gaussienne du coefficient de friction, $\alpha = 2 + \frac{d\log(C_f)}{d\log(Re_s)}$— variant progressivement de $\alpha \simeq 1.5$ pour $Re \simeq 200$ à $\alpha \simeq 1.8$ pour $Re \simeq 10^5$, en accord avec les résultats de Lewis & Swinney (1999) obtenus pour un autre rapport de rayons η. Pour la contrarotation, on remarque une transition plus brutale depuis un plateau où $\alpha \simeq 1.5$ vers $\alpha \simeq 1.75$ pour $Re_s \gtrsim 3200$. Enfin, en cylindre externe seul, la transition est plus brusque et $\alpha \simeq 1.77$ pour $Re_s \gtrsim 5000$. Pour $Re_s \geq 10^4$, les trois exposants locaux sont égaux à ± 0.1 et on a la hiérarchie $C_f(Ro_o) < C_f(Ro_c) < C_f(Ro_i)$. Nous sommes ainsi les premiers à explorer l'effet du nombre de Rotation sur le scaling et les valeurs du couple en écoulement turbulent développé.

Les profils moyens de vitesse azimutale obtenus par PIV stéréoscopique à $Re_s = 1.4 \times 10^4$ pour ces trois nombres de rotation sont tracés en Fig. 18b. Nous avons également mesuré les composantes du tenseur de Reynolds, particulièrement la composante $v'_r v'_\theta$ apparaissant dans l'équation bilan du moment cinétique —le couple étant directement lié au flux de moment cinétique (Marié *et al.*, 2004). Dans le cas du cylindre interne seul, le profil azimutal de vitesse est très plat. La contribution des fluctuations de vitesse au couple représente 25%. Nous rapportons la présence de structures en forme de vortex de Taylor dans l'écoulement moyenné en temps à $Re_s \gtrsim 10^4$, inclinées d'un angle de ±25 ° avec la direction azimutale, et contribuant pour les 75% restant au transport de moment cinétique. Au contraire, dans le cas de la contrarotation parfaite, il n'y a aucune structure dans l'écoulement moyenné en temps. Une petite partie du moment cinétique est transportée par le gradient de vitesse azimutale, et la majeure partie par des fluctuations corrélées faisant penser à des « plumes » (Ravelet *et al.*, 2007). Cette observation semble s'opposer aux résultats numériques de Dong (2008) qui rapporte la présence de vortex de Taylor en contrarotation, mais pour $\eta = 0.5$ et à $Re_s = 8000$.

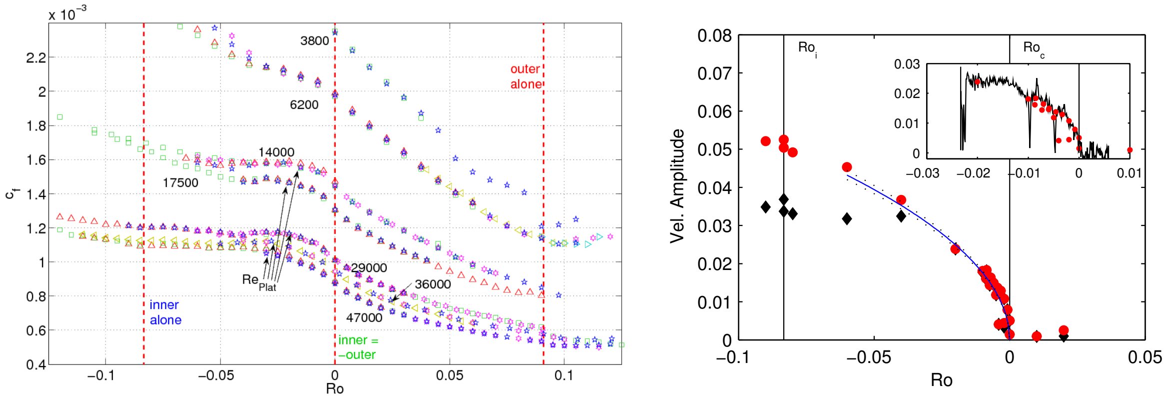

(a) (b)

FIGURE *19 – (a) Coefficient de friction C_f en fonction de Ro à Re_s =* cte. *(b) Amplitude de l'écoulement secondaire en fonction de Ro, à $Re_s = 1.4 \times 10^4$. L'amplitude est le résultat d'un fit sur les champs PIV moyens avec pour modèle de la fonction de courant $\Psi = \sin[\pi(r - r_i)/d] \times \{A_1 \sin[\pi(z - z_0)/\ell] + A_3 \sin[3\pi(z - z_0)/\ell]\}$. Ceci correspond à des rouleaux alternés de longueur d'onde 2ℓ et une vitesse radiale maximale égale à $\pi(A_1/\ell + 3A_3/\ell)$. ♦ : contribution du fondamental, et ● : fondamental + première harmonique. Ligne : fit de la forme $A = a(-Ro)^{1/2}$. Inset : zoom proche de Ro_c avec le résultat d'une expérience quasi-statique avec Ro varié de $Ro = 0.004$ à $Ro = -0.0250$ en 3000 s. L'amplitude est calculée sur des moyennes glissantes de 20 images.*

Nous avons alors étudié la variation des propriétés moyennes de l'écoulement en fonction du nompbre de rotation, en gardant un nombre de Reynolds de cisaillement constant. La variation de C_f en fonction de Ro est tracée en Fig. 19a. Une mesure de la présence de structures de type rouleaux et de leur intensité dans l'écoulement moyenné en temps est présentée en Fig. 19b. La contrarotation parfaite ($Ro = Ro_c = 0$) semble correspondre à un seuil pour l'apparition des rouleaux dans le champ moyenné en temps, et ces rouleaux ont une forme qui se modifie sensiblement autour de $Ro \simeq -0.03$. Aux plus hauts nombres de Reynolds, on observe un plateau de C_f pour $Ro \lesssim -0.035$, contrairement aux travaux récents de van Gils *et al.* (2011); Huisman *et al.* (2012) (groupe de Twente) et de Paoletti & Lathrop (2011) (groupe du Maryland), qui, tous deux pour des $\eta = 0.72$, observent un maximum dans la courbe $C_f(Ro)$ pour $a = 0.4$ [12]. Ceci est attribué à un optimum dans le transport de moment cinétique. On peut remarquer que $a = 0.4$ correspond dans notre géométrie à $Ro = -0.033$. Notre étude a depuis été complétée par des mesures PIV tomographiques, réalisées par Tokgoz *et al.* (2011, 2012) à de plus grands nombres de Reynolds ($Re_s \leqslant 4 \times 10^4$), qui confirment la présence de rouleaux et les modifications de leur forme. Il serait intéressant de réaliser ce genre d'expériences à des nombres de Reynolds ou de Taylor comparables à ceux de Paoletti & Lathrop (2011); van Gils *et al.* (2011) : $Ta \geqslant 10^{12}$, *i.e.* $Re_s \geqslant 10^6$ dans notre géométrie, afin d'établir si la présence de cet optimum dépend du paramètre η, *i.e.* si la présence d'un maximum pour $C_f(a)$ à $Ta \geqslant 10^{12}$ disparait pour $\eta \to 1$.

---

[12] Rapport des vitesses angulaires, voir sa définition en page 43.

2 Axe 2 : Ecoulements dans les machines tournantes

Les travaux exposés ici ont une finalité plus applicative et portent sur l'analyse des écoulements dans plusieurs types de machines tournantes, avec pour objectif l'amélioration de leur conception et de leurs performances. Nous nous intéressons dans un premier temps à l'effet des paramètres géométriques des impulseurs sur les propriétés moyennes de l'écoulement de von Kármán contrarotatif (§ 2.1). Puis nous présentons un ensemble d'études sur les ventilateurs axiaux contrarotatifs (§ 2.2).

2.1 Optimisation des impulseurs pour l'expérience VKS (2002-2006)

Dans l'optique de favoriser l'apparition de la dynamo dans VKS, nous avons effectué un travail d'optimisation de l'écoulement moyenné en temps (Ravelet *et al.*, 2005; Stefani *et al.*, 2006). Nous avons exploré les effets de principalement deux paramètres géométriques des impulseurs sur la topologie de l'écoulement moyen de von Kármán, ainsi que sur la puissance dissipée : le diamètre des disque et l'angle de sortie de pale[1] α défini en Fig. 1c.

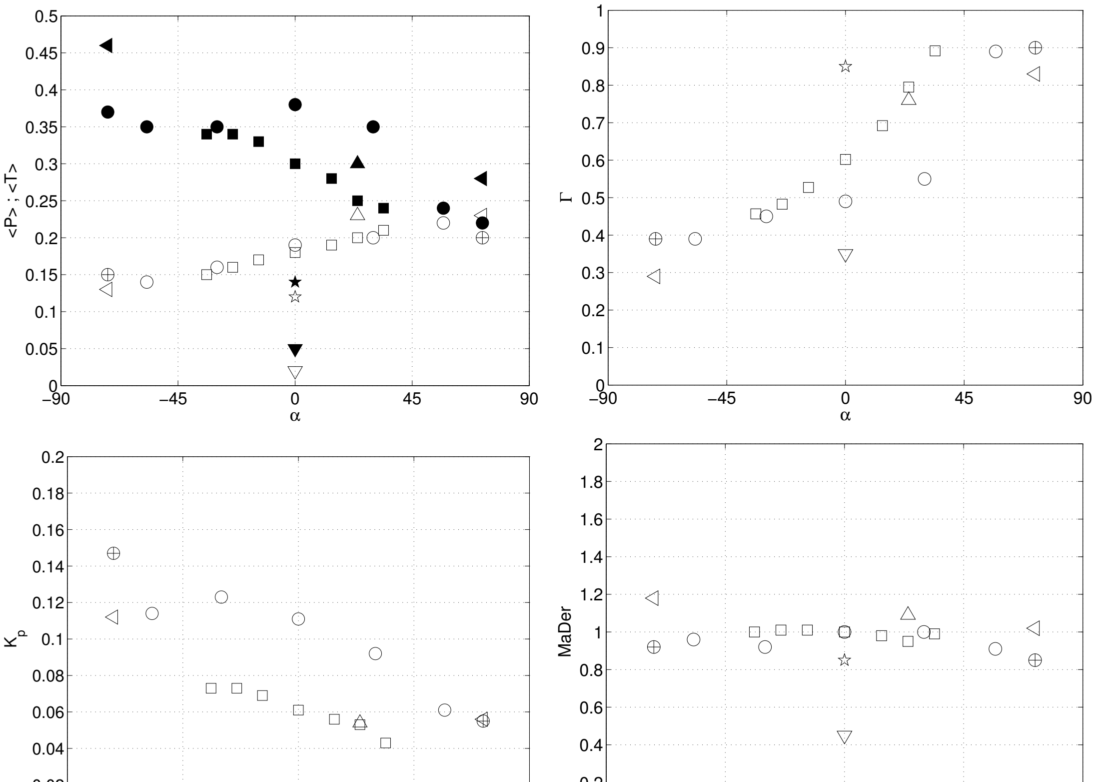

FIGURE *20 – Grandeurs globales hydrodynamiques en fonction de l'angle de sortie de pales* α*, pour les impulseurs de hauteur de pales* $h = 0.2R_c$ *et les disques lisses, en contrarotation à* $Re \gtrsim 10^5$*. (▽) : disques lisses, (○) : disques de rayon* $0.925R_c$ *—les (⊕) ont* 16 *pales—, (□) : disques de rayon* $0.75R_c$*, (★) : disques de rayon* $0.50R_c$*. (△) :* $TM73_2$ *avec anneau. (◁) :* $TM60_2$ *avec anneau. en haut à gauche, symboles vides :* $\langle P\rangle$ *et symboles pleins :* $\langle T\rangle$*.*

---

[1] Angle que nous retrouvons dans la communauté des turbomachinistes, noté usuellement $\beta_{2\infty}$ et qui a un lien direct avec la hauteur manométrique produite, voir § 2.2.

Les grandeurs auxquelles nous nous sommes intéressé sont :

- La moyenne du champ poloïdal $\langle P\rangle$, et du champ toroïdal $\langle T\rangle$;
- Le rapport « poloïdal sur toroïdal » $\Gamma = \frac{\langle P\rangle}{\langle T\rangle}$, dont on montre que l'optimum pour un effet dynamo dû au champ de vitesse moyenné en temps, pour des raisons d'optimum entre hélicité du champ de vitesse et effet Ω axial est $\Gamma = 0.8$ (Ravelet *et al.*, 2005).
- Le préfacteur de couple K_p (voir p. 27) ;
- Le « rendement hydrodynamique » : ce nombre sans dimension, basé sur la vitesse quadratique moyenne, donne une mesure de la quantité d'énergie cinétique stockée par l'écoulement moyen relativement à la puissance injectée dans le fluide au moyen du système d'entrainement :

$$MaDer \; = \; \frac{\langle V^2\rangle^{1/2}}{K_p^{1/3}}$$

Les valeurs de ces paramètres sont tracés en fonction de α en Fig. 20. Les principaux effets ne sont guère surprenants : les disques lisses entrainent très mal le fluide dans le volume ; les impulseurs de plus grand rayon consomment plus de puissance et entrainent plus intensément le fluide ; plus la pale est courbée dans le sens positif, moins elle entraine le fluide en rotation.

Les résultats plus significatifs sont, d'une part la *grande plage de rapports* Γ *réalisables*, et d'autre part la constatation que le *rendement hydrodynamique* $MaDer$ est quasiment *indépendant de la forme du système d'entrainement* pour un entrainement inertiel, ce qui constitue un résultat fort pour VKS où l'un des objectifs était également de tirer le maximum de la puissance disponible (300 kW) en termes de vitesse dans l'écoulement de sodium (*i.e.* de maximiser le R_m à puissance donnée pour avoir une chance d'observer un effet dynamo).

On peut expliquer ce résultat par un raisonnement basé sur les propriétés statistiques de la turbulence localement homogène et isotrope issues de la théorie de Kolmogorov (1991a,b). Tout d'abord, le spectre spatial d'énergie cinétique s'écrit, avec ϵ le taux de dissipation massique, et k le nombre d'onde :

$$E(k) = C_K \; \epsilon^{2/3} \; k^{-5/3}$$

Nous supposons dans la suite que le taux de dissipation massique ϵ est homogène, *i.e.* qu'il est le même en tout point de l'écoulement [2]. $\mathcal{P}$ étant la puissance totale dissipée dans l'écoulement, le taux moyen de dissipation massique est estimé par la relation :

$$\epsilon = \frac{\mathcal{P}}{\rho\pi R_c^2 H_c}$$

Par définition du spectre spatial d'énergie cinétique, on a :

$$\frac{1}{2}\langle v^2\rangle = \int_{k_0}^{\infty} E(k)dk$$

En tirant alors profit de la forte raideur du spectre pour l'intégration, *i.e.* en négligeant la contribution des petites échelles dissipatives, on obtient, avec l'échelle d'injection $k_0 = 2\pi/R_c$ (Cadot *et al.*, 1997; Titon & Cadot, 2003) :

$$E(k_0) = \frac{1}{3}\langle v^2\rangle k_0^{-1}$$

---

[2] Approximation forte : les mesures de Zocchi *et al.* (1994) montrent une forte inhomogénéité, ϵ étant deux fois plus important dans la couche de mélange qu'au niveau des pales.

$$MaDer^2 \simeq 3\pi^{-4/3}(\frac{H_c}{R_c})^{-2/3}C_K \simeq 0.44C_K$$

En prenant pour valeur de la constante de Kolmogorov $1.5 \leqslant C_K \leqslant 1.62$ (Pope, 2000), on obtient la fourchette : $0.81 \lesssim MaDer \lesssim 0.84$, en bon accord avec les résultats reportés en Fig. 20 malgré les approximations les plus fortes de ce modèle (homogénéité du taux de dissipation massique ϵ et choix de l'échelle d'injection k_0).

2.2 Turbomachines axiales contrarotatives (2009-)

Position du problème

Généralités sur les turbomachines en régime incompressible

Nous nous plaçons dans le cadre des turbomachines destinées à véhiculer un fluide en écoulement incompressible (pompes et ventilateurs). Si w représente le *travail massique absorbé par la machine*, en négligeant les variations d'énergie potentielle de pesanteur, on a la relation $w = \Delta h_0$, avec $h_0 = h + \frac{1}{2}V^2$ l'enthalpie massique totale ($\frac{1}{2}V^2$ est l'énergie cinétique par unité de masse, et la variation Δ s'entend entre l'entrée et la sortie de la machine). En appliquant le théorême du moment cinétique, on établit également la loi suivante[3] pour une ligne de courant, qui donne un lien entre énergie échangée et cinématique de l'écoulement : $\Delta h_0 = \Delta\left(Uc_\theta\right)$, avec U la vitesse de rotation de la machine et c_θ la composante de vitesse du fluide selon la direction de la rotation dans le référentiel absolu par rapport auquel U est définie.

On a également la relation $\mathrm{d}h_0 = \frac{\mathrm{d}p}{\rho} + T\mathrm{d}s + \mathrm{d}(\frac{1}{2}V^2)$, avec p la pression, ρ la masse volumique, T la température et s l'entropie massique. Une partie du travail absorbé par la machine peut donc être convertie en élévation d'entropie du fluide. Cette partie constitue une première perte, et on introduit alors la notion d'énergie « hydraulique » communiquée au fluide. Dans le cas d'un fluide en écoulement permanent incompressible, on définit ainsi sur chaque ligne de courant le *travail utile massique* élémentaire $\mathrm{d}w_u$, avec c la vitesse du fluide :

$$\mathrm{d}w_u = \frac{\Delta p}{\rho} + \Delta\left(\frac{1}{2}c^2\right)$$

On a ainsi un premier rendement : le rendement isentropique $\eta_s = w_u/w$. Toutefois, dans une *perspective applicative*, toute l'énergie hydraulique n'est pas aisément exploitable. Ainsi, particulièrement pour les machines axiales, l'énergie cinétique de giration derrière le rotor est difficile à exploiter. On ne considère alors souvent que la partie « utile » de l'énergie hydraulique par unité de masse. Selon l'application, on utilise deux formes, exprimées en termes d'élévations de pression[4] :

- *Elévation de pression « totale »* $\Delta p_t = \Delta\left(p + \frac{1}{2}\rho V_a^2\right)$ pour les pompes et ventilateurs débitant dans un circuit fermé. On lui associe le rendement total $\eta_t = \Delta p_t/\left(\rho w\right)$ au mieux d'un ordre de grandeur $\eta_t \simeq 75\%$ pour un rotor seul et $\eta_t \simeq 80\%$ pour un étage rotor / stator (Vad & Bencze, 1998) ;
- *Elévation de pression « statique »* $\Delta p_s = \Delta p_t - \frac{1}{2}\rho V_{a,2}^2$, avec $V_{a,2}$ la vitesse débitante en aval du ventilateur. Elle trouve sa justification pratique pour les ventilateurs aspirant à une pression d'arrêt p_0 et refoulant dans un circuit débouchant à la pression statique p_0[5].

---

[3] Equation d'Euler des turbomachines, (Dixon & Hall, 2010).

[4] *ISO 5801 - Industrial fans Performance testing using standardized airways.* International Standards for Business, Government and Society, (2007).

[5] Typiquement l'atmosphère. C'est ce Δp_s qui intéresse, par exemple, les acteurs du domaine de la ventilation automobile (Moreau & Bakir, 2002).

On lui associe le rendement statique $\eta_s = \Delta p_s / (\rho w)$, au mieux d'un ordre de grandeur $\eta_s \simeq 55\%$ pour un rotor seul (Yen & Lin, 2006; Sarraf *et al.*, 2011) et $\eta_s \simeq 60\%$ pour un étage rotor / stator (Moreau & Bakir, 2002).

Améliorations des performances, intérêt de la contrarotation et état de l'art

Afin d'améliorer le rendement total d'une machine axiale à un rotor seul, on peut naïvement penser à minimiser la composante giratoire c_θ considérée comme perdue, et à augmenter U. C'est une erreur : certes, on a un rapport $\Delta p_t/(\rho w_u)$ plus proche de 1 pour une machine de plus grand diamètre ou de plus grande vitesse angulaire toutes choses égales par ailleurs, mais il s'avère que le rendement isentropique varie fortement avec la *vitesse angulaire spécifique* Ω et le *rayon spécifique* Λ[6]. En s'écartant du couple $\{\Omega, \Lambda\}$ idéal, on dégrade fortement le rendement isentropique. De plus, augmenter U peut provoquer des problèmes de bruit ou de tenue à la cavitation.

Si les contraintes d'encombrement axial le permettent, une solution est d'utiliser un redresseur (stator) dont le rôle est de convertir l'énergie cinétique de la giration en énergie de pression. Toutefois, il peut s'avérer difficile de redresser complètement l'écoulement et cela se fait au prix de pertes supplémentaires (Moreau & Bakir, 2002).

L'emploi d'un *second rotor contrarotatif* est une troisième solution très séduisante. D'une part on peut redresser l'écoulement, et d'autre part la répartition du travail sur deux rotors constitue une piste intéressante pour l'amélioration de la compacité et du rendement des ventilateurs ou pompes à flux axial (Shigemitsu *et al.*, 2005; Furukawa *et al.*, 2007; Cho *et al.*, 2009; Xu *et al.*, 2009; Shigemitsu *et al.*, 2013). Ce type de système reste toutefois peu utilisé dans les applications subsoniques courantes.

D'une part, de nombreux paramètres additionnels de conception apparaissent, tels que la répartition de chargement entre les deux rotors, la distance axiale, le rapport des vitesses de rotation, le rapport des diamètres, *etc.* Cette difficulté est en même temps une opportunité pour avoir un système de plus grande souplesse d'utilisation.

D'autre part, la zone de mélange entre les deux rotors est le siège de structures très complexes produites par l'interaction d'écoulements hautement instationnaires (convection des sillages, effets potentiels et écoulements secondaires dans les jeux radiaux rotors-carter).

Les travaux menés dans ce contexte visent donc à explorer, principalement expérimentalement, l'effet de quelques paramètres de conception sur les performances globales et sur les interactions dans la zone entre les rotors.

Dispositif expérimental

Au cours de la thèse de Nouri (2012), nous avons conçu et monté un banc d'essai dédié à ces études, dont un schéma se trouve en Fig. 21. Ce banc s'appuie sur la norme ISO-5801 et correspond à une utilisation en aspiration libre et refoulement en conduite. Le diamètre intérieur est $D = 380$ mm. Le système se compose, de l'amont vers l'aval, d'une portion de conduite avec une cloche d'aspiration quart-de-cercle, du système contrarotatif à étudier, d'un dispositif anti-

---

[6] Pour une machine de diamètre D, tournant à la vitesse angulaire ω, communiquant au fluide le travail utile massique w_u au débit Q, on définit :

$$\Omega = \frac{\omega\sqrt{Q}}{w_u^{3/4}}$$

$$\Lambda = \frac{D w_u^{1/4}}{\sqrt{Q}}$$

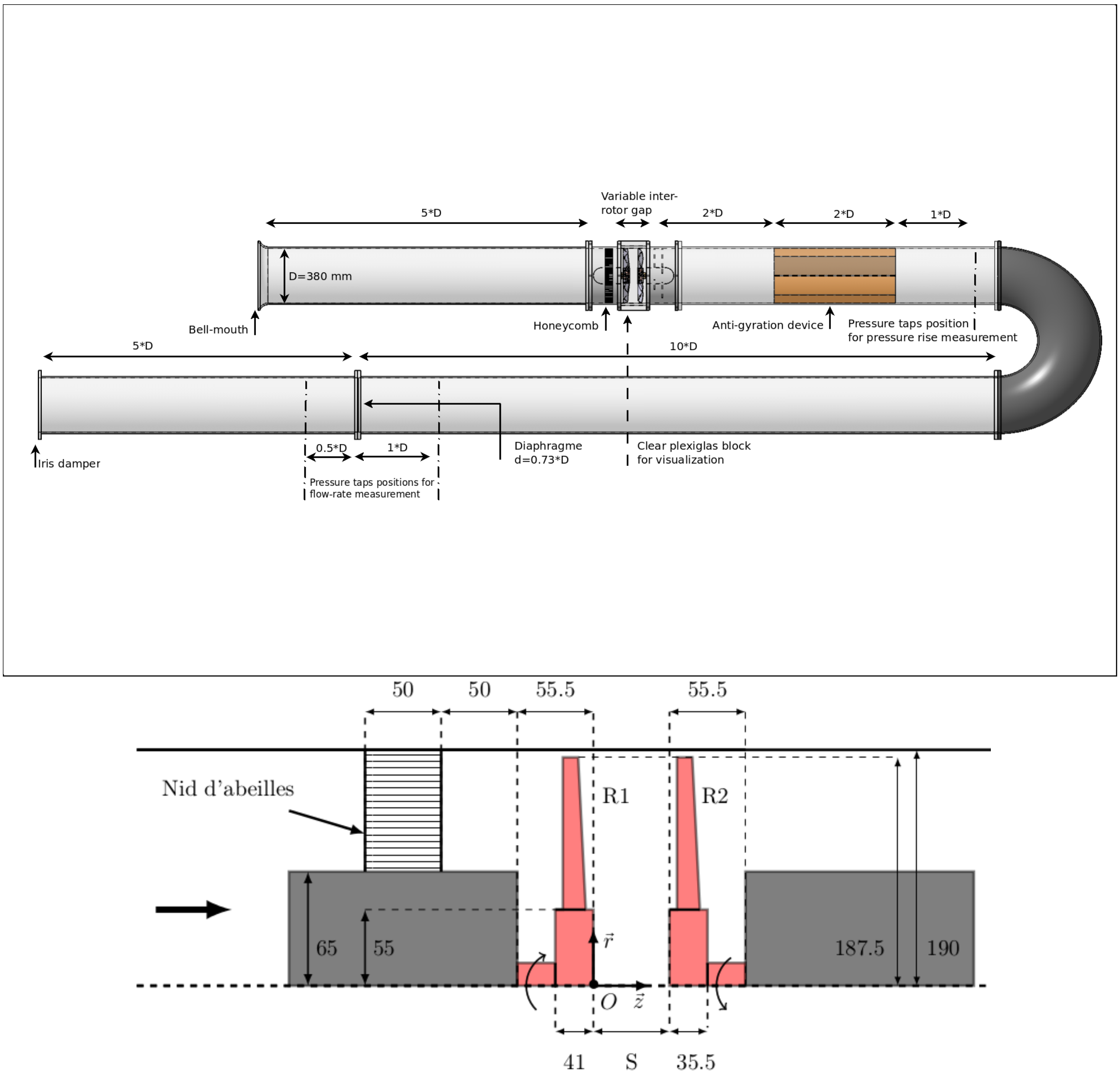

FIGURE *21 – Schéma du banc d'essai* AERO^{2}FANS, *cotes exprimées en mm.*

giration en forme d'étoile derrière lequel s'effectue la mesure de Δp_s, d'un dispositif de mesure de débit par diaphragme en conduite [7], et en sortie d'un obturateur à iris et d'un ventilateur d'extraction afin de varier la perte de charge du circuit au refoulement, partant le débit.

Notre système contrarotatif se compose de deux blocs moteurs indépendants usinés dans la masse contenant chacun un moteur AC sans balais sur lesquels les ventilateurs sont montés directement. Une pièce massive en aluminium, munie de microphones de pression et d'une fenêtre en verre pour les mesures par LDV s'intercale entre ces blocs, assurant une distance nulle entre ventilateurs. La distance entre les ventilateurs est alors variée grâce à des entretoises en plexiglas de diverses épaisseur.

On appelle FR le rotor amont, RR le rotor aval. Les vitesses de rotation en rpm [8] sont notées N_{FR} et N_{RR}. Elles sont non signées. Les vitesses angulaires correspondantes sont notées ω. On

---

[7] *ISO 5167-1 - Mesure de débit des fluides au moyen d'appareils déprimogènes – Partie 1 : Diaphragmes, tuyères et tubes de Venturi insérés dans des conduites en charge de section circulaire*. International Standards for Business, Government and Society, (2003).

[8] tours par minute.

utilisera le rapport des vitesses de rotation $\theta = N_{RR}/N_{FR}$. La distance entre rotors est notée S (voir Fig. 21).

Les principales grandeurs mesurées sont les élévations de pression statique Δp_s, les couples C sur chaque moteur[9], le débit volumique Q, la pression absolue et la température de l'air, les fluctuations de pression en paroi au moyen de microphones de pression à condensateur polarisé, et les vitesses axiales et tangentielles en un point par LDV. Toutes les mesures sont ramenées à une masse volumique $\rho = 1.21$ kg.m^{-3}. Les instruments et les incertitudes de mesures sont présentés dans Nouri *et al.* (2013). Le rendement statique est enfin défini par :

$$\eta_s = \frac{Q\Delta p_s}{C_{FR}\omega_{FR} + C_{RR}\omega_{RR}}$$

Méthode de conception

La plupart des études sur les systèmes contrarotatifs se rapprochant de notre cadre utilisent un second rotor tournant arbitrairement à une vitesse égale à celle du premier, avec un w_u également distribué entre rotors. Le second a de plus un “design” traditionnel identique au premier (souvent en « vortex libre »[10]), l'adaptation des deux rotors étant calculée sur la base du triangle de vitesse théorique au rayon moyen (Shigemitsu *et al.*, 2005; Furukawa *et al.*, 2007; Xu *et al.*, 2009; Shigemitsu *et al.*, 2013) ou du triangle de vitesse au rayon moyen en incluant des modèles de pertes (Cho *et al.*, 2009).

Notre approche a tout d'abord consisté à définir une méthode de conception plus satisfaisante, dans le but de *répondre à un cahier des charges* (débit / Δp_t), et de *redresser complètement l'écoulement* en sortie du système. Cette approche originale, décrite dans (Nouri *et al.*, 2012), se base sur le savoir-faire du laboratoire.

Conception d'un rotor seul

La méthode résumée ici est décrite en détails par Noguera *et al.* (1993) et a fait l'objet d'un logiciel développé et valorisé au laboratoire : MFT3D. Il s'agit d'une approche unidimensionnelle, seules les dépendances radiales étant prises en compte. Le logiciel permet de résoudre pour les turbomachines axiales d'une part le *problème indirect* (définir une géométrie de rotor en se donnant un cahier des charges) et d'autre part le *problème direct* (pour une géométrie de rotor donnée, prédire ses caractéristiques). Les calculs sont basés sur des corrélations empiriques concernant les déflexions et les pertes dans les grilles d'aubes de profil NACA-65 (Emery *et al.*, 1958), et sur des modèles semi-empiriques de pertes développés par Bakir (1992). Les corrélations employées sont synthétisées par Nouri (2012).

Conception du système contrarotatif

A partir des sources de MFT3D, écrit en VISUAL BASIC par F. Bakir, et traduites en C++ par S. Khelladi, j'ai développé un logiciel en C++ avec une interface graphique en QT (voir Fig. 22) incluant une extension pour les machines contrarotatives dont la démarche est la suivante.

Après s'être donné un cahier des charges consistant en un couple $\{Q, \Delta p_t\}$:

- On choisit arbitrairement les paramètres du rotor amont $w^o_{u,FR}$ et N_{FR}, puis on utilise la méthode inverse pour proposer un dessin.

---

[9] Fournis par l'électronique de commande des servo-moteurs AC synchrones à aimants permanents, ils ont été calibrés contre une mesure par couplemètre (Nouri, 2012).

[10] $\mathrm{d}h_0(r) = K$

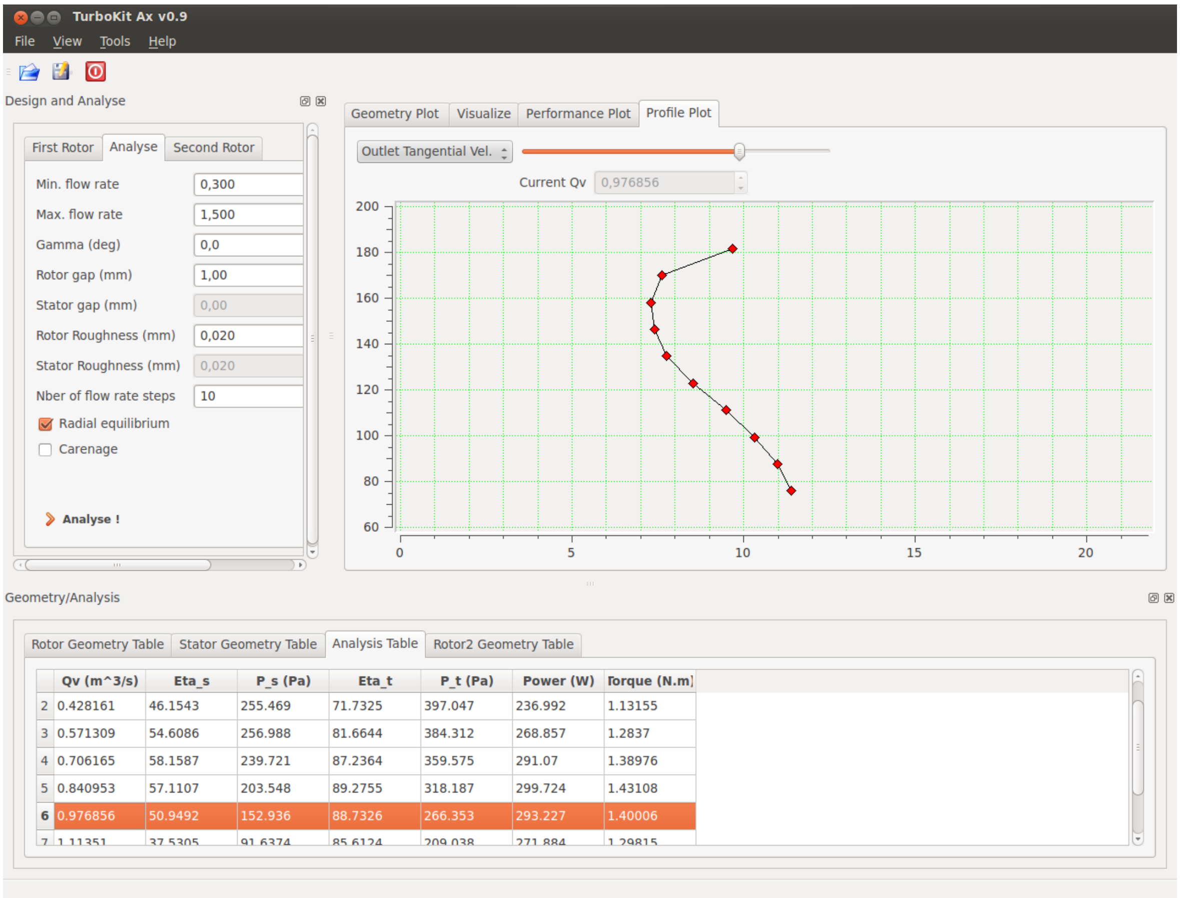

Min. flow rate 0,300
Max. flow rate 1,500
Gamma (deg) 0,0
Rotor gap (mm) 1,00
Stator gap (mm) 0,00
Rotor Roughness (mm) 0,020
Stator Roughness (mm) 0,020
Nber of flow rate steps 10
☑ Radial equilibrium
☐ Carenage

Current Qv 0,976856

	Qv (m^3/s)	Eta_s	P_s (Pa)	Eta_t	P_t (Pa)	Power (W)	Torque (N.m
2	0.428161	46.1543	255.469	71.7325	397.047	236.992	1.13155
3	0.571309	54.6086	256.988	81.6644	384.312	268.857	1.2837
4	0.706165	58.1587	239.721	87.2364	359.575	291.07	1.38976
5	0.840953	57.1107	203.548	89.2755	318.187	299.724	1.43108
6	0.976856	50.9492	152.936	88.7326	266.353	293.227	1.40006
7	1.11351	37.5305	91.6374	85.6124	209.038	271.884	1.29815

FIGURE *22 – Capture d'écran du logiciel de conception de machines axiales incluant les systèmes contrarotatifs.*

- On utilise alors la méthode directe pour analyser ce rotor. On obtient alors pour plusieurs débits une valeur de $w_{u,\,FR}$ ainsi que des profils radiaux des vitesses absolues axiale et tangentielle en sortie de FR : $c_{z,2,FR}(r)$ et $c_{\theta,2,FR}(r)$. Ces profils sont calculés sur typiquement 10 tubes de courant (exemple en Fig. 22).
- Le rotor aval RR est conçu d'une part pour fournir au fluide le reliquat de travail $w_{u,\,RR} = \Delta p_t - w_{u,\,FR}$ et d'autre part de sorte à redresser l'écoulement sortant de FR, *pour chaque tube de courant*. Sa vitesse de rotation N_{RR} est calculée à partir de l'équation d'Euler intégrée sur le rayon (avec une pondération par le débit et un rendement estimé η_g) :

$$\omega_{RR} = \frac{w_{u,\,RR}}{\eta_g} \left(\frac{1}{Q} \sum_{i=1}^{n_{tubes}} \left(r_i \; c_{\theta,2,FR}\,(i) \; dQ_i \right) \right)^{-1}$$

- Le rotor aval est alors dessiné avec les mêmes rayons internes et externes que le rotor amont par une méthode inverse adaptée à la contrainte $c_{\theta,2,RR}(r) = 0$, et en faisant l'hypothèse que le profil de vitesse
- Si la solution obtenue n'est pas réalisable (pales trop cambrées, trop serrées, vitesse de rotation de RR trop importante,...), on recommence à la première étape.

Systèmes contrarotatifs étudiés

Nous nous sommes fixé le cahier des charges suivant pour notre système contrarotatif :

- Un débit nominal $Q = 1$ m^3.s^{-1} ;

- Un travail massique utile $w_u = 347$ m^2.s^{-2}, correspondant à une élévation de pression totale si l'écoulement est parfaitement redressé $\Delta p_t = \rho w_u = 420$ Pa et à $\Delta p_s = 373$ Pa.
- Des vitesses de rotation autour de 2000 *rpm*.
- Un diamètre maximum de 380 mm.

Un premier système, dénommé ci-après HSN a été conçu pour la thèse de Nouri (2012) et a été étudié en détails (Nouri *et al.*, 2013). Nous avons également dessiné un stator adapté au rotor amont du système HSN, pour former le système RSS[11]. Ce dernier a été étudié par Wang *et al.* (2013a), qui comparent les performances globales et les niveaux de fluctuations de pression pariétale de HSN et RSS opérant aux mêmes points de fonctionnement.

Nous avons ensuite dessiné trois nouveaux systèmes contrarotatifs, Jw1, Jw2 et Jw3, en conservant le même cahier des charges, mais en variant certains paramètres de conception comme la répartition du travail effectué par chaque rotor, les vitesses de rotation et le calage des pales. Les premiers résultats comparant uniquement les performances globales des quatre systèmes contrarotatifs font l'objet des travaux de Wang *et al.* (2013b). Les principaux paramètres de ces cinq étages sont décrits en Tab. 2.1. Tous les rotors amonts étudiés ont été dessinés avec un « vortex constant ».[12] Les rotors avals obtenus n'ont pas une forme classique : ils ont des pales « concaves », avec une évolution de calage et de cambrure non monotone du pied à la périphérie (voir le profil typique de prérotation à laquelle sont soumis ces rotors en Fig. 22, ainsi que les caractéristiques des grilles d'aube du système HSN dans Nouri *et al.* (2013)).

	N_{FR}/N_{RR} (*rpm*)	θ	L %	Z_{FR}/Z_{RR}	R_{hub} (mm)	R_{tip} (mm)	Calage des pales du FR	Ψ_{FR}	Ψ_{RR}
HSN	2000/1800	0.9	61	11/7	55	187.5	faible	0.140	0.106
RSS	2000			11/13					
Jw1	2300/2200	0.96	59	10/7	65	187.5	fort	0.100	0.077
Jw2	1800/2600	1.44	49	13/7	65	187.5	faible	0.135	0.069
Jw3	2600/1100	0.42	77	10/7	65	187.5	fort	0.103	0.169

TABLE *2.1 – Paramètres dimensionnant des cinq étages.* $L = w_{u,FR}/w_u$ *;* Z *: nombre de pales ;* R *: rayon ;* $\Psi_{FR} = w_{u,FR}/\left(R_{tip}\omega_{FR}\right)^2$ *;* $\Psi_{RR} = w_{u\,RR}/\left(R_{tip}\omega_{RR}\right)^2$.

Performances globales à distance entre rotors fixée

Les performances globales pour ces cinq étages (quatre contrarotatifs et un étage rotor / stator) sont tracées en Fig. 23, ainsi que les courbes de puissance absorbées en Fig. 24. Nous présentons ici plus particulièrement le système HSN et l'étage RSS comprenant les mêmes rotors amonts (Nouri *et al.*, 2013; Wang *et al.*, 2013a).

Comparaison des performances globales entre les étages HSN et RSS

Expérimentalement, on obtient pour le rotor amont seul $\Delta p_s = 152 \pm 3$ Pa pour $Q = 1$ m^3.s^{-1} et $N_{FR} = 2000$ *rpm* ; et un rendement statique assez faible $\eta_s = 45.7 \pm 1\%$. La valeur obtenue est en bon accord avec la valeur prédite par l'analyse directe du code de dimensionnement. La courbe de pression statique est très plate autour du débit de conception. En ajoutant le stator à $S = 15$ mm en aval, l'élévation de pression mesurée à $Q = 1$ m^3.s^{-1} est $\Delta p_s = 171 \pm 3$ Pa, soit 6% en deçà de la prévision, pour un rendement statique $\eta_s = 51.6 \pm 1\%$. Le gain en points de rendement de +6 est lié d'une part à l'augmentation de Δp_s, mais également d'autre part à

---

[11] pour "Rotor-Stator Stage".

[12] $\mathrm{d}h_0(r) = K\,r$

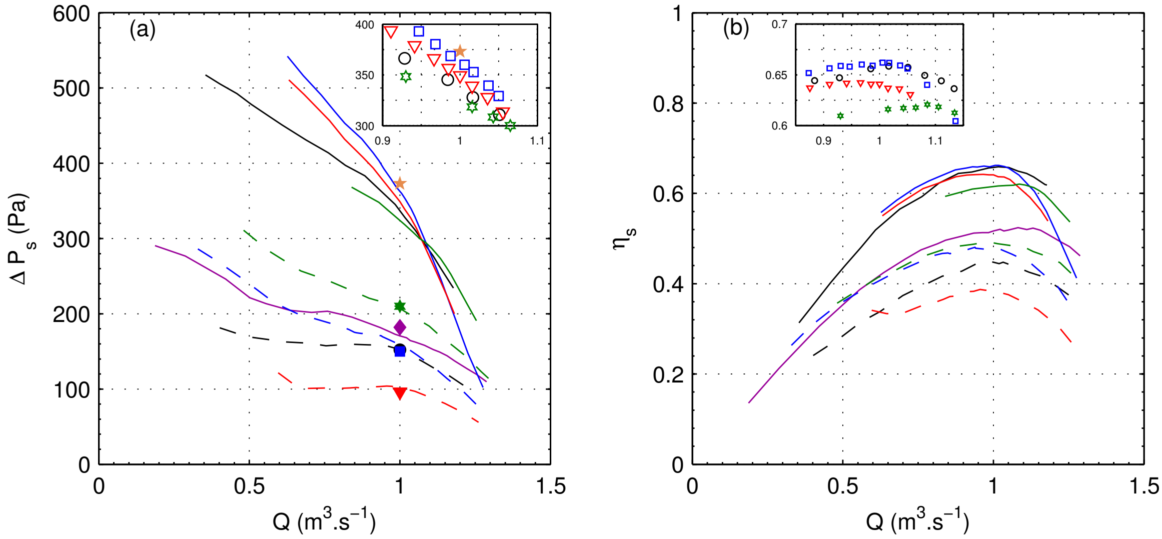

FIGURE *23 – Elévation de pression statique (a) et rendement statique (b) en fonction du débit volumique Q pour les quatre systèmes contrarotatifs (lignes pleines) et les rotors amonts fonctionnant seuls (lignes tiretées). Les symboles pleins sont les valeurs prédites par le code de dimensionnement. En noir et ○ :* HSN*, en bleu et □ :* Jw1*, en rouge et ▽ :* Jw2 *et en vert et ✡ :* Jw3*. A titre de comparaison, les performances de* RSS *sont également tracées en pourpre. Les encarts sont des zooms proches du débit de conception $Q = 1$ m^3.s^{-1}. La taille des symboles correspond à l'incertitude évaluée dans Nouri* et al. *(2013).*

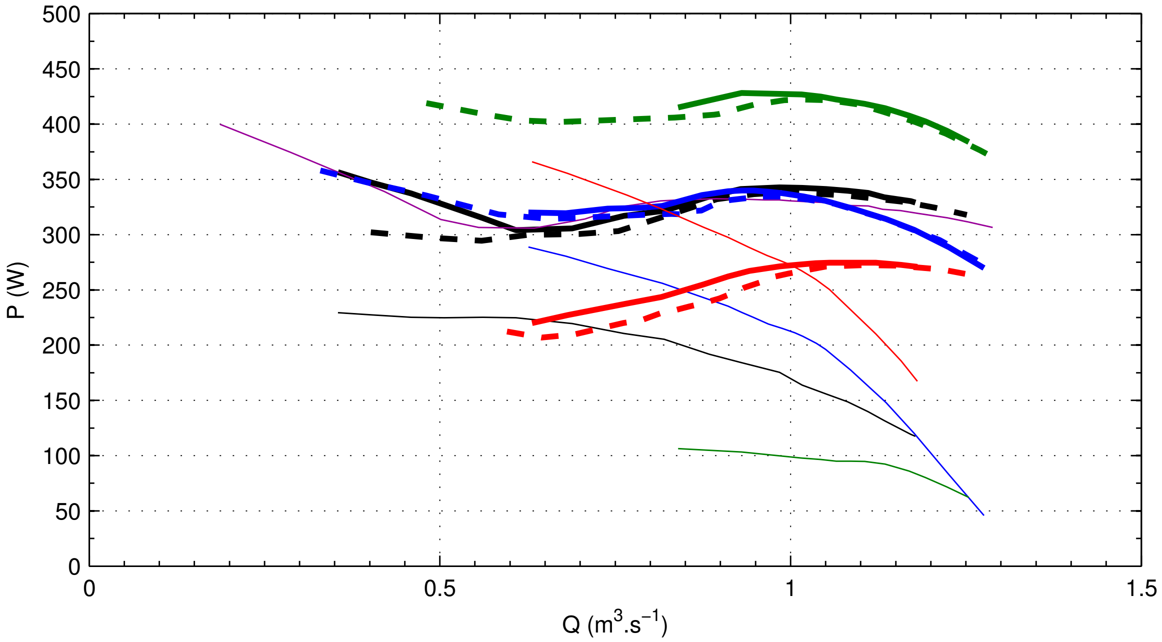

FIGURE *24 – Puissance mécanique appliquée sur les rotors en fonction de Q pour les rotors amonts fonctionnant en système contrarotatif (lignes épaisses) ou fonctionnant seuls (lignes tiretées) et les rotors avals (lignes fines). En noir :* HSN*, en bleu :* Jw1*, en rouge :* Jw2 *et en vert :* Jw3*. La puissance pour* RSS *est également tracée en pourpre. La distance entre rotors est la distance minimale $S = 10$ mm.*

une diminution de la puissance consommée par le rotor de 337 ± 5 à 330 ± 5 W. On remarque enfin que la courbe de pression statique devient plus pentue.

L'étage contrarotatif, pour $S = 10$ mm, fournit une élévation de pression statique $\Delta p_s = 335 \pm 5$ Pa, soit environ 10% en deçà de la prévision, pour un rendement statique $\eta_s = 65.4 \pm 1\%$, soit un gain en points de rendement de +20 par rapport au rotor seul. On a également une plage de débits avec $\eta_s \geqslant 60\%$ de 0.76 à 1.15 fois le débit nominal. La courbe de pression devient beaucoup plus raide, confirmant l'observation de Shigemitsu *et al.* (2009). Cette fois-ci, en revanche, la présence du rotor aval se traduit par une augmentation de la puissance consommée par le rotor amont d'environ 7 W, de l'ordre de l'incertitude de mesure. Cette légère augmentation de puissance sur le rotor amont est observée pour les quatre systèmes contrarotatifs (voir Fig. 24).

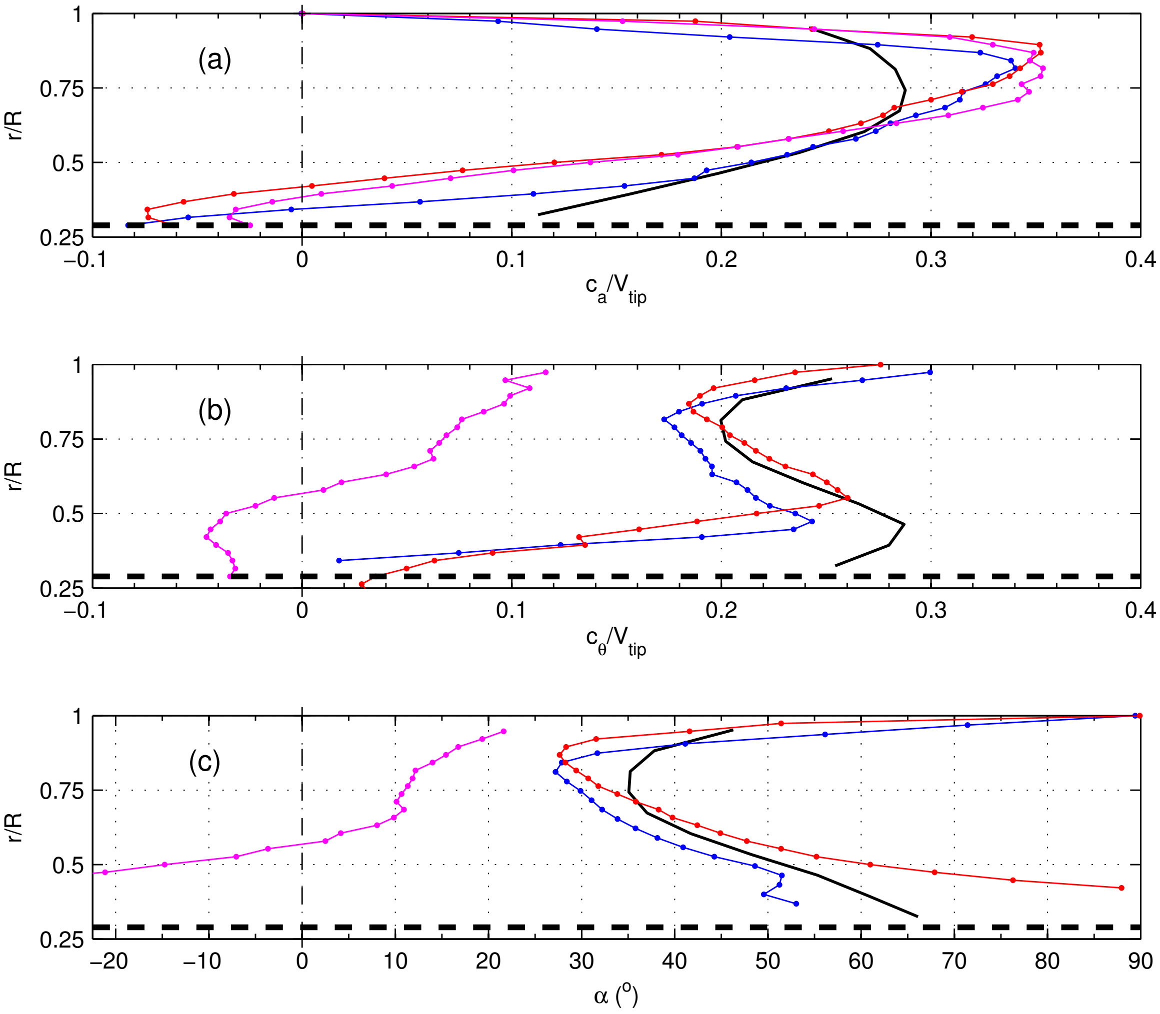

FIGURE 25 – *Profils radiaux des composantes moyennes de vitesse axiale (a), tangentielle (b) et de l'angle entre la vitesse dans le référentiel absolu et la direction axiale (c), pour* HSN, $\theta = 0.9$, $Q = 1\ m^3.s^{-1}$, $N_{FR} = 2000$ *rpm* ($V_{tip} = 39.2 m.s^{-1}$). *En noir : prédiction en aval de FR. En rouge : FR fonctionnant seul, mesure à* 5 *mm du rotor. En bleu : mesure entre les deux rotors,* $S = 10$ *mm mesure à* 5 *mm en aval de FR. En magenta : mesure à* 5 *mm en aval de RR.*

Champs de vitesses dans le système HSN

L'étude des profils moyens de vitesse entre les rotors et en aval du système, tracés en Fig. 25, permettent, d'une part de comparer l'étage effectivement réalisé à l'étage souhaité lors de l'étape de conception, et d'autre part de mettre en relief cette forte interaction entre rotors.

Tout d'abord, lorsque FR est utilisé seul, les profils de vitesse mesurés (en rouge) sont qualitativement proches de ceux donnés par l'analyse directe du logiciel MFT3D (en noir), avec un profil de vitesse axiale présentant un pic vers la moitié de l'envergure de la pale, et un profil de vitesse tangentielle en forme de S. On remarque toutefois que les profils mesurés sont décalés vers la partie externe de la pale, et que l'on a une recirculation significative en pied de pale[13]. Les angles en sortie de rotor FR sont assez proches de ceux donnés par l'analyse directe du logiciel MFT3D.

Lorsqu'on ajoute le rotor aval, à une distance $S = 10$ mm, on a une modification importante des profils (en bleu), liée à un phénomène d'aspiration de RR (la recirculation est supprimée, les profils se décalent vers le pied de pale) et à un ralentissement de la composante giratoire (pré-rotation induite par RR en sens contraire). De plus, les fluctuations de vitesse (non tracées) augmentent de 40% pour la composante c_θ. En conséquence, l'angle α de la vitesse entre les rotors est partout 5 à 10 ° inférieur à la valeur pour laquelle RR a été dessiné : en aval de RR, la vitesse tangentielle est certes faible, mais le redressement est loin d'être parfait. Le profil de vitesse axiale (en magenta) est toutefois similaire à celui en aval de FR, justifiant une des hypothèses de conception.

---

[13] Le rayon du moyeu est inférieur au rayon de la cage contenant le moteur pour HSN ; cela a été corrigé pour les autres systèmes, supprimant cette recirculation, sauf pour JW3 qui en présente une très légère.

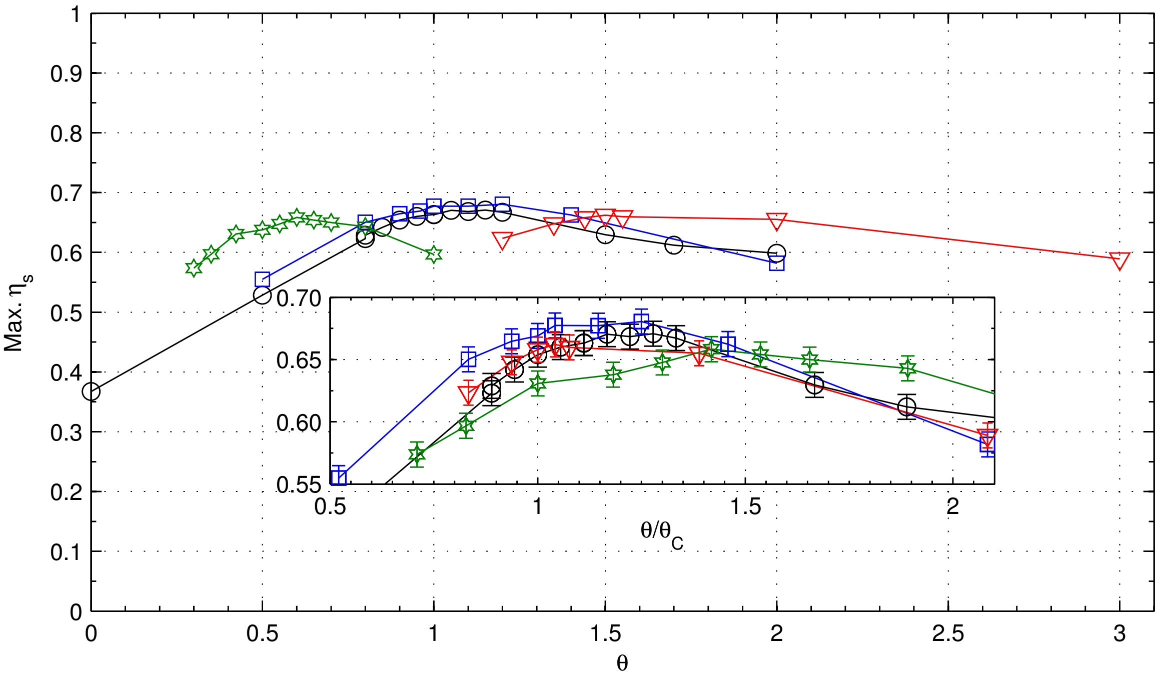

FIGURE 26 – *Rendement statique maximum en fonction de θ pour les quatre systèmes contrarotatifs.* ○ *:* HSN, □ *:* JW1, ▽ *:* JW2 *et* ✡ *:* JW3. *En encart, rendement statique maximum en fonction de θ/θ_c avec θ_c la valeur de conception, voir Tab. 2.1.*

Flexibilité d'un système contrarotatif

En accélérant le rotor aval, *i.e.* en augmentant le rapport de vitesse θ, on améliore la performance du système HSN. Le maximum des maxima de rendement statique vaut $67 \pm 1\%$ pour $\theta = 1.05$ (voir Fig. 26), c'est aussi pour cette valeur de θ que l'écoulement aval est complètement redressé (Nouri *et al.*, 2013). Cette étude de l'influence de θ fait apparaître une autre propriété remarquable, commune à nos quatre systèmes : le rendement statique maximum est supérieur à 60% pour une plage de θ étonnamment grande, de $\theta \simeq 0.8\theta_c$ à $\theta \simeq 2\theta_c$, avec θ_c la valeur de conception.

Effets de la distance sur les interactions entre rotors

Les cas étudiés ci-dessus se limitent à une distance entre rotors faible $S = 10$ mm, soit 17% de la corde au rayon moyen MSC pour le rotor amont du système HSN [14]. Pour cette distance, on a une interaction importante entre rotors, se traduisant par une augmentation de la puissance absorbée par FR, surtout à débit partiel (Fig. 24), et par une modification des profils de vitesse et des fluctuations de vitesse entre les rotors (Fig. 25). Nous étudions ici l'influence de cette distance sur l'interaction entre rotors.

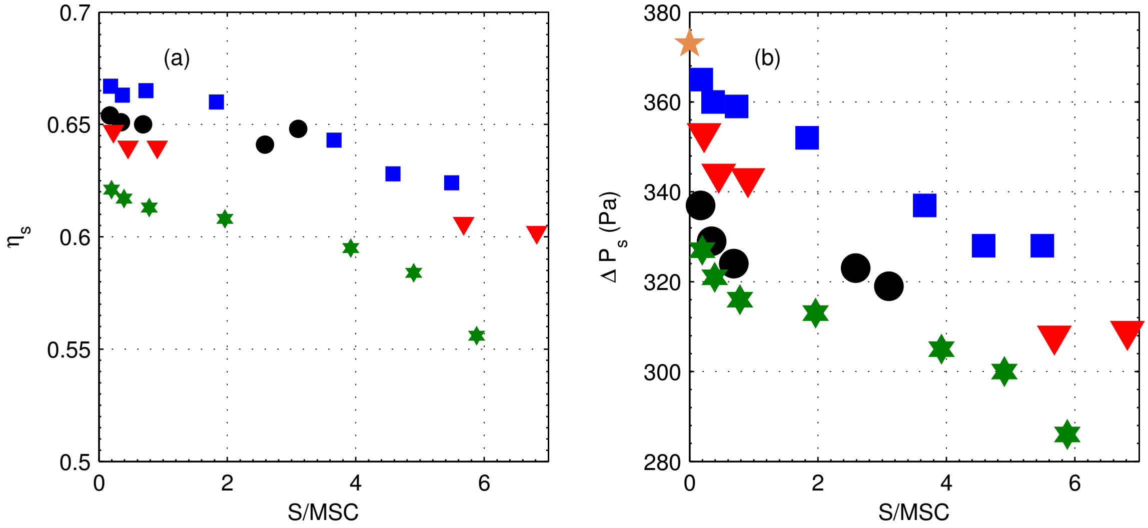

FIGURE 27 – *Rendement statique (a) et élévation de pression statique (b) à $Q = 1\ m^3.s^{-1}$ en fonction de la distance entre rotors S (voir Fig. 21) normalisée par la corde au rayon moyen MSC du rotor amont pour les quatre systèmes contrarotatifs.* ○ *:* HSN, □ *:* Jw1, ▽ *:* Jw2 *et* ✡ *:* Jw3. *La taille des symboles correspond à l'incertitude évaluée dans Nouri* et al. *(2013).*

L'évolution des performances globales au débit de conception avec la distance S est tracée en Fig. 27. Les valeurs de Δp_s et de η_s diminuent de façon monotone pour les quatre systèmes, contrairement aux résultats de Liu *et al.* (2011) montrant une distance optimale de $S = 2MSC$. La chute de rendement est rapide à basse distance avant de devenir plus régulière (-1 point de rendement entre $S \simeq 0.2MSC$ et $S \simeq 2MSC$, -4 points pour $S \simeq 5MSC$). La chute de Δp_s suit une évolution similaire.

La zone entre les deux rotors est une zone où les sillages du rotor amont sont susceptibles

---

[14] On a pour les rotors amonts de HSN : $MSC = 58$ mm, de Jw1 : $MSC = 54.6$ mm, de Jw2 : $MSC = 44$ mm et de Jw3 : $MSC = 51$ mm.

d'interagir avec des effets potentiels créés par la présence du rotor aval. L'analyse du niveau de fluctuations de vitesse et de pression, et du contenu spectral de ces fluctuations peuvent fournir des renseignements utiles sur l'existence de ces interactions et sur leur sensibilité à la distance entre rotors. Les spectres de pression pariétale et les fonctions de corrélations associées sont tracées en Fig. 28 pour deux distances dans le cas du système HSN. D'autres mesures à des distances intermédiaires sont discutées dans Wang *et al.* (2013a), et des analyses de signaux de LDV sont présentés dans Nouri (2012); Nouri *et al.* (2013).

Le résultat principal est tout d'abord l'existence d'interactions non-linéaires entre les fréquences de passage de pales de chaque rotor se traduisant par des pics supplémentaires (sommes et différences de toutes les harmoniques), très visibles à la distance minimale $S = 0.17 MSC$. Les spectres sont dominés par les pics correspondant à RR. Les fonctions d'autocorrélations et l'analyse du retard dans la cross-corrélation montrent une structure très cohérente tournant à la vitesse du rotor aval. D'autre part, ces interactions disparaissent complètement pour $S = 2.58 MSC$ et sont très nettement atténuées dès $S = 0.69 MSC$.

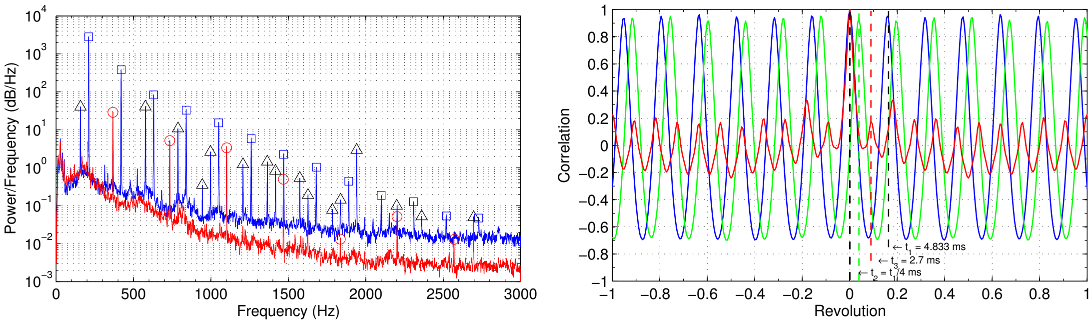

FIGURE *28 – A gauche : densité spectrale de puissance des fluctuations de pression* 5 *mm en aval de FR pour* HSN *à $\theta = 0.9$, $Q = 1$ $m^3.s^{-1}$, $N_{FR} = 2000$ rpm. Courbe bleue : $S = 10$ mm ($S/MSC = 0.17$), courbe rouge : $S = 150$ mm ($S/MSC = 2.58$).* ○ *: fréquence de passage de pale et harmoniques de FR,* □ *: fréquence de passage de pale et harmoniques de RR,* △ *: interactions entre ces fréquences. A droite : fonctions d'autocorrélation et de cross-corrélation des fluctuations de pression. Les microphones sont situés* 5 *mm en aval de FR pour* HSN *à $\theta = 0.9$, $Q = 1$ $m^3.s^{-1}$, $N_{FR} = 2000$ rpm, avec un angle de* 90 ° *entre les microphones* 1 *et* 2*. Le temps est normalisé par la période de rotation de FR. Courbe bleue : autocorrélation microphone* 2*, à $S = 10$ mm ($S/MSC = 0.17$). Courbe verte : cross-corrélation microphones* 1 *et* 2 *aux mêmes conditions. Courbe rouge : autocorrélation microphone* 2*, à $S = 150$ mm ($S/MSC = 2.58$).*

3 Axe 3 : Dynamique et instabilités en écoulements diphasiques

Cet axe regroupe un ensemble de travaux expérimentaux portant sur la dynamique d'écoulements turbulents avec plusieurs phases fluides, dans des géométries les plus simples possibles. Ces travaux sont classés en deux catégories, selon qu'il y ait transfert de masse entre les phases.

3.1 Ecoulements de fluides non miscibles (2006-2011)

Dispersion liquide /liquide en régime turbulent

Une première étude (2006–2007) porte sur la dispersion de deux liquides non-miscibles en régime turbulent, dans le dispositif de Taylor-Couette décrit au § 1.2 p. 42. Les liquides sont une huile de masse volumique $\rho_o = 800$ kg.m^{-3}, de viscosité dynamique $\mu_o = 3.0 \times 10^{-3}$ Pa.s, et une solution acqueuse d'Iodure de Sodium (NaI) à 510 g.L^{-1}[1] afin d'avoir un indice de réfraction identique dans les deux phases (Budwig, 1994). Le processus de dispersion est observé par LIF : la phase acqueuse, de masse volumique $\rho_a = 1500$ kg.m^{-3} et de viscosité dynamique $\mu_a = 2.0 \times 10^{-3}$ Pa.s, est marquée par un traceur fluorescent (Rhodamine B), sensible à la longueur d'onde du laser $Nd : YAg$ (vert, 532 nm) et réémettant dans le jaune. En utilisant un filtre optique passe-bas de longueur de coupure 550 nm, on peut ainsi isoler les phases.

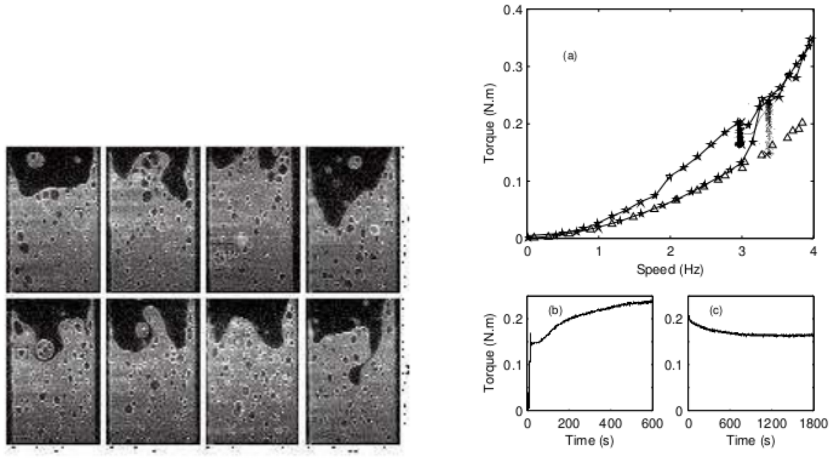

(1) (2)

FIGURE *29 – (1) Images LIF d'une dispersion liquide /liquide en contrarotation (Ro* = 0*) à* 2 *Hz, dans le plan PIV de la Fig. 16. Les régions sombres correspondent à l'huile, et les brillantes à la solution acqueuse. Le cylindre extérieur est à droite. (2) (a) : Couple en fonction de la fréquence pour de l'huile pure* ($\triangle$) *et une solution à* 33% *de solution acqueuse en volume* ($\star$)*, pour Ro* = 0*. La vitesse de rotation augmente de* 0.2 *Hz toutes les* 60 *s de* 0 *à* 4 *Hz, puis diminue à* 0 *Hz. Les points sont les traces des expériences transitoires (b) et (c). (b) : A partir d'un état de repos, la vitesse est imposée brusquement à* 3.5 *Hz. (c) : Dans cet état depuis 20 minutes, la consigne de vitesse est descendue à* 3 *Hz.*

Les évolutions du couple et des interfaces entre les fluides sont observées en régime contrarotatif (Ravelet *et al.*, 2007). Un exemple de visualisation proche du seuil de dispersion et des résultats de mesures de couple pour une concentration volumique donnée sont présentés en Fig. 29. Les deux fluides ont des propriétés proches de l'eau, de sorte que les écoulements

---

[1] Contenant des traces de thiosulfate de sodium ($Na_2S_2O_3$) afin d'éviter une coloration jaunâtre comme suggéré par Narrow *et al.* (2000).

considérés ici sont turbulents. Partant d'un état au repos avec deux fluides séparés par une interface horizontale et augmentant progressivement la vitesse, on observe à 1.5 Hz la formation de quelques gouttes d'huile dans la phase acqueuse. En augmentant encore la vitesse, on observe de plus en plus de gouttes d'huile dans la phase acqueuse et la présence de gouttes multiples dans l'huile, *i.e.* des gouttes d'huile dans des gouttes de phase acqueuse dans l'huile (voir Fig. 29_1). Puis on observe trois régions : une phase continue d'huile avec des gouttes acqueuses, une « mousse » avec des gouttes multiples, et une phase acqueuse continue avec des gouttes d'huile. Au delà de 3.5 Hz, l'écoulement est complètement dispersé.

La puissance dissipée est plus importante en écoulement diphasique dispersé, comme illustré en Fig. 29_2. Le système présente de l'hystérésis et des comportements oscillants à temps très long, pouvant être liés à de l'inversion de phase (Piela *et al.*, 2006). Enfin, nous avons étudié la puissance dissipée massique en régime dispersé établi en fonction de la fraction volumique de phase acqueuse : le maximum est un facteur 2 par rapport au cas monophasique pour une fraction volumique de 33% d'eau. Les résultats sont bien reproduits par le modèle de viscosité effective de Pal (2001).

Rupture d'une bulle

Une seconde étude (2007–2011) porte sur la rupture d'une bulle d'air plongée dans un écoulement moyen turbulent d'eau (Ravelet *et al.*, 2011a).

Position du problème

En l'absence de glissement moyen important entre les phases, comme dans le cas de bulles d'air en microgravité ou bien de gouttes d'huile dans l'eau avec un faible contraste de densité, la déformation d'une inclusion dans un écoulement turbulent est due à l'excitation de modes de surface par la turbulence, en particulier par les structures de taille comparable à son diamètre (Risso & Fabre, 1998; Risso, 2000). Le mode principalement excité est l'harmonique sphérique *axisymétrique* d'ordre 2, dont la fréquence propre d'oscillation et le taux d'amortissement sont assez bien prédits par la théorie linéaire développée par Lamb (1932) puis Miller & Scriven (1968). Pour des inclusions de forme moyenne proches de la sphère, en l'absence de glissement important entre phases, la dynamique de la forme est bien reproduite par un modèle d'oscillateur linéaire forcé par les fluctuations turbulentes, amplifiant certaines fréquences et filtrant les autres (Risso, 2000). La rupture se produit alors lorsque la déformation atteint une valeur critique, comme l'ont montré Risso & Fabre (1998), et peut être causée par des mécanismes de résonnance. Les statistiques des déformations et des taux de ruptures sont alors radicalement différentes de celles de la turbulence.

La question à laquelle nous nous sommes intéressé au cours de ce travail est de savoir si ce type de mécanismes est toujours à l'œuvre pour de grandes bulles d'air dans de l'eau (sur terre). Dans ce cas, une bulle n'est plus sphérique, mais possède une déformation moyenne axisymétrique autour de la direction verticale ; la fréquence propre et l'amortissement des petites déformations sont modifiées (Subramanyam, 1969) ; et les instabilités de sillage conduisent à des trajectoires non rectilignes (Meiron, 1989; Ellingsen & Risso, 2001). Les observations de Veldhuis *et al.* (2008) montrent enfin dans ce cas que les oscillations de forme peuvent être dominés par des modes non-axisymétriques. Notre objectif est d'étudier les mouvements et déformations jusqu'à rupture d'une bulle soumise à sa propre vitesse d'ascension, à ses oscillations de trajectoire et à des fluctuations turbulentes externes.

Dispositif expérimental et traitement d'images

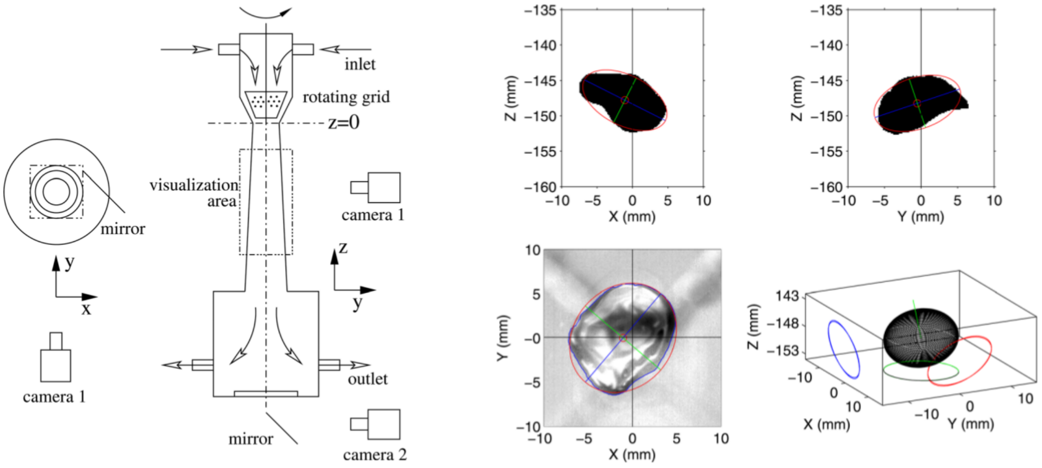

(a) (b)

Figure 30 – *(a) : Schéma de l'expérience vue de dessus et de côté. (b) Exemple d'analyse d'image. En haut à gauche, vue de côté par la caméra 1 dans le plan x ; z. L'image est binarisée (voir texte). L'ellipse équivalente est tracée en rouge, son centre de masse est le point rouge, ses grand et petit axes sont respectivement représentés par les lignes bleues et vertes. En haut à droite, vue de côté par la caméra 1 dans le plan y ; z, mêmes représentations. En bas à gauche, vue de dessous par la caméra 2 dans le plan x ; y, avec le contour actif "snake" tracé en bleu, et l'ellipse équivalente ajustée sur ce contour, dont les caractéristiques ont été représentées avec les conventions précédentes. En bas à droite, ellipsoïde reconstruit à partir des trois vues précédentes. Les trois ellipses utilisées sont tracées dans leur plan en traits pleins, et les projections de l'ellipsoïde sur les trois plans en traits tiretés (on ne voit pas la différence). La ligne verte donne la direction du petit axe de l'ellipsoïde.*

Nous avons construit le dispositif expérimental présenté en Fig. 30a. L'écoulement est en circuit fermé et la partie utile consiste en un tube conique axisymétrique vertical en plexiglas, divergeant avec un demi-angle au sommet de 2.7°. La bulle est injectée en bas de ce cône et est soumise à un écoulement descendant. La forme conique a un effet stabilisant permettant de piéger une bulle dans la zone de visualisation sans avoir à régler très finement le débit. Une grille tournante est placée dans un convergent en amont afin de générer des perturbations turbulentes. La faible rotation permet de maintenir la bulle vers le centre du tube. Les bulles sont injectées au moyen d'une seringue motorisée, à travers un tuyau coudé muni de divers orifices et inclinable horizontalement. En adaptant le diamètre de l'orifice, l'inclinaison et la vitesse de la seringue, on arrive à produire des bulles de diamètre équivalent[2] $d = 9.3$ mm à ± 0.3 mm près.

L'écoulement turbulent en absence de bulle est caractérisé par PIV rapide. La trajectoire et la déformation d'une bulle sont analysées à partir d'images acquises simultanément dans trois plans perpendiculaires. L'éclairage se fait par transmission, au moyen de plaques de LED. Un ellipsoïde équivalent est reconstruit à partir des trois vues perpendiculaires selon la méthode décrite par Kayikcioglu *et al.* (2000). Pour les vues de côtés de la caméra 1, une simple binarisation est effectuée, après soustraction et normalisation par une image de fond sans bulle. Pour extraire l'information de la troisième vue, une méthode plus complexe a été mise en place,

---

[2] Diamètre d'une sphère de même volume d'air injecté.

à cause de la présence de la grille tournante et d'un contraste moins bon. Nous soustrayons tout d'abord une image de fond synchronisée. Puis, les contours de la bulle sont détectés avec l'algorithme SuSan (Smith & Brady, 1997), implémenté en C. Le contour obtenu présentant des lacunes, un contour actif "greedy snake" (Ji & Yan, 2002) est alors utilisé : il s'agit d'une sorte d'« élastique » qui vient se contracter autour des puits de potentiel dans une image de contours. Un exemple du traitement complet est présenté en Fig. 30b, ainsi que des films sur `http://hal.archives-ouvertes.fr/hal-00609136`.

Caractérisation de l'écoulement moyen et des propriétés statistiques turbulentes

L'écoulement moyen et les propriétés statistiques de la turbulence en absence de bulles sont tout d'abord mesurés dans plusieurs plans horizontaux et verticaux au moyen de PIV résolue en temps. L'écoulement moyen dans la direction verticale est un jet axial turbulent avec un profil assez uniforme, de vitesse 0.3 m.s^{-1} au centre de la zone de visualisation. Le taux de turbulence varie de 10% à 20% dans la région centrale. A cet écoulement se superpose un écoulement en rotation solide dans la région centrale, dont les fluctuations sont de l'ordre de 20% de la vitesse axiale. La turbulence est donc plutôt isotrope. La taille typique des bulles ($d \simeq 9$ mm) se situe dans la zone inertielle, l'échelle intégrale et la micro-échelle de Taylor étant respectivement de l'ordre de 30 mm et 5 mm. La fréquence propre du mode 2 pour cette taille de bulle d'air dans de l'eau est $f_2 = \frac{1}{2\pi}\sqrt{\frac{96\sigma}{\rho d^3}} \simeq 15$ Hz (avec ρ la masse volumique de l'eau et σ la tension interfaciale, voir Miller & Scriven, 1968). Du point de vue temporel, là aussi, le temps caractéristique d'oscillation de la bulle est de l'ordre de grandeur des temps de retournement des structures turbulentes.

La contribution de la turbulence à la déformation de la bulle est estimée au moyen d'un nombre de Weber turbulent local instantané $We_t(x,t)$, basé sur la fonction de structure d'ordre 2 à l'échelle d'une bulle. Sa densité de probabilité en temps est asymétrique, et présente une

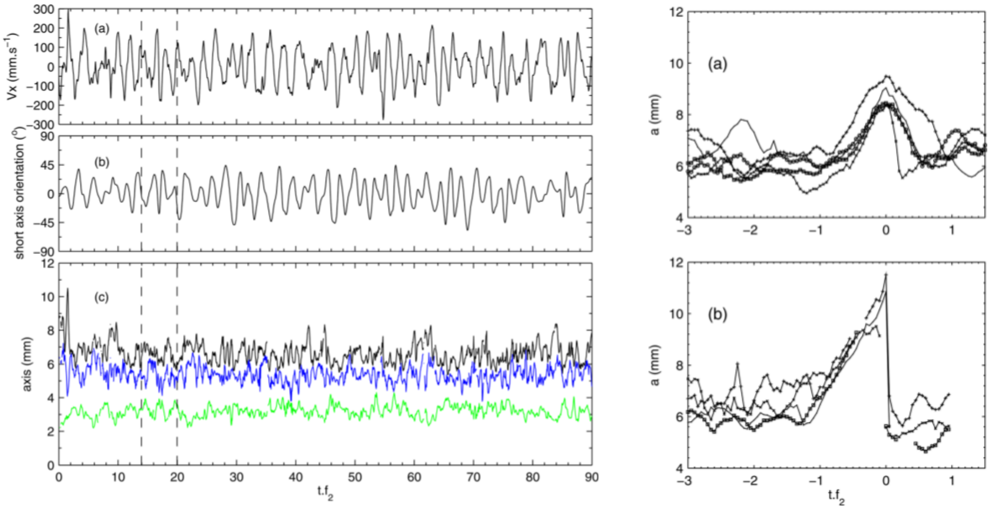

(1) (2)

Figure *31 – (1) Signaux de vitesse selon x dans le plan horizontal (a), de l'orientation par rapport à l'axe vertical du petit axe de l'ellipsoïde équivalent (b), et des longueurs des axes principaux de l'ellipsoïde équivalent (c). (2) Signaux pour différentes bulles de la longueur du grand axe lors de séquences de grandes déformations (a) ou de rupture (b), synchronisés sur le maximum de déformation. Les temps sont adimensionnés par $f_2 \simeq 15$ Hz.*

queue exponentielle vers les grandes valeurs : la valeur moyenne au centre du volume de mesure est $\langle We_t \rangle \simeq 1.3$, et des valeurs $We_t \geqslant 10$ sont atteintes pendant des temps significatifs, avec une distribution de temps d'attentes entre grands évènement de type loi de Poisson.

Dynamique des grandes déformations et mécanismes de rupture

Des signaux typiques de la taille des axes de l'ellipsoïde reconstruit, et de vitesse et d'orientation du petit axe sont tracés en Fig. 31_1. Dans cette expérience, la bulle subit tout d'abord une déformation moyenne imposée par son glissement par rapport au liquide. La forme moyenne est un ellipsoïde axisymétrique autour de son petit axe aligné sur la verticale, de rapport d'aspect élevé (2). En outre, sa trajectoire présente des oscillations quasi-périodiques, de fréquence 8.5 Hz

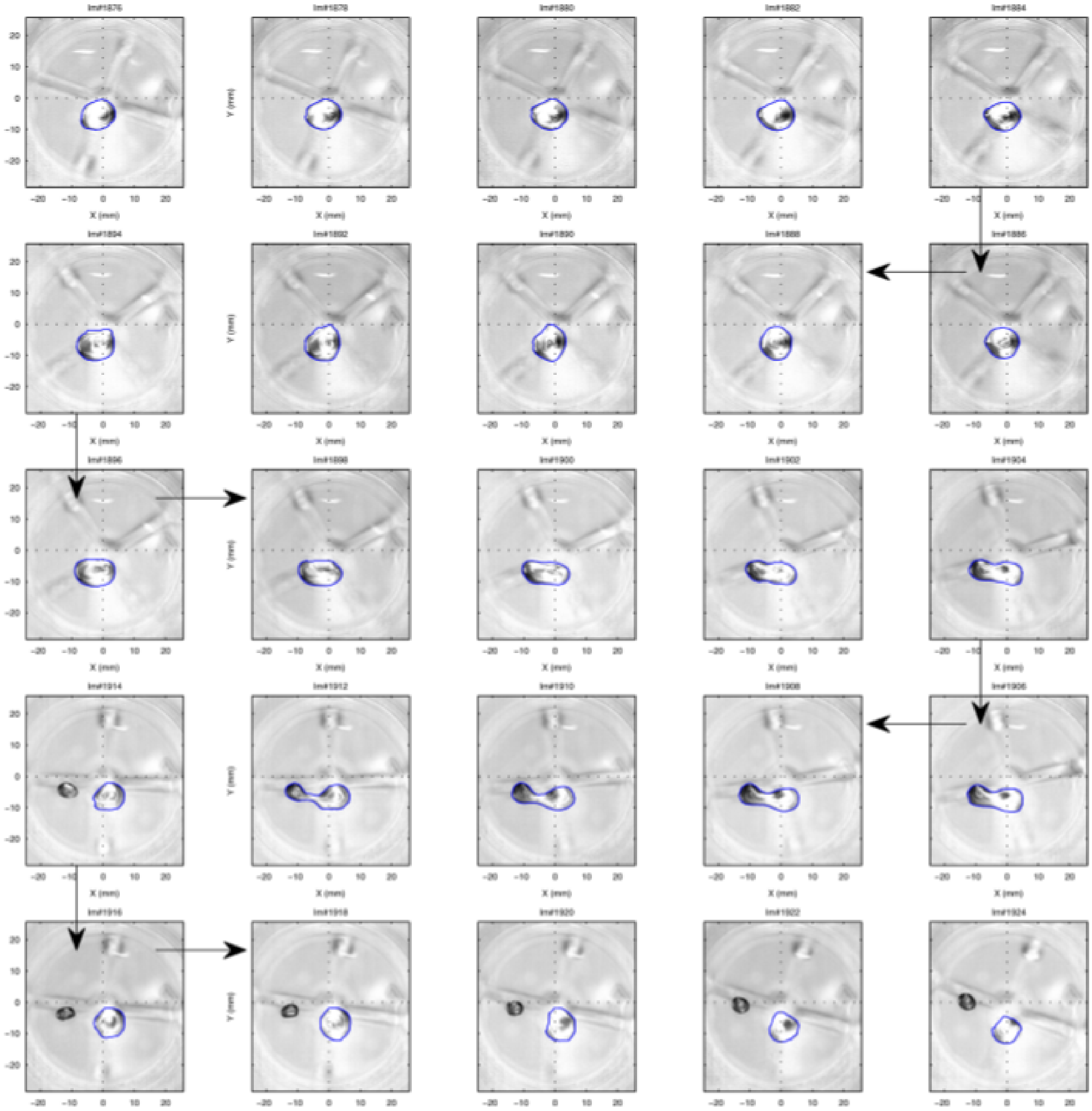

FIGURE *32 – Exemple de rupture observée dans le plan* x *;* y *(caméra 2). Le contour détecté est superposé en bleu. Temps entre chaque image :* $1/150$ *s (soit* $(10 f_2)^{-1}$*). La séquence se suit de gauche à droite pour la première ligne, puis de droite à gauche,* etc*, en suivant les flèches.*

(soit un nombre de Strouhal basé sur le diamètre et la vitesse moyenne de 0.27). Ces deux observations sont cohérentes avec les nombres de Reynolds ($Re_b \simeq 3000$) et de Weber ($We_b \simeq 12$) moyens basés sur la taille de la bulle et la vitesse axiale (Ellingsen & Risso, 2001).

Au contraire, les déformations de la bulle ne montrent aucune oscillation périodique contrairement aux observations effectuées sans glissement significatif entre phases. Toutefois, l'analyse des cross-corrélations entre les trois axes révèle une part de dynamique déterministe et fait clairement apparaître l'échelle de temps basée sur f_2. Le petit axe, vertical en moyenne, joue de plus un rôle particulier dans le cas présent : les déformations importantes sont non-axisymétriques et se produisent dans le plan perpendiculaire au petit axe. Des portions de signaux synchronisés sur une grande déformation et sur une rupture sont tracés en Fig. 31_2, ainsi qu'une séquence d'images dans le plan horizontal menant à la rupture en Fig. 32. On remarque ainsi que les grandes déformations ou ruptures ne correspondent aucunement à des amplifications successives ou à des oscillations à la fréquence f_2, mais que ces phases montrent toutefois une échelle de temps typique de cet ordre de grandeur, ce qui pourrait être le comportement d'un oscillateur très amorti. On observe enfin que la rupture se produit dans un plan *horizontal*, pour des allongements supérieurs à 2 fois le diamètre de la bulle.

En conclusion, par rapport aux cas sans glissement (bulles en microgravité, gouttes d'huile, *etc*) bien décrits par Risso (2000), la situation est radicalement différente. Les grandes déformations menant à la rupture ne sont pas axisymétriques et se produisent dans un plan horizontal. On observe de plus un amortissement exacerbé des oscillations de forme, dont la fréquence se retrouve toutefois dans le temps caractéristique de rupture. La rupture résulte de l'interaction avec une seule structure turbulente et les statistiques de grandes déformations et de ruptures sont identiques à celles de la turbulence.

3.2 Ecoulements cavitants (2009-)

Position du problème

La motivation générale de cet axe de recherche est l'étude des phénomènes instationnaires sur les aubes d'inducteurs axiaux en régime cavitant, dans la continuité d'un thème historique du laboratoire (Bakir *et al.*, 2003; Mejri *et al.*, 2006; Campos-Amezcua *et al.*, 2010). L'existence de différents régimes dynamiques, liés à des instabilités intrinsèques aux poches de cavitation ou à un couplage entre ces poches et le circuit sont bien décrits par notamment Fortes-Patella *et al.* (2007). La problématique sur laquelle porte nos travaux est l'effet des stries d'usinage (rugosités organisées longitudinales) sur la dynamique des poches de cavitation se développant près d'une paroi, dans la perspective d'un éventuel contrôle passif, facilement réalisable et économisant même une étape de polissage dans le cas d'un profil usiné.

La démarche choisie est tout d'abord d'étudier ce problème sur une géométrie simple permettant d'observer une dynamique riche en écoulement turbulent cavitant : il s'agit d'un convergent-divergent ou « venturi ». Le jet rentrant se développant à la fermeture d'une poche de cavitation (De Lange & De Bruin, 1997; Callenaere *et al.*, 2001) peut être à l'origine de cycles de croissance et de découpages périodiques de la poche. Depuis les travaux de notamment Stutz & Reboud (1997), cette géométrie est largement étudiée et constitue un cas de validation pour diverses approches numériques (Barre *et al.*, 2009). Sayyaadi (2010) a mis en évidence la transition entre deux régimes dynamiques différents selon la valeur du nombre de cavitation : à bas nombre de cavitation, un cycle de croissance et de lâchers de nuages que nous désignerons par « régime cyclique de détachement de nuages », et à plus haut nombre de cavitation, un « régime à poches pulsant à basse fréquence ». La transition semble se produire lorsque les poches de cavitation sont « assez grandes », et les limites entre ces régimes en terme par exemple de nombre de Strouhal sont relativement floues. La transition entre ces régimes dépend également du nombre de Reynolds comme le montrent Keil *et al.* (2012), et du confinement latéral ainsi que du rapport d'aspect transverse comme le mettent en évidence Dular *et al.* (2012).

De nombreuses études ont porté sur la réduction de trainée turbulente liée à la présence de stries longitudinales ou "riblets" sur des surfaces, le plus souvent de type plaque plane (voir par exemple Bechert *et al.*, 1997). Les mécanismes de réduction de trainée apportée par ces stries sont liés à des modifications de la couche limite turbulente.

En écoulements cavitants, de nombreux travaux ont porté sur le déclenchement de la cavitation autour de rugosités locales (Arndt & Ippen, 1968). Kawanami *et al.* (1997) montrent comment un petit obstacle sur l'extrados d'un foil peut modifier la dynamique du détachement de nuages. Coutier-Delgosha *et al.* (2005) ont quant-à eux étudié les effets de rugosités aléatoires de type grains de sable sur l'extrados de profils portants. Ils montrent dans le cas des pulsations de poches partielles des variations significatives des longueurs de poches et des fréquences résultant en des nombres de Strouhal plus grands qu'en paroi lisse, ainsi qu'une dégradation de la périodicité et une réduction des fluctuations de pression. A notre connaissance, les effets de stries longitudinales sont peu connus, ce qui nous amène à entreprendre leur étude.

Dispositif expérimental

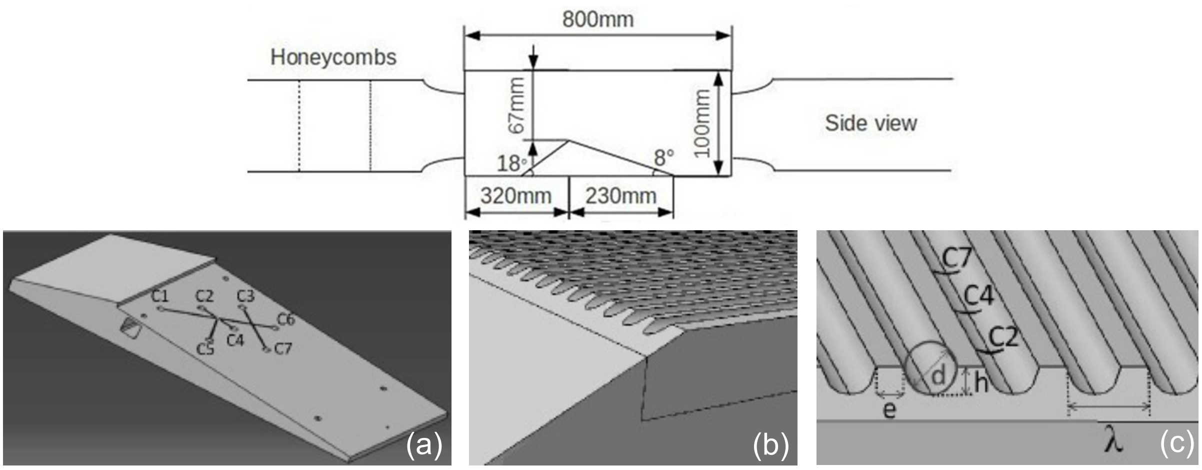

FIGURE 33 – *En haut : schéma de la veine d'essai incluant le venturi. La profondeur de la veine est* 120 *mm. La hauteur du col* $H_{throat} = 67$ *mm est prise comme longueur de référence. En bas, (a) : base portant les plaques avec les logements de capteurs de pression piézoélectriques* $C1$ *à* $C7$*, (b) : zoom au niveau du col montrant la jonction entre une plaque striée et la pièce de base, et (c) : définition des paramètres géométriques des stries longitudinales, usinées à la fraise boule, avec d et h le diamètre de l'outil et la profondeur d'usinage, e la largeur des crêtes, et* λ *la longueur d'onde du motif.*

Le dispositif décrit ici a été conçu et réalisé au cours de la thèse de J.-E. Méhal avec le concours d'A. Danlos. Une veine d'essai de section rectangulaire (voir Fig. 33) a été inclue dans la boucle hydraulique cavitante du laboratoire. Cette veine est précédée de dispositifs tranquiliseurs, grilles en quinconce et nids d'abeilles en amont d'un convergent [3], ce qui assure un écoulement homogène en entrée de veine avec un taux de turbulence de l'ordre de 2%, pour

---

[3] Cette installation s'inspire de celle de l'ENSTA, suivant les conseils de T. Pichon du laboratoire UME.

Plaque	d (mm)	h (mm)	e (mm)	λ (mm)	N	Symbole pour la Fig. 35
A	0	0	0	0	0	×
B	1	0.25	0.1	0.97	124	△
C	2	1	0.1	2.1	57	+
D	2	2	1	3	40	◇
E	2	2	0.1	2.1	57	□

TABLE *3.1 – Paramètres géométriques des stries pour les plaques présentées ici. N est le nombre de stries dans la largeur, pour les autres paramètres, voir Fig. 33.*

un nombre de Reynolds Re basé sur la vitesse débitante et la hauteur de veine de typiquement $Re \simeq 5.5 \times 10^5$.

La partie convergente du venturi possède un angle de 18 ° , et la partie divergente un angle de 8 ° , soit une géométrie proche des cas de Stutz & Reboud (1997); Barre *et al.* (2009); Campos-Amezcua *et al.* (2010); Dular *et al.* (2012). Le venturi se compose d'une base munie de capteurs de pression piézorésistifs sur laquelle se montent des plaques lisses ou munies de différentes stries longitudinales (voir Fig. 33). Les paramètres caractérisant les stries sont rapportés en Tab. 3.1 pour 5 de ces plaques, l'ensemble des cas testés étant rassemblé dans Danlos *et al.* (2013b).

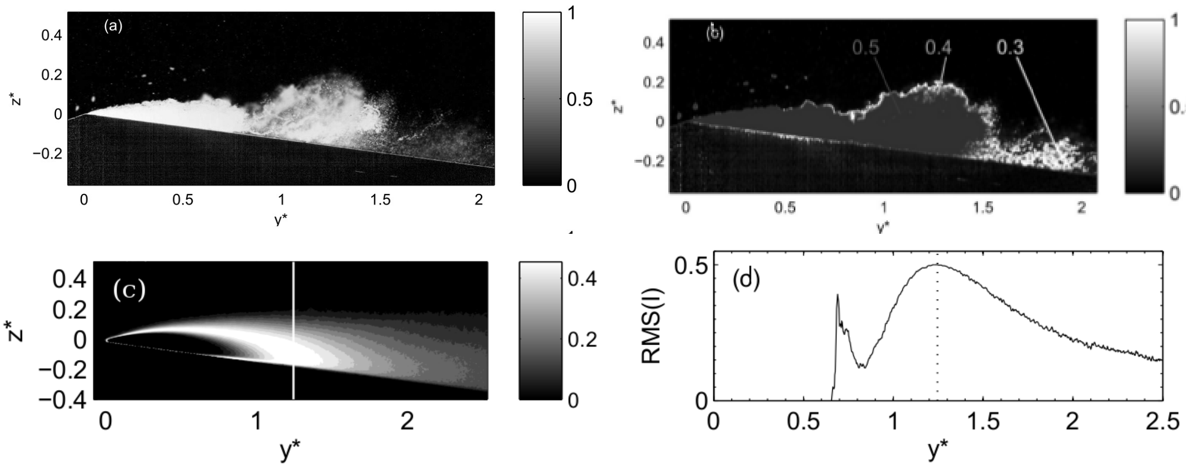

FIGURE *34 – (a) : image normalisée. (b) image binarisée avec différents seuils, puis filtrée par un filtre médian. (c) écart type d'une série de* 4000 *images binarisées, avec la ligne verticale marquant la longueur de la poche détectée. (d) profil selon $z^* = 0$ de l'écart-type, dont le maximum défini la longueur de poche détectée.*

La veine d'essai est constitué de plaques transparentes permettant des visualisations de côté ou de dessus. Les visualisations de côté effectuées par caméra rapide (fréquence d'acquisition 1 kHz) avec un éclairage en transmission par plaques de LED constituent la source d'informations la plus exploitée actuellement. Une illustration du traitement d'image et de la détection de la longueur moyenne des poches est présentée en Fig. 34. Le traitement d'image s'inspire de Ravelet *et al.* (2011a), et la définition retenue pour la longueur moyenne des poches de cavitation L —maximum de l'écart-type sur une série d'images— est celle introduite par Dular *et al.* (2012). Les fréquences de détachement de nuages ou de pulsation de poches f sont obtenues par simple transformée de Fourier temporelle de la moyenne sur une ligne verticale à l'abscisse correspondant à la longueur de poche des niveaux de gris. Enfin, une analyse par la décomposition en modes propres orthogonaux ("Proper Orthogonal Decomposition" ou POD, voir Lumley *et al.* (1993)) est effectuée selon la méthode décrite par Danlos *et al.* (2013a).

Effets de stries longitudinales sur les régimes dynamiques et la forme des poches de cavitation

Cette étude est menée pour une vitesse au col constante $v_{throat} = 8$ m.s^{-1}. Les longueurs de poches L adimensionnées par la hauteur du col H_{throat} et le nombre de Strouhal St_L basé sur cette longueur et sur la vitesse au col sont tracés en fonction du nombre de cavitation σ en Fig. 35. Le nombre de cavitation est défini à partir de la vitesse v_{ref} et de la pression statique p_{ref} en entrée de veine, avec $p_{sat}(T)$ la pression de vapeur saturante à la température T :

$$\sigma = \frac{(p_{ref} - p_{sat})}{\frac{1}{2}\rho v_{ref}^2}$$

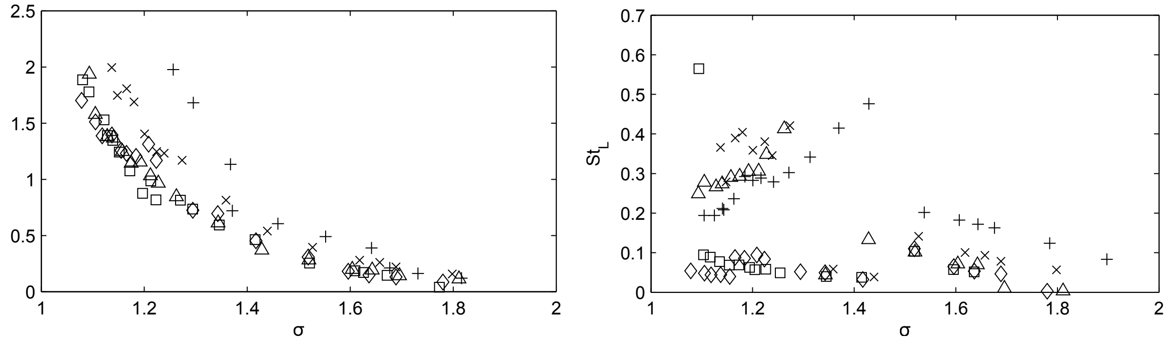

FIGURE *35 – Longueur de poche adimensionnelle L^* et nombre de Strouhal $St_L = \frac{Lf}{v_{throat}}$ en fonction du nombre de cavitation σ. $\times$: plaque lisse A, $\triangle$: plaque B, $+$: plaque C, $\diamondsuit$: plaque D, $\square$: plaque E (voir caractéristiques en Tab. 3.1).*

On retrouve tout d'abord le comportement attendu pour la plaque lisse (symboles : $\times$). Pour les plus grandes valeurs du nombre de cavitation, on observe une poche de faible taille (inférieure à $0.5H_{throat}$), attachée au col, et pulsant sans avoir de nuage convecté dans le sillage ; ce régime se caractérise par $0.05 \leqslant St_L \leqslant 0.15$. A mesure que la pression en entrée de veine diminue, *i.e.* que σ diminue, L croît et f diminue. A $\sigma \simeq 1.3$, où $L^* \simeq 1$, une transition se produit vers le régime à nuage convectés, illustré dans la première colonne de la Fig. 36 pour $\sigma = 1.17$. Ce régime se caractérise par $0.2 \leqslant St_L \leqslant 0.4$. Ces deux plages caractérisant les deux régimes sont cohérentes avec celles rapportées par Sayyaadi (2010).

Dans le cas des plaques munies de stries longitudinales, la tendance générale de la courbe des longueurs de poche est conservée. Toutefois, pour les mêmes paramètres d'écoulement, certaines plaques augmentent les longueurs de poches (C) et d'autres réduisent la taille des poches (B, D et E). De plus, les nombres de Strouhal sont fort différents d'une plaque à l'autre et si les points semblent se grouper en deux nuages, le nombre de Strouhal seul ne semble plus permettre à lui seul la distinction entre deux régimes dynamiques différents, les plages de valeurs se recouvrant (voir en particulier la plaque C, où il semble y avoir une transition autour de $\sigma \simeq 1.5$). On remarque enfin que les plaques D et E gardent un nombre de Strouhal très bas sur toute la gamme de nombre de cavitation exploré, et qu'il semble bien y avoir suppression du lâcher de nuage en aval de la poche pour les bas St_L, comme l'indiquent les images de la seconde colonne de la Fig. 36 (plaque E à $\sigma = 1.17$).

Les premiers modes de la décomposition POD ainsi que leur contribution respective à l'« énergie » totale sont présentés en Fig. 37 pour quatre plaques, aux mêmes conditions hydrodynamiques. Les résultats pour les plaques A (lisse) B (réduisant la taille de poche) et C (aug-

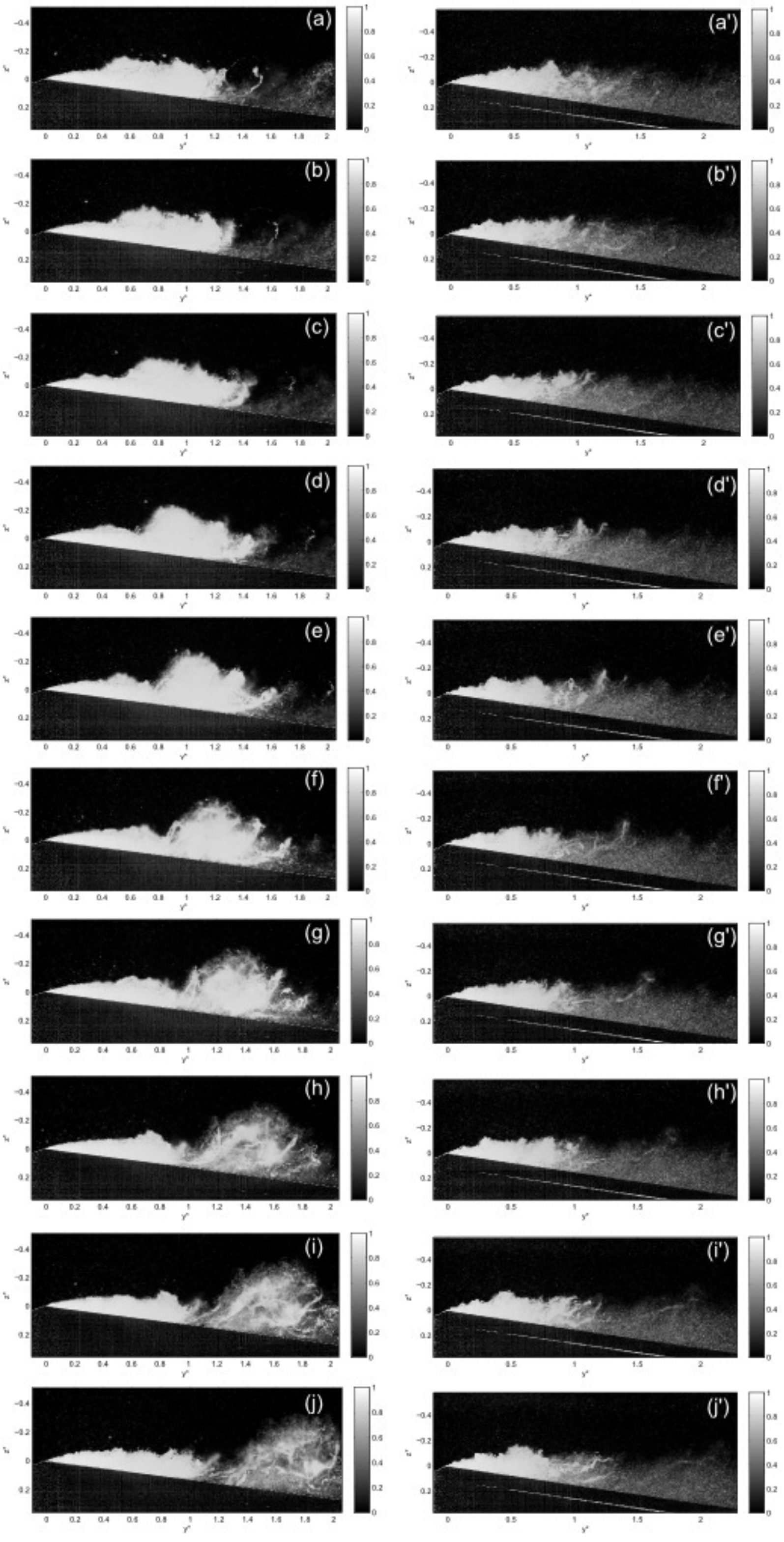

FIGURE *36 – (a-j) : séquences d'images à* $\sigma = 1.17$ *pour la plaque* A *montrant le régime cyclique de détachement de nuages de cavitation. (a'-j') : séquence au même nombre de cavitation pour la plaque* E *illustrant le régime à poches pulsant à basse fréquence (intervalle de temps* $\Delta t = 2$ *ms entre chaque image).*

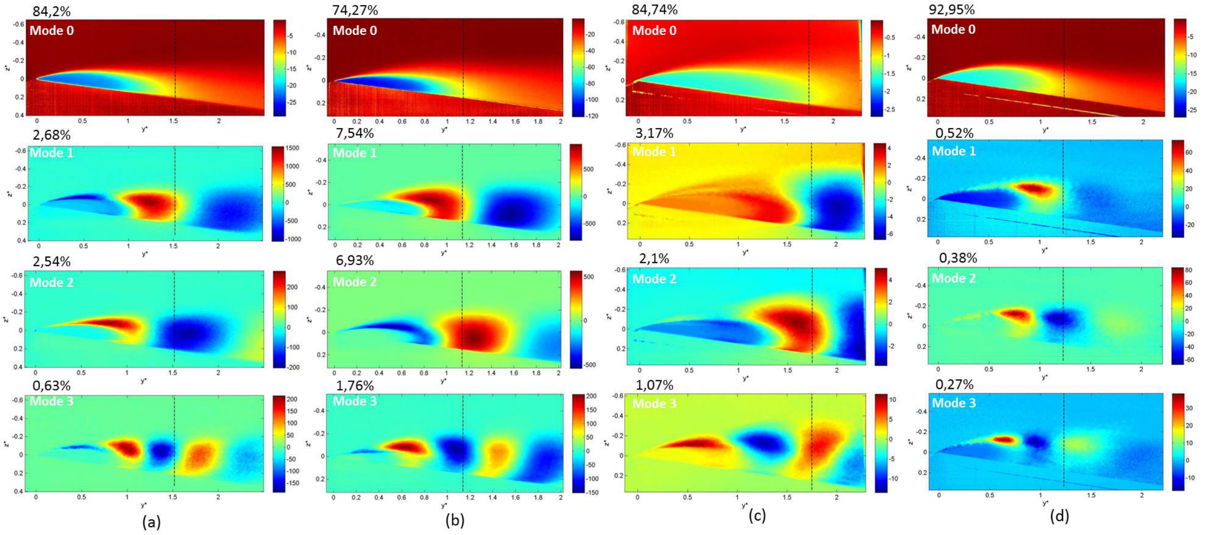

FIGURE *37 – Modes* 0 *à* 3 *issus de la décomposition POD, et contribution à l'énergie totale (en %), à* $\sigma = 1.17$ *pour différentes plaques : (a) plaque lisse A* ($L^* = 1.52$)*, (b) plaque B* ($L^* = 1.14$)*, (c) plaque C* ($L^* = 1.75$) *et (d) plaque E* ($L^* = 1.23$)*.*

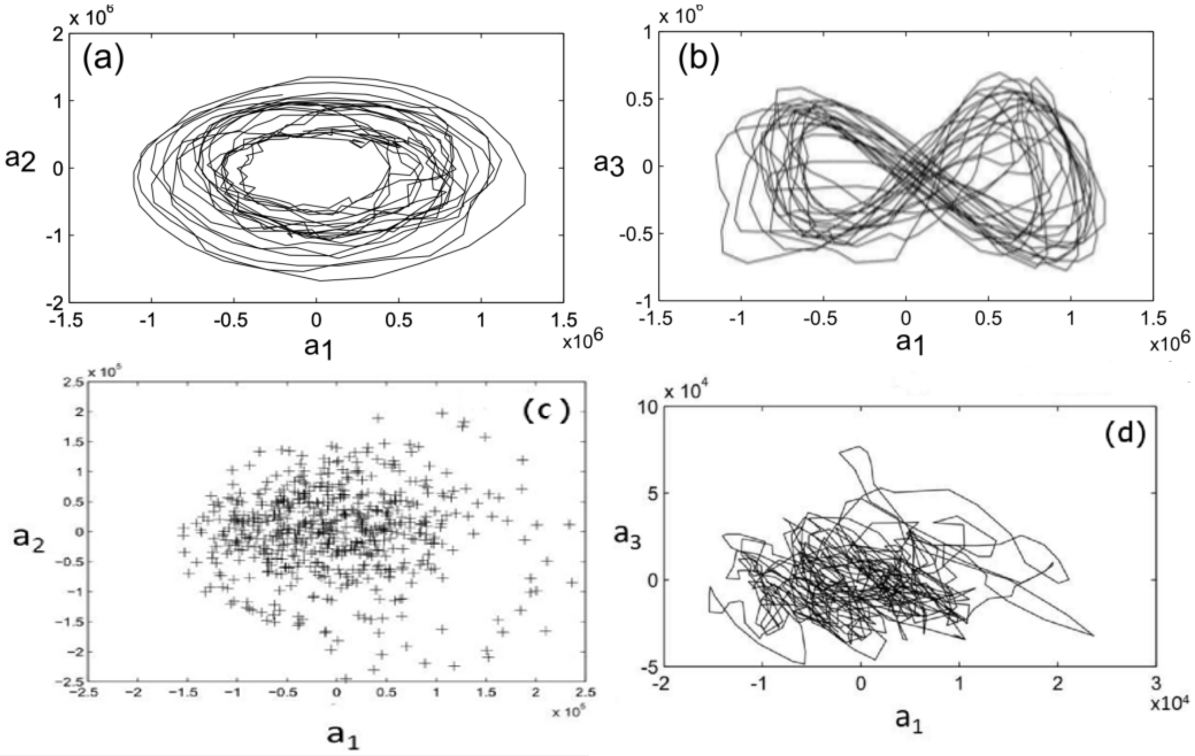

FIGURE *38 – Portrait de phase des coefficients de reconstruction POD à* $\sigma = 1.17$ *pour la plaque B (a-b : coefficients du mode* 2 *et du mode* 3 *en fonction du coefficient du mode* 1*), et pour la plaque E (c-d : coefficients du mode* 2 *et du mode* 3 *en fonction du coefficient du mode* 1*).*

mentant la taille de poche) sont caractéristiques d'un phénomène périodique : les modes 1 à 4 ont une contribution non négligeable, les modes 1 et 2 (puis 3 et 4) ont un poids et ont une forme proches avec un motif décalé d'un quart de longueur d'onde, et le mode 3 (4) semble être une harmonique double du mode 1 (2). Les figures de Lissajous pour la plaque B présentées en Fig. 38 confirment ceci (deux sinus de même fréquence décalés en phase de $\pi/2$ pour a_2 en fonction de a_1 et deux sinus en phase de fréquence unitaire et double pour a_3 en fonction de a_1). Le signal reconstruit pour le mode 1 est ainsi clairement périodique pour les plaques A et B (voir Fig. 39). Notons toutefois que les figures de Lissajous et les signaux reconstruits sont moins clairement caractéristique d'un phénomène périodique pour la plaque C.

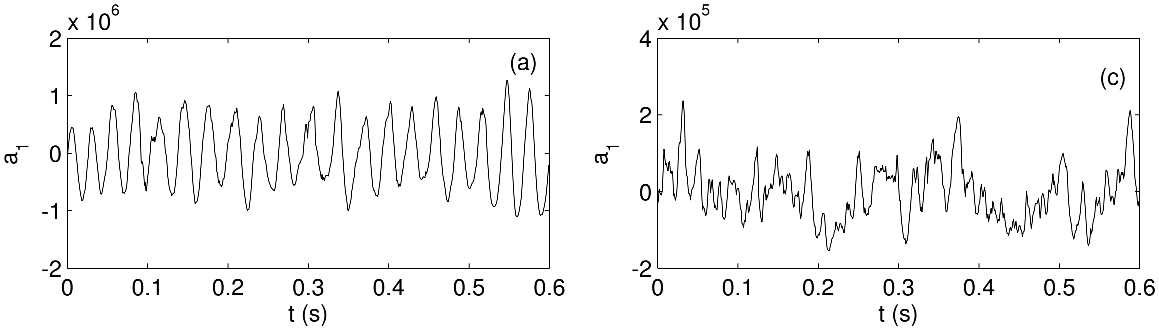

FIGURE *39 – Signaux temporels du coefficient du mode* 1 *de reconstruction POD à* $\sigma = 1.17$ *pour la plaque A et pour la plaque E.*

En revanche, la décomposition modale pour la plaque E est complètement différente : le mode 0 représente plus de 90% de l'énergie, les modes suivants ont des poids différents et ne se ressemblent plus (Fig. 37), les portraits de phases ne font plus apparaître de figures de Lissajous et les signaux ne sont plus purement périodiques (Fig. 38 et 39). On remarque enfin que le premier mode pour la plaque E correspond plutôt à des petites structures se développant sur le haut de la poche.

Ces constatations confirment le changement profond de dynamique pour la poche de cavitation que peuvent apporter la présence de stries d'usinage longitudinale, en plus de la seule modification de la longueur de poche : une exacerbation du cycle de découpage périodique de la poche pour la plaque B (dont les stries ont une profondeur de l'ordre de l'épaisseur de la sous-couche visqueuse), ou une suppression complète du cycle et perte de la périodicité pour les plaques D et E de profondeur 10 fois plus importante. Une analyse approfondie des gradients de pression ainsi que des taux de vide et vitesses en proche paroi par PIV à rayons X ou par sondes optiques (Stutz & Legoupil, 2003) afin de comprendre l'impact des rainures sur la dynamique du jet rentrant permettrait de clarifier ces premiers résultats.

4 Perspectives

Dans les prochaines années, j'envisage de centrer mes activités de recherche autour des axes 2 et 3, tout en entretenant d'une part un lien avec les équipes du CEA-Saclay et de la TU-Delft (axe 1), et en apportant d'autre part un soutien expérimental aux activités du laboratoire sur le transport solide (mesures locales des vitesses et concentrations de particules dans une expérience verticale, et pour l'écoulement à travers une singularité).

Les travaux autour des ***turbomachines axiales contrarotatives*** s'orientent vers la réalisation de mesures plus locales et détaillées, notamment des ***champs de vitesses instationnaires dans la zone entre les rotors***, par des mesures LDV synchronisées sur le premier et le second rotor. Nous souhaitons également développer des mesures PIV dans cette zone, ce qui demande un travail de mise au point des accès optiques et des nappes laser (objectif : thèse de J. Wang). Une expérience identique à échelle réduite est en cours de montage, afin d'une part d'explorer les effets de plus faibles nombres de Reynolds (ANR Scale déposée), et d'autre part de réaliser des mesures de ***rayonnement acoustique*** en chambre anéchoïque et d'explorer les effets de la distance entre rotors sur l'acoustique. Enfin, à plus long terme, dans le cadre par exemple d'un partenariat avec Ensival-Moret / Fapmo, nous envisageons de réaliser une pompe contrarotative sur le banc hydraulique et d'explorer les régimes cavitants.

Un second thème dans cet axe de recherche est en développement : l'étude des ***écoulements internes dans les machines électriques***. Deux études aux problématiques complémentaires sont actuellement en phase de démarrage. Tout d'abord, dans le cadre de l'ANR e-Meca, et de la thèse de J. Antoun-Labib, nous nous intéressons aux pertes dans un écoulement de type ***Taylor-Couette***, à haut rapport de rayon, pour des vitesses périphériques correspondant à des nombres de Mach de l'ordre de 0.7, et avec des cylindres texturés. Enfin, dans le cadre de la thèse de B. Bugeat, nous étudions les ***écoulements axiaux dans des canaux tournants***.

La démarche choisie pour l'évolution des travaux autour des ***instabilités en régime cavitant*** est, d'une part de progresser au niveau des ***mesures locales*** effectuées (mesures du taux de vide et des vitesses dans les poches par sondes optiques), et d'autre part de ***compliquer progressivement la géométrie étudiée*** : deux venturis décalés, puis une grille d'aube fixe, attaquée par un vortex généré en amont, avant d'aller vers une turbomachine.

Enfin, à plus long terme, je souhaite reprendre des études sur les ***dispersions de liquides non-miscibles*** dans un écoulement de ***Taylor-Couette***. Ceci pourra donner lieu à des collaborations internes au laboratoire avec notamment J.-C. Robinet qui développe des approches théoriques pour l'étude des instabilités en diphasique.

Bibliographie

Abi Chebel, N., Masbernat, O., Risso, F., Guiraud, P., Ravelet, F., Dalmazzone, C. & Noïk, C. (2008). *Imaging method for interface rheological characterization.* In *Proceedings of the 13th International Symposium on Flow Visualization, Nice, 1-4 July 2008.* `http://hal.archives-ouvertes.fr/hal-00288844/fr/`.

Abi Chebel, N., Risso, F. & Masbernat, O. (2011). *Inertial modes of a periodically forced buoyant drop attached to a capillary.* Phys. Fluids, **23**, 102104.

Andereck, C. D., Liu, S. S. & Swinney, H. L. (1986). *Flow regimes in a circular Couette system with independently rotating cylinders.* Journal of Fluid Mech., **164**, 155.

Arndt, R. E. A. & Ippen, A. T. (1968). *Rough Surface Effects on Cavitation Inception.* J. Basic Eng., **90**, 249.

Bakir, F. (1992). *Méthode de dimensionnement et d'analyse des machines de compression hélico-centrifuges en régime incompressible.* Thèse de doctorat, École Nationale Supérieure d'Arts et Métiers.

Bakir, F., Kouidri, S., Noguera, R. & Rey, R. (2003). *Experimental analysis of an axial inducer influence of the shape of the blade leading edge on the performances in cavitating regime.* J. Fluids Eng., **125**, 293.

Barre, S., Rolland, J., Boitel, G., Goncalves, E. & Fortes Patella, R. (2009). *Experiments and modelling of cavitating flows in venturi : attached sheet cavitation.* Eur. J. Mech. B, **28**, 444.

Bechert, D. W., Bruse, M., Hage, W., van der Hoeven, J. G. T. & Hoppe, G. (1997). *Experiments on drag-reducing surfaces and their optimization with an adjustable geometry.* Journal of Fluid Mech., **338**, 59.

Berhanu, M., Verhille, G., Boisson, J., Gallet, B., Gissinger, C., Fauve, S., Mordant, N., Pétrélis, F., Bourgoin, M., Odier, P., Pinton, J.-F., Plihon, N., Aumaître, S., Chiffaudel, A., Daviaud, F., Dubrulle, B. & Pirat, C. (2010). *Dynamo regimes and transitions in the VKS experiment.* Euro. Phys. Journal B, **77**, 459.

Boisson, J., Aumaître, S., Bonnefoy, N., Bourgoin, M., Daviaud, F., Dubrulle, B., Odier, P., Pinton, J.-F., Plihon, N. & Verhille, G. (2012). *Symmetry and couplings in stationary von Kármán sodium dynamos.* New Journal of Physics, **14**, 013044.

Bourgoin, M., Marié, L., Pétrélis, F., Gasquet, C., Guigon, A., Luciani, J.-B., Moulin, M., Namer, F., Burguete, J., Chiffaudel, A., Daviaud, F., Fauve, S., Odier, P. & Pinton, J.-F. (2002). *MHD measurements in the von Kármán sodium experiment.* Phys. Fluids, **14**, 3046.

Brauckmann, H. J. & Eckhardt, B. (2013a). *Intermittent boundary layers and torque maxima in Taylor-Couette flow.* Phys. Rev. E, **87**, 033004.

Brauckmann, H. J. & Eckhardt, B. (2013b). *Direct numerical simulations of local and global torque in Taylor–Couette flow up to Re = 30 000.* Journal of Fluid Mech., **718**, 398.

Budwig, R. (1994). *Refractive index matching methods for liquid flow investigations.* Exp. In Fluids, **17**, 350.

BURGUETE, J. & DE LA TORRE, A. (2009). *Hysteresis and vortices dynamics in a turbulent flow.* International Journal of Bifurcation and Chaos, **19**, 2695.

CADOT, O., COUDER, Y., DAERR, A., DOUADY, S. & TSINOBER, A. (1997). *Energy injection in closed turbulent flows : Stirring through boundary layers versus inertial stirring.* Phys. Rev. E, **56**, 427.

CALLENAERE, M., FRANC, J.-P., MICHEL, J.-M. & RIONDET, M. (2001). *The cavitation instability induced by the development of a re-entrant jet.* Journal of Fluid Mech., **444**, 223.

CAMPOS-AMEZCUA, R., KHELLADI, S., BAKIR, F., MAZUR-CZERWIEC, Z., SARRAF, C. & REY, R. (2010). *Numerical analysis of unsteady cavitating flow in an axial inducer.* Journal of Power and Energy, **224**, 223.

CHO, L., CHOI, H., LEE, S. & CHO, J. (2009). *Numerical and experimental analyses for the aerodynamic design of high performance counter-rotating axial flow fans.* In *Proceedings of the ASME 2009 Fluids Engineering Division Summer Meeting - FEDSM2009, Colorado, USA*, pages FEDSM2009–78507.

CORTET, P.-P., DIRIBARNE, P., MONCHAUX, R., CHIFFAUDEL, A., DAVIAUD, F. & DUBRULLE, B. (2009). *Normalized kinetic energy as a hydrodynamical global quantity for inhomogeneous anisotropic turbulence.* Phys. Fluids, **21**, 025104.

CORTET, P.-P., HERBERT, E., CHIFFAUDEL, A., DAVIAUD, F., DUBRULLE, B. & PADILLA, V. (2011). *Susceptibility divergence, phase transition and multistability of a highly turbulent closed flow.* Journal of Statistical Mechanics : Theory and Experiment, **2011**, P07012.

COUGHLIN, K. & MARCUS, P. S. (1996). *Turbulent Bursts in Couette-Taylor Flow.* Phys. Rev. Letters, **77**, 2214.

COUTIER-DELGOSHA, O., DEVILLERS, J., LERICHE, M. & PICHON, T. (2005). *Effect of wall roughness on the dynamics of unsteady cavitation.* J. Fluids Eng., **127**, 726.

DANLOS, A., LALIZEL, G. & PATTE-ROULAND, B. (2013a). *Experimental characterization of the initial zone of an annular jet with a very large diameter ratio.* Exp. In Fluids, **54**, 1418.

DANLOS, A., MEHAL, J.-E., RAVELET, F., COUTIER-DELGOSHA, O. & BAKIR, F. (2013b). *Study of the cavitating instability on a grooved Venturi profile.* Submitted to J. Fluids Eng., `http://hal.archives-ouvertes.fr/hal-00765996`.

DE LA TORRE, A. & BURGUETE, J. (2007). *Slow Dynamics in a Turbulent von Kármán Swirling Flow.* Phys. Rev. Letters, **99**, 054101.

DE LANGE, D. & DE BRUIN, G. (1997). *Sheet cavitation and cloud cavitation, Re-entrant jet and Three-dimensionality.* Applied Scientific Research, **58**, 91.

DIXON, S. L. & HALL, C. A. (2010). *Fluid mechanics and thermodynamics of turbomachinery (6th edition).* Butterworth-Heinemann.

DONG, S. (2008). *Turbulent flow between counter-rotating concentric cylinders : a direct numerical simulation study.* Journal of Fluid Mech., **615**, 371.

DOPPLER, D., GONDRET, P., LOISELEUX, T., MEYER, S. & RABAUD, M. (2007). *Relaxation dynamics of water-immersed granular avalanches.* Journal of Fluid Mech., **577**, 161.

Doron, P., Granica, D. & Barnea, D. (1987). *Slurry Flow in Horizontal Pipes - Experimental and Modeling.* Int. J. Multiphase Flow, **13**, 535.

Douady, S., Couder, Y. & Brachet, M. E. (1991). *Direct Observation of the Intermittency of Intense Vorticity Filaments in Turbulence.* Phys. Rev. Letters, **67**, 983.

Dubrulle, B. & Hersant, F. (2002). *Momentum transport and torque scaling in Taylor–Couette flow from an analogy with turbulent convection.* Euro. Phys. Journal B, **26**, 379.

Dubrulle, B., Dauchot, O., Daviaud, F., Longaretti, P.-Y., Richard, D. & Zahn, J.-P. (2005). *Stability and turbulent transport in Taylor–Couette flow from analysis of experimental data.* Phys. Fluids, **17**, 095103.

Dular, M., Khlifa, I., Fuzier, S., Adama Maiga, M. & Coutier-Delgosha, O. (2012). *Scale effect on unsteady cloud cavitation.* Exp. In Fluids, **53**, 1233.

Eckhardt, B., Grossmann, S. & Lohse, D. (2007). *Torque scaling in Taylor–Couette flow between independently rotating cylinders.* Journal of Fluid Mech., **581**, 221.

Ellingsen, K. & Risso, F. (2001). *On the rise of an ellipsoidal bubble in water : oscillatory paths and liquid-induced velocity.* Journal of Fluid Mech., **440**, 235.

Emery, J. C., Herrig, L. J., Erwin, J. R. & Felix, A. R. (1958). *Systematic two-dimensional cascade tests of NACA 65-series compressor blades at low speeds.* `http://naca.central.cranfield.ac.uk/reports/1958/naca-report-1368.pdf`.

Fauve, S., Laroche, C. & Castaing, B. (1993). *Pressure fluctuations in swirling turbulent flows.* J. Phys. II France, **3**, 271.

Fortes-Patella, R., Coutier-Delgosha, O., Perrin, J. & Reboud, J.-L. (2007). *Numerical Model to Predict Unsteady Cavitating Flow Behavior in Inducer Blade Cascades.* J. Fluids Eng., **129**, 128.

Furukawa, S., Shigemitsu, A. & Watanabe, T. (2007). *Performance test and flow measurement of contra-rotating axial flow pump.* J. Thermal Science, **16**, 7.

Giesecke, A., Stefani, F. & Gerbeth, G. (2010). *Role of Soft-Iron Impellers on the Mode Selection in the von Kármán Sodium Dynamo Experiment.* Phys. Rev. Letters, **104**, 044503.

Gissinger, C. (2012). *A new deterministic model for chaotic reversals.* Euro. Phys. Journal B, **85**, 1.

Gissinger, C. J. P. (2009). *A numerical model of the VKS experiment.* EPL (Europhysics Letters), **87**, 39002.

Goman, M. G., Zakharov, S. B. & Khrabrov, A. N. (1985). *Aerodynamic hysteresis in steady detached flow over extended bodies.* Sov. Phys. Dokl., **30**, 323.

Grossmann, S. & Lohse, D. (2011). *Multiple scaling in the ultimate regime of thermal convection.* Phys. Fluids, **23**, 045108.

Huisman, S. G., van Gils, D. P. M., Grossmann, S., Sun, C. & Lohse, D. (2012). *Ultimate Turbulent Taylor-Couette Flow.* Phys. Rev. Letters, **108**, 024501.

Ji, L. & Yan, H. (2002). *Attractable snakes based on the greedy algorithm for contour extraction.* Pattern Recogn., **35**, 791.

Kawanami, Y., Kato, H., Yamaguchi, H., Tagaya, Y. & M., T. (1997). *Mechanism and control of cloud cavitation.* J. Fluids Eng., **119**, 788.

Kayikcioglu, T., Gangal, A. & Ozer, M. (2000). *Reconstructing ellipsoids from three projection contours.* Pattern Recogn. Lett., **21**, 959.

Keil, T., Pelz, P. & Buttenbender, J. (2012). *On the transition from sheet to cloud cavitation.* In *Proceedings of the Eighth International Symposium on Cavitation.*

Kolmogorov, N. (1991a). *Dissipation of energy in the locally isotropic turbulence.* Proceedings of the Royal Society (London) Series A, **434**, 15. Traduction de l'article original russe de 1941.

Kolmogorov, N. (1991b). *The local structure of turbulence in incompressible viscous fluid for very large Reynolds number.* Proceedings of the Royal Society (London) Series A, **434**, 9. Traduction de l'article original russe de 1941.

La Porta, A., Voth, G. A., Crawford, A. M., Alexander, J. & Bodenschatz, E. (2001). *Fluid particle acceleration in fully developed turbulence.* Nature, **409**, 1017.

Labbé, R., Pinton, J.-F. & Fauve, S. (1996). *Power Fluctuations in Turbulent Swirling Flows.* J. Phys II France, **6**, 1099.

Laguerre, R., Nore, C., Ribeiro, A., Léorat, J., Guermond, J.-L. & Plunian, F. (2008). *Impact of Impellers on the Axisymmetric Magnetic Mode in the VKS2 Dynamo Experiment.* Phys. Rev. Letters, **101**, 104501.

Lamb, H. (1932). *Hydrodynamics.* Cambridge University Press.

Lathrop, D. P., Fineberg, J. & Swinney, H. L. (1992). *Transition to shear-driven turbulence in Couette-Taylor flow.* Phys. Rev. A, **46**, 6390.

Lewis, G. S. & Swinney, H. L. (1999). *Velocity structure functions, scaling, and transitions in high-Reynolds-number Couette–Taylor flow.* Phys. Rev. E, **59**, 5457.

Liu, P., Jin, Y. & Wang, Y. (2011). *Effects of rotor structure on performance of small size axial flow fans.* Journal of Thermal Science, **20**, 205.

Lumley, J. L., Holmes, P. & Berkooz, G. (1993). *The proper orthogonal decomposition in the analysis of turbulent flows.* Ann. Rev. Fluid Mech., **25**, 539.

Marié, L. (2003). *Transport de moment cinétique et de champ magnétique par un écoulement tourbillonaire turbulent : influence de la rotation.* Thèse de doctorat, Université Paris VII. `http://tel.archives-ouvertes.fr/tel-00007755/`.

Marié, L., & Daviaud, F. (2004). *Experimental measurement of the scale-by-scale momentum transport budget in a turbulent shear flow.* Phys. Fluids, **16**, 457.

Meiron, D. I. (1989). *On the stability of gas bubbles rising in an inviscid fluid.* Journal of Fluid Mech., **198**, 101.

Mejri, I., Bakir, F., Rey, R. & Belamri, T. (2006). *Comparison of computational results obtained from a homogeneous cavitation model with experimental investigations of three inducers.* J. Fluids Eng., **128**, 1308.

Miller, C. A. & Scriven, L. E. (1968). *The oscillations of a fluid droplet immersed in another fluid.* Journal of Fluid Mech., **32**, 417.

Moffatt, H. (1978). *Magnetic Field Generation in Electrically Conducting Fluids.* Cambridge University Press, Cambridge, England.

Moisy, F., Willaime, H., Andersen, J. S. & Tabeling, P. (2001). *Passive Scalar Intermittency in Low Temperature Helium Flows.* Phys. Rev. Letters, **86**, 4827.

Monchaux, R. (2007). *Mécanique statistique et effet dynamo dans un écoulement de von Karman turbulent.* Thèse de doctorat, Université Paris-Diderot - Paris VII. `http://tel.archives-ouvertes.fr/tel-00199751`.

Monchaux, R., Berhanu, M., Bourgoin, M., Moulin, M., Odier, P., Pinton, J.-F., Volk, R., Fauve, S., Mordant, N., Pétrélis, F., Chiffaudel, A., Daviaud, F., Dubrulle, B., Gasquet, C., Marié, L. & Ravelet, F. (2007). *Generation of magnetic field by dynamo action in a turbulent flow of liquid sodium.* Phys. Rev. Letters, **98**, 044502.

Monchaux, R., Berhanu, M., Aumaître, S., Chiffaudel, A., Daviaud, F., Dubrulle, B., Ravelet, F., Fauve, S., Mordant, N., Pétrélis, F., Bourgoin, M., Odier, P., Pinton, J.-F., Plihon, N. & Volk, R. (2009). *The von Kármán Sodium experiment : Turbulent dynamical dynamos.* Phys. Fluids, **21**, 035108.

Moreau, S. & Bakir, F. (2002). *Efficient stator designed for automotive engine cooling fan systems.* In *ASME 2002 Fluids Engineering Division Summer Meeting*, pages FEDSM02–31318.

Mujica, N. & Lathrop, D. P. (2006). *Hysteretic gravity-wave bifurcation in a highly turbulent swirling flow.* Journal of Fluid Mech., **551**, 49.

Narrow, T. L., Yoda, M. & Abdel-Khalik, S. I. (2000). *A simple model for the refractive index of sodium iodide acqueous solutions.* Exp. In Fluids, **28**, 282.

Newitt, D. M., Richardson, J. F., Abbott, M. & Turtle, R. B. (1955). *Hydraulic conveying of solids in horizontal pipes.* Trans. Inst. Chem. Eng., **33**, 93.

Noguera, R., Rey, R., Massouh, F., Bakir, F. & Kouidri, S. (1993). *Design and Analysis of Axial Pumps.* In *ASME Fluids Engineering, Second Pumping Machinery Symposium, Washington, USA.*, pages 95–111.

Nore, C., Tuckerman, L. S., Daube, O. & Xin, S. (2003). *The 1 :2 mode interaction in exactly counter-rotating von Kármán swirling flow.* Journal of Fluid Mech., **477**, 51.

Nouri, H. (2012). *Étude expérimentale de l'écoulement et de l'interaction entre deux rotors contrarotatifs subsoniques.* Thèse de doctorat, École Nationale Supérieure d'Arts et Métiers. `http://tel.archives-ouvertes.fr/tel-00795114`.

NOURI, H., RAVELET, F., BAKIR, F., SARRAF, C. & REY, R. (2012). *Design and Experimental Validation of a Ducted Counter-Rotating Axial-Flow Fans System.* J. Fluids Eng., **134**, 104504.

NOURI, H., DANLOS, A., RAVELET, F., BAKIR, F. & SARRAF, C. (2013). *Experimental study of the instationary flow between two ducted Counter-rotating rotors.* J. Eng. Gas Turb. Power, **135**, 022601.

PAL, R. (2001). *Novel viscosity equations for emulsions of two immiscible liquids.* Journal of Rheology, **45**, 509.

PAOLETTI, M. S. & LATHROP, D. P. (2011). *Angular Momentum Transport in Turbulent Flow between Independently Rotating Cylinders.* Phys. Rev. Letters, **106**, 024501.

PÉTRÉLIS, F., FAUVE, S., DORMY, E. & VALET, J.-P. (2009). *Simple Mechanism for Reversals of Earth's Magnetic Field.* Phys. Rev. Letters, **102**, 144503.

PIELA, K., DELFOS, R., OOMS, G., WESTERWEEL, J., OLIEMANS, R. V. A. & MUDDE, R. F. (2006). *Experimental investigation of phase inversion in an Oil-Water flow through a horizontal pipe loop.* Int. J. Multiphase Flow, **32**, 1087.

POPE, S. B. (2000). *Turbulent Flows.* Cambridge University Press.

PRIGENT, A., GRÉGOIRE, G., CHATÉ, H., DAUCHOT, O. & VAN SAARLOS, W. (2002). *Large-scale finite-wavelength modulation within turbulent shear flows.* Phys. Rev. Letters, **89**, 14501.

PÉTRÉLIS, F., MORDANT, N. & FAUVE, S. (2007). *On the magnetic fields generated by experimental dynamos.* Geophys. Astrophys. Fluids Dynamics, **101**, 289.

RACINA, A. & KIND, M. (2006). *Specific power input and local micromixing times in turbulent Taylor-Couette flow.* Exp. In Fluids, **41**, 513.

RAFFEL, M., WILLERT, C. E., WERELEY, S. & KOMPENHANS, J. (2007). *Particle Image Velocimetry : A Practical Guide.* Springer. Cours de PIV du DLR, Göttingen.

RAVELET, F. (2005). *Bifurcations globales hydrodynamiques et magnetohydrodynamiques dans un écoulement de von Kármán turbulent.* Thèse de doctorat, Ecole Doctorale de l'Ecole Polytechnique. `http://tel.archives-ouvertes.fr/tel-00011016/`.

RAVELET, F., MARIÉ, L., CHIFFAUDEL, A. & DAVIAUD, F. (2004). *Multistability and Memory Effect in a Highly Turbulent Flow : Experimental Evidence for a Global Bifurcation.* Phys. Rev. Letters, **93**, 164501.

RAVELET, F., CHIFFAUDEL, A., DAVIAUD, F. & LÉORAT, J. (2005). *Towards an experimental von Kármán dynamo : numerical studies based on experimental flows.* Phys. Fluids, **17**, 117104.

RAVELET, F., DELFOS, R. & WESTERWEEL, J. (2007). *Experimental studies of liquid-liquid dispersion in a turbulent shear flow.* In *Proceedings of the Turbulence and Shear Flow Phenomena, Munich, 27-29 August.* `http://arxiv.org/abs/0707.1414/`.

RAVELET, F., BERHANU, M., MONCHAUX, R., AUMAÎTRE, S., CHIFFAUDEL, A., DAVIAUD, F., DUBRULLE, B., BOURGOIN, M., ODIER, P., PLIHON, N., PINTON, J.-F., VOLK, R., FAUVE, S., MORDANT, N. & PÉTRÉLIS, F. (2008a). *Chaotic Dynamos Generated by a Turbulent Flow of Liquid Sodium.* Phys. Rev. Letters, **101**, 074502.

Ravelet, F., Chiffaudel, A. & Daviaud, F. (2008b). *Supercritical transition to turbulence in an inertially-driven von Kármán closed flow.* Journal of Fluid Mech., **601**, 339.

Ravelet, F., Delfos, R. & Westerweel, J. (2010). *Influence of global rotation and Reynolds number on the large-scale features of a turbulent Taylor-Couette flow.* Phys. Fluids, **22**, 055103.

Ravelet, F., Colin, C. & Risso, F. (2011a). *On the dynamics and breakup of a bubble rising in a turbulent flow.* Phys. Fluids, **23**, 103301.

Ravelet, F., Lemaire, A. & Bakir, F. (2011b). *Etude expérimentale du transport hydraulique de grandes particules en conduite horizontale et en forme de S.* In *20ème Congrès Français de Mécanique, Besançon, 29 août-2 septembre 2011, France.* `http://hal.archives-ouvertes.fr/hal-00575082/fr/`.

Ravelet, F., Dubrulle, B., Daviaud, F. & Ratié, P.-A. (2012). *Kinematic Alpha Tensors and dynamo mechanisms in a von Kármán swirling flow.* Phys. Rev. Letters, **109**, 024503.

Ravelet, F., Bakir, F., Khelladi, S. & Rey, R. (2013). *Experimental study of hydraulic transport of large particles in horizontal pipes.* Exp. Thermal and Fluid Science, **45**, 187.

Risso, F. (2000). *The mechanisms of deformation and breakup of drops and bubbles.* Multiphase Sci. Tech., **12**, 1.

Risso, F. & Fabre, J. (1998). *Oscillations and breakup of a bubble immersed in a turbulent field.* Journal of Fluid Mech., **372**, 323.

Rodriguez Pascual, M., Ravelet, F., Delfos, R., Derksen, J. J. & Witkamp, G. J. (2009). *Large eddy simulations and stereoscopic particle image velocimetry measurements in a scraped heat exchanger crystallizer geometry.* Chem. Eng. Science, **64**, 2127.

Saint-Michel, B., Dubrulle, B., Marié, L., Ravelet, F. & Daviaud, F. (2013). *Forcing-type-dependent stability of steady states in a turbulent swirling flow.* Submitted to Phys. Rev. Letters, `http://hal.archives-ouvertes.fr/hal-00773512`.

Sarraf, C., Nouri, H., Ravelet, F. & Bakir, F. (2011). *Experimental study of blade thickness effects on the overall and local performances of a Controlled Vortex Designed axial-flow fan.* Exp. Thermal and Fluid Science, **35**, 684.

Sarraf, C., Ravelet, F. & Bakir, F. (2013). *Étude expérimentale de l'influence du blocage aval sur les performances d'un ventilateur axial.* In *21ème Congrès Français de Mécanique. Bordeaux, 26-30 août 2013, France.*

Sayyaadi, H. (2010). *Instability of the cavitating flow in a venturi reactor.* Fluid Dynamics Research, **42**, 0555503.

Schewe, G. (1983). *On the force fluctuations acting on a circular cylinder in crossflow from subcritical up to transcritical Reynolds numbers.* Journal of Fluid Mech., **133**, 265.

Shigemitsu, T., Furukawa, A., Watanabe, S. & Okuma, K. (2005). *Air/Water Two-Phase Flow Performance of Contra-Rotating Axial Flow Pump And Rotational Speed Control of Rear Rotor.* In *ASME 2005 Fluids Engineering Division Summer Meeting June 19-23, 2005, Houston, Texas, USA*, volume 1, pages 1069–1074.

SHIGEMITSU, T., FURUKAWA, A., WATANABE, S., OKUMA, K. & FUKUTOMI, J. (2009). *Internal Flow Measurement with LDV at Design Point of Contra-Rotating Axial Flow Pump.* J. Fluid Science and Technology, **4**, 723.

SHIGEMITSU, T., FUKUTOMI, J. & AGAWA, T. (2013). *Internal Flow Condition of High Power Contra-Rotating Small-Sized Axial Fan.* Int. J. Fluid Machinery and Systems, **6**, 25.

SHTERN, V. & HUSSAIN, F. (1999). *Collapse, symmetry breaking, and hysteresis in swirling flows.* Ann. Rev. Fluid Mech., **31**, 537.

SMITH, S. M. & BRADY, J. M. (1997). *SUSAN–A new approach to low level image processing.* Int. J. Comput. Vis., **23**, 45.

SOLIS, M., RAVELET, F., KHELLADI, S. & BAKIR, F. (2010). *Experimental and numerical analysis of the flow inside a configuration including an axial pump and tubular exchanger.* In *3rd Joint US-European Fluids Engineering Summer Meeting, 22nd Symposium on Fluid Machinery, 1-5 August 2010, Montreal, Canada.*, pages FEDSM–ICNMM2010–30723. `http://hal.archives-ouvertes.fr/hal-00505772/fr/`.

SREENIVASAN, K. R., BERSHADSKII, A. & NIEMELA, J. J. (2002). *Mean wind and its reversal in thermal convection.* Phys. Rev. E, **65**, 56306.

STEFANI, F., XU, M., GERBETH, G., RAVELET, F., CHIFFAUDEL, A., DAVIAUD, F. & LÉORAT, J. (2006). *Ambivalent effects of added layers on steady kinematic dynamos in cylindrical geometry : application to the VKS experiment.* Eur. J. Mech. B, **25**, 894.

STUTZ, B. & LEGOUPIL, S. (2003). *X-ray measurements within unsteady cavitation.* Exp. In Fluids, **35**, 130.

STUTZ, B. & REBOUD, J. (1997). *Experiments on unsteady cavitation.* Exp. In Fluids, **22**, 191.

SUBRAMANYAM, S. V. (1969). *A note on the damping and oscillations of a fluid drop moving in another fluid.* Journal of Fluid Mech., **37**, 715.

TAYLOR, G. I. (1923). *Stability of a Viscous Liquid Contained between Two Rotating Cylinders.* Philosophical Transactions of the Royal Society of London. Series A, **223**, 289. `http://rsta.royalsocietypublishing.org/content/223/605-615/289.full.pdf+html`.

TITON, J.-H. & CADOT, O. (2003). *The statistics of power injected in a closed turbulent flow : Constant torque forcing versus constant velocity forcing.* Phys. Fluids, **15**, 625.

TOKGOZ, S., ELSINGA, G., DELFOS, R. & WESTERWEEL, J. (2011). *Experimental investigation of torque scaling and coherent structures in turbulent Taylor-Couette flow.* Journal of Physics : Conference Series, **318**, 082018.

TOKGOZ, S., ELSINGA, G. E., DELFOS, R. & WESTERWEEL, J. (2012). *Spatial resolution and dissipation rate estimation in Taylor–Couette flow for tomographic PIV.* Exp. In Fluids, **53**, 561.

VAD, J. & BENCZE, F. (1998). *Three-dimensional flow in axial-flow fans of non-free vortex design.* Int. J. Heat and Fluid Flow, **19**, 601.

van Gils, D. P. M., Huisman, S. G., Bruggert, G.-W., Sun, C. & Lohse, D. (2011). *Torque Scaling in Turbulent Taylor-Couette Flow with Co- and Counterrotating Cylinders.* Phys. Rev. Letters, **106**, 024502.

Veldhuis, C., Biesheuvel, A. & van Wijngaarden, L. (2008). *Shape oscillations on bubbles rising in clean and in tap water.* Phys. Fluids, **20**, 040705.

Verhille, G., Plihon, N., Bourgoin, M., Odier, P. & Pinton, J.-F. (2010a). *Laboratory Dynamo Experiments.* Space Science Reviews, **152**, 543.

Verhille, G., Plihon, N., Bourgoin, M., Odier, P. & Pinton, J.-F. (2010b). *Induction in a von Kármán flow driven by ferromagnetic impellers.* New Journal of Physics, **12**, 033006.

Wang, J., Ravelet, F. & Bakir, F. (2013a). *Experimental comparison between a counter-rotating axial-flow fan and a conventional rotor-stator stage.* In *ETC2013, 10th European Turbomachinery Conference, 15-19 April 2013, Lappeenranta, Finland.* `http://hal.archives-ouvertes.fr/hal-00795006`.

Wang, J., Ravelet, F., Bakir, F. & Sarraf, C. (2013b). *Influence de la répartition de la charge sur les performances d'une turbomachine axiale contrarotative.* In *21ème Congrès Français de Mécanique. Bordeaux, 26-30 août 2013, France.* `http://hal.archives-ouvertes.fr/hal-00806763`.

Wendt, F. (1933). *Turbulente Strömungen zwischen zwei rotierenden konaxialen Zylindern.* Arch. Appl. Mech., **4**, 577. `http://dx.doi.org/10.1007/BF02084936`.

Xu, J., Tan, C., Chen, H., Zhu, Y. & Zhang, D. (2009). *Influence of tip clearance on performance of a contra-rotating fan.* J. Thermal Science, **18**, 207.

Yen, S. C. & Lin, F. T. (2006). *Exit Flow Field and Performance of Axial Flow Fans.* J. Fluids Eng., **128**, 332.

Zocchi, G., Tabeling, P., Maurer, J. & Willaime, H. (1994). *Measurement of the scaling of the dissipation at high Reynolds numbers.* Phys. Rev. E, **50**, 3693.

Troisième partie

Receuil des principales publications

1 Axe 1

1.1 Supercritical transition to turbulence in an inertially driven von Kármán closed flow

Journal of Fluid Mechanics (2008), vol. 601, pp. 339–364.

We study the transition from laminar flow to fully developed turbulence for an inertially driven von Kármán flow between two counter-rotating large impellers fitted with curved blades over a wide range of Reynolds number (10^2 — 10^6). The transition is driven by the destabilization of the azimuthal shear layer, i.e. Kelvin–Helmholtz instability, which exhibits travelling/drifting waves, modulated travelling waves and chaos before the emergence of a turbulent spectrum. A local quantity —the energy of the velocity fluctuations at a given point— and a global quantity —the applied torque— are used to monitor the dynamics. The local quantity defines a critical Reynolds number Re_c for the onset of time-dependence in the flow, and an upper threshold/crossover Re_t for the saturation of the energy cascade. The dimensionless drag coefficient, i.e. the turbulent dissipation, reaches a plateau above this finite Re_t, as expected for 'Kolmogorov'-like turbulence for $Re \to \infty$. Our observations suggest that the transition to turbulence in this closed flow is globally supercritical : the energy of the velocity fluctuations can be considered as an order parameter characterizing the dynamics from the first laminar time-dependence to the fully developed turbulence. Spectral analysis in the temporal domain, moreover, reveals that almost all of the fluctuation energy is stored in time scales one or two orders of magnitude slower than the time scale based on impeller frequency.

1.2 The von Kármán Sodium experiment : Turbulent dynamical dynamos

Physics of Fluids (2009), vol. 21, pp. 035108.

The von Kármán Sodium (VKS) experiment studies dynamo action in the flow generated inside a cylinder filled with liquid sodium by the rotation of coaxial impellers, the 'von Kármán geometry'. We first report observations related to the self-generation of a stationary dynamo when the flow forcing is $\mathcal{R}_\pi$ -symmetric, i.e., when the impellers rotate in opposite directions at equal angular velocities. The bifurcation is found to be supercritical with a neutral mode whose geometry is predominantly axisymmetric. We then report the different dynamical dynamo regimes observed when the flow forcing is not symmetric, including magnetic field reversals. We finally show that these dynamics display characteristic features of low dimensional dynamical systems despite the high degree of turbulence in the flow.

1.3 Influence of global rotation and Reynolds number on the large-scale features of a turbulent Taylor–Couette flow

Physics of Fluids (2010), vol. 22, pp. 055103.

We experimentally study the turbulent flow between two coaxial and independently rotating cylinders. We determined the scaling of the torque with Reynolds numbers at various angular velocity ratios 'Rotation numbers' and the behavior of the wall shear stress when varying the Rotation number at high Reynolds numbers. We compare the curves with particle image velocimetry analysis of the mean flow and show the peculiar role of perfect counter-rotation for the emergence of organized large scale structures in the mean part of this very turbulent flow that appear in a smooth and continuous way : the transition resembles a supercritical bifurcation of the secondary mean flow.

1.4 Kinematic alpha-Tensors and Dynamo Mechanisms in a von Kármán Swirling Flow

Physical Review Letters (2012), vol. 109, pp. 024503.

We provide experimental and numerical evidence of in-blades vortices in the von Kármán swirling flow. We estimate the associated kinematic α-effect tensor and show that it is compatible with recent models on the von Kármán sodium (VKS) dynamo. We further show that depending on the relative frequency of the two impellers, the dominant dynamo mechanism may switch from α^2 to $\alpha - \Omega$ dynamo. We discuss some implications of these results for VKS experiments.

J. Fluid Mech. (2008), vol. 601, pp. 339–364. © 2008 Cambridge University Press
doi:10.1017/S0022112008000712 Printed in the United Kingdom

Supercritical transition to turbulence in an inertially driven von Kármán closed flow

FLORENT RAVELET†, ARNAUD CHIFFAUDEL AND FRANÇOIS DAVIAUD

Service de Physique de l'Etat Condensé, Direction des Sciences de la Matière,
CEA-Saclay, CNRS URA 2464, 91191 Gif-sur-Yvette cedex, France

(Received 5 December 2006 and in revised form 18 January 2008)

We study the transition from laminar flow to fully developed turbulence for an inertially driven von Kármán flow between two counter-rotating large impellers fitted with curved blades over a wide range of Reynolds number ($10^2 - 10^6$). The transition is driven by the destabilization of the azimuthal shear layer, i.e. Kelvin–Helmholtz instability, which exhibits travelling/drifting waves, modulated travelling waves and chaos before the emergence of a turbulent spectrum. A local quantity – the energy of the velocity fluctuations at a given point – and a global quantity – the applied torque – are used to monitor the dynamics. The local quantity defines a critical Reynolds number Re_c for the onset of time-dependence in the flow, and an upper threshold/crossover Re_t for the saturation of the energy cascade. The dimensionless drag coefficient, i.e. the turbulent dissipation, reaches a plateau above this finite Re_t, as expected for 'Kolmogorov'-like turbulence for $Re \rightarrow \infty$. Our observations suggest that the transition to turbulence in this closed flow is globally supercritical: the energy of the velocity fluctuations can be considered as an order parameter characterizing the dynamics from the first laminar time-dependence to the fully developed turbulence. Spectral analysis in the temporal domain, moreover, reveals that almost all of the fluctuation energy is stored in time scales one or two orders of magnitude slower than the time scale based on impeller frequency.

1. Introduction

Hydrodynamic turbulence is a key feature of many common fluid mechanics problems (Tennekes & Lumley 1972; Lesieur 1990). In a few ideal cases, exact solutions of the Navier–Stokes equations are available, based on several assumptions such as auto-similarity, stationarity, or symmetry (for a collection of examples, see Schlichting 1979). Unfortunately, they are often irrelevant in practice, because they are unstable. Two of the simplest examples are the centrifugal instability of the Taylor–Couette flow between two concentric cylinders, and the Rayleigh–Bénard convection between two differentially heated plates: once the amount of angular momentum or heat becomes too great to be carried by molecular diffusion, a more efficient convective transport arises. Increasing further the control parameter in these two examples, secondary bifurcations occur, leading rapidly to temporal chaos, and/or to spatio-temporal chaos, then to turbulence.

---

† Present address: Laboratory for Aero and Hydrodynamics, Leeghwaterstraat 21, 2628 CA Delft, The Netherlands.

Several approaches have been taken in parallel concerning developed turbulence, focused on statistical properties of flow quantities at small scales (Frisch 1995) or taking into account the persistence of coherent structures in a more deterministic point of view (Tennekes & Lumley 1972; Lesieur 1990). One of the major difficulties concerning a self-consistent statistical treatment of turbulence is that it depends on the flow in which it takes place (for instance wakes, jets or closed flows). At finite Reynolds number, *Re*, most turbulent flows could still keep some average geometrical or topological properties of the laminar flow (for example the presence of a Bénard–von Kármán street in the wake of a bluff body whatever the values of *Re*), which could still influence its statistical properties (Zocchi *et al.* 1994; La Porta *et al.* 2001; Ouellette *et al.* 2006).

Furthermore, we have recently shown for a von Kármán flow that a turbulent flow can exhibit multistability, first-order bifurcations and can even keep traces of its history at very high Reynolds number (Ravelet *et al.* 2004). The observation of this turbulent bifurcation led us to study the transition from the laminar state to turbulence in this inertially driven closed flow.

1.1. *Overview of the von Kármán swirling flow*

1.1.1. *Instabilities of the von Kármán swirling flow between flat disks*

The disk flow is an example where exact Navier–Stokes solutions are available. The original problem of the flow of a viscous fluid over an infinite rotating flat disk was considered by von Kármán (1921). Experimentally, the problem of an infinite disk in an infinite medium is difficult to address. The addition of a second coaxial disk was proposed by Batchelor (1951) and Stewartson (1953). A cylindrical housing can also be added. Instabilities and transitions have been extensively studied in this system for instance Mellor, Chapple & Stokes 1968; Harriott & Brown 1984; Escudier 1984; Sørensen & Christensen 1995; Gelfgat, Bar-Yoseph & Solan 1996; Spohn, Mory & Hopfinger 1998; Gauthier, Gondret & Rabaud 1999; Schouveiler, Le Gal & Chauve 2001; Nore *et al.* 2003, 2004; Nore, Moisy & Quartier 2005). The basic principle of this flow is the following: a layer of fluid is carried near the disk by viscous friction and is thrown outwards by the centrifugal force. By incompressibility of the flow, fluid is pumped toward the centre of the disk. Since the review of Zandbergen & Dijkstra (1987), this family of flow has been called ‘von Kármán swirling flow’. In all cases, it deals with the flow between smooth disks, at low Reynolds numbers, enclosed or not in a cylindrical container.

1.1.2. *The ‘French washing machine’: an inertially driven, highly turbulent von Kármán swirling flow*

Experimentally, the so-called ‘French washing-machine’ has been a basis for extensive studies of very high-Reynolds-number turbulence in the last decade (Douady, Couder & Brachet 1991; Fauve, Laroche & Castaing 1993; Zocchi *et al.* 1994; Cadot, Douady & Couder 1995; Labbé, Pinton & Fauve 1996; Tabeling *et al.* 1996; Cadot *et al.* 1997; La Porta *et al.* 2001; Moisy *et al.* 2001; Bourgoin *et al.* 2002; Titon & Cadot 2003; Leprovost, Marié & Dubrulle 2004; Marié & Daviaud 2004; Ravelet *et al.* 2004). To reach a Kolmogorov regime in these studies, a von Kármán flow is inertially driven between two disks fitted with blades, at a very high Reynolds number ($10^5 \lesssim Re \lesssim 10^7$). Owing to the inertial stirring, very high turbulence levels can be reached, with fluctuations up to 50% of the blade velocity, as we shall see in this article.

Most of the inertially driven von Kármán setups studied in the past dealt with straight blades. Von Kármán flows with curved-blade impellers were first designed by the VKS-team to study dynamo action in liquid sodium (Bourgoin *et al.* 2002; Monchaux *et al.* 2007). With curved blades, the directions of rotation are no longer equivalent. One sign of the curvature, i.e. with the convex face of the blades forward, direction (+), has been shown to be the most favourable for dynamo action (Marié *et al.* 2003; Ravelet *et al.* 2005; Monchaux *et al.* 2007). The turbulent bifurcation (Ravelet *et al.* 2004) has been obtained with the concave face of the blades forward, direction (−). In this last work, the respective role of the turbulent fluctuations and of the changes in the mean flow with increasing the Reynolds number on the multistability were discussed.

1.2. *Outline of the present article*

Our initial motivation for the present study was thus to obtain an overview of the transition to turbulence and to check the range in which multistability exists. We first describe the experimental setup, the fluid properties and the measurement techniques in § 2. The main data presented in this article are obtained by driving our experiment continuously from laminar to turbulent regimes for this negative direction of rotation, covering a wide range of Reynolds numbers. In § 3 and § 4 we characterize the basic flow and describe the transition from the laminar regime to turbulence through quasi-periodicity and chaos and explore the construction of the temporal spectrum of velocity fluctuations. The continuity and global supercriticality of the transition to turbulence is a main result of this article.

In § 5 we obtain complementary data by comparing the two different directions of rotation and the case with a smooth disk. We show how inertial effects clearly lead to differences for the two directions of rotation at high Reynolds numbers. We then summarize and discuss the main results in § 6.

2. Experimental setup

2.1. *Dimensions, symmetries and control parameter*

The cylinder radius and height are, respectively, $R_c = 100$ mm and $H_c = 500$ mm. A sketch of the experiment is shown in figure 1(*a*). We use bladed disks to ensure inertial stirring. The impellers consist of 185 mm diameter stainless-steel disks each fitted with 16 curved blades, of curvature radius 50 mm and of height $h = 20$ mm (figure 1*b*). The distance between the inner faces of the disks is $H = 180$ mm, which defines a flow volume of aspect ratio $H/R_c = 1.8$. With the curved blades, the directions of rotation are no longer equivalent and we can either rotate the impellers anticlockwise, with the convex face of the blades forward, direction (+), or clockwise, with the concave face of the blades forward, direction (−).

The impellers are driven by two independent brushless 1.8 kW motors, with speed servo-loop control. The maximal torque they can reach is 11.5 N m. The motor rotation frequencies $\{f_1; f_2\}$ can be varied independently in the range $1 \leqslant f \leqslant 15$ Hz. Below 1 Hz, the speed regulation is not efficient, and the dimensional quantities are measured with insufficient accuracy. We will take for exact counter-rotating regimes $f_1 = f_2$ the imposed speed of the impellers f.

The experimental setup is thus axisymmetric and symmetric for rotations of π around any radial axis passing through the centre O ($\mathscr{R}_\pi$-symmetry), and we will consider here only $\mathscr{R}_\pi$-symmetric mean solutions, though mean flows breaking this symmetry do exist for these impellers, at least at very high Reynolds numbers

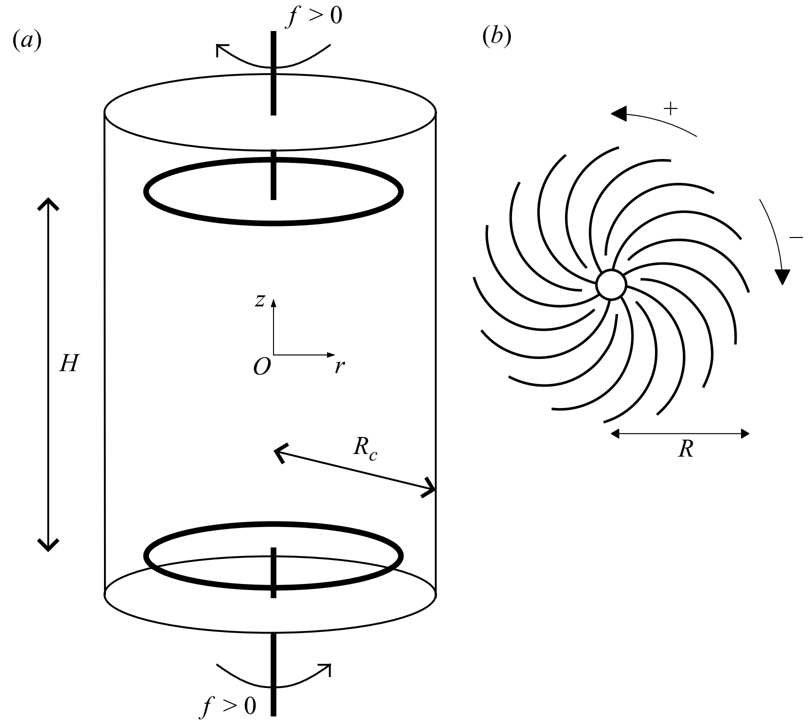

FIGURE 1. (*a*) Sketch of the experiment. The flow volume between the impellers is of height $H = 1.8R_c$. (*b*) Impellers used in this experiment. The disks radius is $R = 0.925R_c$ and they are fitted with 16 curved blades: the two different directions of rotation defined here are not equivalent. This model of impellers has been used in the VKS1 sodium experiment (Bourgoin *et al.* 2002) and is called TM60.

(Ravelet *et al.* 2004). A detailed study of the Reynolds number dependence of the 'global turbulent bifurcation' is outside of the scope of the present article and will be presented elsewhere. Also, since we drive the impellers independently, there is always a tiny difference between f_1 and f_2 and the $\mathcal{R}_\pi$-symmetry of the system cannot be considered as exact. In the following, we will use this symmetry as it is very useful to describe the observed patterns, but we will keep in mind that our system is only an approximation of a $\mathcal{R}_\pi$-symmetric system. The consequences for the dynamics will be analysed in the discussion (§ 6.1).

In the following, all lengths will be expressed in units of R_c. We also use cylindrical coordinates $\{r; z\}$ with origin on the axis of the cylinder and equidistant from the two impellers to take advantage of the $\mathcal{R}_\pi$-symmetry (see figure 1*a*). The time unit is defined using the impeller rotation frequency f. The integral Reynolds number Re is thus defined as $Re = 2\pi f R_c^2 \nu^{-1}$ with ν the kinematic viscosity of the fluid.

As in previous works (Marié & Daviaud 2004; Ravelet *et al.* 2004, 2005), we use water at 20 − 30 °C as working fluid to get Reynolds numbers in the range $6.3 \times 10^4 \lesssim Re \lesssim 1.2 \times 10^6$. To decrease Re down to laminar regimes, i.e. to a few tens, we need a fluid with a kinematic viscosity a thousand times greater than that of water. We thus use 99 %-pure glycerol with kinematic viscosity 0.95×10^{-3} m^2 s^{-1} at 20 °C (Hodgman 1947) and should be able to study the range $50 \lesssim Re \lesssim 900$. To cover a wide range of Reynolds numbers and match these two extreme ranges, we use different mixes of glycerol and water, at temperatures between 15 °C and 35 °C. The physical properties of these mixtures are given in table 1, where C is the mass percentage of glycerol in the mixture. Solutions samples are controlled in a Couette viscometer.

C	μ at 15 °C	μ at 30 °C	ρ	Re range
99%	1700	580	1260	50–2000
93%	590	210	1240	130–5600
85%	140	60	1220	550–19000
81%	90	41	1210	840–28000
74%	43	20	1190	1800–56000
0%	1.1	0.8	1000	570000–1200000

TABLE 1. Dynamic viscosity μ (10^{-3} Pa s) at various temperatures, density ρ (kg m^{-3}) at 20 °C and achievable Reynolds number range for various mass concentrations C of glycerol in water.

The temperature of the working fluid is measured with a platinum thermoresistance (Pt100) mounted on the cylinder wall $\{r=1;\ z=0\}$. To control this temperature, thermoregulated water circulates in two heat exchangers placed behind the impellers. Plexiglas disks can be mounted between the impellers and heat exchangers to reduce the flow on the back side of the impellers. They are at typically 50 mm behind the impellers. However, these disks reduce the thermal coupling: they are used in turbulent water flows and removed at low Reynolds number.

2.2. *Experimental tools, dimensionless measured quantities and experimental errors*

Several techniques have been used in parallel: flow visualizations with light sheets and air bubbles, torque measurements and velocity measurements.

Flow visualizations are made in vertical planes illuminated by approximately 2 mm thick light sheets. We look at two different positions in the flow: either the central meridian plane where the radial and axial components are visualized or in a plane almost tangent to the cylinder wall where the azimuthal component dominates. Tiny air bubbles (less than 1 mm diameter) are used as tracing particles.

Torques are measured using the current consumption in the motors given by the servo drives and have been calibrated by calorimetry. Brushless motors are known to generate electromagnetic noise, due to the pulse-width-modulation supply. We use armoured cables and three-phase sinusoidal output filters (Schaffner FN5010-8-99), and the motors are enclosed in Faraday cages, which enhances the quality of the measurements. The minimal torques we measured are above 0.3 N m, and we estimate the error in the measurements to be ±0.1 N m. The torques T will be presented in the dimensionless form:

$$K_p = T\ \left(\rho R_c^5 (2\pi f)^2\right)^{-1}.$$

Velocity fields are measured by laser Doppler velocimetry (LDV). We use a single-component DANTEC device, with a He–Ne Flowlite Laser (wavelength 632.8 nm) and a BSA57N20 Enhanced Burst Spectrum Analyser. The geometry of the experiment allows us to measure at one point either the axial component $V_z(t)$ or the azimuthal component $V_\theta(t)$. Though the time-averaged velocity field $\boldsymbol{V}$ is not a solution of the Navier–Stokes equations, it is a solenoidal vector field, and it is axisymmetric. We thus use the incompressibility condition $\nabla \cdot \boldsymbol{V} = 0$ to compute the remaining radial component V_r.

The measurements of the time-averaged velocity field are performed on a $\{r \times z\} = 11 \times 17$ grid, weighting velocities by the particles transit time, to remove velocity biases as explained by Buchhave, George & Lumley (1979). This acquisition mode does not have a constant acquisition rate, so we use a different method for the acquisition of well-sampled signals to perform temporal analysis at single points.

In this so-called dead-time mode, we ensure an average data rate of approximately 5 kHz, and the Burst Spectrum Analyser takes one sample every millisecond such that the final data rate is 1 kHz. For practical reasons, this method is well-suited to points close to the cylindrical wall, so we choose the point $\{r=0.9; z=0\}$ for the measurements in figures 3, 4 and 5. The signals are re-sampled at 300 Hz by a 'sample and hold' algorithm (Buchhave *et al.* 1979).

Let us now consider the experimental error in the Reynolds number value. The speed servo-loop control ensures a precision of 0.5 % in f, and an absolute precision of ± 0.002 in the relative difference of the impeller speeds $(f_1 - f_2)/(f_1 + f_2)$. The main error in the Reynolds number is thus a systematic error that comes from the estimation of the viscosity. Taking the variation of the viscosity with temperature to be about 4 % for 1°C and the variation with concentration to be about 5 % for 1 % of mass concentration, we estimate the absolute error in Re as ± 10 % (the temperature is known within 1°C). However, the experimental reproducibility of the Reynolds number is much higher than $\pm 10\%$. In the range $100 \lesssim Re \lesssim 500$ we are able to take Re within ± 5.

3. From order to turbulence: description of the regimes

This section describes the evolution of the flow from the laminar regime to the fully developed turbulence, i.e. for $30 \lesssim Re \lesssim 1.2 \times 10^6$. This wide-range study has been carried for the negative sense of rotation (—) of the propellers.

3.1. *Basic state at very low Reynolds number*

At very low Reynolds number, the basic laminar flow respects the symmetries of the problem. It is stationary, axisymmetric and $\mathscr{R}_\pi$-symmetric. This state is stable at $Re = 90$, for which we present a flow visualization in figure 2(*a*, *b*). In figure 2(*a*), the light sheet passes through the axis of the cylinder. The visualized velocities are the radial and axial components. The poloidal part of the flow consists of two toric recirculation cells, with axial pumping directed towards the impellers.

The flow also contains two counter-rotating cells, separated by an azimuthal flat shear layer, which can be seen in figure 2(*b*) where the light sheet is quasi-tangent to the cylinder wall. Both the azimuthal and axial components vanishs in the plane $z = 0$, which is consistent with the axisymmetry and the $\mathscr{R}_\pi$-symmetry. This flat shear layer is sketched in figure 2(*e*). An LDV velocity field is presented in § 5 (figure 10*c*, *d*).

3.2. *First instability – stationary bifurcation*

The first instability for this flow has been determined by visualization and occurs at $Re = 175 \pm 5$ for both directions of rotation. The bifurcation is supercritical, non-hysteretic, and leads to a stationary regime, with an azimuthal modulation of wavenumber $m = 2$. We present a visualization of this secondary state in figure 2(*c*), at $Re = 185$. The axisymmetry is broken: one can see the $m = 2$ modulation of the shear layer, also sketched in figure 2(*e*). Note also that $\mathscr{R}_\pi$-symmetry is partly broken: the bifurcated flow is $\mathscr{R}_\pi$-symmetric with respect to two orthogonal radial axes only. This first instability is very similar to the Kelvin–Helmholtz instability. Nore *et al.* (2003) made a theoretical extension of the Kelvin–Helmholtz instability in a cylinder. Their model is based on the use of local shear-layer thicknesses and Reynolds numbers to take into account the radial variations in the cylindrical case.

We observe this $m = 2$ shear layer to rotate very slowly in a given direction with a period $7500 f^{-1}$. This corresponds to a very low frequency, always smaller than the maximum measured non-symmetry of the speed servo-loop control between the two

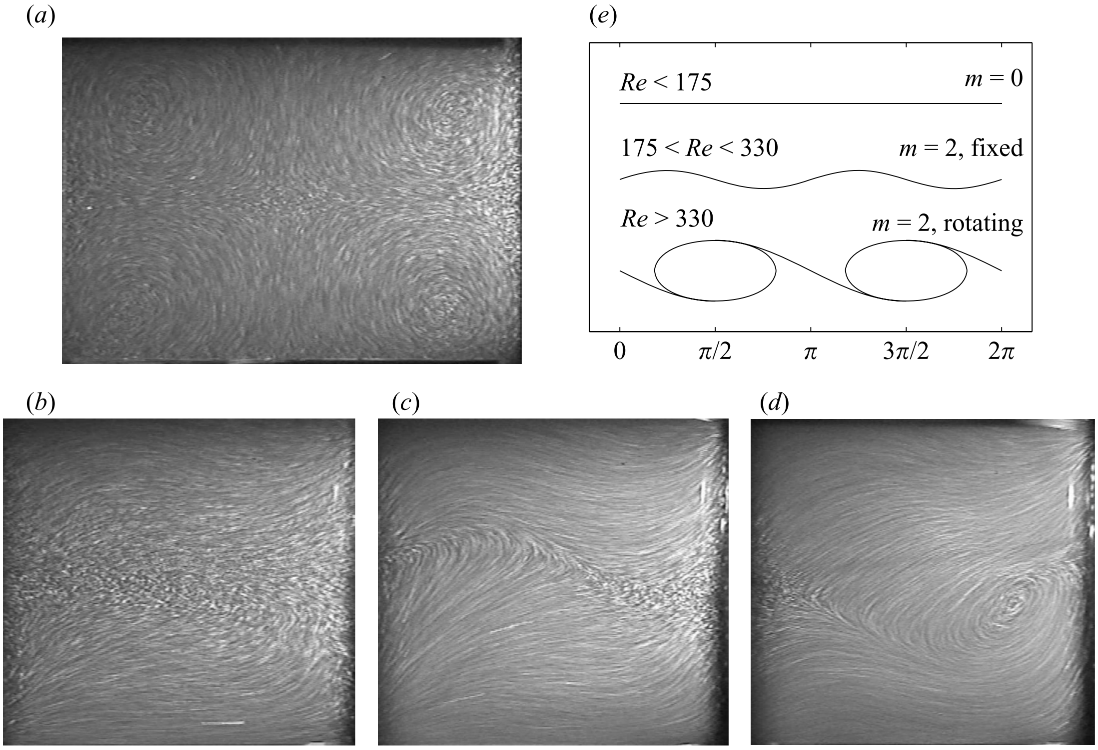

FIGURE 2. Visualization and schematics of the basic laminar flow for impellers rotating in direction (−). The lighting is with a vertical light sheet. Pictures are integrated over 1/25 s with a video camera, and small air bubbles are used as tracers. Picture height is $H - 2h = 1.4R_c$. Laminar axisymmetric flow at $Re = 90$, meridian view (*a*). Views in a plane near the cylinder wall at $Re = 90$ (*b*), $Re = 185$ (*c*) and $Re = 345$ (*d*). The development of the first $m = 2$ instabilities, steady undulation (*c*) and rotating vortices (*d*), is clearly visible in the shape of the shear layer. We give sketches of the shear layer for these Reynolds numbers in (*e*).

independent motors (§ 2.2). This is probably the limit of the symmetry of our system, i.e. the pattern is at rest in the slowly rotating frame where both frequencies are strictly equal (see discussion in § 6.1). For convenience, we will describe the dynamics in this frame.

The laminar $m = 2$ stationary shear-layer pattern is observed up to typically $Re \simeq 300$ where time-dependence arises.

To investigate the time-dependent regimes, we also performed precise velocity measurements at a given point in the shear layer. We measure the azimuthal component v_θ at $\{r = 0.9;\ z = 0\}$, using the dead-time acquisition mode (see § 2).

Below, we describe and illustrate the dynamics observed and the building-up of the chaotic and turbulent spectra. The next § 4 is complementary: we quantitatively characterize the transitions as far as we can, discuss the mechanisms and finally propose a global supercritical view of the transition to turbulence.

3.3. *From drifting patterns to chaos*

We present time series of the velocity and power spectral densities at five Reynolds numbers in figure 3: $Re = 330 \pm 5$, $Re = 380 \pm 5$, $Re = 399 \pm 5$, $Re = 408 \pm 5$ and $Re = 440 \pm 5$.

3.3.1. *Oscillation at the impeller frequency*

The point at $Re = 330 \pm 5$ is the first at which a clear temporal dynamics is observed: a sharp peak in the spectrum (figure 3*b*) is present at the impeller rotation frequency $f_a = f$, shown enlarged in the inset of figure 3(*a*). This oscillation exists for higher

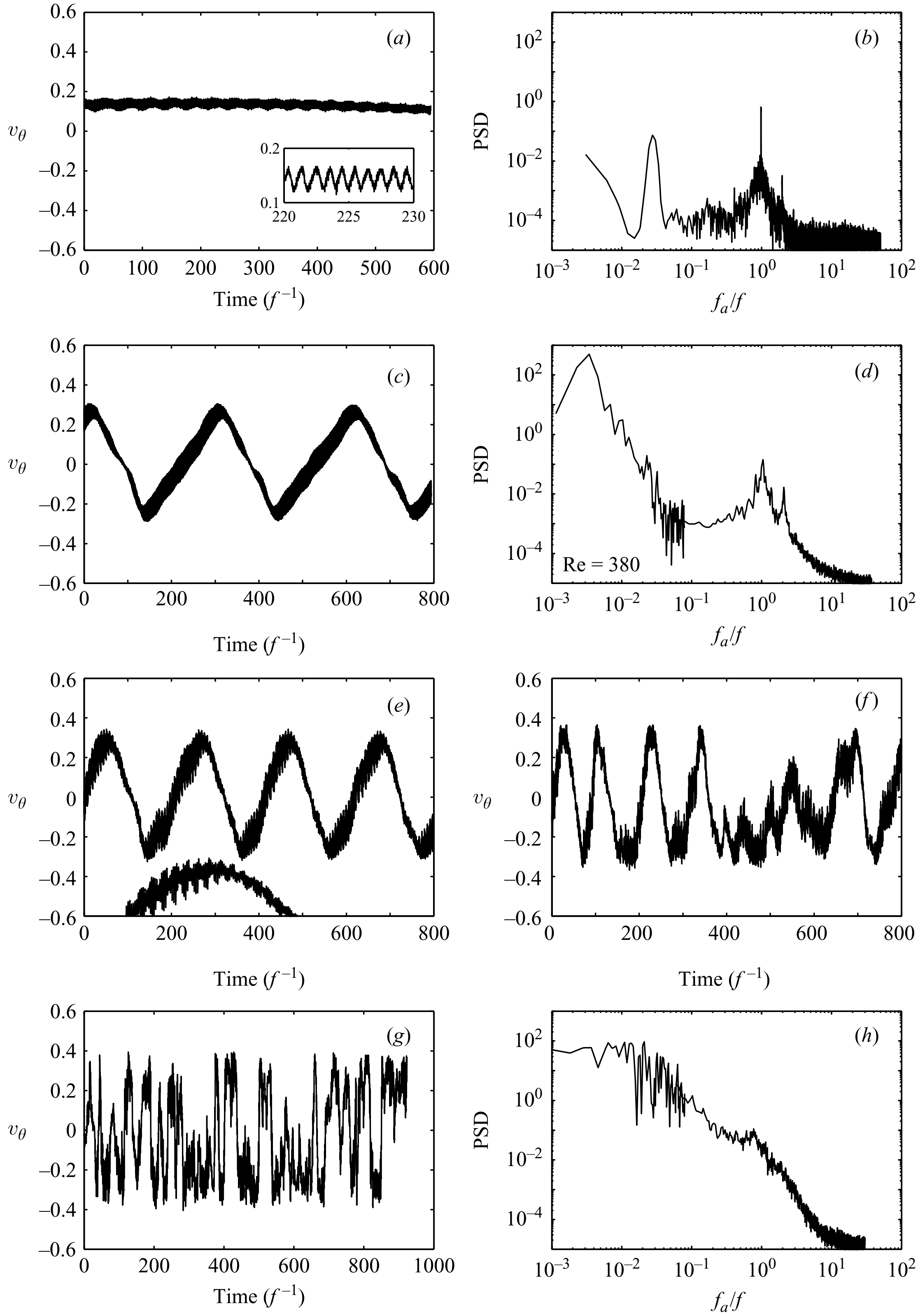

FIGURE 3. Temporal signals $v_\theta(t)$ measured by LDV at $\{r=0.9; z=0\}$ and power spectral densities (PSD), for (*a*,*b*) $Re=330$, (*c*,*d*) $Re=380$, (*e*) $Re=399$, (*f*) $Re=408$ and (*g*, *h*) $Re=440$. f_a is the analysis frequency whereas f is the impeller rotation frequency. Inset in (*a*): zoom of the fast oscillation at frequency f. In (*e*), a small part of the signal is presented with time magnification (×4) and arbitrary shift to highlight the modulation at $6.2f^{-1}$. Power spectra are computed by the Welch periodogram method twice: with a very long window to catch the slow temporal dynamics and with a shorter window to reduce fast-scale noise.

Re with the same small amplitude: it is too fast to be visible on the long time series of figure 3, but it is responsible for the large width of the signal line.

In comparison, a similar measurement performed at $Re \simeq 260$ reveals a flat signal with a very low flat spectrum with just a tiny peak, that is 1/1000 of the amplitude measured at $Re = 330$, at $f_a = f$; we have no data between to check the evolution.

On the spectra, we observe the first harmonic, but do not see the expected blade frequency $8f$ nor a multiple of it. So, it is not clear if it corresponds to the basic fluid instability mode or just to a small precessing mode due to the misaligning of the impeller axis or to mechanical vibrations transmitted to the fluid through the bearings. Since the travelling-wave mode of the next section is much stronger and richer in dynamics we will consider that the signal at $f_a = f$ is a 'minor' phenomenon, i.e. a perturbation of the steady $m = 2$ mode.

In figure 3(*a*) the mean velocity is not zero, but around $v_\theta = +0.17$ during the 600 time units of acquisition, i.e. during 600 disks rotations. This value of the velocity has no special meaning and depends on the phase between the fixed measurement point and the slowly drifting shear layer (§ 3.2). The measurement point stays on the same side of the shear layer for this time series but, on much longer time scales, we measure the typical $m = 2$ shear-layer rotation period.

Further observation of the signal and spectrum of figure 3(*a*, *b*) reveals some energy at low frequency around $f_a \simeq f/30$, corresponding to slowly relaxing modulations: the slowness of this relaxation is the clear signature of the proximity of a critical point.

3.3.2. *Drifting/travelling waves*

For $330 < Re < 389$ the velocity signal is periodic with a low frequency f_D. This is illustrated at $Re = 380$ in figure 3(*c*, *d*). The mean velocity is now zero: the shear layer rotates slowly such that the measurement point is alternately in the cell rotating with the upper impeller ($v_\theta > 0$) and in the cell rotating with the lower impeller ($v_\theta < 0$). Visualizations confirm that this corresponds to a travelling wave (TW) or a drifting pattern and also show that the $m = 2$ shear layer is now composed of two vortices (figure 2*d*) and thus merits the name 'mixing-layer'. Along the equatorial line, the parity is broken or the vortices are tilted (Coullet & Iooss 1990; Knobloch 1996). The velocity varies between $-0.3 \lesssim v_\theta \lesssim 0.3$. The drift is still slow but one order of magnitude faster than the drift described above for the 'steady' $m = 2$ pattern: one can see two periods during 600 time units, i.e. $f_D = f/300$, which is very difficult to resolve by spectral analysis owing to the shortness of the signal (see the caption of figure 3). At $Re = 380$ (figure 3*c*, *d*), the peak at the rotation frequency is still present, but starts to spread and becomes broadband. The power spectral density at frequencies higher than $3f$ decreases extremely rapidly to the noise level. Note that the $\mathscr{R}_\pi$-symmetry remains only with respect to a pair of orthogonal radial axes which rotates with the propagating wave.

3.3.3. *Modulated travelling waves*

For $389 < Re < 408$ the signal reveals quasi-periodicity, i.e. modulated travelling waves (MTW), shown in figure 3(*e*, *f*) at $Re = 399$ and 408. The MTW are regular, i.e. strictly quasi-periodic below $Re = 400$ and irregular above. The modulation frequency (see the magnified (×4) part of the signal in figure 3*e*) is $f_M = f/(6.2 \pm 0.2)$ whatever Re, even above $Re = 400$. It is much faster than the drift frequency ($f_D \sim f/200$) and movies show that it seems to be related to oscillations of the mixing-layer vortex cores.

3.3.4. *Chaotic regime*

The upper limit of the regular dynamics is precisely and reproducibly $Re = 400$ and there is no hysteresis. From the visualizations, we observe that the $m = 2$ symmetry is now broken. The mixing-layer vortices, which are still globally rotating around the cell in the same direction, also behave more and more erratically with increasing Re: their individual dynamics includes excursions in the opposite direction as well as towards one or other impeller. The velocity signal also loses its regularity (see figure 3*e*–*g*).

When this disordered regime is well established, *e.g.* for $Re = 440$ (figure 3*g*), it can be described as series of almost random and fast jumps from one side to the other of the $v = 0$ axis. The peaks reached by the velocity are now in the range $-0.4 \lesssim v_\theta \lesssim 0.4$. The spectral analysis of the signal at $Re = 440$ (figure 3*h*) no longer reveals any well-defined frequency peaks. However, a continuum of highly energetic fluctuations at low frequency, below $f_a = f$ and down to $f_a = f/100$, emerges. A small bump at the rotation frequency f is still visible, and a region of fast fluctuations above the injection frequency also arises. Although we did not carried detailed Poincaré analysis or equivalent and cannot clearly characterize a scenario, we find this transition and this regime typical enough to call it ‘chaos’ (see also § 4.2).

3.4. *From chaos to turbulence: building a continuous spectrum*

Increasing the Reynolds number further, one obtains the situation depicted in figure 4. The time spectrum is now continuous but still evolving. We describe the situations below and above the impeller frequency f separately.

3.4.1. *Slow time scales*

The slow dynamics which has already been described at $Re = 440$ (figure 3*g*, *h*) could be thought to depend only on the largest spatial scales of the flow. It is well established above $Re \simeq 10^3$ (figure 3*b*). The mean velocities corresponding to each side of the mixing layer are of the order of ± 0.6 at $Re = 1.0 \times 10^3$ and above (figure 4*a*, *c*, *g*). The power spectral density below the injection frequency seems to follow a f^{-1} power law over two decades (see discussion § 6.2) for all these Reynolds numbers (figure 4). The spectral density saturates below $10^{-2} f$.

3.4.2. *Fast time scales*

However, the fast time scales, usually interpreted as a trace of fluctuations of small spatial scales evolve between $Re = 1.0 \times 10^3$ and $Re = 6.5 \times 10^3$. At the former Reynolds number, there are few fast fluctuations decaying much faster than $f^{-5/3}$ (figure 4*b*) and the intermittent changeovers are easy to identify in the temporal signal in figure 4(*a*). If the Reynolds number is increased, the fast (small-scale) fluctuations get increasingly bigger and follow a power law over a growing frequency range (figure 4*e*, *f*, *h*). The measured slope is of order of -1.55 over 1.5 decade, i.e. 10% lower than the classical $f^{-5/3}$. This value of the exponent could be ascribed to the so-called ‘bottleneck’ effect (Falkovich 1994) and is compatible with the values given by Lohse & Müller-Groeling (1995) (-1.56 ± 0.01) for a Taylor-microscale Reynolds number $R_\lambda \simeq 100$, which is an estimation for our flow based on the results of Zocchi *et al.* (1994).

4. Quantitative characterization of the transitions

The various dynamic states encountered have been described and illustrated in the previous section. Now, we wish to analyse some characteristic measurements, i.e. the

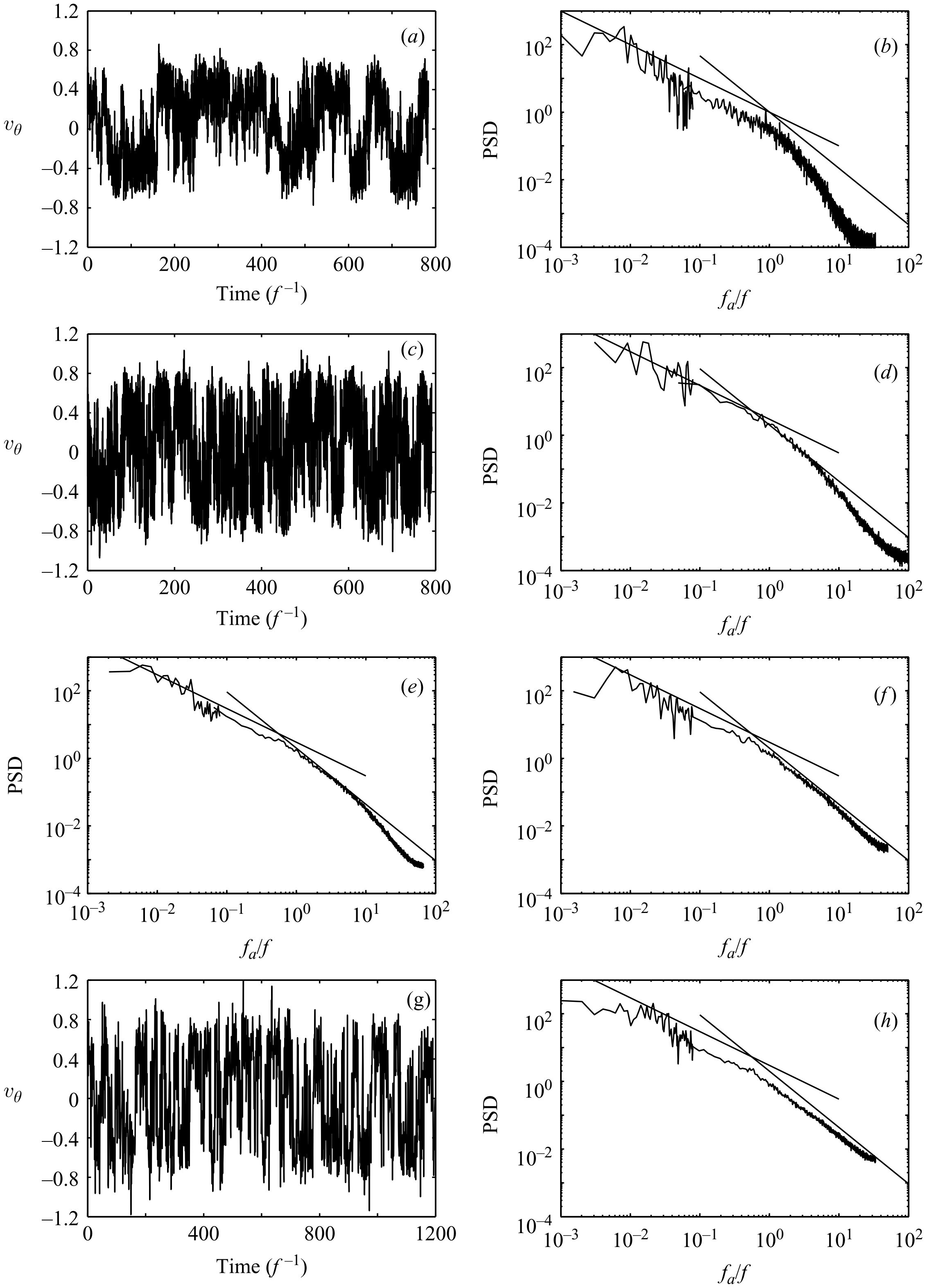

FIGURE 4. (a,b) Temporal signal $v_\theta(t)$ measured by LDV at $\{r = 0.9; z = 0\}$ and power spectral density at $Re = 1.0 \times 10^3$. (c, d) Temporal signal and power spectral density at $Re = 1.7 \times 10^3$. (e, f) Power spectral densities at 2.7×10^3 and 3.8×10^3. (g, h) Temporal signal and power spectral density at 6.5×10^3. Solid lines in the power spectra plots are power-law eye-guides of slope −1 and −5/3. Spectra are computed as explained in the caption of figure 3.

amplitude of the velocity fluctuations and their main frequencies, extract thresholds and critical behaviours and then address the question of the nature of the reported transitions.

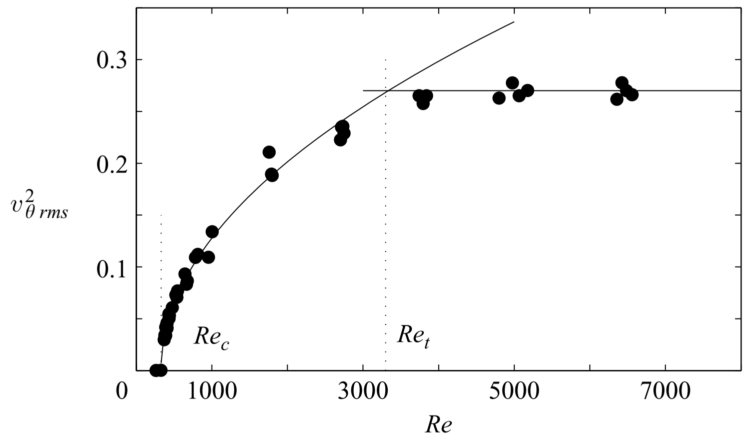

FIGURE 5. Variance of $v_\theta(t)$ measured at $\{r=0.9; z=0\}$ *vs.* Re. Solid curve: nonlinear fit of the form $v^2_{\theta\ rms} = a \times (Re - Re_c)^{1/2}$, fitted between $Re = 350$ and $Re = 2500$. The regression coefficient is $R^2 = 0.990$, and the fit gives $Re_c = 328 \pm 8$ with 95 % confidence interval. The intersection between this fit and the asymptotic value $v^2_{\theta\ rms} \simeq 0.27$ gives $Re_t = 3.3 \times 10^3$.

4.1. *From order to turbulence: a global supercriticality*

It is known that fully turbulent von Kármán flow can generate velocity fluctuations of typically 50 % of the driving impeller velocity. So, we compute the variance $v^2_{\theta\ rms}$ of the LDV time series *versus* the Reynolds number. This quantity is equivalent to a kinetic energy and can be referred to as the azimuthal kinetic energy fluctuations in the mixing layer. With this method, we consider the broadband frequency response of the signal. The results are reported in figure 5 for all the measurements performed between $260 \lesssim Re \lesssim 6500$. Except at the time-dependence threshold, this quantity behaves smoothly: it can be fitted between $Re = 350$ and $Re = 2500$ with a law in the square root of the distance to a threshold $Re_c \simeq 330$ (figure 5):

$$v^2_{\theta\ rms} \propto (Re - Re_c)^{1/2}.$$

Since we will show below that Re_c is precisely the threshold for time-dependence, we can make the hypothesis that $v^2_{\theta\ rms}$ is a global order parameter for the transition to turbulence, i.e. for the transition from steady flow to turbulent flow taken as a whole. With this point of view the transition is globally supercritical.

4.2. *Transitions from order to chaos*

We now turn to the first steps in the transition to time dependence. We monitor the main frequencies of the mixing-layer dynamics in the TW- and MTW-regimes (see § 3.3). In these regimes, even though only a few periods are monitored along single time-series, we carefully estimate the period by measuring the time delay between crossings of the $v = 0$ axis. These values are shown in figure 6(*a*) with circles. In an equivalent way, the periodicity of the travelling of the mixing-layer vortices on the visualizations give complementary data, represented by squares on the same figure.

4.2.1. *Onset of time-dependence*

The drift frequency f_D of the travelling waves behaves linearly with Re above a threshold Re_{TW} very close to 330. Both measurement methods agree though as the visualizations have large error bars in Re due to the shortness of our records and to a poorer thermal control, the fit is made on velocity data only. We observe some imperfection in the quasi-periodic bifurcation, due to the pre-existing slow drift below

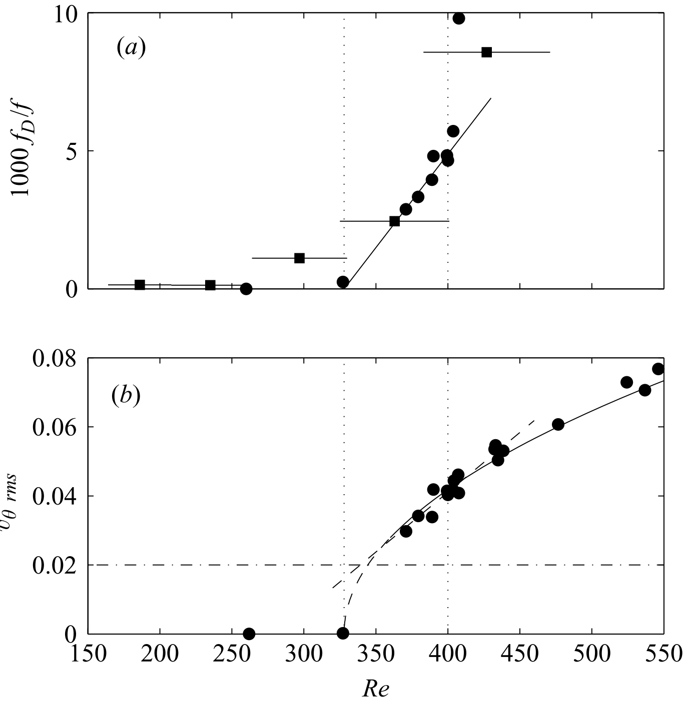

FIGURE 6. (*a*) Low-frequency f_D of the quasi-periodic regime of velocity $v_\theta(t)$ measured at $\{r=0.9; z=0\}$ (circles) and drift frequency of the $m=2$ shear-layer pattern from flow visualizations (squares with large horizontal error bars due to poorer temperature control). The solid line is a linear fit of f_D between the two thresholds $Re_{TW}=330$ and $Re_{chaos}=400$, indicated by vertical dotted lines. (*b*) Enlargement of figure 5. The dashed line is a linear fit of the lowest data between $Re=350$ and $Re=450$. Close to the threshold, it crosses the dash-dotted line which corresponds to the velocity due to the drift and estimates the level of imperfection.

Re_{TW}: we always observe the mixing layer to start rotating in the sense of the initial drift.

We show in figure 6(*b*) an enlargement of figure 5, i.e. the amplitude of the kinetic energy fluctuations. We observe that both the quadratic amplitude fit and the linear frequency fit converge to exactly the same threshold $Re_{TW}=Re_c=328$. We can conclude that the low-frequency mode at $f_a=f_D$ bifurcates at $Re=330\pm5$ through a zero-frequency bifurcation for f_D.

The question is thus precisely how the amplitude behaves at onset. There is obviously a lack of data in the narrow range $300 \lesssim Re \lesssim 350$ (figure 6*b*). It is due to the high temperature dependence of the viscosity in this regime (Reynolds number varied quite fast even with thermal control) and to some data loss at the time of the experimental runs. Despite this lack, we present these observations because of the consistency of the different types of data – visualizations, LDV, torques – over the wide Reynolds number range. The horizontal line $v^2_{\theta\ rms}=0.02$ in figure 6(*b*) corresponds to an amplitude of typically 0.15 for v_θ, which is produced just by the initial shear-layer drift (see the maximum speed in figure 3*a*). This value is in good agreement with a linear extrapolation over the lower range of figure 6(*b*) and thus again with an imperfect bifurcation due to the drift. If we reduce the drift by better motor frequencies matching, the onset value of v_θ will depend on the height of the probe location and the parabola of figure 6(*b*) could perhaps be observed on the $m=2$ shear-layer modes.

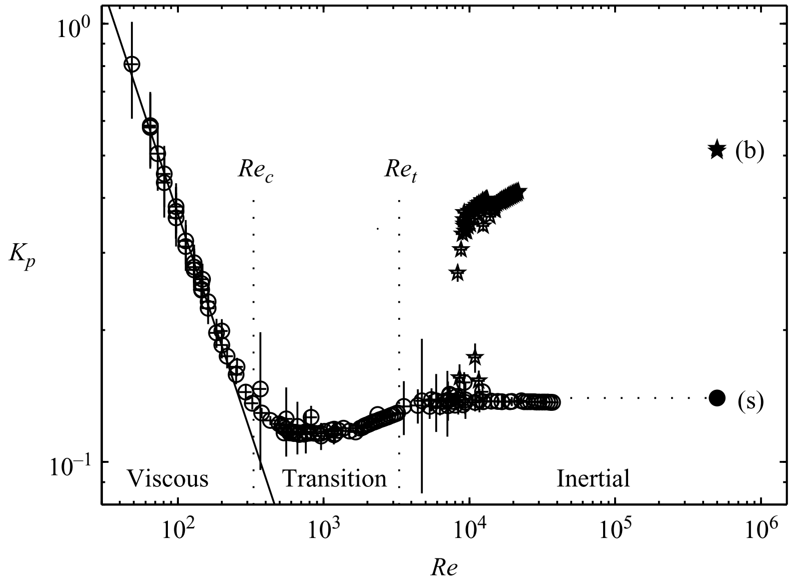

FIGURE 7. Dimensionless torque K_p *vs.* Re in a log-log scale for the negative sense of rotation (—) of the impellers. The main data (○) correspond to the symmetric (s)-flow regime described here. For completeness, the high-torque branch (★) for $Re \gtrsim 10^4$ corresponds to the (b) flow regime (Ravelet *et al.* 2004), i.e. to the 'turbulent bifurcation' (see § 4.4). Since the two motors do not deliver the same torque in this $\mathscr{R}_\pi$-symmetry-broken (b) flow, the average of both values is plotted. Relative error in Re is $\pm 10\,\%$; absolute error of ± 0.1 N m in the torque. Re_c and Re_t are the transition values computed from the fits of figure 5. The single points displayed at $Re = 5 \times 10^5$ correspond to measurements in water, where K_p is extracted from a fit of the dimensional torque by $a + b \times f^2$ for $2 \times 10^5 \lesssim Re \lesssim 9 \times 10^5$ (Ravelet *et al.* 2005).

4.2.2. *Transition to chaos*

The very sharp transition to chaos is observed for $Re > Re_{chaos} = 400$. There is no hysteresis. Just above the chaotic threshold in the MTW regime (figure 3f), the signal sometimes exhibits a few almost-quasi-periodic oscillations, still allowing us to measure a characteristic frequency. The measured values have also been plotted on figure 6(a) and are clearly above the linear fit. This could reveal a vanishing time scale, i.e. a precursor for the very sharp positive/negative jumps of v_θ reported in the chaotic and turbulent regimes.

We do not clearly observe any evidence of mode locking between the present frequencies which are in the progression $f/200 \rightarrow f/6.2 \rightarrow f$ and there is no trace of a sub-harmonic cascade on any of each. This could be linked to a three-frequency scenario like Ruelle–Takens (Manneville 1990).

4.3. *Transition to full turbulence*

4.3.1. *Torque data*

Complementary to the local velocity data, information can be collected on spatially integrated energetic data, i.e. on torque measurements $K_p(Re)$ (figure 7). The low-Reynolds-numbers viscous part will be described below (§ 5) as well as the high-torque bifurcated branch (§ 4.4). In the high-Reynolds-number regimes, the torque reaches an absolute minimum for $Re \simeq 1000$ and becomes independent of Re above 3300.

4.3.2. *From chaos to turbulence*

Is there a way to quantitatively characterize the transition or the crossover between chaos and turbulence? These seems to be no evidence of any special sign to indicate the change between the two regimes. A possible empirical criterion would be the

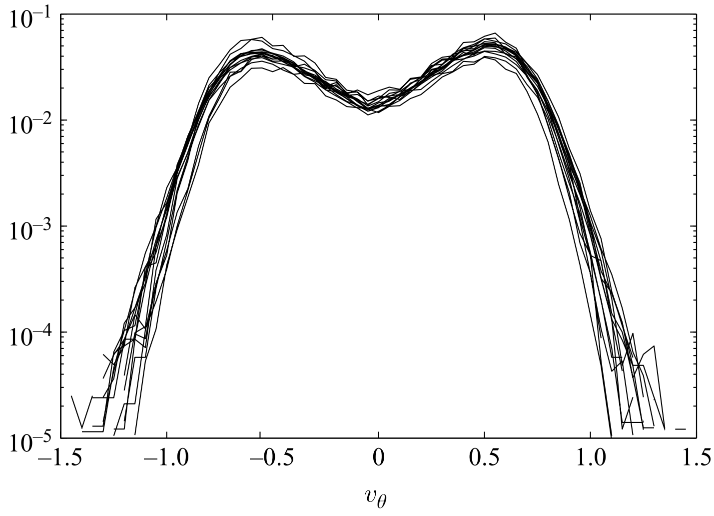

FIGURE 8. Probability density function (PDF) of v_θ for 16 Reynolds numbers in the range $2.5 \times 10^3 \lesssim Re \lesssim 6.5 \times 10^3$.

completeness of the $(f_a/f)^{-1}$ low-frequency part of the spectrum, clearly achieved for $Re = 1000$ (figure 4*b*). This region also corresponds to the minimum of the $K_p(Re)$ curve (figure 7). One could propose that below this Reynolds number, the power injected at the impeller rotation frequency mainly excites low frequencies belonging to the 'chaotic' spectrum, whereas above $Re \simeq 1000$ it also drives the high frequencies through the Kolmogorov–Richardson energy cascade.

4.3.3. *Inertial turbulence*

The $(Re - Re_c)^{1/2}$ behaviour can be fitted through the quasi-periodic and chaotic regimes, up to $Re \sim 3000$. Here, the azimuthal kinetic energy fluctuation level saturates at $v_{\theta\ rms}^2 \simeq 0.27$, i.e. fluctuations of velocities at this point of the mixing layer are of the order of 50 % of the impeller tip speed. This saturation is also revealed by the probability density functions (PDFs) of v_θ presented in figure 8. These PDFs are computed for 16 Reynolds numbers in the range $2.5 \times 10^3 \lesssim Re \lesssim 6.5 \times 10^3$. Note the bimodal character of the PDFs: the two bumps, which are symmetric, correspond to the two counter-rotating cells. Furthermore, all these PDFs collapse and are therefore almost independent of Re in this range. This is also consistent with the spectral data of figure 4(*b–d*) where the $(f_a/f)^{-1}$ slowest time-scale regions which contain most of the energy, below f, appear similar for $Re = 1.0 \times 10^3$ and above (figure 4). The crossover Reynolds number Re_t at which the kinetic energy of fluctuations saturates in figure 5 is estimated by taking the intersection of the horizontal asymptote with the fit: $Re_t = 3.3 \times 10^3$. This value corresponds precisely to the value at which the asymptotic plateau is reached in the K_p *vs.* Re diagram (figure 7). In such an inertially driven turbulent flow, the bulk dissipation is much stronger than the dissipation in boundary layers and the global dimensionless quantities thus do not depend on the Reynolds number past a turbulent threshold (Lathrop, Fineberg & Swinney 1992; Cadot *et al.* 1997).

4.4. *Higher Reynolds number: multistability and turbulent bifurcation*

From all the observations reported above in the negative direction of rotation, we conclude that the transition to turbulence is completed at Re_t and that the azimuthal kinetic energy fluctuation can be considered as an order parameter for the global

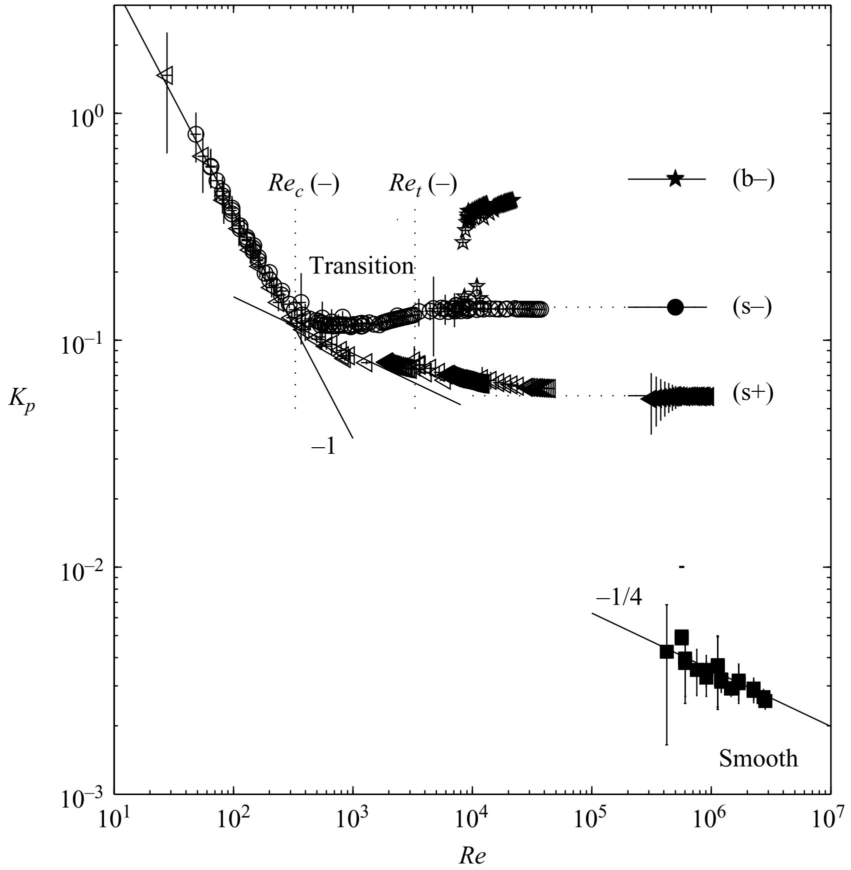

FIGURE 9. Compilation of the dimensionless torque K_p *vs.* Re for various flows. All data are for $\mathscr{R}_\pi$-symmetric von Kármán flows except the branch labelled (b—) ($\star$): see caption of figure 7 for details. $\circ$, direction of rotation (—); $\triangle$ direction of rotation (+); the solid line is a nonlinear fit of equation $K_p = 36.9 \times Re^{-1}$ between $Re = 30$ and $Re = 250$. Some data for flat disks of standard machine-shop roughness, operated in pure water up to 25 Hz (squares) are also displayed with a $Re^{-1/4}$ fit. A $-1/4$ power law is fitted for the positive direction of rotation for $330 \leqslant Re \leqslant 1500$ and is displayed between $Re = 10^2$ and $Re = 10^4$. Relative error in Re is $\pm 10\,\%$; absolute error of ± 0.1 N m on the torque. Re_c and Re_t are the transition values computed from the fits of figure 5.

transition, from the onset of time-dependence $Re_c = 330$ to the fully turbulent state transition/crossover at $Re_t = 3.3 \times 10^3$, i.e. over a decade in Reynolds number.

In the inertial regime above Re_t, the von Kármán flow driven by high-curvature bladed impellers rotating in the negative direction presents another original behaviour: Ravelet *et al.* (2004) have shown that the turbulent von Kármán flow can exhibit multistability at high Reynolds number. To study and analyse this phenomenon, it is necessary to introduce an additional parameter: the rotation velocity difference $\Delta f = f_2 - f_1$ between the two impellers. The so-called ‘turbulent bifurcation’ and multistability are observed exclusively for the negative direction of rotation. So, the $\Delta f = 0$ regime presented here, called (s) for symmetric in Ravelet *et al.* (2004), can be observed only if both motors are started together, i.e. if Δf is kept equal to zero at any time. Once a velocity difference is applied for long enough, depending of the magnitude of $|\Delta f|$, the flow changes abruptly to a one-cell-flow with axial pumping towards one of the impellers only instead of towards each impeller. This new flow, called (b) for bifurcated in Ravelet *et al.* (2004), strongly breaks the $\mathscr{R}_\pi$-symmetry, has no middle shear layer and requires much higher torque from the motors: typically 3 times the value of (s)-flow, with a finite difference between the two motors. The mean reduced torque at $\Delta f = 0$ is plotted with stars in figure 7: branches (s) and (b) co-exist for $Re \gtrsim Re_m = 10^4$. To recover the $\mathscr{R}_\pi$-symmetric flow, one should stop the motors or at least decrease Re below Re_m.

Note that this multistability is only observed above Re_t, i.e. for flows with a well-developed turbulent inertial Kolmogorov cascade. Furthermore, cycles in the parameter plane $\{K_{p2} - K_{p1};\ f_2 - f_1\}$ have been made for various Re between 100 and 3×10^5 (Ravelet 2005). At low Reynolds numbers, $Re \lesssim 800$, this cycle is reduced to a continuous, monotonic and reversible line in the parameter plane. The first appearance of 'topological' transformations of this simple line into multiple discontinuous branches of a more complex cycle is seen at $Re \simeq 5 \times 10^3$, in the neighbourhood of the transitional Reynolds number Re_t, and multistability for $\Delta f = 0$ is first observed for $Re \sim 10^4$. The extensive study of this turbulent bifurcation with varying Re deserves separate treatment and will be reported elsewhere.

From the above preliminary report of our results, we emphasize that the turbulent bifurcation seems specific to fully developed turbulent flows. Whereas the exact counter-rotating flow ($\Delta f = 0$) will never bifurcate (Ravelet *et al.* 2004), for a small Δf $(0 < |\Delta f|/f \ll 1)$ this turbulent bifurcation around $Re_m = 10^4$ will correspond to a first-order transition on the way to infinite-Reynolds-number dynamics: this flow appears an ideal prototype of an ideal system undergoing a succession of well-defined transitions from order to high-Reynolds-number turbulence.

4.5. *The regimes: a summary*

The next section concerns some aspects specific to the inertial stirring. Then follows a discussion (§ 6) about the role of the symmetries and of the spatial scales of the flow which can be read almost independently. The following summary of the observed regimes and transitions is given to support the discussion.

$Re < 175$: $m = 0$, axisymmetric, $\mathscr{R}_\pi$-symmetric steady basic flow (§ 3.1),
$175 < Re < 330$: $m = 2$, discretely $\mathscr{R}_\pi$-symmetric steady flow (§ 3.2),
$330 < Re < 389$: $m = 2$, non $\mathscr{R}_\pi$-symmetric, equatorial-parity-broken travelling waves (§ 3.3.2, § 4.2.1),
$389 < Re < 400$: modulated travelling waves (§ 3.3.3),
$400 < Re < 408$: chaotic modulated travelling waves (§ 3.3.3),
$400 < Re \lesssim 1000$: chaotic flow (§ 3.3.4, § 4.2.2),
$1000 \lesssim Re \lesssim 3300$: transition to turbulence (§ 3.4, § 4.3.2),
$Re \gtrsim 3300$: inertially driven fully turbulent flow (§ 4.3.3),
$Re \gtrsim 10^4$: multivalued inertial turbulence regimes (§ 4.4).

5. Viscous stirring vs. inertial stirring

We now focus on the details of the inertial stirring. So for, a single rotation sense, the negative (−), has been studied. However, relevant information can be obtained from the comparison of data from both senses of impellers rotation, which is equivalent to having two sets of impellers with opposite curvature at any time in the same experiment.

The guideline for this analysis is the global energetic measurements over the whole Reynolds number range. The data for sense (−) have already been partly discussed above (figure 7), but the full set is shown here in figure 9. At low Reynolds number the two curves are identical, which means that the blades have no effect on the viscous stirring. This is analysed in § 5.1. However, at high Reynolds number, there is a factor

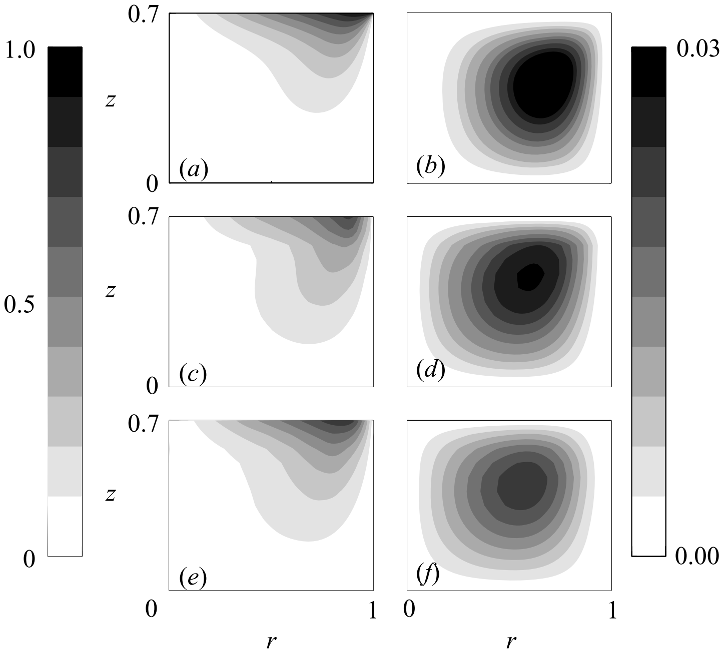

FIGURE 10. Comparison between a numerical simulation (a, b) performed with the code of Nore *et al.* (2003) in a cylinder of aspect ratio $\Gamma = 1.4$ at $Re = 120$ and two experimental velocity fields measured by LDV in direction (+) at $Re = 130$ (c, d) and in direction (−) at $Re = 120$ (e, f). The flow quantities which we present are in (a, c, e) the azimuthal velocity v_θ and in (b, d, f) the poloidal stream function Ψ. Presenting the fields between $0 \leqslant r \leqslant 1$ and $0 \leqslant z \leqslant 0.7$ is sufficient due to axisymmetry and $\mathscr{R}_\pi$-symmetry. Blades or smooth disk are at $z = 0.7$.

3 between the two curves, denoting very different inertial regimes, as discussed in § 5.2.

5.1. *From viscous to inertial stirring*

While $Re \lesssim 300$, the dimensionless torque K_p scales as Re^{-1}. We are in the laminar regime (Schlichting 1979) and the viscous terms are dominant in the momentum balance. These regimes correspond to $m = 0$ or $m = 2$ steady flows, with an eventual slow drift (§§ 3.1 and 3.2).

From the power consumption point of view, both directions of rotations are equivalent. The two curves – circles for direction (−) and left-pointing triangles for direction (+) – collapse for $Re \lesssim 300$ onto a single curve with equation $K_p = 36.9 Re^{-1}$.

We performed velocity field measurements for the two flows at $Re \simeq 120$–130 (figure 10c–f). The differences between the two directions are minor. The order of magnitude of the mean poloidal and toroidal velocities are the same to within 15 % for both directions of rotation in the laminar regime, whereas at very high Re, they strongly differ (by a factor 2) (Ravelet *et al.* 2005).

The flow is thus not sensitive to the shape of the impeller blades in the laminar regime. To explain this, we make the hypothesis that for these large impellers of radius $0.925R_c$, fitted with blades of height $h = 0.2R_c$, the flow at low Re is equivalent to the flow between flat disks with an effective aspect ratio $\Gamma = (H - 2h)/R_c = 1.4$. Nore *et al.* (2004) numerically studied the flow between counter-rotating smooth flat disks enclosed in a cylinder and report the dependence of the first unstable mode wavenumber on the aspect ratio $\Gamma = H/R_c$. In their computations, the critical wavenumber is $m = 1$ for $\Gamma = 1.8$, whereas for $\Gamma = 1.4$, it is $m = 2$ as we observe in our experiments.

We thus compare in figure 10 our experimental velocity fields to a numerical simulation performed by Caroline Nore (personal communication) at the same *Re* and aspect ratio $\Gamma = 1.4$. The three fields are very close. A possible physical explanation for this effect is the presence of viscous boundary layers along the resting cylinder wall. The typical length scale of the boundary layer thickness can be estimated as $\delta = Re^{-1/2}$. At the Reynolds number at which the impellers blades start to have an effect, i.e. at $Re \simeq 300$, this boundary layer thickness is of the order of $\delta \simeq 6$ mm, while the gap between the impellers and the cylinder wall is 7.5 mm. It is also of the order of magnitude of the minimum distance between two blades. For $Re \lesssim 300$, the fluid is thus kept between the blades and cannot be expelled radially: it rotates with the impellers. The stirring cannot be considered as inertial and does not depend on the blade shape.

For $Re \gtrsim 300$, the dimensionless torque starts to shift from a Re^{-1} law and simultaneously there is a difference between the two senses of rotation: the inertial stirring becomes dominant over the viscous stirring. Simultaneously, the steady flow becomes unstable with respect to time-dependence (§§ 3 and 4).

5.2. *Inertial effects*

At high Reynolds number, we observe in figure 9 different behaviours for K_p for the two senses of rotation. Sense (−) passes through a minimum for $Re \simeq 1000$ and then rapidly reaches a flat plateau above $Re_t = 3300$ (see § 4.3), whereas sense (+) asymptotically reaches a regime with only a third of the power dissipation of sense (−). Together with the curved-blade data, figure 9 presents additional data for smooth disks. The dimensionless torque K_p is approximately 30 times smaller for smooth disks than for curved-bladed disks, and does not display any plateaux at high Reynolds number but a $Re^{-1/4}$ scaling law, as described by Cadot *et al.* (1997).

It is tempting to compare our curve $K_p(Re)$ with the classical work of Nikuradse (1932, 1933) consisting of a complete and careful experimental data set on the turbulence in a pipe flow with controlled wall roughness. The data concern the friction factor, equivalent to K_p, measured over a wide range between $Re = 500$ and $Re = 10^6$, which is shown to strongly depend on the wall roughness above $Re \simeq 3000$. The wall roughness is made up of controlled sand grains of diameter in the range 1/507 to 1/15 of the pipe radius, somewhat smaller than our blade height $h/R_c = 1/5$ which can be thought of as an effective roughness.

This data set has defied theoretical interpretation for decades and still motivates papers. Recently, Goldenfeld (2006) and Gioia & Chakraborty (2006) proposed phenomenological interpretations and empirical reduction of Nikuradse's data. In brief, both connect the very high-Reynolds-number inertial behaviour – a plateau at a value which scales with the roughness to the power 1/3 – to the Blasius $Re^{-1/4}$ law for the dissipative region at intermediate *Re*. Goldenfeld (2006), using a method from critical-point physics, finds a scaling for the whole domain above $Re \simeq 3000$, whereas Gioia & Chakraborty (2006) describe the friction factor over the same Reynolds number range according to Kolmogorov's phenomenological model.

Compared with pipe flow results and models, our $K_p(Re)$-curve (figure 9) looks very similar except for the region Gioia & Chakraborty (2006) called the energetic regime. Indeed, in our specific case the basic flow is already dominated by vortices of the size of the vessel. The negative direction (circles in figure 9) shows a minimum followed by a plateau above $Re_t = 3300$ and is in agreement with the general inertial behaviour described above. However for the positive direction (left-pointing triangles in figure 9), the K_p curve seems to be continuously decreasing up to $Re \simeq 10^6$. Looking closer, one can observe a short $Re^{-1/4}$ Blasius regime for Re between 300 and 1500, highlighted by a fit in figure 9, followed by a very slow variation over the next two decades: logarithmic corrections are still visible in the range $10^4 \lesssim Re \lesssim 5 \times 10^4$. For this direction it is more difficult to define a threshold for the plateau observed in pure water (Marié 2003). Nevertheless, this threshold should be of order 10^5, i.e. much higher than with negative rotation.

A possible explanation of this strong difference may lie in the structure of the flow inside the impellers, i.e. between the blades. Let us first assume that this flow is dominated by what happens along the extremities of the blades, on which the pressure is higher. Then we assume that the blade curvature leads to stable boundary layers in positive rotation and to Görtler instability in negative rotation. The former develops Blasius boundary layers, whereas the latter develops turbulent boundary layers with many more vortices. Therefore, when the boundary layer detaches, somewhere along the blades or at least at their end, the Blasius boundary layer in the positive rotation sheds fewer turbulent vortices than the Görtler unstable layer does in the negative rotation.

The above description could be sufficient to explain why the negative rotation is able to produce a Kolmogorov cascade even at quite low Reynolds numbers near Re_t. However if, in the positive rotation case, the flow is only seeded by vortices produced by the stable boundary layer which develops along the smooth blade faces, it is clear that a Blasius $Re^{-1/4}$ regime could be observed in this transition Reynolds range and that a full inertial regime does not occur below a very high Reynolds number owing to the very small roughness of the blade faces. This could be why the two curves in figure 9 look so different: the lower one looks qualitatively like a low-roughness boundary flow and the upper one like a high-roughness boundary flow. However, this may only account for part of the flow driving: the resistive torque is much higher for bladed impellers than for flat disks as shown in figure 9.

Our observation of the closed von Kármán turbulent flow is thus consistent with the claim by Goldenfeld (2006) that full understanding of turbulence requires explicit accounting for boundary roughness.

6. Discussion and conclusion

6.1. *Symmetries and first bifurcations*

As for many flows, the similarity of the flow behaviour at low Reynolds number with an intermediate-size nonlinear system is obvious: breaking of spatial symmetry first, then a temporal symmetry and finally transition to chaos by a quasi-periodic scenario.

A comparable study has been carried both experimentally and numerically on von Kármán flow with flat disk and variable aspect ratio by Nore *et al.* (2003, 2004, 2005). Our results agree well with their results on the first instability mode $m = 2$ if considering the fluid in the blade region as in almost solid-body motion, which reduces the aspect ratio (see § 5.1). However, all thresholds appear at much lower Re for bladed impellers than for flat disks: 175 *vs.* 300 for the first steady bifurcation and 330 *vs.* above 600 for the first temporal instability of the $m = 2$ mode, not observed in Nore *et al.* (2005) study.

Another important difference between the two systems concerns symmetries. Whereas Nore and collaborators deal with exact counter-rotation by using a single motor to drive both disks, our experimental setup uses two independent motors and reaches only an approximation of a counter-rotating regime. As a consequence, the $\mathscr{R}_\pi$-symmetry is *stricto sensu* broken at any Reynolds number and the symmetry group of our problem is $SO(2)$ instead of $O(2)$. To evaluate the level of symmetry breaking we can use a small parameter (Chossat 1993; Porter & Knobloch 2005), e.g. $\epsilon = (f_1 - f_2)/(f_1 + f_2)$ which is between 10^{-4} and 10^{-3} in our runs.

Carefully controlling this parameter is an interesting issue: recently, in a very similar von Kármán flow in the positive sense of rotation at high *Re*, de la Torre & Burguete (2007) reported bistability and a turbulent bifurcation at exactly $\epsilon = 0$ between two $\mathscr{R}_\pi$-symmetric flows. For non-zero ϵ, the mixing layer lies slightly above or below the equator and it randomly jumps between these two symmetric positions when ϵ is carefully set to zero.

With our very small experimental ϵ, we satisfy theoretical predictions (Chossat 1993; Porter & Knobloch 2005) for the 1:2 spatial resonance or $k - 2k$ interaction mechanism with slightly broken reflection symmetry. Instead of mixed mode, pure mode and heteroclinic cycles – specific to $O(2)$ and carefully reported by Nore *et al.* (2003, 2004, 2005) – we only observe drifting instability patterns, i.e. travelling waves and modulated travelling waves, characteristic of $SO(2)$. Also, the drift frequency is very close to zero at the threshold $Re_c = 330$ (figure 6*a*), in agreement with the prediction $f_D \sim O(\epsilon)$ (Chossat 1993; Porter & Knobloch 2005). This bifurcation to travelling waves is similar to the one-dimensional drift instability of steady patterns, observed in many systems (see e.g. Fauve *et al.* 1991). It relies on the breaking of the parity ($\theta \rightarrow -\theta$) of the pattern (Coullet & Iooss 1990): the travelling-wave pattern is a pair of tilted vortices. The bifurcation is an imperfect pitchfork (Porter & Knobloch 2005).

Finally, the comparison can be extended to the travelling waves observed with flat disks above the mixed and pure modes (Nore *et al.* 2003, 2005). The observed wave frequencies are of the same order of magnitude in both cases, which led us to believe that the same kind of hydrodynamics is involved , i.e. the blades again play a minor role at these low Reynolds numbers. However, the frequency ratio between the basic waves (TW) and their modulations (MTW) at onset is much higher (∼32) in our experiment than in the numerical simulations (∼5) (Nore *et al.* 2003). This could be due to the large number of blades.

We also consider the symmetry of the von Kármán flow with respect to the rotation axis. In fact, the time-averaged flow is exactly axisymmetric while the instantaneous flow is not, because of the presence of blades. However, axisymmetry can be considered as an effective property at low Reynolds number and at least up to $Re = 175$, since we have shown that the blades have almost no effect on the flow (see § 5.1). With increasing *Re*, the blades start playing their role and effectively break the axisymmetry of the instantaneous flow.

Finally, we emphasize that the observations made below $Re \sim 400$ closely resemble the route to chaos through successive symmetry breaking for low-degree-of-freedom dynamical systems. Our system can thus be considered as a small system (consistent with the aspect ratio which is of order of 1) until the Reynolds number becomes high enough to excite small dynamical scales in the flow.

6.2. *The three scales of the von Kármán flow*

The observations reported in this article from visualizations and spectra showed three different scales. In particular, time-spectra contain two time–frequency domains, above and below the injection frequency $f_a = f$. Let us first roughly sketch the correspondence between temporal and spatial frequency scales of the whole flow:

(i) the smallest spatial frequencies, at the scale of the vessel, describe the basic swirling flow due to the impeller and produce the intermediate frequency range, i.e. the peak at $f_a = f$ in the time spectrum;

(ii) the intermediate spatial frequencies due to the shear-layer main instabilities produce the lowest time frequencies;

(iii) the highest spatial frequencies produce, of course, the highest temporal frequencies, i.e. the Kolmogorov region.

Taylor's hypothesis is based on a linear mapping between space and time frequencies. It is probably valid for the high part of the spectrum, but the mapping might not be linear and even not monotonic for the low part. We discuss each part of the spectrum in the two following sections.

6.2.1. *The* $1/f$ *low-frequency spectrum*

Once chaos is reached at $Re = 400$, a strong continuous and monotonic low-frequency spectrum is generated (figure 3*h*). In the chaotic regime below $Re \sim 1000$, the spectrum evolves to a neat -1 power law. Then, this part of the spectrum does not evolve any more with Re.

Low-frequency -1 exponents in spectra are common and could be due to a variety of physical phenomena: so-called '$1/f$ noises' have been widely studied, e.g. in the condensed matter field (see for instance Dutta & Horn 1981).

For turbulent von Kármán flows driven by two counter-rotating impellers, this low-time-scale dynamics has been already observed in liquid helium over at least a decade by Zocchi *et al.* (1994) as well as for the magnetic induction spectrum in liquid metals (Bourgoin *et al.* 2002; Volk, Odier & Pinton 2006). However, experiments carried out in a one-cell flow – without turbulent a mixing layer – did not show this behaviour (Marié 2003; Ravelet *et al.* 2004; Ravelet 2005). We therefore conclude that the $1/f_a$-spectrum is related to the chaotic wandering of the mixing layer which statistically restores the axisymmetry. Once again, the mixing layer slow dynamics dominates the whole dynamics of our system, from momentum transfer (Marié & Daviaud 2004) to the very high level of turbulent fluctuations (figures 5 and 8).

Furthermore, we can make the hypothesis that the -1 slope is due to the distribution of persistence times on each side of the bimodal distribution (figure 8): the low-frequency part of the spectrum can be reproduced by a random binary signal. Similar ideas for the low-frequency spectral construction are proposed for the magnetic induction in the von Kármán sodium (VKS) experiment (Ravelet *et al.* 2007). In both cases, longer statistics would be needed to confirm this idea.

6.2.2. *The turbulent fluctuations*

We show above how the flow transitions from chaos to turbulence between $Re \simeq 1000$ and $Re_t = 3300$. We label this region 'transition to turbulence' and observe the growth of a power-law region in the time-spectra for $f_a > f$. Does this slope trace back the Kolmogorov cascade in the space-spectra?

As the classical Taylor hypothesis cannot apply to our full range spectrum, we follow the local Taylor hypothesis idea (Pinton & Labbé 1994) for the high-frequency part $f_a > f$. Whereas Pinton & Labbé (1994) did not apply their technique (using instantaneous velocity instead of a constant advection) to the extreme case of zero advection, we think it can be applied here owing to the shape of the azimuthal velocity PDF (figure 8). These distributions show first that the instantaneous zero velocity is a quite rare event: a local minimum of the curve. The modulus of velocity spends typically 75 % of the time between $\frac{1}{2}V_m$ and $\frac{3}{2}V_m$, where $\pm V_m$ are the positions of the PDF maxima. The sign of the advection has no effect on the reconstructed wavenumber. We can thus conclude that the frequency and wavenumber moduli can be matched to each other at first order by a factor equal to the most probable velocity $|V_m|$ or by the mean of $|v_\theta|$, very close to each other. This approach is consistent with a binary view of the local turbulent signal jumping randomly between two opposite mean values, just as in the turbulent flow reversal model of, e.g. Benzi (2005). Then, the high-frequency part of the spectrum is equivalent to the spectrum obtained by averaging the spectra of every time-series between jumps, while the low-frequency part is dominated by dynamics of the jumps themselves.

Owing to these arguments, we are convinced that an algebraic region dominates the high-frequency part of the k-spectra above Re_t. Observed exponents (−1.55) are of the order of the Kolmogorov exponent, less than 10 % smaller in absolute value. Similar exponents are also encountered at other locations in the vessel.

6.3. *Conclusion and perspectives*

The von Kármán shear flow with inertial stirring has been used for a global study of the transition from order to turbulence. The transition scenario is consistent with a globally supercritical scenario and this system appears to be a very powerful table-top prototype for such a type of study. We have chosen to consider a global view over a wide range of Reynolds number. This allowed us to make connections between information from local (velocities) or global quantities (torques, flow symmetries), as discussed in §§ 5.2, 6.1 and 6.2.

6.3.1. *Further work*

It would be interesting to increase the resolution of the analysis to the different observed thresholds. It would also be worth performing the same wide-range study for the other sense of rotation (+) or another pair of impellers. These studies would enable a comparison of the inertial effects on the turbulent dynamics at very high Reynolds number.

6.3.2. *Controlling the mixing layer*

Many results of the present study proceed from velocity data collected in the middle of the shear layer and we have shown that this layer and its chaotic/turbulent wandering can be responsible for the low-frequency content of the chaotic/turbulent spectrum of the data.

With the slightly different point of view of controlling the disorder level, we have modified the dynamics of the shear layer by adding a thin annulus located in the mid-plane of the flow (Ravelet *et al.* 2005). This property was recently used in the von Kármán Sodium (VKS) experiment conducted at Cadarache, France and devoted to the experimental study of dynamo action in a turbulent liquid-sodium flow. A dynamo has effectively been observed for the first time in this system with a von Kármán configuration using, among other characteristics, an annulus in the mid-plane (Monchaux *et al.* 2007) and is sensitive to the presence of this device. Moreover, clear evidence has been found that the mixing-layer large-scale patterns have a strong effect on the magnetic field induction at low frequency (Volk *et al.* 2006; Ravelet *et al.* 2007). Further studies of this effect in water experiments are in progress.

6.3.3. *Statistical properties of the turbulence*

Studies of the von Kármán flow currently in progress involve both a wider range of data in space, with the use of stereoscopic 3-components particle image velocimetry (SPIV) and a wider range of Reynolds number.

Whereas the SPIV is slower than LDV and will not allow time-spectral analysis, it offers a global view of the flow and allows characterization of statistical properties of the turbulent velocity. Guided by the behaviour of the variance of the local azimuthal velocity revealed in the present article (figure 5), we expect to analyse the evolution of the spatio-temporal statistical properties with Re. Such a study is very stimulating for theoretical advances in statistical mechanics of turbulence in two-dimensional (Robert & Sommeria 1991; Chavanis & Sommeria 1998), quasi-two-dimensional (Bouchet & Sommeria 2002; Jung, Morrison & Swinney 2006) or axisymmetric flows (Leprovost, Dubrulle & Chavanis 2006; Monchaux *et al.* 2006).

We are particularly indebted to Vincent Padilla and Cécile Gasquet for building and piloting the experiment. We acknowledge Caroline Nore for making her simulations available, Arnaud Guet for his help with the visualizations and Frédéric Da Cruz for the viscosity measurements. We have benefited from very fruitful discussions with B. Dubrulle, N. Leprovost, L. Marié, R. Monchaux, C. Nore, J.-F. Pinton and R. Volk.

REFERENCES

Batchelor, G. K. 1951 Note on a class of solutions of the Navier-Stokes equations representing steady rotationally-symmetric flow. *Q. J. Mech. App. Maths* **4**, 29.

Benzi, R. 2005 Flow reversal in a simple dynamical model of turbulence. *Phys. Rev. Lett.* **95**, 024502.

Bouchet, F. & Sommeria, J. 2002 Emergence of intense jets and Jupiter's great red spot as maximum-entropy structures. *J. Fluid Mech.* **464**, 165.

Bourgoin, M., Marié, L., Pétrélis, F., Gasquet, C., Guigon, A., Luciani, J.-B., Moulin, M., Namer, F., Burguete, J., Chiffaudel, A., Daviaud, F., Fauve, S., Odier, P. & Pinton, J.-F. 2002 MHD measurements in the von Kármán sodium experiment. *Phys. Fluids* **14**, 3046.

Buchhave, P., George, W. K. & Lumley, J. L. 1979 The measurement of turbulence with the Laser-Doppler anemometer. *Annu. Rev. Fluid Mech.* **11**, 443.

Cadot, O., Couder, Y., Daerr, A., Douady, S. & Tsinober, A. 1997 Energy injection in closed turbulent flows: Stirring through boundary layers versus inertial stirring. *Phys. Rev.* E **56**, 427.

Cadot, O., Douady, S. & Couder, Y. 1995 Characterization of the low-pressure filaments in a three-dimensional turbulent shear flow. *Phys. Fluids* **7**, 630.

Chavanis, P.-H. & Sommeria, J. 1998 Classification of robust isolated vortices in two-dimensional hydrodynamics. *J. Fluid Mech.* **356**, 259.

Chossat, P. 1993 Forced reflexional symmetry breaking of an *o(2)*-symmetric homoclinic cycle. *Nonlinearity* **6**, 723.

Coullet, P. & Iooss, G. 1990 Instabilities of one-dimensional cellular patterns. *Phys. Rev. Lett.* **64**, 866.

Douady, S., Couder, Y. & Brachet, M. E. 1991 Direct observation of the intermittency of intense vorticity filaments in turbulence. *Phys. Rev. Lett.* **67**, 983.

Dutta, P. & Horn, P. M. 1981 Low-frequency fluctuations in solid: 1/f noise. *Rev. Mod. Phys.* **53**, 497.

Escudier, M. P. 1984 Observations of the flow produced in a cylindrical container by a rotating endwall. *Exps. Fluids* **2**, 189.

Falkovich, G. 1994 Bottleneck phenomenon in developed turbulence. *Phys. Fluids* **6**, 1411.

Fauve, S., Douady, S. & Thual, O. 1991 Drift instabilities of cellular patterns. *J. Phys.* II **1**, 311.

Fauve, S., Laroche, C. & Castaing, B. 1993 Pressure fluctuations in swirling turbulent flows. *J. Phys.* II **3**, 271.

Frisch, U. 1995 *Turbulence – The Legacy of A. N. Kolmogorov*. Cambridge University Press.

Gauthier, G., Gondret, P. & Rabaud, M. 1999 Axisymmetric propagating vortices in the flow between a stationary and a rotating disk enclosed by a cylinder. *J. Fluid Mech.* **386**, 105.

Gelfgat, A. Y., Bar-Yoseph, P. Z. & Solan, A. 1996 Steady states and oscillatory instability of swirling flow in a cylinder with rotating top and bottom. *Phys. Fluids* **8**, 2614.

Gioia, G. & Chakraborty, P. 2006 Turbulent friction in rough pipes and the energy spectrum of the phenomenological theory. *Phys. Rev. Lett.* **96**, 044502.

Goldenfeld, N. 2006 Roughness-induced critical phenomena in a turbulent flow. *Phys. Rev. Lett.* **96**, 044503.

Harriott, G. M. & Brown, R. A. 1984 Flow in a differentially rotated cylindrical drop at moderate Reynolds number. *J. Fluid Mech.* **144**, 403.

Hodgman, C. D. (Ed.) 1947 *Handbook of Chemistry and Physics,* 30th Edn. Chemical Rubber Publishing Co.

Jung, S. W., Morrison, P. J. & Swinney, H. L. 2006 Statistical mechanics of two-dimensional turbulence. *J. Fluid Mech.* **554**, 433.

von Kármán, T. 1921 Über laminäre und turbulente Reibung. *Z. Angew. Math. Mech.* **1**, 233.

Knobloch, E. 1996 Symmetry and instability in rotating hydrodynamic and magnetohydrodynamic flows. *Phys. Fluids* **8**, 1446.

Labbé, R., Pinton, J.-F. & Fauve, S. 1996 Power fluctuations in turbulent swirling flows. *J. Phys* II **6**, 1099.

La Porta, A., Voth, G. A., Crawford, A. M., Alexander, J. & Bodenschatz, E. 2001 Fluid particle acceleration in fully developed turbulence. *Nature* **409**, 1017.

Lathrop, D. P., Fineberg, J. & Swinney, H. L. 1992 Transition to shear-driven turbulence in Couette-Taylor flow. *Phys. Rev.* A **46**, 6390.

Leprovost, N., Dubrulle, B. & Chavanis, P.-H. 2006 Dynamics and thermodynamics of axisymmetric flows: Theory. *Phys. Rev.* E **73**, 046308.

Leprovost, N., Marié, L. & Dubrulle, B. 2004 A stochastic model of torque in von Kármán swirling flow. *Euro. Phys. J.* B **39**, 121.

Lesieur, M. 1990 *Turbulence in Fluids*, 2nd Revised Edn. Kluwer.

Lohse, D. & Müller-Groeling, A. 1995 Bottleneck effects in turbulence: Scaling phenomena in r versus p space. *Phys. Rev. Lett.* **74**, 1747.

Manneville, P. 1990 *Dissipative Structures and Weak Turbulence*. Academic.

Marié, L. 2003 Transport de moment cinétique et de champ magnétique par un écoulement tourbillonaire turbulent: influence de la rotation. PhD thesis, Université Paris VII.

Marié, L., Burguete, J., Daviaud, F. & Léorat, J. 2003 Numerical study of homogeneous dynamo based on experimental von Kármán type flows. *Euro. Phys. J.* B **33**, 469.

Marié, L. & Daviaud, F. 2004 Experimental measurement of the scale-by-scale momentum transport budget in a turbulent shear flow. *Phys. Fluids* **16**, 457.

Mellor, G. L., Chapple, P. J. & Stokes, V. K. 1968 On the flow between a rotating and a stationary disk. *J. Fluid Mech.* **31**, 95.

Moisy, F., Willaime, H., Andersen, J. S. & Tabeling, P. 2001 Passive scalar intermittency in low temperature helium flows. *Phys. Rev. Lett.* **86**, 4827.

Monchaux, R., Berhanu, M., Bourgoin, M., Moulin, M., Odier, Ph., Pinton, J.-F., Volk, R., Fauve, S., Mordant, N., Pétrélis, F., Chiffaudel, A., Daviaud, F., Dubrulle, B., Gasquet, C., Marié, L. & Ravelet, F. 2007 Generation of magnetic field by dynamo action in a turbulent flow of liquid sodium. *Phys. Rev. Lett.* **98**, 044502.

Monchaux, R., Ravelet, F., Dubrulle, B., Chiffaudel, A. & Daviaud, F. 2006 Properties of steady states in turbulent axisymmetric flows. *Phys. Rev. Lett.* **96**, 124502.

Nikuradse, J. 1932 Gesetzmassigkeiten der turbulenten Stromungen in glatten Rohren. *vDI Forshungsheft* 356, (English transl. NASA TT F-10 (1966), p. 359).

Nikuradse, J. 1933 Stromungsgesetz in rauhren Rohren. *vDI Forshungsheft* 361, (English transl. *Tech. Mem.* 1292, NACA (1950)).

Nore, C., Moisy, F. & Quartier, L. 2005 Experimental observation of near-heteroclinic cycles in the von Kármán swirling flow. *Phys. Fluids* **17**, 064103.

Nore, C., Tartar, M., Daube, O. & Tuckerman, L. S. 2004 Survey of instability thresholds of flow between exactly counter-rotating disks. *J. Fluid Mech.* **511**, 45.

Nore, C., Tuckerman, L. S., Daube, O. & Xin, S. 2003 The 1:2 mode interaction in exactly counter-rotating von Kármán swirling flow. *J. Fluid Mech.* **477**, 51.

Ouellette, N. T., Xu, H., Bourgoin, M. & Bodenschatz, E. 2006 Small-scale anisotropy in Lagrangian turbulence. *New J. Phys.* **8**, 102.

Pinton, J.-F. & Labbé, R. 1994 Correction to the Taylor hypothesis in swirling flows. *J. Phys.* II **4**, 1461.

Porter, J. & Knobloch, E. 2005 Dynamics in the 1:2 spatial resonance with broken reflection symmetry. *Physica* D **201**, 318–344.

Ravelet, F. 2005 Bifurcations globales hydrodynamiques et magnétohydrodynamiques dans un écoulement de von Kármán turbulent. PhD thesis, Ecole Polytechnique, France.

Ravelet, F., Chiffaudel, A., Daviaud, F. & Leorat, J. 2005 Toward an experimental von Kármán dynamo: Numerical studies for an optimized design. *Phys. Fluids* **17**, 117104.

Ravelet, F., Marié, L., Chiffaudel, A. & Daviaud, F. 2004 Multistability and memory effect in a highly turbulent flow: Experimental evidence for a global bifurcation. *Phys. Rev. Lett.* **93**, 164501.

Ravelet, F., Volk, R., Behranu, M., Chiffaudel, A., Daviaud, F., Dubrulle, B., Fauve, S., Monchaux, R., Mordant, N., Odier, Ph., Pétrélis, F. & Pinton, J.-F. 2007 Magnetic induction in a turbulent flow of liquid sodium: mean behaviour and slow fluctuations. Phys. Fluids (submitted).

Robert, R. & Sommeria, J. 1991 Statistical equililbrium states for two-dimensional flows. *J. Fluid Mech.* **229**, 291.

Schlichting, H. 1979 *Boundary-Layer Theory*, 7th Edn. McGraw-Hill.

Schouveiler, L., Le Gal, P. & Chauve, M.-P. 2001 Instabilities of the flow between a rotating and a stationary disk. *J. Fluid Mech.* **443**, 329.

Sørensen, J. B. & Christensen, E. A. 1995 Direct numerical simulation of rotating fluid flow in a closed cylinder. *Phys. Fluids* **7**, 764.

Spohn, A., Mory, M. & Hopfinger, E. J 1998 Experiments on vortex breakdown in a confined flow generated by a rotating disc. *J. Fluid Mech.* **370**, 73.

Stewartson, K. 1953 On the flow between two rotating coaxial disks. *Proc. Camb. Phil. Soc.* **49**, 333.

Tabeling, P., Zocchi, G., Belin, F., Maurer, J. & Willaime, H. 1996 Probability density functions, skewness and flatness in large Reynolds number turbulence. *Phys. Rev.* E **53**, 1613.

Tennekes, H. & Lumley, J. L. 1972 *A First Course in Turbulence*. MIT Press.

Titon, J.-H. & Cadot, O. 2003 The statistics of power injected in a closed turbulent flow: Constant torque forcing versus constant velocity forcing. *Phys. Fluids* **15**, 625.

de la Torre, A. & Burguete, J. 2007 Slow dynamics in a turbulent von Kármán swirling flow. *Phys. Rev. Lett.* **99**, 054101.

Volk, R., Odier, P. & Pinton, J.-F. 2006 Fluctuation of magnetic induction in von Kármán swirling flows. *Phys. Fluids* **18**, 085105.

Zandbergen, P. J. & Dijkstra, D. 1987 von Kármán swirling flows. *Annu. Rev. Fluid Mech.* **19**, 465.

Zocchi, G., Tabeling, P., Maurer, J. & Willaime, H. 1994 Measurement of the scaling of the dissipation at high Reynolds numbers. *Phys. Rev.* E **50**, 3693.

PHYSICS OF FLUIDS **21**, 035108 (2009)

The von Kármán Sodium experiment: Turbulent dynamical dynamos

Romain Monchaux,[1] Michael Berhanu,[2] Sébastien Aumaître,[1] Arnaud Chiffaudel,[1]
François Daviaud,[1] Bérengère Dubrulle,[1] Florent Ravelet,[1] Stephan Fauve,[2]
Nicolas Mordant,[2] François Pétrélis,[2] Mickael Bourgoin,[3] Philippe Odier,[3]
Jean-François Pinton,[3] Nicolas Plihon,[3] and Romain Volk[3]
[1]*CEA, IRAMIS, Service de Physique de l'Etat Condensé, CNRS URA 2464, CEA Saclay,*
F-91191 Gif-sur-Yvette, France
[2]*Laboratoire de Physique Statistique, CNRS and École Normale Supérieure, 24 rue Lhomond,*
F-75005 Paris, France
[3]*Laboratoire de Physique de l'École Normale Supérieure de Lyon, CNRS and Université de Lyon,*
F-69364 Lyon, France

(Received 7 July 2008; accepted 19 January 2009; published online 30 March 2009;
publisher error corrected 2 April 2009)

The von Kármán Sodium (VKS) experiment studies dynamo action in the flow generated inside a cylinder filled with liquid sodium by the rotation of coaxial impellers (the von Kármán geometry). We first report observations related to the self-generation of a stationary dynamo when the flow forcing is $\mathcal{R}_\pi$-symmetric, i.e., when the impellers rotate in opposite directions at equal angular velocities. The bifurcation is found to be supercritical with a neutral mode whose geometry is predominantly axisymmetric. We then report the different dynamical dynamo regimes observed when the flow forcing is not symmetric, including magnetic field reversals. We finally show that these dynamics display characteristic features of low dimensional dynamical systems despite the high degree of turbulence in the flow. © *2009 American Institute of Physics*.

[DOI: 10.1063/1.3085724]

I. INTRODUCTION

A. Experimental dynamos

Although it was almost a century ago that Larmor[1] proposed that a magnetic field could be self-sustained by the motions of an electrically conducting fluid,[2] the experimental demonstrations of this principle are quite recent. Using solid rotor motions, Lowes and Wilkinson realized the first (nearly homogeneous) experimental dynamo in 1963;[3] a subcritical bifurcation to a stationary magnetic field was generated and oscillations were later observed in an improved setup in which the angle between the rotors could be adjusted.[4] In this experiment, the main induction source lies in the axial differential rotation between the rotor and the stationary soft iron. Observations of fluid dynamos, however, did not occur before 2000 with the Riga and Karlsruhe experiments. In Riga, the dynamo is generated by the screw motion of liquid sodium. The flow is a helicoidal jet confined within a bath of liquid sodium at rest.[5] The induction processes are the differential rotation and the shear associated with the screw motion at the lateral boundary. The dynamo field has a helical geometry and is time periodic. The bifurcation threshold and geometry of the neutral mode trace back to Ponomarenko's analytical study[6] and have been computed accurately with model velocity profiles[7] or from Reynolds-averaged Navier–Stokes numerical simulations.[8,9] The Karlsruhe dynamo[10] is based on scale separation, the flow being generated by motions of liquid sodium in an array of screw generators with like-sign helicity. The magnetic field at onset is stationary and its large scale component is transverse to the axis of the flow generators. The arrangement follows Roberts' scheme[11] and again the dynamo onset and magnetic field characteristics have been accurately predicted numerically.[12–15]

The approach adopted in the von Kármán Sodium (VKS) experiments builds up on the above results. In order to access various dynamical regimes above dynamo onset,[16–18] it uses less constrained flow generators but keeps helicity and differential rotation as the main ingredients for the generation of magnetic field.[19,20] It does not rely on analytical predictions from model flows, although, as discussed later, many of its magnetohydrodynamics (MHD) features have been discussed using kinematic or direct simulations of model situations. In the first versions of VKS experiment—VKS1, between 2000 and 2002 and VKS2, between 2005 and July 2006—all materials used had the same magnetic permeability ($\mu_r \simeq 1$). However none of these configurations succeeded in providing dynamo action: the present paper analyzes dynamo regimes observed in the VKS2 setup when the liquid sodium is stirred with pure soft-iron impellers ($\mu_r \sim 100$). Although the VKS2 dynamo is therefore not fully homogeneous, it involves fluid motions that are much more fluctuating than in previous experiments. The role of the ferromagnetic impellers is at present not fully understood, but is thoroughly discussed in the text.

Below, we will first describe the experimental setup and flow features. We then describe and discuss in detail in Sec. II our observations of the dynamo generated when the impellers that drive the flow are in exact counter-rotation. In this case the self-sustained magnetic field is statistically stationary in time. We describe in Sec. III the dynamical regimes observed for asymmetric forcing conditions, i.e., when the impeller rotation rates differ. Concluding remarks are given in Sec. IV.

B. The VKS experiment

The VKS experiment studies MHD in a sodium flow generated inside a cylinder by counter-rotation of impellers located near the end plates. This flow has two main characteristics which have motivated its choice. First, its time-averaged velocity field has both helicity and differential rotation, as measured in Refs. 21–23, two features that have long been believed to favor dynamo action.[2] Second, the von Kármán geometry generates a very intense turbulence in a compact volume of space.[24–31]

The topology of the time-averaged velocity field has received much attention because it is similar to the $s_2 t_2$ flow considered in a sphere by Dudley and James.[32] This topology generates a stationary kinematic dynamo[33–35] whose main component is a dipole perpendicular to the rotation axis (an "$m=1$" mode in cylindrical coordinates). The threshold, in magnetic Reynolds number, for kinematic dynamo generation is very sensitive to details of the mean flow such as the poloidal to toroidal velocity ratio,[33–35] the electrical boundary conditions,[34–38] or the details of the velocity profile near the impellers.[38] Specific choices in the actual flow configuration have been based on a careful optimization of the kinematic dynamo capacity of the VKS mean flow.[22,35] The above numerical studies do not take into account the fully developed turbulence of the von Kármán flows, for which velocity fluctuations can be on the order of the mean. In actual laboratory conditions the magnetic Prandtl number of the fluid is very small (about 10^{-5} for sodium) so that the kinetic Reynolds number must be indeed huge in order to generate even moderate magnetic Reynolds numbers. A fully realistic numerical treatment of the von Kármán flows is out of reach. The influence of turbulence on the dynamo onset has thus been studied using model behaviors[39–41] or numerical simulations in the related Taylor–Green (TG) flow.[42–44] These fluctuations may have an ambivalent contribution. On the one hand, they may increase the dynamo threshold compared to estimates based on kinematic dynamo action but, on the other hand, they could also favor the dynamo process. In particular, TG simulations have shown that the threshold for dynamo action may be increased when turbulent fluctuations develop over a well-defined mean flow,[45–47] but that it saturates to a finite value for large kinetic Reynolds numbers. Initial simulations of homogeneous isotropic random flows[48,49] have suggested a possible runaway behavior, although a saturation of the threshold has been observed in the most recent simulations.[50] Finally, we note that many dynamo models used in astrophysics actually rely on the turbulence-induced processes. We will argue here that the VKS dynamo generated when the impellers are counterrotated at equal rates is a dynamo of the α-ω type.

Similar $s_2 t_2$ geometries are being explored in experiments operated by Lathrop and co-workers[51–53] at University of Maryland College Park and by Forest and co-workers[54–56] at University of Wisconsin, Madison. Sodium flows are generated in spherical vessels with a diameter ranging from 30 cm to 1 m. Changes in Ohmic decay times using externally pulsed magnetic fields in Maryland have again suggested that the dynamo onset may significantly depend on fine details of the flow generation.[52,53] Analysis of induction measurements, i.e., fields generated when an external magnetic field is applied in Madison have shown that turbulent fluctuations can induce an axial dipole and have suggested that a bifurcation to a transverse dipole may proceed via an on-off scenario,[55,57,58] as observed also in the Bullard–von Kármán experiment.[59]

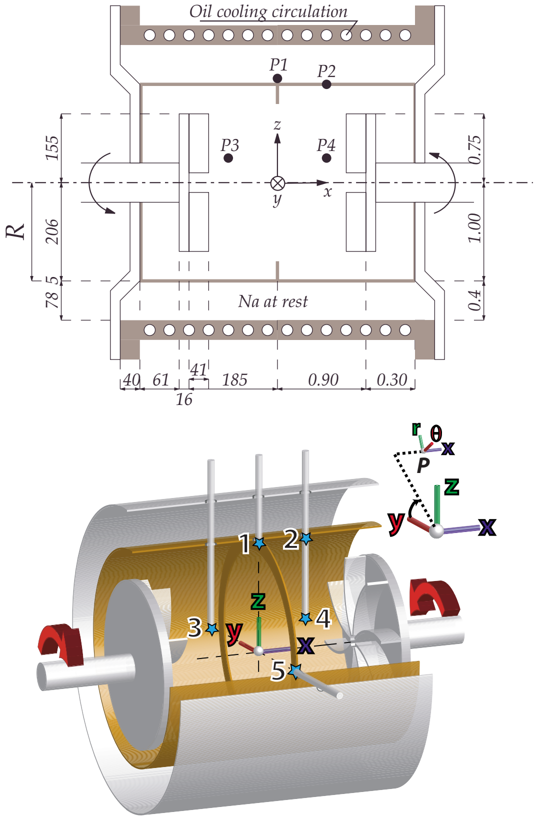

FIG. 1. (Color online) Experimental setup. Note the curved impellers, the inner copper cylinder which separates the flow volume from the blanket of surrounding sodium, and the thin annulus in the midplane. Also shown are the holes through which the 3D Hall probes are inserted into the copper vessel for magnetic measurements. Location in $(r/R,\theta,x/R)$ coordinates of available measurement points: $P_1(1,\pi/2,0)$, $P_2(1,\pi/2,0.53)$, $P_3(0.25,\pi/2,-0.53)$, $P_4(0.25,\pi/2,0.53)$, and $P_5(1,\pi,0)$ (see Table I for details concerning available measurements in different experimental runs). When referring to the coordinates of magnetic field vector **B** measured in the experiment at these different points, we will use either the Cartesian projection (B_x,B_y,B_x) on the frame (x,y,z) or the cylindrical projection (B_r,B_θ,B_x) on the frame (r,θ,x) $(B_\theta=-B_y$ and $B_r=B_z$ for measurements at points P1, P2, and P3). We will use in figures the following color code for the magnetic field components: axial (x) in blue, azimuthal (y) in red, and radial (z) in green.

C. Setup details

In the VKS2 experiment, the flow cell is enclosed within a layer of sodium at rest (Fig. 1). The flow is generated by rotating two impellers with radius of 154.5 mm, 371 mm apart in a thin cylindrical copper vessel, $2R=412$ mm in inner diameter, and 524 mm in length. The impellers are fitted with eight curved blades with height of $h=41.2$ mm; in most experimental runs, the impellers are rotated so as the blades move in a "nonscooping" direction, defined as the positive direction by arrows in Fig. 1. The impellers are driven up to typically 27 Hz by motors with 300 kW available power.

When both impellers rotate at the same frequency $F_1 = F_2$, the complete system is symmetric with respect to any rotation $\mathcal{R}_\pi$ of π around any radial axis in its equatorial plane $(x=0)$. Otherwise, when $F_1 \neq F_2$, the system is not $\mathcal{R}_\pi$-symmetric anymore. For simplicity, we will also refer to symmetric/asymmetric system or forcing.

The kinetic and magnetic Reynolds numbers are

$$\mathrm{Re} = K2\pi R^2 F/\nu$$

and

$$R_m = K\mu_0\sigma 2\pi R^2 F,$$

where $F=(F_1+F_2)/2$, ν is the kinematic viscosity of sodium, μ_0 is the magnetic permeability of vacuum, σ is the electrical conductivity of sodium, and $K=0.6$ is a coefficient that measures the efficiency of the impellers for exact counter-rotation $F_1=F_2=F$.[21–23,35] Re can be increased up to 5×10^6, and the corresponding maximum magnetic Reynolds number is $R_m=49$ (at 120 °C). These definitions of Re and R_m apply to both $\mathcal{R}_\pi$-symmetric and asymmetric forcings, but the K-prefactor correctly incorporates the efficiency of the forcing only in the symmetric case. Reynolds numbers may also be constructed either on F_1 and F_2, e.g., $R_{m,i} = K\mu_0\sigma 2\pi R^2 F_i$. All these definitions collapse for exact counter-rotating, i.e., $\mathcal{R}_\pi$-symmetric regimes.

The flow is surrounded by sodium at rest contained in another concentric cylindrical copper vessel, 578 mm in inner diameter and 604 mm long. An oil circulation in this thick copper vessel maintains a regulated temperature in the range of 110–160 °C. Note that there are small connections between the inner sodium volume and the outer sodium layer (in order to be able to empty the vessel) so that the outer layer of sodium may be moving; however, given its strong shielding from the driving impellers, we expect its motion to be weak compared to that in the inner volume. Altogether the net volume of sodium in the vessel is 150 l—more details are given in Fig. 1.

In the midplane between the impellers, one can attach a thin annulus—inner diameter of 350 mm and thickness of 5 mm. Its use has been motivated by observations in water experiments,[21–23,35] showing that its effect on the mean flow is to make the midplane shear layer steadier and sharper. All experiments described here are made with this annulus attached; in some cases we will mention the results of experiments made without it in order to emphasize its contribution.

Finally, one important feature of the VKS2 experiment described here is that the impellers that generate the flow have been machined from pure soft iron ($\mu_r \sim 100$). One motivation is that self-generation has not been previously observed for identical geometries and stainless steel impellers. Several studies have indeed shown that changing the magnetic boundary conditions can change the threshold for dynamo onset.[60,61] In addition, kinematic simulations have shown that the structure of the sodium flow behind the driving impellers may lead to an increase in the dynamo threshold ranging from 12% to 150%;[38] using iron impellers may protect induction effects in the bulk of the flow from effects occurring behind the impellers. As described in detail below, this last modification allows dynamo threshold to be crossed. We will further discuss the influence of the magnetization of the impellers on its onset.

Magnetic measurements are performed using three-dimensional (3D) Hall probes and recorded with a National Instruments PXI digitizer. We use both a single-point (three components) Bell probe (hereafter labeled G probe) connected to its associated gaussmeter and a custom-made array where the 3D magnetic field is sampled at ten locations along a line (hereafter called SM array), every 28 mm. The array is made from Sentron 2SA-1M Hall sensors and is air cooled to keep the sensors' temperature between 35 and 45 °C. For both probes, the dynamical range is 70 dB, with an ac cutoff at 400 Hz for the gaussmeter and 1 kHz for the custom-made array; signals have been sampled at rates between 1 and 5 kHz.

During runs, we have also recorded other more global data such as torque/power measurements:[28,62]

(a) The temperature of sodium in the vessel. This is important because the electrical conductivity σ of sodium varies in the temperature range of our experiments. In addition, it gives an alternate way of varying the magnetic Reynolds number: one may operate at varying speed or varying temperature. We have used

$$\sigma(T) = 10^8/(6.225 + 0.0345T) \ \ \mathrm{S\ m^{-1}} \tag{1}$$

for $T \in [100, 200]$ °C.

(b) The torque delivered by the electrical supply of the driving motors. It is estimated from outputs of the UMV4301 Leroy-Sommer generators, which provide an image of the torque fed to the motors and of their velocity (regulated during the runs). We stress that this is an industrial indicator—not calibrated against independent/reference torque measurements.

II. DYNAMO GENERATION, SYMMETRIC DRIVING $F_1=F_2$

A. Self-generation

On September 19th, 2006, we observed the first evidence of dynamo generation in the VKS experiment.[16] The flow was operated with the thin annulus inserted and the magnetic field was recorded in the midplane using the G-probe located flush with the inner cylinder (location P1 in Fig. 1).

As the rotation rate of the impeller $F=F_1=F_2$ is increased from 10 to 22 Hz, the magnetic field recorded by the probe develops strong fluctuations and its main component (in the azimuthal direction at the probe location) grows and saturates to a mean value of about 40 G, as shown in Fig. 2(a). This value is about 100 times larger than the ambient magnetic field in the experimental hall, from which the flow volume is not shielded. The hundred-fold increase is also one order of magnitude larger that the induction effects and field

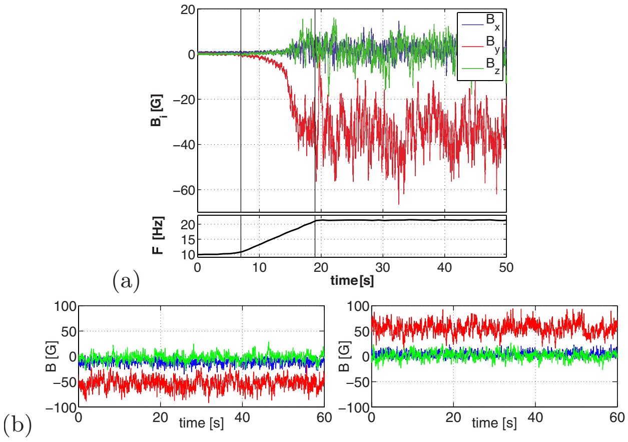

FIG. 2. (Color online) Three components of the magnetic field generated by dynamo action at $F_1=F_2$ measured at point P1 in the experiment VKS2g. (a) Growth of the magnetic field as the impellers' rotation rate F is increased from 10 to 22 Hz. (b) Two independent realizations at same frequency above threshold showing opposite field polarities.

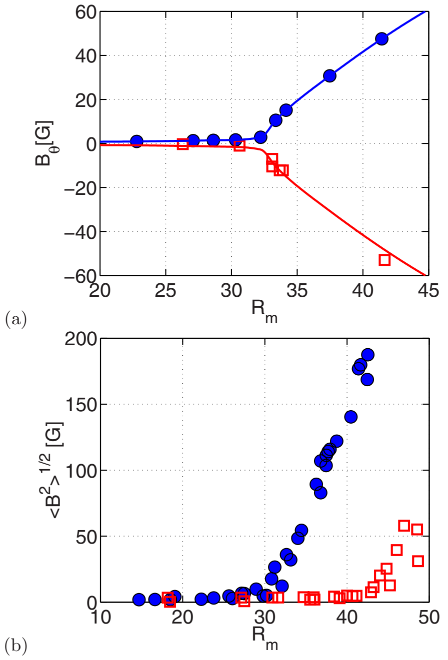

FIG. 3. (Color online) Bifurcation curves. (a) Azimuthal field measured at P1 for VKS2h, growing with either polarity (only measurements with initially demagnetized impellers are shown here). The solid lines correspond to a best fit with a scaling behavior $B_\theta \sim (R_m-32)^{0.77}$ above threshold. (b) Magnetic field amplitude $\langle B^2\rangle^{1/2}=\sqrt{B_x^2+B_y^2+B_z^2}$ at P3 for VKS2i. Impellers are counter-rotating at equal rotation rates in the positive direction shown in Fig. 1 (closed blue circles) or in the opposite direction, i.e., with the blades on the impellers moving in a scooping or negative direction (open red squares). Changes in the efficiency of the stirring are taken into account in the definition of R_m; $R_m=K\mu_0\sigma R^2F$ with $K=K_+=0.6$ in the normal, positive direction of rotation and $K=K_-=0.7$ in the opposite direction.

amplification previously recorded in the VKS experiment with externally applied magnetic field, either homogeneously over the flow volume[19] or localized at the flow boundary.[63] We interpret this phenomenon as evidence of dynamo self-generation in VKS2.

The dynamo field is statistically stationary: the components of the magnetic field measured at the boundary or within the flow display large fluctuations around a nonzero mean value as seen in Fig. 2. When the experiment is repeated, one observes that the azimuthal field at the probe location can grow with either polarity [Fig. 2(b)] as is expected from the $\mathbf{B}\rightarrow-\mathbf{B}$ symmetry of the MHD equations.

The most salient features of this turbulent dynamo have been reported in a letter.[16] They are given in more detail in this section. We first show that the amplitude of the magnetic field behaves as expected for a supercritical (but imperfect) bifurcation; we discuss the structure of the neutral mode and the influence of the magnetization of the iron impellers.

B. Bifurcation

Figure 3(a) shows the evolution of the magnetic field measured at P1 when the magnetic Reynolds number varies. When R_m exceeds $R_m^c \sim 32$, the magnetic field grows spontaneously. In the experiment R_m can be varied either by changing the rotation rate of the impellers, or the working temperature of the sodium in the vessel, and both effects need to be taken into account when building the bifurcation curves in Fig. 3. In other words, the growth of the magnetic field is governed by the proximity to threshold in magnetic Reynolds number $(R_m-R_m^c)$ and not by the single hydrodynamic (rotation rate F) or magnetic (diffusivity $1/\mu_0\sigma$) parameters.

The magnetic field grows from very small values (the induction from the ambient field) and saturates to a value which increases as a function of $(R_m-R_m^c)$. The behavior is identical when the magnetic field grows in one direction or the other. In a canonical supercritical bifurcation, one would expect a scaling region $B_{\text{sat}} \propto (R_m-R_m^c)^a$ with $a=1/2$. Our results are compatible with such a behavior, although a better fit to the data is $B_\theta \sim (R_m-32)^{0.77}$ for the azimuthal component of the magnetic field (the largest component at the measurement point). More measurements and better statistics will, of course, be needed to get a precise scaling behavior; we also stress that one should proceed with caution when ascribing scaling exponents to this bifurcation. The instability grows over a strongly noisy background (the flow hydrodynamic turbulence) and no rigorous theory has been developed in this context—the existence of anomalous exponents is an open question.

Another effect that influences the precise shape of the bifurcation is the magnetic behavior of the iron impellers. As seen in Fig. 2, the dynamo field has a strong azimuthal component. The iron impellers have a direction of easy magnetization in the same direction. The coercitivity of pure iron is weak and the remanent magnetization is of the order of $H_c \sim 100$ A/m, while the saturation flux density exceeds 20 000 G. This magnetization of the impellers induces a bias in the dynamo instability. Experimentally we have observed that once the dynamo grows above the onset with a given polarity of the azimuthal field, then it will always start in the same direction when the flow is driven successively below and above onset. The reverse polarity, as shown in Figs. 2 and 3, are only observed when the impellers have been demagnetized (at least partially) by being exposed to an oscillatory field. The imperfection induced in the bifurcation is

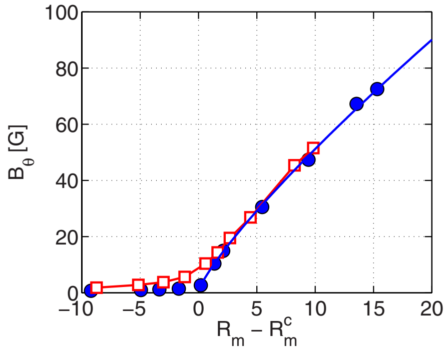

FIG. 4. (Color online) Bifurcation diagrams measured for the azimuthal component at P1 in VKS2h. The curve with closed blue circles is built when increasing F with demagnetized impellers and crossing the dynamo threshold for the first time. Successive cycles in R_m across the bifurcation threshold all lie on the curve with open red square symbols.

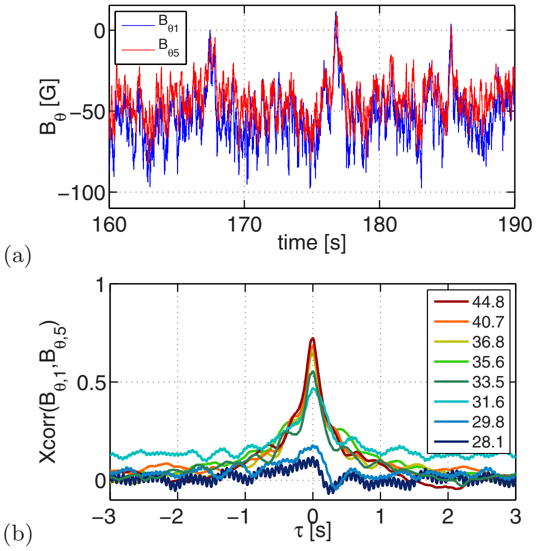

FIG. 5. (Color online) Magnetic field measured at points P1 and P5 in VKS2h: (a) Time traces of the azimuthal magnetic field components. (b) Cross correlation function of the two signals for increasing magnetic Reynolds numbers in the range of 28–45.

shown in Fig. 4. The (circles/blue) curve is obtained when starting the experiment from demagnetized impellers and the bifurcation is crossed for the first time. The (squares/red) curve is obtained for further successive variations in the magnetic Reynolds number below and above the onset. As shown in Ref. 64, the rounding off of the bifurcation curve can be explained in a minimal model for which the magnetization is coupled to a supercritical bifurcation. Other effects that could be *a priori* associated with the ferromagnetism of the driving impellers have not been observed. For instance, after the bifurcation has been crossed for the first time, we have not detected any hysteretic behavior of the dynamo onset, and the smooth continuous increase in the field with $(R_m - R_m^c)$ is at odds with the behavior of solid rotor dynamos.[3,4] Disk dynamos with imposed velocity would also saturate to a value directly fixed by the maximum available mechanical power, in contrast to our observations (cf. Sec. II E).

One last observation strongly ties the self-generated magnetic field with the hydrodynamics of the flow. Features of the flow (mean geometry and fluctuations) can be changed when the driving impellers are counter-rotated in either direction (labeled + or −), or the thin annulus may be inserted or not in the midplane (called the w and w/o configurations).[22,23,31] Bifurcation curves for the +w and −w cases are shown in Fig. 3(b). When the blades of the impellers are rotated in "scooping" (−) or nonscooping (+) directions, we note that the dynamo threshold is changed from $F=16$ Hz in the +w case to $F=18$ Hz in the −w/o case, with corresponding power consumption changing from 40 to 150 kW. Taking into account the change in the efficiency with which the fluid is set into motion, the threshold varies from $R_m^c=32$ to $R_m^c \sim 43$ in terms of the integral magnetic Reynolds number. For the +w/o case (not shown), the onset is again $R_m^c \sim 30$. However, for the −w/o case we have reached $R_m \sim 49$ without observing any dynamo generation. At this stage a detailed comparison of the hydrodynamics and MHD of the four (+, −, w, w/o) flows is not available, but a water prototype allows us to measure the ratio ξ of the mean poloidal velocity to the mean toroidal velocity.[21–23,34,35] For all flows, we get $\xi=0.8$ except for the (−w/o) flow where $\xi=0.5$. In fact, Ravelet and co-workers[22,35] showed that for the VKS2 configuration, $\xi=0.8$ is optimal for kinematic dynamo, while $\xi=0.5$ does not support kinematic dynamo action at all. One may suppose that this ratio has an effect on the fully turbulent dynamo action. Furthermore, strong large scale fluctuations of the flow may hinder dynamo action. Such quantities can be evaluated using the ratio $\delta(t)$ of the instantaneous to the time-averaged kinetic energy densities.[31] Within the four considered flows, the (−w/o) flow presents the highest level for both the mean value and the variance of $\delta(t)$,[31] respectively, 10% and 33% more than the dynamo-generating flow that fluctuates most (+w/o).

C. Geometry of the dynamo field

A central issue is the structure of the magnetic field which is self-sustained above threshold. In order to address it, we have inserted probes and probe arrays at several locations within the sodium flow (cf. Fig. 1). Due to our limited sampling in space, we do not fully map the neutral mode; we only obtain *indications* of its topology. We describe them in detail in this section; measurements reported concern the +w flow case.

In VKS2h runs, simultaneous measurements at points P1 and P5 were performed so that the field is sampled in the midplane at two locations flush with the inner copper cylinder and at a $\pi/2$ angle. As can be observed in the time signals shown in Fig. 5(a), the azimuthal components of the magnetic fields at these two points vary synchronously. The maximum of the autocorrelation function [Fig. 5(b)] occurs for a zero time lag; its value is less than 0.2 below the dynamo onset, jumps to 0.5 at the threshold, and saturates to values around 0.7 for R_m values above 36.

In Fig. 5(b), we have plotted times in seconds and observe that all the curves above the dynamo onset almost collapse. This behavior persists if time is made nondimensional

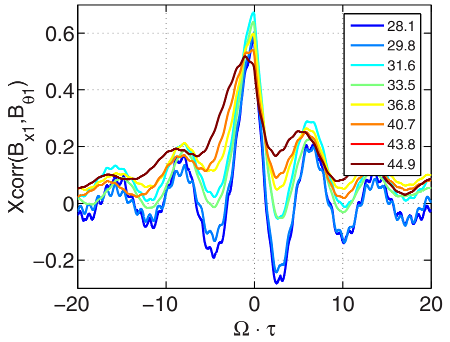

FIG. 6. (Color online) Cross correlation function of the axial component and azimuthal component of the field measured inside the flow for increasing magnetic Reynolds numbers in the range of 28–45. Measurements are done at point P1 in VKS2h.

using the diffusion time $\mu_0 \sigma R^2$ but does not persist when using the impeller rotation rate F (not shown). This shows that the dynamics is linked to a global magnetic mode rather than controlled by hydrodynamic processes. Another observation is that there is also a strong correlation between the axial and azimuthal components of the magnetic field at a given location. Figure 6 shows that its maximum exceeds 0.5 at all R_m, and that it occurs for a time delay increasing with R_m.

In VKS2i runs, the Hall-probe array was set within the bulk of the flow, nearer to one impeller—point P3. For several values above onset (R_m=33.9,35.8,41.4), we observe in Fig. 7 that the normalized field profiles along the array nicely superimpose. Near the rotation axis, the main component is axial; further away the azimuthal component dominates. Outside of the flow volume (beyond the inner copper cylinder) the axial component direction is opposite to that in the center. In the same experiment, the single-point probe was set nearer to the other impeller (symmetrically with respect to the midplane, and close to the rotation axis, point P4). The field measured there is mainly axial with the same direction as at P3. Below threshold, the induction profiles (due to the presence of the Earth's field) have the same geometry: the favored dynamo mode is the most efficient with respect to induction.

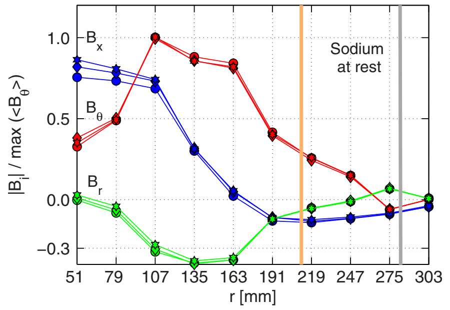

FIG. 7. (Color online) Radial profiles of magnetic field. VKS2i measurements with the probe array inserted at P3. Measurements for +w flows at R_m=33.9,35.8,41.4, above the dynamo onset. The magnetic field components are normalized by the largest value of the θ-component (azimuthal direction): axial (x) is blue, azimuthal (θ) is red, and radial (r) is green. The thick vertical line around the seventh sensor ($r \sim 211$ mm) indicates the position of the inner copper shell; the tenth sensor at r=303 mm is located into the outer copper wall of the vessel.

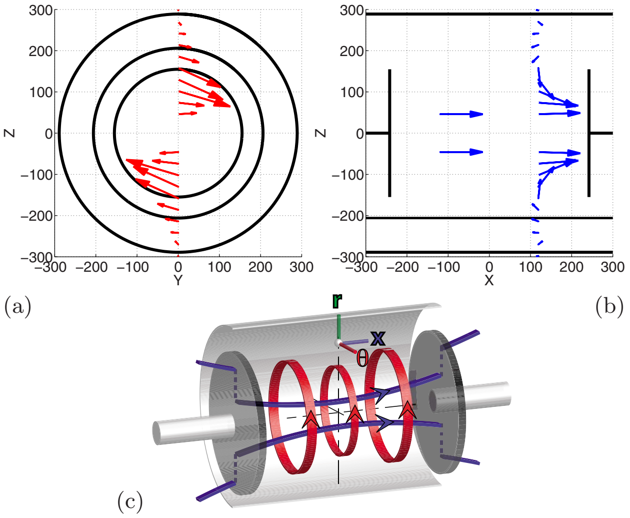

FIG. 8. (Color online) Geometry of the dynamo mode. The magnetic field amplitudes measured along the probe array in Fig. 7 is represented by arrows: (a) toroidal component, (b) poloidal component, and (c) proposed dipole structure for the neutral mode.

The combined results of the two sets of experiments are shown in Figs. 8(a) and 8(b)—the toroidal and poloidal components are displayed and axisymmetry is assumed. The simplest geometry of the magnetic field corresponds to an axisymmetric field whose axial component has one direction at the center of the cylinder and a reversed direction outside, together with a strong azimuthal component—sketched in Fig. 8(c). The dynamo field generated in the VKS2 experiment thus involves a strong axial dipolar component. The determination of its precise geometry (associated higher modes and their relative amplitudes) needs more precise measurements. However, it strongly differs from the prediction of kinematic calculations based on the topology of the mean von Kármán flow[35,36] which tends to favor a transverse dipole. Invoking Cowling's theorem,[2] the axisymmetric nature of the dynamo fields implies that it has not been generated by the mean flow motions alone. However, an axial dipole is expected for an α-ω dynamo. The differential rotation in von Kármán flows can generate an azimuthal field from a large scale axial field by torsion of the field lines—the ω effect.[65] If an α effect takes place, it can produce an azimuthal current from the azimuthal magnetic field component and, in turn, this current will generate an axial magnetic field. One then has a dynamo loop-back cycle that can sustain an axial dipole. For the α component, several mechanisms have been proposed. For an axisymmetric mean flow, it has been shown that nonaxisymmetric fluctuations can generate such an alpha effect provided that they have no mirror symmetry.[66] A scenario was proposed in Ref. 64 using the helicity of the flow ejected by the blades of the driving impellers—this flow is nonaxisymmetric with azimuthal wavenumber m=8, helical, and of much larger amplitude and coherence than small scale turbulent fluctuations. In this case, an azimuthal loop of magnetic field crosses an array of like-sign helical motions that can induce an azimuthal current.[20,67–69] Numerical integration of the mean field induction equation with an α effect localized in the vicinity of the impellers[70] recently displayed the generation of an axial magnetic field. The authors of this study thus claim to show agreement with the scenario proposed in Ref. 64. In mean field theory,[2,71] the most common source of α effect come from the small scale helicity of turbulence. However, the distribution of helicity in 3D turbulence remains a challenging question and measurements in model helical flows[72,73] have failed to show evidence for this kind of contribution. As shown by induction measurements in Refs. 72 and 73, another possible contribution to the α effect lies in the spatial inhomogeneity of the turbulence intensity. As shown in Ref. 74, there is a contribution to the mean-field alpha tensor coming from the inhomogeneity of turbulent fluctuations, with resulting electromotive force $\boldsymbol{\epsilon} \sim (\mathbf{g} \cdot \boldsymbol{\Omega})\mathbf{B}$, where $\boldsymbol{\Omega}$ is the flow vorticity and $\mathbf{g}$ is the normalized gradient of turbulent fluctuations, $\mathbf{g} = (\nabla u^2)/u^2$. It shows again that an azimuthal B_θ field generates a j_θ current and, therefore, an axial magnetic field. Distinguishing between these mechanisms—which may be linked—will need further measurements, ideally from nearby velocity and magnetic probes.

D. Saturation

The amplitude of the magnetic field at saturation is related to the way in which the growing Lorentz forces change the hydrodynamics of the flow. While the value of the threshold can be determined by studying the induction equation for a given velocity field—kinematic dynamo simulations—the saturation is governed by nonlinear effects and one must consider the coupled equations of MHD,

$$\frac{\partial \mathbf{u}}{\partial t} + (\mathbf{u} \cdot \nabla)\mathbf{u} = -\nabla\left(\frac{p}{\rho} + \frac{B^2}{2\mu_0}\right) + \nu\Delta\mathbf{u} + \frac{1}{\rho\mu_0}(\mathbf{B} \cdot \nabla)\mathbf{B}, \tag{2}$$

$$\frac{\partial \mathbf{B}}{\partial t} + (\mathbf{u} \cdot \nabla)\mathbf{B} = (\mathbf{B} \cdot \nabla)\mathbf{u} + \frac{1}{\mu_0\sigma}\Delta\mathbf{B} \tag{3}$$

for divergence-free fields. Dimensionally, the value of the magnetic field at saturation can be written as

$$B_{\text{sat}} = \rho\mu_0 V^2 f(R_m, P_m), \tag{4}$$

where f is a function of the magnetic Reynolds number R_m and magnetic Prandtl number P_m and V is some characteristic velocity scale. Functional forms have been determined in limiting cases of laminar and turbulent dynamos.[64,75,76] In the low (kinetic) Reynolds number limit, the Lorentz force balances the viscous term in the Navier–Stokes equation and one obtains[75,76]

$$B_{\text{sat}}^2 \propto \frac{\rho\nu}{\sigma R^2}(R_m - R_m^c). \tag{5}$$

In the high magnetic Reynolds number limit, the Lorentz force must be balanced by the nonlinear terms and one gets

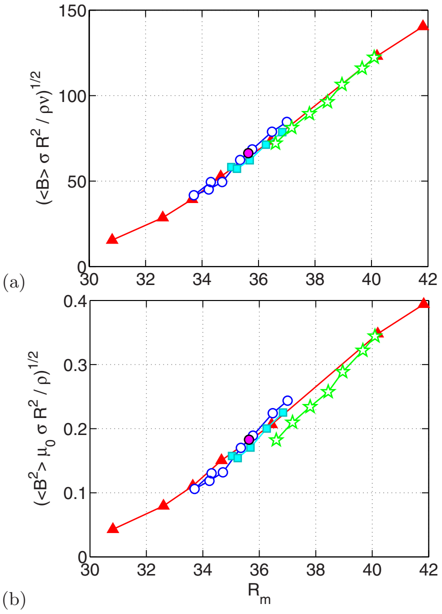

FIG. 9. (Color online) Laminar and turbulent scalings for the magnetic field intensity at saturation. Measurements are shown here for several rotation rates of the impellers and for different operating temperatures T; the magnetic Reynolds number R_m is rescaled accordingly. Measurement at P1 in VKS2h, $\langle B^2\rangle^{1/2}| = \sqrt{B_x^2 + B_y^2 + B_z^2}$: (a) laminar scaling [Eq. (5)] and (b) turbulent scaling [Eq. (6)]. Closed red triangles: $F = 24$ Hz, $T = 127 \to 143$ °C; closed cyan squares: $F = 19$ Hz, $T = 117 \to 137$ °C; open blue circles: $F = 19$ Hz, $T = 117 \to 145$ °C; and open green stars: $F = 21$ Hz, $T = 124 \to 152$ °C.

$$B_{\text{sat}}^2 \propto \frac{\rho}{\mu_0\sigma^2 R^2}(R_m - R_m^c). \tag{6}$$

Both possibilities are shown in Fig. 9, in which the magnetic Reynolds number has been varied either by changing the rotation rate of the driving impellers or by changing the operating temperature and, hence, the sodium's electrical conductivity. Judging from the linearity of the graphs, both seem plausible; however, one may note that the prefactor in the laminar scaling is very large. In other words, a laminar approach, quite doubtful given the high turbulence level in the sodium flow, also underestimates the saturated field by almost two orders of magnitude. We favor the turbulent scaling and note at this point that the fluctuations play an essential role for the generation of the dynamo and that inertial terms in the Navier–Stokes equation control the nonlinear saturation.

E. Power consumption issues

We now turn to the power needed to drive the flow in its steady state, below, or above threshold. Let us call $\mathbf{u}_0(\mathbf{r}, t)$ the velocity field during the linear growth of the dynamo instability, and P_0 the mechanical power needed to drive this velocity field in a stationary forcing. Given the very high kinetic Reynolds number of the experimental flow, one expects the turbulent scaling $P_0 \propto \rho L^2 U_0^3$, where L and U_0 are characteristic length and velocity scales. We define the di-

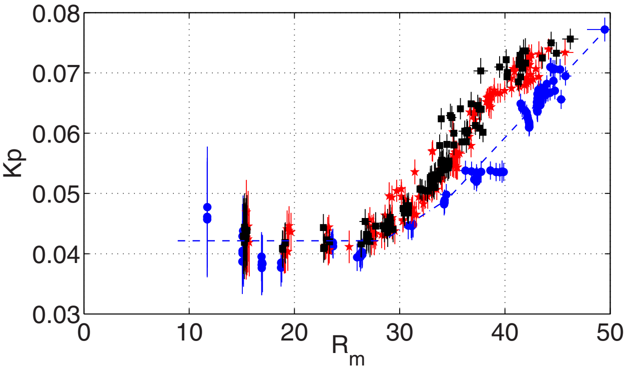

FIG. 10. (Color online) Evolution with R_m of the power number defined in Eq. (7) and measured from the drives of the motors. The blue circles (and dashed line as an eye guide) are from nondynamo runs (VKS2f) with stainless steel impellers. The red stars (VKS2g) and black squares (VKS2h) come from two dynamo runs, with same geometry but with soft-iron impellers and also without any magnetic probes in the flow bulk.

mensionless constant (or power number) K_p, using the torques (Γ_1, Γ_2) or the total power (P_0) delivered by the driving motors, as

$$K_p = \frac{1}{2}\frac{\Gamma_1 + \Gamma_2}{\rho R^5 (2\pi F)^2} = \frac{1}{2}\frac{P_0}{\rho R^5 (2\pi F)^3}, \tag{7}$$

where we have used R as the characteristic length scale and $U_0 = 2\pi RF$ as the associated velocity scale. The 1/2 factor in the definition corresponds to the consumption *per motor*, as used in reports of water-prototype studies.[21,22,35] Please note that the two formulas in Eq. (7) are only equal because $F_1 = F_2$. When a dynamo is generated, the velocity field in the saturated state is $\mathbf{u}_B(\mathbf{r},t)$. The mechanical power is now P_B and it must feed both the hydrodynamic flow and the magnetic field: $P_B = P_B^{\text{hydro}} + P_B^{\text{mag}}$. The field $\mathbf{u}_B$ differs from $\mathbf{u}_0$ because the nonlinear saturation has modified the flow. A likely possibility is that the turbulent fluctuations have been changed,[64,75–77] and this would also change the mean flow via the Reynolds stress tensor. The power needed in order to sustain the magnetic field must be estimated from

$$P_B^{\text{mag}} = \int \frac{j^2}{\sigma} d^3x = \int \frac{(\nabla \times \mathbf{B})^2}{\mu_0^2 \sigma} d^3x, \tag{8}$$

where j is the current density. With the limited measurements at this stage of the experiment, we cannot resolve independently P_B^{hydro} and P_B^{mag}, and we can only use the industrial output of the motors drives as an indicator of P_0 and P_B.

The dimensionless power number is shown in Fig. 10 for three sets of experiments. The blue circles correspond to measurements made when driving the flow with stainless steel impellers, a case for which dynamo action was not observed. A first observation is that the expected turbulent scaling—K_p independent of Re or R_m—is observed only for $R_m < 30$ $(F < 16$ Hz). The $K_p = 0.045$ value is in agreement with measurements made in scaled-down water prototypes.[21–23,31] Above $R_m = 30$, some modification must occur because the flow power consumption climbs, in nondimensional units, from $K_p = 0.045$ to $K_p \sim 0.065$, when $R_m > 40$ $(F > 24$ Hz). This phenomenon, not understood at present, has to be related to the hydrodynamics of the flow because it is observed in nondynamo experiments. However, for identical rotation rates of the impellers, we measure on average that K_p (dynamo) is typically 10% larger than K_p (nondynamo).

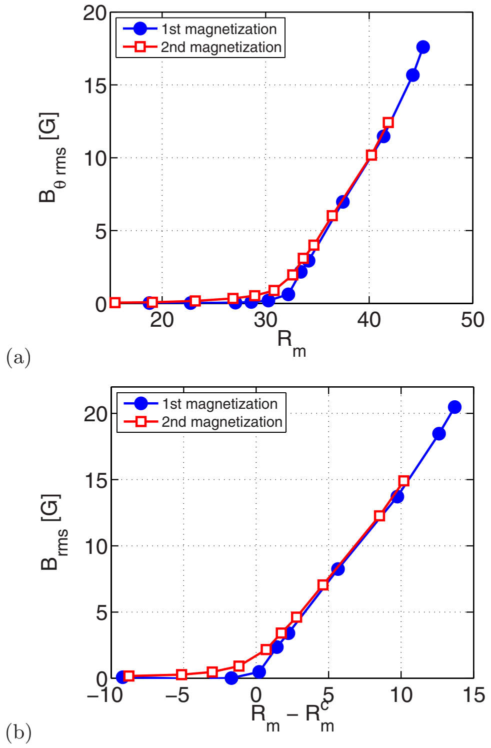

FIG. 11. (Color online) Evolution with R_m of rms values of the magnetic field at saturation. Measurements at point P1 in VKS2h. (a) Azimuthal component $B_{\theta\text{rms}}$. (b) Magnetic field amplitude B_{rms}. The closed blue circles corresponds to a first run with almost demagnetized impellers (see text) and the open red squares to the subsequent runs.

F. Fluctuations

All results presented so far have concerned the average—in time—of the magnetic field recorded by the probes. This section discusses features of the rather large fluctuations about these mean values—as can be seen in Fig. 2. One first observation is that the rms amplitudes in each of the components of the magnetic field increase sharply at dy-

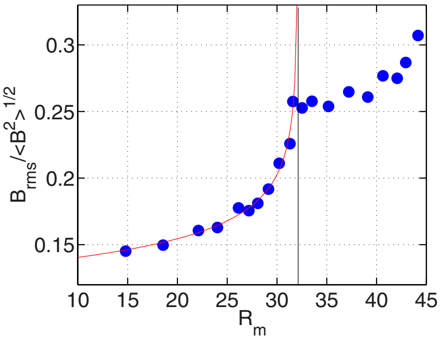

FIG. 12. (Color online) Evolution of the ratio of rms fluctuations to second moment of the magnetic field at point P1.

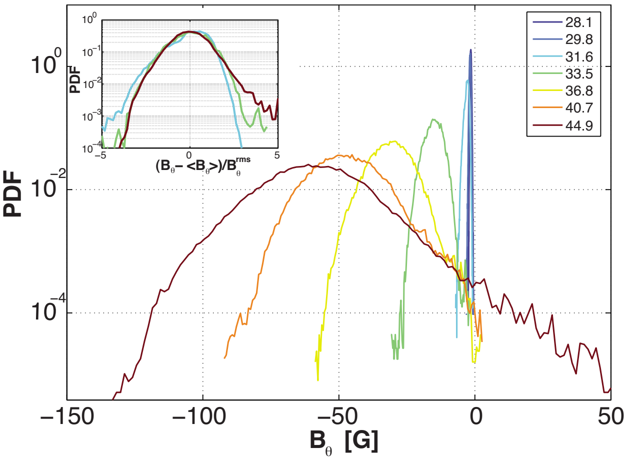

FIG. 13. (Color online) PDFs of local fluctuations of B_θ. Measurement at point P1, VKS2h. Magnetic Reynolds numbers are given in the legend and profiles below onset cannot be distinguished. Inset: PDFs for centered and normalized variables.

namo onset, as shown in Fig. 11. This increase defines the same threshold $R_m^c \sim 32$, as estimated from the behavior of the mean values.

Another interesting observation concerns the evolution of the ratio of rms to second moment. It increases very sharply near onset and then much less rapidly above (cf. Fig. 12). The transition actually allows a determination of the threshold, again at $R_m^c \sim 32$. From a practical point of view, the sharp nonlinear increase in the fluctuations may be a good indicator that one is nearing dynamo onset.

We now study the fluctuations in time of the dynamo field recorded at a fixed location. Each component has instantaneous fluctuations that deviate significantly from the mean values. Figure 13 shows the probability density functions (PDFs) for the azimuthal component measured by the gaussmeter at P1. While sharply peaked about $B_\theta=0$ below threshold, the distributions become wide above threshold. At the highest R_m values, one notes the development of a weak exponential tail to low values with occurrence of events with the reversed polarity. These events, which may also be spatially localized within the flow, are not able to reverse the dynamo. When normalized and centered (inset in Fig. 13), the distributions are still essentially Gaussian in the vicinity of the threshold and there is no evidence that the bifurcation proceeds via on “on-off” scenario.[55,57–59] Gaussian distributions were also observed for most induction measurements carried out in the VKS1 setup,[19] so that self-excitation has not induced significant changes in behavior here—in agreement with measurements in the Karlsruhe dynamo.[10]

The fluctuations whose statistics are given above occur over a wide range of time scales. The time spectra give the distribution of energy among these scales. Since the fluctuations of the magnetic field measured at a given location in the experiment are expected to be sensitive to the local turbulence intensity, we discuss in the following the magnetic energy spectra measured at different locations and at different magnetic Reynolds numbers.

We report in Fig. 14 the magnetic spectra measured above the dynamo threshold at different distances from the axis of the experiment along a radius passing through point P3. We observe a clear dependence of the global shape of the spectra depending on the location. The spectra exhibit ranges to which one may want to ascribe traditional turbulence scaling behavior:

(a) For $f \lesssim F/10$, the spectra are essentially flat; note however a broad frequency peak around $f_{\text{low}} \sim F/10$ (we will see further that $f_{\text{low}} \sim 0.14F$).

(b) In the range $F/10 \lesssim f \lesssim 4F$, the spectra are consistent with power laws: f^{-1} for the azimuthal and the radial components and $f^{-5/3}$ for the axial component.

(c) At larger frequencies, the magnetic energy decays rapidly within a short range $(4F \lesssim f \lesssim 8F)$ possibly consistent with a $f^{-11/3}$ decay, also known to exist in numerous induction experiments with liquid metals[19,65] and an even steeper decay (close to f^{-6}) at larger frequencies.

As we study signals from sensors at increasing radial distances from the axis, these regimes disappear. Harmonics locked to the impellers’ rotation rate become visible: harmonic 8 is particularly intense for sensors at $r \lesssim 215$ mm, inside the inner copper vessel. This is very likely to be related to the fact that the impellers are fitted with eight blades and that those sensors intercept the centrifugal flow ejected at the periphery by the blades. As we move into the layer with sodium at rest $(r \gtrsim 210$ mm), the global energy of the

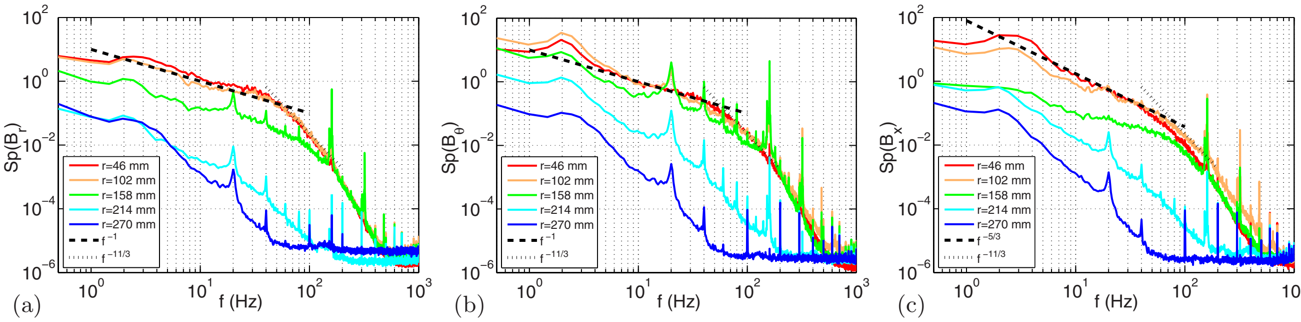

FIG. 14. (Color online) Time spectra of magnetic field fluctuations measured with the probe array at point P3 (location of the innermost sensor) in VKS2i. Different curves on each plot correspond to different sensor depth, labeled in the legend by their distance r to the rotation axis. The rotation frequency of the impellers is 20 Hz: (a) Axial component, (b) azimuthal component, and (c) radial component.

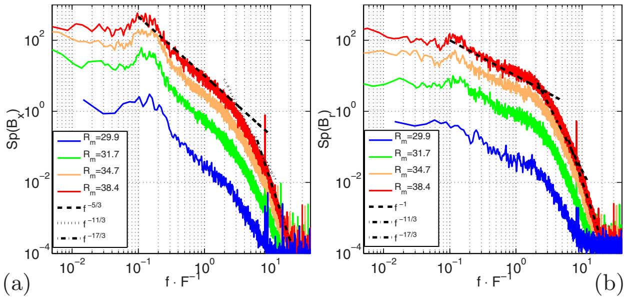

FIG. 15. (Color online) Time spectra of magnetic field fluctuations measured for different values of R_m at point P4 during VKS2i: (a) axial component and (b) radial component.

fluctuations significantly decreases; a decay due to the presence of ohmic dissipation remains visible as well as the first harmonics of the impellers' rotation rate.

We now discuss the evolution of spectra with R_m, measured at the innermost location within the flow (Fig. 15). The different power law regimes remain, with their exponents unchanged for all values of the magnetic Reynolds number. We find that the transition between the different regimes is locked to forcing frequency F. The low frequency peak is systematically present and centered around $f_{\mathrm{low}} \sim 0.14F$ regardless of the Reynolds number. The f^{-1} regime, which remains present for the azimuthal and radial component, may be interpreted as $1/f$ noise due to the presence of several characteristic time scales in the flow. At larger frequencies, above the magnetic diffusion cutoff, the $f^{-11/3}$ regime is expected, under a Taylor hypothesis, from the balance in the induction equation between the magnetic induction term—with a fully turbulent velocity field—and the Ohmic dissipation term. The shortness of the $f^{-11/3}$ regime that we observe and the steeper decrease observed above the eighth harmonic can be attributed to a spatial filtering due to the dimension $l_0 \sim 3$ cm of the tube containing the probe. The spatial integration of magnetic fluctuations at the scale l_0 attenuates the spatial magnetic spectra by a factor k^{-2}, which under a Taylor hypothesis, should lead in the frequency spectral domain to a $f^{-17/3} \sim f^{-5.7}$ regime consistent with the steep energy decrease measured for large frequencies fluctuations. In this scenario the cutoff frequency between the $f^{-11/3}$ and the $f^{-17/3}$ regimes is proportional to $l_0 v$, with v the characteristic local velocity at the probe location. This is consistent with the observation that the transition is locked to the impellers' rotation rate.

Finally, we discuss measurements taken in the midplane, flush with the lateral wall, which have different characteristics. Figure 16 shows the evolution of spectra as the magnetic Reynolds number is increased. The three components have a similar behavior [Fig. 16(a)]. One notes a net magnetic energy increase as the dynamo threshold is crossed. At all magnetic Reynolds number, the spectra exhibit a low frequency peak $f_{\mathrm{low}} \sim 0.14F$ and a peak at a frequency corresponding to the rotation rate of the impellers, also present in the measurements at points P3 and P4 previously discussed. Although the evidence of power law dependence of the spectrum is again restricted to relatively short ranges, different regimes may be identified:

(a) At low frequencies (typically $f \lesssim f_{\mathrm{low}}$) a slow decay with an exponent α_1 changing from $\alpha_1 \sim 0$ below threshold to $\alpha_1 \sim -0.5$ above threshold.
(b) At intermediate frequencies (typically $f_{\mathrm{low}} \lesssim f \lesssim F$) the energy decay is faster with an exponent α_2, changing from $\alpha_2 \sim -2$ below threshold to $\alpha_2 \sim -2.5$ above threshold.
(c) In the high frequency range (typically $f \gtrsim F$), as shown in the semilog representation in Fig. 16(c), the spectra are better described by an exponential decay $\exp(-f/f_{\mathrm{exp}})$. We find that f_{exp} is of the order of $1.4F$.

III. DYNAMICAL REGIMES WITH ASYMMETRIC FORCING $F_1 \neq F_2$

A. Asymmetric flow forcing

In this section, we report results obtained when the impellers rotate at different frequencies ($F_1 \neq F_2$). Different sets of parameters can be used to describe these forcing configurations: (i) F_1 and F_2, the two impellers frequencies; (ii) $F = (F_1 + F_2)/2$ the mean frequency and

$$\Theta = (F_1 - F_2)/(F_1 + F_2)$$

the nondimensional difference; and (iii) any other combinations of F_1 and F_2. In a half-scale water model experiment, it has been shown from torque measurements[21] that there are strong similarities between the von Kármán flow forced by

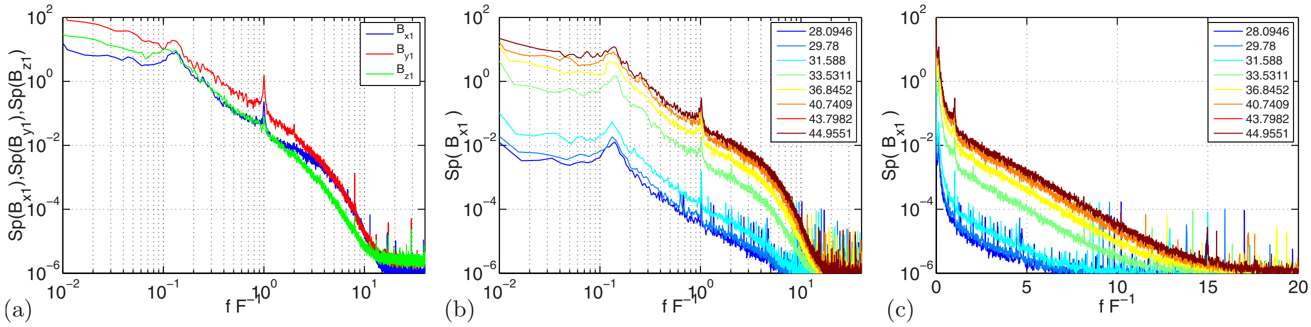

FIG. 16. (Color online) Time spectra of magnetic field fluctuations at point P1. (a) Three components, $R_m \sim 40$; [(b) and (c)] log-log plot and semilog plots of B_x spectra for increasing R_m values.

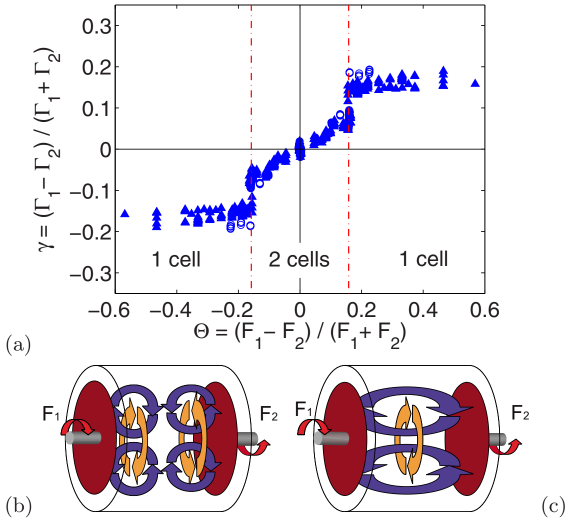

FIG. 17. (Color online) (a) Measurement of the reduced dimensionless torque $\gamma=(\Gamma_1-\Gamma_2)/(\Gamma_1+\Gamma_2)$ vs $\Theta=(F_1-F_2)/(F_1+F_2)$. Data are from VKS2g (open circles) and VKS2h (closed triangles), i.e., without probes in the flow bulk which strongly affect γ in the one-cell regimes. Data have been symmetrized. (b) Schematic configuration of the mean flow in the two-cell regime for small $\Theta(F_1 \simeq F_2)$, as measured in water. (c) Schematic configuration of the mean flow in the one-cell regime for large $\Theta(F_1 \gg F_2)$.

impellers rotating respectively at F_1 and F_2 in the laboratory frame or by impellers rotating at $(F_1+F_2)/2$ in a frame rotating at $(F_1-F_2)/2$. More recently, stereoscopic particle image velocimetry measurements have confirmed this finding.[23] It is thus convenient to choose F and Θ as control parameters since F appears as the effective forcing shear in the rotating frame and $|\Theta|$ measures the relative importance of the global rotation to shear.

These asymmetric regimes have been studied in water experiments allowing a good understanding of the hydrodynamic bifurcations of the flow when breaking the forcing symmetry.[21,22,78] When increasing or decreasing one of the impeller rotation rates from a symmetric configuration, the cell closer to the fastest impeller grows in size and the shear layer is translated toward the slowest impeller. When only one impeller rotates, the flow is made of one single pumping cell rotating with the stirring impeller—similar to the s_1t_1 flow.[32] The evolution between these extreme cases (generally referred to as the "turbulent bifurcation") depends on the impeller and vessel geometry: In some cases, the transition between the two extreme flow topologies (two symmetric cells versus one single cell) is smooth and continuous, but it might also be sudden,[31,78] leading to first order transitions in any order parameter chosen to describe it (average position of the shear layer, torque delivered by the motors, etc.).

Figure 17 shows the evolution of the reduced dimensionless torques

$$\gamma=(\Gamma_1-\Gamma_2)/(\Gamma_1+\Gamma_2)$$

delivered by the motors as a function of Θ. One can see the sudden transition for $|\Theta|=\Theta_c \simeq 0.16$, corresponding, e.g., to $F_1=22$ Hz and $F_2 \simeq 15.8$ Hz. At this point the flow transits between one-cell and two-cell topologies.[22,31,78] The transitions are very sharp and the corresponding hysteresis domains are very narrow.

B. A variety of regimes

We first report observations of dynamo regimes when varying the frequency of rotation of the impellers. Not all possible combinations have been explored—Fig. 18 summarizes the visited regions of parameter space. They are plotted in terms of the experimental control parameters (F_1,F_2) and also as a function of the differential rotation Θ and of an average magnetic Reynolds number based on the global rotation rate $F=(F_1+F_2)/2$. In Fig. 18(b), symmetry between the positive and negative values of Θ has been assumed and observed dynamical regimes will be discussed according to this hypothesis, with F and $|\Theta|$ being the control parameters.

For $R_m(F)\sim 35$, and for increasing $|\Theta|$, one gets successively—Fig. 18(b)—the following main regimes:

1. Stat1: $|\Theta|<0.09$; stationary dynamos of the same type as observed for the symmetric $\Theta=0$ forcing. An example of time trace of the three components of magnetic field measured at P1 is shown in Fig. 19(a).
2. Limit cycle (LC): $|\Theta|\sim 0.1$; for several time-periodic regimes between the Stat1 and Stat2 states [Figs. 19(b) and 19(c)]. These regimes have been studied in detail in Ref. 18.

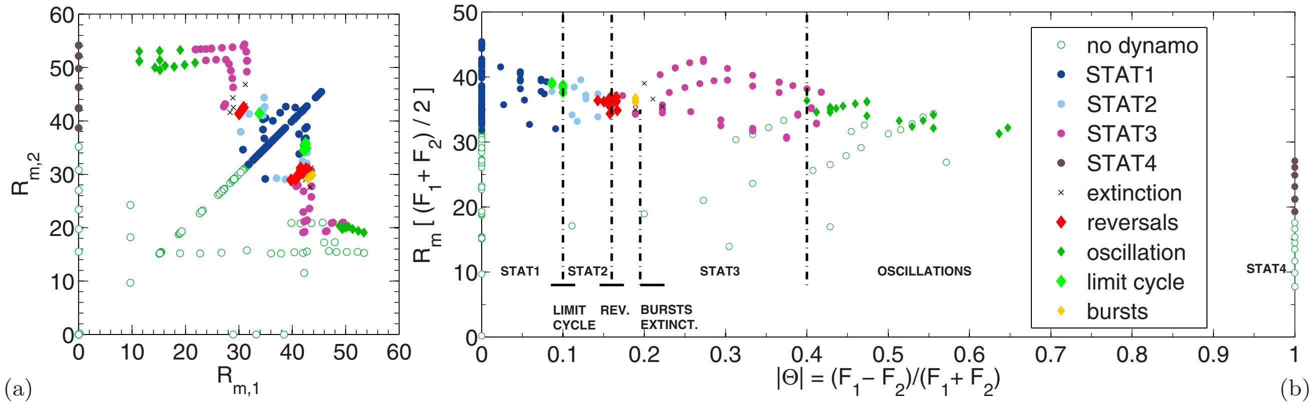

FIG. 18. (Color online) Parameter space and dynamo regimes for VKS2g, VKS2h, and VKS2i. (a) In the $(R_{m,1},R_{m,2})$ plane. (b) In the $[R_m(F),|\Theta|]$ plane, i.e., symmetrized data.

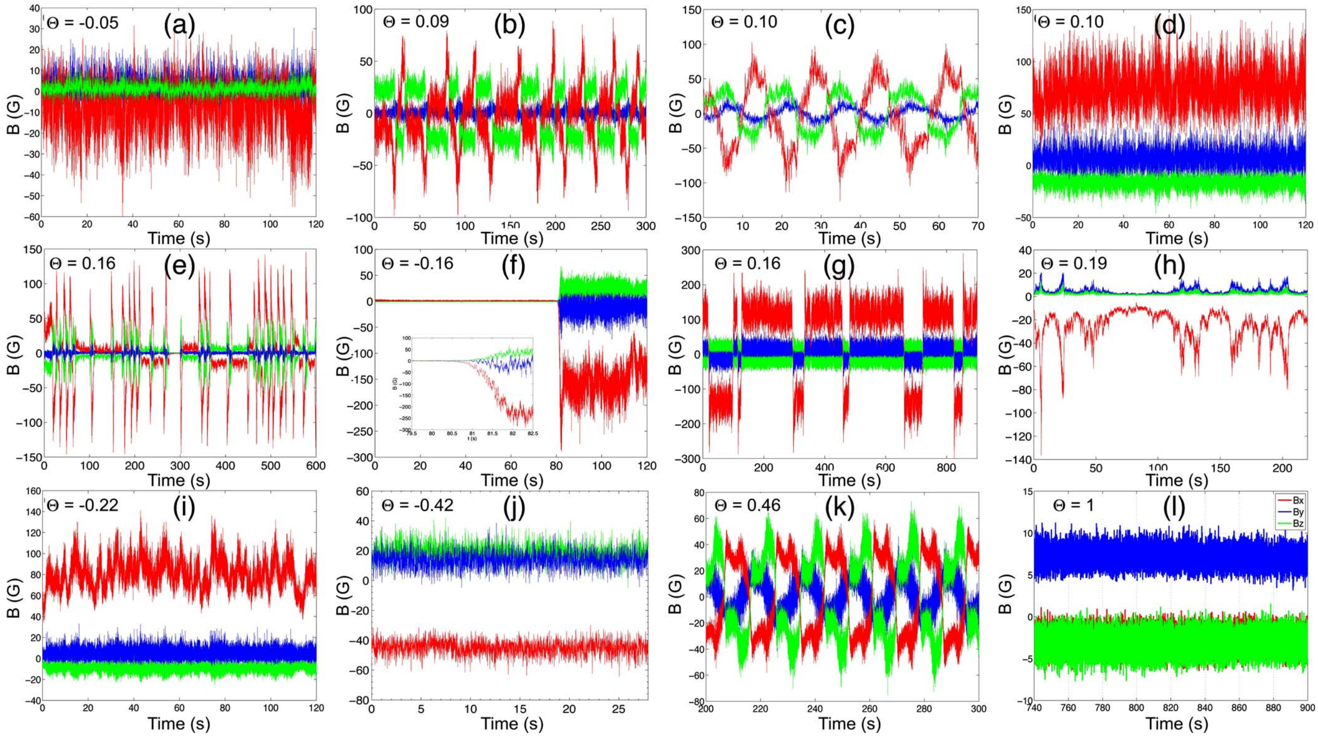

FIG. 19. (Color online) Examples of observed dynamo regimes for increasing values of $|\Theta|$. See text for details. Color code [see caption of Fig. 1 and legend of Fig. 2(a)] for the magnetic field components: axial (x) in blue, azimuthal (y) in red, and radial (z) in green.

(3) Stat2: $0.11 < |\Theta| < 0.13$; stationary regimes [Fig. 19(d)].
(4) Reversal: $|\Theta| \in [0.15-0.18]$; reversing dynamos[17,18] [Fig. 19(g)].
(5) Bursts–ext: $|\Theta| \sim 0.2$; regimes with a "bursting" dynamo field where the magnetic field has on average a low value with sudden "jerks" to much larger intensities [Figs. 19(e) and 19(h)]. In this region we have also observed cases where dynamo action was not observed within 3 minutes test periods, as well as cases when an initial dynamo decays to zero. They have been called "extinctions" [Figs. 19(f) and 25(d)].
(6) Stat3: $0.2 < |\Theta| < 0.4$; stationary dynamos [shown in Figs. 19(i) and 19(j)].
(7) Osc: $|\Theta| > 0.4$; oscillatory dynamos. When increasing further the rotation component of the forcing, oscillatory dynamos are starting from the Stat3 stationary ones. An example is given in Figs. 19(k) and 27(a).
(8) Stat4: at $|\Theta| = 1$, when the flow is driven by the rotation of only one impeller, one observes an abrupt bifurcation to a stationary dynamo of very low (finite) amplitude [Fig. 19(l)]. Note that intermediate forcing conditions ($0.6 \lesssim |\Theta| < 1$) are not reachable at present for mechanical reasons.

We note that at $R_m(F) \simeq 35$ a dynamo is always generated for all explored values of Θ. Θ thus plays an important role in the selection of the dynamo regime; it does not choose it uniquely as we have observed in several cases that the dynamo at given values of (F_1, F_2) depends on the path that has been followed.

C. Stationary dynamo regimes, $\Theta \neq 0$

Although a variety of dynamical regimes have been observed when the flow is driven with impellers counter-rotating at different rates, a large fraction of the phase space is actually populated by stationary regimes (see Fig. 18). In future studies these regimes will need to be fully characterized in terms of mode geometry, type of dynamo bifurcation, etc. For the moment, we classify them in broad classes separated by time-dependent dynamos and consider the three cases for $|\Theta| \lesssim 0.6$. The first one [Stat1; Fig. 19(a) shows a typical time series, see also Fig. 2] appears at low values of Θ ($|\Theta| < 0.09$). The second regime [Stat2; Fig. 19(d)] appears as one increases Θ ($0.11 < |\Theta| < 0.13$), but it is separated from the first by a small range of Θ with a reversing regime. The third stationary regime [Stat3; Fig. 19(j)] appears at larger values of Θ ($0.2 < |\Theta| < 0.4$). The main difference can be observed in the fluctuations, which are dominated by very slow oscillations, with periods of several seconds. This observation is confirmed in Fig. 20(a), showing the power spectrum density for the three stationary regimes. Note that the three spectra collapse when the frequency is rescaled by the mean rotation frequency of the impellers, $F = (F_1 + F_2)/2$, at least for the frequencies larger than F. The small scale fluctuations in the spectrum are thus set by the effective R_m, i.e., turbulence. In Fig. 20(b), the centered and normalized PDFs of the three regimes are presented and display a fairly Gaussian behavior, like in the case of exact counter-rotation (see Fig. 13).

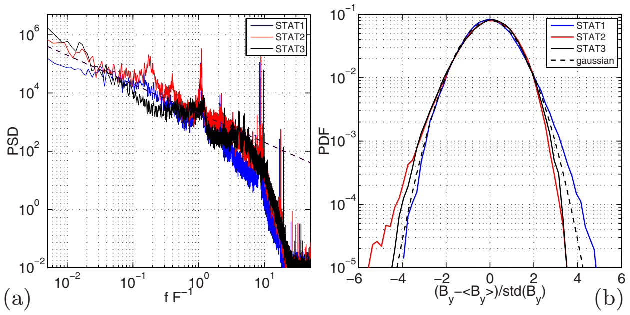

FIG. 20. (Color online) (a) Power spectrum density. Frequency is normalized by the average frequency of the impellers $F=(F_1+F_2)/2$. The dashed line shows the −1 slope as a guide for the eye. (b) Centered PDF, normalized by its rms value. Quantities are computed from the azimuthal component in the time signal in Fig. 19 for the regimes Stat1, Stat2, and Stat3.

Although we have not systematically mapped the (R_m,Θ) plane, some observations can be made about the dynamo bifurcation in these regimes. For the Stat1 regime, the bifurcation seems supercritical with a threshold around $R_m=31$, similar to the counter-rotating case, but the dependence of the threshold on Θ has not been precisely determined. However as one proceeds to more asymmetric regimes, in the case of Stat2 and Stat3, the dependence of the dynamo field on the value of Θ, as well as R_m, is more pronounced. A hysteretic behavior takes place, where the value of the magnetic field at saturation depends on the path followed.

In the limit of the flow being driven by the rotation of a single impeller (the other being kept at rest, i.e., $\Theta=\pm 1$), we observe an abrupt bifurcation to stationary dynamo Stat4. As the rotation rate of the impeller is increased above threshold, the amplitude of the magnetic field increases slightly to reach a maximum at $R_m=23$ Hz, then decreases to almost zero at the maximum rotation rate ($R_m=26$). Such R_m decrease in the dynamo is also observed when the equatorial annulus is removed but then the stationary regime exchanges stability with an oscillatory regime, with a bistability region.[79]

D. Reversals

Decreasing the frequency of one impeller from the stationary dynamo regime at $F_1=F_2=22$ Hz, we performed the first observation of reversals of the magnetic field in a fluid dynamo.[17] These reversals at irregular time intervals are displayed in Fig. 21 for a sensor located at point P2. For each polarity, either positive or negative, the amplitude of the magnetic field has strong fluctuations, with a rms fluctuation level of the order of 20% of the mean. This level of fluctuation is due to the very intense turbulence of the flow, as the kinetic Reynolds number exceeds 10^6. Reversals occur randomly and have been followed for up to 45 min, i.e., 54 000 characteristic time scales of the flow forcing.

The polarities do not have the same probability of observation. Phases with a positive polarity for the largest magnetic field component have, on average, longer duration ($\langle T_+\rangle=120$ s) than phases with the opposite polarity ($\langle T_-\rangle=50$ s). This asymmetry can be due to the ambient magnetic field. Note however that the amplitude of the magnetic field is the same for both polarities. Standard deviations are of the same order of magnitude as the mean values, although better statistics may be needed to make these estimates more precise. The mean duration of each reversal, $\tau\sim 5$ s, is longer than MHD time scales: the flow integral time scale is of the order of the inverse of the rotation frequencies, i.e., 0.05 s, and the Ohmic diffusive time scale is roughly $\tau_\eta\sim 0.4$ s.

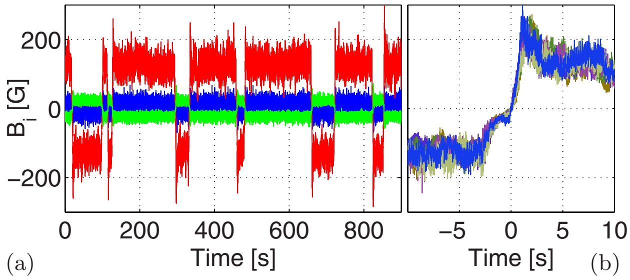

FIG. 21. (Color online) Reversals of the magnetic field generated by driving the flow with counter-rotating impellers at frequencies $F_1=16$ Hz and $F_2=22$ Hz ($\Theta=0.16$, VKS2g). (a) Time recording of the three magnetic field components at P2: axial (x) in blue, azimuthal (y) in red, and radial (z) in green [see legend of Fig. 2(a)]. (b) superimposition of the azimuthal component for successive reversals from negative to positive polarity together with successive reversals from positive to negative polarity with the transformation $B\rightarrow -B$. For each of them the origin of time has been shifted such that it corresponds to $B=0$.

When the amplitude of the magnetic field starts to decay, either a reversal occurs, or the magnetic field grows again with its direction unchanged. Similar sequences, called excursions or aborted reversals,[80,81] are observed in recordings of the Earth's magnetic field. We have also observed that the trajectories connecting the symmetric states **B** and **−B** are quite robust despite the strong turbulent fluctuations of the flow. This is displayed in Fig. 21(a): the time evolution of reversals from positive to negative states can be neatly superimposed by shifting the origin of time such that $B(t=0)=0$ for each reversal. Despite the asymmetry due to the Earth's magnetic field, negative-positive reversals can be superimposed in a similar way on positive-negative ones if $-B$ is plotted instead of B. For each reversal the amplitude of the field first decays exponentially. A decay rate of roughly 0.8 s^{-1} is obtained with a log-linear plot (not shown). After changing polarity, the field amplitude increases linearly and then displays an overshoot before reaching its statistically stationary state. The signal thus clearly breaks the time reversal symmetry, a common feature for many relaxation oscillations or heteroclinic cycles in low dimensional dynamical systems. A similar asymmetry in time, with a slow decay of the field amplitude followed by a fast recovery after changing sign, has been reported in recordings of the Earth magnetic field.[82]

Magnetic field reversals have been found in the same region of parameter space during all the runs (VKS2g, VKS2h, and VKS2i). The characteristics described above have been found reproducible except the nearly perfect superimposition displayed in Fig. 21 (VKS2g). In the following runs where measurements were performed at P1 and P3, although a most probable trajectory clearly appears, some reversals follow a significantly different one between $\pm\mathbf{B}$.

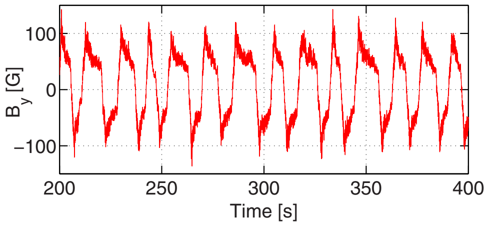

FIG. 22. (Color online) Nearly periodic reversals of the azimuthal magnetic field generated at $F_1=16$ Hz and $F_2=22$ Hz$(\Theta=-0.16)$, VKS2h. Temperature of the outer copper cylinder $T=145$ °C compared to about 120 °C for the regime with irregular reversals shown in Fig. 21.

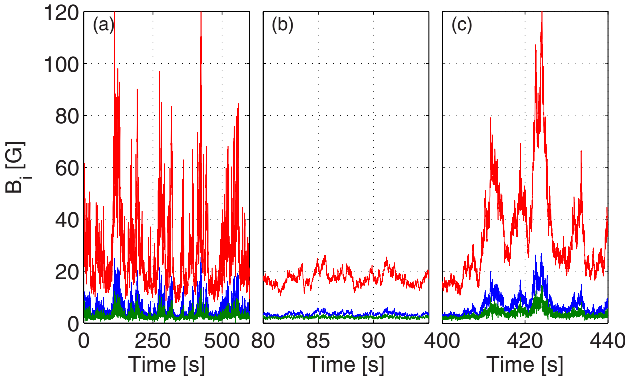

FIG. 23. (Color online) (a) Bursting regimes, VKS2h; $F_1=22$ Hz, $F_2=15$ Hz, $\Theta=0.19$; three components of the magnetic field measured at point P1 [blue: axial component; red: minus azimuthal component; and green: radial component; see legend of Fig. 2(a)]. (b) and (c) are zoomed on, respectively, quiet periods and active bursts.

Another difference concerns the synchronicity with which the three components of the magnetic field switch polarity; in the last runs (VKS2h and VKS2i), the different components have been found to vanish at slightly different times such that the norm of the magnetic field does not vanish during a reversal. These differences can be ascribed to small differences in the three runs. One possibility is that some features of the recordings of the magnetic field during reversals slightly depend on the location of the measurement point in the flow or to slight asymmetries of the setup revealed when $F_1<F_2$ (VKS2g) or $F_1>F_2$ (VKS2h). Furthermore, it is possible that measurements performed in the bulk in the last run (VKS2i) add disturbances to the flow that were not present in the first runs (VKS2g and VKS2h) for which the probes were flush to the lateral boundary. Another difference is related to the correlation of reversals with the global energy budget of the flow. The total power $P(t)$ delivered by the motors driving the flow has been shown to drop significantly below its average during reversals and excursions observed in the first set of runs (VKS2g).[17] However, changes in polarity without noticeable modification of power have also been observed in most other runs.

We note that the randomness of the reversals strongly depends on the magnetic Reynolds number. For instance, starting from a regime with random reversals, we can reach a regime with nearly periodic noisy oscillations between $\pm\mathbf{B}$ by slightly changing the sodium temperature (see Fig. 22; this regime has been observed for 200 s corresponding to 14 periods $T\simeq 14$ s). Reversals can also bifurcate to different types of stationary dynamos or to chaotic regimes involving bursts (see below) by slightly varying the impeller frequencies.

E. Bursts

Bursts occur around $|\Theta|\sim 0.2$ when one impeller rotates at a rate roughly 1.5 times faster than the other one. For instance, when $F_1=22$ Hz and $F_2=15$ Hz we have observed the behavior shown in Fig. 23(a). The magnetic field develops "bursts" from a base state. In this base state [cf. Fig. 23(b)] the magnetic field takes values of the order of 20 G. This is much lower than most other stationary regimes, but nonetheless a dynamo generated field as its amplitude is over 40 times the ambient Earth's field. During the bursts, the dynamo field reaches high field values above 100 G, a level observed in other dynamical regimes such as reversals. Typical bursts, as in Fig. 23(c), have duration of about 2–10 s.

The correlation functions of the magnetic field also display this characteristic time. Figures 24(a) and 24(b) show the normalized correlation functions $\langle B_i(t)B_j(t+\tau)\rangle_t$ for the field components. A characteristic decay time of the order of 2.5 s is observed on all components. Such a characteristic time is long compared to the frequencies of the flow forcing $(F_1,F_2,F_1\pm F_2,\ldots)$ and even compared to the magnetic diffusion time over the radius of the vessel (of the order of 0.4 s). An exponential autocorrelation function is in agreement with a Lorentzian power spectrum as show in Fig. 24(c), where an f^{-2} scaling can be observed for over 2 decades in the case of the azimuthal component of the magnetic field. The statistics of the fluctuations [Fig. 24(d)] displays an ex-

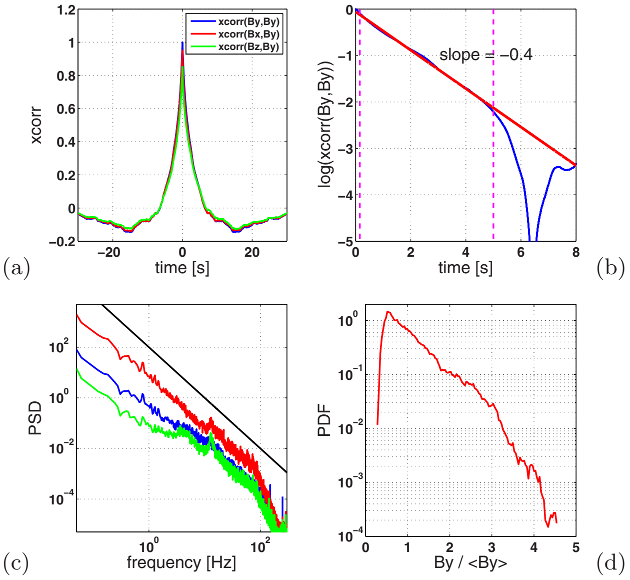

FIG. 24. (Color online) Bursting regimes, VKS2h; $F_1=22$ Hz, $F_2=15$ Hz, $\Theta=0.19$ [cf. Fig. 23]. (a) Time correlations of the magnetic field components. (b) log-linear plot of the autocorrelation of the largest field component $\langle B_y(t)B_y(t+\tau)\rangle_t$. (c) Corresponding time-power spectra—the black solid lines shows an f^{-2} scaling. (d) PDF for $B_y(t)$.

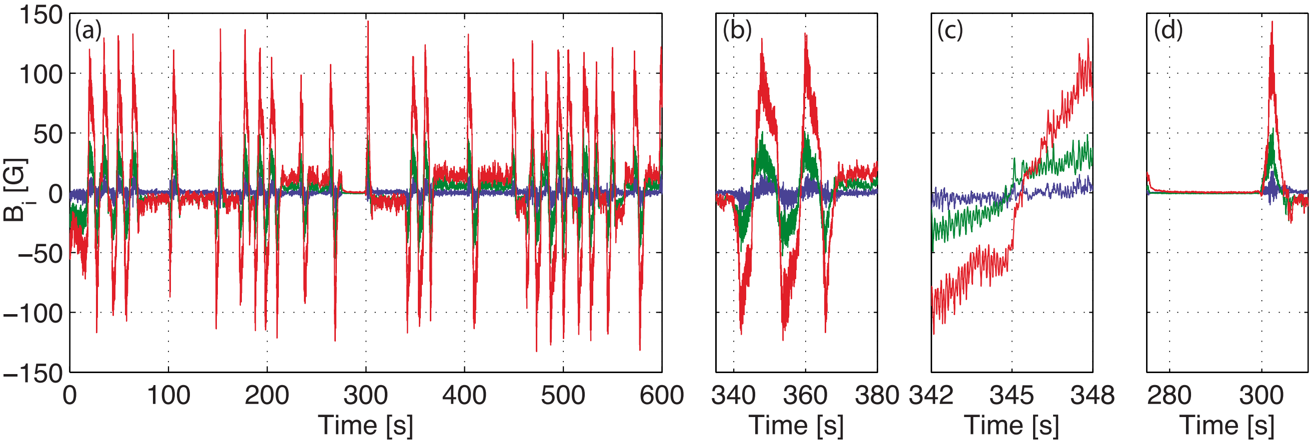

FIG. 25. (Color online) Bursting regimes, VKS2h; $F_1=21$ Hz, $F_2=15$ Hz, and $\Theta=0.167$. (a) Three components of the magnetic field measured at point P1 [blue: axial component; red: azimuthal component; and green: radial component; see legend of Fig. 2(a)]. (b) and (c) are further zoomed on the oscillations (note the change in polarity of the low state mode before and after the oscillations). (d) Zoom including the ending extinction around $t=300$ s.

ponential tail in the PDF, for the bursting events (large amplitudes). The distribution of interarrival times of bursts (not shown) is consistent with a homogeneous Poisson process, indicating that these bursting events are not intercorrelated.

When the velocity of the fastest impeller is slightly lowered, i.e., between the above described bursts domain and the reversals domain, another case of "bursting" events is observed. The dynamo transits from low amplitude states with either positive or negative polarity to the occurrence of oscillations, as seen in Fig. 25. The low amplitude states are again of the order 10–20 G, while the maximum amplitude reached when the oscillations are triggered is over 100 G, as in the oscillatory regimes discussed in Sec. III G. Note the extinction at $t\sim 300$ s, before the dynamo resumes its dynamics in the same regime.

Analysis of the correlation functions [Figs. 26(a) and 26(b)] shows a characteristic time of the order of 15 s with a dynamics such that the radial component of the local magnetic field is slightly ahead of the azimuthal and axial components. Two other peaks can be detected in the power spectra [Fig. 26(c)]: a shallow one at about 4 Hz and another, sharper, at 9 Hz—a frequency clearly visible on the time signal in Fig. 25(c). The PDFs in Fig. 26(d) reveal the low field state and the larger amplitude during the oscillations. Note that PDFs are symmetric so that there is no preferred polarity in this regime.

F. Extinction regimes

In the range of $0.16 \lesssim |\Theta| \lesssim 0.19$, i.e., where reversals, bursting reversals, and bursts occur, we also observe in few cases magnetic field extinctions (Ext). These extinctions consists of a total disappearance of all components of the dynamo field within the absolute precision due to the zero calibration of the probes, i.e., typically 0.5–2 G. They can clearly be distinguished from the low magnetic level (~ 20 G) regimes supporting the bursts [Fig. 23(b)]. Extinctions have been observed as transients or, if not transient, for 3 min test periods for the longest case. The most striking example is a spontaneous extinction observed during the bursting-reversal signal presented in Fig. 25 [see zoom in Fig. 25(d)]. Otherwise, extinctions have been observed when crossing the critical value $\Theta_c \sim 0.16$ where the flow topology changes (see Sec. III A) and may trace back for strong coupling when both flow and magnetic field reorganize. Figure 19(f) shows the reappearance of the dynamo at finite time from a transient extinction regime at $\Theta=-0.158$: The initial condition is Stat3 regime at $\Theta=-0.22$ and the final one is the reversal regime at $\Theta=-0.158$. The dynamo disappears once the control parameter is changed and spontaneously reappears roughly 100 s later through exponential growth [inset in Fig. 19(f)].

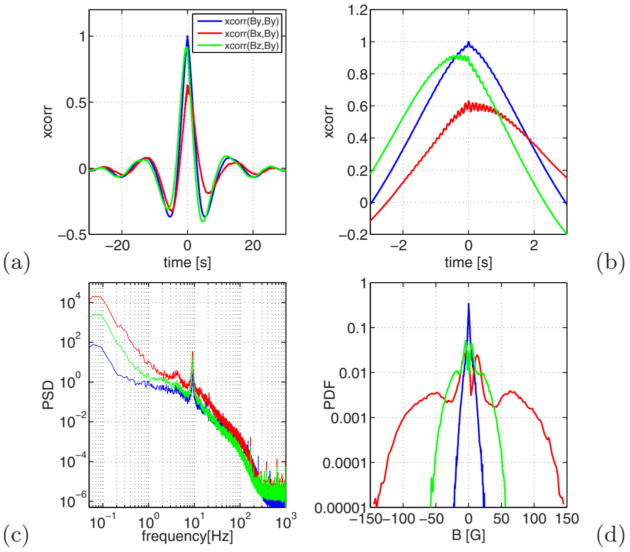

FIG. 26. (Color online) Bursting regimes, VKS2h; $F_1=21$ Hz, $F_2=15$ Hz, $\Theta=0.167$ [cf. Fig. 25]. (a) Time correlations of the magnetic field components. (b) Zoom around zero time lags. (c) Corresponding time-power spectra. (d) PDFs of the three magnetic field components. Color code for (c) and (d) as in Fig. 25.

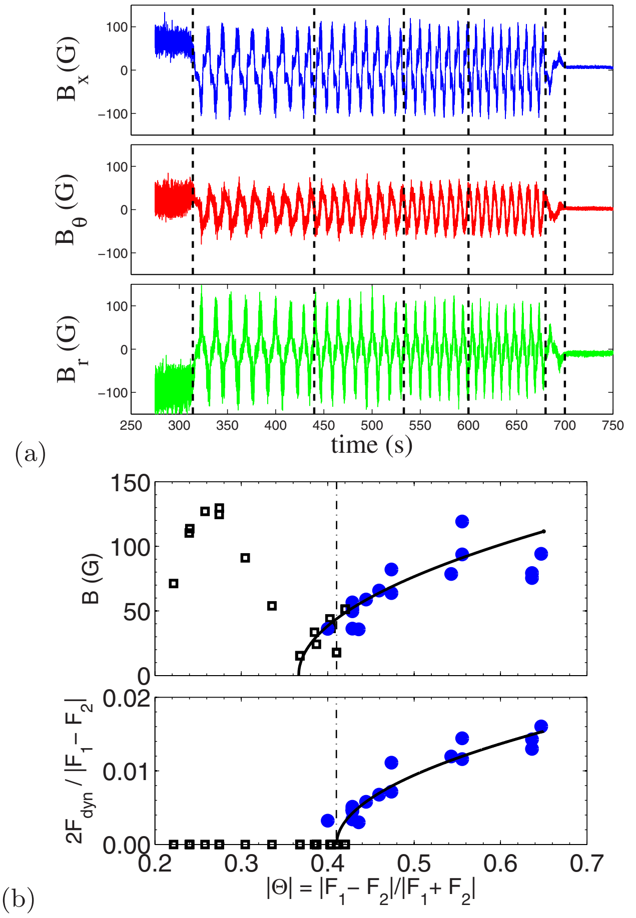

FIG. 27. (Color online) (a) Oscillatory time signals for Θ in the range of 0.44–0.56. The vertical dashed lines denote impeller frequency changes. Starting with $F_1=28$ Hz kept constant, we observe successively: stationary dynamo ($F_2=12$ Hz; $|\Theta|=0.40$) and oscillatory dynamo ($F_1=11,10,9,8$ Hz; $\Theta=0.44,0.47,0.51,0.56$). Then R_m is reduced below dynamo onset by lowering F_2 to 25 Hz (damped oscillations) and 20 Hz (no dynamo). (b): Evolution of the magnetic field amplitude and the dimensionless oscillation frequency with Θ for Osc oscillatory dynamo regimes (closed circles) and Stat3 stationary dynamo regimes (open squares). Amplitude of oscillations is a peak value (see text). Quadratic fits are described in text and the vertical line stands for the oscillatory mode threshold $\Theta_o=0.41$.

G. Oscillatory regimes

Oscillatory dynamos are observed when $|\Theta|>0.4$. Figure 27(a) shows a temporal signal obtained when Θ is varied from 0.44 to 0.56 at constant $F_1=28$ Hz. The frequency of oscillation F_{dyn} increases with $|\Theta|$. Following different paths in the (R_m,Θ) plane, we have observed that the oscillations are reached as a secondary instability of the Stat3 stationary dynamo. Although more systematic studies are needed, we suspect that the oscillatory behavior is path dependent [cf. Fig. 18(b)].

We study the bifurcation as a function of Θ, while R_m is kept in the range[31–36] [cf. Fig. 18(b)]. The evolution of the amplitude of the magnetic field with $|\Theta|$ is plotted in Fig. 27(b) for the Stat3 stationary regime and the oscillatory regime (Osc). One first observes that the amplitude of Stat3 is maximum around $|\Theta|=0.27$, reaches a minimum at $|\Theta|=\Theta_b=0.37$, very close to zero, and starts increasing again. We also observe that the fluctuation level is high below $\Theta_b=0.37$ [Fig. 19(i), $\Theta=-0.22$] and negligible above [see Fig. 19(j), $\Theta=-0.42$]. We conclude that we are in presence of two different stationary regimes (Stat3a and Stat3b exchanging their stability near $\pm\Theta_b$). The second regime Stat3b bifurcates toward oscillations at finite amplitude around $|\Theta|=0.4$. Above, the amplitude of the oscillations is computed as $B^2=B^2_{x,\max}+B^2_{y,\max}+B^2_{z,\max}$, where $B_{i,\max}$ is the peak amplitude of the i-component. With this definition, we observe a continuity between the amplitude of Stat3b and the oscillation regime. A quadratic fit reveals a $B\propto(|\Theta|-\Theta_b)^{1/2}$ dependence and confirms $\Theta_b=0.37$.

The dimensionless oscillation frequency $(2F_{\mathrm{dyn}}/|F_1-F_2|)$ is shown in Fig. 27(b). It behaves as $(|\Theta|-\Theta_o)^{1/2}$, confirming the oscillatory regime threshold value $\Theta_o=0.41$. This low frequency oscillatory dynamo mode appears as a finite-amplitude and zero-frequency secondary bifurcation as in low dimensional dynamical systems. Far from the onset, the almost-saturated frequency F_{dyn} is of the order of 0.014 times the rotation frequency. The corresponding period is much larger than any hydrodynamical or magnetohydrodynamical characteristic time scales. It is two orders of magnitude larger than the period associated with the global rotation $|F_1-F_2|/2$ or to the average frequency $F=(F_1+F_2)/2$ and three orders of magnitude larger than the magnetic diffusion time.

H. Transition and dynamics

We have reported so far a great variety of different dynamical regimes in the parameter space (F_1,F_2): for impellers in counter-rotation at roughly equal frequencies, only statistically stationary dynamos have been observed. Oscillatory regimes exist when one impeller rotates much faster than the other, although a stationary dynamo has been also observed with only one rotating impeller. Experiments on hydrodynamical instabilities have shown since a long time that the competition between a stationary and an oscillatory instability leads to complex behaviors[83–85] that can be understood in the framework of bifurcations of multiple codimension.[86] Competing critical modes have also been considered as phenomenological models of the dynamics of the magnetic fields of the Earth[87,88] or the Sun[89,90] and the same analytical techniques have been used to describe the resulting dynamics. It has been also observed in simulations[91] or mean field models[92] that magnetic field reversals can occur when a stationary and an oscillatory mode is in proximity and a simple analytic model has been designed in this spirit.[93] However, it is far from obvious that these low dimensional dynamical features that have been observed in experiments involving laminar flows, analytical models, and numerical simulations at moderate kinetic Reynolds numbers can survive in strongly turbulent flows. One can, for instance, imagine that strong turbulent fluctuations smear them out by inducing transitions between different dynamo regimes corresponding to different realizations (in the statistical meaning) of the turbulent flow. We will show in this section that this is not the case. Trajectories plotted in low dimensional projections of the phase space are remark-

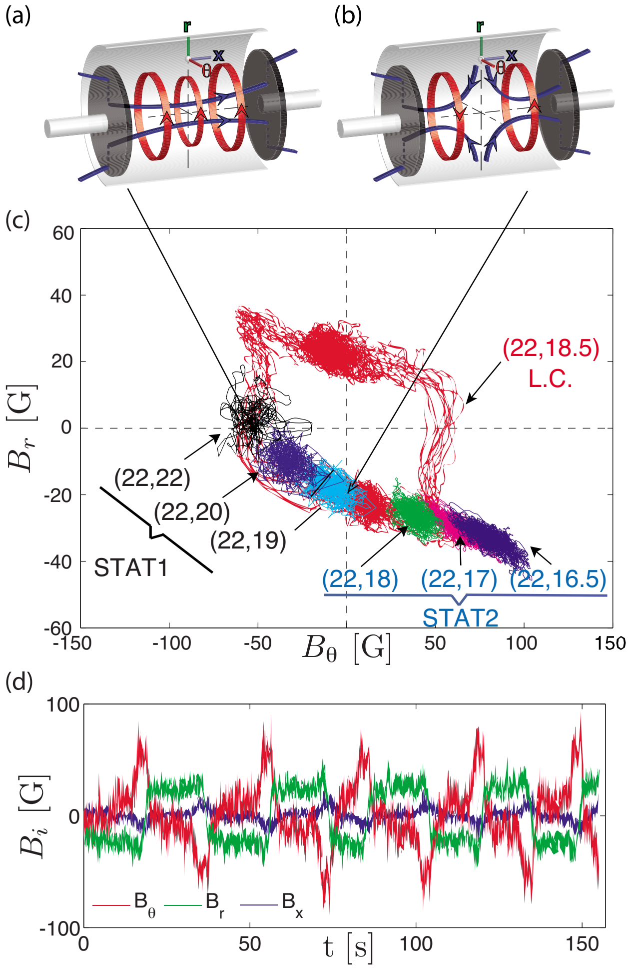

FIG. 28. (Color online) Sketch of the axial dipolar (a) and quadrupolar (b) magnetic modes. (c) Location of the different states in the (B_r, B_θ) plane: fixed points corresponding to the stationary regimes for frequencies (F_1, F_2); limit cycle (LC) observed for impellers counter-rotating at different frequencies (22,18.5) Hz (red cycle). The magnetic field is time averaged over 1 s to remove high frequency fluctuations caused by the turbulent velocity fluctuations. (d) Time recording of the components of the magnetic field for frequencies (22,18.5) Hz $(\Theta = 0.086)$.

ably robust and bifurcations between different dynamo regimes do exhibit well known features of low dimensional dynamical systems. Complex dynamical regimes result from the existence of different stationary dynamo states that become unstable when F_1 or F_2 are varied within a small interval range.

We first consider how the Stat1 dynamo regime bifurcates to a time-dependent regime (LC) when the frequency of an impeller, say F_2, is decreased, while F_1 is kept constant, i.e., starting from $\Theta = 0$ and increasing $|\Theta|$. One starts from a statistically stationary dynamo regime with a dominant azimuthal mean field close to the flow periphery [Fig. 28(a)]. This corresponds to the trace labeled (22,22) in the (B_θ, B_r) plane of Fig. 28(c). As the frequency is decreased, the radial component of the mean field increases and then becomes larger than the azimuthal one [(22,20) and (22,19)]. When we tune the impeller frequencies to (22,18.5) Hz—$\Theta = 0.086$—a global bifurcation to a LC occurs [Figs. 28(c) and 28(d)]. We observe that the trajectory of this LC goes through the location of the previous fixed points related to the stationary regimes. This transition thus looks like the one of an excitable system: an elementary example of this type of bifurcation is provided by a simple pendulum submitted to a constant torque. As the value of the torque is increased, the stable equilibrium of the pendulum becomes more and more tilted from the vertical and for a critical torque corresponding to the angle $\pi/2$, the pendulum undergoes a saddle-node bifurcation to a LC that goes through the previous fixed points. The magnetic field being measured at the periphery of the flow in the midplane between the two impellers, we observe that there is a strong radial component [green trace in Fig. 28(d)] that switches between ±25 G. We propose to ascribe it to a quadrupolar mode [see Fig. 28(b)]. Its interaction with the dipolar mode [Fig. 28(a)] that is the dominant one for exact counter-rotation gives rise to the observed relaxation dynamics. This hypothesis is supported by measurements made outside of the equatorial plane ($x = 109$ mm, $r = 206$ mm) where the radial to azimuthal field ratio is much smaller, as it should if the radial field mostly results from the quadrupolar component. We note that it has been often observed that dipolar and quadrupolar dynamo modes can have their respective thresholds in a narrow range of R_m (Ref. 2) and this has been used to model the dynamics of the magnetic fields of the Earth[87] or the Sun.[90] The relaxation oscillation is observed in a rather narrow range of impeller frequency F_2 (less than 1 Hz). When the frequency of the slowest impeller is decreased further, statistically stationary regimes are recovered [(22,18) to (22,16.5) in Fig. 28(c)]. They also correspond to fixed points located on the trajectory of the LC, except for the case (22,16.5) Hz that separates from it $(\Theta = 0.147)$.

When the rotation frequency of the slowest impeller is decreased further, new dynamical regimes occur. One of them consists in field reversals described in Sec. III D. The three components of the magnetic field reverse at random times [Fig. 21(a)]. Compared to the relaxation cycle described above, the length of phases with given polarity has a wider distribution. However, a variation in temperature of the sodium is enough to transform random reversals to nearly periodic noisy oscillations. Even in the case of random reversals, e.g., for the data in Fig. 21, if we plot the trajectories connecting **B** and **−B** in a phase space reconstruction, we obtain an average LC displayed by a thick dashed black line in Fig. 29. The state with positive polarity corresponds to point P. When a reversals starts, the system leaves P and slows down in the vicinity of point Q that corresponds to the end of the exponential decay of the magnetic field recorded in Fig. 21(b). The trajectory then abruptly changes direction in phase space and leaves Q. This corresponds to the fast recovery of the magnetic field amplitude in Fig. 21(b). Finally, the trajectory reaches the point −P corresponding to the phase of negative polarity by circling around it, which corresponds to the overshoot in the direct time recording [Fig. 21(b)]. As proposed by many authors,[88] it is tempting to understand these field reversals as heteroclinic orbits connecting unstable fixed points in phase space. In the present situation, these fixed points are P, Q together with the symmetric ones −P and −Q obtained by the $\mathbf{B} \to -\mathbf{B}$ transforma-

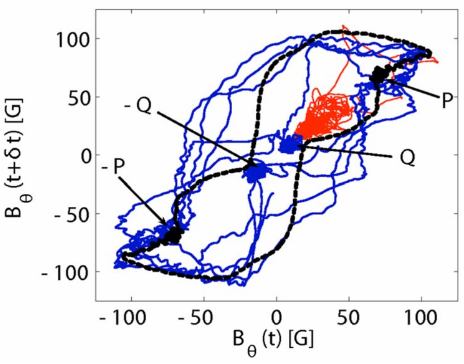

FIG. 29. (Color online) Plot of a cut in a phase space reconstruction $[B_\theta(t), B_\theta(t+\delta t)]$ with $\delta t=1$ s for three regimes: thick dashed black line for field reversals reported in Fig. 21, the magnetic field being rescaled by an *ad hoc* factor accounting for the fact that the probe location is not in the midplane. The medium blue line is for symmetric bursts ($F_1=21$ Hz, $F_2=15$ Hz, $\Theta=0.17$) and the thin red line for asymmetric bursts ($F_1=22$ Hz, $F_2=15$ Hz, $\Theta=0.19$). In these last two plots the magnetic field is time averaged over 0.25 s to remove high frequency fluctuations.

tion. The trajectory in phase space is amazingly robust despite strong velocity fluctuations. These fluctuations set an upper bound on the duration of phases with a given polarity by preventing the system from staying too close to the unstable fixed points and thus to spend too much time in their vicinity. However, this does not suppress the scale separation between the length of the phases with given polarity and the duration of a reversal. In that sense, turbulent fluctuations have a weak effect on the large scale dynamics of the magnetic field. Furthermore, as mentioned in Sec. III D, reversals observed in almost identical conditions in the VKS2h experiments follow a slightly different path in the phase space: at each polarity change a different path in phase space is selected which does not systematically get very close to the unstable fixed points Q and −Q.

We will show next that the fixed points ±P and ±Q are also involved in other dynamical regimes observed in the vicinity of reversals in the parameter space and shown in Fig. 29. For rotation frequencies (22,15) Hz—$|\Theta|=0.19$—the magnetic field displays intermittent bursts in which the most probable value of the azimuthal field is roughly 20 G but bursts up to more than 100 G are observed [see Sec. III E, Fig. 23(a)]. For rotation frequencies (21,15)Hz—$|\Theta|=0.17$—the same type of dynamics occur, but in a symmetric fashion, both positive and negative values of the field being observed [Sec. III E, Fig. 25(a)]. A section of a phase space reconstruction is displayed in Fig. 29 for both regimes of bursts and field reversals. We observe that the asymmetric bursts occur from the unstable fixed point Q in the vicinity of which the signal is located most of the time, whereas symmetric burst involve the two unstable fixed points ±Q. Therefore, these complex dynamics, as well as reversals, can be understood as resulting from the competition between different dynamo modes corresponding to the fixed points ±P and ±Q that bifurcate from stable to unstable in a small region of parameter space.

The different dynamical regimes of the magnetic field generated by the VKS flow thus display several characteristic features of low dimensional dynamical systems, besides fixed points and weakly anharmonic oscillations: global bifurcations from fixed points to a relaxation cycle (Fig. 28), chaotic bursts from unstable fixed points (Fig. 29). These dynamics can be understood as the ones resulting from the competition between a few nearly critical modes.

IV. CONCLUDING REMARKS

The experimental observations reported here make a first step toward a detail investigation of dynamo action and its dynamical regimes in laboratory experiments. This is an essential step between numerical simulations, still far from the realm of realistic fluid dynamos, and planetary and stellar dynamos.

The advantage of the von Kármán geometry investigated here is that fundamental features such as turbulence and global rotation are incorporated. As detailed here, the VKS experiment has brought the following new results:

(a) When the flow is driven with exact counter-rotation, the observed dynamo cannot be explained by the action of the mean flow alone. Turbulence is essential. This is different from previous experiments for which the dynamo's essential features could be predicted by taking into account only the time-averaged flow.

(b) When global rotation is added, a small variation in parameters has allowed for the first time the observation of rich dynamical regimes. Some of these, like intermittent reversals or regular oscillations, are strikingly similar to the behavior of the geomagnetic and solar magnetic fields. A noteworthy feature is that the geometry and time dynamics of these regimes are robust with respect to the turbulent fluctuations, known to be large inside the flow. The turbulent fluctuations do not induce intermittent transitions between magnetic regimes even though they lie in closely adjacent or even overlapping parameter ranges.[79]

There are nevertheless still many open and intriguing questions left from the preliminary observations reported here. To quote but a few:

(a) The effect of the soft-iron impellers. They do change profoundly the self-generation capacity of the flow since identical runs with stainless steel impellers have not self-generated in the same range of flow driving parameters. They may also select a particular type of dynamo. Induction measurements below threshold are indeed quite different from previous VKS observations with stainless steel drives. We finally note that, in two particular runs—at the first dynamo run and after some oscillatory dynamo regime—for which the setup magnetization was probably very low, regimes without dynamo action at $\Theta=0$ were observed above onset between $R_m=31$ ($F=16$ Hz) and $R_m=39$ ($F=20$ Hz).

(b) The dynamics of the Lorentz force during the nonlinear saturation. The way in which it modifies the velocity field when a $(\mathbf{u}, \mathbf{B} \neq 0)$ state is reached must yet be studied, as well as how it acts in the dynamical regimes.

(c) Also open is the interaction between the hydrodynamics and the magnetic field modes. The von Kármán flow displays slow time dynamics and transitions between different flow regimes.[78,94–96]

Finally, the question of dynamo generation in a fully homogeneous container is still an open question. Is the present VKS dynamo a nearly homogeneous dynamo? If the presence of soft-iron just reduces the dynamo threshold into the accessible experimental range without major modification of the nonlinear dynamics, the answer is clearly yes. However, if a coupling responsible for dynamo generation and characteristics, such as mode selection and dynamics, explicitly involves the distribution of ferromagnetic elements, then the VKS2 dynamo will have to be considered as an inhomogeneous one. Future experimental investigations in the VKS experiments are aimed at identifying the essential ingredients for dynamo generation in von Kármán flows—including the role of electrical and magnetic boundary conditions—and the implication of these elements on mode selection and dynamical properties.

ACKNOWLEDGMENTS

We thank M. Moulin, C. Gasquet, J.-B Luciani, A. Skiara, D. Courtiade, J.-F. Point, P. Metz, and V. Padilla for their technical assistance. This work was supported by Grant No. ANR05-0268-03, Direction des Sciences de la Matière et Direction de l'Énergie Nucléaire of CEA, Ministère de la Recherche and CNRS. The experiment was operated at CEA/Cadarache DEN/DTN.

[1] J. Larmor, "How could a rotating body such as the Sun become a magnet?" Br. Assoc. Adv. Sci., Rep., 159 (1919).

[2] H. K. Moffatt, *Magnetic Field Generation in Electrically Conducting Fluids* (Cambridge University Press, Cambridge, 1978).

[3] F. J. Lowes and I. Wilkinson, "Geomagnetic dynamo: A laboratory model," Nature (London) **198**, 1158 (1963).

[4] F. J. Lowes and I. Wilkinson, "Geomagnetic dynamo: An improved laboratory model," Nature (London) **219**, 717 (1968).

[5] A. Gailitis, O. Lielausis, E. Platacis, S. Dementev, A. Cifersons, G. Gerbeth, T. Gundrum, F. Stefani, M. Christen, and G. Will, "Magnetic field saturation in the Riga dynamo experiment," Phys. Rev. Lett. **86**, 3024 (2001).

[6] Yu. B. Ponomarenko, "Theory of the hydromagnetic generator," J. Appl. Mech. Tech. Phys. **14**, 775 (1973).

[7] A. Gailitis, O. Lielausis, E. Platacis, G. Gerbeth, and F. Stefani, "The Riga dynamo experiment," Surv. Geophys. **24**, 247 (2003).

[8] S. Kenjeres and K. Hanjalic, "Numerical simulation of a turbulent magnetic dynamo," Phys. Rev. Lett. **98**, 104501 (2007).

[9] S. Kenjeres and K. Hanjalic, "Numerical insights into magnetic dynamo action in turbulent regime," New J. Phys. **9**, 306 (2007).

[10] R. Stieglitz and U. Müller, "Experimental demonstration of a homogeneous two-scale dynamo," Phys. Fluids **13**, 561 (2001).

[11] G. O. Roberts, "Dynamo action of fluid motions with two-dimensional periodicity," Philos. Trans. R. Soc. London, Ser. A **271**, 411 (1972).

[12] A. Gilbert and P.-L. Sulem, "On inverse cascade in alpha-effect dynamos," Geophys. Astrophys. Fluid Dyn. **51**, 243 (1990).

[13] A. Tilgner, "A kinematic dynamo with a small scale velocity field," Phys. Lett. A **226**, 75 (1997).

[14] A. Tilgner and F. H. Busse, "Saturation mechanism in a model of Karlsruhe dynamo," in *Dynamo and Dynamics: A Mathematical Challenge*, edited by P. Chossat, D. Armbruster, and I. Oprea (Kluwer, Dordrecht, 2001), pp. 109–116.

[15] K.-H. Rädler, E. Apstein, M. Rheinhardt, and M. Schüler, "The Karlsruhe dynamo experiment. A mean field approach," Stud. Geophys. Geod. **42**, 224 (1998).

[16] R. Monchaux, M. Berhanu, M. Bourgoin, M. Moulin, Ph. Odier, J.-F. Pinton, R. Volk, S. Fauve, N. Mordant, F. Pétrélis, A. Chiffaudel, F. Daviaud, B. Dubrulle, C. Gasquet, L. Marié, and F. Ravelet, "Generation of magnetic field by dynamo action in a turbulent flow of liquid sodium," Phys. Rev. Lett. **98**, 044502 (2007).

[17] M. Berhanu, R. Monchaux, M. Bourgoin, M. Moulin, Ph. Odier, J.-F. Pinton, R. Volk, S. Fauve, N. Mordant, F. Pétrélis, A. Chiffaudel, F. Daviaud, B. Dubrulle, C. Gasquet, L. Marié, and F. Ravelet, "Magnetic field reversals in an experimental turbulent dynamo," Europhys. Lett. **77**, 59001 (2007).

[18] F. Ravelet, R. Monchaux, M. Berhanu, S. Aumaître, A. Chiffaudel, F. Daviaud, B. Dubrulle, M. Bourgoin, Ph. Odier, J.-F. Pinton, N. Plihon, R. Volk, S. Fauve, N. Mordant, and F. Pétrélis, "Chaotic dynamos generated by a turbulent flow of liquid sodium," Phys. Rev. Lett. **101**, 074502 (2008).

[19] M. Bourgoin, L. Marié, F. Pétrélis, C. Gasquet, A. Guigon, J.-B. Luciani, M. Moulin, F. Namer, J. Burguete, A. Chiffaudel, F. Daviaud, S. Fauve, Ph. Odier, and J.-F. Pinton, "Magnetohydrodynamics measurements in the von Kármán sodium experiment," Phys. Fluids **14**, 3046 (2002).

[20] F. Pétrélis, M. Bourgoin, L. Marié, J. Burguete, A. Chiffaudel, F. Daviaud, S. Fauve, Ph. Odier, and J.-F. Pinton, "Nonlinear magnetic induction by helical motion in a liquid sodium turbulent flow," Phys. Rev. Lett. **90**, 174501 (2003).

[21] L. Marié, "Transport de moment cinétique et de champ magnétique par un écoulement tourbillonnaire turbulent: Influence de la rotation," Ph.D. thesis, Université de Paris 7, 2003 (http://tel.archives-ouvertes.fr/tel-00007755/en/).

[22] F. Ravelet, "Bifurcations globales hydrodynamiques et magnétohydrodynamiques dans un écoulement de von Kármán turbulent," Ph.D. thesis, École Polytechnique, 2005 (http://tel.archives-ouvertes.fr/tel-00011016/en/).

[23] R. Monchaux, "Mécanique statistique et effet dynamo dans un écoulement de von Kármán turbulent," Ph.D. thesis, Université Diderot, Paris 7, 2007 (http://tel.archives-ouvertes.fr/tel-00199751/en/).

[24] S. Douady, Y. Couder, and M.-E. Brachet, "Direct observation of the intermittency of intense vorticity filaments in turbulence," Phys. Rev. Lett. **67**, 983 (1991).

[25] S. Fauve, C. Laroche, and B. Castaing, "Pressure fluctuations in swirling turbulent flows," J. Phys. II **3**, 271 (1993).

[26] J.-F. Pinton and R. Labbé, "Correction to Taylor hypothesis in swirling flows," J. Phys. II **4**, 1461 (1994).

[27] J. Maurer, P. Tabeling, and G. Zocchi, "Statistics of turbulence between two counter rotating disks in low temperature helium gas," Europhys. Lett. **26**, 31 (1994).

[28] R. Labbé, J.-F. Pinton, and S. Fauve, "Power fluctuations in turbulent swirling flows," J. Phys. II **6**, 1099 (1996).

[29] L. Marié and F. Daviaud, "Experimental measurement of the scale-by-scale momentum transport budget in a turbulent shear flow," Phys. Fluids **16**, 457 (2004).

[30] F. Ravelet, A. Chiffaudel, and F. Daviaud, "Supercritical transition to turbulence in an inertially driven von Kármán closed flow," J. Fluid Mech. **601**, 339 (2008).

[31] P.-P. Cortet, P. Diribarne, R. Monchaux, A. Chiffaudel, F. Daviaud, and B. Dubrulle, "Normalized kinetic energy as a hydrodynamical global quantity for inhomogeneous anisotropic turbulence," Phys. Fluids **21**, 025104 (2009).

[32] M. L. Dudley and R. W. James, "Time-dependent kinematic dynamos with stationary flows," Proc. R. Soc. London, Ser. A **425**, 407 (1989).

[33] L. Marié, C. Normand, and F. Daviaud, "Galerkin analysis of kinematic dynamos in the von Kármán geometry," Phys. Fluids **18**, 017102 (2006).

[34] L. Marié, J. Burguete, F. Daviaud, and J. Léorat, "Numerical study of homogeneous dynamo based on experimental von Kármán type flows," Eur. Phys. J. B **33**, 469 (2003).

[35] F. Ravelet, A. Chiffaudel, F. Daviaud, and J. Léorat, "Toward an experimental von Kármán dynamo: Numerical studies for an optimized design," Phys. Fluids **17**, 117104 (2005).

[36] M. Bourgoin, P. Odier, J.-F. Pinton, and Y. Ricard, "An iterative study of time independent induction effects in magnetohydrodynamics," Phys. Fluids **16**, 2529 (2004).

[37] M. Bourgoin, "Etudes en magnétohydrodynamique, application á l'effet

dynamo," Ph.D. thesis, Ecole Normale Supérieure de Lyon, 2003 (http://tel.archives-ouvertes.fr/tel-00008302/en/).

[38] F. Stefani, M. Xu, G. Gerbeth, F. Ravelet, A. Chiffaudel, F. Daviaud, and J. Léorat, "Ambivalent effects of added layers on steady kinematic dynamos in cylindrical geometry: Application to the VKS experiment," Eur. J. Mech. B/Fluids **25**, 894 (2006).

[39] S. Fauve and F. Pétrélis, in *The Dynamo Effect*, Peyresq Lectures on Nonlinear Phenomena Vol. II, edited by J.-A. Sepulchre (World Scientific, Singapore, 2003), pp. 1–64.

[40] F. Pétrélis, "Effet dynamo: Etudes des mécanismes d'instabilité et de saturation du champ magnétique," Ph.D. thesis, Université Pierre et Marie Curie–Paris VI, 2002 (http://tel.archives-ouvertes.fr/tel-00003842/en/).

[41] F. Pétrélis and S. Fauve, "Inhibition of the dynamo effect by phase fluctuations," Europhys. Lett. **76**, 602 (2006).

[42] M. Brachet, "Direct simulation of three-dimensional turbulence in the Tayor-Green vortex," Fluid Dyn. Res. **8**, 1 (1991).

[43] C. Nore, M. Brachet, H. Politano, and A. Pouquet, "Dynamo action in the Taylor–Green vortex near threshold," Phys. Plasmas **4**, 1 (1997).

[44] Y. Ponty, H. Politano, A. Pouquet, and J.-F. Pinton, "Simulation of induction at low magnetic Prandtl number," Phys. Rev. Lett. **92**, 144503 (2004).

[45] Y. Ponty, P. D. Minnini, D. Montgomery, J.-F. Pinton, H. Politano, and A. Pouquet, "Numerical study of dynamo action at low magnetic Prandtl numbers," Phys. Rev. Lett. **94**, 164502 (2005).

[46] J.-P. Laval, P. Blaineau, N. Leprovost, B. Dubrulle, and F. Daviaud, "Influence of turbulence on the dynamo threshold," Phys. Rev. Lett. **96**, 204503 (2006).

[47] B. Dubrulle, P. Blaineau, O. Mafra Lopes, F. Daviaud, J.-P. Laval, and R. Dolganov, "Bifurcations and dynamo action in a Taylor–Green flow," New J. Phys. **9**, 308 (2007).

[48] A. A. Schekochihin, S. Cowley, G. Hammett, J. Maron, and J. C. McWilliams, "A model of nonlinear evolution and saturation of the turbulent MHD dynamo," New J. Phys. **4**, 84 (2002).

[49] A. A. Schekochihin, S. Cowley, J. Maron, and J. C. McWilliams, "Critical magnetic Prandtl number for small-scale dynamo," Phys. Rev. Lett. **92**, 054502 (2004).

[50] A. B. Iskakov, A. A. Schekochihin, S. C. Cowley, J. C. McWilliams, and M. R. E. Proctor, "Numerical demonstration of fluctuation dynamo at low magnetic Prandtl numbers," Phys. Rev. Lett. **98**, 208501 (2007).

[51] D. P. Lathrop, W. L. Shew, and D. R. Sisan, "Laboratory experiments on the transition to MHD dynamos," Plasma Phys. Controlled Fusion **43**, A151 (2001).

[52] N. L. Peffley, A. G. Goumilevski, A. B. Cawthrone, and D. P. Lathrop, "Characterization of experimental dynamos," Geophys. J. Int. **142**, 52 (2000).

[53] N. L. Peffley, A. B. Cawthorne, and D. P. Lathrop, "Toward a self-generating magnetic dynamo: The role of turbulence," Phys. Rev. E **61**, 5287 (2000).

[54] E. J. Spence, M. D. Nornberg, C. M. Jacobson, C. A. Parada, N. Z. Taylor, R. D. Kendrick, and C. B. Forest, "Turbulent diamagnetism in flowing liquid sodium," Phys. Rev. Lett. **98**, 164503 (2007).

[55] M. D. Nornberg, E. J. Spence, R. D. Kendrick, C. M. Jacobson, and C. B. Forest, "Intermittent magnetic field excitation by a turbulent flow of liquid sodium," Phys. Rev. Lett. **97**, 044503 (2006).

[56] M. D. Nornberg, E. J. Spence, R. D. Kendrick, C. M. Jacobson, and C. B. Forest, "Measurements of the magnetic field induced by a turbulent flow of liquid metal," Phys. Plasmas **13**, 055901 (2006).

[57] D. Sweet, E. Ott, J. M. Finn, T. M. Antonsen, and D. P. Lathrop, "Blowout bifurcations and the onset of magnetic activity in turbulent dynamos," Phys. Rev. E **63**, 066211 (2001).

[58] D. Sweet, E. Ott, T. M. Antonsen, and D. P. Lathrop, "Blowout bifurcations and the onset of magnetic dynamo action," Phys. Plasmas **8**, 1944 (2001).

[59] M. Bourgoin, R. Volk, N. Plihon, P. Augier, and J.-F. Pinton, "A Bullard von Kármán dynamo," New J. Phys. **8**, 329 (2006).

[60] R. Avalos-Zuniga, F. Plunian, and A. Gailitis, "Influence of electromagnetic boundary conditions onto the onset of dynamo action in laboratory experiments," Phys. Rev. E **68**, 066307 (2003).

[61] C. Gissinger, A. Iskakov, S. Fauve, and E. Dormy, "Effect of magnetic boundary conditions on the dynamo threshold of von Kármán swirling flows," Europhys. Lett. **82**, 29001 (2008).

[62] N. Mordant, J.-F. Pinton, and F. Chillà, "Characterization of turbulence in a closed flow," J. Phys. II **7**, 1729 (1997).

[63] R. Volk, R. Monchaux, M. Berhanu, F. Ravelet, A. Chiffaudel, F. Daviaud, B. Dubrulle, S. Fauve, N. Mordant, Ph. Odier, F. Pétrélis, and J.-F. Pinton, "Transport of magnetic field by a turbulent flow of liquid sodium," Phys. Rev. Lett. **97**, 074501 (2006).

[64] F. Pétrélis, N. Mordant, and S. Fauve, "On the magnetic fields generated by experimental dynamos," Geophys. Astrophys. Fluid Dyn. **101**, 289 (2007).

[65] P. Odier, J.-F. Pinton, and S. Fauve, "Advection of a magnetic field by a turbulent swirling flow," Phys. Rev. E **58**, 7397 (1998).

[66] S. I. Braginsky, "Kinematic models of the Earth's hydromagnetic dynamo," Geomagn. Aeron. **4**, 572 (1964).

[67] E. N. Parker, "Hydromagnetic dynamo models," Astrophys. J. **122**, 293 (1955).

[68] F. Plunian and K.-H. Rädler, "Subharmonic dynamo action in the Roberts flow," Geophys. Astrophys. Fluid Dyn. **96**, 115 (2002).

[69] R. Volk, P. Odier, and J.-F. Pinton, "Magnetic induction in a cylindrical array of helical vortices," Phys. Fluids **20**, 016601 (2008).

[70] R. Laguerre, C. Nore, A. Ribeiro, J. Léorat, J.-L. Guermond, and F. Plunian, "Impact of impellers on the axisymmetric magnetic mode in the VKS2 dynamo experiment," Phys. Rev. Lett. **101**, 104501 (2008).

[71] F. Krause and K. H. Radler, *Mean-Field Magnetohydrodynamics and Dynamo Theory* (Pergamon, Oxford, 1980).

[72] R. Stepanov, R. Volk, S. Denisov, P. Frick, V. Noskov, and J.-F. Pinton, "Induction, helicity and alpha effect in a toroidal screw flow of liquid gallium," Phys. Rev. E **73**, 046310 (2006).

[73] R. Volk, "Fluctuations d'induction en magnétohydrodynamique, contributions à l'induction à grande échelle, application à l'effet dynamo," Ph.D. thesis, Ecole Normale Supérieure de Lyon, 2005 (http://tel.archives-ouvertes.fr/tel-00011221/en/).

[74] K.-H. Rädler and R. Stepanov, "Mean electromotive force due to turbulence of a conducting fluid in the presence of mean flow," Phys. Rev. E **73**, 056311 (2006).

[75] F. Pétrélis and S. Fauve, "Saturation of the magnetic field above the dynamo threshold," Eur. Phys. J. B **22**, 273 (2001).

[76] S. Fauve and F. Pétrélis, "Scaling laws of turbulent dynamos," C. R. Phys. **8**, 87 (2007).

[77] P. D. Mininni, Y. Ponty, D. Montgomery, J.-F. Pinton, H. Politano, and A. Pouquet, "Nonlinear behavior of a non-helical dynamo," Astrophys. J. **626**, 853 (2005).

[78] F. Ravelet, L. Marié, A. Chiffaudel, and F. Daviaud, "Multistability and memory effect in a highly turbulent flow: Experimental evidence for a global bifurcation," Phys. Rev. Lett. **93**, 164501 (2004).

[79] M. Berhanu, B. Gallet, R. Monchaux, M. Bourgoin, Ph. Odier, J.-F. Pinton, N. Plihon, R. Volk, S. Fauve, N. Mordant, F. Pétrélis1, S. Aumaître, A. Chiffaudel, F. Daviaud, B. Dubrulle, and F. Ravelet, "Bistability between a stationary and an oscillatory dynamo in a turbulent flow of liquid sodium," J. Fluid Mech. (to be published).

[80] E. Dormy, J.-P. Valet and V. Courtillot, "Numerical models of the geodynamo and observational constraints," Geochem., Geophys., Geosyst. **1**, 62 (2000).

[81] J.-P. Valet, "Time variations in geomagnetic intensity," Rev. Geophys. **41**, 1004 (2003).

[82] J.-P. Valet, L. Meynadier, and Y. Guyodo, "Geomagnetic dipole strength and reversal rate over the past two million years," Nature (London) **435**, 802 (2005).

[83] S. Fauve, C. Laroche, and B. Perrin, "Competing instabilities in a rotating layer of mercury heated from below," Phys. Rev. Lett. **55**, 208 (1985).

[84] R. W. Walden, P. Kolodner, A. Passner, and C. M. Surko, "Traveling waves and chaos in convection in binary fluid mixtures," Phys. Rev. Lett. **55**, 496 (1985).

[85] I. Rehberg and G. Ahlers, "Experimental observation of a codimension-2 bifurcation in a binary fluid mixture," Phys. Rev. Lett. **55**, 500 (1985).

[86] V. Arnold, *Geometrical Methods in the Theory of Ordinary Differential Equations* (Springer, Berlin, 1982).

[87] I. Melbourne, M. R. E. Proctor, and A. M. Rucklidge, in *Dynamo and Dynamics: A Mathematical Challenge*, edited by P. Chossat, D. Armbruster, and I. Oprea (Kluwer, Dordrecht, 2001), pp. 363–370.

[88] P. Chossat and D. Armbruster, "Dynamics of polar reversals in spherical dynamos," Proc. R. Soc. London, Ser. A **459**, 577 (2003), and references therein.

[89] S. M. Tobias, N. O. Weiss, and V. Kirk, "Chaotically modulated stellar dynamos," Mon. Not. R. Astron. Soc. **273**, 1150 (1995).

[90] E. Knobloch and A. S. Landsberg, "A new model of the solar cycle," Mon. Not. R. Astron. Soc. **278**, 294 (1996).

[91] G. R. Sarson and C. A. Jones, "A convection driven geodynamo reversal model," Phys. Earth Planet. Inter. **111**, 3 (1999).
[92] F. Stefani and G. Gerbeth, "Asymmetric polarity reversals, bimodal field distribution, and coherence resonance in a spherically symmetric mean-field dynamo model," Phys. Rev. Lett. **94**, 184506 (2005).
[93] P. Hoyng and J. J. Duistermaat, "Geomagnetic reversals and the stochastic exit problem," Europhys. Lett. **68**, 177 (2004).
[94] R. Volk, P. Odier, and J.-F. Pinton, "Fluctuation of magnetic induction in von Kármán swirling flows," Phys. Fluids **18**, 085105 (2006).
[95] R. Monchaux, F. Ravelet, B. Dubrulle, A. Chiffaudel, and F. Daviaud, "Properties of steady states in turbulent axisymmetric flows," Phys. Rev. Lett. **96**, 124502 (2006).
[96] A. de la Torre and J. Burguete, "Slow dynamics in a turbulent von Kármán swirling flow," Phys. Rev. Lett. **99**, 054101 (2007).

PHYSICS OF FLUIDS **22**, 055103 (2010)

Influence of global rotation and Reynolds number on the large-scale features of a turbulent Taylor–Couette flow

F. Ravelet,[1,a)] R. Delfos,[2] and J. Westerweel[2]
[1]*DynFluid, Arts et Métiers-ParisTech, 151 Blvd. de l'Hôpital, 75013 Paris, France*
[2]*Laboratory for Aero and Hydrodynamics, Mekelweg 2, 2628 CD Delft, The Netherlands*

(Received 25 January 2010; accepted 27 February 2010; published online 7 May 2010)

We experimentally study the turbulent flow between two coaxial and independently rotating cylinders. We determined the scaling of the torque with Reynolds numbers at various angular velocity ratios (Rotation numbers) and the behavior of the wall shear stress when varying the Rotation number at high Reynolds numbers. We compare the curves with particle image velocimetry analysis of the mean flow and show the peculiar role of perfect counter-rotation for the emergence of organized large scale structures in the mean part of this very turbulent flow that appear in a smooth and continuous way: the transition resembles a supercritical bifurcation of the secondary mean flow. © *2010 American Institute of Physics*. [doi:10.1063/1.3392773]

I. INTRODUCTION

Turbulent shear flows are present in many applied and fundamental problems, ranging from small scales (such as in the cardiovascular system) to very large scales (such as in meteorology). One of the several open questions is the emergence of coherent large-scale structures in turbulent flows.[1] Another interesting problem concerns bifurcations, i.e., transitions in large-scale flow patterns under parametric influence, such as laminar-turbulent flow transition in pipes, or flow pattern change within the turbulent regime, such as the dynamo instability of a magnetic field in a conducting fluid,[2] or multistability of the mean flow in von Kármán or free-surface Taylor–Couette flows,[3,4] leading to hysteresis or nontrivial dynamics at large scale. In flow simulation of homogeneous turbulent shear flow it is observed that there is an important role for what is called the *background rotation*, which is the rotation of the frame of reference in which the shear flow occurs. This background rotation can both suppress or enhance the turbulence.[5,6] We will further explicit this in Sec. III.

A flow geometry that can generate both motions—shear and background rotation—at the same time is the Taylor–Couette flow which is the flow produced between differentially rotating coaxial cylinders.[7] When only the inner cylinder rotates, the first instability, i.e., deviation from laminar flow with circular streamlines, takes the form of toroidal (Taylor) vortices. With two independently rotating cylinders, there is a host of interesting secondary bifurcations, extensively studied at intermediate Reynolds numbers, following the work of Coles[8] and Andereck *et al.*[9] Moreover, it shares strong analogies with Rayleigh–Bénard convection,[10,11] which are useful to explain different torque scalings at high Reynolds numbers.[12,13] Finally, for some parameters relevant in astrophysical problems, the basic flow is linearly stable and can directly transit to turbulence at a sufficiently high Reynolds number.[14]

The structure of the Taylor–Couette flow, while it is in a *turbulent* state, is not so well known and only few measurements are available.[15] The flow measurements reported in Ref. 15 and other torque scaling studies only deal with the case where only the inner cylinder rotates.[12,13] In that precise case, recent direct numerical simulations suggest that vortexlike structures still exist at high Reynolds number ($\mathrm{Re} \gtrsim 10^4$),[16,17] whereas for counter-rotating cylinders, the flows at Reynolds numbers around 5000 are identified as "featureless states."[9] The structure of the flow is exemplified with a flow visualization in Fig. 1 in our experimental setup for a flow with only the inner cylinder rotating, counter-rotating cylinders, and only the outer cylinder rotating, respectively.

In the present paper, we extend the study of torques and flow field for independently rotating cylinders to higher Reynolds numbers (up to 10^5) and address the question of the transition process between a turbulent flow with Taylor vortices, and this "featureless" turbulent flow when varying the global rotation while maintaining a constant mean shear rate.

In Sec. II, we present the experimental device and the measured quantities. In Sec. III, we introduce the specific set of parameters we use to take into account the global rotation through a "Rotation number" and the imposed shear through a shear-Reynolds number. We then present torque scalings and typical velocity profiles in turbulent regimes for three particular Rotation numbers in Sec. IV. We explore the transition between these regimes at high Reynolds number varying the Rotation number in Sec. V and discuss the results in Sec. VI.

II. EXPERIMENTAL SETUP AND MEASUREMENT TECHNIQUES

The flow is generated between two coaxial cylinders (Fig. 2). The inner cylinder has a radius of $r_i = 110 \pm 0.05$ mm and the outer cylinder of $r_o = 120 \pm 0.05$ mm. The gap between the cylinders is thus $d = r_o - r_i = 10$ mm and

---

[a)] Electronic mail: florent.ravelet@ensta.org.

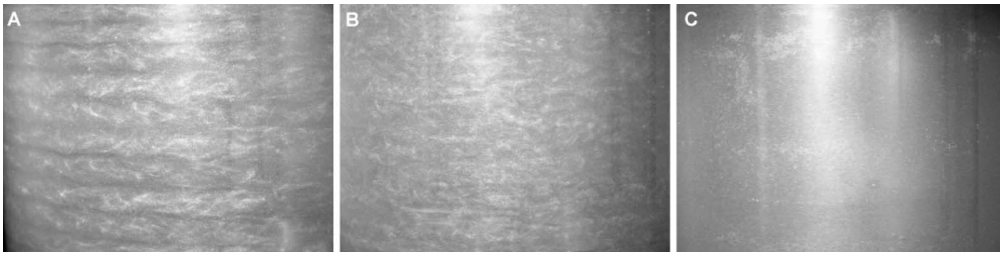

FIG. 1. Photographs of the flow at $\mathrm{Re}=3.6\times 10^3$. Left, A: only the inner cylinder rotating. Middle, B: counter-rotating cylinders. Right, C: only the outer cylinder rotating. The flow structure is visualized using microscopic mica platelets (Pearlessence).

the gap ratio is $\eta=r_i/r_o=0.917$. The system is closed at both ends, with top and bottom lids rotating with the outer cylinder. The length of the inner cylinder is $L=220$ mm (axial aspect ratio is $L/d=22$). Both cylinders can rotate independently with the use of two dc motors (Maxon, 250 W). The motors are driven by a homemade regulation device, ensuring a rotation rate up to 10 Hz, with an absolute precision of ±0.02 Hz and a good stability. A LABVIEW program is used to control the experiment: the two cylinders are simultaneously accelerated or decelerated to the desired rotation rates, keeping their ratio constant. This ratio can also be changed while the cylinders rotate, maintaining a constant differential velocity.

The torque T on the inner cylinder is measured with a corotating torque meter (HBM T20WN, 2 N m). The signal is recorded with a 12 bit data acquisition board at a sample rate of 2 kHz for 180 s. The absolute precision on the torque measurements is ±0.01 N m, and values below 0.05 N m are rejected. We also use the encoder on the shaft of the torque meter to record the rotation rate of the inner cylinder. Since that matches excellently with the demanded rate of rotation, we assume that the outer cylinder rotates at the demanded rate as well.

Since the torque meter is mounted in the shaft between driving motor and cylinder, it also records (besides the intended torque on the wall bounding the gap between the two cylinders) the contribution of mechanical friction such as in the two bearings, and the fluid friction in the horizontal (Kármán) gaps between tank bottom and tank top. While the bearing friction is considered to be marginal (and measured so in an empty, i.e., air filled system), the Kármán-gap contribution is much bigger: during laminar flow, we calculated and measured this to be of the order of 80% of the gap torque. Therefore, all measured torques were divided by a factor of 2, and we should consider the scaling of torque with the parameters defined in Sec. III as more accurate than the exact numerical values of torque.

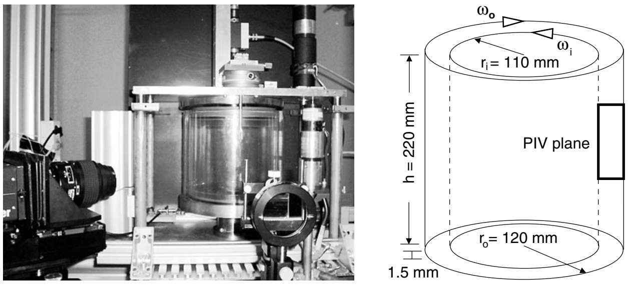

(a) (b)

FIG. 2. Picture and sketch with dimensions of the experimental setup. One can see the rotating torque meter (upper part of the picture), the calibration grid displacement device (on top of the upper plate), one of the two cameras (left side), and the light sheet arrangement (right side). The second camera is further to the right.

A constructionally more difficult, but also more accurate, solution for the torque measurement is to work with three stacked inner cylinders and only measure the torque on the central section, such as is done in the Maryland Taylor–Couette setup,[12] and (under development) in the Twente Turbulent Taylor–Couette setup.[18]

We measure the three components of the velocity by stereoscopic particle image velocimetry (PIV)[19] in a plane illuminated by a double-pulsed Nd:yttrium aluminum garnet laser. The plane is vertical (Fig. 2), i.e., normal to the mean flow: the in-plane components are the radial (u) and axial (v) velocities, while the out-of-plane component is the azimuthal component (w). It is observed from both sides with an angle of 60° (in air) using two double-frame charge coupled device cameras on Scheimpflug mounts. The light-sheet thickness is 0.5 mm. The tracer particles are 20 μm fluorescent (rhodamine B) spheres. The field of view is 11×25 mm^2, corresponding to a resolution of 300×1024 pixels. Special care has been taken concerning the calibration procedure, on which especially the evaluation of the plane-normal azimuthal component heavily relies. As a calibration target we use a thin polyester sheet with lithographically printed crosses on it, stably attached to a rotating and translating microtraverse. It is first put into the light sheet and traversed perpendicularly to it. Typically, five calibration images are taken with intervals of 0.5 mm. The raw PIV images are processed using DAVIS 7.2 by Lavision. They are first mapped to world coordinates, then they are filtered with a min-max filter, then PIV processed using a multipass algorithm, with a last interrogation area of 32×32 pixels with 50% overlap, and normalized using median filtering as postprocessing. Then, the three components are reconstructed from the two camera views. The mapping function is a third-order polynomial, and the interpolations are bilinear. The PIV data acquisition is triggered with the outer cylinder when it rotates in order to take the pictures at the same angular position as used during the calibration.

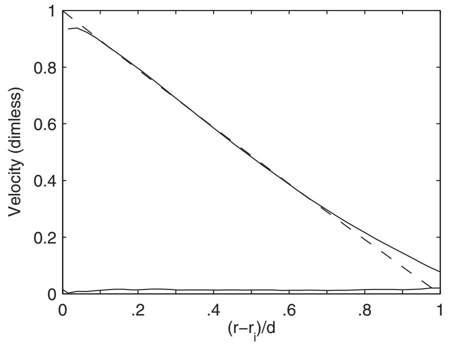

FIG. 3. Dimensionless azimuthal velocity profile $[w/(r_i\omega_i)$ vs $(r-r_i)/d]$ for Ro=Ro$_i$ at Re$_S$=90 (see Sec. III for the definition of the parameters). Solid line: measured mean azimuthal velocity. Dashed line: theoretical profile. The radial component u, which should be zero, is also shown as a thin solid line.

To check the reliability of the stereoscopic velocity measurement method, we performed a measurement for a laminar flow when only the inner cylinder rotates at a Reynolds number as low as Re$_S$=90 using an 86% glycerol-water mixture. In that case, the analytical velocity field is known: the radial and axial velocities are zero, and the azimuthal velocity w should be axisymmetric with no axial dependence, and a radial profile in the form $w(r)=\Omega r_i\eta(r_o/r-r/r_o)/(1-\eta^2)$.[8] The results are plotted in Fig. 3. The measured profile (solid line) hardly differs from the theoretical profile (dashed line) in the bulk of the flow $[0.1\lesssim(r-r_i)/d\lesssim 0.7]$. The discrepancy is, however, quite strong close to the outer cylinder $[(r-r_i)/d=1]$, which may be due to the refraction close to the curved wall that causes measurement errors. The in-plane components, which should be zero, do not exceed 1% of the inner cylinder velocity everywhere. In conclusion, the measurements are very satisfying in the bulk. Further improvements to the technique have been made since this first PIV test, in particular a new outer cylinder of improved roundness, and the measurements performed in water for turbulent cases are reliable in the range $[0.1\lesssim(r-r_i)/d\lesssim 0.85]$. The PIV measurements close to the wall could be further improved by using an outer cylinder that is machined in a block with flat outer interfaces normal to the cameras.

III. PARAMETER SPACE

The two traditional parameters to describe the flow are the inner (respectively, outer) Reynolds numbers Re$_i$ $=(r_i\omega_i d/\nu)$ [respectively, Re$_o$=$(r_o\omega_o d/\nu)$], with the inner (respectively, outer) cylinder rotating at rotation rates ω_i (respectively, ω_o), and ν the kinematic viscosity.

We choose to use the set of parameters defined by Dubrulle *et al.*:[20] a shear Reynolds number Re$_S$ and a Rotation number Ro,

$$\mathrm{Re}_S=\frac{2|\eta\mathrm{Re}_o-\mathrm{Re}_i|}{1+\eta}\mathrm{Ro}=(1-\eta)\frac{\mathrm{Re}_i+\mathrm{Re}_o}{\eta\mathrm{Re}_o-\mathrm{Re}_i}. \qquad (1)$$

With this choice, Re$_S$ is based on the laminar shear rate S: Re$_S$=Sd^2/ν. For instance, with a 20 Hz velocity difference in counter-rotation, the shear rate is around 1400 s^{-1} and Re$_S\simeq 1.4\times 10^5$ for water at 20 °C. A constant shear Reynolds number corresponds to a line of slope η in the $\{\mathrm{Re}_o;\mathrm{Re}_i\}$ coordinate system (see Fig. 4).

The Rotation number Ro compares the mean rotation with the shear and is the inverse of a Rossby number. Its sign defines cyclonic (Ro>0) or anticyclonic (Ro<0) flows. The Rotation number is zero in case of perfect counter-rotation $(r_i\omega_i=-r_o\omega_o)$. Two other relevant values of the Rotation number are Ro$_i$=$\eta-1\simeq-0.083$ and Ro$_o$=$(1-\eta)/\eta\simeq 0.091$ for, respectively, inner and outer cylinders rotating alone. Finally, a further choice that we made in our experiment was the value of $\eta=r_i/r_o$, which we have chosen as relatively close to unity, i.e., $\eta=110/120\simeq 0.91$, which is considered a narrow gap, and is the most common in reported experiments, such as Refs. 8, 9, 21, and 22, although a value as low as 0.128 is described as well.[4] A high η, i.e., $(1-\eta)\ll 1$, is special in the sense that for $\eta\to 1$ the flow is equivalent to a plane Couette flow with background rotation; at high η, the flow is linearly unstable for $-1<\mathrm{Ro}<\mathrm{Ro}_o$.[5,20,23]

In the present study we experimentally explore regions of the parameter space that, to our knowledge, have not been reported before. We present in Fig. 4 the parameter space in $\{\mathrm{Re}_o;\mathrm{Re}_i\}$ coordinates with a sketch of the flow states identified by Andereck *et al.*[9] and the location of the data discussed in the present paper. One can notice that the present range of Reynolds numbers is far beyond that of Andereck, and that with the PIV data we mainly explore the zone between perfect counter-rotation and only the inner cylinder rotating.

IV. STUDY OF THREE PARTICULAR ROTATION NUMBERS

In the experiments reported in this section, we maintain the Rotation number at constant values and vary the shear Reynolds number. We compare three particular Rotation numbers, Ro$_i$, Ro$_c$, and Ro$_o$, corresponding to rotation of the inner cylinder only, exact counter-rotation, and rotation of the outer cylinder rotating only, respectively. In Sec. IV A, we report torque scaling measurements for a wide range of Reynolds numbers—from base laminar flow to highly turbulent flows—and in Sec. IV B, we present typical velocity profiles in turbulent conditions.

A. Torque scaling measurements

We present in Fig. 5 the friction factor c_f $=T/(2\pi\rho r_i^2LU^2)\propto G/\mathrm{Re}^2$, with $U=Sd$ and $G=T/(\rho L\nu^2)$, as a function of Re$_S$ for the three Rotation numbers. A common definition for the scaling exponent α of the dimensionless torque is based on G: $G\propto\mathrm{Re}_S^{\alpha}$. We keep this definition and present the local exponent α in the inset in Fig. 5. We compute α by means of a logarithmic derivative, $\alpha=2+d\log(c_f)/d\log(\mathrm{Re}_S)$.

At low Re, the three curves collapse on a Re^{-1} curve. This characterizes the laminar regime where the torque is proportional to the shear rate on which the Reynolds number is based.

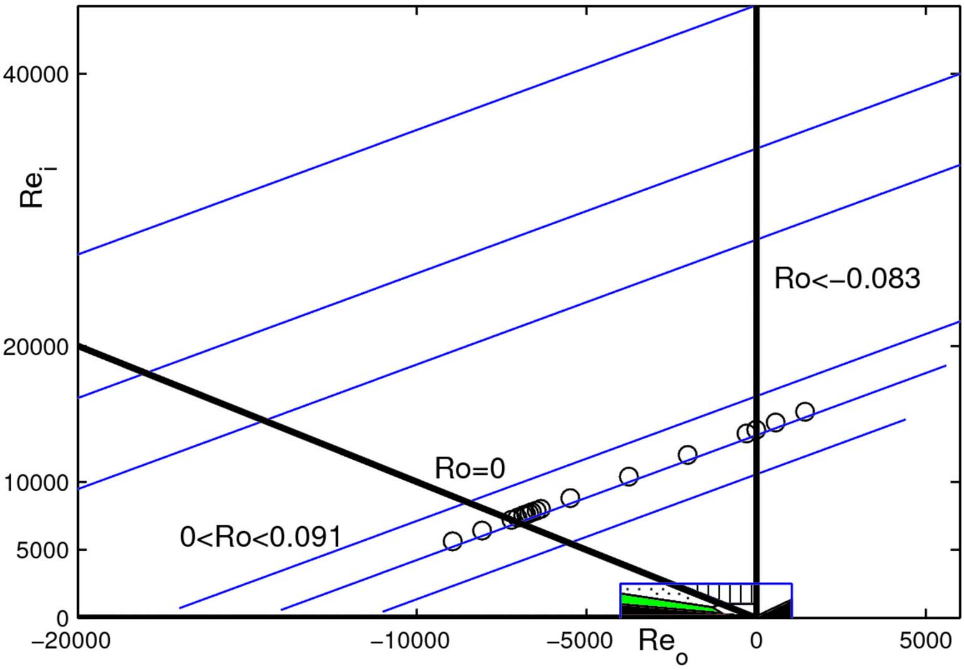

FIG. 4. (Color online) Parameter space in $\{\mathrm{Re}_o;\mathrm{Re}_i\}$ coordinates. The vertical axis $\mathrm{Re}_o=0$ corresponds to $\mathrm{Ro}=\mathrm{Ro}_i=-0.083$ and has been widely studied (Refs. 12, 13, 16, and 17). The horizontal axis $\mathrm{Re}_i=0$ corresponds to $\mathrm{Ro}=\mathrm{Ro}_o=0.091$. The line $\mathrm{Re}_i=-\mathrm{Re}_o$ corresponds to counter-rotation, i.e., $\mathrm{Ro}=\mathrm{Ro}_c=0$. The PIV data taken at a constant shear Reynolds number of $\mathrm{Re}_S=1.4\times10^4$ are plotted with (○). The torque data with varying Ro at constant shear for various Re_S ranging from $\mathrm{Re}_S=3\times10^3$ to $\mathrm{Re}_S=4.7\times10^4$ are plotted as gray (blue online) lines. They are discussed in Fig. 8. We also plot the states identified at much lower Re_S by Andereck *et al.* (Ref. 9) as patches: black corresponds to laminar Couette flow, gray (green online) to "spiral turbulence," dotted zone to "featureless turbulence," and vertical stripes to an "unexplored" zone.

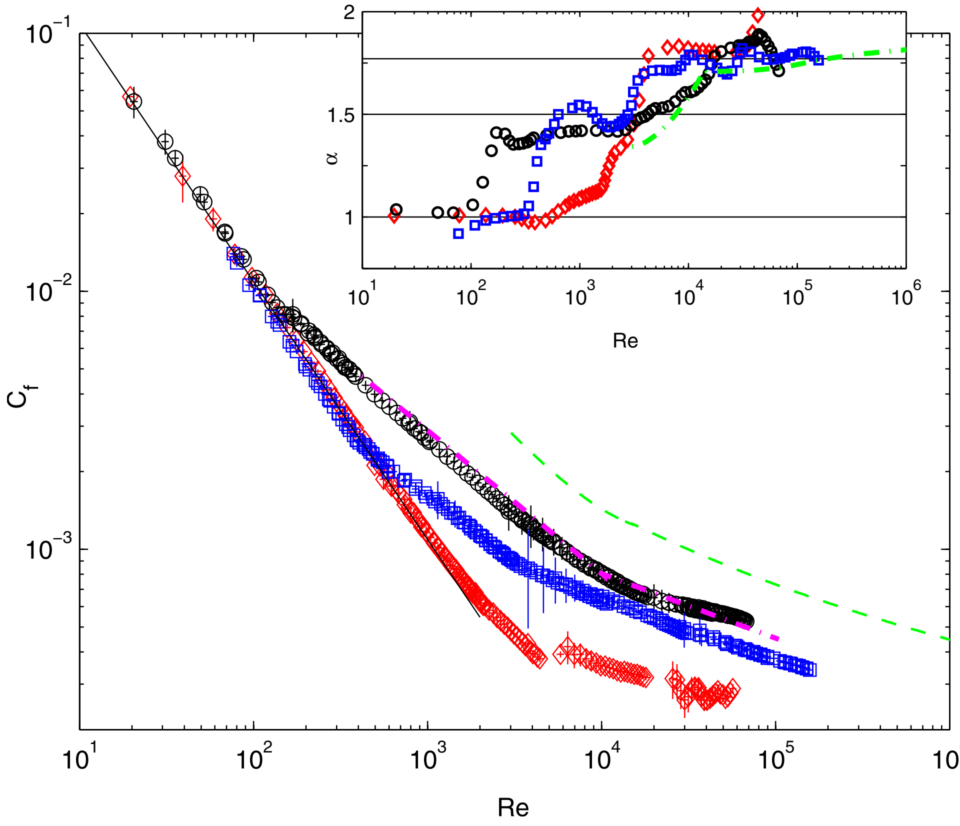

FIG. 5. (Color online) Friction factor c_f vs Re_S for $\mathrm{Ro}_i=\eta-1$ (black ○), $\mathrm{Ro}_c=0$ (blue □), and $\mathrm{Ro}_o=(1-\eta)/\eta$ (red ◇). Relative error on Re_S: ±5%; absolute error on torque: ±0.01 N m. Dashed (green online) line: Lewis' data [Ref. 13, Eq. (3)], for Ro_i and $\eta=0.724$. Dash-dotted (magenta online) line: Racina's data [Ref. 22, Eq. (10)]. Solid thin black line: laminar friction factor $c_f=1/(\eta\,\mathrm{Re})$. Inset: local exponent α such that $C_f\propto\mathrm{Re}_S^{\alpha-2}$, computed as $2+d\log(C_f)/d\log(\mathrm{Re}_S)$, for $\mathrm{Ro}_i=\eta-1$ (black ○), $\mathrm{Ro}_c=0$ (blue □), and $\mathrm{Ro}_o=(1-\eta)/\eta$ (red ◇). Dashed (green online) line: Lewis' data [Ref. 13, Eq. (3)] for Ro_i and $\eta=0.724$.

For $\mathrm{Ro}_i = \eta - 1$, one can notice a transition to a different regime at $\mathrm{Re}_{ci} \simeq 140$ [the theoretical threshold is computed as $\mathrm{Re} = 150$ (Ref. 23)]. This corresponds to the linear instability of the basic flow, leading in this case to the growth of laminar Taylor vortices. The friction factor is then supposed to scale as $c_f \propto \mathrm{Re}^{-1/2}$ ($\alpha = 3/2$), which is the case here (see inset in Fig. 5). For exact counter-rotation ($\mathrm{Ro}_c = 0$), the first instability threshold is $\mathrm{Re}_{cc} \simeq 400$. This is somewhat lower than the theoretical prediction $\mathrm{Re}_{cc} = 515$,[23] which is probably due to our finite aspect ratio. Finally, the Taylor–Couette flow with only the outer cylinder rotating $[\mathrm{Ro}_o = (1-\eta)/\eta]$ is linearly stable whatever Re. We observe the experimental flow to be still laminar up to high Re; then, in a rather short range of Re numbers, the flow transits to a turbulent state at $4000 \lesssim \mathrm{Re}_{to} \simeq 5000$.

Further increase in the shear Reynolds number also increases the local exponent (see inset in Fig. 5). For $\mathrm{Ro}_i = \eta - 1$, it gradually rises from $\alpha \simeq 1.5$ at $\mathrm{Re} \simeq 200$ to $\alpha \simeq 1.8$ at $\mathrm{Re} \simeq 10^5$. The order of magnitude of these values agrees with the results of Lewis *et al.*,[13] although a direct comparison is difficult, owing to the different gap ratios of the experiments. The local exponent is supposed to approach a value of 2 for increasing gap ratio. Dubrulle and Hersant[10] attribute the increase in α to logarithmic corrections, whereas Eckhardt *et al.*[11] attribute the increase in α to a balance between a boundary-layer/hairpin contribution (scaling as $\propto \mathrm{Re}^{3/2}$) and a bulk contribution (scaling as $\propto \mathrm{Re}^2$). The case of perfect counter-rotation shows a plateau at $\alpha \simeq 1.5$ and a sharp increase in the local exponent to $\alpha \simeq 1.75$ at $\mathrm{Re}_{tc} \simeq 3200$, possibly tracing back to a secondary transition. The local exponent then seems to increase gradually. Finally, for outer cylinder rotating alone (Ro_o) the transition is very sharp and the local exponent is already around $\alpha = 1.77$ at $\mathrm{Re} \gtrsim 5000$. Note that the dimensional values of the torque at Ro_o are very small and difficult to measure accurately, and that these may become smaller than the contributions by the two Kármán layers (end effects) that we simply take into account by dividing by 2, as described in Sec. II. One can finally notice that at the same shear Reynolds number, for $\mathrm{Re} \geq 10^4$ the local exponents for the three rotation numbers are equal within ± 0.1 and that the torque with the inner cylinder rotating only is greater than the torque in counter-rotation, the latter being greater than the torque for only the outer cylinder rotating.

B. Velocity profiles at a high shear-Reynolds number

The presence of vortexlike structures at high shear-Reynolds number ($\mathrm{Re}_S \gtrsim 10^4$) in turbulent Taylor–Couette flow with the inner cylinder rotating alone is confirmed in our experiment through stereoscopic PIV measurements.[24] As shown in Fig. 6, the time-averaged flow shows a strong secondary mean flow in the form of counter-rotating vortices, and their role in advecting angular momentum (as visible in the coloring by the azimuthal velocity) is clearly visible as well. The azimuthal velocity profile averaged over both time and axial position w, as shown in Fig. 7, is almost flat, indicating that the transport of angular momentum is due mainly to the time-average coherent structures rather than by the correlated fluctuations as in regular shear flow.

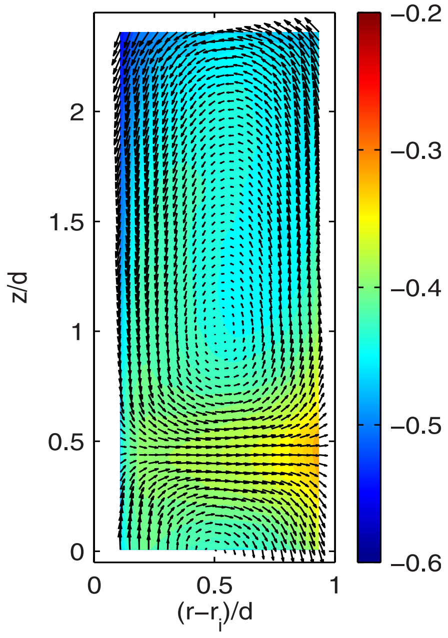

FIG. 6. (Color online) Secondary flow for $\mathrm{Ro} = \mathrm{Ro}_i$ at $\mathrm{Re} = 1.4 \times 10^4$. Arrows indicate radial and axial velocities; color indicates azimuthal velocity (normalized to inner wall velocity).

We then measured the counter-rotating flow at the same Re_S. The measurements are triggered on the outer cylinder position and are averaged over 500 images. In the counter-rotating case, for this large gap ratio and at this value of the shear-Reynolds number, the instantaneous velocity field is really disorganized and does not contain obvious structures like Taylor vortices, in contrast with other situations.[25] No peaks are present in the time spectra, and there is no axial dependency of the time-averaged velocity field. We thus average in the axial direction the different radial profiles; the

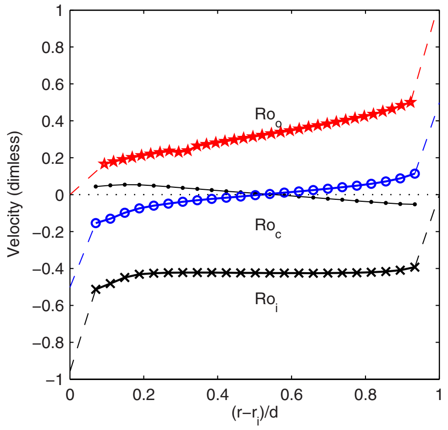

FIG. 7. (Color online) Profiles of the mean azimuthal velocity component for three Rotation numbers corresponding to only the inner cylinder rotating (×, black), perfect counter-rotation (○, blue), and only the outer cylinder rotating (⋆, red) at $\mathrm{Re} = 1.4 \times 10^4$. Thin line (·, black): axial velocity v (for $\mathrm{Ro} = \mathrm{Ro}_i$) averaged over half a period. The velocities are presented in a dimensionless form: $w/(Sd)$ with $Sd = 2r_i(\omega_o - \omega_i)/(1+\eta)$.

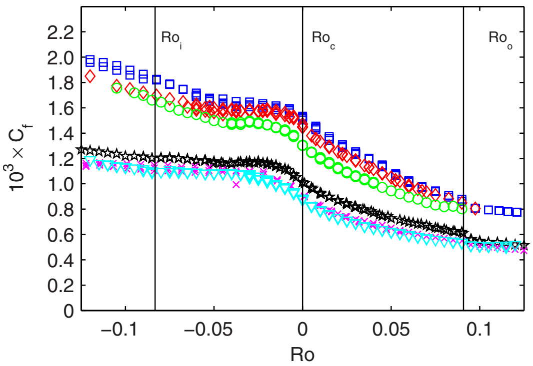

FIG. 8. (Color online) The friction factor c_f as a function of Ro at various constant shear Reynolds numbers: (blue ☐) Re$=1.1\times 10^4$, (red ◇) Re$=1.4\times 10^4$, (green ○) Re$=1.7\times 10^4$, (black ★) Re$=2.9\times 10^4$, (magenta ×) Re$=3.6\times 10^4$, (cyan ▽) Re$=4.7\times 10^4$.

azimuthal component w is presented in Fig. 7 as well. In the bulk, it is low, i.e., its magnitude is below 0.1 between $0.15\lesssim (r-r_i)/d \lesssim 0.85$, that is 75% of the gap width. The two other components are zero within 0.002.

We finally address the outer cylinder rotating alone again at the same Re$_S$. These measurements are done much in the same way as the counter-rotating ones, i.e., again the PIV system is triggered by the outer cylinder. As in the counter-rotating flow, this flow does not show any large scale structures. The gradient in the average azimuthal velocity, again shown in Fig. 7, is much steeper than in the counter-rotating case, which can be attributed to the much lower turbulence, as it also manifests itself in the low c_f value for Ro$_o$.

V. INFLUENCE OF ROTATION ON THE EMERGENCE AND STRUCTURE OF THE TURBULENT TAYLOR VORTICES

To characterize the transition between the three flow regimes, we first consider the global torque measurements. We plot in Fig. 8 the friction factor or dimensionless torque as a function of Rotation number Ro at six different shear Reynolds numbers Re$_S$, as indicated in Fig. 4. We show three series centered around Re$_S$$=1.4\times 10^4$ and three around Re$_S$$=3.8\times 10^4$. As already seen in Fig. 5, the friction factor reduces with increasing Re$_S$. More interesting is the behavior of c_f with Ro: the torque in counter-rotation (Ro$_c$) is approximately 80% of c_f(Ro$_i$), and the torque with outer cylinder rotating alone (Ro$_o$) is approximately 50% of c_f(Ro$_i$). These values compare well with the few available data compiled by Dubrulle *et al.*[20] The curve shows a plateau of constant torque especially at the larger Re$_S$ from Ro$=-0.2$, i.e., when both cylinders rotate in the same direction with the inner cylinder rotating faster than the outer cylinder, to Ro$\simeq -0.035$, i.e., with a small amount of counter-rotation with the inner cylinder still rotating faster than the outer cylinder. The torque then monotonically decreases when increasing the angular speed of the outer cylinder, with an inflexion point close or equal to Ro$_c$. It is observed that the transition is continuous and smooth everywhere and without hysteresis.

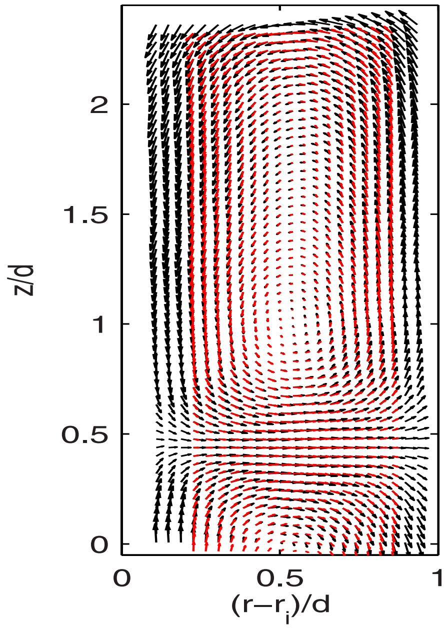

FIG. 9. (Color online) Overlay of measured time-average velocity field at Ro=Ro$_i$ [in gray (red online)] and the best-fit model velocity field (in black). The large third harmonic makes the radial flow being concentrated in narrow bands rather than sinusoidally distributed.

We now address the question of the transition between the different torque regimes by considering the changes observed in the mean flow. To extract quantitative data from the PIV measurements, we use the following model for the stream function Ψ of the secondary flow:

$$\Psi = \sin\left(\frac{\pi(r-r_i)}{d}\right) \times \left[A_1 \sin\left(\frac{\pi(z-z_0)}{\ell}\right) + A_3 \sin\left(\frac{3\pi(z-z_0)}{\ell}\right)\right], \qquad (2)$$

with as free parameters A_1, A_3, ℓ and z_0. This model comprises a flow that fulfills the kinematic boundary condition at the inner and outer walls, r_i, r_i+d, and in between forms in the axial direction alternating rolls, with a roll height of ℓ. In this model, the maximum radial velocity is formed by the two amplitudes and given by $u_{r,\max}=(\partial\Psi/\partial z)_{\max}=\pi(A_1/\ell+3A_3/\ell)$. It is implicitly assumed that the flow is developed sufficiently to restore the axisymmetry, which is checked *a posteriori*. Our fitting model comprises a sinusoidal (fundamental) mode and its first symmetric harmonic (third mode), the latter which appears to considerably improve the matching between the model and the actual average velocity fields, especially close to Ro$_i$ (see Figs. 9 and 10).

We first discuss the case Ro=Ro$_i$. A sequence of 4000 PIV images at a data rate of 3.7 Hz is taken, and 20 consecutive PIV images, i.e., approximately 11 cylinder revolutions, are sufficient to obtain a reliable estimate of the mean flow.[17] It is known that for the first transition the observed flow state can depend on the initial conditions.[8] When starting the inner cylinder from rest and accelerating it to 2 Hz in 20 s, the vortices grow very fast, reach a value with a velocity amplitude of 0.08 ms^{-1}, and then decay to become stabilized at a

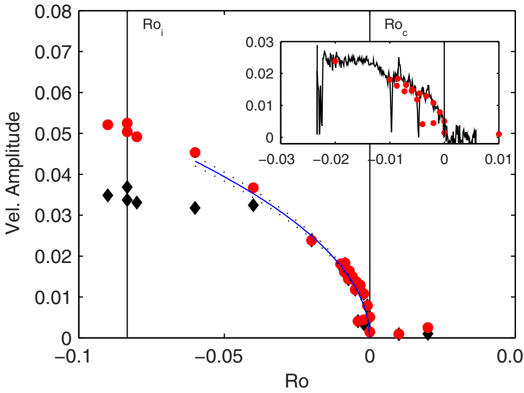

FIG. 10. (Color online) Secondary flow amplitude vs rotation number (Ro) at constant shear rate. Black (◇): model with fundamental mode only; red (○): complete model with third harmonic. Solid line is a fit of the form $A=a(-\mathrm{Ro})^{1/2}$. Inset: zoom close to counter-rotation combined with results from a continuous transient experiment (see text).

value around 0.074 ms^{-1} after 400 s. Transients are thus also very long in turbulent Taylor-vortex flows. For slower acceleration, the vortices that appear first are much weaker and have a larger length scale before reaching the same final state. The final length scale ℓ of the vortices for Ro_i is about 1.2 times the gap width, consistent with the data from Bilson *et al.*[16]

In a subsequent measurement we start from $\mathrm{Ro}=\mathrm{Ro}_i$ and vary the rotation number in small increments, while maintaining a constant shear rate. We allow the system to spend 20 min in each state before acquiring PIV data. We verify that the fit parameters are stationary and compute them using the average of the full PIV data set at each Ro. The results are plotted in Fig. 10. Please note that Ro has been varied both with increasing and decreasing values to check for a possible hysteresis. All points fall on a single curve; the transition is smooth and without hysteresis. For $\mathrm{Ro}\geq 0$, the fitted modes have zero or negligible amplitudes, since there are no structures in the time-average field.[24] One can notice that as soon as $\mathrm{Ro}<0$, i.e., as soon as the inner cylinder wall starts to rotate faster than the outer cylinder wall, vortices begin to grow. We plot in Fig. 10 the velocity amplitude associated with the simple model (single mode, ◇) and with the complete model (modes 1 and 3, ○). Close to $\mathrm{Ro}=0$, the two models coincide: $A_3\simeq 0$ and the mean secondary flow is well described by pure sinusoidal structures. For $\mathrm{Ro}\lesssim -0.04$, the vortices start to have elongated shapes with large cores and small regions of large radial motions in between adjacent vortices; the third mode is then necessary to adequately describe the secondary flow (Fig. 9). The first mode becomes saturated (i.e., it does not grow in magnitude) in this region. Finally, we give in Fig. 10 a fit of the amplitudes close to $\mathrm{Ro}=0$ of the form $A=a(-\mathrm{Ro})^{1/2}$. The velocity amplitude of the vortex behaves like the square root of the distance to $\mathrm{Ro}=0$, a situation reminiscent to a classical supercritical bifurcation, with A as order parameter and Ro as control parameter.

We also performed a *continuous transient* experiment, in which we varied the rotation number quasistatically from $\mathrm{Ro}=0.004$ to $\mathrm{Ro}=-0.0250$ in 3000 s, always keeping the Reynolds number constant at $\mathrm{Re}_S=1.4\times 10^4$. The amplitude of the mean secondary flow, computed on sequences of 20 images, is plotted in the inset of Fig. 10. The curve follows the static experiments (given by the single points), but some downward peaks can be noticed. We checked that these are not the result of a fitting error, and indeed correspond to the occasional disappearance of the vortices. Still, the measurements are done at a fixed position in space. Although the very long time-averaged series leads to well-established stationary axisymmetric states, it is possible that the instantaneous whole flow consists of different regions. Further investigation including time-resolved single-point measurements or flow visualizations needs to be done to verify this possibility.

VI. CONCLUSION

The net system rotation, as expressed in the Rotation number Ro, obviously has strong effects on the torque scaling. Whereas the local exponent evolves in a smooth way for inner cylinder rotating alone, the counter-rotating case exhibits two sharp transitions from $\alpha=1$ to $\alpha\simeq 1.5$ and then to $\alpha\simeq 1.75$. We also notice that the second transition for counter-rotation Re_{tc} is close to the threshold Re_{to} of turbulence onset for outer cylinder rotating alone.

The rotation number Ro is thus a secondary control parameter. It is very tempting to use the classical formalism of bifurcations and instabilities to study the transition between featureless turbulence and turbulent Taylor-vortex flow at constant Re_S, which seems to be supercritical; the threshold for the onset of coherent structures in the mean flow is Ro_c. For anticyclonic flows $(\mathrm{Ro}<0)$, the transport is dominated by large scale coherent structures, whereas for cyclonic flows $(\mathrm{Ro}>0)$, it is dominated by correlated fluctuations reminiscent to those in-plane Couette flow.

In a considerable range of Re_S, counter-rotation (Ro_c) is also close or equal to an inflexion point in the torque curve; this may be related to the crossover point, where the role of the correlated fluctuations is taken over by the large scale vortical structures. The mean azimuthal velocity profiles show that there is only a marginal viscous contribution for $\mathrm{Ro}\leq 0$ but of order 10% at Ro_o.[24] The role of turbulent versus large-scale transport (of angular momentum) should be further investigated from (existing) numerical or PIV velocity data. Since torque scaling with Ro as measured at much higher Re_S that is used for PIV does qualitatively not change, these measurements suggest that the large scale vortices are not only persistent in the flow at higher Re_S, but that they also dominate the dynamics of the flow. An answer to the persistence may be obtained from either a more detailed analysis of instantaneous velocity data or from torque scaling measurements at still higher Reynolds numbers in Taylor–Couette systems such as those under development.[18]

ACKNOWLEDGMENTS

We are particularly indebted to J. R. Bodde, C. Gerritsen, and W. Tax for building up and piloting the experiment. We have benefited very fruitful discussions with A. Chiffaudel, F. Daviaud, B. Dubrulle, B. Eckhardt, and D. Lohse.

[1] P. J. Holmes, J. L. Lumley, and G. Berkooz, *Turbulence, Coherent Structures, Dynamical Systems and Symmetry* (Cambridge University Press, Cambridge, England, 1996).

[2] R. Monchaux, M. Berhanu, M. Bourgoin, M. Moulin, Ph. Odier, J.-F. Pinton, R. Volk, S. Fauve, N. Mordant, F. Pétrélis, A. Chiffaudel, F. Daviaud, B. Dubrulle, C. Gasquet, L. Marié, and F. Ravelet, "Generation of magnetic field by dynamo action in a turbulent flow of liquid sodium," Phys. Rev. Lett. **98**, 044502 (2007).

[3] F. Ravelet, L. Marié, A. Chiffaudel, and F. Daviaud, "Multistability and memory effect in a highly turbulent flow: Experimental evidence for a global bifurcation," Phys. Rev. Lett. **93**, 164501 (2004).

[4] N. Mujica and D. P. Lathrop, "Hysteretic gravity-wave bifurcation in a highly turbulent swirling flow," J. Fluid Mech. **551**, 49 (2006).

[5] D. J. Tritton, "Stabilization and destabilization of turbulent shear flow in a rotating fluid," J. Fluid Mech. **241**, 503 (1992).

[6] G. Brethouwer, "The effect of rotation on rapidly sheared homogeneous turbulence and passive scalar transport. Linear theory and direct numerical simulation," J. Fluid Mech. **542**, 305 (2005).

[7] M. Couette, "Etude sur le frottement des liquids," Ann. Chim. Phys. **21**, 433 (1890).

[8] D. Coles, "Transition in circular Couette flow," J. Fluid Mech. **21**, 385 (1965).

[9] C. D. Andereck, S. S. Liu, and H. L. Swinney, "Flow regimes in a circular Couette system with independently rotating cylinders," J. Fluid Mech. **164**, 155 (1986).

[10] B. Dubrulle and F. Hersant, "Momentum transport and torque scaling in Taylor–Couette flow from an analogy with turbulent convection," Eur. Phys. J. B **26**, 379 (2002).

[11] B. Eckhardt, S. Grossmann, and D. Lohse, "Torque scaling in Taylor–Couette flow between independently rotating cylinders," J. Fluid Mech. **581**, 221 (2007).

[12] D. P. Lathrop, J. Fineberg, and H. L. Swinney, "Transition to shear-driven turbulence in Couette–Taylor flow," Phys. Rev. A **46**, 6390 (1992).

[13] G. S. Lewis and H. L. Swinney, "Velocity structure functions, scaling, and transitions in high-Reynolds-number Couette–Taylor flow," Phys. Rev. E **59**, 5457 (1999).

[14] F. Hersant, B. Dubrulle, and J.-M. Huré, "Turbulence in circumstellar disks," Astron. Astrophys. **429**, 531 (2005).

[15] S. T. Wereley and R. M. Lueptow, "Spatio-temporal character of non-wavy and wavy Taylor–Couette flow," J. Fluid Mech. **364**, 59 (1998).

[16] M. Bilson and K. Bremhorst, "Direct numerical simulation of turbulent Taylor–Couette flow," J. Fluid Mech. **579**, 227 (2007).

[17] S. Dong, "Direct numerical simulation of turbulent Taylor–Couette flow," J. Fluid Mech. **587**, 373 (2007).

[18] D. Lohse, "The Twente Taylor Couette Facility," presented at 12th European Turbulence Conference, 7–10 September 2009, Marburg, Germany.

[19] A. K. Prasad, "Stereoscopic particle image velocimetry," Exp. Fluids **29**, 103 (2000).

[20] B. Dubrulle, O. Dauchot, F. Daviaud, P.-Y. Longaretti, D. Richard, and J.-P. Zahn, "Stability and turbulent transport in Taylor–Couette flow from analysis of experimental data," Phys. Fluids **17**, 095103 (2005).

[21] F. Wendt, "Turbulente Strömungen zwischen zwei rotierenden konaxialen Zylindern," Arch. Appl. Mech. **4**, 577 (1933).

[22] A. Racina and M. Kind, "Specific power input and local micromixing times in turbulent Taylor–Couette flow," Exp. Fluids **41**, 513 (2006).

[23] A. Esser and S. Grossmann, "Analytic expression for Taylor–Couette stability boundary," Phys. Fluids **8**, 1814 (1996).

[24] F. Ravelet, R. Delfos, and J. Westerweel, "Experimental studies of turbulent Taylor–Couette flows," Proceedings of the 5th International Symposium on Turbulence and Shear Flow Phenomena, Munich, 2007, p. 1211.

[25] L. Wang, M. G. Olsen, and R. D. Vigil, "Reappearance of azimuthal waves in turbulent Taylor–Couette flow at large aspect ratio," Chem. Eng. Sci. **60**, 5555 (2005).

Kinematic α Tensors and Dynamo Mechanisms in a von Kármán Swirling Flow

F. Ravelet,[1] B. Dubrulle,[2] F. Daviaud,[2] and P.-A. Ratié[1]
[1]*Arts et Metiers ParisTech, DynFluid, 151 boulevard de l'Hôpital, 75013 Paris, France*
[2]*CEA, IRAMIS, SPEC, CNRS URA 2464, SPHYNX, 91191 Gif-sur-Yvette, France*
(Received 18 January 2012; published 12 July 2012)

We provide experimental and numerical evidence of in-blades vortices in the von Kármán swirling flow. We estimate the associated kinematic α-effect tensor and show that it is compatible with recent models of the von Kármán sodium (VKS) dynamo. We further show that depending on the relative frequency of the two impellers, the dominant dynamo mechanism may switch from α^2 to $\alpha - \Omega$ dynamo. We discuss some implications of these results for VKS experiments.

DOI: 10.1103/PhysRevLett.109.024503 PACS numbers: 47.65.−d, 52.65.Kj, 91.25.Cw

The dynamo effect is the conversion from mechanical energy to magnetic energy. It is at the origin of most magnetic fields in the Universe (the Earth, stars, galaxies, etc.) and therefore deserves special attention. The von Kármán sodium experiment (VKS) is at present time one of the three successful liquid metal dynamo experiments. In this experiment, the mechanical energy is provided by two iron counter-rotating impellers in a cylindrical vessel, and the spontaneous conversion into magnetic energy is obtained as soon as one of the impellers rotates faster than 16 Hz [1–3]. The process of how this conversion occurs is, however, still a matter of debate. Indeed, a quasi axial axisymmetric mean magnetic dynamo field is observed in VKS experiment, while an equatorial dipole is expected if the dynamo process only involves the time averaged axisymmetric mean flow [4]. Several models have recently been suggested to explain this observation, based upon the now classical α effect in mean field theory of dynamo [5,6]: in the presence of a nonaxisymmetric fluctuating velocity field, the mean VKS magnetic field satisfies

$$\partial_t\langle\mathbf{B}\rangle = \nabla\times(\langle\mathbf{u}\rangle\times\langle\mathbf{B}\rangle + \langle\overline{\overline{\alpha}}\mathbf{B}\rangle - \overline{\overline{\beta}}\nabla\times\langle\mathbf{B}\rangle), \qquad (1)$$

where u_i and B_i are the velocity and magnetic field, $\langle\rangle$ denotes time-azimuthal average and $\overline{\overline{\alpha}}$ and $\overline{\overline{\beta}}$ are second-order tensors depending on $\langle u\rangle$ and $u' = u - \langle u\rangle$. Specifically, it was suggested that vortical coherent structures in between the impeller blades such as pictured in Fig. 1(c) generate highly-correlated nonaxisymmetric velocity-vorticity fluctuations that would result in a non-negligible $\overline{\overline{\alpha}}$ tensor able to produce an axial dipole [7,8]. Kinematic simulations using a numerical model of such vortices indeed reproduce the growth of an axisymmetric axial field as observed in VKS experiments [9]. Numerical simulations [8,10] using *ad hoc* $\overline{\overline{\alpha}}$ tensors in the induction equation and different boundary conditions satisfactorily reproduce the large scale structure of the dynamo magnetic field, provided the nondimensional α parameter is of the order of 2 (ferromagnetic boundary conditions, [8]) or 0.02 if variations of the permeability due to soft iron are taken into account [10]. However, no measurements of the velocity structure in between the blades has been available so far, preventing check of the plausibility of these estimates, and, thus, the soundness of these α models. In the present Letter, we first provide some experimental evidence of these in-blades vortical structures and give more quantitative information on their averaged properties using Reynolds averaged Navier-Stokes (RANS) computational fluid dynamics (CFD) calculations. We then use these results to compute the resulting kinematical α effect. Some implications of these results for VKS experiments are finally discussed. Depending on the relative frequency of the two impellers, the dominant dynamo mechanism may switch from α^2 to $\alpha - \Omega$ dynamo, resulting in onset of dynamical regimes.

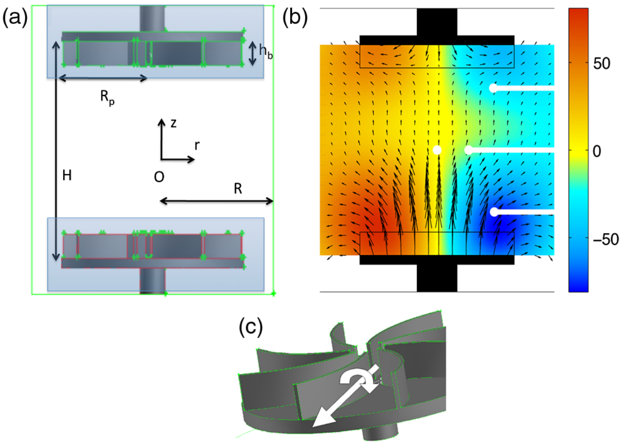

FIG. 1 (color online). (a) Geometry of the experiment. The shaded blue zone denote the rotating fluid volume used in the numerical simulation. (b) Reconstruction of the dynamo magnetic field in a meridional plane in a VKS experiment with rotating bottom disk and stationary upper disk (after [3]). The poloidal (resp. toroidal) component is coded with arrows (resp. color) from blue to red (jet color map). Measuring probes are in white. (c) Putative in-blades vortice creating the α effect.

To observe the vortices potentially responsible for the α effect, we use a von Kármán water experiment which is a 1/2 scale reproduction of the first successful VKS dynamo experiment described in [1]. Its geometry is summarized in Fig. 1: the fluid contained in a Plexiglas cylinder of radius $R = 100$ mm is stirred by a pair of coaxial impellers that can be rotated independently at rotation frequencies f_1 and f_2 ranging from 1 to 12 Hz. The impellers are flat disks of diameter $2R_p = 150$ mm fitted with either straight blades or radial blades of constant height $h_b = 20$ mm and curvature radius 92.5 mm. The inner faces of the discs are $H = 180$ mm apart. Velocity measurements are performed with a laser doppler velocimetry (LDV) and a stereoscopic particle image velocimetry (PIV) system provided by DANTEC dynamics. In the sequel, we use R and $T = 1/\pi(f_1 + f_2)$ as units of length and time.

In the VKS experiment, dynamo regimes have been observed for a wide variety of rotating frequencies (f_1, f_2) [2]. For simplification, we focus here on the simplest case where the top disk is fixed and the bottom disk is rotating, with the convex face of the blades pushing the fluid forward: $(f_1, f_2) = (1/(\pi T), 0)$. In such a case, dynamo action is observed for $f_1 > 16$ Hz through a nearly axisymmetric dipolar dynamo field, with azimuthal component localized at each impeller [[3,11] and Fig. 1(b)]. Figure 2(a) shows the mean time-averaged nondimensional velocity on a half meridional plane measured by PIV in the experiment. It consists in a fully nonsymmetric flow, with the outside radial part rotating as a block almost at the impeller's velocity. Due to the observing angle, this representation does not allow for velocity measurements inside the blades. Additional measurements using a LDV system and impellers with straight blades allow the measurement of the instantaneous azimuthal velocity component at one point located inside a blade [Fig. 2(b)]. In this measurement, one observes a modulation of the azimuthal velocity, over a period of $1/8f_1$ sec corresponding to one blade crossing. During a period, the azimuthal velocity first drops, and then catches again with the velocity of the blade. This drop results in a smaller averaged velocity (black lower curve) than the impeller velocity (blue upper curve) and is an experimental evidence of the presence of in-blades vortical movements.

To characterize further these motions, we now perform numerical experiments with the CFD finite-volume solver code FLUENT 6.3. The model that has been used is the stationary realizable k-ϵ RANS model [12]. We ran several different mesh configurations before reaching a satisfactory converged solution. It corresponds to a case where the fluid volume is divided into three parts: one central part with a typical element size of 3 mm and two volumes surrounding the impellers 15 mm and 15 mm apart from the blade tips in resp. the axial and radial direction, with conformal interfaces. The mesh is refined to 1 mm close to the blades. The equations are solved in a moving reference frame in one of these volumes to simulate the impeller's rotation. A grid convergence check has been performed and a stable converged solution with one rotating disk was found, with torques at both impellers equal to those measured in the experimental flow within 10 percent. The result is presented in Fig. 2(c) for the azimuthally averaged flow. One observes a one cell circulation close to the experimental one. To quantify this, we present in Fig. 3 a comparison between the numerical and the experimental velocity radial profiles at three locations: $z = \pm 0.53$; $z = 0$. The agreement is within 5% in most of the flow. The CFD solution enables the description of the in-blades velocity. On Fig. 2(c), one observes an intensification of the azimutal velocity at the edge of the rotating impeller, as well as some edge vortices near the top and the bottom edge. In the stationary impeller, the azimuthal velocity is slightly negative, so there is a huge differential rotation at the blades shrouds and tips. The streamlines displayed in Fig. 2(d) enables the clear visualization of in-blades radial trailing vortices, that are located behind the blades. Such vortices can be responsible for a deceleration of the azimuthal velocity observed in Fig. 2(b).

Using the CFD velocity field, one can compute the (nondimensional) azimuthally averaged helicity tensor,

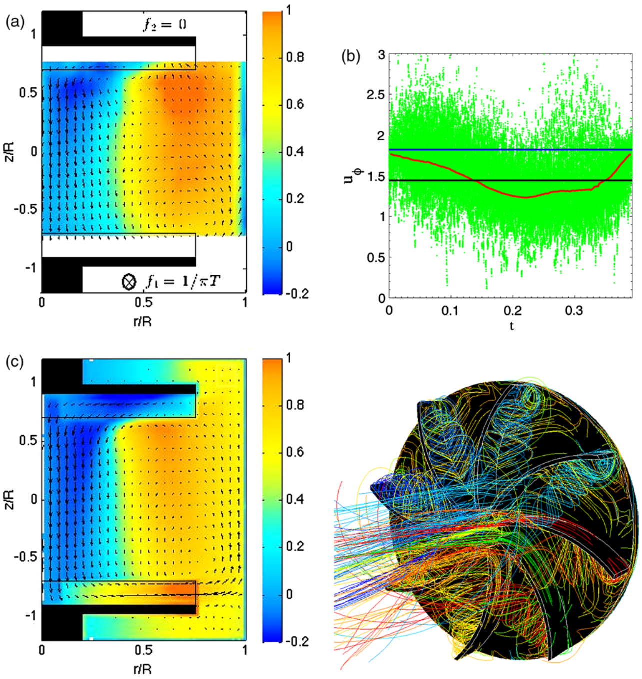

FIG. 2 (color online). (a) Nondimensional experimental mean velocity in a meridional plane. (b) nondimensional azimuthal velocity in the blades synchronized on the blade crossing vs nondimensional time. Green points: LDV measurements; red middle curve: running average; black lower curve: time average; blue upper curve: blade velocity. (c) Nondimensional numerical mean velocity. (d) Radial vortices as observed with streamlines in the CFD simulation.

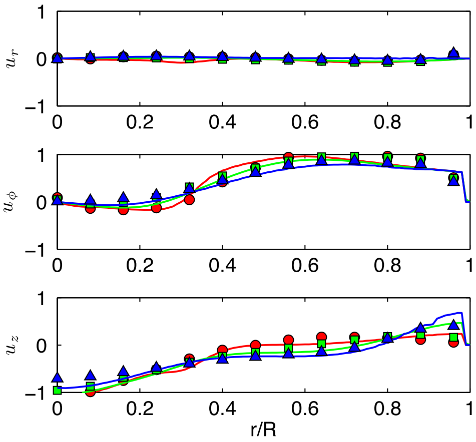

FIG. 3 (color online). Comparison between numerical (line) and experimental (symbols) profiles at $z = -0.53$ (red circles), $z = 0$ (green squares), and $z = 0.53$ (blue triangles). Error bars are of the order of the size of the symbols.

$$h_{ij} = \epsilon_{ikn}\langle u'_k \partial_j u'_n\rangle, \tag{2}$$

where $u' = u - \langle u\rangle$ is the fluctuating velocity field, $h_{ii} = \mathrm{Tr}(h) = -\langle u'_i \omega'_i\rangle$ is minus the helicity of the fluctuations, ω is the vorticity, and the symbol $\langle\rangle$ denotes azimuthal average. The result is displayed in Fig. 4. One sees that the helicity is mainly concentrated in the impellers, with a maximum absolute nondimensional value around 1 (corresponding to 100 ms^{-2} for impeller rotating at 10 Hz). In the rotating impeller, the largest helicity component is $h_{\phi\phi}$ with a value of the order of -0.5. Its value in the stationary impeller is of opposite sign and slightly larger, 1. This difference may be explained by the existence of a very large vertical differential rotation at the stationary impeller, which can generate a large toroidal vorticity. In the rotating impeller, other nonnegligible helicity components are found as $h_{\phi r}$ and h_{rz}. In the stationary impeller, other fairly large helicity components are h_{rr}, $h_{r\phi}$, h_{rz},$h_{z\phi}$, and h_{zr} (of the order of ± 1). We also computed the (nondimensional) azimuthally averaged Reynolds tensor $r_{ij} = \langle u'_i u'_j\rangle$ (not shown). We observed a similar localization of the tensor in the impellers, with a much smaller value, of the order of 5×10^{-2} (corresponding to 0.5 $\mathrm{m}^2\,\mathrm{s}^{-2}$ for impeller rotating at 10 Hz). The exact dynamo properties of such a velocity field would require solving the full kinematic problem, like in [9]. To get an order of magnitude estimates of the dynamo efficiency, we may, however, approximate the fluctuations by a short in time field, since the magnetic Reynolds number in VKS experiment is rather large (between 10 and 70) and the turbulence correlation time is much smaller than the magnetic field diffusive time. In such a case, one can use the computation of [13], equation (29); see also [14] to link the helicity and Reynolds tensor to $\bar{\alpha}$ and $\bar{\bar{\beta}}$ as

$$\alpha_{ij} = \tau h_{ij}, \qquad \beta_{ij} = \tau r_{ij}, \tag{3}$$

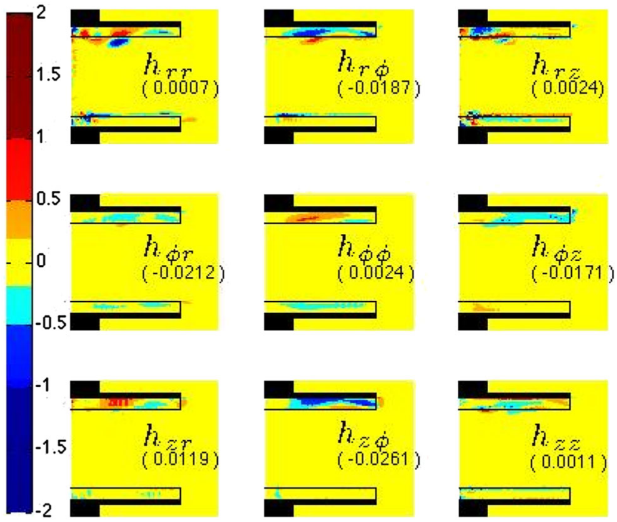

FIG. 4 (color online). Components of the (nondimensional) azimuthally averaged helicity tensor h_{ij} in numerics. The number in parentheses is the volume averaged value.

where τ is the correlation time of the nonaxisymmetric velocity perturbations. The CFD simulation provides a time-independent solution and cannot be used to compute this correlation time. However, we can use the LDV measurements in water (see Fig. 2) to estimate that this time is at most of the order of $1/8f_1$. Therefore, in nondimensional units, $\tau \le \pi/8$. This estimate leads to maximal nondimensional $\bar{\alpha}$ tensors of the order of ± 0.4 (resp. -0.2) in the stationary (resp. rotating) impeller, and maximal nondimensional $\bar{\bar{\beta}}$ tensors of the order of 2×10^{-2}. Our estimate of $\bar{\alpha}$ using CFD simulations and experiments can be compared with existing models of the VKS dynamo. First, we observe that the largest component of the tensor in the rotating impeller is $\alpha_{\phi\phi}$, as assumed in [8,10]. It is negative, as required for instability [8]. However, its maximal value is an order of magnitude smaller than the value $|\alpha_c| = 2.1$ needed to obtain dynamo action with ferromagnetic boundary conditions at magnetic Reynolds number reached in the VKS experiment [8]. On the other hand, it is one order of magnitudes larger than the value needed to obtain a dynamo action in VKS according to the model with localized permeability distribution [10]. Given the uncertainty in evaluation of the correlation time, we may say that our findings clearly validate the hypotheses of model of [10], but do not rule those of the model of [8]. Dynamo action may be impeded by a large enough turbulent resistivity, parameterized by $\bar{\bar{\beta}}$. This effect has been discarded in the numerical models so far [8,10]. Our estimate shows that this approximation is marginally legitimate in VKS, where the critical magnetic Reynolds number $Rm_c \sim 50$ in our time and length units, resulting in a nondimensional molecular magnetic diffusivity of the order of $1/Rm_c \sim 0.02$, i.e., of the order of the maximal value for the turbulent magnetic diffusivity, resulting in a 100 percent increase of the total magnetic diffusivity at $Rm = 50$. Our finding is in agreement with a recent estimate of [15] who observed a 50 percent increase of magnetic diffusivity at $Rm = 30$, in a nonstationary turbulent flow of liquid sodium, generated in a closed toroidal channel.

The present computation shows that the in-blade velocity is the VKS impellers is able to generate sufficient α effect to produce a dynamo mechanism, provided adequate boundary conditions [8] or localized permeability distributions [10] are taken into account. The special localization of this α effect found in the present study however calls for further discussion about a qualitative picture of the VKS one disk dynamo. Indeed, using Eq. (1), one can show that the poloidal field (r, z component) is generated from the toroidal field (ϕ component) through the α effect. In contrast, there are two possibilities (possibly concomitant) to generate toroidal field from poloidal field: either through the mean differential rotation $\Omega' = (1/r)d\langle u_\phi \rangle/dz$ (Ω effect) possibly reinforced by the jump of permeability or conductivity at the impellers [16] and (or) through α effect. The first case corresponds to a $\alpha - \Omega$ dynamo, while the second corresponds to an α^2 dynamo. Since the $\bar{\bar{\alpha}}$ tensor varies over a region of size h_b, the crossover in between the two mechanism lies at the critical value $R_p\Omega' \sim \alpha_{rr}/h_b$. This induces a dissymmetry in between the two impellers: at the rotating one, the differential rotation is almost zero $\Omega' \sim 0$ while at the stationary one, the differential rotation occurs over the height of the blades, so that in nondimensional shape $R_p\Omega' \sim R_p/h_b \sim 4$, i.e., is of the order of $\alpha_{rr}R/h_b \sim 4$. Therefore, the dynamo generation is α^2 at the rotating impeller, while it can be a combination of an α^2 and an $\alpha - \Omega$ at the stationary one (an $\alpha^2 - \Omega$) dynamo). Such a dissymmetry may explain generically the field dissymmetry observed in the VKS configuration with one rotating disk, where the field is much more intense near the rotating impeller, than near the stationary impeller cf. Fig. 1.

If the α effect computed in the present case is not strongly modified when the two impellers are rotating, we may draw interesting implications about the VKS dynamo in more general rotating regimes. Indeed, the location of the azimuthal velocity shear layer strongly depends on the relative velocity of the two impellers $\theta = (f_1 - f_2)/(f_1 + f_2)$ [17]: as long as $|\theta| \leq \theta_c$, the azimuthal velocity shear layer is in-between the two impellers, and there is a constant shear at the two impellers, of the order of $\Omega' \approx \pi(f_1 - f_2)/H$. Once $|\theta| \geq \theta_c$, the shear layer is at the slowest impeller, like in the one rotating disk case explored in the present Letter: the differential rotation is almost zero at the fastest impeller, and very strong at the slowest one [18]. This peculiar property however offers possible very different generic dynamo behavior under and above θ_c. For $|\theta| < \theta_c$, the Ω effect is of the order $O(1/H)$, so that it is too weak to supersede the α effect, of the order $1/h_b$ (since $h_b/H \ll 1$). In such case, the dominant dynamo mechanism is α^2 at each impellers. For $|\theta| > \theta_c$, the differential rotation switches to $O(1/h_b)$ at the slowest impeller, and the Ω effect becomes comparable to the α effect. There is therefore the possibility of an $\alpha^2 - \Omega$ mechanism at the slowest impeller, with an α^2 dynamo mechanism at the fastest impeller. This natural switch, induced by the behavior of the shear layer, opens interesting perspectives in terms of possible dynamical regimes in the VKS experiments. Indeed, an homogeneous α^2 dynamo is generically steady, with dynamo threshold $Rm_c = O(k/\alpha)$, while an homogeneous $\alpha - \Omega$ dynamo is generically oscillatory with dynamo threshold $Rm_c = O(k^2\sqrt{(2/\alpha k R_p \Omega')})$, with a rotating frequency bifurcating from a finite value at the dynamo onset $\omega_{osc} = \sqrt{(\alpha k R_p \Omega'/2)}$ [19]. [Meridional circulation and (or) parity properties with respect to the equator of α can steady $\alpha - \Omega$ dynamos.] In our setting, this translates in $Rm_c = O(R/h_b)$ for α^2 dynamos, and $Rm_c = O(R/h_b)/\sqrt{\theta_c/\theta}$ and $\omega_{osc} = O(R/h_b)\sqrt{\theta_c/\theta}$ for the $\alpha - \Omega$ dynamo. Due to inhomogeneities and possible nonlinear coupling in between the two dynamo mechanism at each impeller [3], it is not guaranteed that these generic features will persist. However, we observe that for $\theta < \theta_c$, dynamos observed in VKS are indeed steady, while both steady and dynamical regimes with oscillations appear for $\theta \geq \theta_c$ [20], with oscillation frequency bifurcating from finite value [2]. The scale separation in the VKS experiment, with α and Ω effects occurring in region of size $h_b \ll R$ is in any case a very interesting result, since it validates the main hypotheses underlining the α effect and opens the way to homogenization techniques [21]. It would also be interesting in the VKS experiment to vary the blade's height to see how it affects both the threshold and the oscillation frequencies and check their potential R/h_b scaling.

We thank A. Chiffaudel and F. Bakir for fruitful discussions, P.-P. Cortet for PIV measurements of Fig. 2, and the VKS team for magnetic field measurements used for Fig. 1.

[1] R. Monchaux *et al.*, Phys. Rev. Lett. **98**, 044502 (2007).
[2] R. Monchaux *et al.*, Phys. Fluids **21**, 035108 (2009).
[3] J. Boisson *et al.*, New J. Phys. **14**, 013044 (2012).
[4] F. Ravelet, A. Chiffaudel, F. Daviaud, and J. Léorat, Phys. Fluids **17**, 117104 (2005).
[5] F. Krause and K.-H. Rädler, *Mean-Field Magnetohydrodynamics and Dynamo Theory* (Pergamon, New York, 1980).
[6] H. K. Moffat, *Magnetic Field Generation in Electrically Conducting Fluids* (Cambridge University Press, Cambridge, England, 1978).
[7] F. Petrelis, N. Mordant, and S. Fauve, Geophys. Astrophys. Fluid Dyn. **101**, 289 (2007).

[8] R. Laguerre, C. Nore, A. Ribeiro, J. Léorat, J.-L. Guermond, and F. Plunian, Phys. Rev. Lett. **101**, 104501 (2008); Phys. Rev. Lett. **101**, 219902(E) (2008).
[9] C. J. P. Gissinger, Europhys. Lett. **87**, 39002 (2009).
[10] A. Giesecke, F. Stefani, and G. Gerbeth , Phys. Rev. Lett. **104**, 044503 (2010).
[11] B. Gallet *et al.*, Phys. Rev. Lett. **108**, 144501 (2012).
[12] "FLUENT 6.3 User's Guide," http://hpce.iitm.ac.in/website/Manuals/Fluent_6.3/fluent6.3/help/index.htm.
[13] K.-H. Rädler and M. Rheinhardt, Geophys. Astrophys. Fluid Dyn. **101**, 117 (2007).
[14] A. Brandenburg and K. Subramanian, Astron. Nachr. **328**, 507 (2007).
[15] P. Frick, V. Noskov, S. Denisov, and R. Stepanov, Phys. Rev. Lett. **105**, 184502 (2010).
[16] G. Verhille, N. Plihon, M. Bourgoin, P. Odier, and J.-F. Pinton, New J. Phys. **12**, 033006 (2010).
[17] P.-P. Cortet, P. Diribarne, R. Monchaux, A. Chiffaudel, F. Daviaud, and B. Dubrulle, Phys. Fluids **21**, 025104 (2009).
[18] The value of θ_c is of the order of 0.1 and slightly depends on the blades curvature, the aspect ratio of the experiment, or on the presence of different additional appendices in the flow (ring, baffles, etc.) [17].
[19] P. H. Roberts, Phil. Trans. R. Soc. A **272**, 663 (1972).
[20] M. Berhanu *et al.*, Eur. Phys. J. B **77**, 459 (2010).
[21] B. Dubrulle and U. Frisch, Phys. Rev. A **43**, 5355 (1991).

2 Axe 2

2.1 Toward an experimental von Kármán dynamo : Numerical studies for an optimized design

Physics of Fluids (2005), vol. 17, pp. 117104.

Numerical studies of a kinematic dynamo based on von Kármán type flows between two counterrotating disks in a finite cylinder are reported. The flow has been optimized using a water model experiment, varying the driving impellers' configuration. A solution leading to dynamo action for the mean flow has been found. This solution may be achieved in VKS2, the new sodium experiment to be performed in Cadarache, France. The optimization process is described and discussed ; then the effects of adding a stationary conducting layer around the flow on the threshold, on the shape of the neutral mode and on the magnetic energy balance are studied. Finally, the possible processes involved in kinematic dynamo action in a von Kármán flow are reviewed and discussed. Among the possible processes, we highlight the joint effect of the boundary-layer radial velocity shear and of the Ohmic dissipation localized at the flow/outer-shell boundary.

2.2 Study of the Aerodynamics/Aeroacoustics of an Axial-Flow Fan : Experimental Validation of a LES/LPCE/Brinkman Penalization Method

31st AIAA Aeroacoustics Conference (2010). AIAA paper n^o 2010-3869.

The seek for an efficient aerodynamic and aeroacoustic design of axial-flow fans is an important field of investigation for both academic and applied research. Improvements can only be made with a better understanding of the physical mechanisms arising in these machines that combine strong interactions between rotating and non-rotating parts of highly complex geometries. One way is to couple well-suited experimental investigations and innovative computational methods, that overtake the weaknesses of methods based for instance on aeroacoustic analogy. In this paper we study an axial fan using a new numerical method based on LES/LPCE Brinkman Penalization Method. This method is developed in the Department of Mechanical Engineering at Korea University. The experimental tests and validations are performed in the Laboratory of Fluid Dynamics at Arts et Metiers ParisTech in Paris. Detailed analysis of numerical and experimental results are in progress within the two partner teams. In this paper we present preliminary encouraging results.

2.3 Experimental study of blade thickness effects on the overall and local performances of a Controlled Vortex Designed axial-flow fan

Experimental Thermal and Fluid Science (2011), vol. 35, pp. 684-693.

The purpose of this work is to study the effects of blade thickness on the performances of an axial-flow fan. Two fans that differ only in the thickness of their blades were studied. The first fan was designed to be part of the cooling system of an automotive vehicle power unit and has very thin blades. The second fan has much thicker blades compatible with the rotomoulding conception process. The overall performances of the fans were measured in a test bench designed according to the ISO-5801 standard. The curve of aerodynamics characteristics (pressure head versus flow-rate) is slightly steeper for the fan with thick blades, and the nominal point is shifted towards lower flow-rates. The efficiency of the thick blades fan is lower than the efficiency of the fan with thin blades but remains high on a wider flow-rate range. The mean velocity fields downstream of the rotors are very similar at nominal points with less centrifugation for the thick blades fan. Moreover, the thick blades fan maintains an axial exit-flow on a wider range of flow-rates. The main differences concern local properties of the flow : phase-averaged velocities and wall pressure fluctuations strongly differ at the nominal flow-rates. The total level of fluctuations is lower for the thick blades fan that for the thin blades fan and the spectral decomposition of the wall fluctuations and velocity signals reveal more harmonics for the thick blades fan, with less correlation between the different signals. For this kind of turbomachinery, the use of thick blades could lead to a good compromise between aerodynamic and acoustic performances, on a wider operating range.

2.4 Experimental Study of the Instationary Flow Between Two Ducted Counter-Rotating Rotors

Journal of Engineering for Gas Turbines and Power (2013), vol. 135, pp. 22601.

The purpose of this work is to study experimentally the aerodynamic characteristics of a subsonic counter-rotating axial-flow fans system operating in a ducted configuration. The fans of diameter D=375 mm were designed to match the specification point using an original iterative method : the front rotor blade cascade is designed with a conventional inverse method, setting the radial distribution of the Euler work. The through-flow is then computed using an axisymmetric and radial equilibrium assumption, with empirical models of losses. The rear rotor is not conventional but is designed to straighten the radial profile of the tangential velocity. The design of the front rotor is then modified until the stage meets the requirements. The experimental setup is arranged such that the rotation rate of each fan is independently controlled and that the axial distance between the rotors can be varied from 17% to 310% of the midspan chord length. Systematic measurements of the global performances and local measurements of the velocity field and of the wall pressure fluctuations are performed, in order to first validate the design method, and to explore the effects of the two specific free parameters of the system, the axial spacing and the ratio of rotation rates. The results show that the efficiency is strongly increased compared to a conventional rotor or to a rotor-stator stage. The developed design method slightly overpredicts the pressure rise and slightly underpredicts the best ratio of rotation rates. Flow angle measurements downstream of the stage show that the outflow is not completely straightened at the design point. Finally, the system is highly efficient on a wide range of flow rates and pressure rises : this system has thus a very flexible use, with a large patch of high efficient operating points in the parameter space.

PHYSICS OF FLUIDS **17**, 117104 (2005)

Toward an experimental von Kármán dynamo: Numerical studies for an optimized design

F. Ravelet, A. Chiffaudel,[a] and F. Daviaud
Service de Physique de l'Etat Condensé, DSM/DRECAM/SPEC, CNRS/SPM URA 2464, CEA/Saclay, 91191 Gif-sur-Yvette Cedex, France

J. Léorat
LUTH, Observatoire de Paris-Meudon, 92195 Meudon, France

(Received 19 October 2004; accepted 1 September 2005; published online 15 November 2005)

Numerical studies of a kinematic dynamo based on von Kármán type flows between two counterrotating disks in a finite cylinder are reported. The flow has been optimized using a water model experiment, varying the driving impellers' configuration. A solution leading to dynamo action for the mean flow has been found. This solution may be achieved in VKS2, the new sodium experiment to be performed in Cadarache, France. The optimization process is described and discussed; then the effects of adding a stationary conducting layer around the flow on the threshold, on the shape of the neutral mode and on the magnetic energy balance are studied. Finally, the possible processes involved in kinematic dynamo action in a von Kármán flow are reviewed and discussed. Among the possible processes, we highlight the joint effect of the boundary-layer radial velocity shear and of the Ohmic dissipation localized at the flow/outer-shell boundary.
[DOI: 10.1063/1.2130745]

I. INTRODUCTION

In an electrically conducting fluid, kinetic energy can be converted into magnetic energy, if the flow is both of adequate topology and sufficient strength. This problem is known as the dynamo problem,[1] and is a magnetic seed-field instability. The equation describing the behavior of the magnetic induction field **B** in a fluid of resistivity η under the action of a velocity field **v** is writen in a dimensionless form:

$$\frac{\partial \mathbf{B}}{\partial t} = \nabla \times (\mathbf{v} \times \mathbf{B}) + \frac{\eta}{\mathcal{V}^* \mathcal{L}^*} \nabla^2 \mathbf{B}, \tag{1}$$

where $\mathcal{L}^*$ is a typical length scale and $\mathcal{V}^*$ is a typical velocity scale. In addition, one must take into account the divergence-free nature of **B**, the electromagnetic boundary conditions and the Navier-Stokes equations governing the fluid motion, including the backreaction of the magnetic field on the flow through the Lorentz force.

The magnetic Reynolds number $R_m = \mathcal{V}^* \mathcal{L}^* \eta^{-1}$, which compares the advection to the Ohmic diffusion, controls the instability. Although this problem is simple to set, it is still open. Although some flows lead to the dynamo instability with a certain threshold R_m^c, other flows do not, and antidynamo theorems are not sufficient to explain this sensitivity to flow geometry.[1] The two recent experimental success of Karlsruhe and Riga[2–6] are in good agreement with analytical and numerical calculations;[7–10] these two dynamos belong to the category of constrained dynamos: the flow is forced in pipes and the level of turbulence remains low. However, the saturation mechanisms of a dynamo are not well known, and the role of turbulence on this instability remains misunderstood.[11–17]

The next generation of experimental homogeneous unconstrained dynamos (still in progress, see, e.g., Frick *et al.*, Shew *et al.*, Marié *et al.*, and O'Connell *et al.* in the Cargèse 2000 workshop proceedings[18]) might provide answers to these questions. The VKS liquid-sodium experiment in Cadarache, France,[19–21] belongs to this category. The VKS experiment is based on a class of flows called von Kármán type flows. In a closed cylinder, the fluid is inertially set into motion by two coaxial counterrotating impellers fitted with blades. This paper being devoted to the hydrodynamical and magnetohydrodynamical (MHD) properties of the mean flow, let us first describe briefly the phenomenology of such mean flow. Each impeller acts as a centrifugal pump: the fluid rotates with the impeller and is expelled radially by the centrifugal effect. To ensure mass conservation the fluid is pumped in the center of the impeller and recirculates near the cylinder wall. In the exact counterrotating regime, the mean flow is divided into two toric cells separated by an azimuthal shear layer. Such a mean flow has the following features, known to favor dynamo action: differential rotation, lack of mirror symmetry and the presence of a hyperbolic stagnation point in the center of the volume. In the VKS experimental devices, the flow, inertially driven at kinetic Reynolds number up to 10^7 (see the following), is highly turbulent. As far as full numerical MHD treatment of realistic inertially driven high-Reynolds number flows cannot be carried out, this study is restricted to the kinematic dynamo capability of von Kármán mean flows.

Several measurements of induced fields have been performed in the first VKS device (VKS1),[20] in rather good agreement with previous numerical studies,[22] but no dynamo

---

[a] Author to whom correspondence should be addressed. Electronic mail: arnaud.chiffaudel@cea.fr

was seen: in fact the achievable magnetic Reynolds number in the VKS1 experiment remained below the threshold calculated by Marié *et al.*[22] A larger device—VKS2, with diameter 0.6 m and 300 kW power supply—is under construction. The main generic properties of mean-flow dynamo action have been highlighted by Marié *et al.*[22] on two different experimental von Kármán velocity fields. Further, various numerical studies in comparable spherical flows confirmed the strong effect of flow topology on dynamo action.[23,24] In the experimental approach, many parameters can be varied, such as the impellers' blade design, in order to modify the flow features. In addition, following Bullard and Gubbins,[25] several studies suggest adding a layer of stationary conductor around the flow to help the dynamo action. All these considerations lead us to consider the implementation of a static conducting layer in the VKS2 device and to perform a careful optimization of the mean velocity field by a kinematic approach of the dynamo problem.

Looking toward the actual VKS2 experiment, one should discuss the major remaining physical unexplored feature: the role of hydrodynamical turbulence. Turbulence in an inertially driven closed flow will be very far from homogeneity and isotropy. The presence of hydrodynamical small scale turbulence could act in two different ways: on the one hand, it may increase the effective magnetic diffusivity, inhibiting the dynamo action.[26] On the other hand, it could help the dynamo through a small-scale α effect.[27] Moreover, the presence of a turbulent mixing layer between the two counterrotating cells may move the instantaneous velocity field away from the time-averaged velocity field for large time scales.[28] As the VKS2 experiment is designed to operate above the predicted kinematic threshold presented in this paper, it is expected to give an experimental answer to this question of the role of turbulence on the instability. Further, if it exhibits dynamo action, it will shed light on the dynamical saturation regime which is outside the scope of the present paper.

In this paper, we report the optimization of the time-averaged flow in a von Kármán liquid sodium experiment. We design a solution which can be experimentally achieved in VKS2, the new device held in Cadarache, France. This solution particularly relies on the addition of a static conducting layer surrounding the flow. The paper is organized as follows. In Sec. II we first present the experimental and numerical techniques that have been used. In Sec. III, we present an overview of the optimization process which lead to the experimental configuration chosen for the VKS2 device. We study the influence of the shape of the impellers both on the hydrodynamical flow properties and on the onset of kinematic dynamo action. In Sec. IV, we focus on the understanding of the observed kinematic dynamo from a magnetohydrodynamical point of view: we examine the structure of the eigenmode and the effects of an outer conducting boundary. Finally, in Sec. V, we review some possible mechanisms leading to kinematic dynamo action in a von Kármán flow and propose some conjectural explanations based on our observations.

II. EXPERIMENTAL AND NUMERICAL TOOLS

A. What can be done numerically

The bearing of numerical simulations in the design of experimental fluid dynamos deserves some general comments. Kinetic Reynolds numbers of these liquid sodium flows are typically 10^7, well beyond any conceivable direct numerical simulation. Moreover, to describe effective MHD features, it would be necessary to treat very small magnetic Prandtl numbers, close to 10^{-5}, a value presently not within computational feasibility. Several groups are progressing in this way on model flows, for example, with large eddy simulations[15] which can reach magnetic Prandtl numbers as low as $10^{-2}-10^{-3}$. Another strong difficulty arises from the search of realistic magnetic boundary conditions treatment which prove in practice also to be difficult to implement, except for the spherical geometry.

An alternative numerical approach is to introduce a given flow in the magnetic induction equation (1) and to perform *kinematic dynamo* computations. This flow can be either analytical,[8,23] computed by pure hydrodynamical simulations (which may now be performed with Reynolds numbers up to a few thousands), or measured in laboratory water models[22,24] by laser Doppler velocimetry (LDV) or by particle imaging velocimetry. Such measurements lead to a map of the time-averaged flow and to the main properties of the fluctuating components: turbulence level, correlation times, etc. Kinematic dynamo computations have been successfully used to describe or to optimize the Riga[7] and Karlsruhe[8] dynamo experiments.

We will follow here the kinematic approach using the time-averaged flow measured in a water model at realistic kinetic Reynolds number. Indeed, potentially important features such as velocity fluctuations will not be considered. Another strong limitation of the kinematic approach is its linearity: computations may predict if an initial seed field grows, but the study of the saturation regime will rely exclusively on the results of the actual MHD VKS experiment.

B. Experimental measurements

In order to measure the time-averaged velocity field—hereafter simply denoted as the mean field—we use a water-model experiment which is a half-scale model of the VKS2 sodium device. The experimental setup, measurement techniques, and methods are presented in detail in Refs. 22 and 29. However, we present in the following an overview of our experimental issues and highlight the evolutions with respect to those previous works.

We use water as the working fluid for our study, noting that its hydrodynamical properties at 50 °C (kinematic viscosity ν and density ρ) are very close to those of sodium at 120 °C.

A sketch of the von Kármán experiments is presented in Fig. 1. The cylinder is of radius R_c and height $H_c=1.8R_c$. In the following, all the spatial quantities are given in units of $R_c=\mathcal{L}^*$. The hydrodynamical time scale is based on the im-

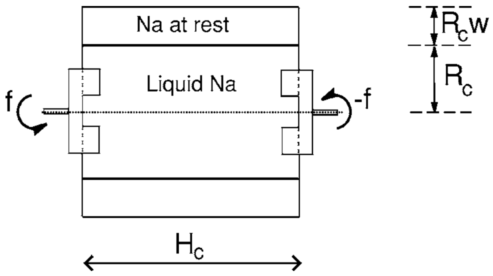

FIG. 1. Sketch of the VKS2 experiment. The container radius R_c is taken as unit scale. w is the dimensionless thickness of sodium at rest.

peller driving frequency f: if $\mathbf{V}$ is the measured velocity field for a driving frequency f, the dimensionless mean velocity field is thus $\mathbf{v}=(2\pi R_c f)^{-1}\mathbf{V}$.

The integral kinetic Reynolds number Re is typically 10^6 in the water-model, and 10^7 in the sodium device VKS2. The inertially driven flow is highly turbulent, with velocity fluctuations up to 40% of the maximum velocity.[20,22] In the water model, we measure the time-averaged velocity field by LDV. Data are averaged over typically 300 disk rotation periods. We have performed velocity measurements at several points for several driving frequencies: as expected for so highly turbulent a flow, the dimensionless velocity $\mathbf{v}$ does not depend on the integral Reynolds number $\mathrm{Re}=\mathcal{V}^*\mathcal{L}^*\nu^{-1}$.[30]

Velocity modulations at the blade frequency have been observed only in and very close to the interblade domains. These modulations are thus time averaged and we can consider the mean flow as a solenoidal axisymmetric vector field.[31] So the toroidal part of the velocity field V_θ (in cylindrical coordinates) and the poloidal part (V_z, V_r) are independent.

In the water-model experiment dedicated to the study reported in this paper, special care has been given to the measurements of velocity fields, especially near the blades and at the cylinder wall, where the measurement grid has been refined. The mechanical quality of the experimental setup ensures good symmetry of the mean velocity fields with respect to rotation of π around any diameter passing through the center of the cylinder ($\mathcal{R}_\pi$ symmetry). The fields presented in this paper are thus symmetrized by $\mathcal{R}_\pi$ with no noticeable changes in the profiles but with a slightly improved spatial signal-to-noise ratio. With respect to Ref. 22, the velocity fields are neither smoothed, nor stretched to different aspect ratios.

Figure 2 shows the mean flow produced by the optimal impeller. The mean flow respects the phenomenology given in the Introduction: it is composed of two toroidal cells separated by a shear layer, and two poloidal recirculation cells. High velocities are measured over the whole volume: the inertial stirring is actually very efficient. Typically, the average over the flow volume of the mean velocity field is of order of $0.3\times(2\pi R_c f)$.

In addition to velocity measurements, we perform global power consumption measurements: torques are measured through the current consumption in the motors given by the servo drives and have been calibrated by calorimetry.

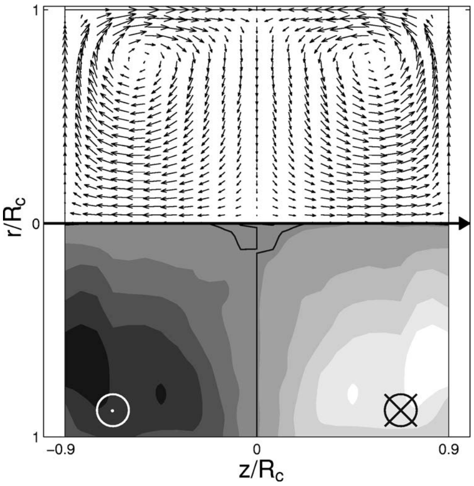

FIG. 2. Dimensionless mean velocity field measured by LDV and symmetrized for kinematic dynamo simulations. The cylinder axis is horizontal. Arrows correspond to the poloidal part of the flow and shading to the toroidal part. We use cylindrical coordinates (r,θ,z), with origin at the center of the cylinder.

C. Kinematic dynamo simulations

Once we know the time-averaged velocity field, we integrate the induction equation using an axially periodic kinematic dynamo code, written by J. Léorat.[32] The code is pseudospectral in the axial and azimuthal directions while the radial dependence is treated by a high-order finite difference scheme. The numerical resolution corresponds to a grid of 48 points in the axial direction, 4 points in the azimuthal direction (corresponding to wave numbers $m=0,\pm 1$) and 51 points in the radial direction for the flow domain. This spatial grid is the common basis of our simulations and has been refined in some cases. The time scheme is second-order Adams-Bashforth with diffusive time unit $t_d=R_c^2\eta^{-1}$. The typical time step is 5×10^{-6} and simulations are generally carried out over 1 time unit.

Electrical conductivity and magnetic permeability are homogeneous and the external medium is insulating. Implementation of the magnetic boundary conditions for a finite cylinder is difficult, due to the nonlocal character of the continuity conditions at the boundary of the conducting fluid. In contrast, axially periodic boundary conditions are easily formulated, since the harmonic external field then has an analytical expression. We thus choose to look for axially periodic solutions, using a relatively fast code, which allows us to perform parametric studies. To validate our choice, we compared our results with results from a finite cylinder code (F. Stefani, private communication, 2002) for some model flows and a few experimental flows. In all these cases, the periodic and the finite cylinder computations give comparable results. This remarkable agreement may be due to the peculiar flow and to the magnetic eigenmodes symmetries: we do not claim that it may be generalized to other flow geometries. Indeed, the numerical elementary box consists of two mirror-symmetric experimental velocity fields in order to avoid strong velocity discontinuities along the z axis. The magnetic eigenmode could be either symmetric or antisymmetric with respect to this artificial mirror symmetry.[33] In almost all of our simulations, the magnetic field is mirror-antisymmetric, and we verify that no axial currents cross the mirror boundary. The few exotic symmetric cases we encountered cannot be used for optimization of the experiment.

Further details on the code can be found in Ref. 32. We use a mirror-antisymmetric initial magnetic seed field optimized for a fast transient.[22] Finally, we can act on the electromagnetic boundary conditions by adding a layer of stationary conductor of dimensionless thickness w, corresponding to sodium at rest surrounding the flow exactly as in the experiment (Fig. 1). This extension is made while keeping the grid radial resolution constant (51 points in the flow region). The velocity field we use as input for the numerical simulations is thus simply in an homogeneous conducting cylinder of radius $1+w$:

$$\mathbf{v} \equiv \mathbf{v}_{\text{measured}} \quad \text{for} \quad 0 \leq r \leq 1,$$

$$\mathbf{v} = 0 \quad \text{for} \quad 1 \leq r \leq 1+w.$$

III. OPTIMIZATION OF THE VKS EXPERIMENT

A. Optimization process

The goal of our optimization process is to find the impeller whose mean velocity field leads to the lowest R_m^c for the lowest power cost. We have to find a solution feasible in VKS2, i.e., with liquid sodium in a 0.6 m diameter cylinder with 300 kW power supply. We performed an iterative optimization loop: for a given configuration, we measure the mean velocity field and the power consumption. Then we simulate the kinematic dynamo problem. We try to identify features favoring dynamo action and modify parameters in order to reduce the threshold and the power consumption and go back to the loop.

B. Impeller tunable parameters

The impellers are flat disks of radius R fitted with 8 blades of height h. The blades are arcs of circles, with a curvature radius C, whose tangents are radial at the center of the disks. We use the angle $\alpha = \arcsin(R/2C)$ to label the different curvatures (see Fig. 3). For straight blades $\alpha = 0$. By convention, we use positive values to label the direction corresponding to the case where the fluid is set into motion by the convex face of the blades. In order to study the opposite curvature ($\alpha < 0$) we just rotate the impeller in the other direction. The two counterrotating impellers are separated by H_c, the height of the cylinder. We fixed the aspect ratio H_c/R_c of the flow volume to 1.8 as in the VKS device. In practice we successively examine the effects of each parameter h, R, and α on global quantities characterizing the mean flow. We then varied the parameters one by one, until we found a relative optimum for the dynamo threshold. We tested 12 different impellers, named TMxx, with three radii ($R = 0.5$, 0.75, and 0.925), various curvature angles α and different blade heights h.

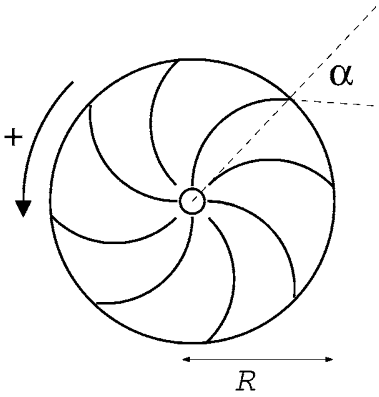

FIG. 3. Sketch of the impeller parameters. R is the dimensionless radius and α is the blade curvature angle. The sign of α is determined by the sense of rotation: positive when rotated anticlockwise.

C. Global quantities and scaling relations

We know from empirical results[22–24] that the poloidal to toroidal ratio Γ of the flow has a great impact on the dynamo threshold. Moreover, a purely toroidal flow is unable to sustain dynamo action,[34,35] whereas it is possible for a purely poloidal flow.[36,37] We also note that, for a Ponomarenko flow, the pitch parameter plays a major role.[7,16,17] All these results lead us to first focus on the ratio

$$\Gamma = \frac{\langle P \rangle}{\langle T \rangle},$$

where $\langle P \rangle$ is the spatially averaged value of the poloidal part of the mean flow and $\langle T \rangle$ the average of the toroidal part.

Another quantity of interest is the velocity factor $\mathcal{V}$: the dimensionless maximum value of the velocity. In our simulations, the magnetic Reynolds number R_m is based on the velocity factor, i.e., on a typical *measured* velocity in order to take into account the stirring efficiency:

$$\mathcal{V} = \frac{\max(\|\mathbf{V}\|)}{2\pi R_c f},$$

$$R_m = 2\pi R_c^2 f \mathcal{V}/\eta.$$

We also define a power coefficient K_p by dimensional analysis. We write the power $\mathcal{P}$ given by a motor to sustain the flow as follows:

$$\mathcal{P} = K_p(\text{Re}, \text{geometry}) \rho R_c^5 \Omega^3,$$

with ρ the density of the fluid and $\Omega = 2\pi f$ the driving pulsation. We have checked[29] that K_p does not depend on the Reynolds number Re as expected for so highly turbulent inertially driven flows.[30]

The velocity factor measures the stirring efficiency: the greater $\mathcal{V}$, the lower the rotation frequency needed to reach a given velocity. Besides, a lower K_p implies that less power is needed to sustain a given driving frequency. The dimensionless number which we need to focus on compares the velocity effectively reached in the flow to the power consumption. We call it the MaDo number:

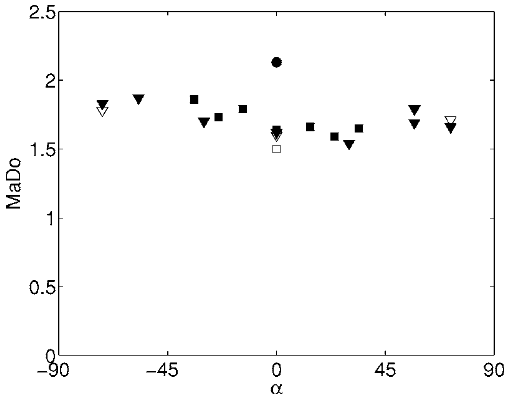

FIG. 4. MaDo number vs α for all the impellers we have tested. $R=0.925$ (▼), $R=0.75$ (■), and $R=0.5$ (●). Closed symbols: $h=0.2$ and open symbols: $h\leq 0.1$.

$$\mathrm{MaDo}=\frac{\mathcal{V}}{K_p^{1/3}}.$$

The greater MaDo, the less power needed to reach a given velocity (i.e., a given magnetic Reynolds number). The MaDo number is thus a hydrodynamical efficiency coefficient. To make the VKS experiment feasible at laboratory scale, it is necessary both to have great MaDo numbers and low critical magnetic Reynolds numbers R_m^c. The question underlying the process of optimization is to know if we can, on the one hand, find a class of impellers with mean flows exhibiting dynamo action, and, on the other hand, if we can increase the ratio MaDo/R_m^c. This means that we have to look both at the global hydrodynamical quantities and at the magnetic induction stability when varying the impellers' tunable parameters h, R, and α.

Figure 4 presents MaDo for the entire set of impellers. For our class of impellers, the MaDo number remains of the same order of magnitude within ±10%. Only the smallest diameter impeller ($R=0.5$) exhibits a slightly higher value. In the ideal case of homogeneous isotropic turbulence, far from boundaries, we can show that what we call the MaDo number is related to the Kolmogorov constant $C_K\simeq 1.5$.[38] The Kolmogorov constant is related to the kinetic energy spatial spectrum:

$$E(k)=C_K\epsilon^{2/3}k^{-5/3},$$

where ϵ is the dissipated power per unit mass and k the wave number. If we assume that ϵ is homogeneous and that $\mathcal{P}$ is the total dissipated power we measure, we have

$$\epsilon=\frac{\mathcal{P}}{\rho\pi R_c^2H_c}.$$

Using the definition

$$\frac{1}{2}\langle v^2\rangle=\int E(k)dk$$

and assuming $\frac{1}{2}\langle v^2\rangle\simeq\frac{1}{2}\mathcal{V}^2$ and using the steepness of the spectrum, we obtain

$$E(k_0)=\tfrac{1}{3}\mathcal{V}^2k_0^{-1},$$

with $k_0=2\pi/R_c$ the injection scale. Then the relation between the MaDo number and C_K is

$$\mathrm{MaDo}^2\simeq 3\pi^{-4/3}\left(\frac{H_c}{R_c}\right)^{-2/3}C_K\simeq 0.44C_K,$$

i.e., with $C_K=1.5$, we should have, for homogeneous isotropic turbulence $\mathrm{MaDo}\simeq 0.81$. In our closed system with blades, we recover the same order of magnitude, and the fact that MaDo is almost independent of the driving system. Thus, there is no obvious optimum for the hydrodynamical efficiency. Between various impellers producing dynamo action, the choice will be dominated by the value of the threshold R_m^c.

Let us first eliminate the effect of the blade height h. The power factor K_p varies quasilinearly with h. As MaDo is almost constant, smaller h impellers require higher rotation frequencies, increasing the technical difficulties. We choose $h=0.2$, a compromise between stirring efficiency and the necessity to keep the free volume sufficiently large.

D. Influence of the poloidal/toroidal ratio Γ

In our cylindrical von Kármán flow without a conducting layer ($w=0$), there seems to be an optimal value for Γ close to 0.7. Since the mean flow is axisymmetric and divergence-free, the ratio Γ can be changed numerically by introducing an arbitrary multiplicative factor on, say, the toroidal part of the velocity field. In the following, Γ_0 stands for the experimental ratio for the measured mean velocity field $\mathbf{v}^{\mathrm{exp}}$, whereas Γ stands for a numerically adjusted velocity field $\mathbf{v}^{\mathrm{adj}}$. This flow is simply adjusted as follows:

$$v_\theta^{\mathrm{adj}}=v_\theta^{\mathrm{exp}},$$

$$v_r^{\mathrm{adj}}=(\Gamma/\Gamma_0)\cdot v_r^{\mathrm{exp}},$$

$$v_z^{\mathrm{adj}}=(\Gamma/\Gamma_0)\cdot v_z^{\mathrm{exp}}.$$

In Fig. 5, we plot the magnetic energy growth rate σ (twice the magnetic field growth rate) for different values of Γ, for magnetic Reynolds number $R_m=100$ and without conducting layer ($w=0$). The two curves correspond to two different mean velocity fields which have been experimentally measured in the water model (they correspond to the TM71 and TM73 impellers, see Table I for their characteristics). We notice that the curves show the same shape with maximum growth rate at $\Gamma\simeq 0.7$, which confirms the results of Ref. 22.

For $\Gamma\lesssim 0.6$, oscillating damped regimes (open symbols in Fig. 5) are observed. We plot the temporal evolution of the magnetic energy in the corresponding case in Fig. 6: these regimes are qualitatively different from the oscillating regimes already found in Ref. 22 for *non*-$\mathcal{R}_\pi$ symmetric $\Gamma=0.7$ velocity fields, consisting of one mode with a complex growth rate: the magnetic field is a single traveling wave, and the magnetic energy, integrated over the volume, evolves monotonically in time.

In our case, the velocity field is axisymmetric and $\mathcal{R}_\pi$ symmetric, i.e., corresponds to the group O(2).[33] The evolu-

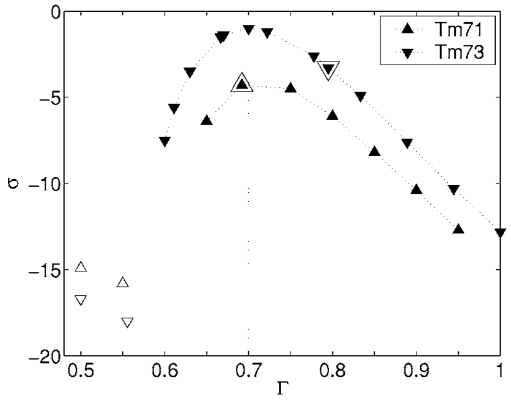

FIG. 5. Magnetic energy growth rate σ vs numerical ratio Γ. $R_m=100$ and $w=0$. Simulations performed for two different mean velocity fields [impellers TM71 (▲) and TM73 (▼) of radius $R=0.75$]. Larger symbols correspond to natural Γ_0 of the impeller. The vertical dashed line corresponds to optimal $\Gamma=0.7$. Closed symbols stand for stationary regimes whereas open symbols stand for oscillating regimes for $\Gamma \lesssim 0.6$.

tion operator for the magnetic field also respects these symmetries. It is known that symmetries strongly constrain the nature of eigenvalues and eigenmodes of linear stability problems. We observe two types of nonaxisymmetric $m=1$ solutions consistent with the O(2) group properties:

- A steady bifurcation with a real eigenvalue. The eigenmode is $\mathcal{R}_\pi$ symmetric with respect to a certain axis. We always observed such stationary regimes for $\Gamma \gtrsim 0.6$.
- Oscillatory solutions in the shape of standing waves associated with complex-conjugate eigenvalues.

The latter oscillatory solutions are observed for $\Gamma \lesssim 0.6$. Since the temporal integration starts with a $\mathcal{R}_\pi$ symmetric initial condition for the magnetic field, we obtain decaying standing waves corresponding to the sum of two modes with complex-conjugate eigenvalues and the same amplitudes. The magnetic energy therefore decays exponentially while pulsating [Fig. 6(a)].

The same feature has been reported for analytical "$s_2^0t_2^0$-like flows" in a cylindrical geometry with a Galerkin analysis of neutral modes and eigenvalues for the induction equation.[29] A major interest of the latter method is that it gives the structure of the modes: one mode is localized near one impeller and rotates with it, the other is localized and rotates with the other impeller. Growing oscillating dynamos are rare in our system: a single case has been observed, for TM71(–) ($\Gamma_0=0.53$) with a $w=0.4$ conducting layer at

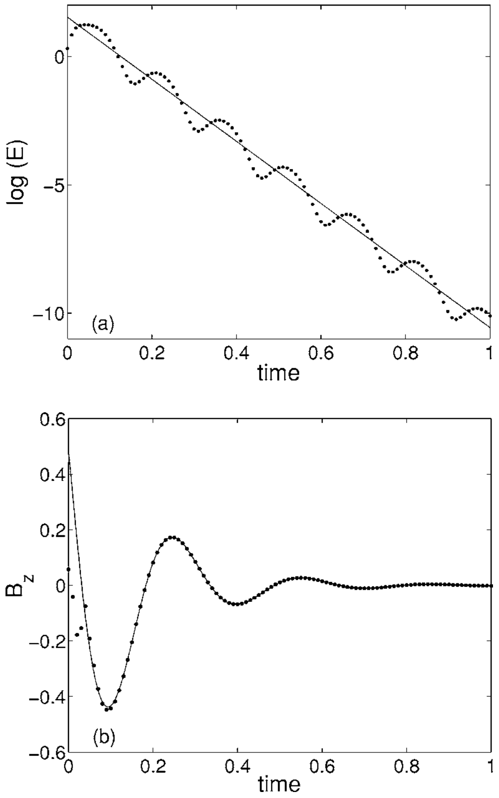

FIG. 6. Typical damped oscillating regime for impeller TM70 at $\Gamma=0.5$, $w=0$, and $R_m=140$. (a) Temporal evolution of the magnetic energy $E=\int \mathbf{B}^2$. The straight line is a linear fit of the form $E(t)=E_0\exp(\sigma t)$ and gives the temporal growth rate $\sigma=-12.1$. (b) Temporal evolution of the z component of $\mathbf{B}$ at the point $r=0.4$, $\theta=0$, and $z=-0.23$ with a nonlinear fit of the form: $B_z(t)=a\exp(\sigma t/2)\cos(\omega t+\phi)$ which gives $\sigma=-12.2$ and $\omega=20.7$.

TABLE I. Global hydrodynamical dimensionless quantities (see text for definitions) for the radius $R=0.75$ impeller family, rotating counterclockwise (+), or clockwise (−) (see Fig. 3). The last two columns present the thresholds for kinematic dynamo action with ($w=0.4$) and without ($w=0$) conducting layer. Optimal values appear in bold font. Most negative curvatures have not been investigated (n.i.) but the TM71-, which presents an oscillatory (o) dynamo instability for $R_m^c=197$ with $w=0.4$. (1): the TM70 impeller ($\Gamma_0=0.60$) has a tricky behavior, exchanging stability between steady modes, oscillatory modes and a singular mode which is mirror symmetric with respect to the periodization introduced along z and thus not physically relevant.

Impeller	α (deg)	$\langle P\rangle$	$\langle T\rangle$	$\Gamma_0=\dfrac{\langle P\rangle}{\langle T\rangle}$	$\langle P\rangle\cdot\langle T\rangle$	$\langle H\rangle$	$\mathcal{V}$	K_p	MaDo	R_m^c ($w=0$)	R_m^c ($w=0.4$)
TM74-	−34	0.15	0.34	0.46	0.052	0.43	0.78	0.073	1.86	n.i.	n.i.
TM73-	−24	0.16	0.34	0.48	0.055	0.41	0.72	0.073	1.73	n.i.	n.i.
TM71-	−14	0.17	0.33	0.53	0.057	0.49	0.73	0.069	1.79	n.i.	197 (o)
TM70	0	0.18	0.30	0.60	0.056	0.47	0.65	0.061	1.64	(1)	(1)
TM71	+14	0.19	0.28	**0.69**	0.053	0.44	0.64	0.056	1.66	**179**	51
TM73	+24	0.20	0.25	**0.80**	0.051	0.44	0.60	0.053	1.60	180	**43**
TM74	+34	0.21	0.24	0.89	0.050	0.44	0.58	0.043	1.65	∞	44

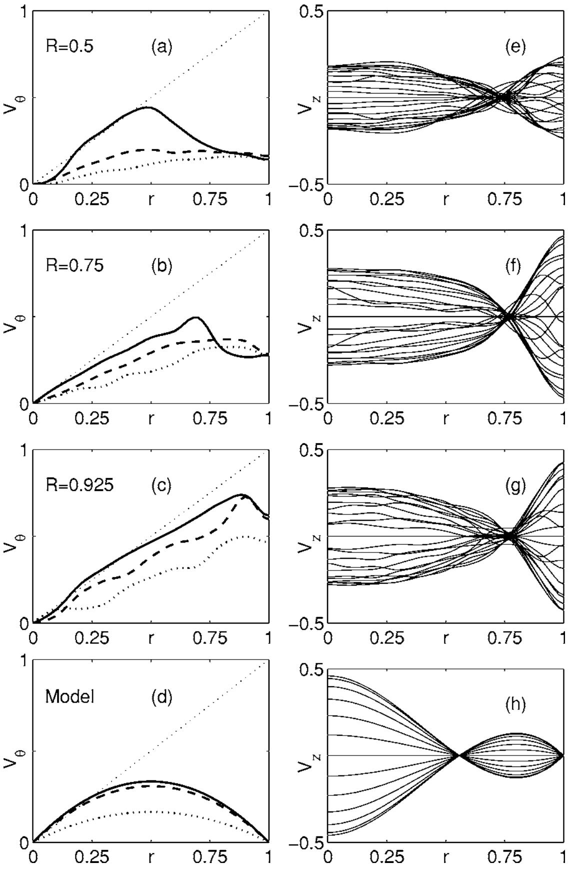

FIG. 7. [(a)–(d)] Radial profiles of toroidal velocity v_θ for $z=0.3$ (dotted line), 0.675 (dashed line), and 0.9 (solid line) and [(e)–(h)] axial velocity v_z for various equidistant z between the two rotating disks. From top to bottom: experimental flow for [(a) and (e)]: $R=0.5$, [(b) and (f)]: $R=0.75$, [(c) and (g)]: $R=0.925$ impeller, and [(d) and (h)]: model analytical flow [see Eq. (3) and discussion in the text].

$R_m=215$ ($R_m^c=197$, see Table I). Such high a value for the magnetic Reynolds number is out of the scope of our experimental study, and is close to the practical upper limit of the numerical code.

Experimental dynamo action will thus be sought in the stationary regimes domain $\Gamma \gtrsim 0.6$. Without a conducting layer, we must look for the optimal impeller around $\Gamma_0 \simeq 0.7$.

E. Effects of the impeller radius *R*

One could *a priori* expect that a very large impeller is favorable to the hydrodynamical efficiency. This is not the case. For impellers with straight blades, MaDo slightly decreases with R: for respectively $R=0.5$, 0.75, and 0.925, we respectively get MaDo=2.13, 1.64, and 1.62. This tendency is below the experimental error. We thus consider that MaDo does not depend on the impeller.

Nevertheless one should not forget that $\mathcal{V}$ varies quasilinearly with impeller radius R: if the impeller becomes smaller it must rotate faster to achieve a given value for the magnetic Reynolds number, which may again cause mechanical difficulties. We do not explore radii R smaller than 0.5.

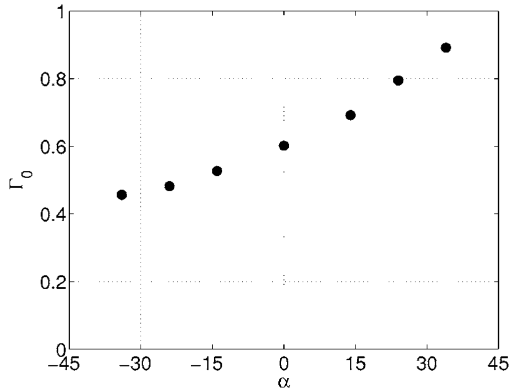

FIG. 8. Γ_0 vs α for four impellers of radius $R=0.75$ rotated in the positive and the negative directions (see Table I).

Concerning the topology of the mean flow, there are no noticeable effects of the radius R on the poloidal part. We always have two toric recirculation cells, centered at a radius r_p close to 0.75 ± 0.02 and almost constant for all impellers [see Figs. 7(e)–7(h)]. The fluid is pumped to the impellers for $0<r<r_p$ and is reinjected in the volume $r_p<r<1$. This can be interpreted as a geometrical constraint to ensure mass conservation: the circle of radius $r=\sqrt{2}/2$ (very close to 0.75) separates the unit disk into two regions of the same area.

The topology of the toroidal part of the mean flow now depends on the radius of the impeller. The radial profile of v_θ shows stronger departure from solid-body rotation for smaller R [Figs. 7(a)–7(d)]: this will be emphasized in the discussion. We performed simulations for three straight blades impellers of radii $R=0.5$, $R=0.75$, and $R=0.925$; without a conducting shell ($w=0$) and with a conducting layer of thickness $w=0.4$. We have integrated the induction equation for the three velocity fields numerically set to various Γ and compared the growth rates. The impeller of radius $R=0.75$ close to the radius of the center of the poloidal recirculation cells systematically yields the greatest growth rate. Thus, radius $R=0.75$ has been chosen for further investigations.

F. Search for the optimal blade curvature

The hydrodynamical characteristics of the impellers of radius $R=0.75$ are given in Table I. For increasing blade curvature the average value of the poloidal velocity $\langle P\rangle$ increases whereas the average value of the toroidal velocity $\langle T\rangle$ decreases: the ratio Γ_0 is a continuous growing function of curvature α (Fig. 8). A phenomenological explanation for the $\langle T\rangle$ variation can be given. The fluid pumped by the impeller is centrifugally expelled and is constrained to follow the blades. Therefore, it exits the impeller with a velocity almost tangent to the blade exit angle α. Thus, for $\alpha<0$ (respectively, $\alpha>0$), the azimuthal velocity is bigger (respectively, smaller) than the solid body rotation. Finally, it is possible to adjust Γ_0 to a desired value by choosing the appropriate curvature α, in order to lower the threshold for dynamo action.

Without a conducting shell, the optimal impeller is the

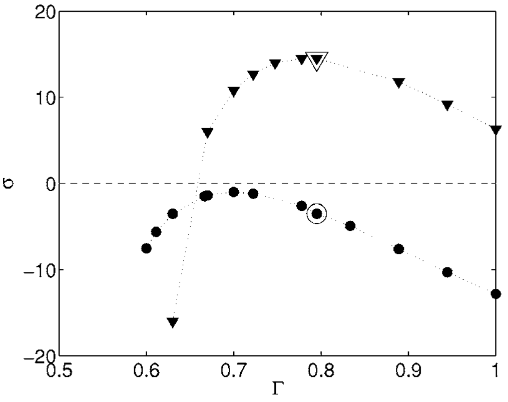

FIG. 9. Shift in the optimal value of Γ when adding a conducting layer. Magnetic energy growth rate σ vs Γ for $w=0$ (●) and $w=0.4$ (▼). Impeller TM73, $R_m=100$. Larger symbols mark the natural Γ_0 of the impeller.

TM71 ($\Gamma_0=0.69$). But its threshold $R_m^c=179$ cannot be achieved in the VKS2 experiment. We therefore must find another way to reduce R_m^c, the only relevant factor for the optimization.

G. Optimal configuration to be tested in the VKS2 sodium experiment

As in the Riga experiment,[4,7] and as in numerical studies of various flows,[25,39,40] we consider a stationary layer of fluid sodium surrounding the flow. This significantly reduces the critical magnetic Reynolds number, but also slightly shifts the optimal value for Γ. We have varied w between $w=0$ and $w=1$; since the experimental VKS2 device is of fixed overall size (diameter 0.6 m), the flow volume decreases while increasing the static layer thickness w. A compromise between this constraint and the effects of increasing w has been found to be $w=0.4$ and we mainly present here results concerning this value of w. In Fig. 9, we compare the curves obtained by numerical variation of the ratio Γ for the same impeller at the same R_m, in the case $w=0$, and $w=0.4$. The growth rates are much higher for $w=0.4$, and the peak of the curve shifts from 0.7 to 0.8. We have performed simulations for velocity fields achieved using four different impellers (Fig. 10), for $w=0.4$ at $R_m=43$: the result is very robust, the four curves being very close.

In Fig. 11, we plot the growth rates σ of the magnetic energy simulated for four experimentally measured mean velocity fields at various R_m and for $w=0.4$. The impeller TM73 was designed to create a mean velocity field with $\Gamma_0=0.80$. It appears to be the best impeller, with a critical magnetic Reynolds number of $R_m^c=43$. Its threshold is divided by a factor 4 when adding a layer of stationary conductor. This configuration (TM73, $w=0.4$) will be the first one tested in the VKS2 experiment. The VKS2 experiment will be able to reach the threshold of kinematic dynamo action for the mean part of the flow. Meanwhile, the turbulence level will be high and could lead to a shift or even disappearance of the kinematic dynamo threshold. In Sec. IV, we examine in detail the effects of the boundary conditions on the TM73 kinematic dynamo.

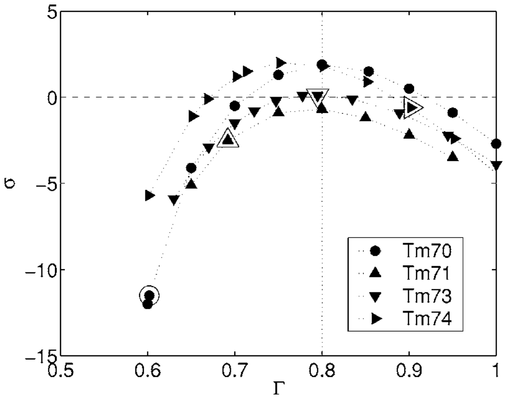

FIG. 10. Growth rate σ of magnetic energy vs numerical ratio Γ. $R_m=43$ and $w=0.4$ for four different $R=0.75$ impellers: TM70 (●), TM71 (▲), TM73 (▼), and TM74 (▶). Larger symbols mark the natural Γ_0 of each impeller.

H. Role of flow helicity versus poloidal/toroidal ratio

Most large scale dynamos known are based on helical flows.[1,41] As a concrete example, while successfully optimizing the Riga dynamo experiment, Stefani *et al.*[7] noticed that the best flows were helicity maximizing. The first point we focused on during our optimization process, i.e., the existence of an optimal value for Γ, leads us to address the question of the links between Γ and mean helicity $\langle H\rangle$. In our case, for aspect ratio $H_c/R_c=1.8$ and impellers of radius $R=0.75$, the mean helicity at a given rotation rate $\langle H\rangle=\int \mathbf{v}\cdot(\nabla\times\mathbf{v})rdrdz$ does not depend on the blade curvature (see Table I). Observation of Fig. 12 also reveals that the dominant contribution in the helicity scalar product is the product of the toroidal velocity $(v_\theta \propto \langle T\rangle)$ by the poloidal recirculation cells vorticity $[(\nabla\times\mathbf{v})_\theta \propto \langle P\rangle]$. We can therefore assume the scaling $\langle H\rangle \propto \langle P\rangle\langle T\rangle$, which is consistent with the fact that the product $\langle P\rangle\cdot\langle T\rangle$ and $\langle H\rangle$ are both almost constant (Table I).

To compare the helicity content of different flows, we now consider the mean helicity at a given R_m, $\langle H\rangle/\mathcal{V}^2$, more relevant for the dynamo problem. Figure 13 presents $\langle H\rangle/\mathcal{V}^2$

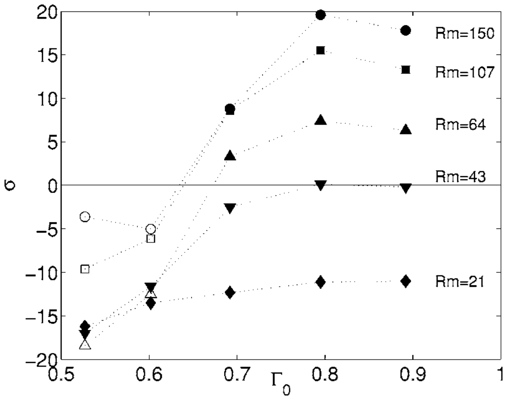

FIG. 11. Growth rate σ vs natural ratio Γ_0 for five impellers at various R_m and $w=0.4$. From left to right: TM71- ($\Gamma_0=0.53$), TM70 ($\Gamma_0=0.60$), TM71 ($\Gamma_0=0.69$), TM73 ($\Gamma_0=0.80$), and TM74 ($\Gamma_0=0.89$) (see also Table I). Closed symbols: stationary modes and open symbols: oscillating modes.

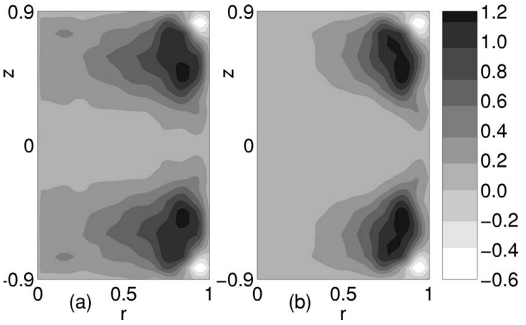

FIG. 12. Contours of kinetic helicity $H=\mathbf{v}\cdot(\nabla\times\mathbf{v})$ for TM73 velocity field. (a) Total helicity and (b) azimuthal contribution $v_\theta\cdot(\nabla\times\mathbf{v})_\theta$ is dominant.

vs Γ_0 for all $h=0.2$ impellers. The $R=0.75$ family reaches a maximum of order of 1 for $\Gamma_0\simeq 0.9$. This tendency is confirmed by the solid curve which shows a numerical variation of Γ for the TM73 velocity field and is maximum for $\Gamma=1$. In addition, even though $R=0.925$ impellers give reasonably high values of helicity near $\Gamma=0.5$, there is an abrupt break in the tendency for high curvature: TM60 (see Ref. 22) exhibits large $\Gamma_0=0.9$ but less helicity than TM74. Inset in Fig. 13 highlights this optimum for $\langle H\rangle/\mathcal{V}^2$ versus impeller radius R. This confirms the impeller radius $R=0.75$ we have chosen during the optimization described previously.

Since the optimal value toward dynamo action for the ratio Γ (close to 0.7–0.8, depending on w) is lower than 1, the best velocity field is not absolutely helicity maximizing. In other words, the most dynamo promoting flow contains more toroidal velocity than the helicity-maximizing flow. As shown by Leprovost,[42] one can interpret the optimal Γ as a quantity that maximizes the product of mean helicity by a measure of the ω effect, i.e., the product $\langle H\rangle\langle T\rangle\sim\langle P\rangle\langle T\rangle^2$.

IV. IMPACT OF A CONDUCTING LAYER ON THE NEUTRAL MODE AND THE ENERGY BALANCE FOR THE VKS2 OPTIMIZED VELOCITY FIELD

In this section, we discuss the mean velocity field produced between two counterrotating TM73 impellers in a cylinder of aspect ratio $H_c/R_c=1.8$, like the first experimental configuration chosen for the VKS2 experiment. See Table I for the characteristics of this impeller, and Fig. 2 for a plot of the mean velocity field. We detail the effects of adding a static layer of conductor surrounding the flow and compare the neutral mode structures, the magnetic energy and spatial distribution of current density for this kinematic dynamo.

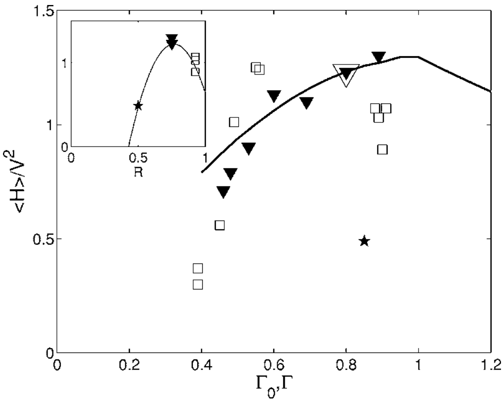

FIG. 13. Mean helicity at a given R_m ($\langle H\rangle/\mathcal{V}^2$) vs poloidal over toroidal ratio. The $R=0.75$ impeller series (▼) is plotted as a function of Γ_0. The large open symbol stands for TM73 at Γ_0 and the solid line stands for the same quantity plotted vs numerical variation of TM73 velocity field (Γ). We also plot $\langle H\rangle/\mathcal{V}^2$ vs Γ_0 for the $R=0.5$ (★) and $R=0.925$ (□) impellers. The inset presents $\langle H\rangle/\mathcal{V}^2$ vs impeller radius R for impellers of $0.8\lesssim\Gamma_0\lesssim 0.9$.

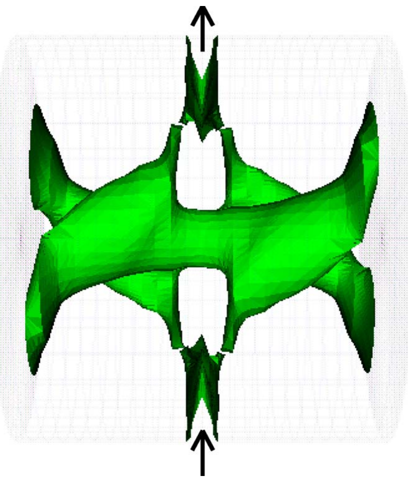

FIG. 14. Isodensity surface of magnetic energy (50% of the maximum) for the neutral mode without conducting layer ($w=0$). Cylinder axis is horizontal. Arrows stand for the external dipolar field source regions.

A. Neutral mode for $w=0$

Without a conducting layer, this flow exhibits dynamo action with a critical magnetic Reynolds number $R_m^c=180$. The neutral mode is stationary in time and has an $m=1$ azimuthal dependency. In Fig. 14, we plot an isodensity surface of the magnetic energy (50% of the maximum) in the case $w=0$ at $R_m=R_m^c=180$. The field is concentrated near the axis into two twisted banana-shaped regions of strong axial field. Near the interface between the flow and the outer insulating medium, there are two small sheets located on either side of the plane $z=0$ where the magnetic field is almost transverse to the external boundary and dipolar. The topology of the neutral mode is very close to that obtained by Marié *et al.*[22] with different impellers, and to that obtained on analytical $s_2^0t_2^0$-like flows in a cylindrical geometry with the previously described Galerkin analysis.[22]

In Fig. 15 we present sections of the $\mathbf{B}$ and $\mathbf{j}$ fields, where $\mathbf{j}=\nabla\times\mathbf{B}$ is the dimensionless current density. The scale for $\mathbf{B}$ is chosen such that the magnetic energy integrated over the volume is unity. Since the azimuthal dependence is $m=1$, two cut planes are sufficient to describe the neutral mode. In the bulk where twisted-banana-shaped structures are identified, we note that the toroidal and poloidal parts of $\mathbf{B}$ are of the same order of magnitude and that $\mathbf{B}$ is concentrated near the axis, where it experiences strong stretching due to the stagnation point in the velocity field. Around the center of the flow's recirculation loops ($r\simeq 0.7$ and $z\simeq\pm 0.5$ see Fig. 2) we note a low level of magnetic field: it is expelled from the vortices. Close to the outer boundary, we mainly observe a strong transverse dipolar field [Fig. 15(a)] correlated with two small loops of very

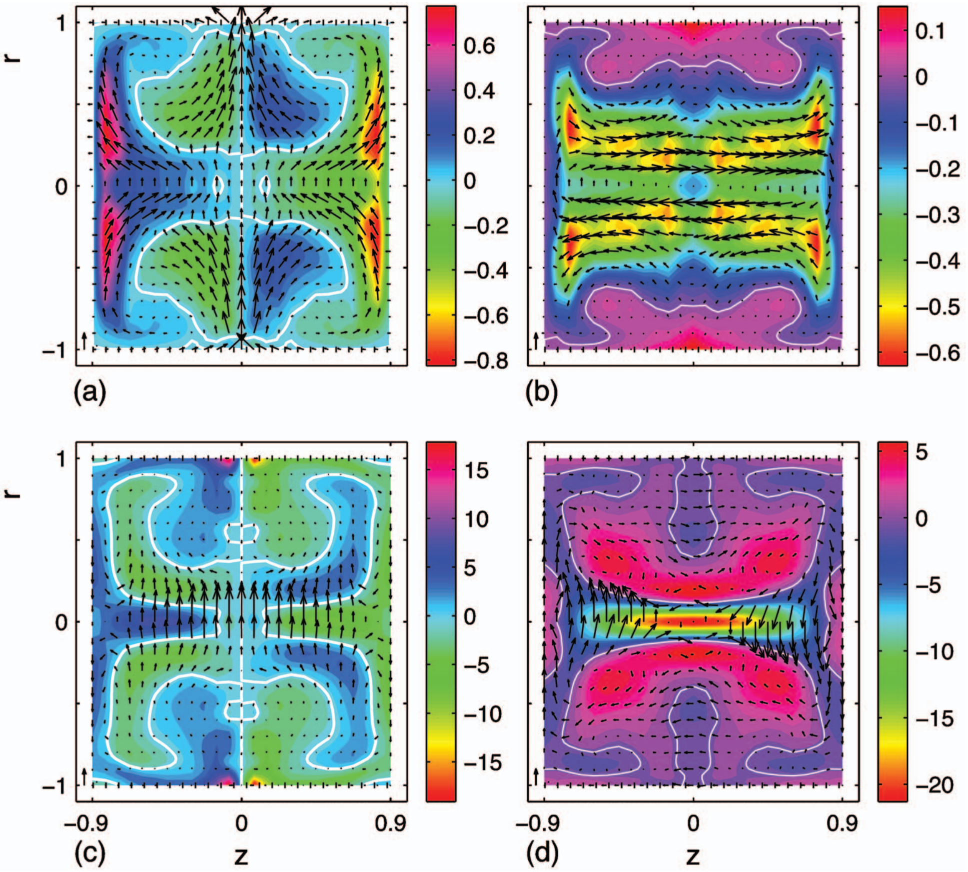

FIG. 15. (Color). Meridional sections of **B** and **j** fields for the neutral mode with $w=0$. **B** is normalized by the total magnetic energy. Arrows correspond to components lying in the cut plane, and color code to the component transverse to the cut plane. A unit arrow is set into the lower left corner of each panel: (a) **B** field, $\theta=0$; (b) **B** field, $\theta=\pi/2$; (c) **j** field, $\theta=0$; and (d) **j** field, $\theta=\pi/2$.

strong current density **j** [Fig. 15(c)]. These current loops seem constrained by the boundary, and might dissipate a great amount of energy by the Joule effect (see discussion below).

B. Effects of the conducting layer

As indicated in the first section, the main effect of adding a conducting layer is to strongly reduce the threshold. In Fig. 16, we plot the critical magnetic Reynolds number for increasing values of the layer thickness. The reduction is significant: the threshold is already divided by 4 for $w=0.4$ and the effects tends to saturate exponentially with a characteristic thickness $w=0.14$ (fit in Fig. 16), as observed for an α^2 model of the Karlsruhe dynamo by Avalos *et al.*[40] Adding the layer also modifies the spatial structure of the neutral mode. The isodensity surface for $w=0.6$ is plotted in Fig. 17 with the corresponding sections of **B** and **j** fields in Fig. 18. The two twisted bananas of the axial field are still present in the core, but the sheets of magnetic energy near the $r=1$ boundary develop strongly. Instead of thin folded sheets on both sides of the equatorial plane, the structures unfold and grow in the axial and azimuthal directions to occupy a wider volume and extend on both sides of the flow/conducting-layer boundary $r=1$. This effect is spectacular and occurs even for low values of w.

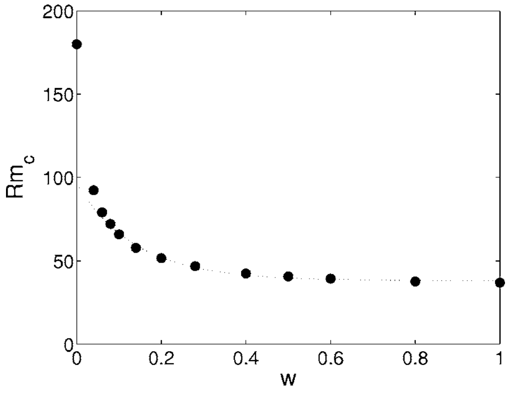

FIG. 16. Critical magnetic Reynolds number vs layer thickness w. TM73 velocity field. Fit: $R_m^c(w)=38+58\exp(-w/0.14)$ for $w\geqslant0.08$.

Small conducting layers are a challenge for numerical calculations: since the measured tangential velocity at the wall is not zero, adding a layer of conductor at rest gives rise to a strong velocity shear, which in practice requires at least 10 grid points to be represented. The maximal grid width used is 0.005: the minimal nonzero w is thus $w=0.05$. The exponential fit in Fig. 16 is relevant for $w\gtrsim0.1$. It is not clear whether the departure from exponential behavior is of numerical origin, or corresponds to a crossover between different dynamo processes.

The analysis of the **B** and **j** fields in Fig. 18 first reveals smoother **B** lines and much more homogeneous a distribution for the current density. The azimuthal current loops responsible for the transverse dipolar magnetic field now develop in a wider space [Fig. 18(c)]. Two poloidal current loops appear in this plane, closing in the conducting shell.

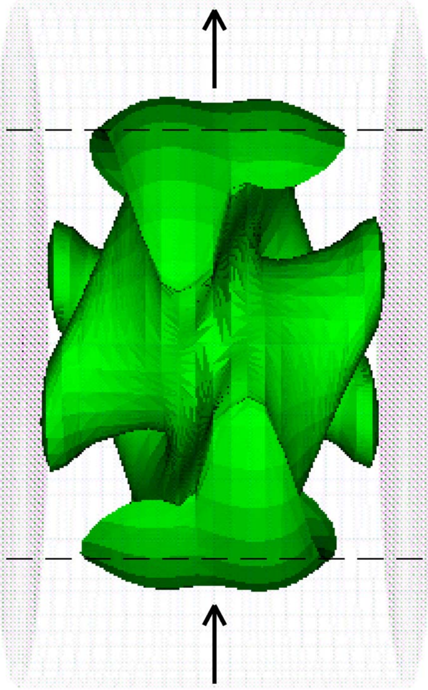

FIG. 17. Isodensity surface of magnetic energy (50% of the maximum) for the neutral mode with $w=0.6$.

These loops are responsible for the growth of the azimuthal magnetic field at $r=1$ [Fig. 18(a)]. Changes in the transverse plane ($\theta=\pi/2$) are less marked. As already stated in Refs. 39 and 40, the positive effect of adding a layer of stationary conductor may reside in the subtle balance between magnetic energy production and Ohmic dissipation.

C. Energy balance

In order to better characterize which processes lead to dynamo action in a von Kármán flow, we will now look at the energy balance equation. Let us first separate the whole space into three domains:

- Ω_i: $0<r<1$ (inner flow domain);
- Ω_o: $1<r<1+w$ (outer stationary conducting layer);
- Ω_∞: $r>1+w$. (external insulating medium).

In any conducting domain Ω_α, we write the energy balance equation:

$$\frac{\partial}{\partial t}\int_{\Omega_\alpha}\mathbf{B}^2 = R_m\int_{\Omega_\alpha}(\mathbf{j}\times\mathbf{B})\cdot\mathbf{V} - \int_{\Omega_\alpha}\mathbf{j}^2 + \int_{\partial\Omega_\alpha}(\mathbf{B}\times\mathbf{E})\cdot\mathbf{n}. \quad (2)$$

The left-hand side of Eq. (2) is the temporal variation of the magnetic energy E_{mag}. The first term in the right-hand side is the source term which writes as a work of the Lorentz force. It exists only in Ω_i and is denoted by W. The second term is the Ohmic dissipation D, and the last term is the Poynting vector flux P which vanishes at infinite r.

We have checked our computations by reproducing the results of Kaiser and Tilgner[39] on the Ponomarenko flow.

At the dynamo threshold, integration over the whole space gives

$$0 = W - D_o - D_i.$$

In Fig. 19, we plot the integrands of W and D at the threshold for dynamo action, normalized by the total instantaneous magnetic energy, as a function of radius r for various w. For $w=0$, both the production and dissipation mostly take place near the wall between the flow and the insulating medium ($r=1$), which could not have been guessed from the cuts of **j** and **B** in Fig. 15. The $w=0$ curve in Fig. 19 has two peaks. The first one at $r\simeq 0.1$ corresponds to the twisted bananas, while the second is bigger and is localized near the flow boundary $r=1$. A great deal of current should be dissipated at the conductor-insulator interface due to the "frustration" of the transverse dipole. This can explain the huge effect of adding a conducting layer at this interface: the "strain concentration" is released when a conducting medium is added. Thus if we increase w, the remaining current concentration at $r=1+w$ decreases very rapidly to zero, which explains the saturation of the effect. In the meantime, the curves collapse on a single smooth curve, both for the dissipation and the production (solid black curves in Fig. 19). For greater values of w, the production density and the dissipation in the core of the flow $r<0.2$ are smaller, whereas a peak of production and dissipation is still visible at the flow-conducting shell interface $r=1$. The conducting layer does not spread but reinforces the localization of the dynamo process at this interface. This can help us to understand the process which causes the dynamo in a von Kármán type flow.

Let us now look at the distribution between the dissipation integrated over the flow D_i and the dissipation integrated over the conducting shell D_o (Fig. 20). The ratio D_o/D_i increases monotonically with w and then saturates to 0.16. This ratio remains small, which confirms the results of Avalos *et al.*[40] for a stationary dynamo. We conclude that the presence of the conducting layer—allowing currents to flow—is more important than the relative amount of joule energy dissipated in this layer.

D. Neutral mode structure

From the numerical results presented above in this section, we consider the following questions: Is it possible to identify typical structures in the eigenmode of the von Kármán dynamo? If so, do these structure play a role in the dynamo mechanism? We have observed magnetic structures in the shape of bananas and sheets (see Figs. 14 and 17). In the center of the flow volume, there is a hyperbolic stagnation point equivalent to α-type stagnation points in ABC flows (with equal coefficients).[43] In the equatorial plane at the boundary the merging of the poloidal cells resembles β-type stagnation points in ABC flows. In such flows, the magnetic field is organized into cigars along the α-type

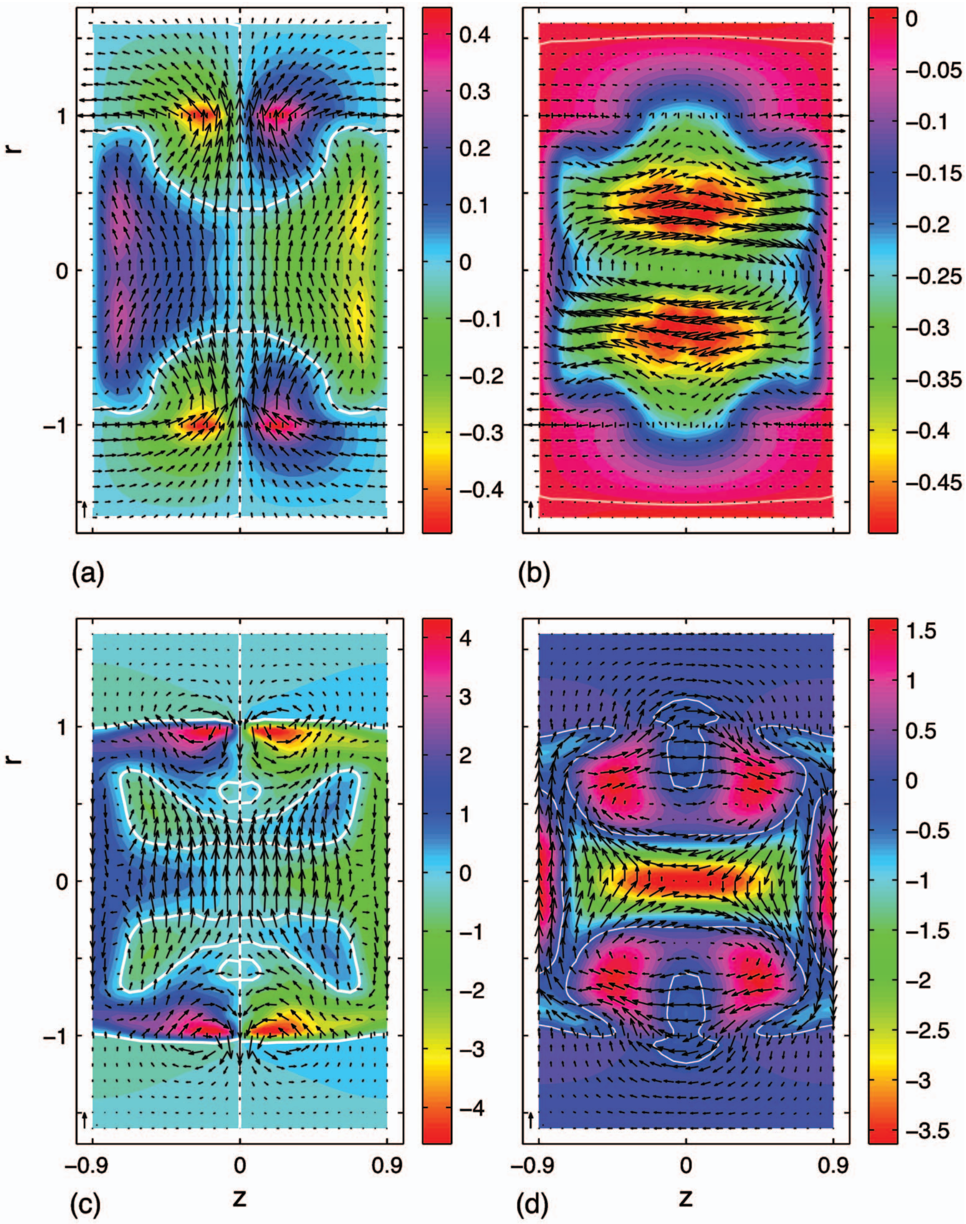

FIG. 18. (Color). Meridional sections of **B** and **j** fields for the neutral mode with $w=0.6$. **B** is normalized by the total magnetic energy. Arrows correspond to components lying in the cut plane, and color code to the component transverse to the cut plane. A unit arrow is set into the lower left corner of each panel: (a) **B** field, $\theta=0$; (b) **B** field, $\theta=\pi/2$; (c) **j** field, $\theta=0$; and (d) **j** field, $\theta=\pi/2$.

stagnation points and sheets on both sides of the β-type stagnation points:[44] this is very similar to the structure of the neutral mode we get for $w=0$ (Fig. 14). We also performed magnetic induction simulations with an imposed axial field for the poloidal part of the flow alone. We obtain a strong axial stretching: the central stagnation point could be responsible for the growth of the bananas/cigars, which are then twisted by the axial differential rotation. One should nevertheless not forget that the actual instantaneous flows are highly turbulent, and that such peculiar stagnation points of the mean flow are especially sensitive to fluctuations.

The presence of the conducting layer introduces new structures in the neutral mode (see Figs. 14, 17, 15, and 18). In order to complete our view of the fields in the conducting layer, we plot them on the $r=1$ cylinder for $w=0.6$ (Fig. 21). As for $w=0$, the dipolar main part of the magnetic field enters radially into the flow volume at $\theta=\pi$ and exits at $\theta=0$ [Fig. 21(a)]. However, looking around $z=0$, we observe that a part of this magnetic flux is azimuthally diverted in the conducting shell along the flow boundary. This effect does not exist without a conducting shell: the outer part of the dipole is anchored in the stationary conducting layer.

Another specific feature is the anticolinearity of the current density **j** with **B** at ($z=0$; $\theta=0,\pi$, $r=1$), which resembles an "α" effect. However, while the radial magnetic field is clearly due to a current loop [arrows in the center of Fig. 21(b)], j_r is not linked to a **B** loop [Fig. 21(a)], which is not obvious from Fig. 18. Thus, the anticolinearity is restricted to single points ($z=0$; $\theta=0,\pi$; $r=1$). We have checked this, computing the angle between **j** and **B**: the isocontours of this angle are very complex and the peculiar values corresponding to colinearity or anticolinearity are indeed restricted to single points.

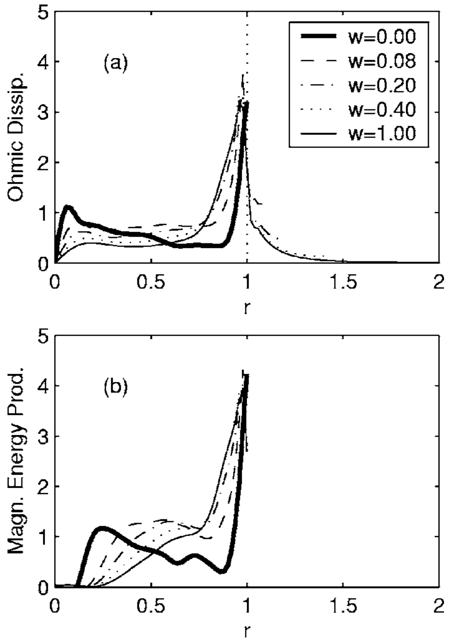

FIG. 19. (a) Radial profile of Ohmic dissipation integrated over θ and z: $\int_0^{2\pi}\int_{-0.9}^{0.9} r\mathbf{j}^2(r)dzd\theta$ for increasing values of w. (b) Radial profile of magnetic energy production integrated over θ and z: $\int_0^{2\pi}\int_{-0.9}^{0.9} r((\mathbf{j}\times\mathbf{B}).\mathbf{V})(r)dzd\theta$ for increasing values of w.

E. Dynamo threshold reduction factor

We have shown that the threshold for dynamo action is divided by four when a conducting layer of thickness w $=0.4$ is added. This effect is very strong. Following Avalos and Plunian,[40] let us compare the threshold reduction factor $\Lambda=1-R_m^c(w)/R_m^c\ (w=0)$ for various kinematic dynamos. The threshold reduction for TM73-flow ($\Lambda=0.78$) is much higher than for the Karlsruhe ($\Lambda=0.11$) and Riga ($\Lambda=0.56$) dynamos. Reduction rate can also be radically different between model flows: the α^2 model for Karlsruhe dynamo gives a low R_m^c dynamo for $w=0$ and benefits very little from a finite w ($\Lambda=0.11$), while the Ponomarenko flow does not lead to dynamo action without a conducting layer ($\Lambda=1$). The reduction factors considered above are maximal values obtained either for high w in stationary dynamos or for the optimal w in oscillatory dynamos.[39,40]

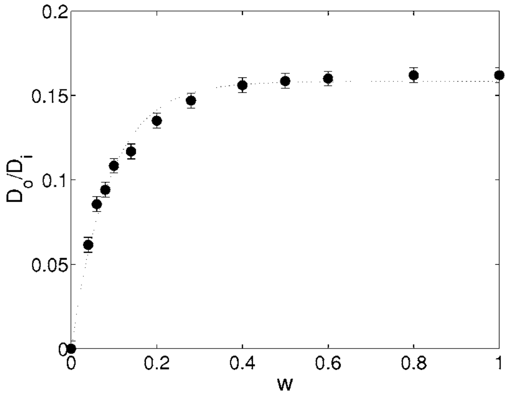

FIG. 20. Ratio of the integrated dissipation in the outer region and in the inner region D_o/D_i vs w. Fit: $D_o/D_i(w)=0.16(1-\exp(-w/0.089))$.

In order to understand why Λ is so high for our TM73-flow, we propose to compare our experimental flow with an optimal analytical model-flow proposed by Marié,[29] in collaboration with Ch. Normand and F. Daviaud in the same geometry. The Galerkin method used by these authors does not include the effect of a conducting layer. We thus perform kinematic dynamo simulations with our usual approach, and then study the effects of adding a conducting layer on the following velocity field for $\epsilon=0.7259$ corresponding to Γ $=0.8$:[29]

$$v_r=-\frac{\pi}{2}r(1-r)^2(1+2r)\cos(\pi z),$$

$$v_\theta=4\epsilon r(1-r)\sin(\pi z/2), \qquad (3)$$

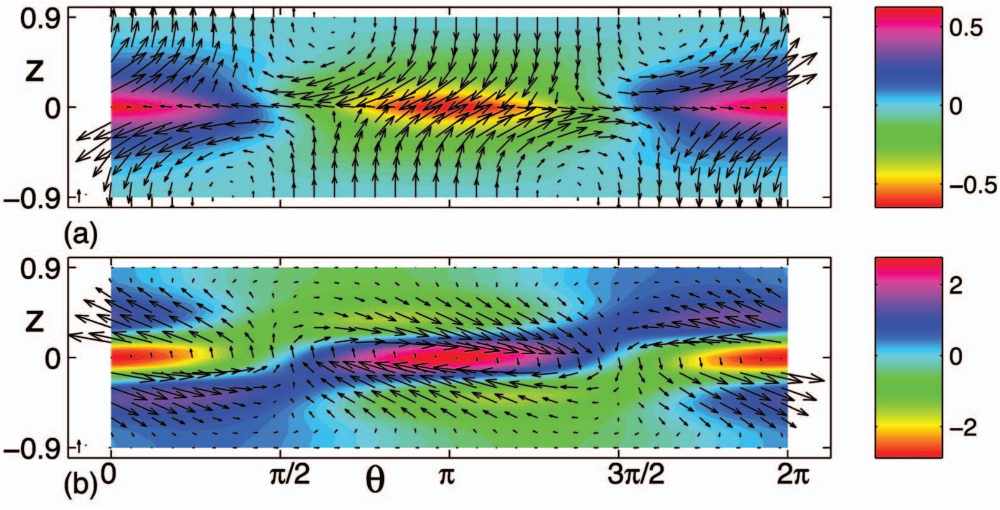

FIG. 21. (Color). (a) [Respectively, (b)] $\mathbf{B}$ (respectively, $\mathbf{j}$) field at $r=1$ for $w=0.6$. Color code corresponds to B_r (respectively, j_r) and arrows to B_z and B_θ (respectively, j_z and j_θ).

$$v_z=(1-r)(1+r-5r^2)\sin(\pi z).$$

This is the velocity field plotted in Fig. 7(d). The kinematic dynamo threshold is found at $R_m^c=58$ for $w=0$, in good agreement with the Galerkin analysis. With a $w=1$ conducting layer, we get a low $\Lambda=0.26$ reduction rate, i.e., $R_m^c=43$, close to the TM73 threshold for $w=1$: $R_m^c=37$. The threshold reduction is also found to show an exponential behavior with w, of characteristic thickness 0.20, as in Fig. 16.

Let us describe the model flow features represented in Fig. 7(d). The velocity is very smooth at the cylindrical boundary: the toroidal velocity is maximum at $r=0.5$ and slowly decreases to zero at $r=1$. The poloidal recirculation loops are centered at $r_p=0.56$ and the axial velocity also decreases slowly to zero at the cylindrical boundary. Thus, mass conservation requires the axial velocity to be much higher in the central disk $(0<r<r_p)$ than outside. These constraints make analytical models somewhat different from experimental mean flows [Figs. 7(a)–7(c)]. In particular, high kinetic Reynolds numbers forbid smooth velocity decrease near boundaries. This explains why experimental flows do not lead to low thresholds unless a conducting layer is added.

We now consider the effect of a conducting shell on the model flow's eigenmode structure. First note that without a conducting shell, the model's neutral mode structure is already very similar to that of TM73 with a conducting shell: the transverse dipole is not confined into thin sheets but develops into wider regions connected to bananas of axial field in the center. Adding the conducting layer mainly leaves the neutral mode structure unchanged and thus quantitatively reduces its impact compared to the experimental case.

Finally, from the very numerous simulations of experimental and model von Kármán flows performed, we conclude that the addition of a static conducting layer to experimental flows makes the eigenmode geometry closer to optimal model eigenmodes, and makes the critical R_m^c approach moderate values (typically 50). It may thus be conjectured that the puzzling sensitivity of dynamo threshold to flow geometry is lowered when a static layer is present. We conclude that this feature renders the dynamo more robust to flow topology details. This could also act favorably in the nonlinear regime.

V. CONJECTURES ABOUT DYNAMO MECHANISMS

In this section, we intend to relate the results of the optimization process to some more elementary mechanisms. As emphasized in Sec. I, there is no sufficient condition for dynamo action and although numerical examples of dynamo flows are numerous, little is known about the effective parameters leading to an efficient energy conversion process. For example, the classical α and axial ω mechanisms have been proposed to be the main ingredients of the von Kármán dynamo.[19] Our starting point is the observation that dynamo action results from a constructive coupling between magnetic field components due to velocity gradients, which, in the present axisymmetric case, reduce to derivatives with respect to r (radial gradients) and to z (axial gradients). The gradients of azimuthal velocity generate a toroidal field from a poloidal one (the ω effect[1]), while regeneration of the poloidal field is generally described as resulting from a helicity effect (denoted as the α effect if scale separation is present[27]). How do these general considerations apply to the present flow? As in the Sun, which shows both a polar-equatorial differential rotation and a tachocline transition, our experimental flow fields present azimuthal velocity shear in the axial and radial directions (see Fig. 2). We will therefore consider below the role of both the axial and the radial ω effect.

We will discuss these mechanisms and then suggest that, for a flow surrounded by a static conducting layer, the dynamo mechanism is based on the presence of a strong velocity shear (at the boundary layer $r=1$) which lies in this case in the bulk of the overall electrically conducting domain.

A. Axial ω effect

Induction simulations performed with the toroidal part of the velocity show an axial ω effect which converts an imposed axial field into toroidal field through $\partial v_\theta/\partial z$. Such a R_m-linear effect has been demonstrated in the VKS1 experiment.[20] This effect is concentrated around the equatorial shear layer $(z=0)$ as visible in Fig. 2. Thus, we may surmise that the axial ω effect is involved in the dynamo process: for dynamo action to take place, there is a need for another process to convert a toroidal magnetic field into a poloidal field.

B. α effect, helicity effect

R_m-nonlinear conversion from transverse to axial magnetic field has also been reported in the VKS1 experiment.[21] This effect is not the usual scale-separation α effect[27] and has been interpreted as an effect of the global helicity as reported by Parker[41] (in the following, it will be denoted "α" effect). We believe it to take place in the high kinetic helicity regions of the flow (see Fig. 12).

C. Is an α ω mechanism relevant?

Bourgoin *et al.*[45] performed a study of induction mechanisms in von Kármán-type flows, using a quasi-static iterative approach. They show that α ω dynamo action, seen as a three-step loop-back inductive mechanism, is possible, but very difficult to obtain, since fields are widely expelled by the vortices. The authors highlight the fact that the coupling between the axial ω effect and the α effect is very inefficient for our velocity fields, because of the spatial separation of these two induction effects. Our observations of the velocity and helicity fields confirm this separation.

The authors also discovered an induction effect—the BC effect—related to the magnetic diffusivity discontinuity at the insulating boundary that could be invoked in the dynamo mechanism. This BC effect, illustrated on our TM73-velocity field (Fig. 14 in Ref. 45), is enhanced in the case of strong velocity and vorticity gradients at the boundaries, characteristic of high Reynolds number flows. We are therefore convinced that for experimental flow fields at $w=0$, the BC effect helps the dynamo. This is consistant with our observations of high tangential current density near the boundaries and high magnetic energy production at $r=1$ even for $w=0$ (Fig. 19). Such a current sheet formation and BC effect was reported by Bullard and Gubbins.[25]

When a large layer of sodium at rest is added, the BC effect vanishes because the conductivity discontinuity occurs at $r=1+w$ whereas the currents still are concentrated at the flow boundary $r=1$. However, with a conducting layer, we have presented many features favoring the dynamo. In the next subsection, we propose a possible origin for this conducting-layer effect.

D. Radial ω effect, boundary layers and static shell

With a layer of steady conducting material surrounding the flow, we note the occurrence of two major phenomena:

- the possibility for currents to flow freely in this shell (Fig. 19), and
- the presence of a very strong velocity shear localized at the boundary layer which now lies in the bulk of the electrically conducting domain.

Let us again consider the shape of the velocity shear. Any realistic (with real hydrodynamical boundary conditions) von Kármán flow obviously presents negative gradients of azimuthal velocity $\partial v_\theta / \partial r$ between the region of maximal velocity and the flow boundary. This region can be divided into two parts: a smooth decrease in the bulk $(R \lesssim r \lesssim 1)$ and a sharp gradient in the boundary layer at $r=1$ (Fig. 7).

These gradients are responsible for a radial ω effect, producing B_θ with B_r, in both insulating and conducting cases. However, without a conducting layer, only the smooth part of the gradient which lies in the bulk will be efficient for dynamo action. Indeed, owing to the huge value of the kinetic Reynolds number and the very small value of the magnetic Prandtl number, the sharp boundary layer gradient is confined to a tiny domain, much smaller than the magnetic variation scale. No significant electrical currents can flow in it and we did not resolve this boundary layer with the numerical code: it is totally neglected by our approach.

The role of both types of gradients is illustrated by the observation [Fig. 7(c)] of impellers of large radius $(R=0.925)$. For such impellers there is almost no departure from solid body rotation profiles in the flow region and these impellers lead to dynamo action only with conducting shell,[22] i.e., due to the sharp gradient. On the other hand, our $R=0.75$ selected impellers present a stronger bulk-gradient and achieve dynamo in both cases [Fig. 7(b)].

In fact, the way we numerically modelized the von Kármán flow surrounded by a static conducting layer—considering an equivalent fluid system in which the boundary layer appears as a simple velocity jump in its bulk—is consistent with the problem to solve. The velocity jump, just as any strong shear, is a possible efficient source for the radial ω effect.

E. A shear and shell dynamo?

We pointed out above that the regions of maximal helicity (the α-effect sources, see Fig. 12) are close to those of radial shear where the radial ω-effect source term is large. Dynamo mechanism could thus be the result of this interaction. In the absence of a static shell, one can suppose that the dynamo arises from the coupling of the α effect, the ω effect and the BC effect.[45] With a static conducting layer, as explained previously, the radial ω effect is especially strong: the radial dipole, anchored in the conducting layer and azimuthally stretched by the toroidal flow (see Fig. 21) is a strong source of azimuthal field. This effect coupled with the α effect could be the cause of the dynamo.

For small conducting layer thickness w, one could expect a crossover between these two mechanisms. In fact, it appears that the decrease of R_m^c (Fig. 16) with the conducting shell thickness w is very fast between $w=0$ and $w=0.08$ and is well fitted for greater w by an exponential, as in Ref. 40. We can also note that for typical $R_m=50$, the dimensionless magnetic diffusion length $R_m^{-1/2}$ is equal to 0.14. This value corresponds to the characteristic length of the R_m^c decrease (Fig. 16) and is also close to the cross-over thickness and characteristic lengths of the Ohmic dissipation profiles [Figs. 19(a) and 20].

We propose to call the mechanism described previously a “shear and shell” dynamo. This interpretation could also apply to the Ponomarenko screw-flow dynamo which also principally relies on the presence of an external conducting medium.

VI. CONCLUSION

We have selected a configuration for the mean flow feasible in the VKS2 liquid sodium experiment. This mean flow leads to kinematic dynamo action for a critical magnetic Reynolds number below the maximum achievable R_m. We have performed a study of the relations between kinematic dynamo action, mean flow features and boundary conditions in a von Kármán-type flow.

The first concluding remark is that while the dynamo without a static conducting shell strongly depends on the bulk flow details, adding a stationary layer makes the dynamo threshold more robust. The study of induction mechanisms in three-dimensional cellular von Kármán type flows performed by Bourgoin *et al.*[45] suggests that this sensitivity comes from the spatial separation of the different induction mechanisms involved in the dynamo process: the loop-back between these effects cannot overcome the expulsion of magnetic flux by eddies if the coupling is not sufficient. Secondly, the role of the static layer is generally presented as a possibility for currents to flow more freely. But, instead of spreading the currents, the localization at the boundary of both magnetic energy production and dissipation (Fig. 19) appears strongly reinforced. Actually, strong shears in the bulk of the electrically conducting domain imposed by material boundaries are the dominating sources of dynamo action. They result in a better coupling between the inductive mechanisms. We also notice that there seems to be a general value for the minimal dynamo threshold (typically 50) in our class of flows, for both best analytical flows and experimental flows with a static conducting layer.

Although the lowering of the critical magnetic Reynolds number due to an external static envelope seems to confirm previous analogous results,[16,39,40] it must not be considered as the standard and general answer. In fact, in collaboration with Frank Stefani and Mingtian Xu from the Dresden MHD group, we are presently examining how such layers, when situated at both flat ends, i.e., besides the propellers, may lead to some increase of the critical magnetic Reynolds number. This option should clearly be avoided to optimize fluid dynamos similar to VKS2 configuration. However, a specific study of this latter effect may help us to understand how dynamo action, which is a global result, also relies on the mutual effects of separated spatial domains with different induction properties.

ACKNOWLEDGMENTS

The authors thank the other members of the VKS team, M. Bourgoin, S. Fauve, L. Marié, P. Odier, F. Pétrélis, J.-F. Pinton, and R. Volk, as well as B. Dubrulle, N. Leprovost, C. Normand, F. Plunian, F. Stefani, and L. Tuckerman for fruitful discussions. They are indebted to V. Padilla and C. Gasquet for technical assistance. They also thank the GDR dynamo for support.

[1] H. K. Moffatt, *Magnetic Field Generation in Electrically Conducting Fluids* (Cambridge University Press, Cambridge, England, 1978).
[2] A. Gailitis, O. Lielausis, S. Dement'ev, E. Platacis, and A. Cifersons, "Detection of a flow induced magnetic field eigenmode in the Riga dynamo facility," Phys. Rev. Lett. **84**, 4365 (2000).
[3] R. Stieglitz and U. Müller, "Experimental demonstration of a homogeneous two-scale dynamo," Phys. Fluids **13**, 561 (2001).
[4] A. Gailitis, O. Lielausis, E. Platacis, S. Dement'ev, A. Cifersons, G. Gerbeth, T. Gundrum, F. Stefani, M. Christen, and G. Will, "Magnetic field saturation in the Riga dynamo experiment," Phys. Rev. Lett. **86**, 3024 (2001).
[5] A. Gailitis, O. Lielausis, E. Platacis, G. Gerbeth, and F. Stefani, "Colloquium: Laboratory experiments on hydromagnetic dynamos," Rev. Mod. Phys. **74**, 973 (2002).
[6] U. Müller, R. Stieglitz, and S. Horanyi, "A two-scale hydromagnetic dynamo experiment," J. Fluid Mech. **498**, 31 (2004).
[7] F. Stefani, G. Gerbeth, and A. Gailitis, "Velocity profile optimization for the Riga dynamo experiment," *Transfer Phenomena in Magnetohydrodynamic and Electroconducting Flows*, edited by A. Alemany, Ph. Marty, and J.-P. Thibault (Kluwer Academic, Dordrecht, The Netherlands, 1999), pp. 31–44.
[8] A. Tilgner, "Numerical simulation of the onset of dynamo action in an experimental two-scale dynamo," Phys. Fluids **14**, 4092 (2002).
[9] A. Tilgner and F. H. Busse, "Simulation of the bifurcation diagram of the Karlsruhe dynamo," Magnetohydrodynamics **38**, 35 (2002).
[10] F. Plunian and K.-H. Rädler, "Subharmonic dynamo action in the Roberts flow," Geophys. Astrophys. Fluid Dyn. **96**, 115 (2002).
[11] D. Sweet, E. Ott, J. M. Finn, T. M. Antonsen, and D. P. Lathrop, "Blowout bifurcations and the onset of magnetic activity in turbulent dynamos," Phys. Rev. E **63**, 066211 (2001).
[12] A. Gailitis, O. Lielausis, E. Platacis, G. Gerbeth, and F. Stefani, "The Riga dynamo experiment," Surv. Geophys. **24**, 247 (2003).
[13] F. Cattaneo, D. W. Hughes, and E.-J. Kim, "Suppression of chaos in a simplified nonlinear dynamo model," Phys. Rev. Lett. **76**, 2057 (1996).
[14] F. Pétrélis and S. Fauve, "Saturation of the magnetic field above the dynamo threshold," Eur. Phys. J. B **22**, 273 (2001).
[15] Y. Ponty, H. Politano, and J.-F. Pinton, "Simulation of induction at low magnetic Prandtl number," Phys. Rev. Lett. **92**, 144503 (2004).
[16] F. Pétrélis, "Effet dynamo: Etude des mécanismes d'instabilité et de saturation du champ magnétique," Ph.D. thesis, Université Paris VI (2002).
[17] S. Fauve and F. Pétrélis, "The dynamo effect," in *Peyresq Lectures on Nonlinear Phenomena*, edited by J.-A. Sepulchre (World Scientific, Singapore, 2003), Vol. II.
[18] *Dynamo and Dynamics, a Mathematical Challenge, Cargèse (France) August 21–26, 2000*, edited by P. Chossat, D. Armbruster, and I. Oprea, NATO ASI series (Kluwer Academic, Dordrecht, The Netherlands, 2001).
[19] L. Marié, F. Pétrélis, M. Bourgoin, J. Burguete, A. Chiffaudel, F. Daviaud, S. Fauve, P. Odier, and J.-F. Pinton, "Open questions about homogeneous fluid dynamos: the VKS experiment," Magnetohydrodynamics **38**, 156 (2002).
[20] M. Bourgoin, L. Marié, F. Pétrélis, C. Gasquet, A. Guigon, J.-B. Luciani, M. Moulin, F. Namer, J. Burguete, A. Chiffaudel, F. Daviaud, S. Fauve, P. Odier, and J.-F. Pinton, "MHD measurements in the von Kármán sodium experiment," Phys. Fluids **14**, 3046 (2002).
[21] F. Pétrélis, M. Bourgoin, L. Marié, J. Burguete, A. Chiffaudel, F. Daviaud, S. Fauve, P. Odier, and J.-F. Pinton, "Nonlinear magnetic induction by helical motion in a liquid sodium turbulent flow," Phys. Rev. Lett. **90**, 174501 (2003).
[22] L. Marié, J. Burguete, F. Daviaud, and J. Léorat, "Numerical study of homogeneous dynamo based on experimental von Kármán type flows," Eur. Phys. J. B **33**, 469 (2003).
[23] N. L. Dudley and R. W. James, "Time-dependent kinematic dynamos with stationary flows," Proc. R. Soc. London, Ser. A **425**, 407 (1989).
[24] C. B. Forest, R. O'Connell, R. Kendrick, E. Spence, and M. D. Nornberg, "Hydrodynamic and numerical modeling of a spherical homogeneous dynamo experiment," Magnetohydrodynamics **38**, 107 (2002).
[25] E. C. Bullard and D. Gubbins, "Generation of magnetic fields by fluid motions of global scale," Geophys. Astrophys. Fluid Dyn. **8**, 43 (1977).
[26] A. B. Reighard and M. R. Brown, "Turbulent conductivity measurements in a spherical liquid sodium flow," Phys. Rev. Lett. **86**, 2794 (2001).
[27] F. Krause and K. H. Rädler, *Mean Field MHD and Dynamo Theory* (Pergamon, New York, 1980).
[28] L. Marié and F. Daviaud, "Experimental measurement of the scale-by-scale momentum transport budget in a turbulent shear flow," Phys. Fluids **16**, 457 (2004).
[29] L. Marié, "Transport de moment cinétique et de champ magnétique par un écoulement tourbillonaire turbulent: influence de la rotation," Ph.D. thesis, Université Paris VII (2003).
[30] U. Frisch, *Turbulence—The Legacy of A. N. Kolmogorov* (Cambridge University Press, New York, 1995).
[31] F. Ravelet, "Etude expérimentale de l'écoulement tourbillonnaire de von Kármán et application à l'effet dynamo," M.S. thesis, Université Paris VI (2002).
[32] J. Léorat, "Numerical simulations of cylindrical dynamos: Scope and method," in *Progress in Turbulence Research*, Progress in Astronautics and Aeronautics, Vol. 162 (AIAA, Washington, 1994), pp. 282–292.
[33] E. Knobloch, "Symmetry and instability in rotating hydrodynamic and magnetohydrodynamic flows," Phys. Fluids **8**, 1446 (1996).
[34] E. C. Bullard and H. Gellman, "Homogeneous dynamos and terrestrial magnetism," Philos. Trans. R. Soc. London, Ser. A **247**, 213 (1954).
[35] G. E. Backus, "A class of self-sustaining dissipative spherical dynamos," Ann. Phys. **4**, 372 (1958).
[36] J. J. Love and D. Gubbins, "Dynamos driven by poloidal flow exist," Geophys. Res. Lett. **23**, 857 (1996).
[37] M. R. E. Proctor, "An extension of the toroidal theorem," Geophys. Astrophys. Fluid Dyn. **98**, 235 (2004).
[38] M. Lesieur, *Turbulence in Fluids*, 2nd ed. (Kluwer Academic, Dordrecht, The Netherlands, 1990).
[39] R. Kaiser and A. Tilgner, "Kinematic dynamos surrounded by a stationary conductor," Phys. Rev. E **60**, 2949 (1999).
[40] R. Avalos-Zuniga and F. Plunian, "Influence of electromagnetic boundary conditions onto the onset of dynamo action in laboratory experiments," Phys. Rev. E **68**, 066307 (2003).
[41] E. N. Parker, "Hydromagnetic dynamo models," Astrophys. J. **122**, 293 (1955).

[42] N. Leprovost, “Influence des petites échelles sur la dynamique à grande échelle en turbulence magnétohydrodynamique,” Ph.D. thesis, Université Paris VI (2004).

[43] S. Childress and A. D. Gilbert, *Stretch, Twist, Fold: The Fast Dynamo* (Springer, New York, 1995).

[44] V. Archontis, S. B. F. Dorch, and A. Nordlund, “Numerical simulations of kinematic dynamo action,” Astron. Astrophys. **397**, 393 (2003).

[45] M. Bourgoin, P. Odier, J.-F. Pinton, and Y. Ricard, “An iterative study of time independent induction effects in magnetohydrodynamics,” Phys. Fluids **16**, 2529 (2004).

Study of the Aerodynamics/Aeroacoustics of an Axial-Flow Fan: Experimental Validation of a LES/LPCE/Brinkman Penalization Method

Florent Ravelet[*], Sofiane Khelladi[†], Hussain Nouri[‡], Farid Bakir[§]
Laboratoire de Dynamique des Fluides, Arts et Métiers ParisTech, Paris, France
Hoyeon Kim[¶], Youngmin Bae[‖], Young J. Moon[**]
Department of Mechanical Engineering, Korea University, Seoul, 136-713, Korea

The seek for an efficient aerodynamic and aeroacoustic design of axial-flow fans is an important field of investigation for both academic and applied research. Improvements can only be made with a better understanding of the physical mechanisms arising in these machines that combine strong interactions between rotating and non-rotating parts of highly complex geometries. One way is to couple well-suited experimental investigations and innovative computational methods, that overtake the weaknesses of methods based for instance on aeroacoustic analogy. In this paper we study an axial fan using a new numerical method based on LES/LPCE Brinkman Penalization Method. This method is developed in the Department of Mechanical Engineering at Korea University. The experimental tests and validations are performed in the Laboratory of Fluid Dynamics at Arts & Métiers ParisTech in Paris. Detailed analysis of numerical and experimental results are in progress within the two partner teams. In this paper we present preliminary encouraging results.

I. Introduction

Efficient aerodynamic and aeroacoustic design of axial-flow fans remains an important field of investigation for both academic and applied research. A better understanding of the physical mechanisms arising in these machines is the only way to improve their performances. The aerodynamical and acoustical fields are strongly interdependent. Difficulties encountered in this type of application, both experimentally and numerically, are mainly due to the nature of the flows that combine strong interactions between rotating and non-rotating parts of highly complex geometries. One way is to couple well-suited experimental investigations and innovative computational methods, that overtake the weaknesses of methods based for instance on aeroacoustic analogy.[1, 2]

One of the problems concerning the validation of CFD codes dealing with flows in highly complex geometries, is the absence of reliable test cases including experimental data.

In this paper we propose a setup of a normalized test bench to perform in-situ highly accurate measurements on axial fans. The measurements will be used as a reference data base to validate a new numerical method based on LES/LPCE Brinkman Penalization Method (BPM).

Two axial fans were tested: a thin- and a thick-blades fans, see figure (1). The thin-blades fan was designed following a classical procedure and is the reference. The thick-blades fan has the very same geometry. Their aerodynamic performances are compared in details in.[3] BPM is more efficient when using thick virtual solid boundaries,[4] a thick-blades is thus more indicated for a first application of BPM to turbomachines.

---

[*] Associate Professor
[†] Associate Professor
[‡] Ph.D student
[§] Professor
[¶] Ph.D student, student Member of AIAA
[‖] Post-doctoral staff, Member of AIAA
[**] Professor, Senior Member of AIAA, Corresponding Author (yjmoon@korea.ac.kr)

The paper is organized as follow: section II is devoted to the description of the test bench, BPM is presented in section III. In section IV we present preliminaries results concerning fans and validation. In section V we give concluding remarks.

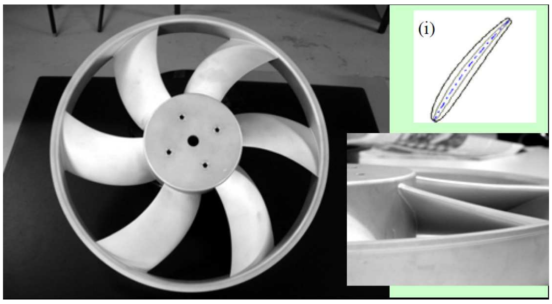

Figure 1. The thick-blades fan. (i) Cross-section of thick and thin profiles.

II. Experimental setup

An ISO 5801[5] normalized test bench have been built in order to perform in-situ highly accurate measurements of pressure fluctuations and velocity fields on an axial blowing fan interacting with a stator.[1] The test bench consists of a pipe of inner diameter $D = 380$ mm.

The used fan has been developed for an automotive engine cooling system application. The fan has six blades. The hub-to-tip radius ratio for the blades is $\Phi_{int}/\Phi_{max} = 0.366$, with $\Phi_{max} = 358$ mm. A circular collar has been added, with an external diameter of 376 mm. The radial gap between the pipe and the fan is thus 2 mm thick. The rotor is built up from blades of circular-arc camber lines, with a thin profile of maximum thickness 4 mm along the camber lines (NACA 4 digits based, clipped at $0.95\,x/c$).

The fans were designed to meet the following specifications point: a pressure head of 270 Pa, a rotational speed of 2500 rpm and a flow rate of 0.73 m^3/s for a rotor-alone situation.

The upstream face of the fan is at a distance D from the entrance of the pipe. A DC-motor is hidden in a casing of diameter 0.30 D and length 0.7 D, terminated in a warhead shape. The binding of it to the tube is ensured by five rods of diameter 8 mm, i.e. 0.021 D, in order to minimize their influence, regardless the flow rate, and the distance between the upstream face of the fan and the binding rods is 0.26 D, see figure 2.

According to the ISO-5801 norm, an eight blades star-shaped part with thickness 1.5 mm and length 2 D is placed 2 D downstream of the rotor-stator set. It is supposed to prevent the outgoing flow from having any rotating component, and converts the rotational kinetic energy into static pressure. The static pressure of the axial fan is measured 1 D downstream of the star, with an average over four flush-mounted pressure probes. The flow rate is measured with a diaphragm according to the ISO-5167 norm, 10 D downstream of the star, and 5 D upstream of the exit of the pipe. The diaphragm has a diameter of 0.73 D.

The pressure fluctuations are measured simultaneously by eight G.R.A.S 40BP 1/4" polarized pressure microphones, with G.R.A.S 26AC preamplifiers and a G.R.A.S 12AG power supply module.

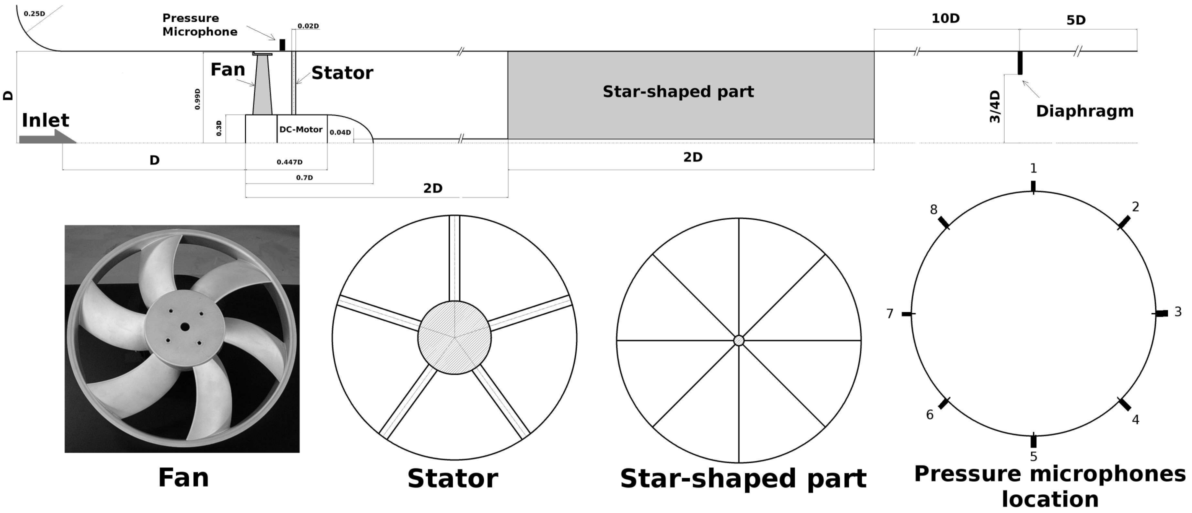

Figure 2. Test bench scheme.

III. Computational Methodology

Computation is carried out to study the aerodynamic/aeroacoustic characteristics of the axial-flow fan. The targeted axial-flow fan revolves with a rotational speed of 2500 rpm in a circular duct (maximal blade-tip speed of 49.2 m/s or M=0.15). Apart from generation and propagation of the noise, the flow field of the axial-flow fan may be considered incompressible, realizing the fact that noise generation in this case is more or less a one-way compressibility effect. So, a hydrodynamic/acoustic splitting approach[6,7] is employed, where the total flow variables are decomposed into the incompressible and perturbed compressible variables as,

$$\begin{aligned} \rho(\vec{x},t) &= \rho_0 + \rho(\vec{x},t) \\ \vec{u}(\vec{x},t) &= \vec{U}(\vec{x},t) + \vec{u}'(\vec{x},t) \\ p(\vec{x},t) &= P(\vec{x},t) + p'(\vec{x},t) \end{aligned} \tag{1}$$

Here, the incompressible variables represent hydrodynamic turbulent flow field, while acoustic fluctuations and other compressibility effects are resolved by perturbed quantities denoted by ('). The basic idea behind this approach is such that the turbulent flow field of axial fan is computed by incompressible large eddy simulation (LES), whilst acoustic field is computed by the linearized perturbed compressible equations (LPCE)[8,9] with acoustic sources acquired from the LES solutions.

In the present study, the three-dimensional, hydrodynamic flow field within a circular duct with rotating fans and stationary struts is computed by employing a Brinkman penalization method (BPM)[10] to the incompressible large eddy simulation. This method is simple and efficient to treat objects of arbitrary shape, moving or stationary in the flow region. The accuracy of the present BPM is secured at the immersed boundaries by using a concept of body-fitted, Cartesian-like grid. More details on this issue can be found in reference.[4] The filtered, incompressible Navier-Stokes equations using the Brinkman penalization method are written as

$$\begin{aligned} \frac{\partial \tilde{U}_j}{\partial x_j} &= 0 \\ \frac{\partial \tilde{U}_i}{\partial t} + \frac{\partial}{\partial x_j}\left(\frac{\tilde{U}_i\tilde{U}_j}{\epsilon}\right) + \frac{\partial}{\partial x_j}M_{ij} &= -\frac{\partial \tilde{P}}{\partial x_i} + \nu\frac{\partial}{\partial x_j}\left(\frac{\partial \tilde{U}_i}{\partial x_j} + \frac{\partial \tilde{U}_j}{\partial x_i}\right) - \frac{\nu}{K}(\tilde{U}_i - U_{0i}) \end{aligned} \tag{2}$$

where $(\tilde{\ })$ indicates the superficial, volume-averaged quantity, ν represents the kinematic viscosity of the fluid, ϵ is the porosity defined as the ratio of the volume occupied by the fluid to the total volume, K is the permeability, M_{ij} is the sub-grid tensor, and U_{0i} denotes the velocity of the rotating fan blades.

The main advantage of this penalization technique is that no additional treatment is needed to impose the boundary condition. A single set of governing equations with penalty terms is applied to the whole computational domain, in which different porosity ϵ and permeability K are assigned for fluids and solids (see Fig. 3(a)). For example, porosity is equal to unity and permeability becomes infinite in the fluid region so that Eq. 1 returns to incompressible LES. On the contrary, when porosity and permeability approach to zero for solids, the inertia terms become negligible compared to the penalty terms in the momentum equations so that no-slip condition is asymptotically satisfied at the impermeable surfaces.

Once LES solution reaches a pseudo-periodic stage, acoustic field is solved by the linearized perturbed compressible equation (LPCE) coupled with the Brinkman penalization method.[4] The LPCE/BPM equations are written as

$$\begin{aligned}
\frac{\partial \rho'}{\partial t} + \frac{1}{\epsilon}\left(U_j \frac{\partial \rho'}{\partial x_j} + \rho_0 \frac{\partial u'_j}{\partial x_j}\right) &= 0 \\
\frac{\partial u'_i}{\partial t} + \frac{\partial u'_j U_j}{\partial x_j} + \frac{1}{\rho_0}\frac{\partial p'}{\partial x_i} - R_{ij}(u'_j - U_{0i}) &= 0 \\
\frac{\partial p'}{\partial t} + \frac{1}{\epsilon}\left(U_j \frac{\partial p'}{\partial x_j} + \gamma P \frac{\partial u'_j}{\partial x_j} + u'_j \frac{\partial P}{\partial x_j}\right) &= -\frac{DP}{Dt}
\end{aligned} \tag{3}$$

where DP/Dt represents the explicit noise source term acquired from the LES solutions and U_{0i} denotes the velocity of the rotating fan blades. As in Eq. 2, a single set of governing equations is applied to the whole computational domain with different porosity ϵ and permeability K assigned for fluids and solids as shown in Fig. 3(a). In Eq. 3, a slip boundary condition is imposed at the impermeable surface by introducing an anisotropic permeability tensor R_{ij},

$$R_{xx} = \frac{1}{K} s_y n_x, \;\; R_{xy} = \frac{1}{K} s_y n_y, \;\; R_{yx} = -\frac{1}{K} s_x n_x, \;\; R_{yy} = -\frac{1}{K} s_x n_y \tag{4}$$

where $\vec{s} = (s_x, s_y)$ and $\vec{n} = (n_x, n_y)$ are the unit vectors tangential and normal to the impermeable boundaries, respectively. The left hand sides of LPCE represent the effects of acoustic wave propagation and refraction in an unsteady, inhomogeneous flow, while the right hand side contains only the acoustic source term.

To solve the governing equations related to the aerodynamics and aeroacoustics of the axial-flow fan, the highorder compact/filtering schemes are employed for spatial discretization, while a four-stage Runge-Kutta method is used for temporal integration with implicit treatment of penalization terms in the momentum equations. The central compact scheme widely used in CAA is efficient and high-order accurate but cannot deal with the steep gradients associated with the abrupt change of permeability, because the scheme has no numerical diffusion. To resolve this matter, we also employ the compact spatial-filtering schemes,[11,12] in which the numerical diffusion can be controlled by the filtering coefficient and the order of accuracy. These high-order compact/filtering schemes combined with one-side differencing/filtering technique[4] produce sufficient numerical diffusion in the region where the steep gradients exist.

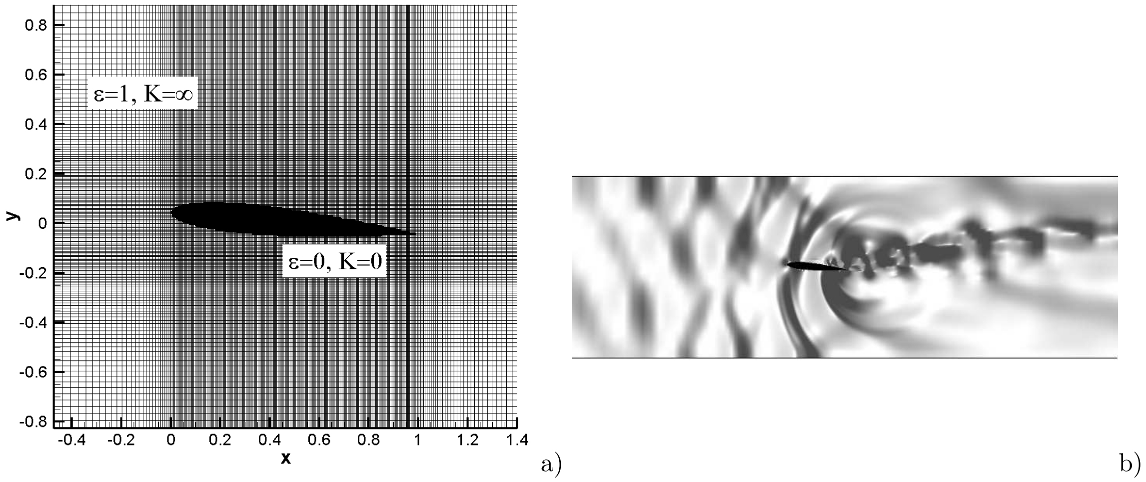

Figure 3. a) Cartesian grids mapped with different porosity and permeability for blade and air and b) instantaneous pressure fluctuation field within the duct

IV. Results and Discussion

A. Experiments

The characteristics of the two fans are shown in Figure 4 together with the designed specifications point of the thin-blades fan. The design point thus corresponds to a flow coefficient $\Phi = 0.156$ and a pressure coefficient $\Psi = 0.200$. The curves are the results of five measurements proceeded at nominal rotation speed. The error bars in Figure 4a stand for the RMS (root mean square) values of the five measurements of Φ and Ψ, magnified by a factor three for better visualization. The pressure coefficient distributions are globally relatively similar to each other. The thin-blades fan matches the specifications point plotted in Figure 4a. At the design flow rate, the thick-blades fan produces a depression 8% below the specified depression.

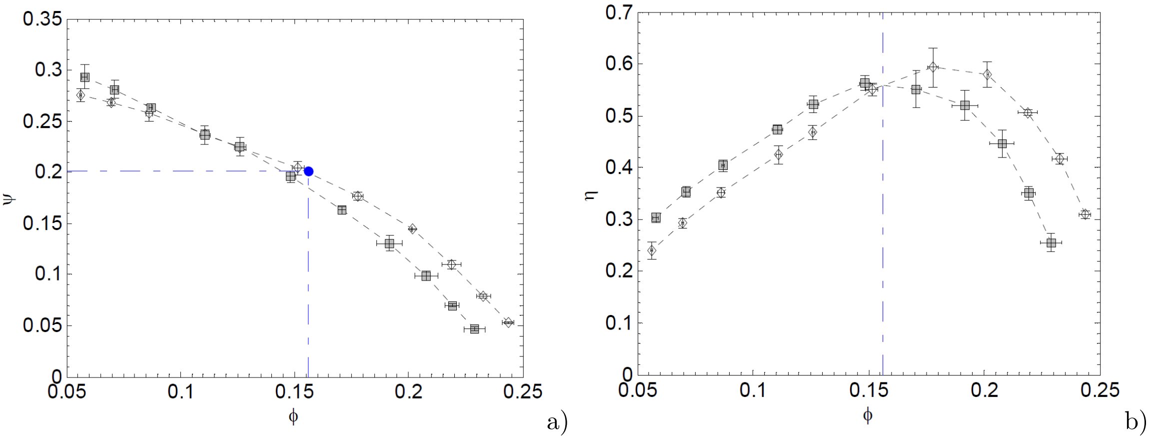

Figure 4. Aerodynamic characteristic curve: a) Pressure coefficient Ψ vs. flow coefficient Φ, b) Fan efficiency η vs. flow coefficient Φ. ■ thick blades fan, ◊ thin blades fan. • design specification point.

The efficiencies of both fans are shown in figure 4b with the specifications flow rate coefficient of the thin-blades fan.The efficiencies distributions have a classical shape, skewed toward partial flow rates, with a strong fall after the nominal flow rate which is fairly set around an overflow of about 20%. At $\Phi = 0.18$ and $\Psi = 0.17$, the thin-blades fan reaches its maximum efficiency of 0.58 ± 0.005. The maximum of efficiency is shifted toward overflow with respect to the design point. One open question is whether this is due to the forward swept or not. The maximum efficiency of the thick-blades fan reaches a value 0.55 ± 0.005. The thickening of the blades has led to a decrease of 0.03 of efficiency. The maximum of efficiency is shifted toward a partial flow of about 30% with respect to the nominal flow rate of the thin-blades fan and the thick-blades fan thus gives its best efficiency for a flow rate $\Phi = 0.15$ very close to the design point. The corresponding pressure coefficient is $\Psi = 0.19$.

The squared amplitude spectra of wall pressure at $\Phi = 0.18$ are plotted in Figure 5a. The sampling time is 10s, corresponding to approximately 330 fan rotations, and the spectra is an average of eight 50% overlapping parts, windowed with a Hamming window. The spectra are displayed between 150 and 850 Hz. Both fans exhibit relatively high discrete peaks, corresponding to the blade passing frequency fbpf (200 Hz for the thin-blades fan and 202 Hz for the thick-blades one) and its harmonics. They are high above the broadband noise. The two fans differ however strongly by the repartition of energy between the different harmonics.
The squared amplitude spectra of wall pressure at the nominal flow rate of the thick blades fan $\Phi = 0.15$ are plotted in Figure 5b. The blade passing frequency is now 200 Hz for the thick-blades fan and 193 Hz for the thin-blades fan. Please not that the angular velocity ratio needed to reach the same dimensional static pressure elevation and flow rate, equal to 1.037, is the same as the ratio discussed in the last paragraph of the section dedicated to the fan global characteristics. The results are very similar to the previously described flow rate: for the thin-blades fan, the fundamental frequency and the first harmonic are the only visible peaks in the spectrum.

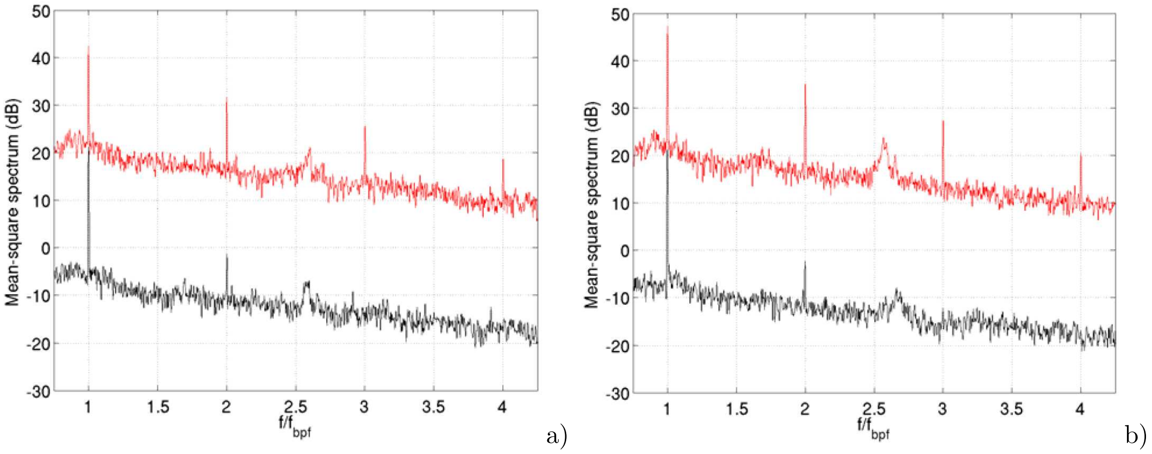

Figure 5. Square amplitude spectra of wall pressure fluctuations for thin-blades axial-flow fan (black) and thick-blades axial-flow fan (red). a) A flow rate $\Phi = 0.18$. The thin-blades rotates $\omega = 209.5$ rad/s and thick-blades rotates at $\omega = 211.5$ rad/s. b) A flow rate $\Phi = 0.15$. The thin-blades rotates $\omega = 202.7$ rad/s and thick-blades rotates at $\omega = 209.5$ rad/s. The thick-blades flow spectrum has been shifted by +30 dB for clarity.

Figure 6 presents autocorrelation and cross-correlation functions of wall pressure fluctuations for the two fans. One can notice that the functions present a periodicity that corresponds to six events in one rotation that is the blade passing frequency. The time lag for the strongest peak in the cross-correlation function does match the angular distance between the microphones which is one half of a turn here. Another common feature between the two fans is that secondary peaks height for the autocorrelation function are close to the peaks height for the cross-correlation function. Some strongly coherent flow structures might be involved in this zone between the rotor and the binding static part. The strong difference between the thin-blades fan and the thick-blades fan is the value of the cross-correlation coefficient. It is significantly lower for the thick blades fan. Local velocity measurements that give access to flow structure such as PIV measurements would be of great interest in order to better understand this difference.

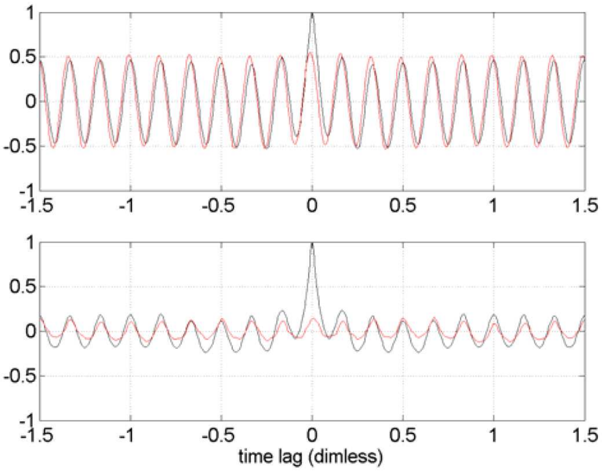

Figure 6. Black curves: autocorrelation function of pressure fluctuations at position 1 (see Figure 2). Red curves: cross- correlation function of pressure fluctuations between position 1 and position 5 (see Figure 2). Top graph corresponds to the thin-blades fan fan at $\Phi = 0.18$, bottom graph corresponds to the thick-blades fan at $\Phi = 0.18$. The time is made non-dimensional with reference to $\tau = t \times \frac{\omega}{2\pi}$ one period of rotation:

B. Computation

The present LES/LPCE/BPM method is first tested for blade noise within a duct (simplified 2D laminar case). At $Re = 3 \times 10^4$, $M = 0.5$, and angle of attack= 5 deg, a laminar boundary layer is separated over the suction side of two-dimensional NACA0012 airfoil, where vortices are shed toward the trailing-edge of the blade. Figure 2(a) shows the blade immersed in Cartesian grids with different porosity and permeability assigned for blade and air within the duct. In Fig 2(b), an instantaneous pressure fluctuation field computed by the present method shows a certain duct mode of noise generated at the trailing-edge of the blade via edge-scattering of the shed vortices. It is noted that a substantial part of the noise is propagating upstream in the duct.

From this result, one could find a possibility on the prediction of aerodynamic/aeroacoustic characteristics of the axial fan with the simple and efficient Brinkman penalization method. The present computational method is now applied to the targeted three-dimensional axial-flow fan. Figure 7 shows the axial-flow fan immersed in single-block, structured, H(axial)-O-H(cross-section)-type grids with different porosity and permeability assigned for fan and air in a circular duct. It is expected that about 8 million grid points will be distributed over the whole test bench configuration for LES/BPM computation. For LPCE/BPM calculation, much coarser mesh will be used, considering the fact that scales of pressure fluctuations (possible noise sources, DP/Dt) is considerably larger than those of velocity fluctuations.

There are many details in computations such as resolving the turbulent boundary layers over the fan blades, interpolation of hydrodynamic variables between LES/LPCE grids, acquiring the noise sources from LES grids, etc., all of which are to be validated in the final manuscript. The first part is especially important to resolve the broadband noise of the fan. Besides, physics of three-dimensional axial fan flows are needed to be understood more clearly in terms of noise generation processes.

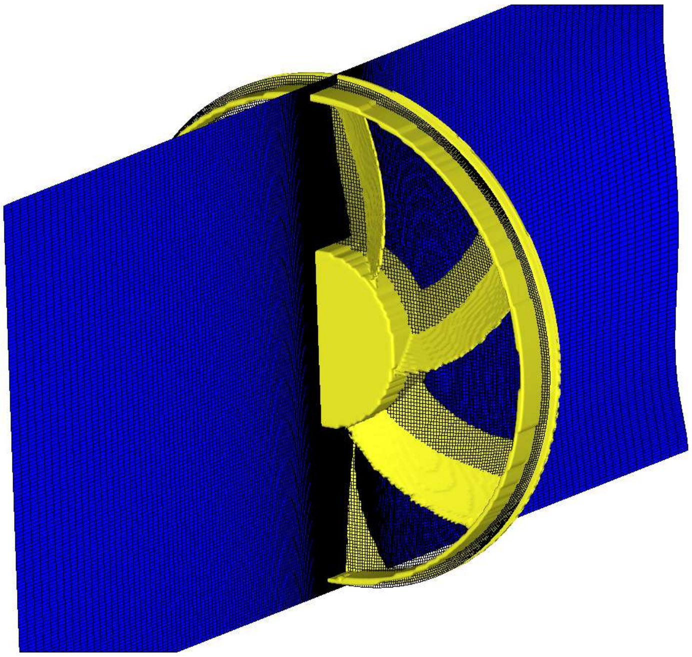

Figure 7. Single-block, structured, H-O-H-type grids mapped with different porosity and permeability for axial fan and air within a circular duct

V. Conclusion

A setup of a normalized test bench to perform in-situ highly accurate measurements on axial fans was presented in this paper. The measurements will be used as a reference data base to validate a numerical method based on LES/LPCE Brinkman Penalization Method (BPM). For practical reasons, thick solid parts are more indicated for a first use of BPM to turbomachines. Two axial fans were tested: a thin- and a thick-blades fans. The thin-blades fan was designed following a classical procedure and is the reference. The thick-blades fan has the very same geometry. The later is used to validate BPM. The numerical results of BPM will be presented soon.

References

[1] Maaloum, A., Kouidri, S., Bakir, F., and Rey, R., “Effect of inlet duct contour and lack thereof on the noise generated of an axial flow fan,” *Applied Acoustics*, Vol. 64, No. 10, 2003, pp. 999–1010.

[2] Khelladi, S., Kouidri, S., Bakir, F., and Rey, R., “Predicting tonal noise from a high rotational speed centrifugal fan,” *Journal of Sound and Vibration, Vol. 313, Issues 1-2, pp. 113-133*, 2008.

[3] Sarraf, C., Ravelet, F., Nouri, H., and Bakir, F., “Experimental Study of Blade Thickness Effects on the Global and the Local Performances of Axial-Flow Fans,” *HEFAT2010, 7th International Conference on Heat Transfer, Fluid Mechanics and Thermodynamics, Antalya, Turkey*, 19-21 July 2010.

[4] Bae, Y. M. and Moon, Y. J., “Brinkman Penalization Method for Computation of Acoustic Scattering from Complex Geometry,” *submitted to 16th AIAA/CEAS Aeroacoustics Conference, Stockholm, Sweden*, June 2010.

[5] “ISO 5801 - Industrial fans – Performance testing using standardized airways,” 2007.

[6] Hardin, J. and Pope, D., “An Acoustic/Viscous Splitting Technique for Computational Aeroacoustics,” *Computational Fluid Dynamics*, Vol. 6, No. 56, 1994, pp. 323–340.

[7] Goldstein, M., “A Generalized Acoustic Analogy,” *Journal of Fluid Mechanics*, Vol. 488, 2003, pp. 315–333.

[8] Seo, J. H. and Moon, Y. J., “The Linearized Perturbed Compressible Equations for Aeroacoustic Noise Prediction at Very Low Mach Numbers,” *AIAA-Paper*, 2005, pp. 2005–2927.

[9] Seo, J. H. and Moon, Y. J., “Linearized Perturbed Compressible Equations for Low Mach Number Aeroacoustics,” *Journal of Computational Physics*, Vol. 218, 2006, pp. 702–719.

[10] Liu, Q. and Vasilyev, O. V., “A Brinkman penalization method for compressible flows in complex geometries, Journal of Computational Physics,” *Journal of Computational Physics*, Vol. 227, 2007, pp. 946–966.

[11] Lele, S. K., “Compact Finite Difference Schemes with Spectral-like Resolution,” *Journal of Computational Physics*, Vol. 103, 1992, pp. 16–42.

[12] Gaitonde, D., Shang, J. S., and Young, J. L., “Practical Aspects of Higher-Order Numerical Schemes for Wave Propagation Phenomena,” *International Journal for Numerical Methods in Engineering*, Vol. 45, No. 12, 1999, pp. 1849–1869.

Experimental Thermal and Fluid Science 35 (2011) 684–693

Contents lists available at ScienceDirect

Experimental Thermal and Fluid Science

journal homepage: www.elsevier.com/locate/etfs

Experimental study of blade thickness effects on the overall and local performances of a Controlled Vortex Designed axial-flow fan

C. Sarraf, H. Nouri, F. Ravelet *, F. Bakir

Arts et Metiers ParisTech, DynFluid, 151 boulevard de l'Hôpital, 75013 Paris, France

ARTICLE INFO

Article history:
Received 30 July 2010
Received in revised form 3 December 2010
Accepted 3 January 2011
Available online 9 January 2011

Keywords:
Axial-flow fan
Turbomachinery
Blades thickness
Overall performance
Pressure fluctuations
Phase-averaged anemometry

ABSTRACT

The purpose of this work is to study the effects of blade thickness on the performances of an axial-flow fan. Two fans that differ only in the thickness of their blades were studied. The first fan was designed to be part of the cooling system of an automotive vehicle power unit and has very thin blades. The second fan has much thicker blades compatible with the rotomoulding conception process. The overall performances of the fans were measured in a test bench designed according to the ISO-5801 standard. The curve of aerodynamics characteristics (pressure head versus flow-rate) is slightly steeper for the fan with thick blades, and the nominal point is shifted towards lower flow-rates. The efficiency of the thick blades fan is lower than the efficiency of the fan with thin blades but remains high on a wider flow-rate range. The mean velocity fields downstream of the rotors are very similar at nominal points with less centrifugation for the thick blades fan. Moreover, the thick blades fan maintains an axial exit-flow on a wider range of flow-rates. The main differences concern local properties of the flow: phase-averaged velocities and wall pressure fluctuations strongly differ at the nominal flow-rates. The total level of fluctuations is lower for the thick blades fan that for the thin blades fan and the spectral decomposition of the wall fluctuations and velocity signals reveal more harmonics for the thick blades fan, with less correlation between the different signals. For this kind of turbomachinery, the use of thick blades could lead to a good compromise between aerodynamic and acoustic performances, on a wider operating range.

1. Introduction

The low-speed axial-flow fans, used for instance in the cooling system of automotive vehicles power units, have very complex three-dimensional geometries that can affect both their overall and acoustical performances. An example of one parameter that dramatically modifies the performances is for instance the blade sweep [1–4]. A second parameter that should affect the performances is the blade thickness. Low-speed axial-flow fans usually have conventional thin blades. However, following motivations such as active control of the blade shape or the use of the rotomoulding process [5,6], the designers would have now to face profiles with thicker blades. The control of blade shape may help to reduce the radiated noise or to extend the operating range and the need for actuators then implies thicker blades. The rotomoulding process—previously tested for wind turbine blades—leads to thick hollow blades and may be more economic because of material gain. The blades can have more stiffness with greater inertia moment. Complex shapes with blade recovering are moreover easier to manufacture than with traditional plastic injection methods, and the blades can be filled for instance with noise-absorbing foam.

In aeronautics and in the automotive industry, changing the blade thickness has been used for many years as an efficient way to modify the lift and drag characteristics and the boundary layers detachment process [7,8]. Applied to low-speed axial-flow fans, one could *a priori* think that the extra thickness may increase the dissipation of energy in the von Kármán street behind the blades so that the performances of the fan decrease and the pressure fluctuations in its wake increase. The effects of blade thickness on the overall performances are not so well known [9–12] and to the best of our knowledge the influence on the dynamics remains an open question.

Therefore this study intends to compare the aerodynamical performances of two axial-flow fans that only differ in the thickness of their blades. The geometry of the fans and the experimental setup are presented in Section 2. The results on the mean features are presented and discussed in Section 3: the overall characteristics of the two fans are presented in Section 3.1; the mean velocity fields downstream of the fans are compared in Section 3.2 and these results are briefly discussed in Section 3.3. Some results on local fluctuating quantities are presented and discussed in Section 4: measurements of the wall pressure fluctuations that are an

---

* Corresponding author.
E-mail address: florent.ravelet@ensta.org (F. Ravelet).

0894-1777/$ - see front matter © 2011 Elsevier Inc. All rights reserved.
doi:10.1016/j.expthermflusci.2011.01.002

image of the acoustical performances are presented in Section 4.1 and finally, phase-averaged velocity signals that are measured on one point are then compared in Section 4.2. Concluding remarks are then given in Section 5.

2. Experimental setup

2.1. Geometry of the two fans

The fans used in this study are two prototypes developed for automotive engine cooling system applications following the methods detailed in [13]. The fans are made out of aluminium and have the same geometrical characteristics except the blade thickness. The thin blades axial-flow fan is the reference and is labeled F_A. The thick blades fan is labeled F_B. Pictures of the thick blades fan are displayed in Fig. 1 with a drawing of a section of the F_A and F_B blades at hub, mid-span and tip. The main characteristics of the blade cascade are given in Table 1.

Each of these fans has six blades. The rotor is built up from blades of circular-arc camber lines, with NACA-65 profiles of mean chord $c = 74$ mm clipped at $0.95x/c$. The hub-to-tip radius ratio is $R_{int}/R_{max} = 0.365$ with tip radius $R_{max} = 179$ mm. The rotors are moreover shrouded with a zigzag circular collar in order to close the radial gap in the free-flow experimental facility (see Section 2.2 below). The spanwise load of the blades is prescribed following a controlled vortex design method [3,13]: in the present case the absolute tangential velocity downstream of the rotor V_θ increases linearly with the radius such that the Euler work per unit mass $\omega r V_\theta$ increases quadratically from the hub to the tip of the blades. The blade loading that is the ratio of the Euler work to the square of the peripheral velocity is moreover constant along the radial direction. With this design the hub losses are reduced and the blades are less twisted [3]. The blades are stacked on the trailing edge. The blades are finally swept forward in order to benefit from lower tonal noise as suggested by several studies [1–4]. The forward sweep may also increase or decrease the overall performance, depending on the blade loading distribution, as reported in Refs. [3,4].

The maximum blade thickness of the thin blade axial-flow fan F_A is 4 mm, *i.e.* 5.6% of the chord length at mid-span (conventional axial-flow fans usually have a relative maximum thickness varying from roughly 10% at hub to 7% at tip [13]). The blades of the second fan F_B are thickened to reach a maximum thickness of 10 mm, *i.e.* 13.5% of the chord length at mid-span. The thickness distribution e of fan F_B is: $e_B = 2e_A + 2$ mm. The Fan F_A was designed to meet the specifications point $\Delta p_{des} = 270$ Pa, $Q_{N,\,des} = 0.736$ m^3 s^{-1} for a nominal angular velocity $\omega_N = 260$ rad s^{-1}. The corresponding specific speed $\Omega = \frac{\omega\sqrt{Q}}{(\Delta p/\rho)^{3/4}}$ is $\Omega = 3.89$.

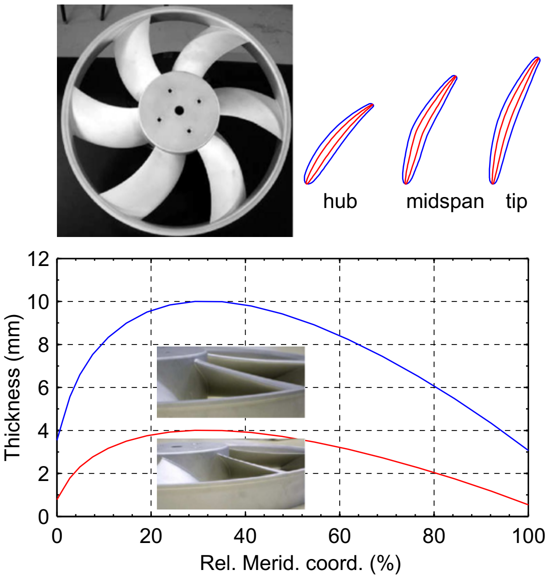

Fig. 1. Views of the two fans. Front view, sections of thick and thin profiles at various span locations and thickness distribution law along the meridional coordinate.

Table 1
Blade cascade parameters for the reference fan F_A. Radius R (mm). Chord length c (mm). Cascade solidity σ. Stagger angle γ (°). Profile designation according to the nomenclature given in Ref. [13]: NACA 65(*xx*)*yy* with (*xx*) representing the relative camber and *yy* standing for the relative thickness. Lieblein's diffusion factor D.

	R	c	σ	γ	Profile	D
Hub	65.4	66.6	0.97	53	NACA 65(07)06	0.372
Mid-span	122.2	74.0	0.58	66	NACA 65(10)05	
Tip	179.0	81.3	0.43	70	NACA 65(11)05	0.650

2.2. Normalized test benches and measurement techniques

2.2.1. Free-flow experimental facility

The Fig. 2a shows the experimental facility used to determine the overall performances of axial-flow fans in open-flow configuration. The air suction test bench was designed and built at the Dynfluid laboratory of Arts et Métiers ParisTech according to the ISO-5801 standard. It consists of a cuboid of size 1.3 × 1.3 × 1.8 m. A pierced plate inside it prevents the flow from having pre-rotation. The fans are placed at one end, the zigzag circular collar being tightly fitted to the bench. The air flow-rate is set and measured according to the ISO-5167 standard by setting the hydraulic impedance of the bench through diaphragms of various sizes that are placed at the other end.

Pressure rise Δp is measured with an absolute precision of ±0.1 Pa. The torque C on the fan shaft is measured with a HBM strain gauge transducer. The uncertainty of torque measurements corresponds to 0.1% of the maximum measured torque. The angular velocity ω is measured with a tachymeter of relative precision ±0.2%. The power adsorbed on the fan shaft is then estimated through the product $C\omega$. The accuracy of the whole system leads to a determination of the efficiency within about ±0.5%.

The mean velocity field in the wake of the fans has been measured with Two-Component Laser Doppler Anemometry (LDA), using a DANTEC "FlowExplorer"system. The method to get the three components of the mean velocity field downstream of the fan relies on the axisymmetry of the mean flow, that is *a posteriori* checked. The definition of the laboratory Cartesian coordinate system $\{X;Y;Z\}$ and of the two measuring planes is pictured in Fig. 3. The LDA system measures the velocities on the Y axis and on the Z axis. The measurement is first performed in the $\{Y;Z\}$ plane at a certain radial distance r from the axis of rotation, and at an (axial) distance z from the trailing edges of the fan in the Y direction (point 1 in Fig. 3). The measured velocities, in polar coordinates, are thus the radial velocity $V_r(r,z)$ and the axial velocity $V_z(r,z)$. The measuring volume is then precisely traversed to the same radial and axial distances r and z, but in the $\{X;Y\}$ plane (point 2 in Fig. 3). Special care has been given to the alignment of the system. The velocities that are measured at this second point, in polar coordinates, are thus the opposite of the tangential velocity $-V_\theta(r,z)$ and the axial velocity $V_z(r,z)$ that is measured two times. We then check that the two measurements give the same mean axial velocities: the difference between $V_z(r,z)$ in the two planes is less than 1% everywhere.

Constant Temperature Anemometry (CTA) with a 2D Dantec 55R51 hot fiber film probe has also been used to study more

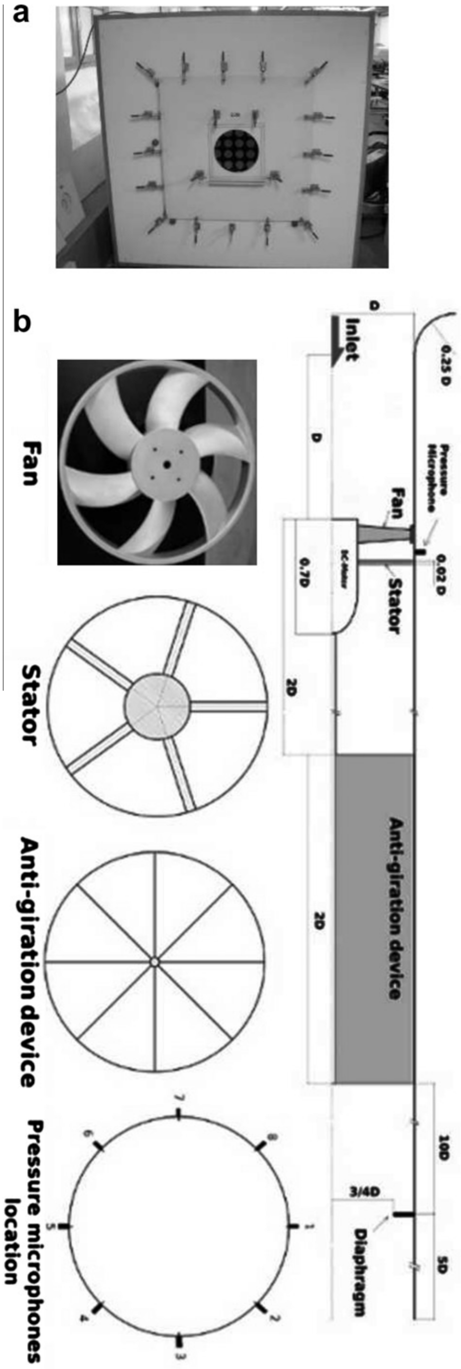

Fig. 2. ISO-5801 test benches. (a) Open-flow facility. The dimensions are 1.3 × 1.3 × 1.8 m. The fans suck the flow through the test bench. (b) Ducted-flow facility. This configuration is dedicated to the local measurements of wall pressure fluctuations. The fans blow the flow into the pipe.

specifically the velocity fluctuations and the phase-averaged velocity signals. The method to get the three velocity components is the same as described in Refs. [2,4] and is based on two measurements at different angular positions of the probe.

2.2.2. Ducted-flow experimental facility

In order to compare the behavior of the two fans in a ducted-flow configuration and to measure the wall pressure fluctuations, a second test bench was built according to the ISO-5801 standard (see Fig. 2b).

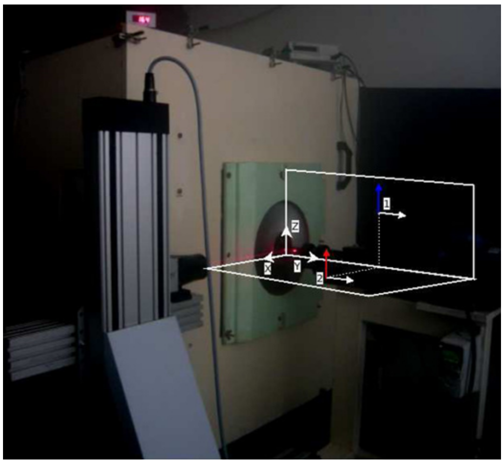

Fig. 3. Measurement of the mean exit-flow field with a Two-component LDA system. The measurements are taken in the two planes that are displayed with white lines. The origin of the coordinate system is centered on the rotation axis, and the axial position of the origin corresponds to the plane that contains the fans blades trailing edges. The LDA system measures the velocity in the Y and Z directions. At point 1 this corresponds to the axial V_z and radial velocities V_r. At point 2 this corresponds to the axial V_z and to the opposite of the tangential velocities $-V_\theta$.

It consists of a cylindrical pipe of inner diameter $D = 380$ mm. A bell mouth is flush-mounted at the inlet of the duct. The upstream face of the fan is at a distance D from the pipe inlet. A DC-motor is hidden in a casing of diameter 0.3D and length 0.7D, with a warhead-shape end. The binding to the tube is ensured by five rods of diameter 8 mm, i.e. 0.02D, in order to minimize their influence, regardless the flow-rate. The distance between the upstream face of the fan and the binding rods is 0.26D. An anti-gyration device made of eight metal sheets of thickness 1.5 mm and length 2D is placed 2D downstream of the rotor-stator set. It prevents the outgoing flow from having any rotating component. The static pressure of the axial fan is measured 1D downstream of the anti-gyration device, with an average over four flush-mounted pressure taps. The flow-rate is measured with a normalized diaphragm, located 10D downstream of the anti-gyration device and 5D upstream of the pipe outlet. The diaphragm has a diameter of 0.73D. Other diaphragms of various sizes are placed at the exit of the pipe to vary the test bench hydraulic impedance and thereby to vary the operating point of the studied axial-flow fan.

Wall pressure fluctuations are measured simultaneously by eight microphones that are evenly distributed on the circumference of the duct. They are mounted downstream of the fan, halfway between the fan and the five rods that ensure the binding to the tube (see Fig. 2b). The microphones are G.R.A.S 40BP 1/4″ polarized pressure microphones of sensitivity 1.65 mv Pa^{-1}, with G.R.A.S 26AC preamplifiers and a G.R.A.S 12AG power supply module. The signals are amplified with a gain of +30 dB and high-pass filtered with a three-pole Butterworth filter with cut-off frequency of 20 Hz. The signals are then digitalized using a NI Data Acquisition Card (M 6211, 16 bits) at a sample rate of 12 kHz.

3. Comparison of the mean features of the two fans

3.1. Overall characteristics

The characteristics of the two fans are shown in Fig. 4a together with the design operation point of the reference fan. The flow-rate coefficient (Φ) and pressure rise coefficient (Ψ) are defined respectively by Eqs. (1) and (2):

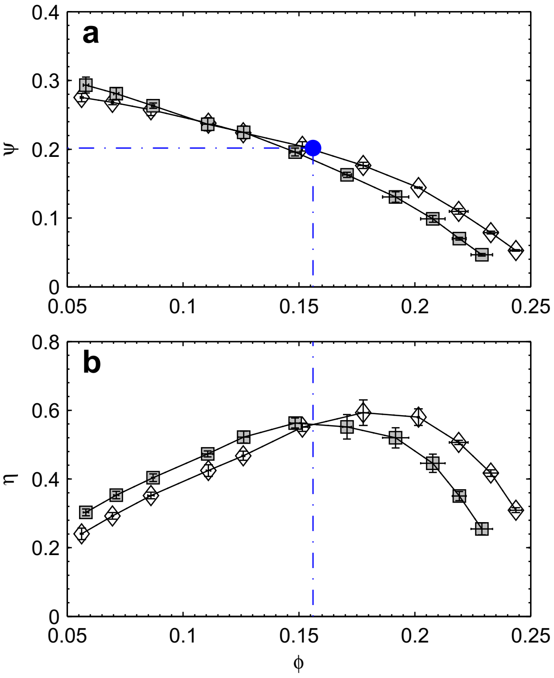

Fig. 4. Fans characteristics: (a) pressure rise coefficient Ψ *vs.* flow-rate coefficient Φ and (b) fans efficiency η *vs.* flow-rate coefficient Φ. (◇): thin blades fan F_A, (□): thick blades fan F_B and (•): design specification point. The reproducibility is evaluated from five independent experiments and displayed are errorbars magnified by a factor 3 for (a) and a factor 6 for (b).

$$\Phi = \frac{Q}{\pi \omega R_{max}^3} \qquad (1)$$

$$\Psi = \frac{\Delta p}{\frac{1}{2}\rho\omega^2 R_{max}^2} \qquad (2)$$

The design point thus corresponds to $\Phi_{des} = 0.156$ and $\Psi_{des} = 0.200$ and is indicated by a dot in Fig. 4a.

The curves are the results of five measurements at the nominal rotation rate $\omega_N = 260\ \mathrm{rad\ s^{-1}}$. The error bars in Fig. 4a stand for the standard deviation of the five measurements of Φ and Ψ, magnified by a factor three for better visualization. The pressure coefficient distributions are relatively similar to each other. The thin blades fan F_A matches the specifications point plotted in Fig. 4. At the design flow-rate, the thick blades fan F_B produces a pressure rise that is 8% below the specified pressure rise. The curve of F_B is moreover steeper than the curve of F_A and there is a cross-over between the two fans: at partial flow-rates below $\Phi = 0.11$, F_B produces more pressure rise than F_A; at overflow-rates, approximately beyond $\Phi = 0.2$, F_A produces this time more pressure rise than F_B and the difference of pressure rise between the two fans remains almost constant.

The efficiency coefficient (η) is defined by Eq. (3):

$$\eta = \frac{\Delta p Q}{C\omega} \qquad (3)$$

The efficiencies of both fans are shown in Fig. 4b with the flow-rate coefficient of the design point highlighted by the vertical dash-dotted line. The efficiencies distributions have a classical shape, with a slow evolution for partial flow-rates and a strong drop after the nominal flow-rate. The nominal flow-rate for F_A is $\Phi_{N,A} = 0.18$ and the corresponding pressure coefficient is $\Psi_{N,A} = 0.17$. The efficiency is then $\eta_{max,A} = 0.58 \pm 0.005$ which is pretty fair for this type of turbomachinery [13]. The maximum of η is shifted towards overflow with respect to the design point. This point is discussed below in Section 3.3.

The maximum efficiency for the thick blades fan F_B is $\eta_{max\ ,B} = 0.55 \pm 0.005$. The thickening of the blades has led to a decrease of 0.03 of η_{max}. The nominal flow-rate of F_B is shifted toward a partial flow-rate of about 17% with respect to the nominal flow-rate of F_A and the thick blades fan thus gives its best efficiency for a flow-rate $\Phi_{N,B} = 0.15$ very close to the design point $\Phi_{des} = 0.156$. The corresponding pressure coefficient is $\Psi_{N,B} = 0.19$. The distribution of the efficiency of F_B is moreover flatter than that of F_A: quantitatively, the range of flow-rates corresponding to a decrease of 3% of η from η_{max} is $\pm 0.3\ \Phi/\Phi_N$ for F_B, while it is only $\pm 0.2\ \Phi/\Phi_N$ for F_A.

As a partial conclusion please also note that although the thick blades fan F_B does not meet the specification point at the nominal angular velocity $\omega_N = 260\ \mathrm{rad\ s^{-1}}$, the desired point in a dimensional point of view ($\Delta p = 270\ \mathrm{Pa}$, $Q_N = 0.736\ \mathrm{m^3\ s^{-1}}$) can be reached with this fan rotating at $\omega =\ 270\ \mathrm{rad\ s^{-1}}$. Since the efficiency of the two fans is the same at such flow-rates ($\eta \simeq 0.55$), the use of F_B at $\omega = 270\ \mathrm{rad\ s^{-1}}$ in the automotive cooling application would lead to the very same power consumption as the use of F_A at $\omega_N = 260\ \mathrm{rad\ s^{-1}}$.

3.2. Comparison of the mean exit-flow fields

The mean exit-flow downstream of the rotors may give further information that help to understand the differences that have been observed on the overall characteristics. To compare the two fans F_A and F_B, two sets of measurement of the flow field have been performed. Each set consists in choosing one dimensional operating point (fixed diaphragm at the inlet of the free-flow experimental facility, flow-rate Q and pressure rise Δp) and in adjusting the rotation rates of the two fans to make them operating at this very same point.

The first set was made very close to the nominal flow-rate of F_B ($\Phi_{N,B} = 0.15$) and is presented in Fig. 5. The second set was made very close to the nominal flow-rate of F_A ($\Phi_{N,A} = 0.18$) and is presented in Fig. 6. The flow fields have been measured on a Cartesian grid that extends typically from $z = 20$ mm to $z = 150$ mm with a spacing of 10 mm (14 points in the axial direction) and from $r = 40$ mm to $r = 220$ mm or from $r = 65$ mm to $r = 255$ mm with a spacing of 5 mm (38 points in the radial direction). The mean data rate is 2000 Hz and the signal has been acquired for 15 s, *i.e.* roughly 500 revolutions of the rotor, at each position. The mean value and the standard deviation are thus well converged.

3.2.1. Discharge flow components

The flow fields in meridional plane, *i.e.* the discharging component $V_z(r,z)$ and the centrifugal component $V_r(r,z)$, are displayed in Figs. 5 and 6a and b.

One common feature of the two fans, regardless of the flow-rate, is the presence of a large recirculation, with small upstream velocities close to the hub: the discharged flow exits only for $r > 100$ mm. Measurements of the flow field close to the hub with CTA that do not give access to the velocity direction should be considered with caution. The main difference lies in the centrifugation of the flow by the two fans.

The meridional flow for F_A at a partial flow-rate of $\Phi/\Phi_{N,A} = 83\%$ is plotted in Fig. 5a. The flow downstream of the fan already has a very important radial component as noticed by Kergoulay et al. [2]. The discharging flows for the two fans at their respective nominal flow-rate (Fig. 6a for F_A and Fig. 5b for F_B) are very similar with smaller centrifugation for F_B. The meridional flow for F_B at an over-flow-rate of $\Phi/\Phi_{N,B} = 120\%$ is plotted in Fig. 6b and presents barely no centrifugation. There thus seems to be a tendency for the thick blades fan F_B to maintain a mainly axial exit-flow on a wider range of operating points.

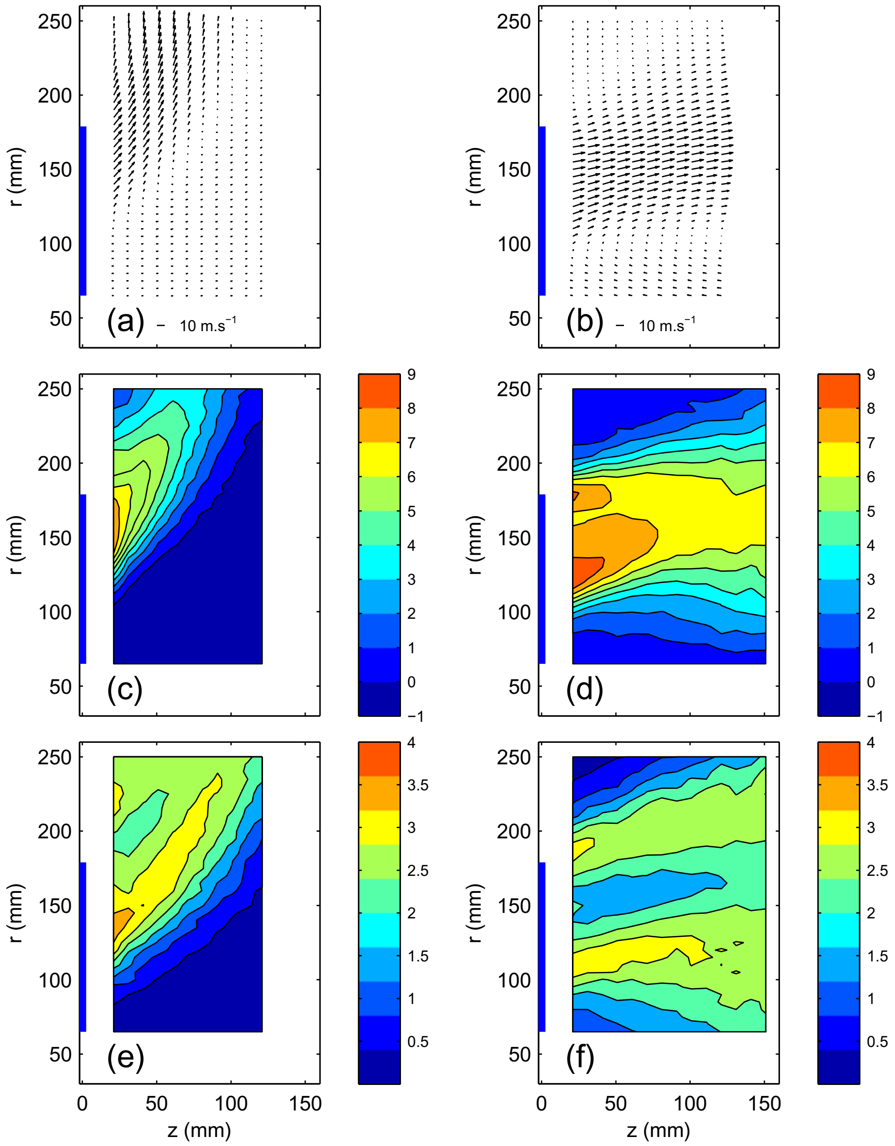

Fig. 5. Mean exit-flow measured by LDA close to the nominal point of F_B. (a, c and e) F_A rotating at $\omega = 209.5$ rad s^{-1} for a flow-rate $Q = 0.557$ m^3 s^{-1} and a pressure rise $\Delta p = 164$ Pa corresponding to a flow coefficient $\Phi_A = 0.148$. The discharge velocity $Q/(\pi R^2_{max})$ is 5.6 m s^{-1}. (b, d and f) F_B rotating at $\omega = 214.2$ rad s^{-1} to give the same flow-rate and pressure rise, that corresponds then to a flow coefficient $\Phi_B = 0.144$. (a and b) Mean meridional flow $\{V_r(r,z);\ V_z(r,z)\}$. (c and d) Mean tangential velocity V_θ. (e and f) Standard deviation of the tangential velocity $V_{\theta\ \mathrm{rms}}$. The blue patch in each figure stands for the position of the blades.

3.2.2. Mean tangential velocity

Contours of the tangential velocity field $V_\theta(r,z)$ are plotted in Figs. 5 and 6c and d. As a common feature for both fans, one can notice that the tangential velocity downstream of the rotors has significant values, of the order of the discharge velocity $Q/(\pi R^2_{max})$. At the design flow-rate, an extra static pressure rise of roughly $1/2\rho V_\theta^2 = 30$ Pa could be obtained by the use of a stator. That corresponds to 20% of the pressure rise and would lead to a significant increase of the efficiency. The tangential velocity fields are moreover strongly correlated to the meridional velocity field for both fans, regardless of the flow-rate. It is almost zero outside the discharge jet. The 3D structure of the exit-flow thus resembles an annular rotating jet. Close to the fans, there are two local maxima for nominal (Fig. 5d for F_B and 6c for F_A) and overflow-rates (Fig. 6d for F_B). The radial positions of these maxima are adjacent to the edges of the discharge jets.

The differences between the two fans lie in the magnitude and the axial attenuation of the tangential velocities. The velocities are stronger for the thick blades fan F_B—which is consistent with its overall lower efficiency—and the axial velocity decay is also slower. These two points are discussed below in Section 3.3.

3.2.3. Standard deviation of the tangential velocity

Contours of the standard deviation (or the root mean square *rms*) of the tangential velocity field $V_{\theta\ \mathrm{rms}}$ are plotted in Figs. 5 and 6e and f. The maxima of fluctuations are located at the edge of the discharge jet where the radial gradient in tangential velocity is steep, and the core of the jet corresponds to a local minimum of fluctuations. Finally, one can notice that the global level of fluctuations in the exit-flow of F_A is stronger than that in the exit-flow of F_B.

3.3. Remarks and discussion on the modifications of overall performances and of exit-flow topology

The nominal flow-rates of the two fans are different and furthermore do not match the design point (see Fig. 4b). The latter could be an effect of the forward sweep as noticed in Refs.

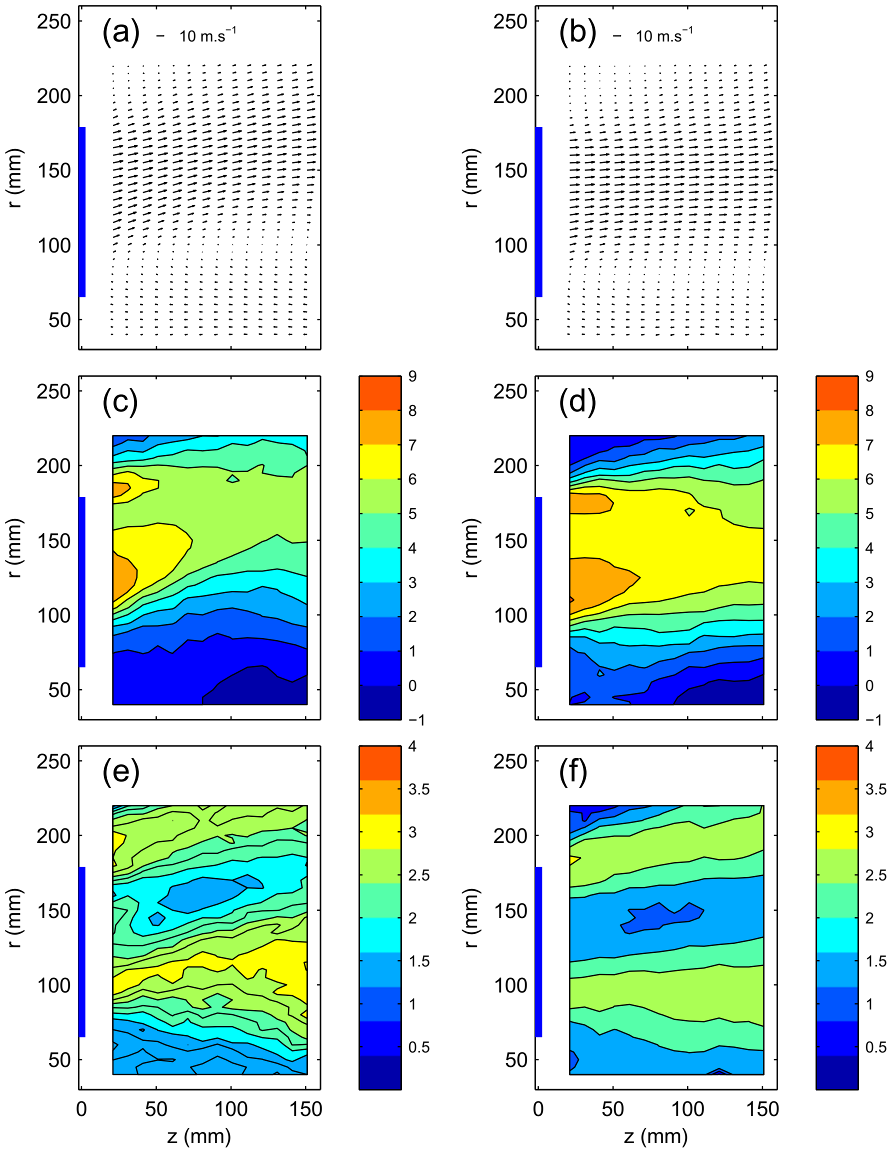

Fig. 6. Mean exit-flow measured by LDA close to the nominal point of F_A. (a, c and e) F_A rotating at $\omega = 209.5$ rad s^{-1} for a flow-rate $Q = 0.668$ m^3 s^{-1} and a pressure rise $\Delta p = 140$ Pa corresponding to a flow coefficient $\Phi_A = 0.178$. The discharge velocity $Q/(\pi R^2_{max})$ is 6.7 m s^{-1}. (b, d and f) F_B rotating at $\omega = 218.1$ rad s^{-1} to give the same flow-rate and pressure rise, that corresponds then to a flow coefficient $\Phi_B = 0.170$. (a and b) Mean meridional flow $\{V_r(r,z);\ V_z(r,z)\}$. (c and d) Mean tangential velocity V_θ. (e and f) Standard deviation of the tangential velocity $V_{\theta\ \mathrm{rms}}$. The blue patch in each figure stands for the position of the blades.

[3,4]: for comparable Controlled Vortex Design fans—of relative thickness 10% and pressure rise coefficient $\Psi_N \simeq 0.3$ for Vad [3] and of relative thickness 9% and pressure rise coefficient $\Psi_N \simeq 0.3$ for Hurault et al. [4] – both studies reported a decrease of the flow-rate and efficiency with respect to the design point when the fan blades are swept forward. However, the trend is not systematic and first depends on the blade loading that is directly linked to half of the pressure rise coefficient Ψ_N. Indeed, for a more loaded fan with more load near the tip, Hurault et al. [14] reported an increase of the nominal flow-rate with forward sweep. The fact that the nominal flow-rates of F_A is greater than the design point – computed with a method that had been validated for conventional thickness of roughly 7% [13] – while it is lower for F_B in the present study suggests that the shift of nominal flow-rate with respect to the design point could not be ascribed to the blade sweep alone but that blade thickness also plays a major role because it somehow modifies the blade loading and the balance between lift and losses.

Some results concerning the effects of thickness on the aerodynamic behavior of isolated profiles may help to explain the relative position, *i.e.* the cross-over between the two curves (see Fig. 4a). In general the thickening of isolated profiles leads to a reduction of the aerodynamic efficiency (lift to drag ratio) [7,8]. Even at the most efficient angle of attack, significant boundary layer separations are observed on thick profiles—of relative thickness above 10%—while not on thin profiles [11] and the lift is reduced. The viscous dissipation is moreover greater for thick profiles, especially when they have rounded trailing edge as it is the case here [10]. Despite these drawbacks, the thick profiles have the advantage of having a more progressive stall than thin profiles, at higher angles of attack. The first two points are most likely responsible for the lower pressure rise and the lower efficiency of F_B at nominal and overflow-rates where the angle of attack of the blade cascade is low: at high flow-rates the lift is increased for the thin blades fan F_A that means more pressure rise and the viscous losses are reduced and this could explain the shift of the nominal point towards higher flow-rates. The last feature is almost probably at the origin of the gain of pressure rise and of efficiency at partial flow-rates as observed for F_B in the present experiment: the losses that are dominated by the separation on the suction side are reduced and the lift is increased.

The effects of the thickness on the overall performances close to the nominal flow-rates could also be informed by the modifications of the exit-flow topology (see Figs. 5 and 6). The tangential velocities downstream of the fan F_B (Fig. 5d and Fig. 6d) are stronger than for the fan F_A (Fig. 5c and Fig. 6c). Since the velocity fields for the two fans have been measured at the same flow-rate and pressure rise, F_B rotating a little bit faster than F_A for that, the Euler work for F_B is thus greater than the Euler work for F_A and its static efficiency is lower. However, if one would have to use a stator, the fan F_B would lead to a greater recovery of static pressure which would increase the static efficiency of the stage. The regions of high velocity also extend further away axially and are moreover larger in radius for F_B: a stator could be positioned in a wider range of axial distance from the fans, which should be beneficial regarding interaction noise. And at last, the fact that the thick blades fan F_B maintains a mainly axial flow on a wider range of flow-rates (less centrifugation) would also increase the efficiency of a stator downstream of it.

4. Study of local fluctuations

The increase of blade thickness thus leads to strong differences in the mean-flow features of those two fans. The purpose of the present section is to study the influence of the blade thickness on local dynamics such as pressure and velocity fluctuations.

4.1. Wall pressure fluctuations

The results of this paragraph concern the two axial-fans operating in a ducted-flow configuration (see Fig. 2b). In that case there is a radial gap of 1.5 mm between the pipe and the collar surrounding the fan. It should be also noted that for technical reasons, the ducted experiments have been performed for an angular velocity $\omega = 209.5$ rad s^{-1} (2000 rpm). The presence of the gap substantially reduces the efficiency of the fans without modifying the nominal flow-rate: F_A reaches a maximum efficiency $\eta = 0.49$ for a flow coefficient $\Phi = \Phi_{N,A} = 0.18$. The pressure coefficient is $\Psi = 0.15$, slightly lower than in the free-flow experiment which presents no radial gap. The F_B fan reaches a maximum efficiency $\eta = 0.48$ at a flow coefficient $\Phi = \Phi_{N,B} = 0.15$ and a pressure coefficient $\Psi = 0.18$. The characteristic curves show similar behavior as in the free-flow case for nominal and overflow-rates. The behaviors at partial flow-rates are completely different owing to the presence of the tube that prevents the flow from being centrifuged. The results reported here are thus limited to flow-rates above $\Phi = 0.15$.

The wall pressure fluctuations are compared for two different flow-rates, corresponding to the nominal point of the thin blades fan $\Phi_{N,A} = 0.18$ and to the nominal point of the thick blades fan $\Phi_{N,B} = 0.15$. In every case, for a fixed diaphragm at the pipe exit, the angular velocity of one of the two fans has been set to $\omega = 209.5$ rad s^{-1} and the angular velocity of the second fan has been adjusted in order to give the same dimensional pressure rise and flow-rate for the two fans.

The squared amplitude spectra of wall pressure at flow-rate $\Phi_{N,A}$ are plotted in Fig. 7. The spectra $S(f)$ are expressed in dB using the formula:

$$S(f) = 20\,\log_{10}(p'(f)/p_0)$$

$p'(f)$ being the modified Welch-average Fourier Transform of the fluctuating pressure. The sampling time is 10 s, corresponding to approximately 330 fan rotations, and the spectra are an average of eight 50% overlapping parts, windowed with a Hamming window. The spectra are displayed between 150 and 850 Hz. The reference pressure is $p_0 = 1$ Pa.

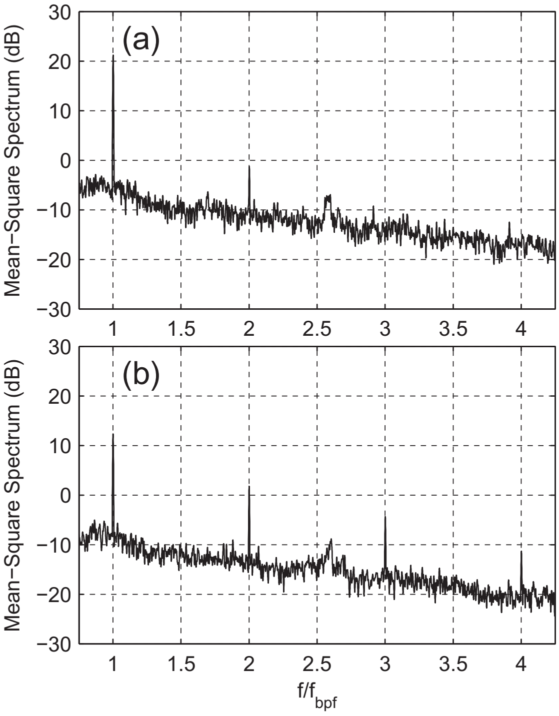

Fig. 7. Square amplitude spectra of wall pressure fluctuations for thin blades axial-flow fan F_A (a) and thick blades axial-flow fan F_B (b) at a flow-rate $\Phi = \Phi_{N,A} = 0.18$. F_A rotates at $\omega = 209.5$ rad s^{-1} and F_B rotates at $\omega = 211.5$ rad s^{-1} in order to give the same flow-rates and pressure rises.

Both fans exhibit relatively high discrete peaks, corresponding to the blade passing frequency f_{bpf} (200 Hz for F_A and 202 Hz for F_B) and its harmonics. The corresponding values are reported in Table 2. They are high above the broadband noise. The two fans differ however strongly by the repartition of energy between the different harmonics. For F_A, only the fundamental frequency f_{bpf} and the first harmonic $2f_{bpf}$ are visible. The level at f_{bpf} is 21 dB, and the level at $2f_{bpf}$ is −1.5 dB.

For F_B fan, the first three harmonics clearly appear. At the blade passing frequency f_{bpf} the level is 12 dB. At $2f_{bpf}$ it is 2 dB, at $3f_{bpf}$ it is −4 dB and at $4f_{bpf}$ it is −11 dB. For this flow-rate, the increase of blades thickness thus seems to lead to a decrease of the first peak level, and to an increase of the harmonics. The global level of fluctuations, *i.e.* $10\,\log_{10}(\sigma_p'^2/p_0^2)$, is moreover lower for the thick blades fan (F_B:19 dB) than for the thin blades fan (F_A: 23 dB).

The previously described features regarding both the spectral composition and the relative fluctuations levels could be due to the fact that the F_A fan is working at its nominal flow-rate while the F_B fan is working at overflow-rate. To answer this question we have performed the same experiment at the nominal flow-rate of the F_B fan.

Table 2
Level of wall pressure fluctuations at the blade passing frequency and its harmonics (dB) for both fans at flow-rate $\Phi_{N,A}$.

	f_{bpf}	$2f_{bpf}$	$3f_{bpf}$	$4f_{bpf}$	Total
F_A	21	−1.5	–	–	23
F_B	12	2	−4	−11	19

The squared amplitude spectra of wall pressure at the nominal flow-rate of the thick blades fan $\Phi_{tck} = 0.15$ are plotted in Fig. 8 and the levels of the discrete peaks are reported in Table 3. The blade passing frequency is now $f_{bpf} = 200$ Hz for F_B and 193 Hz for F_A. Please note that the angular velocity ratio needed to reach the same dimensional static pressure rise and flow-rate $\omega_B/\omega_A = 1.037$ is the same as the ratio discussed in Section 3.1 dedicated to the fan overall characteristics.

The results are very similar to the previously described flow-rate: for the F_A fan, the fundamental frequency f_{bpf} and the first harmonic $2f_{bpf}$ are still the only visible peaks in the spectrum. The level at f_{bpf} is 21 dB, and the level at $2f_{bpf}$ is -2 dB. For the F_B fan, the first three harmonics clearly appear. At the blade passing frequency f_{bpf} the level is 17 dB. At $2f_{bpf}$ it is 5 dB, at $3f_{bpf}$ it is -2.5 dB and at $4f_{bpf}$ it is -9.5 dB. The decrease of the first peak level and the increase of the level of the harmonics is also present at this flow-rate. The global level of fluctuations is 20 dB for the thick blades fan and 22.5 dB for the thin blades fan.

Fig. 9 presents autocorrelation and cross-correlation functions of wall pressure fluctuations for the two fans. The black curves correspond to the autocorrelation function:

$$A(\tau) = \frac{\langle p'_1(t)p'_1(t-\tau)\rangle}{\sigma^2_{p'1}}$$

and the red curves correspond to the cross-correlation function between microphones 1 and 5:

$$C_{1-5}(\tau) = \frac{\langle p'_1(t)p'_5(t-\tau)\rangle}{\sigma_{p'_1}\sigma_{p'_5}}$$

One can notice that the functions present a periodicity that corresponds to six events in one rotation that is the blade passing frequency. The time lag for the main peak in the cross-correlation function does match the angular distance between the microphones which is one half of a turn here. Another common feature between the two fans is that secondary peaks height for the autocorrelation function are close to the peaks height for the cross-correlation function. Some strongly coherent flow structures might be involved in this zone between the rotor and the binding static part. The strong difference between the F_A fan and the F_B fan is the value of the cross-correlation coefficient. It is significantly lower for the thick blades fan. This might be an imprint of structures dissipating more quickly in the wake of the thick blades fan F_B. Local velocity measurements in the wake of the fans may help to better understand this difference and the links between exit-flow dynamics and wall pressure fluctuations.

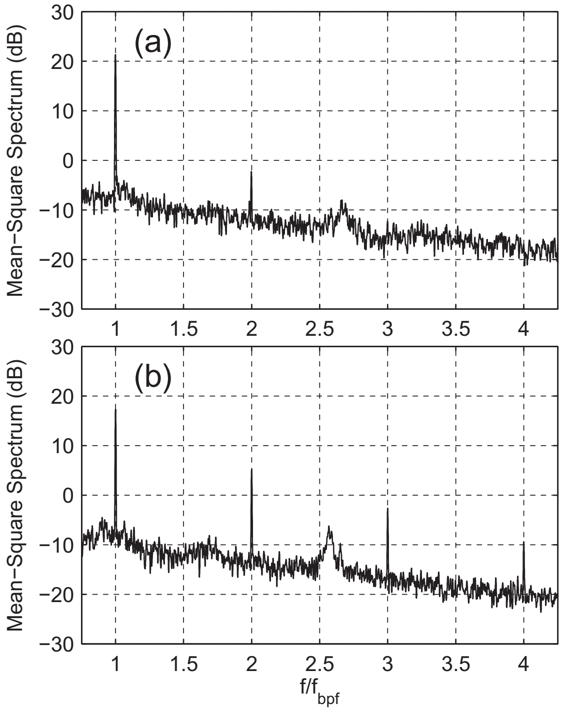

Fig. 8. Square amplitude spectra of wall pressure fluctuations for thin blades axial-flow fan F_A (a) and thick blades axial-flow fan F_B (b) at a flow-rate $\Phi = \Phi_{N,B} = 0.15$. F_B rotates at $\omega = 209.5$ rad s^{-1} and F_A rotates at $\omega = 202.7$ rad s^{-1}.

Table 3
Level of wall pressure fluctuations at the blade passing frequency and its harmonics (dB) for both fans at flow-rate $\Phi_{N,B}$.

	f_{bpf}	$2f_{bpf}$	$3f_{bpf}$	$4f_{bpf}$	Total
F_A	21	−2	–	–	22.5
F_B	17	5	−2.5	−9.5	20

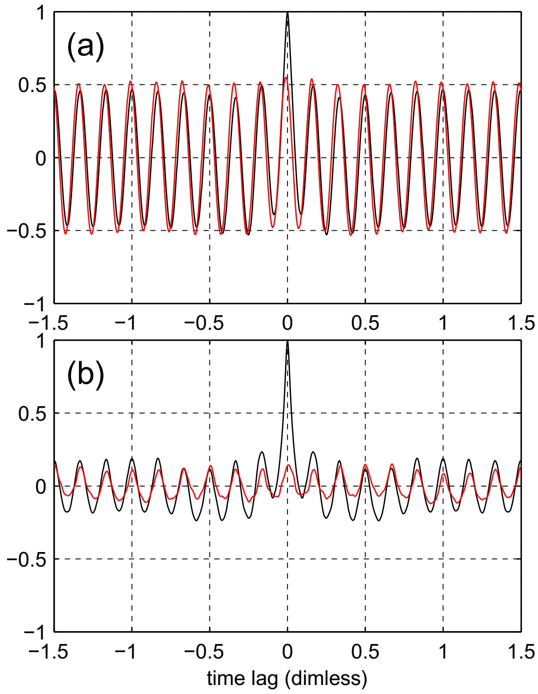

Fig. 9. Black curves: autocorrelation function of pressure fluctuations at position 1 (see Fig. 2b). Red curves: cross-correlation function of pressure fluctuations between position 1 and position 5 (see Fig. 2b). Top graph corresponds to F_A at $\Phi_{N,A} = 0.18$, bottom graph corresponds to F_B at $\Phi_{N,B} = 0.15$. The time is made non-dimensional with reference to one period of rotation: $t' = \frac{t\omega}{2\pi}$. (For interpretation of the references to colour in this figure legend, the reader is referred to the web version of this article.)

4.2. Local velocity measurements in the wake of the fans

Time-resolved signals of the tangential velocity downstream of the fans have been measured by Constant Temperature Anemometry (CTA) at an axial distance $z = 24$ mm downstream of the fan and at a radius $r = 120$ mm that corresponds to mid-span. The rotation rates of the fans have been adjusted to give the same operating point (fixed diaphragm at the inlet of the free-flow experimental facility, flow-rate Q and pressure rise Δp). This point is close to the nominal flow-rate of F_A ($\Phi_{N,A} = 0.18$) and the fans rotate at an angular velocity close to $\omega = 209$ rad s^{-1} (2000 rpm). An amount of 2^{19} samples have been recorded at an acquisition rate of

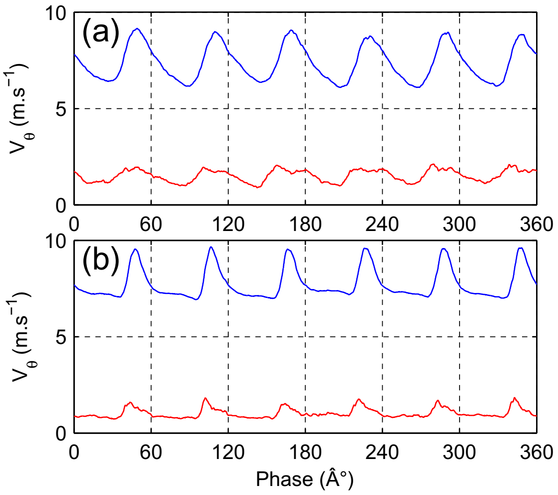

Fig. 10. Phase-averaged tangential velocity $V_\theta(\phi)$ (blue) and phase-averaged *rms* of the tangential velocity $V_{\theta\ \mathrm{rms}}(\phi)$ (red) at an axial distance $z = 24$ mm downstream of the fan and at mid-span $r = 120$ mm. The operating point is close to the nominal point of F_A. (a): F_A rotating at $\omega = 205.5$ rad s^{-1} for a flow-rate $Q = 0.620$ m^3 s^{-1} and a pressure rise $\Delta p = 125$ Pa corresponding to a flow coefficient $\Phi_A = 0.178$. (b): F_B rotating at $\omega = 209$ rad s^{-1} to give the same flow-rate and pressure rise, that corresponds then to a flow coefficient $\Phi_B = 0.170$. (For interpretation of the references to colour in this figure legend, the reader is referred to the web version of this article.)

120 kHz. That corresponds to roughly 150 revolutions of the fans and to approximately 3600 samples per revolution. The rotation rates have been measured with an encoder, synchronized to the CTA data acquisition, in order to perform analysis of phase-averaged signals [2]. This point has been chosen as close as possible to the fans blades, and such that the three components of the velocity are close for both fans, as can be seen in Fig. 6.

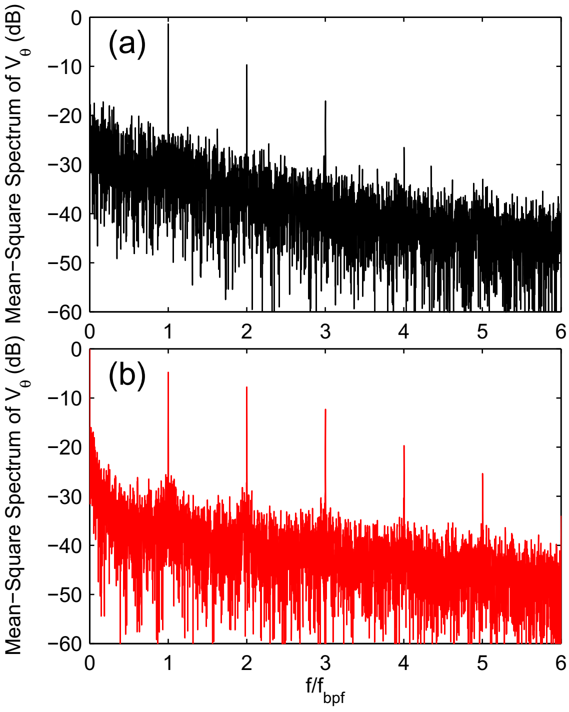

Fig. 11. Square amplitude spectra of $V_\theta(t)$ under the conditions of Fig. 10. (a) F_A fan. (b) F_B fan.

Table 4
Level of tangential velocity fluctuations at the blade passing frequency and its harmonics (dB) for both fans close to flow-rate $\Phi_{N,A}$.

	f_{bpf}	$2f_{bpf}$	$3f_{bpf}$	$4f_{bpf}$	$5f_{bpf}$
F_A	−1.4	−9.7	−17.1	−26.5	–
F_B	−4.8	−7.8	−12.3	−19.7	−25.4

The phase-averaged signals of the tangential velocity $V_\theta(\phi)$ are plotted in Fig. 10, ϕ being the phase on one revolution, in degree. Portions of signal of length corresponding to one revolution have been averaged. The signals for F_A (Fig. 10a) and for F_B (Fig. 10b) are periodic with a periodicity of 60° that corresponds to the blade passages. The shape of the signal for each blade is very similar owing to the very good symmetry and alignment of the system. The mean velocity is respectively 7.4 m s^{-1} for F_A and 7.7 m s^{-1} for F_B. For F_A, the signal has a more regular shape than for the thick blades fan F_B, and the peak-to-peak amplitude is bigger. These peak-to-peak phase-averaged fluctuations give the biggest contribution to the total standard deviation of the velocity. They should also give the biggest contribution to the peaks at blade passing frequency and its harmonics in velocity spectra as reported by Kergoulay et al. [2] and as can be seen from the phase-averaged *rms* of the tangential velocity $V_{\theta\ \mathrm{rms}}(\phi)$ plotted in red in Fig. 10.

The local tangential velocity spectra are plotted in Fig. 11. The peaks at the blade passing frequency and its harmonics are clearly visible and are reported in Table 4. The same features as for the wall pressure fluctuations studied in Section 4.1 are present: F_A has a stronger peak at f_{bpf} but smaller and fewer secondary peaks. This is consistent with the shape of the phase-averaged velocity signals (Fig. 10) and the fact that the main contribution to the peaks arises from this phase-averaged component of the velocity signal.

5. Conclusions

Two fans that differ only in the thickness of their blades were studied in order to highlight the effects of thickness on overall performances and the pressure and velocity fluctuations that are generated. The first fan, which has very thin blades, was designed to be part of the cooling system of an automotive vehicle power unit. The second compatible with the rotomoulding conception process, that generates only hollow parts with large edge radius, has much thicker blades.

The performances of the fans were measured and the results indicate that the overall performances were substantially equivalent, with a drop of 8% of pressure rise at conception flow-rate for the thick blades fan and a maximum efficiency that is 3% lower than the efficiency of the thin blades fan and that is shifted towards lower flow-rates.

Contrary to what one could a priori think the thick blades fan does present a certain number of interesting features:

1. The overall performances are only slightly decreased. The conception point can be reached by a relative increase of rotational speed of 4% for the same power consumption. The fact that the characteristic curve is steeper could be positive: the flow-rate is more stable with respect to small variations of the circuit hydraulic impedance. Finally, at very partial flow-rates, the thick blades fan produces more pressure rise than the thin blades fan, which could be beneficial concerning stall instabilities.
2. The mean exit-flow fields present significant differences. The tangential velocity component is stronger and remains high further away downstream of the thick blades fan F_B, which may increase the efficiency of a potential stator. The exit-flow

moreover remains axial on a wider operating range. The thin blades fan F_A leads to a more centrifuged discharging flow, which may be a configuration of interest in some applications, for instance for automotive cooling with the fan sucking air through the heat exchanger.

3. The wall pressure fluctuations just downstream of the fan are lower for the thick blades and their spectral decomposition is completely different. The same features are observed on velocity fluctuations. The spectral decomposition that shows stronger peaks at the blade passing frequency and less harmonics for the thin blades fan than for the thick blades fan, together with the phase-averaged analysis of velocity signals suggest that the pressure fluctuations are due to strong coherent wakes that are more dissipated with the use of thick blades. These measurements will be used as a benchmark for high-order finite volume CFD codes developed for aeroacoustics in the laboratory [15], and data are also available on request.

Further numerical and experimental investigations are planed to better understand the origins of the observed features that are reported in the present Article. The open questions that remain concern the influence of the blade thickness and of its distribution from leading edge to trailing edge on the blade loading and how this affects the efficiency and shift of the nominal flow-rate, the centrifugation of the exit-flow and the modifications of the pressure and velocity spectra.

References

[1] T. Fukano, Y. Kodama, Y. Takamatsu, Noise generated by low pressure axial flow fans, iii: effects of rotational frequency, blade thickness and outer blade profile, Journal of Sound and Vibration 56 (1978) 261–277.

[2] G. Kergourlay, S. Kouidri, G.W. Rankin, R. Rey, Experimental investigation of the 3d unsteady flow field downstream of axial fans, Flow Measurement and Instrumentation 17 (2006) 303–314.

[3] J. Vad, A.R.A. Kwedikha, Cs. Horváth, M. Balczó, M.M. Lohász, T. Régert, Aerodynamic effects of forward blade skew in axial flow rotors of controlled vortex design, Proceedings of the Institution of Mechanical Engineers, Part A: Journal of Power and Energy 221 (2007) 1011–1023.

[4] J. Hurault, S. Kouidri, F. Bakir, R. Rey, Experimental and numerical analysis of the sweep effect on three-dimensional flow downstream of axial flow fans, Flow Measurement and Instrumentation 21 (2010) 155–165.

[5] M. Anandha Rao, J.L. Throne, Principles of rotational molding, Polymer Engineering & Science 12 (1972) 237–264.

[6] A. Tcharkhtchi, J. Verdu, Structure-processibility relationships during rotational moulding of plastics, Advanced Engineering Materials 6 (2004) 983–992.

[7] B. Thwaites, Incompressible Aerodynamics, An Account of the Theory and Observation of the Steady Flow of incompressible Fluid past Aerofoils, Wings, and Other Bobies, Dover Publication, Inc., 1987.

[8] S.F. Hoerner, Fluid-Dynamic Lift, Hoerner Fluid Dynamics, 1985.

[9] R.J. Roelke, J.E. Haas, The effect of rotor blade thickness and surface finish on the performance of a small axial flow turbine, Journal of Engineering for Power 105 (1983) 377–382.

[10] J. Estevadeordal, S. Gorgineni, W. Copenhaver, G. Bloch, M. Brendel, Flow field in a low-speed axial fan: a dpiv investigation, Experimental Thermal Fluid Science 23 (2000) 11–21.

[11] C. Sarraf, H. Djeridi, S. Prothin, J.Y. Billard, Thickness effect of naca foils on hydrodynamic global parameters, boundary layer states and stall establishment, Journal of Fluids and Structures 26 (2010) 559–578.

[12] K.-S. Lee, K.-Y. Kim, A. Samad, Design optimization of low-speed axial flow fan blade with three-dimensional RANS analysis, Journal of Mechanical Science and Technology 22 (2008) 1864–1869.

[13] R. Noguera, R. Rey, F. Massouh, F. Bakir, S. Kouidri, Design and analysis of axial pumps, in: ASME Fluids Engineering, Second Pumping Machinery Symposium, Washington, USA, 1993, pp. 95–111.

[14] J. Hurault, S. Koudri, F. Bakir, R. Rey, Experimental and numerical investigation of downstream turbulence in axial flow fan, in: Fan Noise 2007 International Symposium, Lyon, 2007.

[15] F. Ravelet, S. Khelladi, H. Nouri, F. Bakir, H. Kim, Y. Bae, Y.J. Moon, Study of the aerodynamics/aeroacoustics of an axial-flow fan: experimental validation of a les/lpce/brinkman penalization method, in: 16th AIAA/CEAS Aeroacoustics Conference, 7–9 June 2010, Stockholm, Sweden, AIAA, 2010, pp. 2010–3869.

Experimental Study of the Instationary Flow Between Two Ducted Counter-Rotating Rotors

H. Nouri

A. Danlos
e-mail: amelie.danlos@gmail.com

F. Ravelet

F. Bakir

C. Sarraf

Arts et Metiers ParisTech,
DynFluid Lab.,
151 Boulevard de l'Hôpital,
75013 Paris, France

The purpose of this work is to study experimentally the aerodynamic characteristics of a subsonic counter-rotating axial-flow fans system operating in a ducted configuration. The fans of diameter $D = 375$ mm were designed to match the specification point using an original iterative method: the front rotor blade cascade is designed with a conventional inverse method, setting the radial distribution of the Euler work. The through-flow is then computed using an axisymmetric and radial equilibrium assumption, with empirical models of losses. The rear rotor is not conventional but is designed to straighten the radial profile of the tangential velocity. The design of the front rotor is then modified until the stage meets the requirements. The experimental setup is arranged such that the rotation rate of each fan is independently controlled and that the axial distance between the rotors can be varied from 17% to 310% of the midspan chord length. Systematic measurements of the global performances and local measurements of the velocity field and of the wall pressure fluctuations are performed, in order to first validate the design method, and to explore the effects of the two specific free parameters of the system, the axial spacing and the ratio of rotation rates. The results show that the efficiency is strongly increased compared to a conventional rotor or to a rotor-stator stage. The developed design method slightly overpredicts the pressure rise and slightly underpredicts the best ratio of rotation rates. Flow angle measurements downstream of the stage show that the outflow is not completely straightened at the design point. Finally, the system is highly efficient on a wide range of flow rates and pressure rises: this system has thus a very flexible use, with a large patch of high efficient operating points in the parameter space. [DOI: 10.1115/1.4007756]

1 Introduction

In the early studies in the 1930s [1,2], the counter-rotating machines aroused greater interest in the turbomachinery field, particularly for their potential improvement of the efficiency with respect to conventional machines by recovering more kinetic energy from the front rotor exit-flow. The first counter-rotating machines have appeared in aeronautic [1–3] and marine [4–6] applications, in open configuration. Nowadays, these machines with two coaxial axial-flow fans that rotate in opposite direction see a revival of interest in several distinct configurations, open and ducted flows, shrouded or not shrouded rotors, in various subsonic regime applications [7–10].

The previous studies concluded that the presence of the rear rotor improves the global efficiency [11,12] and also increases the operating flow-rate range. In the case of two counter-rotating rotors, there are at least two supplementary parameters that can influence the behavior of the system, the axial spacing between the two rotors, and the possibility of adjusting the rotation rate ratio [13]. The axial spacing may have a strong influence both on the global and local performances of the system [11,12]. An increase of this parameter leads to a decrease of the efficiency on the one hand, and to a decrease of the acoustic noise on the other hand. It is thus necessary to cope with this parameter in view of optimizing a counter-rotating fans system. Besides, in the case of two independent rotation rates, the variation of the rotation rate ratio may be a very interesting means to widen the operating range. In the industry, the use of frequency inverters and of industrial robots is moreover becoming widespread in order to save energy, which may favor the development of a lot of industrial applications of counter-rotating fans system in the near future. Furthermore, in the open literature only a few studies deal with rapid design methods applicable in industry without a systematic comings and goings between theoretical and CFD analysis.

The general aim of this study is to contribute to the development of a fast and reliable design method for such systems that take into account the effects of the various supplementary free parameters.

A system with two counter-rotating axial-flow fans (CRS) in a ducted flow configuration have been designed according to a method developed in the DynFluid Laboratory [14,15]. The two rotors can rotate independently and the distance between the rotors can be varied on a wide range. The first results show that the overall performances at the nominal design point are slightly lower than predicted, with a static pressure rise 10.2% lower. The static efficiency is however remarkably high ($\eta_s \simeq 65\%$) and corresponds to a 20 points gain in efficiency with respect to the front rotor maximal efficiency and to a 10 points gain with respect to the rear rotor. The overall measurements give the first clues that allow us to validate the design method. The first results on the effects of the rotation rate ratio and the axial spacing moreover confirm that the counter-rotating system has a very flexible use that allows work at a constant flow rate on a wide range of static pressure rises or to work at constant pressure rise on a wide range of flow rates, with static efficiency bigger than 60% [14].

This paper first presents an extension of the study of the global performances to a wider range of relative axial spacings A and rotation rate ratios θ. Emphasis is then placed on the interaction between the two rotors through local measurements of the velocity field with laser Doppler anemometry and local measurements of the wall pressure fluctuations on the casing. These local measurements give new light to the effects of the parameters A and θ on the performances.

The method that was specifically developed for the design of the CRS is first briefly presented in Sec. 2. The experimental setup is then described in Sec. 3. The global performances of the system

---

Contributed by the International Gas Turbine Institute (IGTI) of ASME for publication in the Journal of Engineering for Gas Turbines and Power. Manuscript received August 12, 2012; final manuscript received September 14, 2012; published online January 8, 2013. Editor: Dilip R. Ballal.

Table 1 Design point of the counter-rotating system for air at $\rho = 1.21$ kg m^{-3}

	CRS	Front rotor	Rear rotor
D (mm)	380	380	380
R_{tip} (mm)	187.5	187.5	187.5
R_{hub} (mm)	55	55	55
Z	—	11	7
Δp_t (Pa)	420	260	160
N (rpm)	1900	2000	1800
Q (m^3 s^{-1})	1	1	—
$\Omega = \dfrac{\omega\sqrt{Q}}{(\Delta p_t/\rho)^{3/4}}$	2.46	3.71	—
Other constraints	Axial exit-flow	Constant vortex	$\alpha_{1\mathrm{RR}}(r) = \alpha_{2\mathrm{FR}}(r)$ $C_{a1\mathrm{RR}}(r) = C_{a2\mathrm{FR}}(r)$

for the design parameters are given in Sec. 4.1. The effects of the relative axial spacing A on the local features are explored in Sec. 4.2. The potential of improving the performances with adjusting the rotation rate ratio θ is then discussed in Sec. 4.3. Finally, conclusive remarks are given in Sec. 5.

2 Design of the Rotors

The design of the rotors is based on the use of the software MFT (mixed flow turbomachinery) developed by the DynFluid Laboratory [15]. The front rotor is conventional: the radial distribution of the outflow tangential component, i.e., of the Euler work, is imposed following classical laws. The design of the second rotor is not conventional as far as, on the one hand, it is adapted to the actual outflow velocity profile downstream of the front rotor that is predicted by MFT, and on the other hand, it is designed to have a pure axial exit-flow. More details about the method can be found in Ref. [14].

The design point of the counter-rotating system (CRS) is given in Table 1. The system is designed to achieve a total-pressure rise $\Delta p_t = 420$ Pa at flow rate $Q = 1$ m^3 s^{-1} for a mean rotation rate $N = 1900$ rpm with air at density $\rho_{\mathrm{des}} = 1.21$ kg m^{-3}. The CRS is moreover constrained to have a solely axial discharge flow at the nominal flow rate.

The two rotors, i.e., the front rotor (FR) and the rear rotor (RR), are then designed following an iterative procedure:

- The pressure rise of the front rotor is initially chosen and FR is designed with the MFT software, that is based on the inverse method with simplified radial equilibrium [15].
- The behavior of the designed FR is then analyzed with MFT, using a direct method. The effects of the real fluid are partially taken into account with the introduction of an axial-velocity distribution which considers the boundary layers at the hub and casing. If the design point is not met, the blade cascade can be slightly modified by hand, for instance by changing the value of the hub and tip Lieblein's diffusion factors or the number of blades.
- The total pressure rise of FR $\Delta p_{t\mathrm{FR}}$ is computed. The profiles of axial and tangential velocities ($C_{a2\mathrm{FR}}(r) = C_{a1\mathrm{RR}}(r)$ and $C_{u2\mathrm{FR}}(r) = C_{u1\mathrm{RR}}(r)$, respectively) and the profile of flow angle $\alpha_{2\mathrm{FR}}(r)$ at the trailing edge of the FR blades are also computed (see Fig. 1), in contrast to other design methods [7–9]. The RR is drawn in such a way that the exit flow is purely axial, that is $\alpha_{2\mathrm{RR}} = 0$ deg, using a Matlab script, assuming that the axial velocity profile is kept constant across RR, i.e., $C_{a2\mathrm{RR}}(r) = C_{a1\mathrm{RR}}(r)$. Under these assumptions, the total pressure rise of RR should be $\Delta p_{t\mathrm{RR}} = \eta_{\mathrm{est}}\rho_{\mathrm{des}}U_{m\mathrm{RR}}C_{u2\mathrm{FR}}$, with $\eta_{\mathrm{est}} = 60\%$ an estimate of the rotor efficiency.
- The total pressure rise of the CRS is computed as $\Delta p_{t\mathrm{CRS}} = \Delta p_{t\mathrm{FR}} + \Delta p_{t\mathrm{RR}}$. If the design point is not met, the design pressure rise of FR is varied and the calculations are made again.

The drawback of this method is that the losses and interactions in-between the two rotors are not taken into account. The effects of the relative axial spacing A in particular are not taken into account. In the present case, this direct analysis of FR predicts a mean absolute tangential velocity downstream of the front rotor $C_{u2\mathrm{FR}} \simeq 9.6$ m s^{-1} with a radial distribution uniform within $\pm 5\%$ (constant vortex design) at the design flow rate. The Reynolds number based on the inlet relative velocity and on the chord length $\mathrm{Re} = (W_1 c)/\nu$ varies from $\mathrm{Re}_{\mathrm{hub}} = 0.6 \times 10^5$ at the hub to $\mathrm{Re}_m = 3 \times 10^5$ at midspan and $\mathrm{Re}_{\mathrm{tip}} = 7 \times 10^5$ at the tip. The geometrical characteristics of the rotor blades obtained with this method are summarized in Table 2, and pictures of the front and

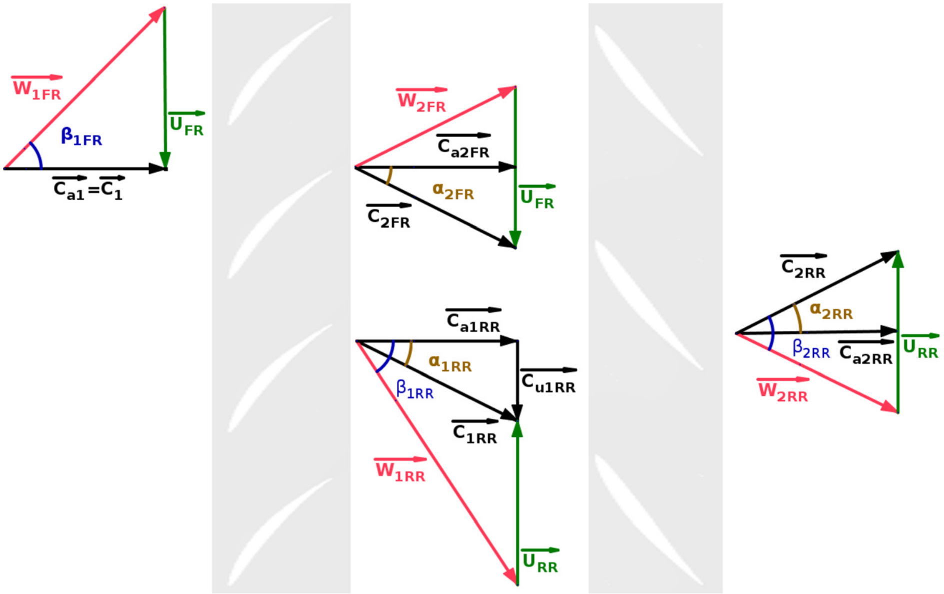

Fig. 1 Velocity triangles for the CRS. The fluid is flowing from left to right. Please see the Nomenclature for the meaning of the capital letters and subscripts. Please also note that this is a general case where the exit-flow is not constrained to be solely axial.

Table 2 Blade cascade parameters for the two rotors. Radius R (mm), chord length c (mm), cascade solidity σ, stagger angle γ (deg). Profile designation according to the nomenclature given in Ref. [15]: NACA65(xx)yy with (xx) representing the relative camber and yy standing for the relative thickness. Lieblein's diffusion factor $\mathcal{D}$.

Radial position	R	c	σ	γ	Profile	$\mathcal{D}$
Front rotor (blade thickness 4.5 mm)						
Hub	55	40.3	1.28	23	NACA 65(26)11	0.62
Midspan	121.25	58.0	0.84	57	NACA 65(12)07	
Tip	187.5	75.7	0.71	69	NACA 65(07)06	0.44
Rear rotor (blade thickness 6 mm)						
Hub	55	58.8	1.18	73	NACA 65(03)10	0.61
Midspan	121.25	72.9	0.66	65	NACA 65(05)08	
Tip	187.5	87.1	0.51	75	NACA 65(04)07	0.46

rear rotors are given in Fig. 2. The profiles of $C_{a2\mathrm{FR}}(r)$ and $C_{u2\mathrm{FR}}(r)$ computed with MFT, on which the design of RR is based, are plotted in Fig. 5 below.

The behavior of the designed machine resulting from the above method can then be measured in order to answer the following questions:

- Is the design-point achieved?
- What are the characteristics of the machine at the neighborhood of the design point?

3 Experimental Setup

3.1 Test Bench. The counter-rotating system is studied in a ducted-flow test rig, AERO^{2}FANS, that has been built according to the ISO-5801 standards (installation of category B) [16,17]. Figure 2 shows this test rig. It consists of a cylindrical pipe of inner diameter $D = 380$ mm. A bell mouth is flush-mounted at the inlet of the duct to reduce the energy loss due to fluid friction and flow separation of the inlet flow. The upstream face of the FR is at a distance $5D$ from the pipe inlet. A honeycomb is placed upstream of the FR to homogenize the incoming flow. Two brushless PANASONIC A4 motors drive each rotor separately and are hidden in a casing of diameter $0.33D$ and of length $0.45D$, with a warhead-shape end. The front and the rear motors are bound to the tube by two rod rows (3 and 5 rods, the first row being at $0.1D$ from the rear rotor). For the front motor the honeycomb is placed between the two rows to reduce the rods effect on the incoming flow at the inlet of the FR. An antigyration device made of eight metal sheets of thickness 1.5 mm and length $2D$ is placed $2D$ downstream of the CRS. It prevents the outgoing flow from having any rotating component by converting the dynamic pressure of the rotational component to thermal energy. Therefore, as the outgoing flow is supposed to contain only an axial component perpendicular to the pressure taps with no radial dependence, the static pressure that is measured $1D$ downstream of the antigyration device with an average over four flush-mounted pressure taps, is equal to the average pressure in the section. To make the installation more compact, a tube bend of 180 deg is placed $1D$ downstream of the pressure taps. The flow rate is measured with a normalized diaphragm, located $10D$ downstream of the tube bend and $5D$ upstream of the pipe outlet. The diaphragm has a diameter of $0.73D$. An iris damper, originally used for air flow regulation in ducts, is placed at the exit of the pipe to vary the test-bench hydraulic impedance and thereby to vary the operating point of the studied axial-flow fan. Finally, an axial blower can also be used at the exit of the pipe to widen the explored flow-rate range.

3.2 Measurements Methodology and Accuracy

3.2.1 Control Parameters. The study focuses on the influence of the gap between the rotors (relative axial spacing A) as well as on the influence of the ratio of rotation rates $\theta = N_{\mathrm{RR}}/N_{\mathrm{FR}}$. Six axial spacings, from $S = 10$ mm to $S = 180$ mm were investigated. They correspond to relative axial spacings with respect to the chord

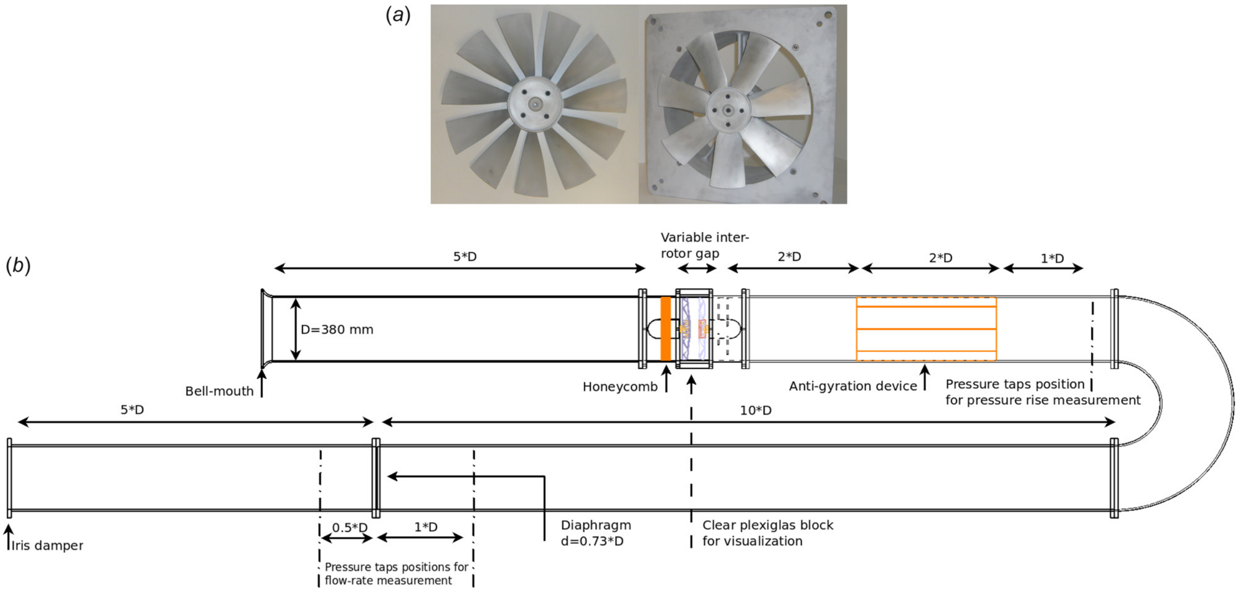

Fig. 2 Experimental facility for CRS, AERO^{2}FANS

of FR at midspan ($c_{m\mathrm{FR}} = 58$ mm) $A = S/c_{m\mathrm{FR}} \in [0.17, 0.34, 0.69, 0.86, 2.58, 3.10]$. Blocks of different thicknesses are used to change the axial spacing. Unless specified, the default relative axial spacing is $A = 0.17$.

Regarding the ratio θ, each rotor is driven separately so all combinations are possible. The default configuration is $\theta = 0.9$ (see Table 1). The motors are driven with two servo-controllers with a close loop regulation that is excellent; their rotation rate is constant within ±2 rpm.

3.2.2 Static Pressure Rise. According to the ISO-5801 standard [16], the static pressure rise is defined as the difference between the static pressure downstream of the fan and the total pressure at the duct inlet,

$$\Delta p_s = p_{s\mathrm{RR2}} - p_{\mathrm{atm}}$$

It is of practical interest for applications where a fan sucks air from the atmosphere and blows it into a circuit with an exit to the atmosphere (open circuit). In the present article, only the static pressure rise is considered and all figures relative to the CRS performances are performed with the above definition. The measurements are corrected with the static pressure drop due to the entrance loss, the honeycomb, the rotor casings, and the antigyration device that has been measured separately; the rotors have been removed and the blower has been used to create a flow.

In the design of the CRS, it has been imposed a pure axial-flow at the exit of RR. In that specific case the static pressure rise of the CRS should be $\Delta p_s = \Delta p_t - 1/2\rho(Q/(\pi D^2/4))^2 \simeq 373$ Pa. The only way to measure the total pressure rise of the system in a general case that includes radial dependence of the discharge flow with axial, radial, and tangential components is to measure the whole velocity and pressure fields on a section downstream of RR.

The atmospheric pressure, the dry temperature and the wet temperature have been measured. The density of the air is then computed for each measurement. It has been found that the maximum variation in density, relative to the design density, $\rho_{\mathrm{des}} = 1.21$ kg m^{-3} is $\pm 2.2\%$. Therefore, in order to present homogeneous results, the pressure rise that is discussed in the following has been multiplied by the ratio of the design density ρ_{des} over the experimentally measured density, ρ, i.e., ρ_{des}/ρ.

The static pressure rise is measured with an absolute precision of ±1 Pa. The correction for the losses also introduces an error of ±3 Pa. Finally, the relative uncertainty of the measurement of ρ is $\pm 1\%$. Therefore, the error bars that are displayed in the following figures for the static pressure rise stand for the uncertainty of the normalized pressure rise, computed using standard uncertainty evaluations methods.

3.2.3 Volumetric Flow-Rate Measurement. The measurement of the volumetric flow rate is done by measuring a singular pressure drop $\Delta p_{\mathrm{diaph}}$ on a diaphragm, $Q \propto \sqrt{\Delta p_{\mathrm{diaph}}/\rho}$. The relative uncertainty of the measured flow rate is of the order of $\pm 0.5\%$ at the nominal flow rate.

3.2.4 Static Efficiency. The static efficiency is defined by Eq. (1), with Q the volumetric flow rate, ΔP_s the measured static pressure rise, T the torque, and ω the angular velocity,

$$\eta_s = \frac{\Delta P_s Q}{(T_{\mathrm{FR}}\omega_{\mathrm{FR}}) + (T_{\mathrm{RR}}\omega_{\mathrm{RR}})} \tag{1}$$

The torque T was measured using the drivers provided with the motors. A calibration measurement has been performed with a conventional torque-meter. This calibration step shows that the measure of the torque supplied by the driver is very precise, the difference between the two measurements is below $\pm 0.5\%$. The relative uncertainty of the static efficiency is of the order of $\pm 1\%$.

3.2.5 Velocity Measurements and Flow Visualization. Laser Doppler anemometry (LDA) measurements have been performed locally in-between the rotors in order to study the influence of the axial spacing on the flow in this mixing region. The axial and tangential components of the velocity along the radial direction were measured using a one-component LDA system through a thin ($e = 2.5$ mm) and flat window, integrated to the duct. Beside these local and unstationary measurements, original measurements of the absolute flow angle were performed with a high speed camera and a thin wind vane. This method is inspired from the wool tufts visualization technique but instead of wool tufts, a small and light plate is used in order to determine the flow angle downstream of the rear rotor. The images are analyzed with Matlab, using the pattern recognition algorithms described in Ref. [18] in order to compute the average value of the absolute flow angle and its fluctuations.

3.2.6 Wall Pressure Fluctuations. Wall pressure fluctuations are measured simultaneously by four microphones that are evenly distributed on the circumference of the duct. They are mounted downstream of the front rotor, at various axial distances. The microphones are G.R.A.S 40BP 1/4 in. polarized pressure microphones of sensitivity 1.65 mV Pa^{-1}, with G.R.A.S 26AC preamplifiers and a G.R.A.S 12AG power supply module. The signals are amplified with a gain of +30 dB and high-pass filtered with a three-pole Butterworth filter with cut-off frequency of 20 Hz. The signals are then digitalized using a NI Data Acquisition Card (PCI 6123 S, with simultaneously sampled channels, 16 bits) at a sample rate of 6 kHz.

4 Results and Discussion

4.1 Overall Performances of the Reference System ($\{\theta = 0.9; A = 0.17\}$). The characteristics of the FR rotating alone (RR has been removed from its shaft in that case), of the RR rotating alone (FR has been removed) and of the counter-rotating system are shown in Fig. 3. The operating rotation rates are the design rotation rates, i.e., 2000 rpm for the front rotor and 1800 rpm for the rear rotor. The nominal flow rates of the three systems, i.e., the flow

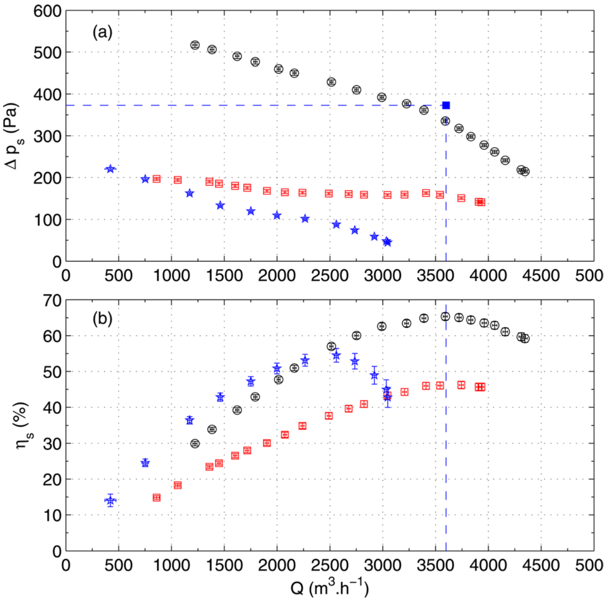

Fig. 3 Fans characteristics (*a*) static pressure rise Δp_s versus flow rate Q; (*b*) static efficiency η_s versus flow rate Q. The axial spacing is $A = 0.17$. Red □: FR rotating alone at $N_{\mathrm{FR}} = 2000$ rpm (RR has been removed), blue ★: RR rotating alone at $N_{\mathrm{RR}} = 1800$ rpm (FR has been removed) and black ○: CRS at $N_{\mathrm{FR}} = 2000$ rpm and $\theta = 0.9$. The blue ■ and the dashed lines stand for the design point of the CRS. The error bars stand for the measurement uncertainty.

Table 3 Nominal points of FR rotating alone at $N_{FR} = 2000$ rpm, RR rotating alone at $N_{RR} = 1800$ rpm, and CRS at $N_{FR} = 2000$ rpm and $\theta = 0.9$ (see also Fig. 3)

	Front rotor	Rear rotor	CRS
Maximum efficiency (%)	46.2 ± 1	54.4 ± 1	65.4 ± 1
Nominal Q ($m^3\ s^{-1}$)	1.01 ± 0.01	0.70 ± 0.01	1.00 ± 0.01
Δp_s (Pa)	157 ± 3	88 ± 3	335 ± 5

rates at maximum efficiency, are reported in Table 3 together with the corresponding static pressure rises and efficiencies.

The front rotor rotating alone has a very flat curve (red □ in Fig. 3). The characteristic curve could not be explored for flow rates higher than 3800 $m^3\ h^{-1}$, i.e., 1.06 $m^3\ s^{-1}$, even with the help of the blower. The measured static pressure rise at the design point is 157 Pa, with a relatively low static efficiency of 46%. Numerical analysis performed with MFT [15] and with Fluent 6.3 give very similar results for the static pressure rise ($142 \leq \Delta p_s \leq 153$ Pa). The total pressure rise predicted by these two different numerical methods, a model using semiempirical correlations versus computational fluid dynamics, is roughly 260 Pa. The predicted global performances of FR can thus be considered as validated. The remaining question is about the prediction of the exit-flow velocity components, i.e., of the exit-flow angles. The comparison of the predicted and measured velocity profiles is presented in Sec. 4.2.

The rear rotor rotating alone has a steeper curve (blue ★ in Fig. 3) and its nominal flow rate $Q \simeq 2550$ $m^3\ h^{-1}$ is lower than the design flow rate of FR and CRS. First, this is consistent with the bigger stagger angle of the blades (see Table 2). This rotor is not conventional. Let us be reminded that it has been designed to be adapted to a flow rate $Q = 1$ $m^3\ s^{-1}$ with prerotation.

Let us examine the velocity triangles in Fig. 1 and consider the case with the front coupled to the rear rotor: the incoming velocity $C_{1RR} = C_{2FR}$ has an axial component as well as a tangential component. Hence, the flow angle in the relative reference frame reads

$$\tan(\beta_{1RR}) = \frac{U_{RR} + C_{u1RR}}{C_{a1RR}} \tag{2}$$

Now the case without the front rotor is considered and it is assumed that the flow through the honeycomb is axial. Since the tangential component does not exist anymore and the incoming velocity has only the axial component, Eq. (2) becomes

$$\tan(\beta_{1RR}) = \frac{U_{RR}}{C_{a1RR}} \tag{3}$$

One can compute the result of Eq. (2) for the mean radius and at the nominal flow rate of the CRS, and by assuming that the tangential velocity is well predicted by MFT, that is $\langle U_{RR} \rangle \simeq 22.9$ m s^{-1}, $\langle C_{a1RR} \rangle \simeq 8.8$ m s^{-1}, and $\langle C_{u1RR} \rangle = \langle C_{u2FR} \rangle \simeq 9.6$ m s^{-1}. This leads to $\langle \tan(\beta_{1RR}) \rangle \simeq 3.69$. Supposing that RR rotating alone has its maximum efficiency when the tangent of the inlet flow-angle is equal to this value, Eq. (3) implies that this is for a flow rate, such that $\langle C_{a1RR} \rangle = \langle U_{RR} \rangle / \tan(\langle \beta_{1RR} \rangle) \simeq 6.2$ m s^{-1}, i.e., $Q \simeq 0.705$ $m^3\ s^{-1}$ or 2540 $m^3\ h^{-1}$. This is exactly the nominal flow rate of the RR rotating alone (see Fig. 3 and Table 3).

The characteristic curve of the CRS (black ○ in Fig. 3) is steeper than the characteristic curve of the FR. It is roughly parallel to the RR curve. The nominal flow rate of the CRS matches well with the design flow rate, i.e., 1 $m^3\ s^{-1}$. The static pressure rise at the nominal discharge ($\Delta p_{sCRS} = 335$ Pa) is 10.2% lower than the design point (373 Pa), which is not so bad in view of the rough approximations used to design the system.

The CRS has a high static efficiency ($\eta_{sCRS} = 65\%$) compared to a conventional axial-flow fan or to a rotor-stator stage with similar dimensions, working at such Reynolds numbers [19,20]. The gain in efficiency with respect to the front rotor is 20 points, while an order of magnitude of the maximum gain using a stator is typically 10 points [19,20]. The efficiency curve is moreover very flat, the flow-rate range for which the static efficiency lays in the range $60\% \leq \eta_s \leq 65\%$ is $2750 \lesssim Q \lesssim 4150$ $m^3\ h^{-1}$, that is, from 76% of the nominal flow rate up to 115% of the nominal flow rate. One open question is to what extent the global performances of the CRS are affected by the axial spacing and the ratio of rotation rates, and whether the efficient range could be extended by varying this ratio.

4.2 Influence of the Relative Axial Spacing *A*

4.2.1 Global Performances. Figure 4 shows the characteristics curves at the design rotation rates, i.e., $N_{FR} = 2000$ rpm and $\theta = 0.9$. For all axial spacings, the overall performances hardly change near the nominal flow rate. They tend however to decrease by less than 5% when increasing A. The efficiency decreases by only 2 points and the nominal flow rate (defined by the highest efficiency) does not change for the different cases. The relative axial spacing parameter A, does not seem to affect global performances. This would be the case if the axial and tangential components of the velocity fields do not vary significantly with A. This point is addressed in the following paragraph, where, unless specified, more local studies are performed at the design point of the system ($N_{FR} = 2000$ rpm, $\theta = 0.9$, and $Q = 1$ $m^3\ s^{-1}$).

4.2.2 Mean Velocity Field in Between the Two Rotors. Local LDA measurements of the axial and tangential components were performed along the spanwise direction for three relative axial spacings, $A = \{0.17; 0.86; 3.1\}$. The radial profiles at a distance $d = 5$ mm downstream of FR of the time-average of both components are plotted in Fig. 5 and compared to the values predicted by MFT (□). First, the flow rate that is computed with an integration of the axial velocity is $Q = 1.00 \pm 0.02$ for all the presented cases, in excellent agreement with the flow rate measured with the in-duct diaphragm. The measured axial profiles (Fig. 5(*a*)) are not

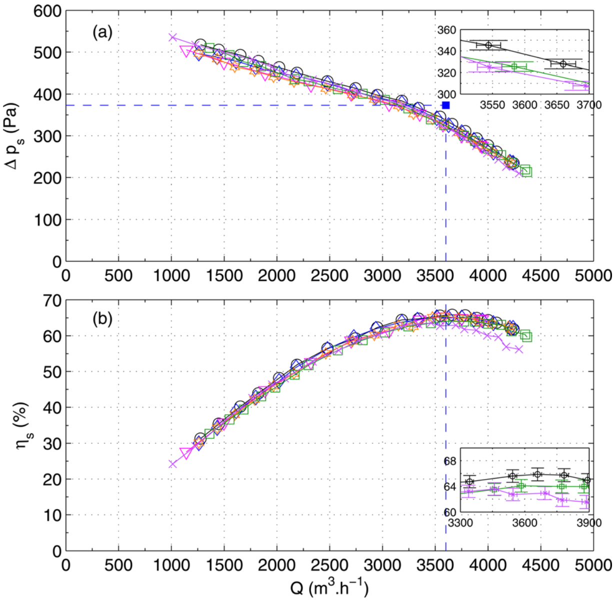

Fig. 4 CRS characteristics at various axial spacing (*a*) static pressure rise Δp_s versus flow rate *Q*; (*b*) static efficiency η_s versus flow rate *Q*. The rotation ratio of FR is $N_{FR} = 2000$ rpm and $\theta = 0.9$. Black ○: $A = 0.17$, blue ◇: $A = 0.34$, magenta ∇: $A = 0.69$, orange ☼: $A = 0.86$ mm, dark green □: $A = 2.58$, purple ×: $A = 3.1$. The blue ■ and the dashed lines stand for the design point of the CRS.

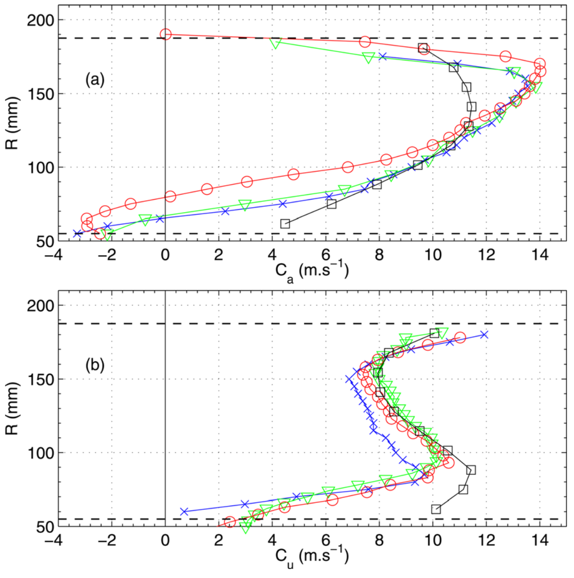

Fig. 5 Comparison of the radial profiles at a distance of 5 mm downstream of FR of the axial and tangential components, C_a (*a*) and C_u (*b*), respectively for $A = 0.17$ (blue ×), $A = 0.86$ (green ∇) and $A = 3.1$ (red ○). The black □ stand for the values predicted by MFT. The dashed lines represent the hub and the blade tip. $N_{FR} = 2000$ rpm and $\theta = 0.9$.

homogeneous, the flow rate is discharged mainly through the upper part of the blade. This tendency is slightly underpredicted by MFT. In the lower part of the blade, negative values of the axial velocity in the experimental profiles indicate a recirculating flow and thus the presence of a radial component at least in this region of the blade. This behavior is not predicted with MFT, because of the simplified radial equilibrium hypothesis that forces the radial component to be equal to zero. The deficit in term of flow rate shown by the measured profile in the lower region is counterbalanced by higher velocities in the upper region in comparison with the predicted values.

For $A = 0.17$ (blue × in Fig. 5) and $A = 0.86$ (green ∇), the profiles are very similar, whereas for $A = 3.1$ (red ○), the bigger spacing between the rotors seems to lead to a greater recirculation and the whole profile is slightly shifted to the upper part of the pipe.

Regarding the tangential component (Fig. 5(*b*)), the measured profiles are consistent with the predicted value from MFT particularly for $A = 0.86$ and $A = 3.1$. For the same reasons as for the axial component, in the lower region MFT is unable to detect the velocity deficit. For $A = 0.17$, the tangential velocity is lower than in the other two cases. This might be due to the proximity of the rear rotor; at each blade passage, the velocity is slowed down by the blade which results in an averagely lower value.

These profiles, measured 5 mm downstream of the FR, point out a local effect that may be due to the rear rotor but globally, the variation of the axial spacing does not affect drastically the mean velocity field close to FR. Let us examine the velocity evolution along the axial direction for a fixed spacing between the two rotors $A = 3.1$. The profiles of mean velocity at a distance $d = 5$ mm downstream of the front rotor and at a distance $d = 5$ mm upstream of the rear rotor are compared in Fig. 6. According to the axial components, the recirculating region is smaller near the rear rotor. Moreover, while traveling from the FR to RR, the tangential component become more homogenized in the upper region. Again globally the velocity is not affected significantly which explains why the global performances do not drastically change when A is increased to the maximum value that was explored in the present study. Finally, the profiles of the flow angle in the absolute reference frame are plotted in Fig. 6(*c*). The agreement between the predicted value on which the design of the rear rotor is based (black □) and the angles just downstream of the FR (red ○) and just upstream of the RR (blue +) is at first sight very good. The angle is however slightly underestimated close to the blade tip, and overestimated close to the hub, in agreement with the discussion on the actual axial velocity profile.

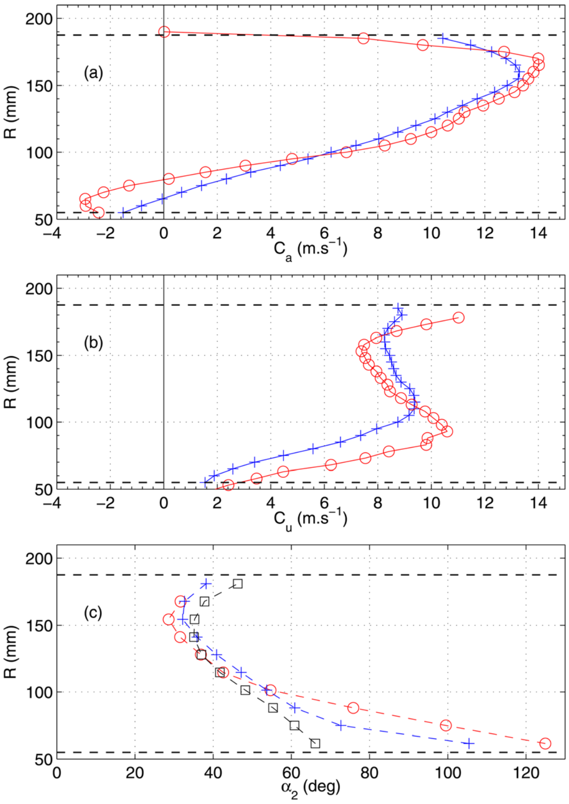

Fig. 6 Comparison of the radial profiles of the axial and tangential components, C_a (*a*) and C_u (*b*) and of the absolute flow angle α (*c*), respectively, 5 mm downstream of FR (red ○) and 175 mm downstream of FR (blue +). The dashed lines represent the hub and the blade tip. $A = 3.1$, $N_{FR} = 2000$ rpm, and $\theta = 0.9$. The black □ in (*c*) stand for the predicted angles.

In other studies [11,12] it was reported that the axial spacing had a more significant influence on the overall performances. This was noticed as well in this study. In the present study, the global performance when $A = 3.10$ is still excellent (see Fig. 4). In the following paragraph, measurements of the wall pressure fluctuations and analysis of the velocity fluctuations are performed to check whether the axial spacing has an influence on more local quantities.

4.2.3 Wall Pressure and Velocity Fluctuations. The wall pressure fluctuations have been recorded for two axial spacings, $A = 0.17$ and $A = 2.86$. For both configurations, four microphones were regularly spaced around the duct circumference and 5 mm downstream of the front rotor. Figure 7 shows the power spectral density for $A = 0.17$ (blue curve) and $A = 2.86$ (red curve).

One can see that the blue curve has much more frequency components, higher peaks, and higher signal-to-noise ratio than the red curve. Among those frequency peaks, there are the blade passing frequencies (and its harmonics) of the front rotor, $f_{\text{bpFR}} = 112{,}000/60 = 366.7$ Hz and the blade passing frequency (and its harmonics) of the rear rotor, $f_{\text{bpRR}} = 71{,}800/60 = 210$ Hz. Please notice that f_{bpFR} peaks of the blue curve are hidden by those of the red curve. The peaks of the rear rotor blade passing frequencies are much higher than those of the front rotor despite the fact that the rear rotor rotation rate is lower than the front rotor rotation rate. This is consistent with the fact that the RR has fewer

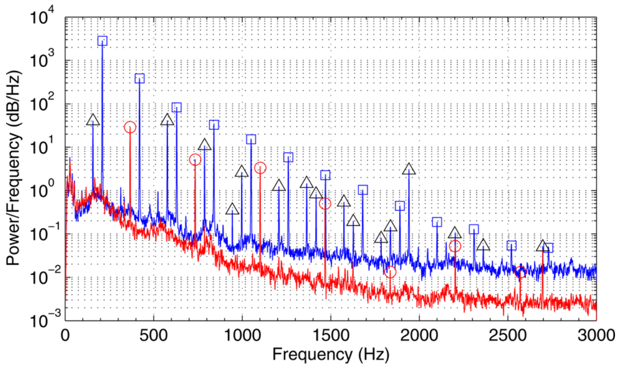

Fig. 7 Power spectral density of the wall pressure fluctuations 5 mm downstream of the front rotor. The blue curve stands for the axial spacing $A = 0.17$ and the red curve for $A = 2.86$. The red ○ stand for the blade passing frequency and the harmonics of the front rotor and the blue □ stand for that of the rear rotor. The black Δ stand for the various interactions of these frequencies.

blades than the FR and performs more static pressure rise than the FR alone (assuming that the FR does the same pressure rise with and without the RR). The RR's blades are therefore more loaded which results in higher peak levels as can be observed in Fig. 7. Moreover, along the blade passing frequencies other peaks are visible for the shortest axial spacing (blue curve in Fig. 7). The corresponding frequencies are the interactions of the two rotors blade passing frequencies that are equal to

$$f = mf_{\text{bpFR}} + nf_{\text{bpRR}} \tag{4}$$

where m and n are two integers. The same spectral analysis was carried out on signals from LDA measurements at two radii away from the wall duct, $-R = 120$ mm and $R = 170$ mm, for $A = 0.17$. The results are plotted in Fig. 8. Again the blade passing frequencies of the front and rear rotors are well detected as well as some interaction frequencies. The strong interaction between the rotors is not only located near the wall but is also present along the blade height.

Figure 9 graphs the autocorrelation coefficients of the microphone number 2 (blue curve) and the cross correlation between microphone numbers 1 and 2 (green curve) for $A = 0.17$. The rear rotor rotation direction is from microphone 1 to microphone 2. The abscissa axis represents the front rotor rotation (dimless); 1 corresponds to one revolution of the front rotor.

In the case of $A = 0.17$, both curves (blue and green) are periodic and highly correlated. The main period $t_1 = 4.833$ ms corresponds to $f_1 = 210$ Hz. This is the blade passing frequency of the rear rotor, f_{bpRR}. According to the cross correlation curve, the flow structure near by the microphone number 1 is very similar to that of the microphone number 2. The green curve is shifted by $t_2 = t_1/4$ and that is the time to go from microphone one to microphone two. This observation could mean that there is a strongly coherent structure (located at least in the tip region), traveling at the same rotation rate as the rear rotor and in the same direction. All these remarks lead us to think that the rear rotor generates and imposes its frequency to the flow structure in the interrotors region.

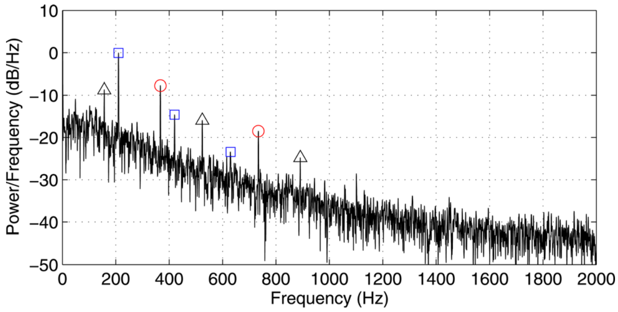

Fig. 8 Power spectral density of the LDA signals for $A = 0.17$, 5 mm downstream the front rotor at $R = 120$ mm. The LDA signal is resampled before computing the PSD. The red ○ and blue □ stand for the blade passing frequencies and their harmonics of the front rotor and the rear rotor, respectively. The black Δ are the rotor interaction peaks.

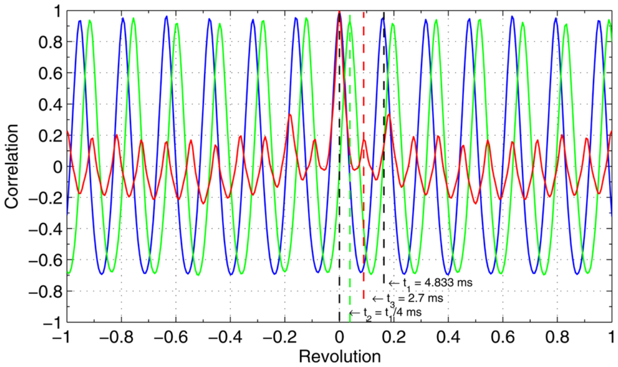

Fig. 9 Auto- and cross-correlation functions of the wall pressure fluctuations. The time on the abscissa axis is made dimensionless, i.e., $t' = tf_{\text{FR}}$ and represents two revolutions of the front rotor. The t_1 periodic blue curve stands for the autocorrelation coefficients of the microphone 2 at $A = 0.17$. The t_2 shifted green curve stands for the cross correlation of the microphones 1 and 2 at $A = 0.17$, t_2 being the time lag of the first maximum of the green curve. The t_3 periodic red curve stands for autocorrelation of the microphone 2 at $A = 2.86$.

Let us now consider the case where $A = 2.86$. Recall that the microphones are still 5 mm downstream of the front rotor and thus 145 mm upstream of the rear rotor. The power spectral density in Fig. 7 (red curve) shows only the blade passing frequencies of the front rotor. The blade passing frequencies of the rear rotor do not appear any more. The peak levels are noticeably the same. In the same way, the autocorrelation coefficients of the microphone number 2, red curve in Fig. 9, are very low for $A = 2.86$. One can count 11 periods on the red curve, and that is the number of blade of the front rotor and the period $t_3 = 2.7$ ms corresponds to $f_3 = 370.4$ Hz which is very near to the front rotor blade passing frequency. It is clear from above that the interaction between rotors tends to decrease when increasing the axial spacing, at least, the FR does not see the influence of the RR. On the other hand, it does not mean that the RR does not contribute to the whole noise emission or that the rotors interaction does not exist anymore when the axial spacing is increased.

In the present study, the axial distance has thus much more important effects on local and fluctuating characteristics of the system than on the global performances. This is very interesting for instance for an acoustic optimization.

4.3 Influence of the Rotation Ratio θ.

The overall performances of the CRS for various θ at a constant relative axial spacing $A = 0.17$ and at a constant $N_{\text{FR}} = 2000$ rpm are plotted in Fig. 10. As expected, the more the rotation rate of RR increases, the more the static pressure rise of the CRS increases and the nominal flow rate of the CRS increases. The maximal static efficiency and the corresponding nominal flow rate as a function of θ are moreover plotted in Fig. 11 (black ○: $N_{\text{FR}} = 2000$ rpm).

For very low rotation rates of RR, i.e., for $\theta = 0$ (dark green ✡ in Fig. 10) and $\theta = 0.5$ (black ◁ in Fig. 10), the system is very inefficient: in the first case when the RR is at rest the maximum efficiency hardly reaches 35% which is below the maximal

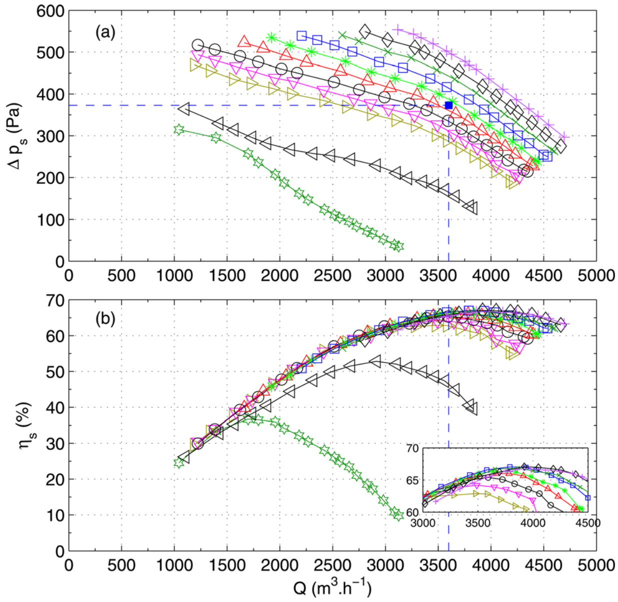

Fig. 10 CRS characteristics at $N_{FR} = 2000$ rpm, $A = 0.17$, and $\theta \in [0; 1.2]$. (*a*) Static pressure rise Δp_s versus flow rate Q; (*b*) static efficiency η_s versus flow rate Q. Dark green ☆: $\theta = 0$, black ◁: $\theta = 0.5$, mustard yellow ▷: $\theta = 0.8$, magenta ∇: $\theta = 0.85$, black ○: $\theta = 0.9$, red Δ: $\theta = 0.95$, green ∗: $\theta = 1$, blue □: $\theta = 1.05$, dark green ×: $\theta = 1.1$, black ◇: $\theta = 1.15$, and purple +: $\theta = 1.2$. The blue ■ and the dashed lines stand for the design point of the CRS.

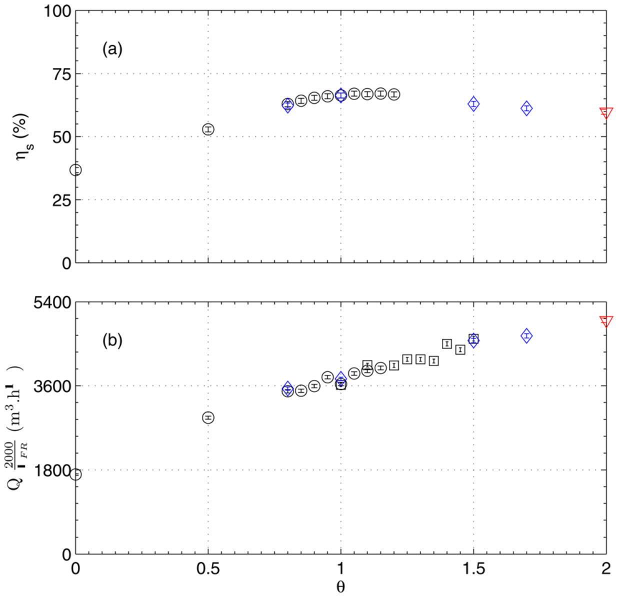

Fig. 11 Maximal static efficiency η_s (*a*) and corresponding nominal flow rate Q (*b*) versus θ for the CRS with $A = 0.17$. Black ○: $N_{FR} = 2000$ rpm, blue ◇: $N_{FR} = 1600$ rpm, and red ∇: $N_{FR} = 1300$ rpm. Please note that the presented nominal flow rate has been scaled by $2000/N_{FR}$.

efficiencies of both FR and RR alone. The maximum flow rate that can be reached is moreover very low in both cases compared to the discharge goal of 3600 $m^3\ h^{-1}$.

In the range $\theta \in [0.8; 1.2]$, i.e., $N_{RR} \in [1600; 2400]$ rpm for $N_{FR} = 2000$ rpm, the system is highly efficient. The maximum efficiency slightly increases with θ to reach a maximum value of $67 \pm 1\%$ for $\theta \in [1.05; 1.15]$ and then seems to decrease slightly ($\eta_s = 66 \pm 1\%$ for $\theta = 1.20$).

On the one hand, this is a very interesting feature of the counter-rotating system. One could imagine, simply by varying the rear rotor rotation rate, to work at a constant pressure rise with an efficiency greater than 60% for a large flow-rate range. For instance, in the present case, the system could give a constant static pressure rise of 375 Pa with $\eta_s \geq 60\%$ for $3000 \leq Q \leq 5000\ m^3\ h^{-1}$ with $N_{FR} = 2000$ rpm, $A = 0.17$, and $\theta \in [0.85; 1.5]$. One could also imagine working at a constant flow rate with high static efficiency. For instance, in the present case, the system could give a constant flow rate of 3600 $m^3\ h^{-1}$ with $\eta_s \geq 60\%$ for $290 \leq \Delta p_s \leq 680$ Pa with $N_{FR} = 2000$ rpm, $A = 0.17$, and $\theta \in [0.8; 1.5]$.

On the other hand, the maximum of the best efficiencies as a function of θ is not reached at the design point ($\theta = 0.9$), but for a slightly greater ratio of the rotation rates. This point requires further studies and the first question that is addressed is until which value the rear rotor can be accelerated keeping a great efficiency of the system. In order to extend the range of explored θ to $\theta > 1.2$, it is necessary to reduce the rotation rate of the front rotor, because of the maximal power that the motors can deliver. The maximum efficiency for four values of θ at $N_{FR} = 1600$ rpm (blue ×) and for $\theta = 2$ at $N_{FR} = 1300$ rpm (red +) are plotted in Fig. 11(*a*) together with the values previously discussed and that were obtained at $N_{FR} = 2000$ rpm (black ○). For $\theta = 0.8$ and $\theta = 1$, the two values are equal to those that were measured with $N_{FR} = 2000$ rpm. The ratio Q/N_{FR} is moreover the same for those two points as can be seen in Fig. 11(*b*): the efficiency thus does not depend on the Reynolds number in the explored range (at midspan, the Reynolds number is $Re = 3 \times 10^5$ at $N_{FR} = 2000$ rpm, and $Re = 2.4 \times 10^5$ at $N_{FR} = 1600$ rpm). This may be the same for $N_{FR} = 1300$ rpm with $Re = 2 \times 10^5$.

The maximal efficiency for $\theta > 1.2$ decreases (see Fig. 11) as could be expected but surprisingly, the maximal efficiency at $\theta = 2$ is still quite high, $\eta_s(\theta = 2) = 60 \pm 1\%$.

The measurement of the velocity field between the two rotors that have been presented in Sec. 4.2 may help to understand these features. At $\theta = 0.9$ and $Q = 1\ m^3\ s^{-1}$, the measured angles on the upper part of the blades are indeed smaller than the prediction on which the design of RR is based. In order to match the design, the RR requires more tangential velocity (see the velocity triangles in Fig. 1). This may explain why the maximal efficiency first increases when $\theta > 0.9$. On the other hand, the faster RR rotates, the higher the discharge flow should be to match the velocity triangle. The flow rate at which the system is the most efficient indeed quasilinearly increases with θ (see Fig. 11(*b*)). However in this case the front rotor is in an overflow regime. This rotor then gives reduced pressure rise and lower tangential component in the exit flow. This is consistent with the decrease of the maximal efficiency for greater θ. The characteristic curve of FR (see red □ in Fig. 3) is very flat, and this could also explain why the system is still so efficient for relatively large values of θ.

The last question that is discussed is whether the flow at the exit of the CRS is solely axial at the design point or not, and to what extent the exit absolute flow angles are correlated to the behavior of the system at the nominal points when varying θ.

The flow angle downstream of the CRS has been measured by image processing. A wind vane of length 100 mm, thickness 1.5 mm, and width 10 mm has been placed between the CRS and the antigyration device, at a radius 160 mm. It is illuminated from beneath with a LED plate and imaged from above with a high-speed video camera (Optronis CamRecord 600) at 250 Hz. The images are then treated with algorithm described in Ref. [18] after normalization with a background image. An equivalent ellipsoid is fitted, the orientation of which is computed. The measured angle is stable within ±1°. The results are plotted in Fig. 12. The negative orientation corresponds to the direction of rotation of FR, and the positive orientation to the direction of rotation of RR. At the design point $\theta = 0.9$, the exit-flow still has a nonnegligible rotating component ($\alpha \simeq -15$ deg), indicating that the RR does

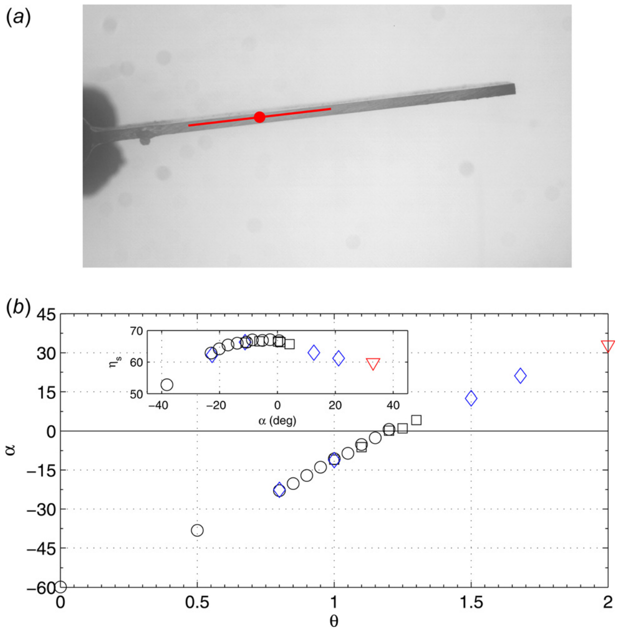

Fig. 12 Measurement of the absolute flow angle α_{2CRS} with image processing. Example of the processing with the detected centroid (red ○) and the equivalent ellipsoid great axis (straight red line). Absolute flow angle α at the nominal flow rate versus θ. Inset: static efficiency at the nominal flow rate η_s versus α for the same data set. Black ○: $N_{FR} = 2000$ rpm, black □: $N_{FR} = 1800$ rpm, blue ◇: $N_{FR} = 1600$ rpm, and red ▽: $N_{FR} = 1300$ rpm.

not completely straighten the flow. The angle is reduced when increasing θ and $\alpha = 0$ deg is obtained for $\theta \simeq 1.2$. The swirl is then reversed in the direction given by RR for $\theta > 1.2$. One can furthermore notice that the angle varies linearly with θ and that α and η_s are highly correlated (see inset in Fig. 12). Efficiencies greater than 62% are obtained for $\theta \in [0.8; 1.7]$ corresponding to $\alpha \in [-22 \text{ deg}; 22 \text{ deg}]$. The range of flow rates that could be reached with a very high efficiency is thus extremely high.

5 Conclusion

A counter-rotating axial-flow fan has been designed according to an iterative method that is relatively fast. It is based on semiempirical modelization that partly takes into account the losses, boundary layers at hub and casing, and the effects of low Reynolds numbers (below 2×10^5). The rear rotor is adapted to the radial profile of the flow downstream of the front rotor that is predicted by the model.

The overall performances at the nominal design point are slightly lower than predicted, with a static pressure rise 10.2% lower. The static efficiency is however remarkably high ($\eta_s \simeq 65\%$) and corresponds to a 20 points gain in efficiency with respect to the front rotor maximal efficiency and to a 10 points gain with respect to the rear rotor.

The overall measurements give first clues that allow us to validate the design method. Local measurements of the velocity field and flow visualization show that the simplified radial equilibrium hypothesis used in the design method is responsible for the slight underprediction. The measured tangential velocity and the predicted value between the rotors are consistent within 10% for 75% of the blade span, in the upper portion. However, there are recirculating flows close to the hub that are not predicted. The variation of relative axial distances for $A \in [0.17; 3.10]$ quite surprisingly does not affect the overall performances so much; the efficiency is decreased by 2 points and the static pressure rise by 5%. The best efficient configuration ($\eta_s = 67\%$) is moreover obtained for a small increase of the rear rotor rotation rate from $N_{RR} = 0.9N_{FR}$ to $N_{RR} = 1.15N_{FR}$, which is consistent with the velocity field measurements and with the visualizations.

The counter-rotating system has furthermore a very flexible use that allows to work at constant flow rate on a wide range of static pressure rises or to work at constant pressure rise on a wide range of flow rates, with static efficiency bigger than 60%, simply by varying the rear rotor rotation rate. For the design point $(Q_{des}; \Delta p_{s,des})$, the system could respectively give the constant pressure rise $\Delta p_{s,des}$ for $0.83Q_{des} \leq Q \leq 1.39Q_{des}$ or deliver the constant volumetric flow rate Q_{des} and $0.77\Delta p_{s,des} \leq \Delta p_s \leq 1.79\Delta p_{s,des}$ with a static efficiency $\eta \geq 60\%$ by varying N_{RR} in the range $N_{RR} \in [0.8; 1.5]N_{FR}$. One could thus imagine an efficient closed-loop-controlled axial-flow fan. Besides, this feature may not be general but related to the flat characteristic of the front rotor in the present system. Other studies with a different design of the front rotor (other load distribution, thickening of the blades [17]) may give answers to this point.

Finally, the wall pressure fluctuations investigation, which is representative of the very near-field noise emission, shows a strong influence of the rear rotor over the flow structure between rotors when they are close to each other. The spectral composition of the fluctuating pressure is very sensitive to the axial spacing. An increase of A leads to a suppression of the rotors interaction peaks close to the FR without decreasing a lot the overall performances. This parameter can thus be of great interest with respect to an acoustic optimization problem. These results are encouraging to study deeper the effect of the axial spacing on the far-field noise emission.

Acknowledgment

The authors finally wish to thank Robert Rey for very fruitful discussions.

Nomenclature

Roman Characters

A = relative axial spacing
c = chord length
C = flow velocity in the absolute reference frame
CRS = counter-rotating system
d = distance
D = ducting pipe diameter
$\mathcal{D}$ = Lieblein's diffusion factor
f = frequency
FR = front rotor
LDA = laser Doppler anemometry
MFT = mixed flow turbomachinery
N = rotation rate in rpm
Q = volumetric flow rate
R = radial coordinate
Re = Reynolds number
RR = rear rotor
S = axial distance between the rotors
t = time
t' = dimensionless time
T = torque supplied by the shaft
U = velocity of the moving reference frame
W = flow velocity in the relative reference frame
Z = number of blades

Greek Characters

α = flow angle in the absolute reference frame
β = flow angle in the relative reference frame
γ = stagger angle
Δp = pressure rise
η = efficiency
ν = kinematic viscosity
ω = angular velocity

Ω = specific speed
ρ = density
σ = blade solidity
θ = rotation ratio N_{RR}/N_{FR}

Subscripts

1 = rotor inlet
2 = rotor outlet
a = axial component
atm = atmospheric
bp = blade passing
des = design
diaph = diaphragm
est = estimate
m = midspan
r = radial component
s = static
t = total
u = tangential component

References

[1] Lesley, E., 1933, "Experiments With a Counter-Propeller," Technical Report No. 453, National Advisory Committee for Aeronautics.

[2] Lesley, E., 1939, "Tandem Air Propellers," Technical Report No. 689, National Advisory Committee for Aeronautics.

[3] Playle, S. C. D., Korkan, K., and von Lavante, E., 1986, "A Numerical Method for the Design and Analysis of Counter-Rotating Propellers," J. Propul. Power, **2**, pp. 57–63.

[4] van Gunsteren, L. A., 1971, "Application of Momentum Theory in Contra-Rotating Propellers," Int. Shipbuild. Prog., **206**, p. 359.

[5] Chen, B. Y.-H., and Reed, A. M., 1989, "A Design Method and an Application for Contrarotating Propellers," Technical Report DTRC-90/003, David Taylor Research Center, Bethesda, MD.

[6] Min, K.-S., Chang, B.-J., and Seo, H.-W., 2009, "Study on the Contra-Rotating Propeller System Design and Full-Scale Performance Prediction Method," Int. J. Naval Architecture Ocean Eng., **1**, pp. 29–38.

[7] Cho, L., Choi, H., Lee, S., and Cho, J., 2009, "Numerical and Experimental Analyses for the Aerodynamic Design of High Performance Counter-Rotating Axial Flow Fans," Proceedings of the ASME 2009 Fluids Engineering Division Summer Meeting (FEDSM2009), Vail, CO, August 2–6, ASME Paper No. FEDSM2009-78507.

[8] Shigemitsu, T., Fukutomi, J., and Okabe, Y., 2010, "Performance and Flow Condition of Small-Sized Axial Fan and Adoption of Contra-Rotating Rotors," J. Therm. Sci., **19**, pp. 1–6.

[9] Shigemitsu, A., Watanabe, T., and Furukawa, S., 2007, "Performance Test and Flow Measurement of Contra-Rotating Axial Flow Pump," J. Therm. Sci., **16**(1), pp. 7–13.

[10] Pin, L., Yingzi, J., and Yanping, W., 2011, "Effects of Rotors Structure on Performance of Small Size Axial Flow Fans," J. Therm. Sci., **20**, pp. 205–210.

[11] Sharma, P., Jain, Y., and Pundhir, D., 1988, "A Study of Some Factors Affecting the Performance of a Contra-Rotating Axial Compressor Stage," Proc. Inst. Mech. Eng., Part A. Power and Process Eng., **202**, pp. 15–21.

[12] Sharma, P., Pundhir, D., and Chaudhry, K., 1991, "A Study of Aeroacoustic Performance of a Contra-Rotating Axial Flow Compressor Stage," Def. Sci. J., **41**, pp. 165–180.

[13] Shigemitsu, T., Furukawa, A., Watanabe, S., and Okuma, K., 2005, "Air/Water Two-Phase Flow Performance of Contra-Rotating Axial Flow Pump and Rotational Speed Control of Rear Rotor," ASME 2005 Fluids Engineering Division Summer Meeting (FEDSM2005), Houston, TX, June 19–23, Vol. 1, pp. 1069–1074, ASME Paper No. FEDSM2005-77002.

[14] Nouri, H., Ravelet, F., Bakir, F., Sarraf, C., and Rey, R., 2011, "Design and Experimental Validation of a Ducted Counter–Rotating Axial–Flow Fans System," ASME J. Fluids Eng., **134**(10), p. 104504.

[15] Noguera, R., Rey, R., Massouh, F., Bakir, F., and Kouidri, S., 1993, "Design and Analysis of Axial Pumps," ASME Fluids Engineering, Second Pumping Machinery Symposium, Washington, DC, June 20–24, pp. 95–111.

[16] ISO, 2007, "ISO 5801—Industrial Fans Performance Testing Using Standardized Airways," International Standards for Business, Government and Society.

[17] Sarraf, C., Nouri, H., Ravelet, F., and Bakir, F., 2011, "Experimental Study of Blade Thickness Effects on the Global and Local Performances of a Controlled Vortex Designed Axial-Flow Fan," Exp. Therm. Fluid Sci., **35**, p. 684.

[18] Ravelet, F., Colin, C., and Risso, F., 2011, "On the Dynamics and Breakup of a Bubble Rising in a Turbulent Flow," Phys. Fluids, **23**, p. 103301.

[19] Moreau, S., and Bakir, F., 2002, "Efficient Stator Designed for Automotive Engine Cooling Fan Systems," ASME 2002 Fluids Engineering Division Summer Meeting (FEDSM2002), Montreal, Canada, July 14–18, ASME Paper No. FEDSM2002-31318.

[20] Bakir, F., and Moreau, S., 2003, "Detailed Study of an Efficient Small Diameter Automotive Engine Cooling Fan System," ASME 2003 Fluids Engineering Division Summer Meeting (FEDSM2003), Honolulu, HI, July 6–10, ASME Paper No. FEDSM2003-45117.

3 Axe 3

3.1 On the dynamics and breakup of a bubble rising in a turbulent flow

Physics of Fluids (2011), vol. 23, pp. 103301.

Experimental investigations of the dynamics of a deformable bubble rising in a uniform turbulent flow are reported. The turbulence is characterized by fast particle image velocimetry. Time-resolved evolutions of bubble translation, rotation, and deformation are determined by three-dimensional shape recognition from three perpendicular camera views. The bubble dynamics involves three mechanisms fairly decoupled : (1) average shape is imposed by the mean motion of the bubble relative to liquid ; (2) wake instability generates almost periodic oscillations of velocity and orientation ; (3) turbulence causes random deformations that sometimes lead to breakup. The deformation dynamics is radically different from that observed in the absence of a significant sliding motion due to buoyancy. Large deformations that lead to breakup are not axisymmetric and correspond to elongations in the horizontal direction. The timescale of decay of shape oscillations is of the same order as their natural frequency f_2, so that breakup always results from the interaction with a single turbulent eddy. This overdamping causes the statistics of large deformations and the statistics of breakup identical to the statistics of turbulence. The bubble response time f_2^{-1} however controls the duration of individual breakup events.

3.2 Study of the cavitating instability on a grooved Venturi profile

submitted to Journal of Fluid Engineering (2013).

Instabilities of a partial cavity developed on an hydrofoil, a converging-diverging step or in an inter-blade channel, have already been investigated in many previous works. The aim of this study is to evaluate a passive control method of the sheet cavity. According to operating conditions, cavitation can be described by two different regimes : an unstable regime with a cloud cavitation shedding and a stable regime with only a pulsating sheet cavity. Avoiding cloud cavitation can limit structure damages since this regime is less agressive. The surface condition of a converging-diverging step is here studied as a solution to control the cavitation regime. This study discusses the effect of longitudinal grooves, on the developed sheet cavity. Analyzes conducted with Laser Doppler Velocimetry, visualisations and pressure measurements show that the grooves geometry, and especially the groove depth, acts on the sheet cavity dynamics and can even suppress the cloud cavitation shedding.

3.3 Experimental study of hydraulic transport of large particles in horizontal pipes

Experimental Thermal and Fluid Science (2013), vol. 45, pp. 187-197.

This article presents an experimental study of the hydraulic transport of very large solid particles (above 5 mm) in an horizontal pipe. Two specific masses are used for the solids. The solids are spheres that are large with respect to the diameter of the pipe (5%, 10% and 15%) or real stones of arbitrary shapes but constant specific mass and a size distribution similar to the tested spherical beads. Finally, mixtures of size and/or specific mass are studied. The regimes are characterized with differential pressure measurements and visualizations. The results are compared to empirical models based on dimensionless numbers, together with 1D models that are based on mass and momentum balance. A model for the transport of large particles in vertical pipes is also proposed and tested on data available in the Literature, in order to compare the trends that are observed in the present experiments in a horizontal pipe to the trends predicted for a vertical pipe. The results show that the grain size and specific mass have a strong effect on the transition point between regimes with a stationary bed and dispersed flows. The pressure drops are moreover smaller for large particles in the horizontal part contrary to what occurs for vertical pipes, and to the predictions of the empirical correlations.

PHYSICS OF FLUIDS **23**, 103301 (2011)

On the dynamics and breakup of a bubble rising in a turbulent flow

F. Ravelet,[1,2,a)] C. Colin,[2] and F. Risso[2,b)]
[1]*Arts et Metiers ParisTech, DynFluid, 151 boulevard de l'Hôpital, 75013 Paris, France*
[2]*Institut de Mécanique des Fluides de Toulouse, Université de Toulouse and CNRS, Allée du Prof. C. Soula, 31400 Toulouse, France*

(Received 1 July 2011; accepted 14 September 2011; published online 11 October 2011)

Experimental investigations of the dynamics of a deformable bubble rising in a uniform turbulent flow are reported. The turbulence is characterized by fast particle image velocimetry. Time-resolved evolutions of bubble translation, rotation, and deformation are determined by three-dimensional shape recognition from three perpendicular camera views. The bubble dynamics involves three mechanisms fairly decoupled: (1) average shape is imposed by the mean motion of the bubble relative to liquid; (2) wake instability generates almost periodic oscillations of velocity and orientation; (3) turbulence causes random deformations that sometimes lead to breakup. The deformation dynamics is radically different from that observed in the absence of a significant sliding motion due to buoyancy. Large deformations that lead to breakup are not axisymmetric and correspond to elongations in the horizontal direction. The timescale of decay of shape oscillations is of the same order as their natural frequency f_2, so that breakup always results from the interaction with a single turbulent eddy. This overdamping causes the statistics of large deformations and the statistics of breakup identical to the statistics of turbulence. The bubble response time f_2^{-1} however controls the duration of individual breakup events. *© 2011 American Institute of Physics*. [doi:10.1063/1.3648035]

I. INTRODUCTION

In the absence of a strong rise velocity of the bubble due to buoyancy, the deformation of a bubble in a turbulent flow results from the response of surface modes to the turbulent forcing.[1,2] The deformation is well described by axisymmetric mode 2,[3] the shape of which corresponds to the spherical harmonic of order 2, and the frequency and damping rate of which are well predicted by the linear theory.[4,5] The turbulent forcing is well described by the instantaneous turbulent Weber number experienced by the bubble along its trajectory. Furthermore, the breakup is observed to occur when the instantaneous deformation reaches a critical value. Due to the major role played by the bubble dynamics, the statistics of bubble shape and breakup occurrence are radically different from those of turbulence.

One open question is whether this description is still valid for a large bubble rising in water. Even in the absence of turbulence, a large rising bubble is no more spherical but flattened in the vertical direction. This may change the natural frequency and the damping rate of the oscillations.[6–8] Moreover, due to the instability of its wake, the bubble does not rise on a straight path but follows helical or zigzagging path.[9] Shape oscillations also occur and are observed to involve non-axisymmetric modes.[10,11]

When a rising bubble is immersed in a turbulent flow, the action of the turbulent fluctuations is thus combined to both a non-zero average deformation and self-sustained oscillations.

This paper reports an experimental investigation on the dynamics of a rising bubble in a turbulent flow. The objective is to determine how a bubble moves and deforms under the combined action of its rise velocity, wake-induced oscillations, and turbulent fluctuations. First, this requires an experimental set-up in which a rising bubble can be observed over a long time. Following the idea of Wichterle *et al.*,[12] this has been obtained by immersing a bubble in a slightly rotating downward flow through a slightly divergent pipe. Second, it also requires to generate a calibrated turbulent flow with an intensity large enough to cause the bubble breakup. Ideally, this flow should be as uniform as possible to avoid considering changes in turbulence properties as the bubble moves. Third, we need to track the three-dimensional motion and shape of the bubbles, which requires time-resolved records of at least three perpendicular view of the bubble.

The experimental setup is presented in Sec. II. An original technique of image processing has been developed to track the three-dimensional dynamics and is presented in Sec. III. The turbulent flow has been characterized with fast particle image velocimetry (PIV) and the results are presented in Sec. IV. Section V A is devoted to the study of bubbles dynamics at moderate deformations. The breakup process is finally analyzed in Sec. V B and the concluding remarks are given in Sec. VI.

II. EXPERIMENTAL SETUP

The experimental device consists of a closed flow loop. A sketch is shown in Fig. 1. The test section is a vertical conical pipe out of Plexiglas in which water flows downward. It is of height 320 mm with an inner diameter of 50 mm at inlet and 80 mm at outlet (half-angle of the cone is thus 2.7°). Perturbations are generated in the flow with a rotating grid made

---

[a)]Electronic mail: florent.ravelet@ensta.org.
[b)]Electronic mail: frederic.risso@.imft.fr.

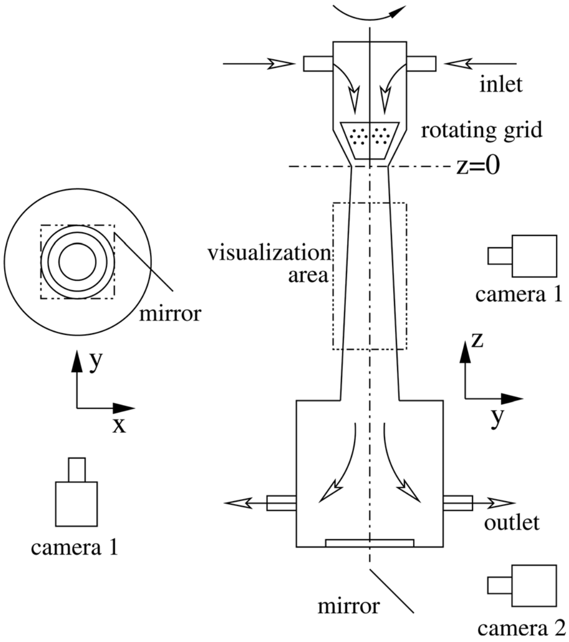

FIG. 1. Sketch of the experimental setup. Left: top view. Camera 1 gives two side views in the planes $x-z$ and $y-z$ with the help of a 45° mirror. The visualization area is surrounded by a square glass box filled with water. Right: side view. Camera 2 gives the bottom view in the plane $x-y$ with the help of another 45° mirror. Two LED plates of 120×120 mm are used for lighting of the vertical planes, and the horizontal plane is illuminated with the help of an halogen lamp above the experiment. The rotating grid is covered with luminescent paint and is illuminated from its sides in order to have as bright as possible a background for the horizontal plane.

with four blades (right trapezoid of height 45 mm, top side 40 mm, and bottom side 22 mm). This impeller is surrounded by a converging conical casing, leaving a layer of 2 mm between the blade tips and the wall. The bottom of this conical housing is the z reference (see Fig. 1). The grid consists of 3 mm holes every 5 mm in an hexagonal pattern and thus has a solidity (ratio of blocked area and unit area) of 0.67. The grid is rotated between 1 and 3 Hz, corresponding to tip speeds in the range 0.25–0.75 m s^{-1}.

The flow rate, produced with a centrifugal pump, is measured with a Bürker flow transmitter and can be set in the range 0.5–0.7 L s^{-1}, corresponding to average velocities in the range 0.10–0.35 m s^{-1} in the test section.

Air bubbles are injected at the bottom of the test section, with a pipe of inner diameter 4 mm, at the end of which different pipe elbows can be connected. A way to get regular sized bubbles is to inject a known quantity of air with a motorized syringe and to have the exit of the elbow pointing down. In the study reported here, the bubbles have an equivalent diameter of $d = 9.3 \pm 0.3$ mm.

The visualization volume extends from $z = -100$ mm to $z = -180$ mm and is surrounded by a square glass box filled with water to minimize optical distortions. Two cameras and two mirrors are used to get three different views of the bubble in the visualization volume (see Fig. 1). Two components of the flow field have been measured in several planes with fast PIV. More details about the PIV measurements are given in Sec. IV.

III. IMAGE PROCESSING

Every experiment with bubbles consists of a sequence of 2000 images taken simultaneously by the two cameras, at a rate of 300 Hz. In order to extract quantitative information about the bubble shape and its dynamics, the three images taken by the two cameras are processed under MATLAB software following the procedure illustrated in Figs. 2 and 3. This procedure can be decomposed into three steps: ellipses that are equivalent to the side views of the bubble on camera 1 are first defined using simple algorithm, then an ellipse equivalent to the bottom view on camera 2 is fitted with a different algorithm, and at last a resulting ellipsoid is rebuilt from these three perpendicular projection contours. Quantities such as the velocity of the center of mass or the large-scale deformation, that is relevant in the context of breakup mechanism, are then computed from the equivalent ellipsoid.

A. Algorithm for side views detection

For the two side views of camera 1, we use simple binarization after subtraction and normalization by a background image taken without bubbles. The stability of the LED plates illumination is very good, and a single threshold of -0.20 has been used for all the images. An example showing the sharpness of the gray level profile at the bubble boundary can be found in Fig. 2. The typical number of pixels inside the detected bubble is around 3000. The center of mass and the second-order moments of the shape are then computed. That defines an equivalent ellipse displayed with red lines in the upper quadrants of Fig. 3. We have compared this method with some edge detection algorithms, to test the accuracy of the measured features. For the Canny method implemented in MATLAB, the mean discrepancy between the two techniques is less than 1% for the area and for the length of the equivalent ellipse axes. The discrepancy is moreover less than 0.3° for the orientation of the axes. The simple binarization has been retained because it is more robust and the threshold can be chosen once and for all.

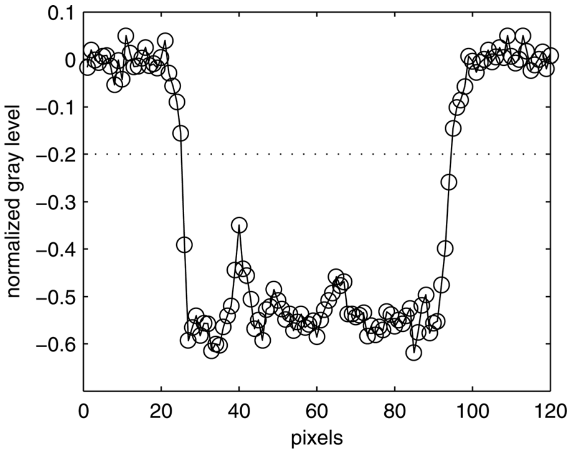

FIG. 2. Normalized gray level profile along constant height $z = -146.5$ mm for view 1 of image 39 of sequence $B5$ (see also top left quadrant in Fig. 3). Horizontal dotted line: threshold used for binarization. Bubble corresponds to values below the threshold. Calibration factor: 6.5 pixels correspond to 1 mm.

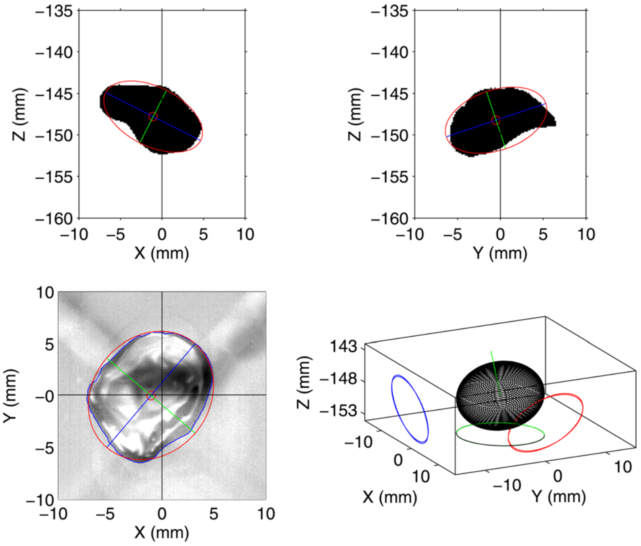

FIG. 3. (Color online) Illustration of image processing on image 39 of sequence *B*5 (see Table I). Top left: side view in the plane $x-z$ (camera 1) with the equivalent ellipse (mid-gray line, red online), its center of mass (mid-gray dot, red online), and major (dark gray line, blue online) and minor axes (light gray line, green online). Top right: side view in the plane $y-z$ (camera 1) with the same conventions. Bottom left: bottom view of camera 2 in the plane $x-y$ with the snake active contour (dark gray line, blue online) and the ellipse fitted on this contour (mid-gray line, red online) with its center of mass (mid-gray dot, red online) and major (dark gray line, blue online) and minor axes (light gray line, green online). Bottom right: ellipsoid reconstructed with the three projections. The ellipses used to compute the ellipsoid are plotted as solid lines on the three planes together with the three projections of the reconstructed ellipsoid, which are displayed as dashed lines. Solid light gray line (green online) gives the direction of the ellipsoid minor axis.

B. Algorithm for bottom view detection

For the bottom view of camera 2, the problem is slightly different because of the lighting from the top with an halogen lamp and because of the presence of the rotating grid in the field of view. These constraints lead to poor contrast and render simple binarization with a single threshold impossible. The images of camera 2 are thus treated with the following procedure.

We first take a set of pictures without bubbles and have thus a moving background which we synchronize and then subtract from the images, as shown in the lower left quadrant of Fig. 3. One can still guess the position of the rotating grid which is blurred in the background of the resulting image. The background is non-uniform and the contrast between the bubble and the background is not very high. However, one can distinguish the contour of the bubble, finding sharp edges, and rebuilding the contour by extrapolation.

We have implemented such a method with MATLAB. The first step uses a SuSan edge detection algorithm[13] that has been implemented in C for efficiency. The values for the kernel radius (3 pixels) and for the threshold (10%) that are used are claimed to be optimal and universal.[13] Only sharp edges are captured by this algorithm and there are still holes in the contour. We then use active contours to capture the bubble interface. We use a greedy snake algorithm,[14] with weighting parameters $\alpha=0.3$ for continuity/elasticity, $\beta=0.7$ for curvature/rigidity, and $\gamma=3$ for the attraction to edge map. The snake is initialized by hand for the first image of a sequence and then dilated in every direction by an amount of 10 pixels from the converged state to give an initial value for the next image. These parameters were modified by hand for images close to breakup where the projection of the bubble on the horizontal plane has strong concave curvatures. An ellipse is then fitted on the converged snake contour (see blue and red lines in the lower left quadrant of Fig. 3).

C. Ellipsoid reconstruction and relevant parameters

The ellipses that have thus been fitted on the projections of the bubble in three perpendicular planes give 9 parameters. An ellipsoid has 6 independent parameters (3 lengths and 3 orientations). It is thus possible to reconstruct an equivalent ellipsoid by minimization.[15] The lower right quadrant of Fig. 3 presents the reconstructed ellipsoid, the three ellipses used to determine it, and the three back projections of the ellipsoid onto the planes. One can notice that they hardly distinguish from each other. We have defined an error function for the reconstructed shape as the maximum of the radial distance between the fitted ellipses and the back-projected ellipses. The point is rejected when the error exceeds 0.8 mm, i.e., roughly 10% of the semi major axis length.

The whole process requires 10 h of computation on a desktop computer for the first pass on a sequence of 2000 images. After this first pass, typically 5% of the images have been rejected and are retreated by hand in a second pass. The final rate of rejection excluding the breakup phase is below 1% for all the sequences.

The physical quantities that are extracted from the image processing may help to understand how the turbulence affects the deformation of the bubble. The rising bubbles that are studied are relatively large and are thus no more spherical. Their wake is moreover unstable and this leads to a complicated path[9] that may also affect the deformation dynamics. The extracted quantities are thus the lengths of the three semi-axes of the ellipsoid (a, b, and c), the velocity of the center of mass V that is computed as the derivative of the position, and the orientation θ of the short axis of the ellipsoid with respect to the vertical axis.

IV. CHARACTERIZATION OF THE FLOW FIELD

A. Mean features of the large-scale flow

The flow field has been measured in the absence of bubbles with 2D-2C fast PIV in one vertical plane containing the symmetry axis, then in eight horizontal planes, 10 mm apart from each other. The data acquisition rate is 600 Hz and time series of 6000 images have been recorded. The PIV analysis consists of standard correlation of two successive images on windows of 32×32 pixels with an overlap of 50% in a first pass, and then on windows of 16×16 pixels with 0% overlap in two successive passes. Normalized median test[16] has been used to discard outliers, which were reconstructed with a bilinear interpolation. The rate of outliers is always below 4%.

The mean flow consists of an axial spreading jet superimposed with rotation. We have studied three cases: a case with rotating grid and no mean flow rate, a second case with an imposed mean flow rate and no rotation, and the case with both pumping and rotation which is relevant for bubble dynamics and breakup studies. In the experiments reported here, the flow rate is 0.62 L s^{-1} and if so, the rotation rate of the rotating grid is 1.5 Hz.

The first two cases are first briefly discussed. The flow is turbulent in every case. On one hand, when the grid does not rotate, the mean vertical particle displacement is of the order of 6 pixels—or -300 mm s^{-1}—in the middle of the test section, and the mean flow is axisymmetric. The standard deviation of the vertical component of the velocity σ_{uz} is around 8% of the time-averaged velocity everywhere, while a typical PIV evaluation error of 0.1 pixel corresponds to a fluctuation rate of 2%. On the other hand, when the grid rotates alone it creates an upward pumping of typical velocity 45 mm s^{-1} on the center line with recirculation cells close to the cone edges. The flow is moreover no more axisymmetric. And last, the flow in the center line is very fluctuating (fluctuation rate 35%).

Figures 4, 5, and 6 present velocity measurements that have been performed in the relevant case with pumping and rotation. The vertical and horizontal velocity profiles along the x-axis at $z=-140$ mm are plotted in Fig. 4. The mean axial jet is directed downward and has a flat profile of constant velocity around $u_z \simeq -300\,\mathrm{mm\,s^{-1}}$. The fluctuation rate of the vertical component of the velocity is above 10% and even exceeds 20% in the core region.

Concerning the horizontal velocities, the grid creates solid body rotation within an annulus of diameter 15 mm. The horizontal velocities are of the order of 2/3 of the vertical velocity, and in the center, their fluctuation rates are of the order of 35% of the maximal horizontal speed, i.e., of the order of 20% of the vertical speed. The mean flow is not axisymmetric as can be seen in Fig. 5 where the center-line of the vortex slightly deviates from the z-axis. The bubbles are however trapped inside the vortex annular core in a zone that extends from $z \simeq -110$ mm to $z \simeq -160$ mm (see Fig. 5). The rotation rate inside the vortex core that is deduced from velocity measurements is bigger than the impeller rotation rate of 1.5 Hz: the velocity measured 20 mm away from the center corresponds to 2 Hz at $z=-100$ mm and to 1.6 Hz at $z=-180$ mm. This can be due to the fact that the impeller is a trapezoid tightly enclosed in a housing.

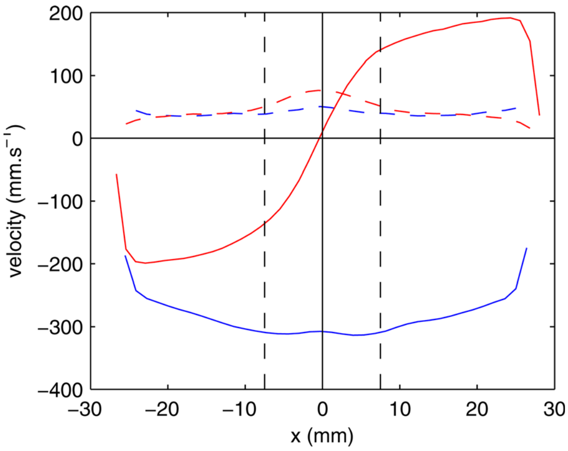

FIG. 4. (Color online) Velocity profiles at $z=-140$ mm along x-axis, for a flow rate of 0.62L s^{-1} and a rotation rate of 1.5 Hz. Dark gray (blue online): vertical velocity u_z (solid line) and its standard deviation σ_{uz} (dashed line). Mid-gray (red online): tangential velocity u_y (solid line) and its standard deviation σ_{uy} (dashed line). The vertical dashed lines stand for the core region of diameter 15 mm.

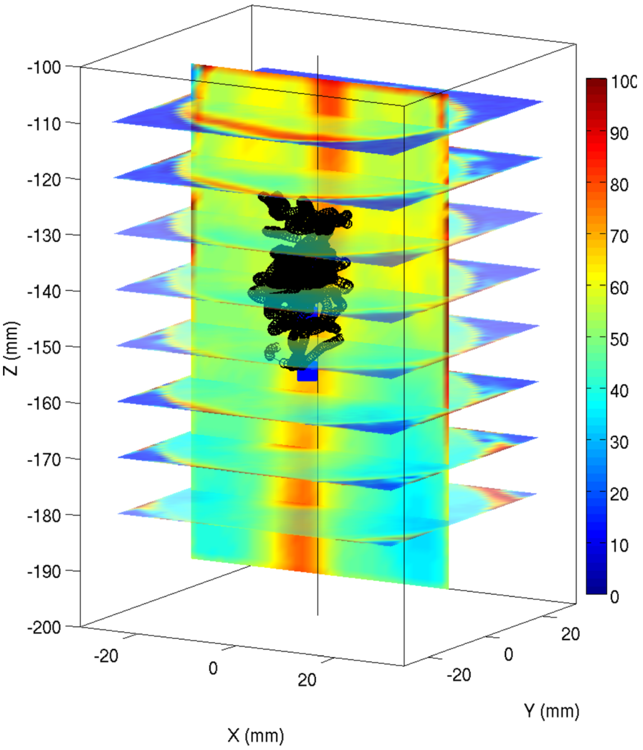

FIG. 5. (Color online) Standard deviation of the velocity measured in one vertical plane and eight horizontal planes superimposed with the trajectory of bubble $B5$ (black) and mean positions of the six bubbles (blue squares).

A time signal of the vertical velocity at a point close to the center of the region where the bubbles are trapped is plotted in Fig. 6 together with the corresponding power spectrum. The flow is turbulent and the spectrum exhibits a large inertial range with a $-5/3$ power law. The integral time scale Θ that could be estimated from the autocorrelation function of the time signal in Fig. 6 is $\Theta \simeq 0.10$ s, i.e., an integral length scale $\Lambda \simeq 30$ mm deduced from the Taylor's hypothesis of frozen turbulence. This approximately corresponds to three times the bubble diameter, which is close to 10 mm. The estimated Taylor micro-scale is roughly 0.016 s that corresponds to $\lambda \simeq 5$mm, i.e., half the bubble diameter. The arrows in Fig. 6(b) that stand for three length scales surrounding the mean bubble diameter are in the inertial range of the spectrum. The bubble thus locally experiments the turbulent nature of the flow.

In conclusion, the bubbles are trapped within a core region of 15 mm width where they experience a turbulent flow that is roughly isotropic: the fluctuations of velocity are of the same order of magnitude $(60\ \mathrm{mm\ s^{-1}})$ for the three components of the velocity. The mean axial flow is moreover homogeneous in this region, and the horizontal velocity resembles solid-body rotation.

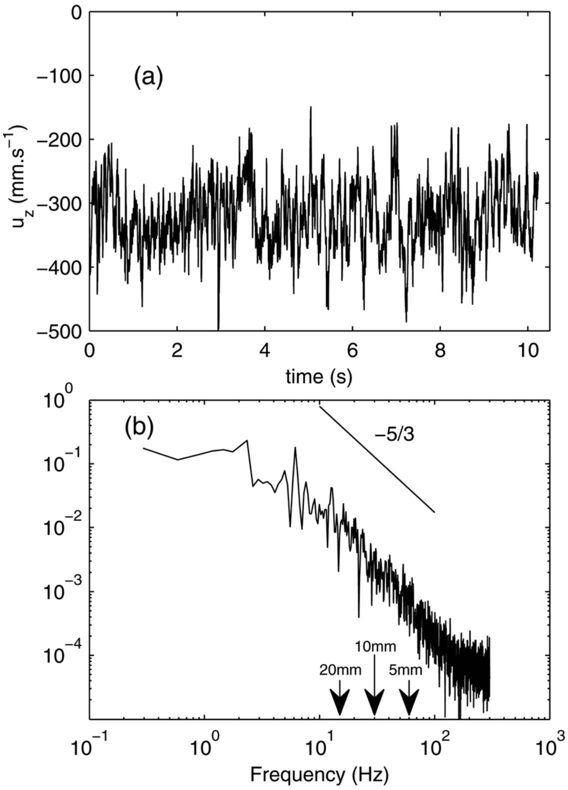

FIG. 6. Velocity measurements for a flow rate of 0.62 L s^{-1} and a rotation rate of 1.5 Hz. (a) Time signal of the vertical velocity u_z at point $x=-0.3$, $y=0$, $z=-140$ (in mm). (b) Corresponding power spectrum. Arrows stand for corresponding length scales using Taylor's hypothesis.

B. Consequences on the bubbles

With these velocity measurements, we can now estimate the ratio of deforming forces and stabilizing forces acting on the bubbles. For our air bubbles in water, the viscous shear is negligible: a capillary number Ca based on the measured shear rate of the mean flow, on the viscosity of water, and on the interfacial tension between air and water $\sigma = 70$ mN m^{-1} is $Ca \leq 5\times 10^{-4}$. The relevant numbers are thus Weber numbers comparing inertia to capillarity.

The bubble of mean diameter $d=9.3\pm 0.3$ mm has a mean rising velocity $U_b = 300$ mm s^{-1} and is in a region where the fluid is in solid body rotation at angular velocity $\Omega = 9.4$rad s^{-1}. The bubble Reynolds number is $Re_b = U_b d/\nu \simeq 2800$ with $\nu = 10^{-6}$m^2 s^{-1}, the kinematic viscosity of water. The Weber number based on the mean rising velocity is $We = \rho d U^2/\sigma \simeq 11.6$, with $\rho = 10^3$kg m^{-3}, the density of the continuous phase. These values of Re_b and We correspond to a situation with a large mean deformation of the bubble that should be an elongated ellipsoid rising with an oscillating path[8,9] as confirmed by the results discussed in Sec. V A. The Weber number We_Ω based on the solid body rotation is very small: $We_\Omega = \rho d(d\Omega/2)^2/\sigma \simeq 0.25$. The solid body rotation plays no role in the deformation of the bubble. It will actually maintain the bubble in the central zone of the flow (see Fig. 5).

The eigenfrequency of mode 2 for the deformation of the bubble[4,5] is $\omega_2 = \sqrt{\frac{96\sigma}{\rho d^3}} \simeq 92.7$rad s^{-1} ($f_2 = 14.8$ Hz). In the following, all the temporal features will be compared to this time scale. The Reynolds number based on this oscillation frequency is $Re_{osc} = 1/2 d^2\omega_2/\nu \simeq 3900$. It is fairly high, which implies a small damping rate of the free oscillations of a bubble at rest:[4,5] $\beta = \frac{80\nu}{d^2} \simeq 0.9$ s^{-1}. The rising velocity of the bubble is thus of the same order of magnitude as the shape oscillation velocity: $Re_b/Re_{osc} = 0.7$. The rising velocity may thus have significant effects on the shape dynamics. Finally, the level of turbulent fluctuations in the velocity field is high ($\sigma_u/U_b \simeq 1/5$) and may also have a significant impact on the shape dynamics.

To take into account the contribution of turbulent fluctuations, we define an instantaneous turbulent Weber number $We_t(\mathbf{x}, t)$ at each point, based on the velocity scale $\delta\hat{u}^2(\mathbf{x}, t) = \max(u'(\mathbf{x}+\mathbf{b}, t) - u'(\mathbf{x}-\mathbf{b}, t))^2$. This velocity scale $\delta\hat{u}$ is the maximum of the second order structures functions computed for distance d ($\mathbf{b}$ is a vector of length $d/2$ and various orientations, the maximum being taken on these orientations). The spatial distribution of this turbulent Weber number is very similar to the distribution of the velocity fluctuations that is presented in Fig. 5, and the time-averaged value of the turbulent Weber number is less than 1.8 in the test region.

The temporal features of this signal at a point close to the center of the visualization volume are given in Fig. 7. At this point, the mean turbulent Weber number is 1.3 and the standard deviation is 1.2. One can notice in Fig. 7(b) that the probability density function of We_t is skewed towards high values: very rare events with high values of the turbulent Weber number arise. One event is highlighted in the inset of Fig. 7(a): we notice that the Weber number exceeds a significant value ($We_t \geq 5$) for a non-negligible time with respect to the time scale given by f_2, that is roughly $We_t \geq 5$ during $0.75 f_2^{-1}$. The distribution of the waiting times between these high We_t events resembles a Poisson process as can be seen in Fig. 7(c) where the distribution of time intervals between two successive events with $We_t \geq 2$ is reported. The distribution is exponential with a time constant of 0.04 s or $0.6 f_2^{-1}$ in this case.

V. INTRODUCTION TO THE STUDY OF BUBBLE DYNAMICS

The mean features of the large-scale flow and the turbulent statistics that may be relevant towards the shape dynamics of bubbles of mean diameter 9.3 mm have thus been characterized. The following two sections deal with the bubble shape dynamics. As described thereafter, the breakup rate is very low and the breakup process does not seem to depend on the history of the bubble—in other words, no resonant breakup is observed. The dynamics during moderate deformations phases is thus first presented (Sec. V A), and the breakup phase is then specifically analyzed (Sec. V B).

A. Dynamics of moderate deformations

This section is devoted to the behavior of bubbles of typical diameter $d=9.3\pm 0.3$ mm that are injected in the previously described velocity field, excluding the breakup phase. The results reported hereafter concern six sequences

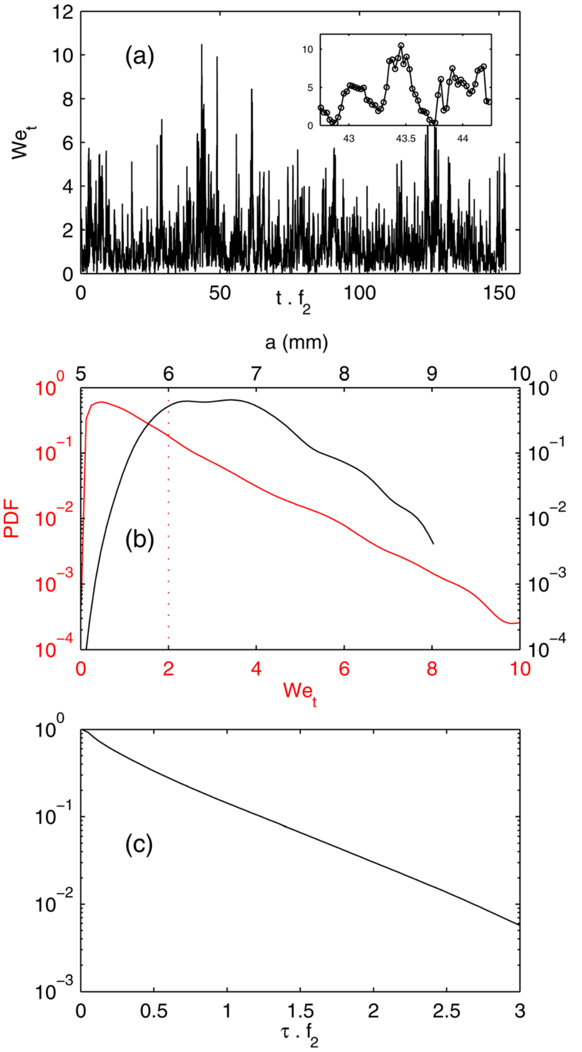

FIG. 7. (Color online) Measurement of the turbulent Weber number $We_t(\mathbf{x},t)$ at point $x=-0.3$, $y=0$, $z=-140$ (in mm) for a flow rate of 0.62 L s^{-1} and a rotation rate of 1.5 Hz. (a) Time signal. (b) Corresponding probability density function, in gray (left and bottom axis, red online). The black curve (top and right axis) is the probability density function of major axis a for bubble $B5$. (c) Distribution of time intervals between two successive events corresponding to $We_t \geq 2$. This threshold is highlighted by the vertical dotted line in (b). All the times are made non-dimensional with $f_2 \simeq 15$ Hz.

of 2000 images taken at 300 Hz for six independent bubbles, dimensions of which are presented in Table I. These values have been extracted from the images with the procedure described in Sec. III. A sequence of 25 side view images in the plane $x-z$ (camera 1) is displayed in Fig. 8 and may be considered as a typical example to illustrate the deformations and motion of the bubble. This sequence has been chosen because the major axis of the equivalent ellipsoid lies in this $x-z$ plane during the selected time interval. The time series of the three ellipsoid semi-axis of the horizontal velocity V_x and of the orientation of the short axis θ for sequence $B5$ are moreover plotted in Fig. 9.

1. Mean shape

The instantaneous shape of the bubble strongly differs from an ellipsoid as can be seen in Fig. 8. The semi-axis lengths are moreover strongly fluctuating (Fig. 9(c)): the fluctuating rate of the three axes is of the order of 10%. One can also notice in Table I that the volume of the equivalent ellipsoid is not conserved: the fluctuation rate of $(abc)^{1/3}$ is nevertheless small, around 2%. Finally, the following observations can be drawn:

- the mean shape of the bubbles is an ellipsoid with a symmetry axis around the short axis;
- the mean aspect ratio of this ellipsoid χ is 1.91 ± 0.11 and seems to increase with the equivalent radius;
- the short axis is pointing in the vertical direction on average, as can be seen in Fig. 9(b).

2. Position and motion of the bubble

The mean positions of the six bubbles are displayed with blue squares in Fig. 5. The trajectory of bubble $B5$ is also displayed in this figure. The trajectory of a bubble is quite complicated and frequently exhibits loops but the six bubbles are however trapped inside the vortex annular core as described in Sec. IV. The fluctuations of the position are of the same order of magnitude for every bubble: the standard deviation of the vertical position is $\sigma_z \simeq 7$mm and the fluctuations in the horizontal positions are $\sigma_x = \sigma_y \simeq 4$mm. These last two could be translated in polar coordinates centered on the mean bubble position and would give a fluctuation of radial position $\sigma_r \simeq 2.5$mm.

Though the bubble path seems erratic, the time series of the horizontal velocity (Fig. 9(a)) and of the short axis orientation (Fig. 9(b)) are more regular and may exhibit a periodic behavior. The horizontal velocity has a standard deviation of the order of 100 mm s^{-1}. The temporal spectra of horizontal velocity and of orientation are plotted in Fig. 10. Some peaks are clearly visible and give a typical harmonic component for the path at 8.5 Hz. The cross-correlation between V_x and θ moreover shows a peak at -0.73, with a time delay between two successive peaks in the cross-correlation function that corresponds to this frequency of 8.5 Hz. This

TABLE I. Fitted ellipsoid dimensions in mm for six bubbles. Mean half major axis, $\langle a \rangle$; half medium axis, $\langle b \rangle$; half short axis, $\langle c \rangle$; equivalent radius, $\langle (abc)^{1/3} \rangle$; aspect ratio $\chi = \langle (a+b)/2c \rangle$; standard deviations σ_a, σ_b, σ_c, and $\sigma_{abc^{1/3}}$.

Bubble	$\langle a \rangle$	$\langle b \rangle$	$\langle c \rangle$	$\langle (abc)^{1/3} \rangle$	χ	σ_a	σ_b	σ_c	$\sigma_{abc^{1/3}}$
$B1$	6.05	4.98	3.05	4.49	1.83	0.48	0.38	0.29	0.07
$B2$	6.10	4.94	3.04	4.49	1.84	0.52	0.40	0.30	0.09
$B3$	6.22	5.13	3.14	4.62	1.84	0.52	0.41	0.33	0.09
$B4$	6.50	5.24	3.11	4.71	1.92	0.67	0.45	0.34	0.12
$B5$	6.65	5.39	3.19	4.82	1.92	0.62	0.49	0.35	0.13
$B6$	7.03	5.49	3.00	4.84	2.14	0.75	0.55	0.38	0.13

behavior is consistent with a wake instability. The strouhal number built with this frequency, the mean bubble rising velocity, and the bubble diameter is $St = \frac{fd}{U_b} \simeq 0.27$. According to the works of Lindt,[17] the prediction for the strouhal number of the wake is $St = 0.28$.

3. Dynamics of deformation

The significant deformations that the bubbles undergo on the contrary do not exhibit any periodic behavior, as can be seen in Fig. 9(c) on the time series of the three semi-axes of the equivalent ellipsoid and in Fig. 10 where no peak is visible in the power spectrum of a. There thus seem to be no trace of a periodic shape oscillation at the eigenfrequency f_2 at first glance, contrary to what is observed without buoyancy.[1,2] The deformations still have a part of deterministic dynamics that is highlighted with the analysis of the cross-correlations between the three axes lengths.

Figure 11 presents an average on all sequences excluding breakup phases of the cross-correlation functions of the two largest axes lengths $a - b$ (blue dashed-dotted line), of the big and short axes lengths $a - c$ (red dashed line), and of the medium and short axes lengths $b - c$ (black line). The cross-correlation function is defined as

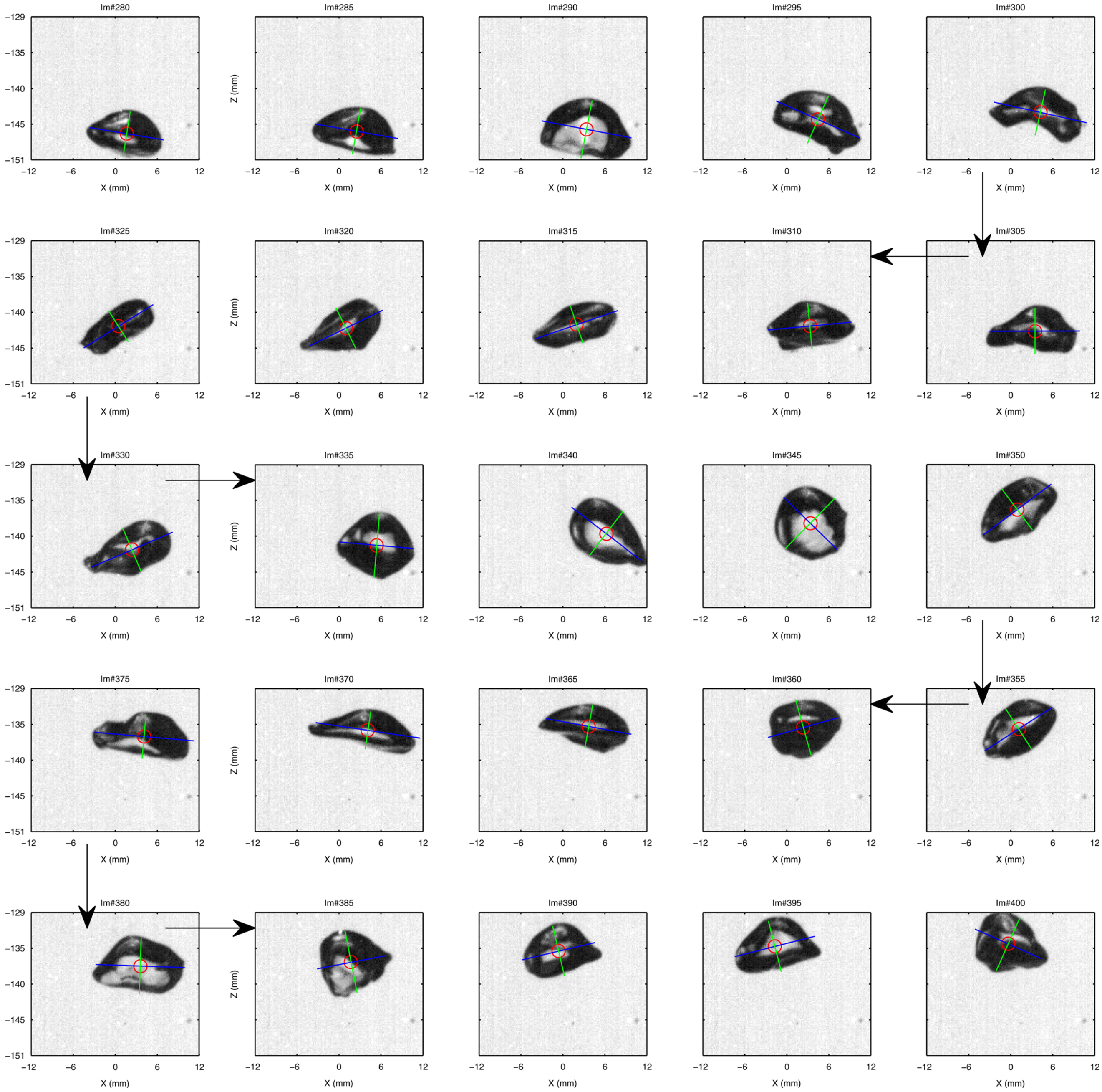

FIG. 8. (Color online) Illustration of a deformation sequence on case $B5$. Side view in the plane $x - z$ (camera 1) with the center of mass (mid-gray dot, red online), the major (dark gray line, blue online) and minor axes (light gray line, green online) of the equivalent ellipse. One image over 5 is displayed and the time lag between each image thus corresponds to $1/60$ s $((4f_2)^{-1})$. Please note that the sequence reads from top left to top right then the second line reads from right to left, and so on, following the arrows.

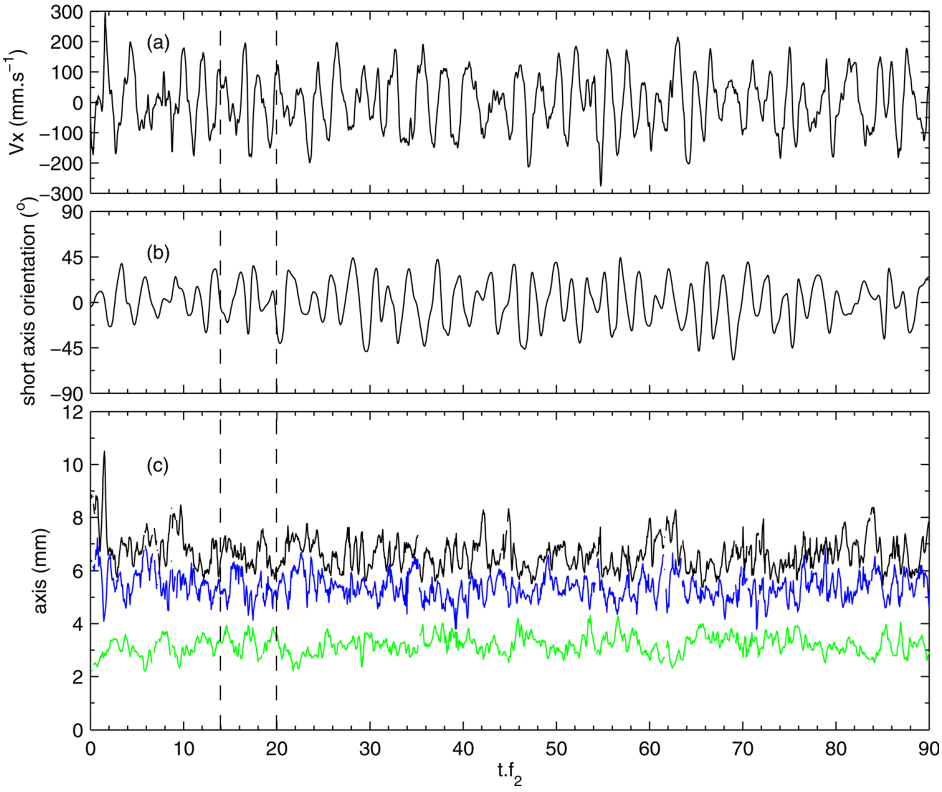

FIG. 9. (Color online) Time signals of (a) horizontal velocity V_x, (b) orientation θ of the short axis relative to vertical direction, and (c) semi-axis lengths (black, a; dark gray (blue online), b; light gray (green online), c; for sequence $B5$. All the times are made non-dimensional with $f_2 \simeq 15$ Hz. The vertical dashed lines stand for the time interval corresponding to the sequence depicted in Fig. 8.

$$C_{a-b}(\tau) = \frac{\langle a(t)\, b(t-\tau)\rangle}{\sigma_a\, \sigma_b},$$

where $\langle\rangle$ stands for time average, τ is a time lag, and σ is the standard deviation. The short axis is significantly anti-correlated to the two biggest axes, at 0 time-lag. The cross-correlation coefficient of a and c, and b and c is indeed close to -0.6 at $\tau = 0$ ($C_{a-c}(\tau = 0) \simeq -0.62$ and $C_{b-c}(\tau = 0) \simeq -0.54$). Concerning the two biggest axes, they have very few correlation: their cross-correlation coefficient at $\tau = 0$ is $C_{a-b}(\tau = 0) \simeq 0$. The deformations of the bubbles are thus non-axisymmetric, as already observed for large rising bubbles.[10,11] The cross-correlation function C_{a-b} presents two local maxima around 0.15 for $\tau \simeq -0.6$ and $\tau \simeq 0.5$. This may be a trace of exchanges between a

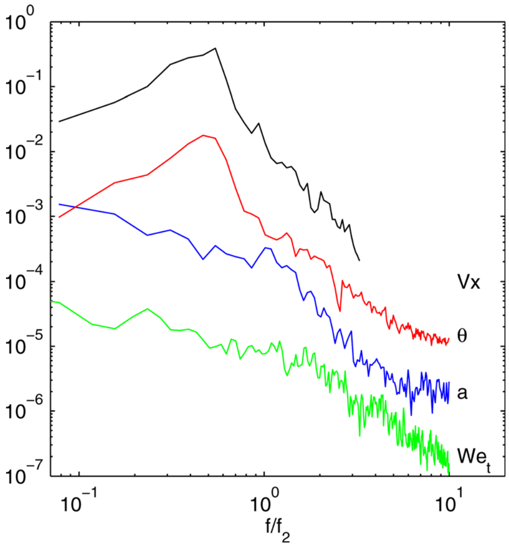

FIG. 10. (Color online) Power spectra of V_x (black), θ (mid-gray, red online), a for sequence $B5$ (please see also the time signals in Fig. 9) (dark gray, blue online), and We_t at point $x = -0.3$, $y = 0$, $z = -140$ mm (please see the time signal in Fig. 7) (light gray, green online). The frequencies are made non-dimensional with $f_2 \simeq 15$ Hz. The different spectra have been vertically shifted for the sake of clarity.

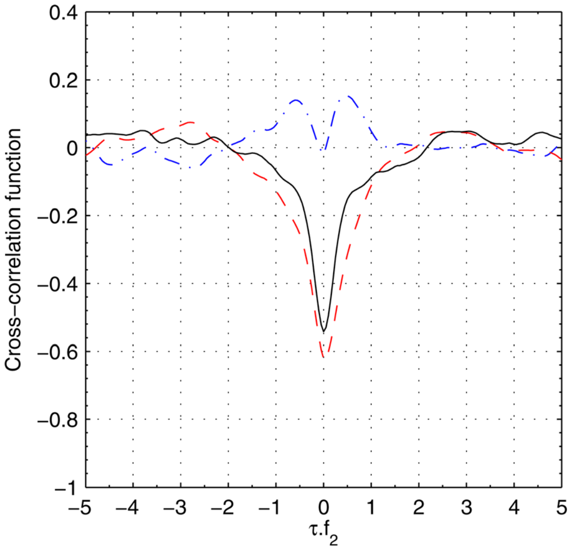

FIG. 11. (Color online) Cross-correlation functions of $a-b$ (dashed-dotted, blue online), $a-c$ (dashed, red online), and $b-c$ (black). An average has been made on all the sequences excluding breakup phases. The time lag is made non-dimensional with $f_2 \simeq 15$ Hz.

and *b* when the two main axes are close in length. Finally, one can notice that the cross-correlation function goes to zero rapidly with increasing time lags: one can estimate that the dynamics of the three axes is uncorrelated after 1 to 2 f_2^{-1}.

The short axis thus seems to play a particular role with respect to the deformations. As previously noticed, it is pointing in the vertical direction on average, i.e., it is aligned with the gravity. The analysis of the correlations suggest that the significant deformations take place in the horizontal direction and are not axisymmetric, and that though no oscillations are observed, the characteristic time based on the eigenfrequency f_2 should be present.

In order to check this hypothesis, Sec. V B will focus on the dynamics of the most intense deformations and on the breakup process.

B. Large deformations and breakup

The probability distribution function (PDF) of *a* for bubble *B*5 is plotted in black in Fig. 7(b). This PDF is clearly not Gaussian and is asymmetric: the PDF has a positive skewness 0.5. A number of events that correspond to high values of *a* should thus be detectable. We propose $a \geq \langle a \rangle + 1.5\sigma_a$, i.e., $a \geq 7.5$ mm for bubble *B*5, as an arbitrary threshold to qualify a large deformation. One question is to what extent these events are rare or frequent.

The distribution of the waiting times between two overtakings of this threshold is plotted in red in Fig. 12. The statistics is exponential with a characteristic time around 7 f_2^{-1}. This behavior is reminiscent of the statistics for the turbulent Weber number that have been shown in Fig. 7(c). For bubbles of equivalent diameter 9.3 mm, the breakup rate is however very low, of the order of 50 s^{-1}. In order to allow the determination of breakup statistics in a reasonable time, experimental measurements for the same flow conditions, but with larger bubbles, have been carried out. The black curve in Fig. 12 shows the statistics of breakup time of bubbles of equivalent diameter 12 mm. These measurements show that the distribution of the life-time before breakup is also an exponential law. This is consistent with waiting for an instantaneous turbulent Weber number bigger than a certain threshold to lead to breakup.

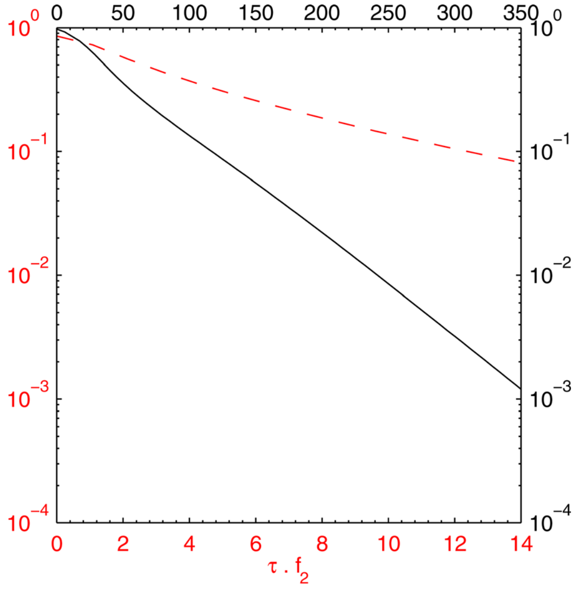

FIG. 12. (Color online) Dashed line (red online), bottom and left axis: distribution of time intervals between two successive overtakings of a threshold for *a* ($a \geq 7.5$ mm), for sequence *B*5. Black solid line, top and right axis: distribution of bubbles breakup times, for 76 breakup time measurements. (Please note that for breakup statistics, the velocity field is the same but the equivalent diameter of the bubbles has been increased to 12 mm, in order to increase breakup rate. In that case, the time-scale that has been used to present dimensionless times is based on $f_2 \simeq 10$ Hz).

Some large deformations that do not lead to breakup have been identified and selected for the six experiments. They correspond to maximum deformations $8.3 \lessapprox a \lessapprox 9.5$mm. The time series of *a* have been synchronized to a reference time t_0 that corresponds to the maximum of *a* and are gathered in Fig. 13(a). They are plotted between $t_0 - \text{g}3\ f_2$ and $t_0 + 1\ f_2$. The corresponding series of images in the plane $x - y$ (camera 2) for the sequence concerning bubble *B*4 is displayed in Fig. 14.

These series show the following common features for the large deformations. First, there are neither successive amplifications of the deformation nor periodic shape oscillations at the eigenfrequency f_2 as observed when stochastic resonance occurs.[1] A strong increase of *a* is immediately followed by a decrease back to the mean level. Once

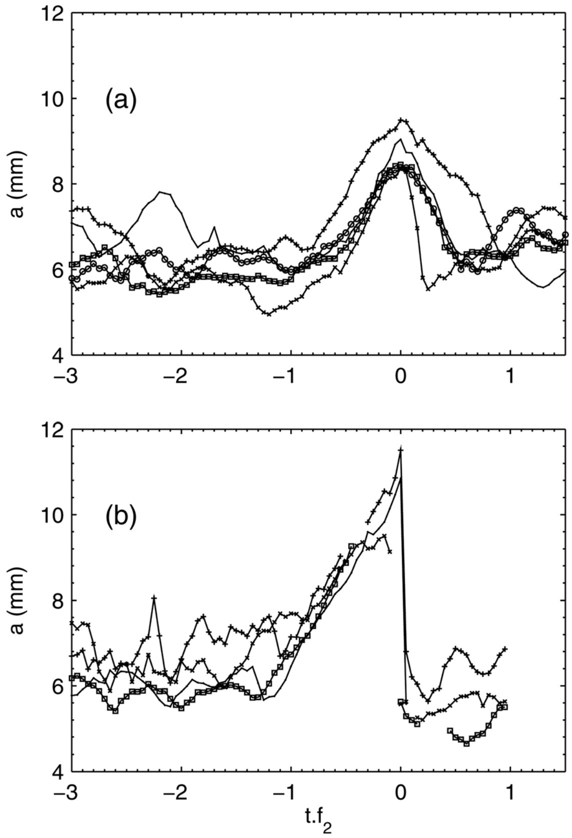

FIG. 13. Superposition of large deformation phases (a) and breakup events (b) for the different bubbles. The sequences have been synchronized on the maximum of *a*. The time is made non-dimensional with $f_2 \simeq 15$Hz. (a) case *B*2 (□ and ○), case *B*3 (×), case *B*4 (black line), and case *B*6 (+). (b) case *B*2 (□), case *B*3 (×), case *B*4 (black line), and case *B*6 (+).

synchronized to the maximum deformation, the phases of growth and decay nevertheless exhibit a distinct time-scale around f_2^{-1}. This is reminiscent of the behavior of a strongly damped oscillator. The large deformations moreover correspond to strongly elongated shapes of the bubble as can be seen in Fig. 14. In that case, the three dimensional aspect ratio at maximum deformation in picture #1434 is $\chi \simeq 2.5$, and the aspect ratio in the horizontal plane is $a/b \simeq 2.0$. For all the large deformations, the bubble is elongated in an almost horizontal direction, the short axis being vertical within ±15°. This shape is not axisymmetric and its decomposition into spherical harmonics involves a major contribution of mode $n=2$, $m=2$ where n stands for the poloidal wave number and m stands for the azimuthal wave number.

Finally, the breakup phases have been identified and the time series of axis a synchronized to the breakup time are gathered in Fig. 13(b). The corresponding series of images in the plane $x-y$ (camera 2) for bubble $B2$ is displayed in Fig. 15. The breakups are very similar to the previously described large deformations. The four bubbles break in a horizontal plane when a exceeds the value $a_{break} \simeq 10.5$mm, which corresponds to approximately twice the equivalent bubble

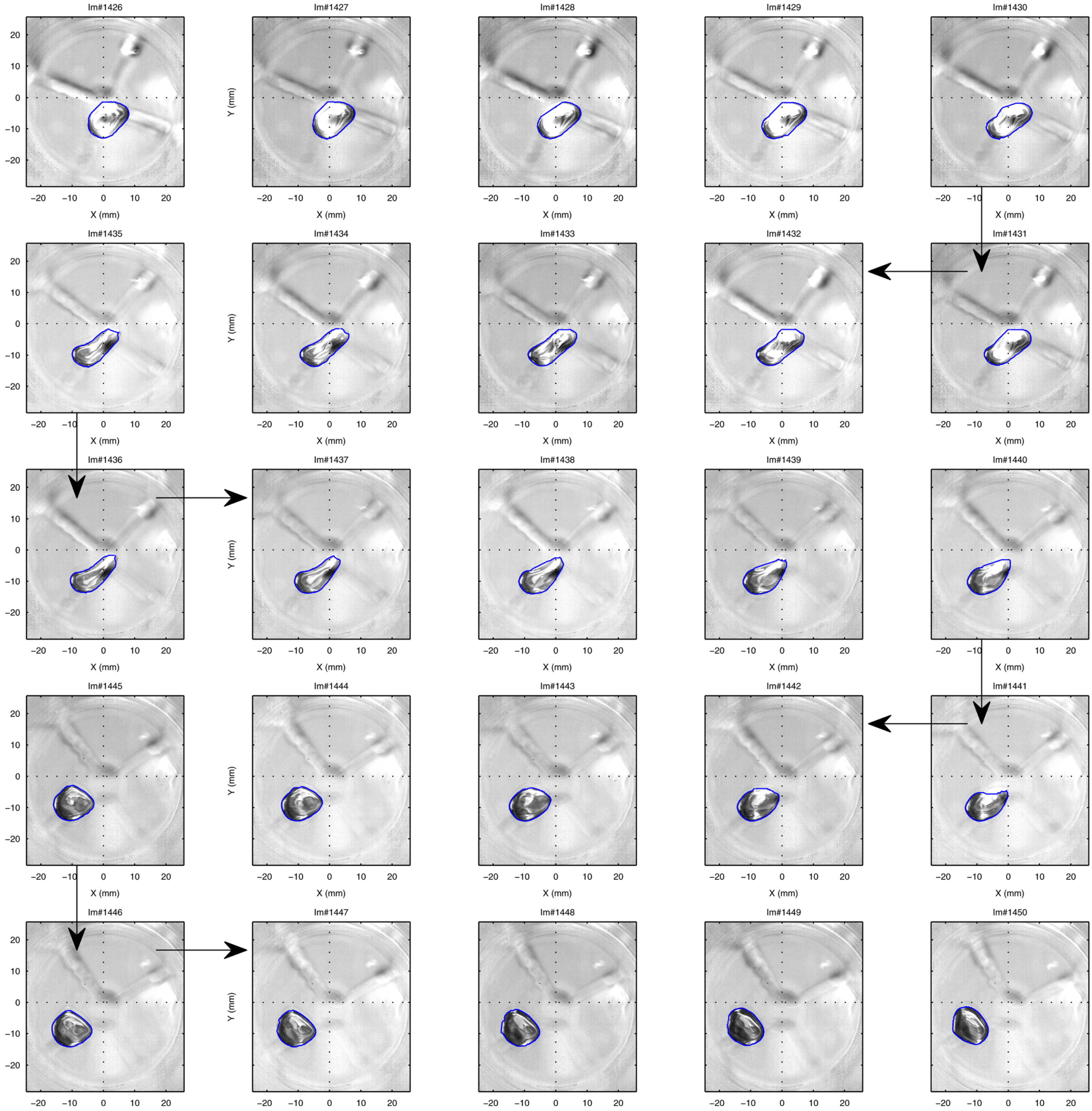

FIG. 14. (Color online) Illustration of a large deformation sequence that do not lead to breakup on case $B4$. Bottom view in the plane $x-y$ (camera 2) with the detected contour in dark gray (blue online). The time lag between each image corresponds to $1/300$ s ($(20f_2)^{-1}$). Please note that the sequence reads from top left to top right then the second line reads from right to left, and so on, following the arrows. The maximum deformation is reached in picture #1434 with $a \simeq 9$mm and thus corresponds to time t_0 in Fig. 13.

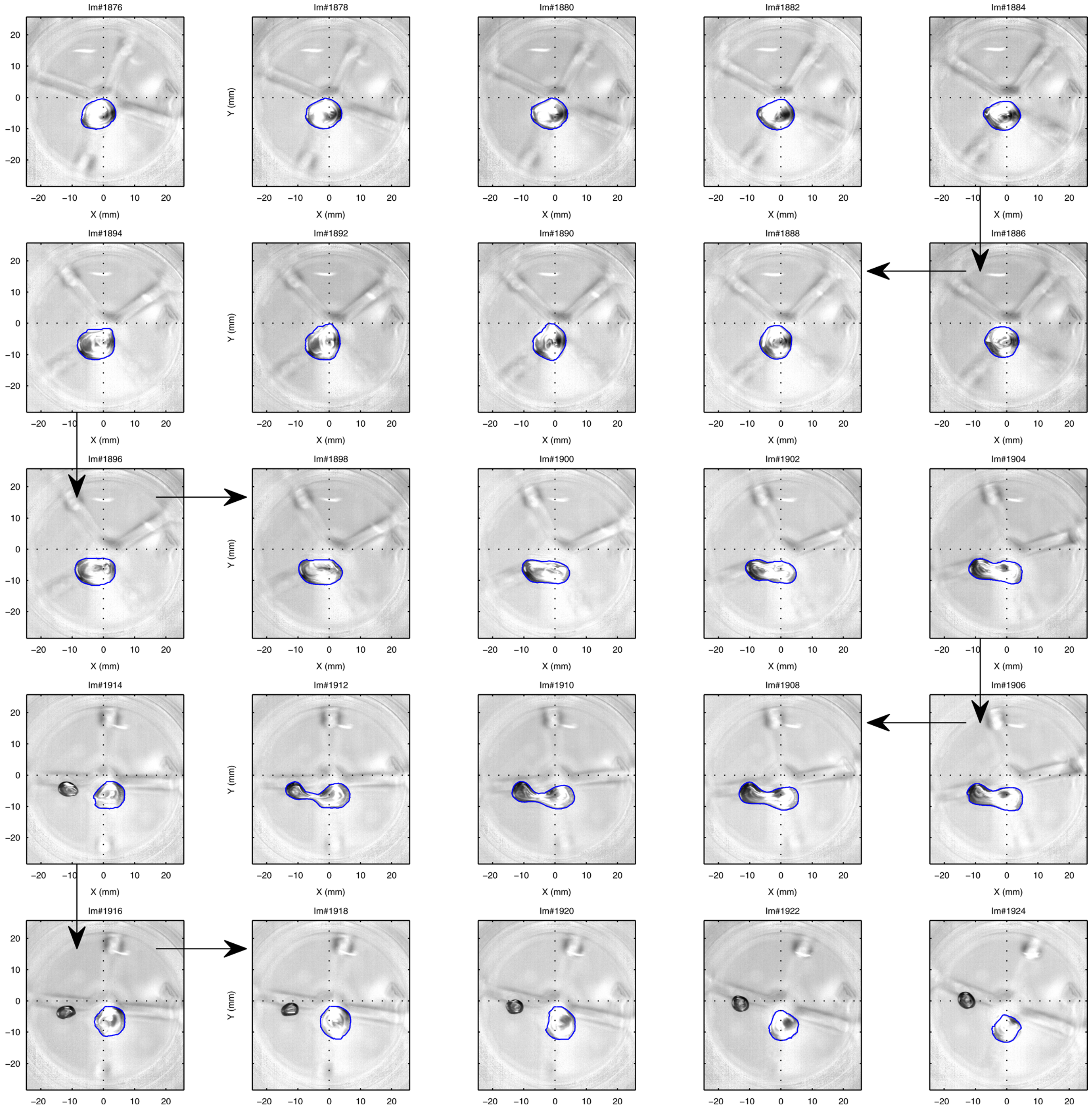

FIG. 15. (Color online) Illustration of a breakup on case $B2$. Bottom view in the plane $x-y$ (camera 2) with the detected contour in dark gray (blue online). One image over 2 is displayed and the time lag between each image thus corresponds to $1/150$ s ($(10f_2)^{-1}$). Please note that the sequence reads from top left to top right then the second line reads from right to left, and so on, following the arrows.

radius. This value of the critical deformation leading to breakup is in agreement with results obtained in the absence of buoyancy for both a bubble in a homogeneous turbulence[1] or a drop in a strongly heterogeneous turbulence.[2]

The final phase of growth of a is collapsing for the four cases, with a characteristic breakup time t_b again on the order of f_2^{-1}. In the situation investigated here, there is no stochastic resonance and the breakup results from the interaction with a single turbulent eddy. Depending on the duration t_i of this interaction, the scaling of t_b may be different. On the one hand, if t_i is short compared to the natural relaxation time f_2^{-1}, then t_b is expected to be proportional to $f_2^{-1}(\approx 0.06\ \mathrm{s})$. On the other hand, if t_i is large compared to f_2^{-1}, the forcing flow can be considered as steady and the numerical simulation of a bubble in a constant uniaxial straining flow by Rodríguez-Rodríguez *et al.*[18] can be considered as a reasonable model of the present breakup process. From our observations, the magnitude of the instantaneous Weber number leading to breakup is of order 10. From Fig. 6 of Ref. 18, the breakup time corresponding to this Weber number is slightly larger than $\frac{d/2}{\delta\bar{u}(d)} \approx 1.7\times 10^{-2}$ s, which is approximately equal to $f_2^{-1}/4$. In fact, Fig. 7(a) shows that the duration of the largest turbulent fluctuation is of order of f_2^{-1}. We are thus probably in between these two extreme cases. However, as the expected breakup rate is similar in both cases, we are not surprised to observe that t_b is close to f_2^{-1}.

VI. CONCLUDING REMARKS

The purpose of this study was to determine the dynamics of a deformable bubble rising in a turbulent flow. In particular, we are interested in understanding the role of the sliding motion induced by buoyancy upon the bubble deformation and breakup.

In the absence of significant sliding motion, the shape dynamics of a bubble in a turbulent low-viscosity liquid was already fairly well understood.[1,2] The bubble essentially responds to turbulent eddies of scales comparable to its diameter by experiencing deformations described by the axisymmetric spherical harmonics $n=2$, $m=0$. After interaction with an intense turbulent eddy, either the bubble breaks or performs weakly damped oscillation at the frequency f_2 given by the linear theory[4,5] of shape oscillations for this mode. The shape dynamics can be modeled by a linear oscillator forced by turbulent fluctuations, which amplifies frequencies close to f_2 and filters out others. Deformation statistics are therefore radically different from those of turbulence, and since breakup occurs whenever the bubble elongation is larger than a certain threshold, the breakup probabilities also strongly differ from those of turbulence.

The present work reports an experimental investigation of an air bubble immersed in a uniform downward turbulent flow of water, which has been characterized by means of fast PIV. Thanks to rapid imaging of three perpendicular views combined with three-dimensional shape recognition, temporal evolutions of bubble translation, rotation, and deformation have been measured.

The dynamics of the bubble involves three mechanisms fairly decoupled:

- The average shape of the bubble is imposed by the sliding between the phases. It is approximately an oblate spheroid with its small axis in the direction of motion. It therefore mainly involves spherical harmonic $n=2$, $m=0$.
- The wake instabilities lead to quasi-periodic oscillations of velocity and orientation but only cause slight shape oscillations, which are not axisymmetric in agreement with previous works dealing with bubbles rising in a quiescent fluid.[10,11] These deformations do not play a significant role in the breakup.
- Turbulence generates random deformations that may cause breakup when the bubble elongation exceeds twice the equivalent diameter, a value in agreement with results obtained in the absence of buoyancy.

A large deformation occurs when the bubble encounters an intense turbulent eddy. It corresponds to an elongation in a horizontal direction, which breaks the axial symmetry of the average shape and mainly involves spherical harmonic $n=2$, $m=2$. After interaction with the eddy, the bubble either breaks or relaxes towards its average shape on a time scale close to f_2^{-1}, without experiencing any oscillations. The existence of a large sliding motion between the phases thus radically changes the shape dynamics: it could still be modeled by an oscillator—which describes now the amplitude of mode $n=2$, $m=2$—with a proper frequency f_2 but with a damping rate comparable to f_2. With such an overdamped oscillator, breakup cannot result from stochastic resonance and is always caused by the interaction with a single intense eddy.

This absence of memory of the shape dynamics has a major consequence for breakup. The statistics of waiting times between two large deformations and, similarly, the statistics of bubble residence time before breakup, do not involve the characteristic timescale f_2^{-1} of the bubble deformation and are identical to the statistics of turbulence. The response time f_2^{-1} however controls the effectiveness of turbulent bursts—through the Weber number—and the duration of the breakup phenomenon.

Unexpectedly, breakup statistics in a turbulent flow eventually turn out to be easier to model for a large bubble rising on an oscillatory path than for a non-sliding bubble in microgravity condition. It is due to the strong enhancement of the damping of shape oscillations. The reason of this enhancement and its relation with the existence of a significant sliding remains an open question that deserves to be addressed in a future work.

[1] F. Risso and J. Fabre, "Oscillations and breakup of a bubble immersed in a turbulent field," J. Fluid Mech. **372**, 323 (1998).

[2] S. Galinat, F. Risso, O. Masbernat, and P. Guiraud, "Dynamics of drop breakup in inhomogeneous turbulence at various volume fractions," J. Fluid Mech. **578**, 85 (2007).

[3] F. Risso, "The mechanisms of deformation and breakup of drops and bubbles," Multiphase Sci. Technol. **12**, 1 (2000).

[4] C. A. Miller and L. E. Scriven, "The oscillations of a fluid droplet immersed in another fluid," J. Fluid Mech. **32**, 417 (1968).

[5] A. Prosperetti, "Free oscillations of drops and bubbles: The initial-value problem," J. Fluid Mech. **100**, 333 (1980).

[6] S. V. Subramanyam, "A note on the damping and oscillations of a fluid drop moving in another fluid," J. Fluid Mech. **37**, 715 (1969).

[7] O. A. Basaran, T. C. Scott, and C. H. Bayers, "Drop oscillations in liquid-liquid systems," AIChE J. **440**, 1263 (1989).

[8] D. I. Meiron, "On the stability of gas bubbles rising in an inviscid fluid," J. Fluid Mech. **198**, 101 (1989).

[9] K. Ellingsen and F. Risso, "On the rise of an ellipsoidal bubble in water: Oscillatory paths and liquid-induced velocity," J. Fluid Mech. **440**, 235 (2001).

[10] K. Lunde and R. J. Perkins, "Shape oscillations of rising bubbles," Appl. Sci. Res. **58**, 387 (1997).

[11] C. Veldhuis, A. Biesheuvel, and L. van Wijngaarden, "Shape oscillations on bubbles rising in clean and in tap water," Phys. Fluids **20**, 040705 (2008).

[12] K. Wichterle, J. Wichterlová, and L. Kulhánková, "Breakup of bubbles rising in liquids of low and moderate viscosity," Chem. Eng. Commun. **192**, 550 (2005).

[13] S. M. Smith and J. M. Brady, "SUSAN—A new approach to low level image processing," Int. J. Comput. Vis. **23**, 45 (1997).

[14] L. Ji and H. Yan, "Attractable snakes based on the greedy algorithm for contour extraction," Pattern Recogn. **35**, 791 (2002).

[15] T. Kayikcioglu, A. Gangal, and M. Ozer, "Reconstructing ellipsoids from three projection contours," Pattern Recogn. Lett. **21**, 959 (2000).

[16] J. Westerweel and F. Scarano, "Universal outlier detection for PIV data," Exp. Fluids **39**(6), 1096 (2005).

[17] J. T. Lindt, "On the periodic nature of the drag on a rising bubble," Chem. Eng. Sci. **27**, 1775 (1972).

[18] J. Rodríguez-Rodríguez, J. M. Gordillo and C. Martínez-Bazán, "Breakup time and morphology of drops and bubbles in a high-Reynolds-number flow," J. Fluid Mech. **548**, 69 (2006).

Study of the cavitating instability on a grooved Venturi profile

Amélie Danlos
Post-Doctoral student
DynFluid Laboratory, EA 92
Arts et Métiers ParisTech
151 Boulevard de l'Hôpital
75013 Paris, France
Email: amelie.danlos@ensam.eu

Jean-Elie Méhal

PhD student
DynFluid Laboratory, EA 92
Arts et Métiers ParisTech
151 Boulevard de l'Hôpital
75013 Paris, France

Florent Ravelet

Associate Professor
DynFluid Laboratory, EA 92
Arts et Métiers ParisTech
151 Boulevard de l'Hôpital
75013 Paris, France
Email: florent.ravelet@ensam.eu

Olivier Coutier-Delgosha

Professor
Laboratoire de Mécanique de Lille, UMR 8107
Arts et Métiers ParisTech
8 Boulevard Louis XIV
59046 Lille, France
Email: olivier.coutier@ensam.eu

Farid Bakir

Professor
DynFluid Laboratory, EA 92
Arts et Métiers ParisTech
151 Boulevard de l'Hôpital
92290 Paris, France
Email: farid.bakir@ensam.eu

ABSTRACT

Instabilities of a partial cavity developed on an hydrofoil, a converging-diverging step or in an inter-blade channel, have already been investigated in many previous works. The aim of this study is to evaluate a passive control method of the sheet cavity. According to operating conditions, cavitation can be described by two different regimes: an unstable regime with a cloud cavitation shedding and a stable regime with only a pulsating sheet cavity. Avoiding cloud cavitation can limit structure damages since this regime is less agressive. The surface condition of a converging-diverging step is here studied as a solution to control the cavitation regime. This study discusses the effect of longitudinal grooves, on the developed sheet cavity. Analyzes conducted with Laser Doppler Velocimetry, visualisations and pressure measurements show that the grooves geometry, and especially the groove depth, acts on the sheet cavity dynamics and can even suppress the cloud cavitation shedding.

Nomenclature

C_f	Friction coefficient
H	Sheet cavity mean height
H^*	Undimensional sheet cavity mean height
H_{throat}	Height of the section at the Venturi throat
K	Karman constant
L	Sheet cavity mean length
L^*	Undimensional sheet cavity mean length
N	Number of grooves
P	Relative pressure
Q	Flow rate
$Re_{y_{throat}}$	Reynolds number
T	Water temperature
St_L	Strouhal number
d	Diameter blur of grooves
e	Width of the ridge
f	Shedding frequency
f_L	Frequency of the sheet cavity closure position variation
h	Depth of grooves
p_{ref}	Inlet pressure
p_{vap}	Saturation pressure of water
v_{ref}	Inlet discharge velocity
v_{throat}	Velocity measured at the Venturi throat
v_y	Longitudinal component of flow velocity
v'_y	Flow velocity component parallel to the bottom wall Venturi slope
v'_y*	Undimensional flow velocity component parallel to the bottom wall Venturi slope
v'_∞	Flow velocity component parallel to the bottom wall Venturi slope measured far from the plate wall
x,y,z	Cartesian coordinate system
x,y',z'	Cartesian coordinate system inclined, parallel to the bottom wall Venturi slope
x^*,y^*,z^*	Dimensionless space variables
y'^*,z'^*	Dimensionless space variables
δ_v	Viscous sublayer thickness
λ	Distance between the middle of two adjacent grooves
ν	Water viscosity
ρ	Water density

σ Cavitation number

* Symbol for undimensional variables: lengths are divided by H_{throat} and velocities by v'_∞

1 Introduction

Cavitation is a crucial phenomenon encountered in fluid mechanics and for instance in turbomachinery domain. The unsteady character of the sheet cavity behavior on suction side of hydrofoils, on converging-diverging obstacles or on blades in turbines and propellers is responsible for many issues like erosion, noise and vibrations. However, in many industrial devices, cavitation inception can not be avoided, so the challenge consists in a better understanding of the two-phase flow dynamics once cavitation has appeared, in order to reduce its negative effects. Simple geometries like 2D foil sections, or converging-diverging steps like Venturi-type sections are used to approach sheet cavitation dynamics [1]. A low pressure zone appears in the flow, downstream this type of obstacles. When this pressure becomes lower than the fluid saturation pressure, cavitation is induced and and a two-phase flow is obtained.

Sheet cavity dynamics can be described with a well-known cycle [2–7]. Sheet cavity grows from the Venturi throat until a re-entrant jet appears in the sheet cavity closure, and flows upstream, near the wall, below the cavity. The re-entrant jet separates then the sheet cavity when it reaches the liquid-gas interface of the flow. A large vapour cloud is shed and convected downstream the flow, while the sheet cavity length is substantially reduced. Then, the cloud of vapor collapses in a higher pressure region and sustains the re-entrant jet due to cloud implosion, which later produces a new shedding of vapor cloud [5, 8, 9]. This cycle is characterized by the shedding frequency f. Such oscillatory behaviour of the sheet cavity is a witness of two-dimensional and three-dimensional cavity instabilities. These instabilities induce vibrations which are a disability for many industrial applications, as for inducers [10–12].

Many studies have analyzed this sheet cavity cycle observed on cavitating hydrofoils or Venturi profiles. They have resulted in the definition of two types of oscillatory behaviors [5, 13]: the first one called cloud cavitation regime appears when the sheet cavity is long enough and generates periodical shedding as it has been described previously. But when the sheet cavity length is shorter because of a higher pressure level [5] and/or a Reynolds number smaller than a critical value [14, 15], no cloud cavitation shedding occurs. In this regime, the sheet cavity pulses but the cavity closure is always at the same location and no large scale detached cavitation structure is observed. In order to characterize these two regimes, a Strouhal number St_L is defined (as it is presented in section 3.4). For a sheet cavity regime, $St_L \simeq 0.1$ while a cloud cavitation regime is characterized by $0.2 \leq St_L \leq 0.4$. The cloud cavitation regime is more aggressive and leads to increased damages of the solid structures.. It is thus interesting to find a way to control the sheet cavity instability in order to limit erosion and/or noise. A passive control method of the sheet cavity regime has therefore to be evaluated by its ability to reduce the sheet cavity length, in order to favorise nearly stable regimes in front of periodical unsteady behaviors.

Some studies have already been conducted to delay cavitation inception by modifying the foil surface roughness using local protuberances with different geometries or distributed irregularities [16, 17]. This modification acts on the turbulent boundary layer which drives the onset of sheet cavitation. However, in many industrial applications, the effect of developped cavitation on surface drag and/or performance is also of primary importance. Therefore, attention should be paid not only on delaying cavitation inception, but also on moderating fully developped cavitation. Only a few studies exist about the role of the surface condition in a fully developed cavitating flow. Some of these works show that roughness is able to decrease sheet cavity length, to increase oscillation frequency of the cavity or even to change cavitation regime [18–20]. The roughness distribution and geometry is a major characteristic of this passive method of cavitation control: tranversal or longitudinal grooves, with smooth or straight edges, for different depths or interval lengths [21].

The present study investigates the effect of different grooved suction side surfaces of a Venturi-type section with convergent and divergent angles respectively 18° and 8°. Different grooved plates have been studied in order to emphasize the crucial geometric parameter of this organized roughness to obtain a passive control of cavitation. High speed visualizations of the cavitating flow show the effect of flow modifications near the wall on the sheet cavity development, and next, velocity measurements in non-cavitating conditions clarify the effect of the grooved surface on the flow structure.

2 Experimental set-up

Experiments were conducted in the closed loop test rig of the DynFluid laboratory water tunnel. This rig is composed of two storage tanks with a capacity of $4\,\mathrm{m}^3$ each. The centrifugal pump can reach 1450 rpm. The test-section for experiments is presented in Fig. 1. The study flow volume, which is presented in Fig. 1, measures $120 \times 100 \times 800\,\mathrm{mm}^3$. The bottom wall is made of a convergent (18° angle) and a divergent (8° angle), which results in a minimum height $H_{throat} = 67\,\mathrm{mm}$ at the Venturi throat. The flow rate is fixed for all measurements at $Q = 240\,\mathrm{m}^3.\mathrm{h}^{-1}$, which gives a maximun velocity at the Venturi throat $v_{throat} \simeq 8\,\mathrm{m.s}^{-1}$. Considering that the water viscosity in the operating conditions is $\nu = 1.007\ 10^{-6}\,\mathrm{m}^2.\mathrm{s}^{-1}$, then the Reynolds number is $Re_{throat} = v_{throat} H_{throat} / \nu \simeq 5.5\ 10^5$, for the water at a temperature $T = (19 \pm 1)^{\circ}\mathrm{C}$. Several honeycombs followed by a circular contraction provide the flow a velocity top hat profile upstream the Venturi with an inlet velocity equal to $v_{ref} = 5.56\,\mathrm{m.s}^{-1}$, for all experimental configurations, with less than 3% of turbulence intensity (Fig. 2), measured at a distance $y = 300\,\mathrm{mm}$ upstream the Venturi throat (at an undimensional distance $y^* = y/H_{throat} \simeq -4.5$ from the throat). A vacuum pump can decrease the pressure in the test rig by decreasing pressure at the free surface in each storage tanks in order to acts on the cavitation number $\sigma = (p_{ref} - p_{vap})/(\frac{1}{2}\rho {v_{ref}}^2)$, with p_{ref} the pressure measured at $y = 250\,\mathrm{mm}$ upstream the Venturi throat (at $y^* = y/H_{throat} \simeq -3.73$). The test section includes four plexiglas windows to permit three-dimensional visualisations of the flow.

The bottom wall of the test section, in the divergent part of the Venturi, is made of interchangeable plates of dimensions 7 mm thick, 242 mm long, and 120 mm wide, to cover the entire Venturi surface downstream the Venturi throat. The junction between the plate and the Venturi basis is done upstream the Venturi throat to minimize its disturbances on the flow. So disturbances are expected to be smoothed before the flow comes on the throat, thanks to the favorable pressure gradient. Seven 2 MI-PAA KELLER absolute pressure sensors even out with the Venturi basis wall and distributed on the Venturi basis surface (Fig.3 and table 2). These sensors, which are 4.5 mm in diameter, acquire pressure measurements during 1 min at a sampling rate of 1000 Hz. Their sensitivity is $35\,\mathrm{mV.bar}^{-1}$. The plate is screwed on the basis by ensuring the sealing between both components with a vacuum grease. Table 1 presents the different grooved plates used for experiments. Plate 0 will be considered as the reference case, with a smooth surface on the suction side of the Venturi. The other plates, from 1

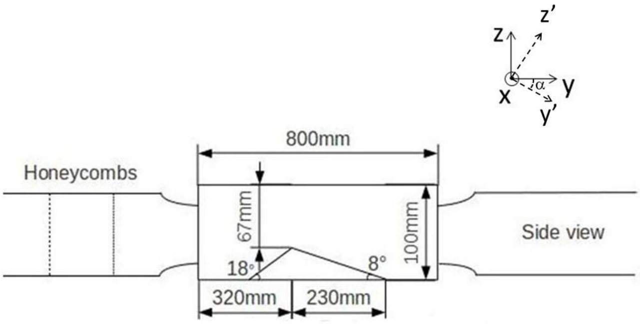

Fig. 1. Test section of the experimental device using a Venturi profile (the origin of the cartesian coordinate system is located at the throat, in the middle of the test section wide, $\alpha = 8^\circ$ is the angle for the LDV measurements system $xy'z'$ and $H_{throat} = 67\,\mathrm{mm}$ is the reference length).

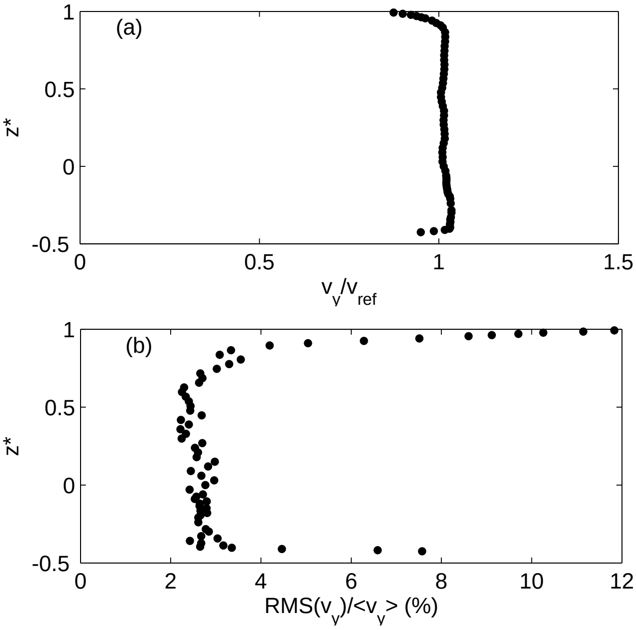

Fig. 2. Characterisation of the flow in the test section inlet: (a) undimensional longitudinal velocity profile $v_y^* = v_y/v_{ref}$ (the line represents the mean value of the velocity $v_{ref} = 5.56\,\mathrm{m.s^{-1}}$) and ($b$) the profile of the turbulence intensity $\frac{RMS(v_y)}{<v_y>}$, where $< v_y >$ is the time-averaged velocity, $y^* \simeq -4.5$ and $x^* = 0$ (Results come from LDV measurements, presented in the section 4.1).

to 8, have grooved surfaces. These grooves are made with a 1 mm or 2 mm diameter bur d, with a h depth and the width of the ridge is e. The distance between the middle of two adjacent grooves is equal to $\lambda = e + 2\sqrt{dh - h^2}$ for plates 1 to 6 and $\lambda = e + d$ for plates 7 and 8. Grooves open to the throat, so roughness effects already from the onset of the sheet cavity. All positions in the test section are expressed with undimensional values $x^* = x/H_{throat}$, $y^* = y/H_{throat}$ and $z^* = z/H_{throat}$, and the origin of the cartesian coordinate system is located in the throat, in the middle of the test section width.

The test of these grooved plates and their comparison with the results obtained with the smooth reference plate 0 allow to evaluate the effects the effect of the surface condition of the Venturi bottom wall on the flow dynamics near the wall, with or without cavitation.

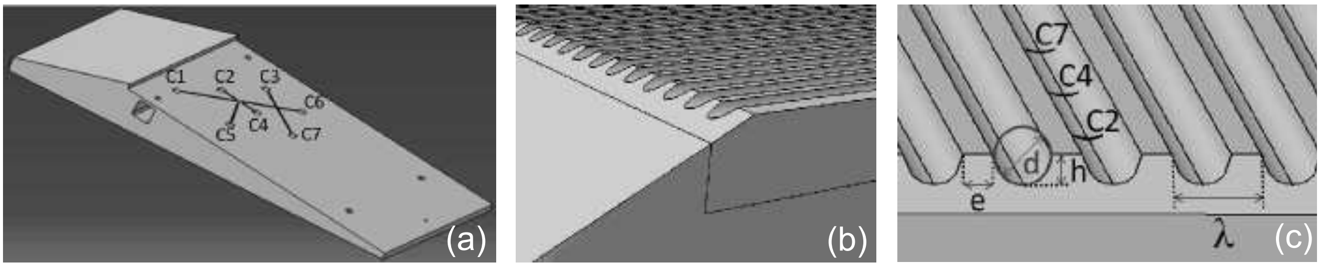

Fig. 3. Venturi components: (a) Venturi basis with $C1$ to $C7$ pressure sensors on the basis surface, (b) junction between the Venturi basis and a plate and (c) zoom of a grooved plate with the definition of the grooves geometric parameters (d and h are respectively the grooves diameter and depth, e is the width of the ridge and λ is the grooves wavelength).

Table 1. Characteristics of the studied plates used on the Venturi suction side (N is the number of grooves) and description os symbols used in following graphics

Plate	d (mm)	h (mm)	e (mm)	λ (mm)	N	Symbol
0	0	0	0	0	0	×
1	1	0.15	0.1	0.81	147	★
2	1	0.25	0.1	0.97	124	△
3	1	0.5	0.1	1.1	109	▲
4	1	0.5	1	2	60	•
5	2	0.5	0.1	1.83	65	✶
6	2	1	0.1	2.1	57	+
7	2	2	1	3	40	♢
8	2	2	0.1	2.1	57	□

Table 2. Pressure sensors on the Venturi suction side

Pressure sensor	y'(mm)	y'^*	x(mm)	x^*
C1	16.75	0.25	30	0.4478
C2	33.50	0.5	0	0
C3	50.25	0.75	-30	-0.4478
C4	67	1	0	0
C5	67	1	30	0.4478
C6	83.75	1.25	-30	-0.4478
C7	100.5	1.5	0	0

3 Effect of grooved surfaces on cavitating flow

Visualisations are conducted for each plate (the smooth and the grooved ones), for different values of cavitation number σ defined as $\sigma = (p_{ref} - p_{vap})/(\frac{1}{2}\rho {v_{ref}}^2)$. In this definition, p_{ref} and v_{ref} represent the inlet pressure and velocity of the test section, measured 250 mm upstream the Venturi throat, while p_{vap} is the vapor pressure at temperature T =292 K of the fluid with a density ρ. Temperature deviation during measurements is small enough (about 1 K) to neglect temperature effect on results but in order to have precise values of σ, the flow temperature is measured at each acquisition (with an uncertainty of 0.1 K). Temperature for all measurements is then considered as the ambient temperature and $p_{vap} \simeq 2200\,\mathrm{Pa}$. For each studied configuration, σ ranges from 0.9 to 1.7 with 1% of uncertainty.

3.1 Sheet cavity visualisations

Visualisations of the sheet cavity developed on the Venturi consist in the acquisition of 4000 images for each configuration (for a given cavitation number and a given grooved plate geometry), in the (y0z) plane. A CamRecord 600 Optronics camera is used with a Zeiss Makro-planar T* which has a focal length of 100 mm. This high-speed CMOS camera records images with a 1280×512 pixels resolution, a rate of 1000 fps and an exposure time equal to $0.167\,\mu$s. The pixels size is $12\,\mu\mathrm{m} \times 12\,\mu\mathrm{m}$ for an active area of $15.35\,\mathrm{mm} \times 12.29\,\mathrm{mm}$. The flow is illuminated by a Super Long Life Ultra Bright (SLLUB) White Led Backlight from Phlox on a $200\,\mathrm{mm} \times 200\,\mathrm{mm}$ light output area. Its minimal luminance is $3000\,\mathrm{cd.m}^{-2}$ in continuous mode and its uniformity is 99.54%. This light source gives then images integrated on the entire width of the test section, but the focusing is made as far as possible in the middle of the section, in order to prevent side walls effects.

3.2 Effects of the Venturi surface condition on the sheet cavity size

In order to determine the cavity mean length, mean values and standard deviation of the grey levels are calculated with the 4000 images recorded in each flow configuration, in the (y0z) plane (side views of the attached sheet cavity dynamics). The instantaneous images are normalised by a reference image. Normalised images are then binarised with a threshold level equal to 0.4 and the noise is filtered with a median filter as presented in Fig. 4. The thresehold level is chosen with the Otsu's method [22] and validated with comparisons with the initial normalised images (Fig. 4(b)). The mean cavity length extends from the Venturi throat to the cloud cavitation separation location. This closure of the sheet cavity is detected by localising the maximum value of the standard deviation of the grey levels according to [6] (Fig. 5). Figure 6 shows the evolution of the cavity mean length L according to the cavitation number σ, for all plates. The uncertainty of L is less than 2% (by evaluating the effect of images processing) and σ is calculated with 1% of uncertainty. Plates 1,3, 4 and 5 provide a sheet cavity length close to the one obtained with the reference plate 0. Conversely, plates 2, 6, 7 and 8 lead to significant differences of the cavity lengths. The results obtained with these three plates are thus detailed hereafter. It can be observed that for the plate 2, the cavity mean length decreases as it has been encountered in litterature, for random distributed roughness [20]. This plate has a large number of grooves ($N = 124$ and $\lambda = 0.97\,\mathrm{mm}$) and is characterized by a small depth $h = 0.25\,\mathrm{mm}$. But other types of grooves have the opposite effect, i.e. an increase of the mean length of the sheet cavity, as we can see for the plate 6, which has a small number of grooves ($N = 57$ and $\lambda = 2.1\,\mathrm{mm}$) with a large depth $h = 1\,\mathrm{mm}$. This difference between the effects of surface condition is larger for small cavitation numbers. When σ is greater than 1.2 i.e. for small sheet cavities, the influence of the surface condition on the mean cavity length seems to be less important. The major difference between plates 2 and 6, is the depth parameter h, the diameter d and the number of grooves on the bottom wall of the Venturi. In comparison with plates 3, 4 and 5 which do not affect significantly the sheet cavity length with respect to the reference plate 0, the depth h seems to be the criterion that drives the change of effects on the sheet cavity. Indeed, the plate 2 is one of the plates which has the smallest depth. Plate 1 has an even smaller depth, but this plate seems to have no effect on the cavitation dynamics. The depth of plate 1 has been chosen in order to be of the order of the viscous sublayer thickness δ_v calculated on a flat plate (zone of the boundary layer where the velocity increases linearly from the wall, beyond this zone, the velocity increases logarithmically with the height). In the case of a plane plate [23], δ_v is defined by:

$$\frac{\delta_v}{y^*} = \frac{50}{Re_{y^*}\sqrt{\frac{C_f}{2}}} \tag{1}$$

where Re_y is the critical Reynolds number which determines the distance y^* from the beginning of the plate where the boundary layer becomes turbulent ($Re_{y^*} = 5\ 10^5$ for a plane plate) and C_f is the coefficient of friction expressed as:

$$C_f = 2\left(\frac{\mathrm{K}}{\log Re_{y^*}}\mathrm{G}\left(\log Re_{y^*}\right)\right)^2 \tag{2}$$

with $\mathrm{K} = 0.41$ the Karman constant and G a function that gives $\mathrm{G}\left(\log\left(Re_{y^*}\right)\right) = 1.5$ in the studied zone $10^5 < Re_{y^*} < 10^6$ [23].

If we assume that our experimental set-up used is a fat plate, without pressure gradient, δ_v is inferior to 0.20 mm ($\delta_v/H_{throat} \simeq 0.003$) at the end of the plate (at $y^* \simeq 3.4$). This calculation allows us to obtain an order of magnitude of the viscous sublayer thickness of our experimental set-up, even if we have to consider the adverse pressure gradient and the effects of grooves on the boundary layer development to have a more accurate value of the viscous sublayer thickness.

Indeed, results obtained with plate 1 (with a grooves depth inferior to the viscous sublayer thickness of a plane plate without pressure gradient δ_v) are identical to the one measured with plate 0. Conversely, if the depth of the grooves is too large, then the sheet cavity length increases.

However, if the depth is increased up to $h = 2$ mm, results are different: for plates 7 and 8, we can see a decrease of the sheet cavity length, like for the plate 2 which presents a small depth. These two plates 7 and 8 are special because the geometry of the grooves is different. Grooves for plates 1 to 6 are arcuate hollows while grooves are cylindrical gutters for plates 7 and 8 ($h > \frac{d}{2}$). This geometry leads to a decrease of the sheet cavity length. This phenomenon may be related to the fluid flow inside the grooves, which may be different with plate 6, compared with plates 7 and 8. Indeed, the number of grooves N is the same for these three plates. It can thus be deduced that this parameter is not crucial for the effect of grooves on the sheet cavity length. Only the depth h is different from plate 6 to plates 7 and 8. It implies that a reduction or an increase of the sheet cavity length can both be obtained with appropriate grooves, depending on their depth h.

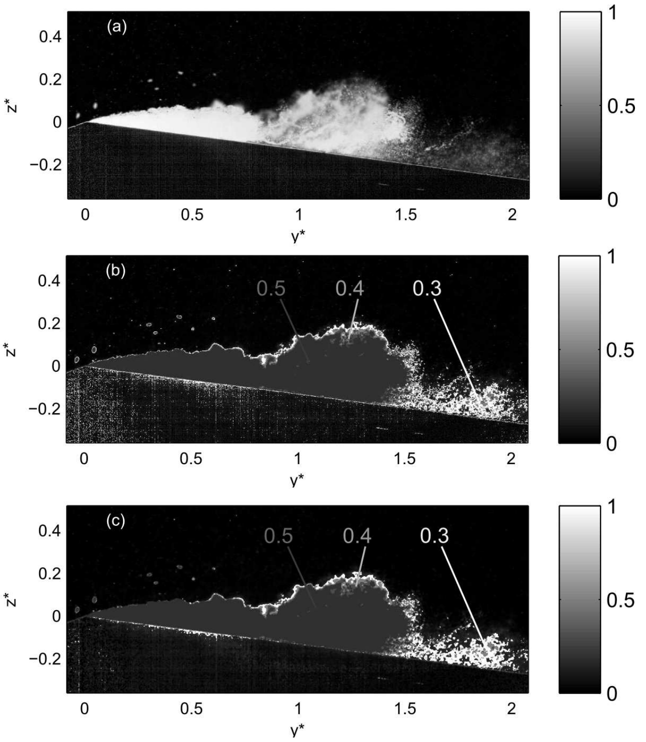

Fig. 4. Images processing for the sheet cavity length measurements: (*a*) normalized instantaneous image, (*b*) image binarization with different threshold levels 0.5, 0.4 or 0.3 and (*c*) median filter applied on the binarized image.

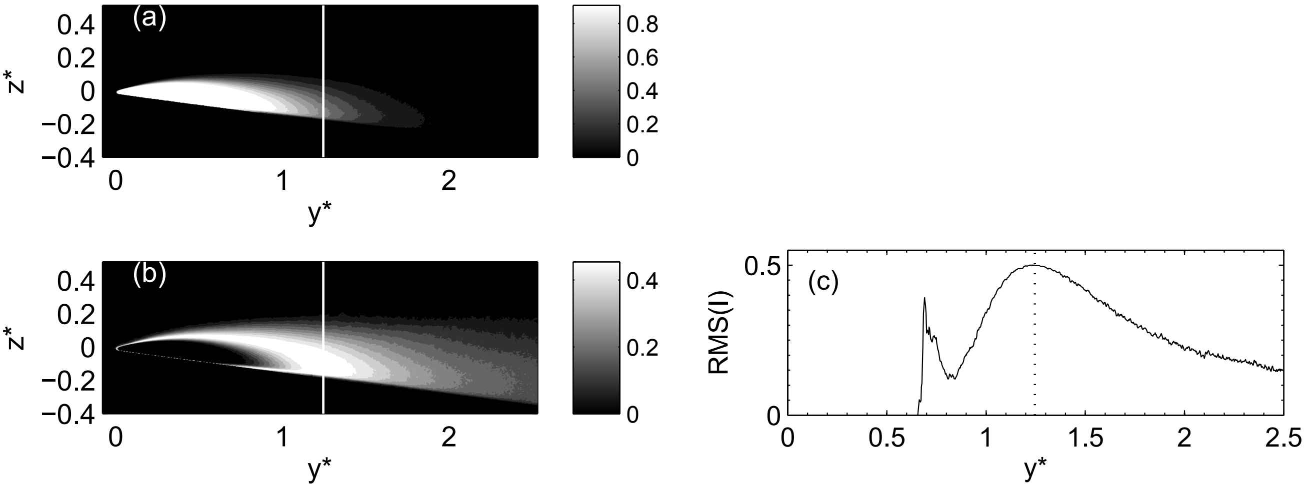

Fig. 5. Sheet cavity on the smooth plate 0 for $\sigma = 1.18$: (*a*) normalized average image, (*b*) root mean square of normalized images (the line represents the undimensional sheet cavity length $L^* = L/H_{throat} \simeq 1.62$) and (*c*) a profile of the root mean square of normalized images $\mathrm{RMS}(I)$ plotted in z*=0.

The former analysis was focused on the effects of the grooves on the sheet cavity length. In addition, the effects on the mean height of the sheet cavity are also investigated hereafter: for that purpose, the maximum height of the sheet cavity is detected. The calculation of the mean value of all these maximum heights (which can variate in position) gives information about the shape of the sheet cavity, according to the grooved surfaces. Figure 7 displays the undimensional sheet cavity mean height $H^* = H/H_{throat}$ (with 2% of uncertainty) according to the undimensional sheet cavity mean length $L^* = L/H_{throat}$,

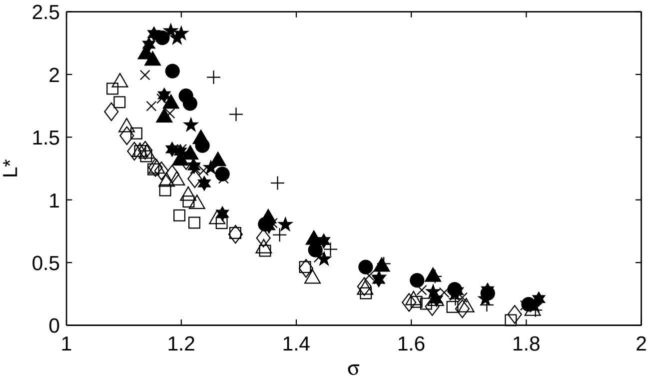

Fig. 6. Undimensional sheet cavity length $L^* = L/H_{throat}$ according to the cavitation number σ: ×: plate 0, ★: plate 1, △: plate 2, ▲: plate 3 , +: plate 4, ✶: plate 5, +: plate 6, ◇: plate 7, □: plate 8.

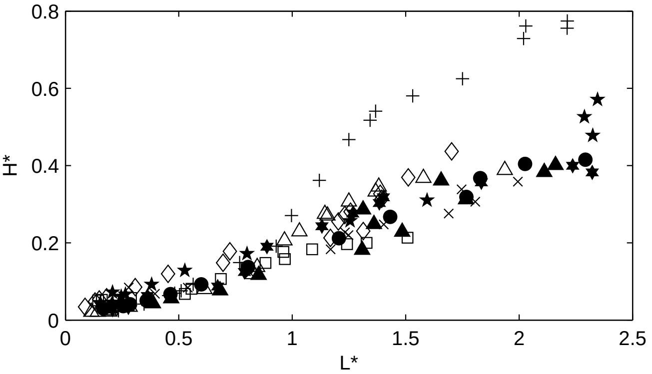

Fig. 7. Undimensional sheet cavity mean height $H^* = H/H_{throat}$ according to the undimensional sheet cavity mean length $L^* = L/H_{throat}$: ×: plate 0, ★: plate 1, △: plate 2, ⋆: plate 3 , +: plate 4, ✶: plate 5, +: plate 6, ◇: plate 7, □: plate 8.

which depends on the cavitation number, for all different studied plates. It can be observed that results obtained with plate 6 are significantly different from all other data. As grooved plates introduce a three-dimensional geometry with different grooves wavelengths, these Venturi surfaces induce a changing in the sheet cavity dynamics: the grooves wavelength forces the flow, and especially the inception of the sheet cavity, in the grooves hollow, but also the development of the sheet cavity or the re-entrant jet. This phenomen, with a three-dimensional wavelength imposed to the flow is different from the smooth case, with the plate 0. The cavity closure line is actually inclined [24] and the cloud cavitation shedding is linked to three-dimensional instabilities [25–27], three-dimensional effects are then to be taken into account to evaluate the efficiency of the passive control. As each plate presents a different spanwise distribution, we can say that depth is a crucial parameter but that the grooves wavelength λ is also important. Plates 6, 7 and 8 have largest wavelength ($\lambda > 2\,\mathrm{mm}$ and $N < 60$). For small sheet cavities characterised by $0 < L^* \leq 1$, which corresponds to $1.2 \leq \sigma \leq 1.9$, all curves are nearly superimposed, which suggests that grooves play a less crucial role.

Figure 8 which presents the aspect ratio H/L according to the cavitation number for all grooved plates, shows that most of grooved plates present large variations of the aspect ratio values with different cavitation numbers while the reference plate case 0 leads to a nearly constant aspect ratio. The grooved plates 3, 4 and 5 for which the sheet cavity length is almost equal to the reference case, for all cavitation numbers, are characterized by an aspect ratio $0.1 \leq \frac{H}{L} \leq 0.2$. These values are still close to the reference case. On the other hand, the plate 1, with a grooves depth h too small to modify the sheet cavity

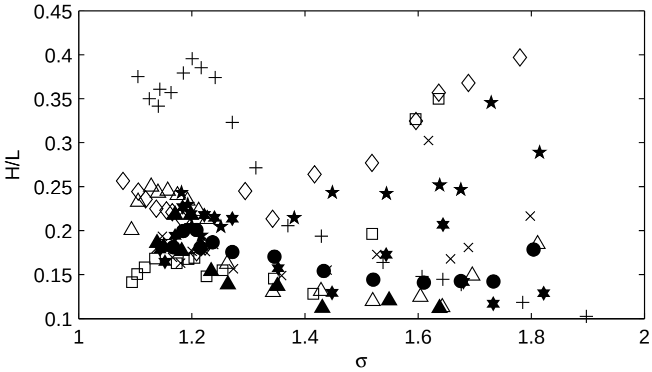

Fig. 8. Aspect ratio H/L according to the cavitation number σ: $\times$: plate 0, $\bigstar$: plate 1, $\triangle$: plate 2, $\star$: plate 3 , $+$: plate 4, $\bigstar$: plate 5, $+$: plate 6, $star$: plate 7, $\square$: plate 8.

length, has an aspect ratio very different from the smooth plate 0. This result shows that the grooves have effects not only on the sheet cavity length but also on its shape. Plates 7 and 8 present an evolution of the aspect ratio H/L similar to the plate 1. The most obvious observation is that the evolution is inversed for plate 6. Indeed, for plate 6, the ratio H/L is high for $1 \leq \sigma \leq 1.4$ and small for $1.4 \leq \sigma \leq 1.9$ ($0.2 \leq \frac{H}{L} \leq 0.4$ for the first range of σ and $0.1 \leq \frac{H}{L} \leq 0.2$ for the second), while, for plates 7 and 8, H/L is first in the range of $0.1 \leq \frac{H}{L} \leq 0.2$ when $1 \leq \sigma \leq 1.4$ and then $0.2 \leq \frac{H}{L} \leq 0.4$ when $1.4 \leq \sigma \leq 1.9$. Cavitation dynamics is thus completely different for plates 6 and other plates, which have a smaller grooves wavelength λ, excluding plates 7 and 8 for which the grooves geometry is quite different. It confirms that the crucial parameter in the action of the grooves is *i*) the depth, which may modify the re-entrant jet progression, *ii*) the wavelength, which can force the cavitation dynamics in the spanwise component. As it was reminded in the introduction, the cavity regime depends on the mean size of the sheet cavity [5]. An analysis of the Strouhal number based on the characteristic frequency of the sheet cavity is conducted to determine the effects of grooved surfaces on the unsteady behavior of the cavity.

3.3 Pressure measurements

In order to analyze the different cavitation dynamics detected with the grooved surfaces, pressure measurements have been acquired at the bottom wall of the Venturi. Relative pressure measurements have been first conducted with no velocity and no use of the vacuum pump to define the zero setting state for each sensor.

The analysis of the pressure fluctuations obtained with plates 0, 2, 6, 7 and 8, on the Fig. 9, indicates that the maximum amplitude of fluctuations of each pressure sensor corresponds to the sheet cavity closure [5]. For example, for $\sigma = 1.5$, the undimensional sheet cavity length is $L^* < 0.5$ on the plate 0 (Fig. 6). The sensor $C1$ is the only sensor located in the sheet cavity. Fluctuations of pressure measurements is thus an indicator of sheet cavity length. This figure confirms the results obtained with the image processing: if we look at the sensor $C1$, the maximum of pressure fluctuations is at $\sigma = 1.5$ for the smooth plate 0, $\sigma < 1.5$ for the plate 2 and $\sigma > 1.5$ for the plate 6, with larger grooves. This result shows that the length of sheet cavities is smaller on plate 2 than on plate 0 and a longer sheet cavity is obtained on plate 6 than on the others. As it was observed for the plate 8 previously, pressure fluctuations are a witness of the cavity regime changing. Indeed, in the Fig. 9(e), which represents results for the plate 8, no clear maximum of $\frac{\text{RMS}}{<P>}$ can be identified, so we are not able to detect the

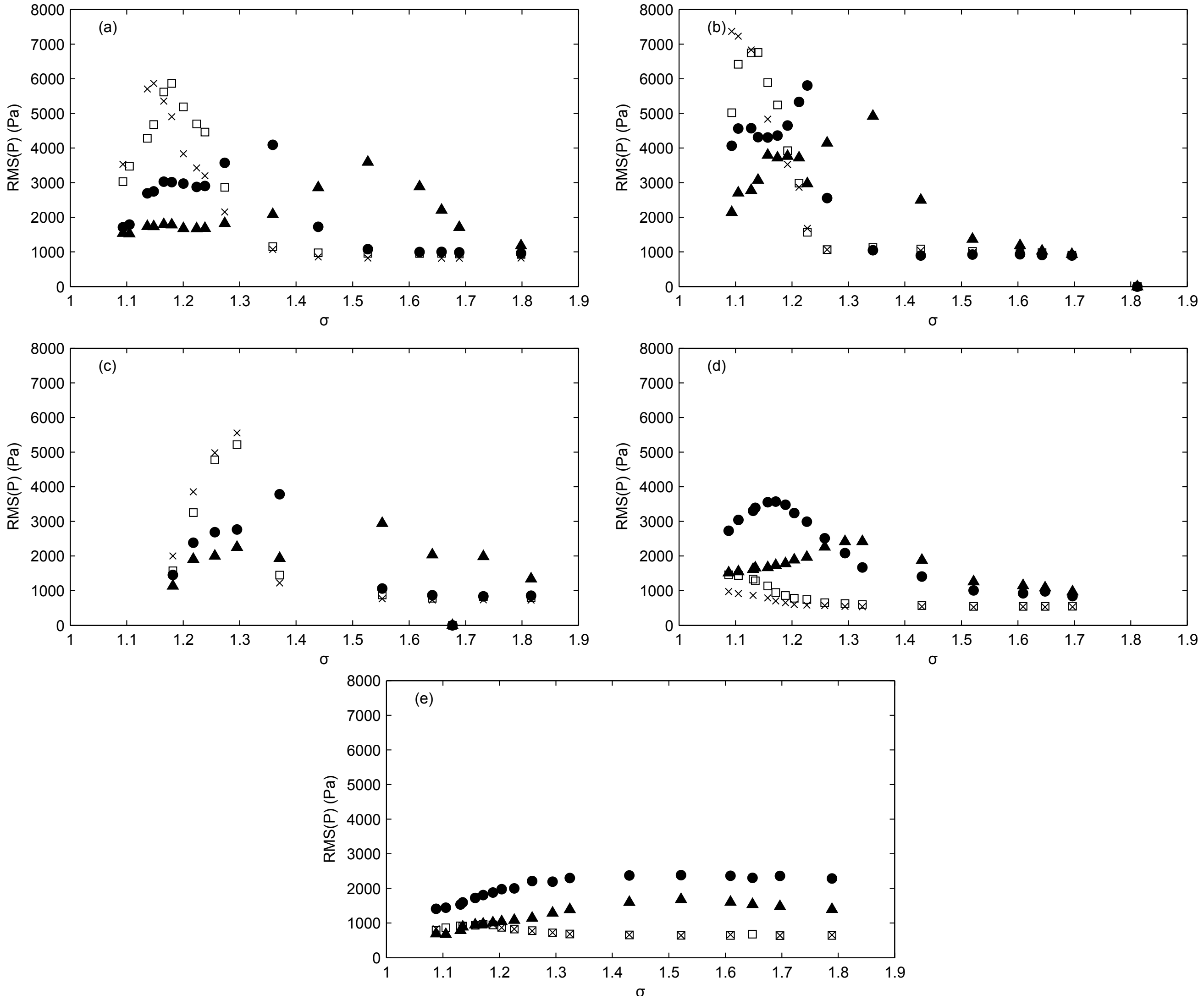

Fig. 9. Pressure fluctuations $\mathrm{RMS}(P)$ on the Venturi bottom wall according to the cavitation number σ, at different distances from the ventrui throat:(a) for plate 0,(b) for plate 2, (c) for plate 6, (d) for plate 7 and (e) for plate 8. ▲: C1, ●: C2, □: C4, ×: C6. (see positions of sensors in Table 2)

sheet cavity length by analyzing pressure measurements. This is an other indicator of the sheet cavity regime. The difference between a sheet cavity regime and a cloud cavitation regime can thus be demonstrated also by the analysis of the pressure measurements.

3.4 Two cavitation regimes

The fluctuations of the two-phase area in the sheet cavity regime or the shedding of the cloud of vapor in the cloud cavitation regime are both periodical. The frequency of these phenomena is determined by studying the evolution of the grey levels at the sheet cavity closure position (by selecting the vertical line of pixels situated in the mean position of the sheet cavity closure determined previously). The power spectral density of this sheet cavity length evolution allows to determine the characteristic frequency of the sheet cavity according to the mean cavity length for each studied case of Venturi profile grooved surface (Fig.10), with 0.2% of uncertainty.

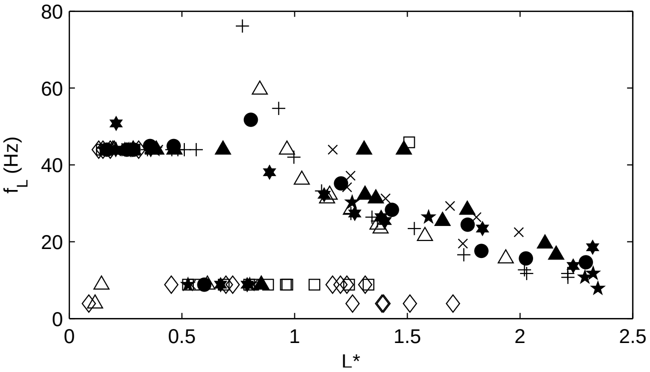

Fig. 10. Frequency of the sheet cavity length oscillation f_L according to the undimensional sheet cavity mean length L^*: ×: plate 0, ★: plate 1, △: plate 2, ⋆: plate 3 , +: plate 4, ✶: plate 5, +: plate 6, ◇: plate 7, □: plate 8.

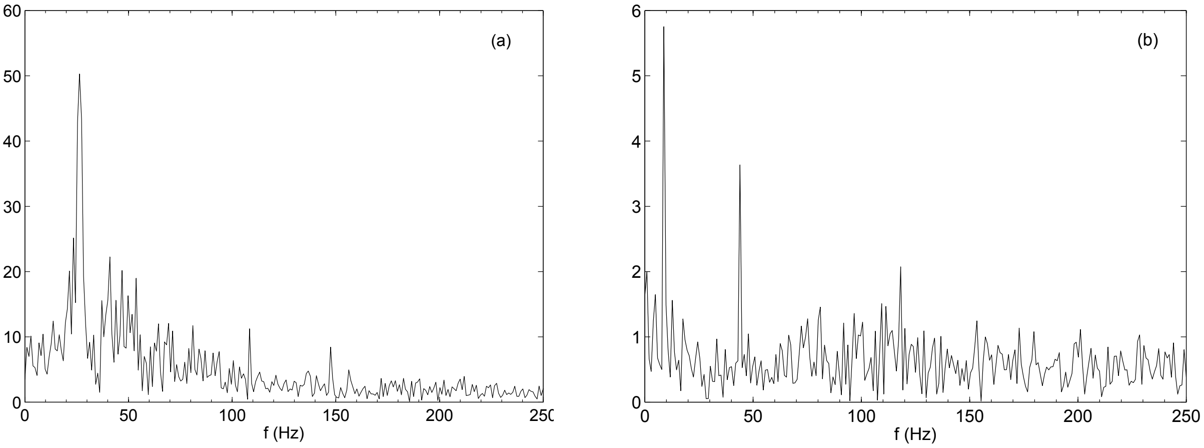

Fig. 11. Frequency spectrum of the variation of the gray level in the closure of the sheet cavity, on the plate 0: (a) for $\sigma = 1.17$, (b) for $\sigma = 1.44$

Here, the frequency difference between the smooth Venturi surface and the other grooved plates is greater when the mean cavity length is large (it means for small cavitation numbers). It can be observed in the range $0 < L^* < 1$, which corresponds to $1.3 < \sigma < 1.9$, two peaks on the frequency spectrum, with similar amplitudes, at 43.95 Hz and 8.79 Hz. These two frequencies are harmonics and are both present in this studied range, as it is shown in Fig. 11 for the plate 0. This frequency of 43.95 Hz is the blade passing frequency of the centrifugal pump used to impose the flow rate: as the pump with 5 blades operates at 528 rpm, the blade passing frequency is 44 Hz. It means that smallest cavities oscillate then at the blade passing frequency. For largest sheet cavities, so for a cavitation number σ in the range $1 < \sigma < 1.3$, there is only one peak on the frequencies spectrum (Fig.11 (a) presents results for $\sigma = 1.17$). This peak corresponds to the shedding frequency of the cloud cavitation and it decreases when the sheet cavity length increases. Plates 7 and 8 lead to a different feature for the frequency derived from the grey level analysis in the closure of the sheet cavity. The cavitation number σ has no effect on the frequency peak of spectra, which is always $f_L = 43.95$ Hz. This result shows again that the cavitation dynamics is particular for these two plates 7 and 8. Figure 12 shows frequency spectra obtained for plate 7 (Fig. 12(a)) and plate 8 (Fig. 12(b)) for $\sigma = 1.17$.

The characteristic frequency of the sheet cavity is also represented on the Fig. 13 with the undimensional Strouhal

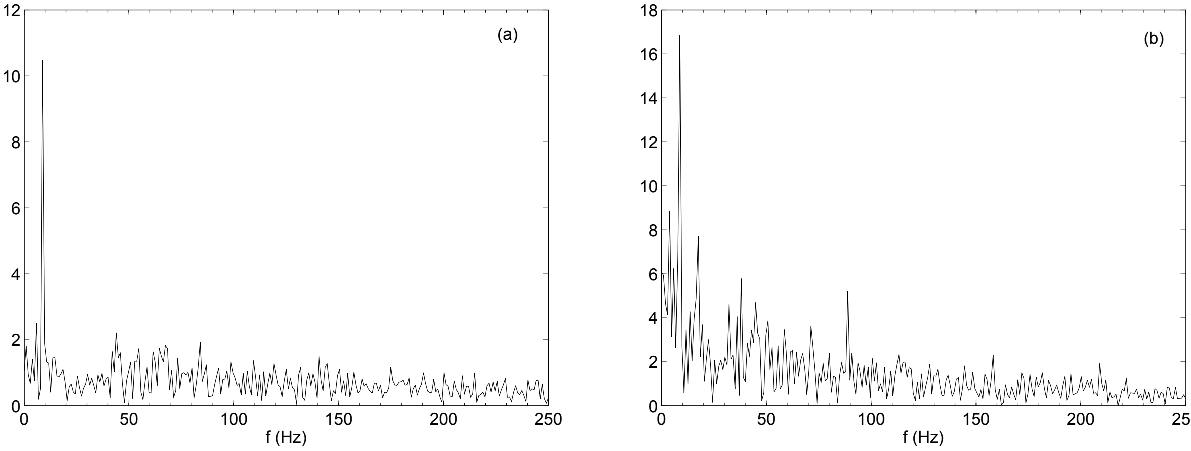

Fig. 12. Frequency spectrum of the variation of the gray level in the closure of the sheet cavity, for $\sigma = 1.17$ for: (a) the plate 7, (b) the plate 8

number $St_L = Lf_L/v_{throat}$, with 6% of uncertainty. If we look at all plates excluding plates 7 and 8, we can observe that for $1 \leq \sigma \leq 1.3$, the Strouhal number is around 0.3, as it has been reported in previous experiments in [7]. This range of cavitation numbers leads to a cloud cavitation regime, characterized by large fluctuations of the cavity closure position and large cloud cavitation shedding. On the other hand, for $1.3 \leq \sigma \leq 1.9$, the Strouhal number decreases until reaching a value smaller than 0.15. This range corresponds to a sheet cavity regime, for which there is no convected cloud cavitation, the cavity closure position is almost at a constant distance from the Venturi throat. In the sheet cavity regime, the sheet cavity pulses. These two types of variation of the Strouhal number exist for grooved plates but also for the smooth one (plate 0), and have been brought out by other authors [28,29]. It can be also observed in Fig. 13 that the grooved plates surfaces can modify the Strouhal number. Indeed, smooth surface plate 0 presents Strouhal numbers larger than grooved plates, essentially for small cavitation numbers.

Plates 7 and 8 have a quite constant Strouhal number $0.05 \leq St_L \leq 0.15$, which is characteristic of the sheet cavity regime, with a pulsating sheet cavity and no cloud cavitation shedding. Figure 14 compares the sheet cavity evolutions at a same $\sigma = 1.17$, for the reference smooth plate 0 and the grooved plate 8. It can be seen that in the case of the plate 8 the sheet cavity pulses (Fig. 14(a)) without any shedding contrary to a smooth surface of the Venturi profile (Fig.14(b)). Then, the grooves depth h controls the cavitation regime and can suppress the cloud cavitation for a large range of σ. Plates 7 and 8 are thus able to stabilize the sheet cavity and to reduce its length.It is thus possible to obtain a passive control by using specific geometrical parameters of grooves.

With the study of the sheet cavity height evolution (section 3.2), we can also determine the frequency f_H of the sheet cavity height. This frequency f_H and the frequency f_L of the sheet cavity length evolution have been compared for plates 0 to 6. Results for plates 7 and 8 are not compared because for all the studied range of σ, there is no cloud cavitation shedding. For all grooved plates and for the smooth plate 0, the curve $f_H = g(f_L)$ is linear so the frequency of the height evolution is linked to the length evolution frequency.

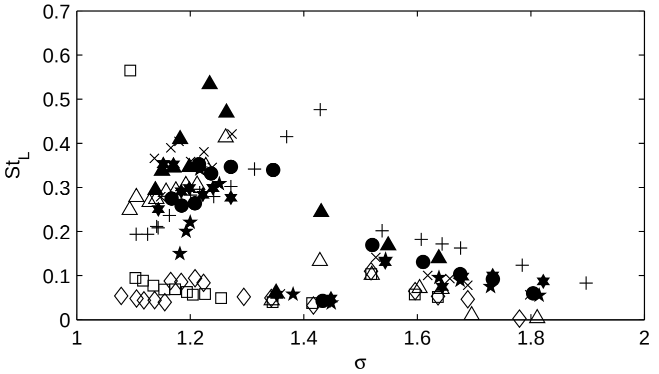

Fig. 13. Strouhal number $St_L = \frac{Lf_L}{v_{throat}}$ according to the cavitation number σ: ×: plate 0, ★: plate 1, △: plate 2, ⋆: plate 3, +: plate 4, ✱: plate 5, +: plate 6, ◇: plate 7, □: plate 8.

4 Grooved surfaces effect on a non cavitating flow

To discuss the reasons for the modifications of cavitating flows with the grooved surfaces, the velocity profiles are measured in the non cavitating flow, and more especially in the boundary layer, as it is the cavitation inception zone. Therefore, velocity measurements with Laser Doppler Velocimetry have been conducted.

4.1 Laser Doppler Velocimetry measurements (LDV)

A one dimensional FlowExplorer Mini LDA system of Dantec Dynamics has been used to measure the longitudinal componant v_y of the flow. This system consists in a factory-aligned and calibrated optical probe, with a focal lens of 300 mm, and a signal processor. The optical head provides two laser beams with 25 mW power and a wave length 660 nm. The measurement volume dimensions are 0.1 mm in diameter and 1 mm in length. The measurable velocity fluctuation is 0.002% of the velocity range. This sytem has a high accuracy, as the calibration coefficient uncertainty is lower than 0.1%. In each measurement position, 10000 samples are acquired, with a limiting time of acquisition fixed of 60 s. The data rate is near 300 Hz, while the validation rate is upper than 60%. For measurements downstream the Venturi throat, the optical head is inclined at 8° in order to align the laser beams with the Venturi slope. In this way, measurements can be acquired very near the wall so velocity measurements can be used to analyze the effect of surface condition on the boundary layer of the flow. Then, the acquired velocity component is not the longitudinal velocity of the test section but the velocity component parrallel to the slope of the Venturi bottom wall. In the discussion of LDV results, this component is then called v'_y in order to clarify explanations.

On the other hand, velocity measurements presented on Fig.2 were made with a horizontal optical head, so the component is really the longitudinal velocity v_y in this case.

4.2 Effects of the grooves on the velocity profile of the non cavitating flow

Figure 15 shows undimensional velocity profiles $v_y^{'*} = v'_y/v'_\infty$, where v'_y is the flow velocity component parallel to the bottom wall Venturi slope and v'_∞ is the same velocity component measured far from the plate wall, at $z^{'*} = z'/H_{throat}$ =0.9 (this zone is not shown on the figure). Velocity profiles are represented here at different distances from the throat, in y^* =0.5, y^* =1 and y^* =2. We can see on this Fig.15 that grooves modify the flow, near the wall, up to $z^{'*}$ =0.07 for plates 2, 6 and 7

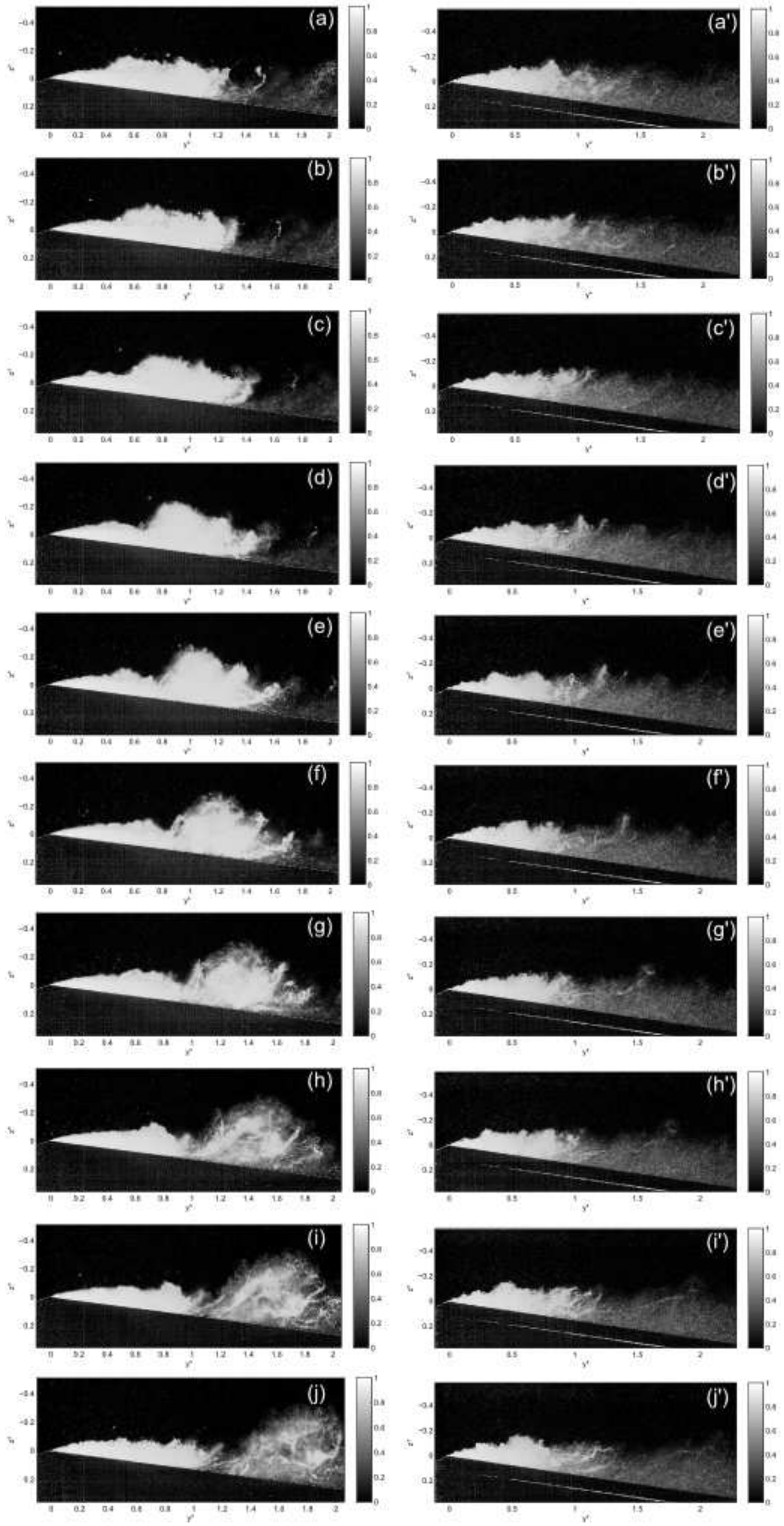

Fig. 14. Visualisation of (a-j) the cloud cavitation shedding for the smooth plate 0 and (a'-j') the sheet cavity pulsation for the plate 8, when $\sigma = 1.17$ ($\Delta t = 2\,\mathrm{ms}$ between two images)

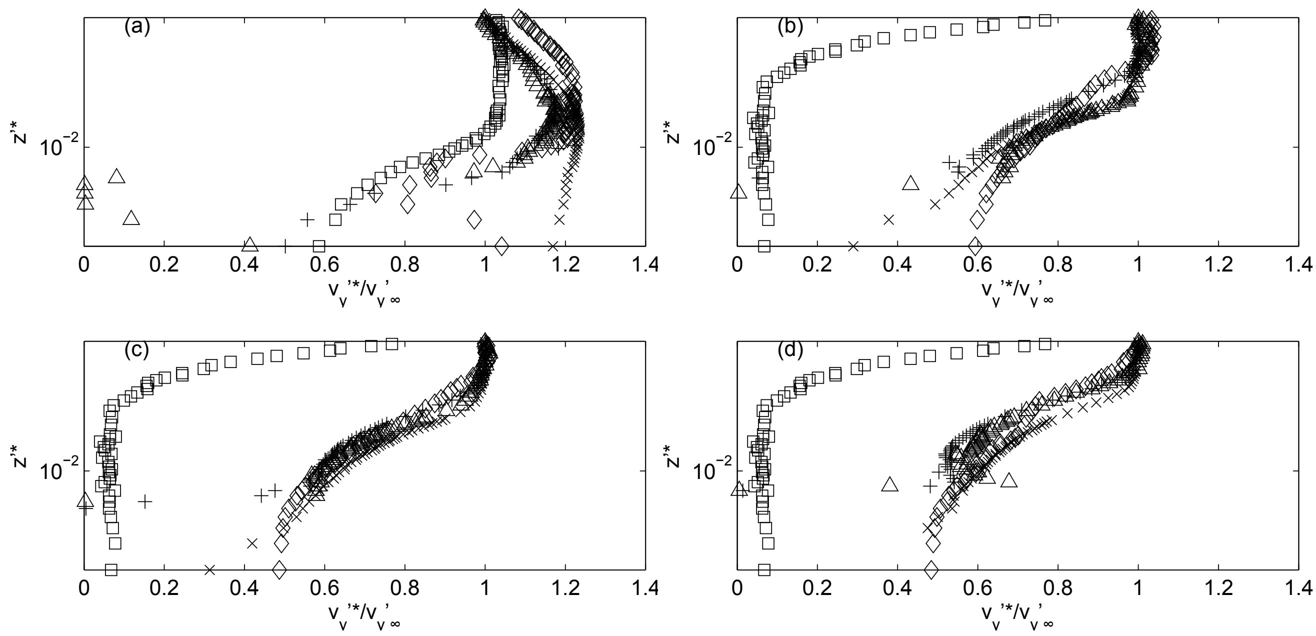

Fig. 15. Longitudinal non-dimensional velocity profile $v_y'^*/v'_{y_\infty}$ of the non-cavitant flow, at (*a*) $y^* = 0$, (*b*) $y^* = 0.5$, (*c*) $y^* = 1$ and (*d*) $y^* = 2$. ×: plate 0, ◇: plate 2, +: plate 6, ◇: plate 7, □: plate 8.

and until $z'^* = 0.3$ for plate 8. This modification depends on the geometry of the grooves. For all values of y^*, excluding the plate 8 for which the velocity profile is totally different, the velocity is always lower for the plate 6, which is the plate with larger grooves and minimum number N of grooves. On the other hand, for smaller grooves, with the plate 2 for example ($d = 1\,\text{mm}$, $h = 0.25\,\text{mm}$ and $e = 0.1\,\text{mm}$) which has a large grooves number $N = 124$, in $y^* = 0.5$, the velocity profile is similar to the velocity profile of the reference plate 0, without grooves. At station $y^* = 1$ or $y^* = 2$ the velocity for the plate 2 becomes lower than for the reference plate 0. The effect of plate 2 on the grooves overlaps even the curve obtained with plate 6. Then the effect of the grooves geometry disapears from $y^* = 2$, but grooves still play the role of a brake for the flow. Very close to the wall, from $z'^* = 0$ until $z'^* = 0.02$, the velocity profile $v_y'^*$ for the plate 7 is superimposed on the velocity profile of the plate 0, when $0 \leq y'^* \leq 2$. This feature explains why plate 7 reduces sheet cavity length like plate 2. If $z'^* > 0.02$, then $v_y'^*$ is lower than other plates 2 and 6. On the other hand, the velocity profile obtained for the plate 8 is totally different. $v_y'^*$ is very low from $z'^* = 0.3$ for $0.5 \leq y^* \leq 2$. This analysis permits to bring out the effect of structured roughness surface on the flow but also the importance of the geometric parameters of the grooves. The grooves wavelength is thus a crucial parameter to influence the sheet cavity dynamics, since plates 7 and 8 have the same grooves geometry but present different grooves wavelength.

In order to investigate in more details the effects of each groove on the velocity profile, two specific velocity profiles have been acquired for each plate: the first one is located in the middle of the test section wide, at $x^* = 0$, above the recess of the groove, while the second one is measured at $x^* = \lambda/2$, above the edge of the groove. It can be observed (Fig. 16) that the relative difference between the two curves is always lower than 3%. The effect of the grooves is thus not local but global, by the way it changes the flow instabilities.

This non-cavitating flow analysis provides a basis for analysis of measurements performed in cavitating conditions. As it was reported previously, the use of plate 6 results in a decrease of the velocity flow near the wall. The fluid encountered a

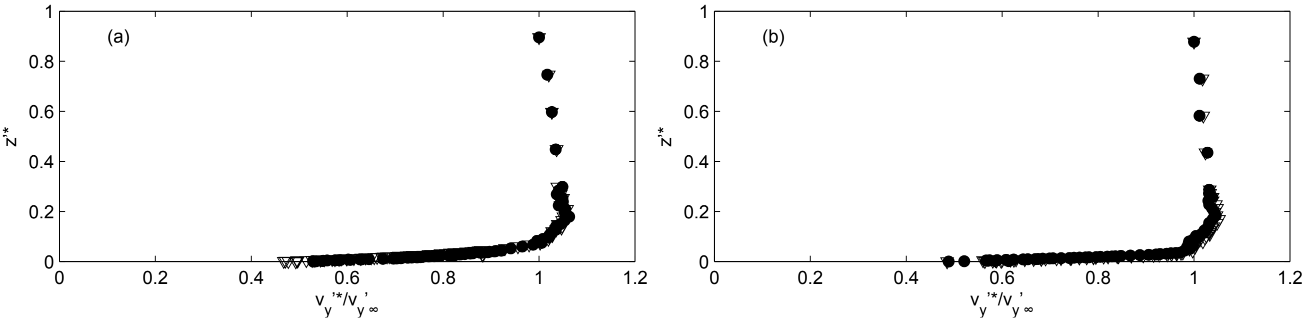

Fig. 16. Longitudinal non-dimensional velocity profile $v_y'^*/v_{y_\infty}'$ of the non-cavitating flow, at $y^* = 0.5$, for (*a*) the grooved sheet 6 and (*b*) the grooved sheet 2. ●: $x^* = 0$, △: $x^* = \frac{\lambda}{2}$

larger surface to flow with larger grooves, so the velocity is considerably decreased. But with the analysis of the mean sheet cavity length, we can say that larger grooves decreases the cavity length. Moreover, with larger grooves, the re-entrant jet can travel further upstream before reaching the interface and cutting the sheet cavity, in order to extract a cloud cavitation. The immediate consequence is that the mean sheet cavity length should be smaller with large grooves. An hypothesis that can be proposed is that some grooves provide small recirculation zones that prevent the re-entrant jet to flow upstream, underneath the sheet cavity, as it is discussed in [30], for the study of a non-cavitant flow boundary layer. Then the re-entrant jet is stopped by these recirculation zones. Not only re-entrant jet is crucial for the cavitation shedding but also side-entrant jets [31]. The three-dimensional distribution of grooves and their geometry have of course effects on the side-entrant jets dynamics.

5 Conclusions

Effects of the surface condition of a Venturi profile have been investigated using visualisation, Laser Doppler Velocimetry, and pressure measurements. The aim of this study was to evaluate the importance of grooved surfaces provided by machining. Geometry of these grooved surfaces have been observed in order to identify crucial parameters. Results show that the depth of grooves is a determining factor. It is demonstrated that a grooves depth smaller than the viscous sublayer thickness has no effect on the sheet cavity length. Some plates lead to a cavitation instabilities changing: essentially plates 7 and 8, for which the sheet cavity length is reduced and the plate 6 which increases this sheet cavity length. These three plates have a large depth $h \geq 1\,\text{mm}$. If the depth is $h > \frac{d}{2}$, then the grooved plate is able to reduce the sheet cavity length. The study of the shedding frequency of cloud cavitation, by image processing highlighted two cavitation regimes: for small cavitation numbers ($1 < \sigma < 1.3$), cavitation is in an unstable regime, with large sheet cavity and large shedding of cloud cavitation. This regime is characterized by a Strouhal number $St_L = 0.3$. The second cavitation regime is a stable regime, with $1.3 < \sigma < 1.9$, which presents sheet cavities with only oscillations in the downstream part (this oscillation being related to the blade passing frequency of the circulation pump used in the test rig). A large grooves depth h, can modify the sheet cavity regime. Plates 7 and 8, with $h = 2\,\text{mm}$, are examples of roughness surfaces that can suppress the cloud cavitation shedding in a large range of cavitation number σ. This study has thus demonstrated the feasability of a passive control of cavitation on a Venturi profile by modifying the surface condition of the bottom wall using distributed organized roughness.

References

[1] Barre, S., Rolland, J., Boitel, G., Goncalves, E., and Fortes Patella, R., 2009. "Experiments and modelling of cavitating flows in venturi: attached sheet cavitation". *European Journal of Mechanics - B/Fluids 28,* **3**, pp. 444–464.

[2] Knapp, R., 1955. "Recent investigation on the mechanics of cavitation and erosion damage". *Trans. ASME,* **77**, pp. 1045–1054.

[3] Avellan, F., Dupont, P., and Farhat, M., 1991. "Cavitation erosion power". *ASME-FED,* **16**, p. 135140.

[4] Stutz, B., and Reboud, J., 1997. "Experiments on unsteady cavitation". *Experiments in Fluids,* **22**, pp. 191–198.

[5] Callenaere, M., Franc, J., Michel, J., and Riondet, M., 2001. "The cavitation instability induced by the development of a re-entrant jet". *J. Fluid Mech.,* **444**, pp. 223–256.

[6] Dular, M., Bachert, B., Stoffel, B., and Sirok, B., 2004. "Relationship between cavitation structures and cavitation damage ". *Wear,* **257**, pp. 1176–1184.

[7] Coutier-Delgosha, O., Devillers, J., Pichon, T., Vabre, A., Woo, R., and Legoupil, S., 2006. "Internal structure and dynamics of sheet cavitation". *Physics of Fluids,* **18**, pp. 017103 1–12.

[8] De Lange, D., and De Bruin, G., 1997. "Sheet cavitation and cloud cavitation, Re-entrant jet and Three-dimensionality.". *Applied Scientific Research,* **58**, pp. 91–114.

[9] Bergerat, L., Khelladi, S., and Bakir, F., 2012. "Cavitation modeling of thermosensitive fluids using compressible phases approach.". *Proceedings of the 8th International Symposium on Cavitation, Cav2012, no.185*, pp. 1–6.

[10] Bakir, F., Kouidri, S., Noguera, R., and Rey, R., 2003. "Experimental analysis of an axial inducer influence of the shape of the blade leading edge on the performances in cavitating regime". *Journal of Fluids Engineering,* **125(2)**, pp. 293–301.

[11] Mejri, I., Bakir, I., Bakir, F., and Belamri, T., 2006. "Comparison of computational results obtained from a homogeneous cavitation model with experimental investigations of three inducers". *Journal of Fluids Engineering, Transactions of the ASME,* **128(6)**, pp. 1308–1323.

[12] Campos-Amezcua, R., Khelladi, S., Bakir, F., Mazur-Czerwiec, Z.and Sarraf, C., and Rey, R., 2010. "Numerical analysis of unsteady cavitating flow in an axial inducer". *Proceedings of the Institution of Mechanical Engineers, Part A: Journal of Power and Energy,* **224(2)**, pp. 223–238.

[13] Sayyaadi, H., 2010. "Instability of the cavitating flow in a venturi reactor ". *Fluid Dynamics Research,* **42**.

[14] Keil, T., Pelz, P., Cordes, U., and Ludwig, G., 2011. "Cloud cavitation and cavitation erosion in convergent divergent nozzle". *WIRMC 3rd International Cavitation Forum*.

[15] Keil, T., Pelz, P., and Buttenbender, J., 2012. "On the transition from sheet to cloud cavitation". *Proceedings of the Eighth International Symposium on Cavitation*.

[16] Arndt, R., and Ippen, A., 1968. "Rough surface effects on cavitation inception". *ASME J. Basic Eng.,* **90**, pp. 249–261.

[17] Arndt, R., 1981. "Cavitation in fluid machinery and hydraulic structures". *Ann. Rev. Fluid Mech.,* **13**, pp. 273–328.

[18] Kawanami, Y., Kato, H., Yamaguchi, H., Tagaya, Y., and Tanimura, M., 1997. "Mechanism and control of cloud cavitation". *Journal of Fluids Engineering,* **119**, pp. 788–795.

[19] Stutz, B., 2003. "Influence of roughness on the two-phase flow structure of sheet cavitation". *Transactions of the ASME,* **125**, July, pp. 2652–659.

[20] Coutier-Delgosha, O., Devillers, J., Leriche, M., and Pichon, T., 2005. "Effect of wall roughness on the dynamics of unsteady cavitation". *Journal of Fluids Engineering,* **127(4)**, pp. 726–733.

[21] Yonjian, L., Haosheng, C., Jiadao, W., and C., D., 2010. "Effects of grooves on cavitation around the body of revolution". *Journal of Fluids Engineering,* **132**.

[22] Otsu, N., 1979. "A Threshold Selection Method from Gray-Level Histograms". *IEEE Transactions on Systems, Man, and Cybernetics,* **9**.

[23] Schlichting, H., and Gersten, K., 2004. *Boundary-layer theory*. Springer-Verlag Berlin Heidelberg.

[24] De Lange, D., 1996. "Observation and modelling of cloud formation behind a sheet cavity.". PhD thesis, University of Twente, The Netherlands.

[25] Laberteaux, K., and Ceccio, S., 1998. "Partial attached cavitation on two- and three-dimensional hydrofoils". *Proc. 22nd ONR Symp. on Naval Hydrodynamics, Washington DC*.

[26] Duttweiler, M., and Brennen, C., 1998. "Partial cavity instabilities". *Proc. US-Japan Seminar: Abnormal Flow Phenomena in Turbomachines, Osaka, Japon (ed. Y. Tsujimoto and J. Katz*.

[27] Foeth, E.-J., van Terwisga, T., and van Doorne, C., 2008. "On the collapse structure of an attached cavity on a three-dimensional hydrofoil". *Journal of Fluids Engineering,* **130**.

[28] Farhat, M., 1994. "Contribution ltude de lrosion de cavitation: mcanismes hydrodynamiques et prdiction.". *Phd Thesis, EPFL, Suisse*.

[29] Dular, M., Khlifa, I., Fuzier, S., Adama Maiga, M., and Coutier-Delgosha, O., 2012. "Scale effect on unsteady cloud cavitation". *Exp. Fluids*.

[30] Coustols, E., 2001. "Effet des parois rainures ("riblets") sur la structure d'une couche limite turbulent.". *Mec. Ind.,* **2**, pp. 421–434.

[31] Koop, A., and Hoeijmakers, H., 2010. "Unsteady sheet cavitation on three-dimensional hydrofoil.". *7th International Conference on Multiphase flow ICMF 2010, Tamp, FL USA*.

Experimental Thermal and Fluid Science 45 (2013) 187–197

Contents lists available at SciVerse ScienceDirect

Experimental Thermal and Fluid Science

journal homepage: www.elsevier.com/locate/etfs

Experimental study of hydraulic transport of large particles in horizontal pipes

F. Ravelet *, F. Bakir, S. Khelladi, R. Rey

Arts et Metiers ParisTech, DynFluid, 151 Boulevard de l'Hôpital, 75013 Paris, France

A R T I C L E   I N F O

Article history:
Received 5 September 2011
Received in revised form 23 October 2012
Accepted 7 November 2012
Available online 1 December 2012

Keywords:
Hydraulic transport
Solid–liquid two-phase flow
Bed friction
Deep sea mining

A B S T R A C T

This article presents an experimental study of the hydraulic transport of very large solid particles (above 5 mm) in an horizontal pipe. Two specific masses are used for the solids. The solids are spheres that are large with respect to the diameter of the pipe (5%, 10% and 15%) or real stones of arbitrary shapes but constant specific mass and a size distribution similar to the tested spherical beads. Finally, mixtures of size and/or specific mass are studied. The regimes are characterized with differential pressure measurements and visualizations. The results are compared to empirical models based on dimensionless numbers, together with 1D models that are based on mass and momentum balance. A model for the transport of large particles in vertical pipes is also proposed and tested on data available in the Literature, in order to compare the trends that are observed in the present experiments in a horizontal pipe to the trends predicted for a vertical pipe. The results show that the grain size and specific mass have a strong effect on the transition point between regimes with a stationary bed and dispersed flows. The pressure drops are moreover smaller for large particles in the horizontal part contrary to what occurs for vertical pipes, and to the predictions of the empirical correlations.

1. Introduction

The hydraulic transport of solid particles is a method widely used in chemical and mining industries. Many predictive models exist in the case of slurries transported under homogeneous regime, that is to say when the particle diameter is small compared to the flow length scales and the velocity of the carrier fluid is high compared to the settling velocity of a particle [1–4]. It is then possible to predict the pressure losses in horizontal or vertical pipes with sufficient accuracy. In recent years, the sharp increase in demand for raw materials makes it interesting exploitation of new resources, particularly the use of fields at the bottom of the ocean [5,6]. In this case, the solids may be large with respect to the pipe diameter and the circuit would have complex shapes, including vertical parts, horizontal parts, and potentially bends and S-shapes in order to absorb the deformations caused by surface waves. For transport of large particles in vertical pipe, a predictive model based on the work of Newitt et al. [7] and Richardson et al. [8] is proposed and validated on a set of experimental data [9–11]. However, in horizontal, and a fortiori in geometries in S-shape, there are few models [1–4,12–15]and the effects of specific mass and more specifically of very large particle size have not been systematically explored. One major difficulty in the case of transport of large particles and high specific mass comes from the various flow regimes that may be observed [1,2,4,12,13,16,17]: when the speed of transportation increases, several transitions arise from regimes with a layer of solids at the bottom of the pipe that is at rest or that flows backwards in inclined pipes [13,16,17] to regimes with a moving bed and eventually to heterogeneous and pseudo-homogeneous suspensions at high mixture velocities.

The knowledge of the velocity above which the bed starts to move forward is of great interest with respect to operation of a production line. Below this limit the system may indeed plug. In the present study, experiments are carried out in order to better understand the effects of solid size and specific mass on this velocity and on the pressure drop.

The experimental set-up is presented in Section 2. Some general considerations on the typical regimes and pressure drop curves that are specific to an horizontal pipe and an overview of few models are presented in Section 3. The experimental results are presented and discussed in Section 4. The main results that concern mono-disperse calibrated solid spheres of two different sizes and two different specific masses flowing in the horizontal pipe are presented in Section 4.1. Mixture of spheres and rough stones of arbitrary shapes are also tested in Section 4.2, in order to check to what extent the results obtained for spheres may represent an actual application. Several models are proposed and compared to the experiments in Section 4.3. Conclusions and perspectives are then given in Section 5.

---

* Corresponding author.
E-mail address: florent.ravelet@ensta.org (F. Ravelet).

0894-1777/$ - see front matter © 2012 Elsevier Inc. All rights reserved.
http://dx.doi.org/10.1016/j.expthermflusci.2012.11.003

2. Experimental set-up

2.1. Test loop

The test loop is shown schematically in Fig. 1. It consists of a first rigid, transparent horizontal pipe of internal diameter $D = 100$ mm and 10 m long in which flows the liquid/solid mixture. The return occurs in a clear flexible PVC hose reinforced with a steel coil, of internal diameter $D = 100$ mm and total length 20 m. This return pipe first follows a 180° horizontal curve of curvature diameter 1.7 m, then a climb, a descent and an ascent in a vertical plane. The present study focuses on the horizontal pipe.

The mixture of solids and water that flows in the rigid horizontal pipe and the return flexible pipe is then passed through a separator consisting of a closed box fitted with a side hatch and whose bottom side consists of a grid of stainless steel. The water then falls into the tank 2, and the solids flow in a chute that is inclined at 45°. This chute provides at its end an adjustable flap in order to control the solids flow rate. The end of the chute is above a grid container of known capacity that is immerged in tank 1 and connected with a grid pipe to the outlet of tank 1. The separated water flows from tank 2 into tank 1 through a pipe with an electromagnetic flowmeter. The mixture is sucked by a vortex pump (Ensival Moret MT 100-100-250) connected to the outlet of tank 1 and delivered in the circuit.

2.2. Characteristics of the solids

Solids with different sizes and specific masses are used. Their physical and geometrical characteristics are summarized in Table 1. The particles are relatively large, with sizes ranging from 5% to 18% of the pipe diameter. Calibrated beads of Glass (SiLi, SiLibeads type M, with a relative dispersion of sizes of 4%) and of Alumina (Umicore, Alumina Degussit 92%, with a relative dispersion of sizes of 10%) are used. The real solids that are used from the perspective of an actual application have irregular shapes, as can be seen in the picture in Table 1. The specific mass of a sample of fifty solids have been measured with a densimeter. It is constant within 2700 ± 10 kg m^{-3}.

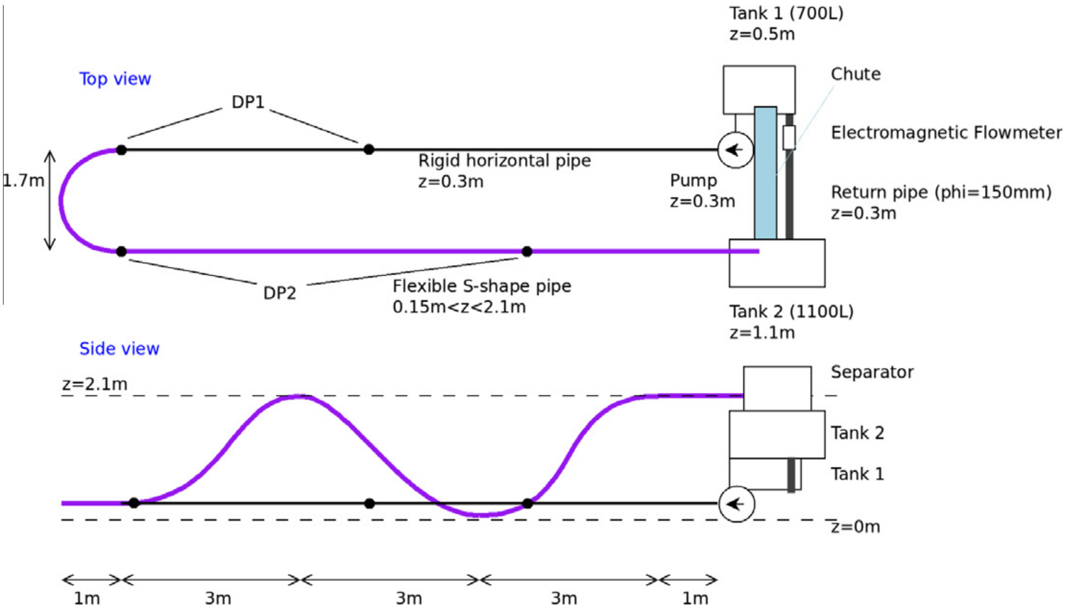

Fig. 1. Sketch of the test loop. Top and side views.

Table 1
Physical characteristics of the calibrated beads and of the different mixtures. The mean diameter D_{50} is such that 50% of the solids are greater than this size.

Type	Glass beads	Alumina beads	Mixture 1 (Alumina)	Mixture 2 (Alumina)	Mixture 3 (Alumina/Glass)	Stones
Size	5 mm 10 mm 16 mm	6 mm 15 mm	50% 6 mm 50% 15 mm D_{50}:10.5 mm	75% 6 mm 25% 15 mm D_{50}:8.25 mm	50% 6 mm Alumina 50% 5 mm Glass D_{50}:5.5 mm	8–18 mm D_{50}:10 mm
Specific mass	2500 kg m^{-3}	3650 kg m^{-3}	3650 kg m^{-3}	3650 kg m^{-3}	3075 kg m^{-3}	2700 kg m^{-3}
Picture						

2.3. Control parameters and measured quantities

The aim of the present work is to measure the pressure drops in different parts of the test loop as a function of concentration and velocity. Several choices can be made for the definition of these quantities. The natural control parameters, i.e. the parameters that are really adjusted with experimental means, are the volumetric flow rates of the liquid (Q_l) and of the solids (Q_s).

The following set of parameters is chosen for presenting the results. The first is the mixture velocity V_{mix} and the second is the *transport* or *delivered* concentration C:

$$V_{mix} = \frac{Q_l + Q_s}{A}$$
$$C = \frac{Q_s}{Q_s + Q_l}$$

with A the cross-section area of the pipe. This mixture velocity is a volumetric average of the velocities of each phase. It is convenient for comparison with models.

Concerning the concentration, please note that on the one hand, the solids do not flow with the same velocity as water, because of their large size and of the large density ratio—in other words there is a non-negligible *slip* velocity. On the other hand, in horizontal parts, among the various regimes that may be observed there exist regimes with a stationary layer of solids at rest at the bottom of the pipe [4,12,13]. There could thus be a great difference between the *transport* or *delivered* concentration C and the *in situ*, *local* or *volumetric* concentration ϵ_s that is the ratio between the area occupied by the solids and the area of the pipe. Further, the volumetric concentration is a key parameter in the modelisation, as illustrated in Sections 3.1 and 3.3. This concentration is however not a control parameter but results from the geometry, the physical properties of the phases and the boundary conditions.

The present experimental study is to perform measurements with varying V_{mix} in the range 0–5 m s^{-1}, for constant delivered concentrations of 5%, 10%, 15%, and 20%.

The water flow-rate is measured using an electromagnetic flowmeter (KROHNE Optiflux 2000) and adjusted by varying the rotation rate of the vortex pump. The solids flow-rate is set through a hatch and is measured by filling the buffer zone of known capacity located in the tank 1. Finally, the pressure drop are measured using two differential pressure sensors (VEGADIF65): a first that is located at the end of the straight line, 60 diameters downward of the pump, and a second that is located at the hose in the S-shaped part (see the position of the pressure taps in Fig. 1). After a stationary state is reached, the data are recorded for 30 s at a sample rate of 130 Hz. Measuring the rate of fluctuation of flow and pressure is used as a validation criterion of the measurements. The losses are expressed in terms of hydraulic gradients (meters of water column per meter of pipe) and with a dimensionless pressure drop coefficient:

$$I(m/m) = \frac{\Delta P}{\rho_l g L}$$
$$\lambda = \frac{\Delta P}{\frac{1}{2}\rho_l V_{mix}^2}\frac{D}{L}$$

with ΔP the measured static pressure drop, ρ_l the specific mass of the carrying liquid (water) and L the curvilinear distance between the pressure taps. The velocity scale that is used to present dimensionless results is the terminal velocity of the particle falling in the fluid at rest V_0. Finally, the relative specific mass of the solids with respect to water is $s = \frac{\rho_s}{\rho_l}$.

In order to compare the present data to existing theories and correlations [4,15], the following quantity is also introduced:

$$\Phi = \frac{I - I_f}{I_f}$$

with I_f the hydraulic gradient that would be observed for water flowing alone at the mixture velocity. It corresponds to the dimensionless excess of pressure drop caused by the presence of the particles. Similarly, two dimensionless groups are introduce for the mixture velocity:

$$F_D = V_{mix}/\sqrt{gD}$$

a “Froude” number based on the mixture velocity and the pipe diameter and

$$F_{d_p} = V_0/\sqrt{gd_p}$$

a “Froude” number based on the terminal velocity and the size of the particle.

In the following, I_h stands for the hydraulic gradient in the horizontal line, and I_s stands for the hydraulic gradient in the S-shape pipe. The case of the S-shape part is not fully developed here and will be discussed in a forthcoming paper with new experimental data including a better discretisation of the different inclined parts and bends. The symbol I_v is used for the hydraulic gradient that would be observed in a vertical pipe.

Optical measurements are also performed with a high-speed camera (Optronis CamRecord600). Typically 3200 images are recorded with a resolution of 1280 × 1024 pixels at a frame rate of 200 Hz. The flow is illuminated backwards with a LED plate from Phlox. The visualization area is surrounded by a square plexiglas box filled with water in order to minimize optical distorsions.

3. Observed regimes and overview of a few models

A common feature of multiphase flows is the existence of very different flow patterns, which makes modeling much more complicated. In the case of the transport of large solid particles by a carrying liquid, several intermittent, stratified and dispersed regimes are observed in horizontal and inclined flows [1,2,4,17]. For the specific case of vertical ascending flows, though plug or slug flows are observed in the pneumatic transport of small particles [18], to the best of our knowledge only dispersed regimes are observed for the hydraulic transport of large ($d_p \geqslant 1$ mm) and massive ($s \geqslant 1.5$) particles [2,9–11]. The present section first presents a model for vertical ascending flows and then the typical regimes that are encountered in the horizontal experiment and the different possible models.

3.1. Validation of a model for the hydraulic transport of large particles in ascending vertical pipelines

The case of vertical flow is reasonably straightforward. The pressure force exerted on a column of fluid of height z balances two forces: the hydrostatic weight of the mixture and the friction on pipe wall due to the fluid shear stress [1,2]. In the following, the hydrostatic weight of the column of water is removed in order to present the hydraulic gradients that are due to the flow of a mixture in the pipe.

The vertical hydraulic gradient I_v can thus be decomposed into two parts: $I_v = I_{stat} + I_f$, with I_{stat} the hydrostatic contribution and I_f the wall shear-stress contribution. The hydrostatic contribution reads:

$$I_{stat} = (s-1)\epsilon_s$$

The *in situ* concentration ϵ_s is *a priori* unknown. Following the seminal work of Newitt et al. [7], the average velocity difference between the solids and the surrounding water, or *slip* velocity V_{slip} reads:

$$V_{slip} = \frac{1-C}{1-\epsilon_s} V_{mix} - \frac{C}{\epsilon_s} V_{mix} \tag{1}$$

This slip velocity would be the terminal velocity V_0 for a single solid of diameter d_p and of drag coefficient $c_d = 0.44$ falling in an infinite medium of fluid at rest:

$$V_0 = \sqrt{\frac{4 d_p g (s-1)}{3 c_d}} \tag{2}$$

However, it must be corrected in the case of a concentrated mixture flowing in a pipe. Owing to the range of parameters that we are interested in, we have chosen to use the Richardson and Zaki correlation [8] for the *hindered* average slip velocity:

$$V_{slip} = (1-\epsilon_s)^{2.4} V_0 \tag{3}$$

The *in situ* concentration is obtained by solving the non-linear system of Eqs. (1) and (3) in an iterative way, with a trust-region dogleg algorithm.

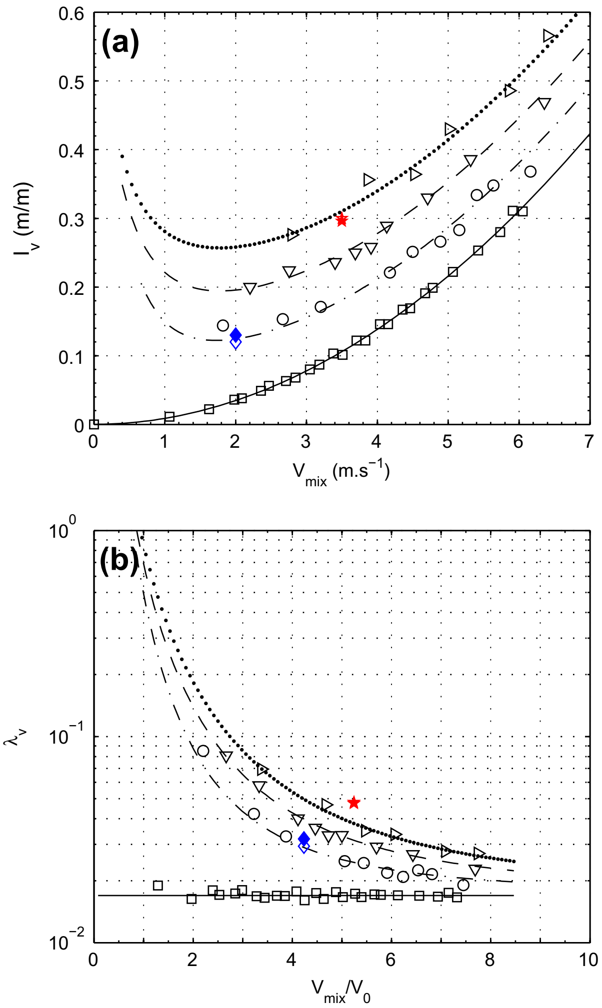

Fig. 2. Validation of the vertical model on different data sets. Vertical hydraulic gradient I_v vs. mixture velocity V_{mix}. Black symbols: data of Yoon et al. [11] for spherical beads of diameter $d_p = 20$ mm, $s = 2.15$ flowing in a pipe of diameter $D = 100$ mm, compared to the results of the model (black lines) for various concentrations (□ and filled line: $C = 0\%$, ○ and dash-dotted line: $C = 5\%$, ▽ and dashed line: $C = 10\%$ and ▷ and dotted line: $C = 15\%$). Red ★: data (open symbol) of Xia et al. [9] for spherical beads of diameter $d_p = 15$ mm, $s = 2$ flowing in a pipe of diameter $D = 100$ mm, at $C = 15\%$, compared to the result of the model (closed symbol). Blue ◇: data (open symbol) of Hong et al. [10] for spherical beads of diameter $d_p = 5$ mm, $s = 2.5$ flowing in a pipe of diameter $D = 50$ mm, at $C = 3.85\%$, compared to the result of the model (closed symbol). (For interpretation of the references to color in this figure legend, the reader is referred to the web version of this article.)

The model for the wall shear-stress contribution I_f is based on some assumptions. As noticed by Engelmann [5] or Hong et al. [10], large particles tend to migrate away from the wall due to hydrodynamic lift [2]. Assuming that the near-wall velocity profile is only slightly affected by the presence of particles in the core region, the wall shear-stress is modeled by water flowing at the water velocity:

$$I_f = \lambda \frac{\left(V_{mix} \frac{1-C}{1-\epsilon_s}\right)^2}{2gD}$$

This model for vertical ascending flow has been validated on various experimental data available in the Literature [9–11]. The comparison between the model and the data is plotted in Fig. 2. The agreement is very good. When dealing with a mixture of liquid and solids, the pressure drops are significantly higher than for pure fluid for the whole range of mixture velocity that corresponds here to $V_0 \leqslant V_{mix} \leqslant 8V_0$: it is for instance twice as large at $C = 5\%$ and $V_{mix} = 4V_0$ for the beads of diameter $d_p = 0.2D$ and $s = 2.15$ (data of Yoon et al. [11], ○ in Fig. 2). A remarkable feature of the curves is the presence of a local minimum: the hydraulic gradient does not vary monotonically with the velocity. This is due to the fact that the hydrostatic gradient is the dominant term and that it is a decreasing function of the mixture velocity. In the case of ascending flows, the *in situ* concentration ϵ_s is indeed much larger than the *delivered* concentration C for mixture velocities of the order of V_0 and decreases slowly with increasing V_{mix}. For instance, for the data plotted with ○ in Fig. 2, $V_0 = 0.83$ m s^{-1} and the values of the computed *in situ* concentration are: $\epsilon_s = 13\%$ for $V_{mix} = V_0$, $\epsilon_s = 11\%$ for $V_{mix} = 1.2V_0 = 1$ m s^{-1}, $\epsilon_s = 10\% = 2C$ for $V_{mix} = 1.4V_0$ and $\epsilon_s = 6\%$ for $V_{mix} = 4V_0$. The contribution of the hydrostatic gradient to the total hydraulic gradient is respectively 96%, 93%, 90% and 43%. The velocity which corresponds to the minimum of the pressure drop curve ($V_{mix} \simeq 1.8V_0$ for ○ in Fig. 2) is of great practical importance and the line should not be operated below this velocity.

The model is thus used with the parameters of the present experiments to compare the order of magnitude of hydraulic gradients and critical velocities between horizontal and vertical flows (see for instance Figs. 3 and 4b).

3.2. Description of the typical regimes in horizontal pipes

The Fig. 3 presents a typical evolution of the hydraulic gradients I_h and I_s in the present experimental setup. The solids are Glass beads of diameter 5 mm and the delivered concentration is $C = 5\%$.

The thick black line in Fig. 3 stands for the measured hydraulic gradient in the horizontal part in the case with water flowing alone. The typical Reynolds number is 2×10^5 and the flow is fully turbulent. The curve is a fit of the form $I_f = \lambda \frac{V^2}{2gD}$ that gives a value for the friction coefficients $\lambda_h = 0.156$ and $\lambda_s = 0.160$. Corresponding rugosities can be deduced with the Colebrook formula. The estimated rugosity is 20 μm for the horizontal pipe.

The shape of the pressure drop curve with particles (red[1] ●: I_h and blue ■: I_s in Fig. 3) is very similar to the ascending vertical case with a large increase of the pressure drop for the whole range of tested mixture velocity (here, $V_{mix} \leqslant 10.5V_0$). The presence of a local minimum is also observed: the hydraulic gradient does not vary monotonically with the velocity. The mixture velocity for which

---

[1] For interpretation of color in Figs. 3, 4, and 6, the reader is referred to the web version of this article.

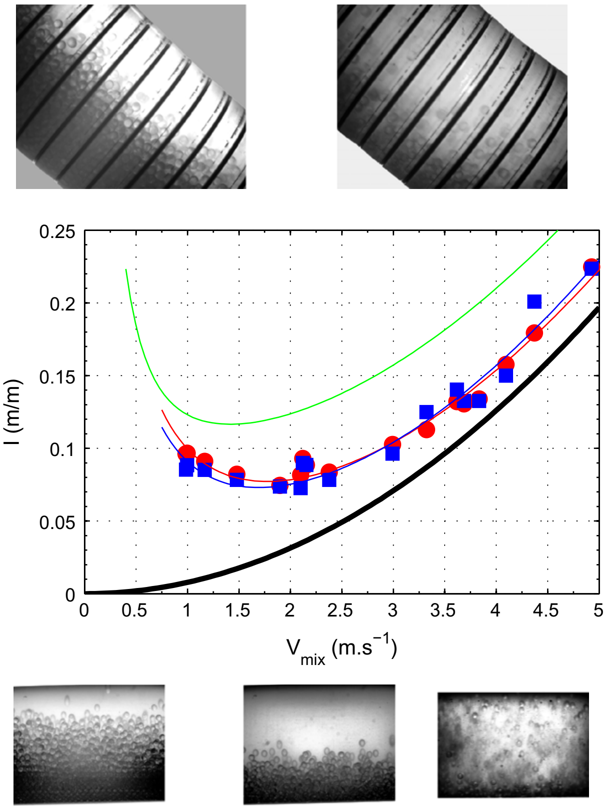

Fig. 3. Illustration of the different regimes. Hydraulic gradient vs. V_{mix}, Glass beads of 5 mm, $C = 5\%$. Solid black line: water flowing alone I_f, red ●: I_h, blue ■: I_s. The blue and red solid lines are fits of the type $a/V_{mix} + bV_{mix}^2$ (see Section 3.3). The green solid line stands for I_v predicted with the model developed for vertical pipelines (see Section 3.1).

the minimum hydraulic gradient is observed will be termed the *critical velocity* V_{crit}, following the definition of Doron et al. [12]. In the present case and in the horizontal pipe, the critical velocity is $V_{crit,h} \simeq 1.8$ m s^{-1} (i.e. $V_{crit,h} \simeq 3.8V_0$). All these observations are consistent with all the previous studies that dealt with similar large particles [4,12,14,15].

For $V_{mix} < V_{crit}$ in the horizontal pipes, flow regimes with a stationary bed above which a compact layer of beads is flowing are observed (see bottom left picture in Fig. 3 that corresponds to $V_{mix} = 1.2$ m s^{-1}, i.e. $V_{mix} = 2.5V_0$). The more the mixture velocity decreases, the more the solids tend to settle down. These regimes are thus such that $\epsilon_s \gg C$ ($\epsilon_s \simeq 32\%$ for bottom left picture in Fig. 3) and are characterized by a large pressure drop that is caused by a decrease in the discharge section. In the ascending part of the flexible pipe, a layer of solids located at the bottom of the pipe and that is flowing backwards is even observed for these low velocities, as already observed by Yamaguchi et al. [17] (see top left picture in Fig. 3 that is taken at $V_{mix} = 0.9$ m s^{-1}). The flow in this regime is very unstable and the transit time needed to reach a stationary state is very long, of the order of twenty minutes—the typical time for a solid to flow through the whole pipe being 30 s.

Slightly above the critical velocity—for $V_{mix} \gtrsim V_{crit}$—a moving bed on the bottom of the pipe is observed both in the horizontal pipe and in the S-shaped part (see bottom central picture and top right picture in Fig. 3 that are both taken at $V_{mix} = 2.1$ m s^{-1}, i.e. $V_{mix} = 4.1V_0$). Very few beads are also transported by saltation. The mean height of this moving bed is roughly 25 mm in the present case (Glass beads, $d_p = 5$ mm and $C = 5\%$), that corresponds to approximately five layers of beads. There is a velocity gradient between the upper layer of the moving bed and the lower layer that moves more slowly, as usually observed for hydraulic transport of sediment in two-dimensional open channels [19]. Please note that there may be substantial differences between the present experiments and usual bed-load models for the transport of sediments [19], because of three-dimensional and geometrical effects due to the cylindrical section of the pipe and of the large particle diameter to pipe diameter ratio. The average velocity of this bed is small compared to the mixture velocity and $\epsilon_s > C$ here, $\epsilon_s \simeq 10\%$.

Increasing further the mixture velocity, more and more solid beads get suspended and transported by the flow, there is no more bed, the flow is fully dispersed. The pressure drop curves behave as the clear-water pressure drop curve and follow the same trend at high velocities. In that case, $\epsilon_s \gtrsim C$ and the regime is called “pseudo-homogeneous” [12] or “heterogeneous” [4] (see bottom right picture in Fig. 3 that is taken at $V_{mix} = 4.9$ m s^{-1}, i.e. $V_{mix} = 10.3V_0$).

The green line is the results of the model for pressure drop in ascending vertical flow, presented in Section 3.1. The main contribution to the increase of the total hydraulic gradient in the vertical model comes from the hydrostatic pressure of the mixture. On the contrary, in the case of the horizontal pipe, the increase in the total hydraulic gradient originates in the bed formation that causes more friction. Some partial conclusions concerning the comparison of a vertical ascending pipe and an horizontal pipe in view of an application with complicated shapes can be drawn. Firstly, the hydraulic gradient in the horizontal part is lower than the one that would be observed in an ascending vertical pipe at least for this specific mass and solid size. Secondly, the critical velocity in the horizontal pipe is greater than that of a vertical pipe. The effects of size, concentration and specific mass that may be very different for a vertical and an horizontal pipe will be further explored in Section 4.

3.3. Correlations and models

This paragraph is a brief overview of some of the correlations and models that are commonly used.

Empirical correlations The first quantity of interest to be presented is the critical velocity V_{crit}. One correlation has been proposed by Durand and Condolios [14]:

$$V_{crit} = F_l\{2D\,g(s-1)\}^{1/2} \tag{4}$$

with F_l a constant of order unity, that depends on the delivered concentration and the particle size.

Concerning the prediction of the hydraulic gradient, a first empirical correlation is the one proposed by Durand and coworkers [15]. They used sand particles of one specific mass with diameter up to 25.4 mm in pipes ranging from 38 mm to 558 mm in diameter (the maximum relative diameter in the pipe of 104 mm was 4.5%). The dimensionless excess of pressure drop caused by the presence of the particles Φ is expressed using the two “Froude” numbers F_D and F_{d_p}. These two parameters are grouped to form $\Psi = F_D^2 F_{d_p}^{-1}$. They found a general correlation that best represents all their data:

$$\Phi = 180\;C(\Psi)^{-1.5} \tag{5}$$

It is recommended to use this correlation in the vicinity of the critical velocity (from mixture velocities slightly below to three or four times greater). This correlation was then modified to take into account the specific mass of the particles, as reported by Newitt et al. [4]. In the case of particles of a few millimeters flowing in water, the particle Reynolds number is sufficiently high to assume that the settling velocity is given by Eq. (2) with a constant drag coefficient c_d. This form of the correlation reads:

$$\Phi = 121\;C\left(\frac{V_{mix}^2}{gD(s-1)}\sqrt{\frac{3}{4}c_d}\right)^{-1.5}$$

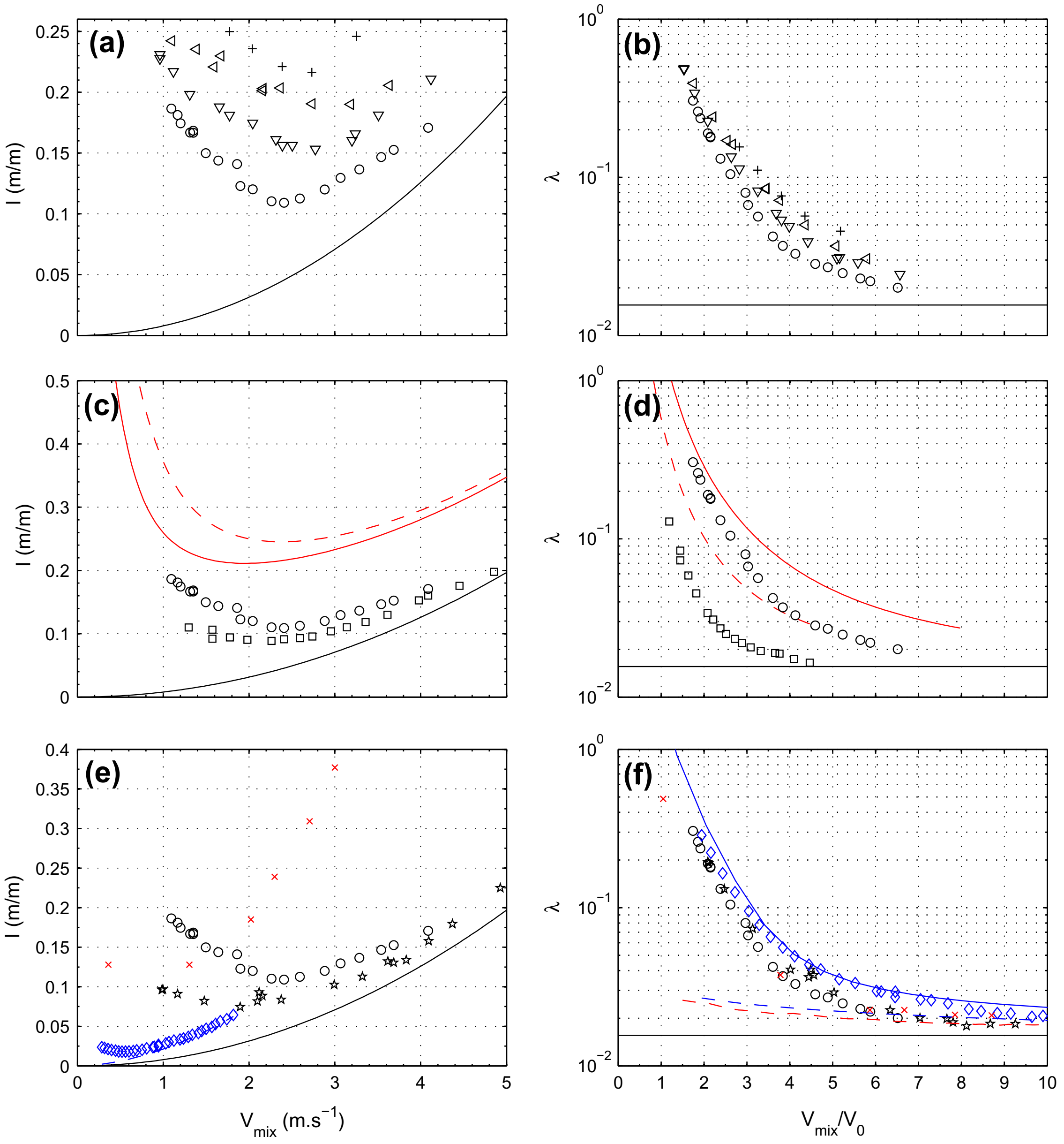

Fig. 4. (a,c, and e): Hydraulic gradient I_h *vs.* mixture velocity V_{mix}. (b,d, and f): dimensionless plot of λ_h vs. V_{mix}/V_0. (a and b): Experimental data for Alumina beads of $d_p = 6$ mm at various concentrations: $C = 5\%$ (○), $C = 10\%$ (▽), $C = 15\%$ (◁) and $C = 20\%$ (+). Solid black line: water flowing alone. (c and d): Experimental data in the horizontal pipe (symbols) and predictions of the model presented in Section 3.1 for a similar vertical pipe (red lines), for Alumina beads at $C = 5\%$ and two sizes: $d_p = 6$ mm (○ and solid red line) and $d_p = 15$ mm (□ and dashed red line). (e and f): Experimental data for $d_p = 5$ and 6 mm and $C = 5\%$ for two specific masses: Alumina (○) and Glass (★). Blue ◇: data extracted from Fig. 3 of Ref. [12] (particles of diameter $d_p = 3$ mm, $s = 1.24$ flowing in an horizontal pipe of diameter $D = 50$ mm at $C = 4.2\%$), solid blue line: validation of the two-layer model, dashed blue line: single phase pressure drop. Red ×: data extracted from Fig. 12 of Ref. [4] (gravels of mean diameter $d_p = 2.6$ mm, $s = 2.55$ flowing in an horizontal pipe of diameter $D = 25.4$ mm at $C = 5\%$), red dashed line: single phase pressure drop.

The functional form of I_h that is predicted by this model is thus: $I_h = I_f\left(1 + AV_{mix}^{-3}\right) = bV_{mix}^2 + aV_{mix}^{-1}$, as displayed in Figs. 3 and 6.

This correlation have been widely discussed [1,2,4,12]. The main criticisms are that it does not take into account the size of the particles and that a single correlation may not be applicable to all flow regimes. The value of the constant that is reported in the Literature is moreover different according to various authors, the term $F_{d_p}^{-1}$ being sometimes abruptly replaced by $\sqrt{C_d}$.

Semi-empirical correlations Newitt et al. [4] have lead experiments in a 25.4 mm in diameter horizontal pipe, with various particles covering four specific masses ($s = 1.18$, $s = 1.4$, $s = 2.6$ and $s = 4.1$) and various sizes, the largest being of equivalent diameter 2.6 mm (10% of the pipe diameter). Theoretical considerations are used to derive expressions of the hydraulic gradient for different flow regimes (homogeneous, heterogeneous and flow with moving beds), and of the transition velocities between those regimes. For heterogeneous flows, i.e. for $17V_0 \leqslant V_{mix} \leqslant \sqrt[3]{1800gDV_0}$, the excess of friction is considered proportional to the energy dissipated by the particles as they fall under the action of gravity. This hypothesis leads to:

$$\frac{\Phi}{\epsilon_s} \propto (s-1)V_0V_{mix}^{-3} \tag{6}$$

For flows with a moving bed, i.e. for $\sqrt{2gD(s-1)} \lesssim V_{mix} \leqslant 17V_0$, the effect of the solids is proportional to the solid–solid friction between the solids and the bottom of the pipe:

$$\frac{\Phi}{\epsilon_s} \propto (s-1)V_{mix}^{-2} \tag{7}$$

The main assumption in Ref. [4] is the use of C for ϵ_s, that is equivalent to assume that the particles move at the same speed as the water or at a constant fraction of it. The suspension of particles through turbulence or Bagnold forces is moreover not taken into account. This is obviously not the case in the present experiment as can be seen with the pictures in Fig. 3 and the values of ϵ_s/C that are reported in Section 3.2.

Analytical model based on mass and momentum balance Doron et al. [12] have established such a model. It is based on the decomposition of the cross-section of the pipe into two layers. It is thus a one dimensional model. The bottom of the pipe is assumed to be filled with a stationary or moving bed of packed particles. The height of this bed is y_b and the volumetric concentration in this layer is $C_b = 0.52$. All the particles are assumed to move at the same velocity in the bed. An heterogeneous mixture of solids and fluid is flowing in the upper part of the pipe. The mixture is treated as an homogeneous fluid with averaged physical properties and no slip between the phases is considered. The mass and momentum balance are then written in each layer. The shear stresses at the walls and at the interface between the two layers are modeled with frictions coefficients, and with a static friction force for the lower layer. In addition, the dispersion process of the solid particles in the upper layer is modeled by a turbulent diffusion process balanced by the gravitational settling of particles, leading to an advection–diffusion equation. The size of the particles is taken into account, firstly to define the roughness of the interface between the two layers, and secondly in the definition of the turbulent diffusion coefficient and the advection velocity that is the hindered terminal velocity (the Richardson and Zaki correlation [8], Eq. (3), is used). This model leads to a non-linear system of five equations with five unknowns: the bed height (y_b), the velocity of the upper layer (U_h), the velocity of the lower layer (U_b), the concentration in the upper layer (C_h) and the pressure gradient (∇P). The parameters of the model are: the solid friction coefficient between the pipe wall and the particles (η), an angle of internal friction that models the normal stress transmitted by the shear stress at the interface between the fluid and the bed (φ), the packing concentration (C_b) and the correlations for fluid friction coefficients. This model have been implemented in Matlab, using an iterative procedure with a trust-region dogleg algorithm to solve the non-linear system. This implementation has been validated on the data of Ref. [12] in Fig. 4f.

4. Results and discussion

4.1. Effects of the physical characteristics of the beads

This paragraph is devoted to the comparison of the pressure drop curves with various concentrations, specific masses and sizes for identical spherical beads. The reference case is the Alumina beads of diameter 6 mm, of specific mass $s = 3.65$, and at a delivered concentration $C = 5\%$. In this case, the order of magnitude of the minimal pressure drop at critical velocity $V_{crit,h} \simeq 2.4\ \mathrm{m\ s^{-1}}$ is $I_{crit,h} \simeq 0.11$ m/m.

The effects of the concentration are presented in Fig. 4a and b. Only results for the horizontal part are plotted. On the one hand, increasing the delivered concentration leads to an increase of the pressure drop, as expected. The relative increase of the pressure drop at the critical point with respect to $C = 5\%$ is roughly 40% for $C = 10\%$ and 70% for $C = 15\%$. Very few points are available for the concentration $C = 20\%$ owing to the large power required; these points are nevertheless on both sides of the critical point. The relative increase in pressure drop at the critical point for $C = 20\%$ is around 100%. On the other hand, changing the concentration seems to increase only very slightly the critical velocity (see Section 4.3 for a discussion of this point).

The comparison of two sizes of beads of same specific mass at the same concentration is presented in Fig. 4c and d: the experimental measurements for Alumina beads of diameter $d_p = 6$ mm are plotted with ○ and the results for Alumina beads of diameter $d_p = 15$ mm are plotted with □. The pressure drop that would be observed in an ascending vertical pipe according to the prediction of the model (see Section 3.1) is plotted with, respectively a solid red line for $d_p = 6$ mm and a dashed red line for $d_p = 15$ mm. The main effects of the size are first that the pressure drop is decreased for the large particles in the horizontal pipe, and secondly that the critical velocity does not seem to be affected by the particle size. This feature is quite surprising to the best of our knowledge has not been reported in previous works that mainly dealt with particles below 4 mm (see Section 3.3). It is moreover robust as it is confirmed on the Glass beads (see ★ and ◇ in Fig. 8). The decrease of pressure drop with larger particles and the constancy of the critical velocity are a distinguishing feature between horizontal and vertical flows: owing to the dependence of the slip velocity on the square root of the particle diameter, the hydraulic gradient and the critical velocity are greater for larger solids in vertical flows as a direct result of the model presented in Section 3.1.

Finally, the experimental measurements of the pressure drop for two beads of similar size ($d_p \simeq 5$ mm) and two different specific masses, respectively $s = 3.65$(○) and $s = 2.5$(★) are plotted in Fig. 4e

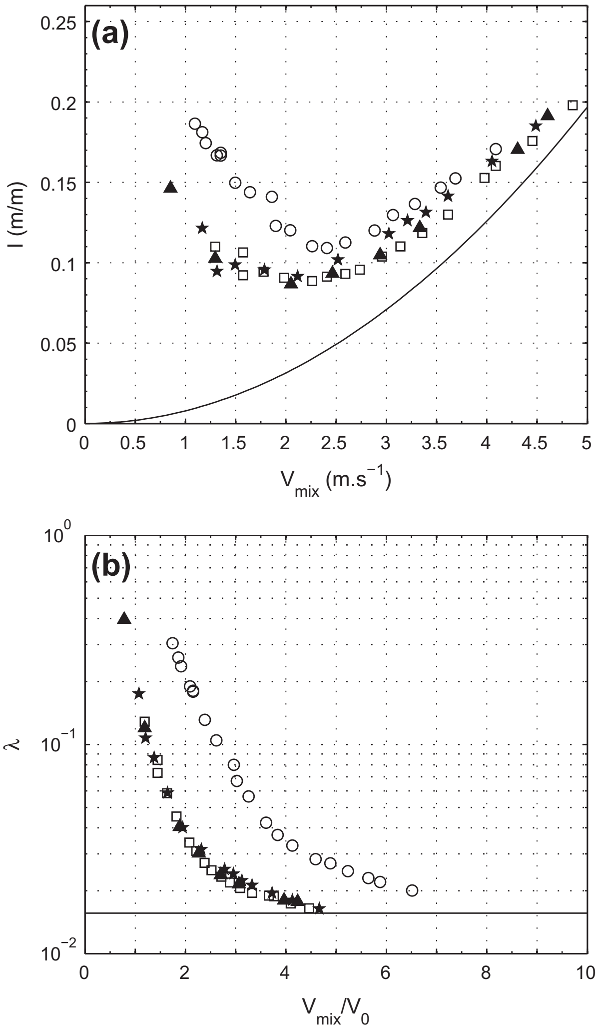

Fig. 5. (a): Hydraulic gradient I_h *vs.* mixture velocity V_{mix} and (b): dimensionless plot of λ_h vs. V_{mix}/V_0, at $C = 5\%$ *vs.* for ○: Alumina 6 mm, □: Alumina 15 mm, △: mixture 1 and ★: mixture 2.

and f. Increasing the specific mass leads to both an increase of the pressure drop and of the critical velocity. Experimental data on particles of similar size that are available in the Literature [4,12] are also plotted in this figure. Please note that they have been collected in pipes of smaller diameters. The shape of the present curves is very similar to previously reported works, particularly when presented in a dimensionless form (λ vs. V_{mix}/V_0, in Fig. 4f). Please nonetheless notice that the single-phase flow pressure drop coefficients are different (black solid line, blue and red dashed lines in Fig. 4f).

4.2. Mixes of beads and rough solids

This paragraph deals with mixtures of spheres and rough stones of arbitrary shapes in order to check to what extent the results obtained for mono-disperse spheres may represent an actual application.

The Fig. 5 presents the horizontal hydraulic gradient I_h vs. V_{mix} for different mixtures of Alumina beads of diameter 6 mm and 15 mm. Contrary to what one might think *a priori*, the pressure drop of the mixtures is not a simple linear combination of the pressure drop of each bead size: for a 50% of 6 mm mixture (mixture 1) the pressure drop curve coincides with that of the 15 mm beads. The pressure drop is thus low. This effect is even still present for a proportion of 75% of 6 mm beads in the mixture (mixture 2) but only at low mixture velocities corresponding to $V_{mix} \lesssim V_{crit}$, i.e. to regimes with a stationary bed. For higher velocities the pressure drop lies between the other two and is closer to the pressure drop of the 6 mm beads.

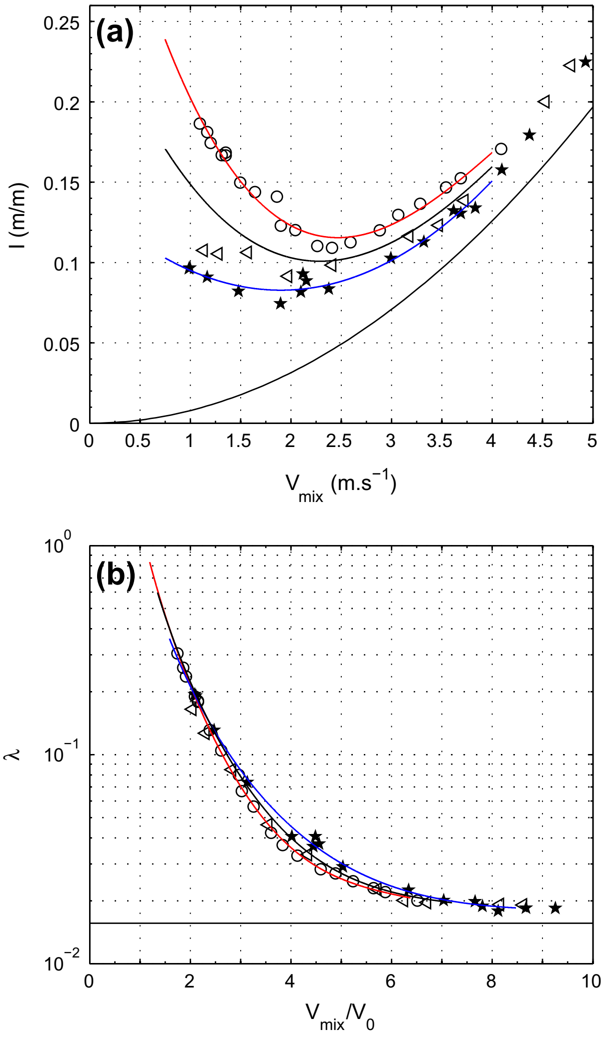

Fig. 6. (a): Hydraulic gradient I_h *vs.* mixture velocity V_{mix} and (b): dimensionless plot of λ_h vs. V_{mix}/V_0, at $C = 5\%$ for ∘: Alumina 6 mm with a fit corresponding to the red line, ★: Glass 5 mm with a fit corresponding to the blue line and ◁: mixture 3. The black solid line is the mean of the two fits.

The Fig. 6 presents the comparison of $I_h(V_{mix})$ for three mixtures of beads of same size but different specific mass: Glass beads of 5 mm (★), Alumina beads of 6 mm (∘) and mixture 3 (50% Glass/50% Alumina, ◁). The pressure drop curve for the mixture lies between the two single-type cases and seems to be well modelised by the mean of the two curves: the solid red line in Fig. 6 is a fit for the Alumina, the solid blue line a fit for Glass and the black line is the mean of these two curves.

The effects that have been observed for mixtures, particularly in the horizontal part, may be ascribed to segregation phenomena. This is illustrated in Fig. 7 for mixture 2 of Alumina of two sizes (see Table 1). A tendency of having two layers of beads, with the small beads being transported at the bottom of the pipe while the large beads are transported on top of this bed, is indeed observed. This phenomenon is reminiscent of the so-called “Brazil nut effect”. Likewise, for the mixture of beads of different specific masses, the heaviest tend to settle at the bottom of the pipe.

All the previous results concern experiments with spherical beads of unique size and specific mass or mixtures of at most two different types of spherical beads. The pressure drop curves for stones are plotted in Fig. 8. Their physical characteristics are given and illustrated in Table 1. The specific mass of a sample of 50 solids have been measured with a densimeter. It is constant within 2700 ± 10 kg m^{-3}. Their specific mass is thus very close to that of Glass. Their size distribution is between 8 and 18 mm, with 50% of the solids having a size lower than 10 mm. The pressure drop I_h for these solids is very close to the case of 10 mm Glass beads. The irregular shape of the solids that leads to different drag coefficients thus does not seem to play an important role with respect to the hydraulic gradient, as already reported by Yoon et al. [11]. It may be a second order effect with respect to the size and specific mass effects.

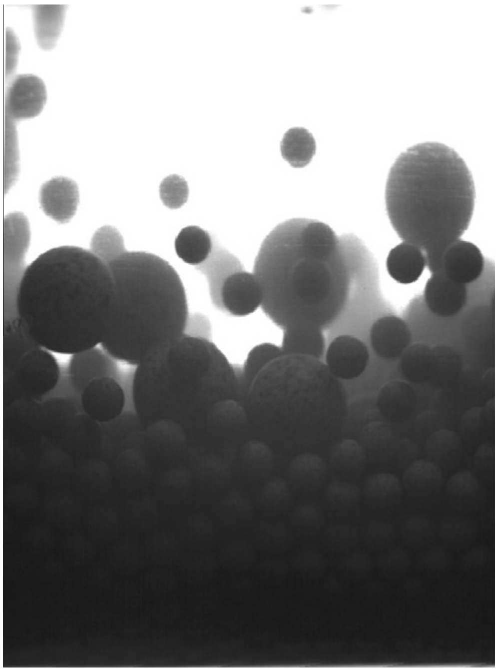

Fig. 7. Illustration of segregation for mixture 2. In that case, $C = 5\%$ and $V_{mix} \simeq 1$ m s^{-1}.

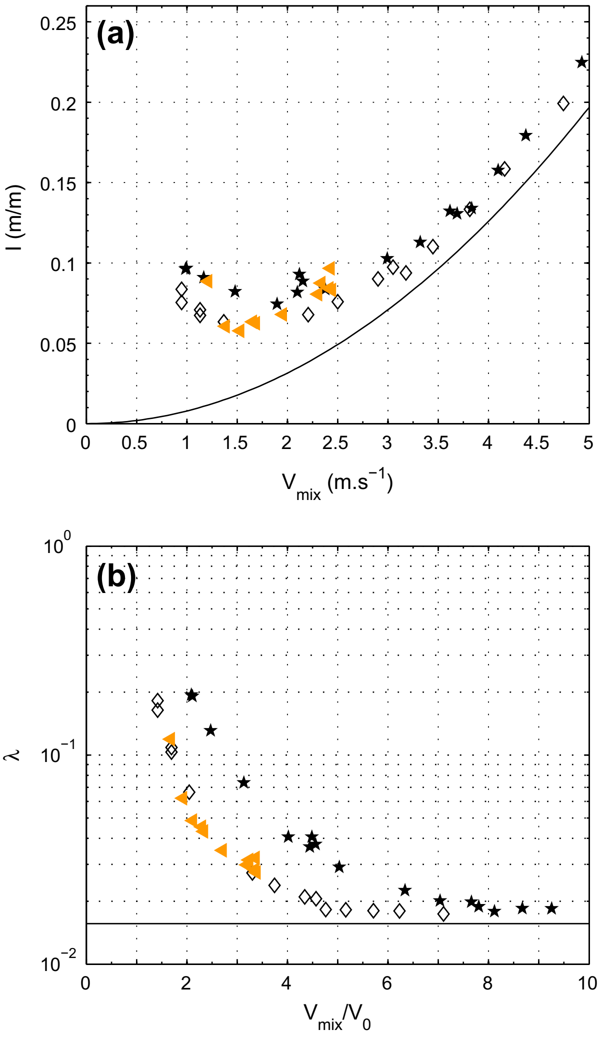

Fig. 8. (a): Hydraulic gradient I_h vs. mixture velocity V_{mix} and (b): dimensionless plot of λ_h vs. V_{mix}/V_0, at $C = 5\%$ for ★: Glass 5 mm, ◇: Glass 10 mm and orange ◁: stones. (For interpretation of the references to color in this figure legend, the reader is referred to the web version of this article.)

Table 2
Critical velocity V_{crit} (m s^{-1}) experimentally measured for Alumina and Glass beads, compared to the values predicted with the correlation (4).

	Glass 5 mm, $C = 5\%$	Alumina 6 mm, $C = 5\%$
Experiment	1.8	2.4
Eq. (4) with $F_l = 1$	1.7	2.3
Eq. (4) with $F_l = 1.05$	1.8	2.4

4.3. Analysis and discussion

This section is devoted to the application of various models to the present data and to their discussion.

Semi-empirical correlations The first quantity that could be checked is the critical velocity V_{crit} that is the mixture velocity for which the minimum hydraulic gradient is observed. The present results suggest that the critical velocity does not strongly depend on the particle size but depends on the specific mass (Fig. 4c–e). The terminal settling velocity furthermore does not seem to be the velocity scale that drives the pressure drop curve as can be seen in Fig. 4d. The correlations that use the “Froude” number F_D (Eqs. (4) and (5)) may be applicable.

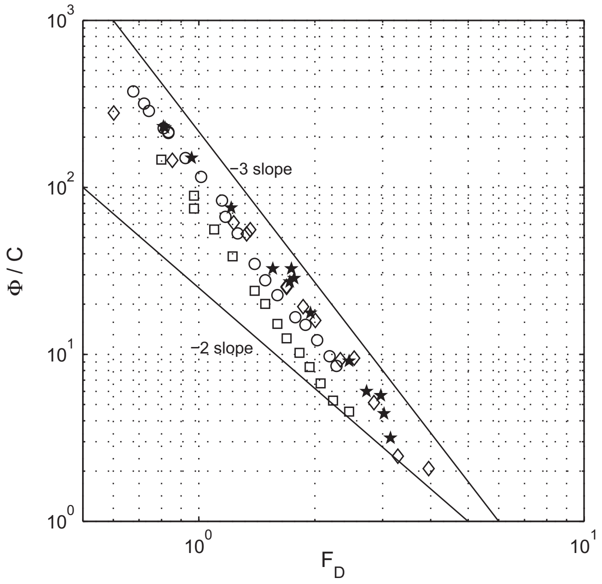

Fig. 9. Dimensionless excess of head loss divided by the delivered concentration Φ/C vs. Fr for ★: Glass beads of 5 mm ($C = 5\%$), ◇: Glass beads of 5 mm ($C = 10\%$), ∘: Alumina beads of 6 mm ($C = 5\%$) and □: Alumina beads of 15 mm ($C = 5\%$).

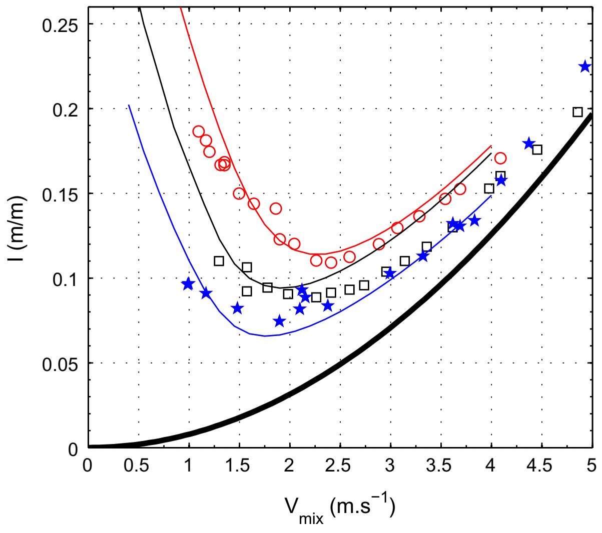

Fig. 10. Results of the model (solid lines) compared to the present experimental data (symbols) at $C = 5\%$. Blue line and ★: Glass 5 mm. Red line and ∘: Alumina 6 mm. Black line and □: Alumina 15 mm. Parameters for the model: $C_b = 0.52$, $\eta = 0.25$, $\tan\varphi = \infty$ (see text).

The results concerning the prediction of the critical velocity are reported in Table 2. The predicted values are in excellent agreement with the experimental values for Glass and Alumina beads of various sizes and at various concentrations (see Fig. 4 for Alumina and Fig. 8 for Glass).

The value of the dimensionless excess of head loss Φ, normalized by the delivered concentration C is plotted as a function of the Froude number F_D for various data sets in Fig. 9. All the data follow the same trend. The effect of the concentration is moreover well described by a linear dependence: the data points for Glass beads of 5 mm at a concentration $C = 5\%$ (★) and at a concentration $C = 10\%(\diamondsuit)$ collapse on a single curve. A -3 power law $\Phi = C\,K\,F_D^{-3}$ fits quite well the data in the range $0.7 \lesssim F_D \lesssim 3$. The effect of specific mass that is included in the definition of the Froude number seems to be well taken into account: the data points for Glass beads of 5 mm at a concentration $C = 5\%$, $C = 10\%$ (★ and ◇) and for Alumina beads of 6 mm at a concentration $C = 5\%$ (○) are very close, the values of the constant K being respectively 130 ± 4 and 123 ± 3. All these considerations are consistent with the empirical correlation (Eq. (5)) and the theoretical equation (Eq. (6)) with $V_0 \propto \sqrt{s-1}$ for large particles. On the contrary, the -2 power law and the dependency in $(s-1)$ of Φ that are predicted by Eq. (7) does not seem to be consistent with the present measurements. As already noticed, the size of the particles, that is not taken into account in the model, has a strong influence on the hydraulic gradient: the value of the constant for Glass beads of 10 mm (not represented in Fig. 9) is indeed $K = 87$ and the value for Alumina beads of 15 mm (□) is $K = 75$. This is predicted neither by Eq. (5) (no dependence in d_p) nore by Eq. (6) (Φ increases as $\sqrt{d_p}$). The model that leads to Eqs. (6) and (7) relies on the hypothesis that $\epsilon_s \propto C$. This is not the case in the present experiments: for Glass beads of $d_p = 5$ mm at $C = 5\%$, the values of the *in situ* concentration estimated with imaging are indeed: $\epsilon_s \simeq 32\%$, 10% and 7% for $V_{mix}/V_{crit,h} = 0.67$, 1.17 and 2.72. For the Alumina beads of $d_p = 6$ mm and $d_p = 15$ mm, the measured concentrations are $\epsilon_s \simeq 11\%$ and 9% for $V_{mix}/V_{crit,h} = 0.83$ and 1.66.

Analytical model based on mass and momentum balance The question that is addressed is to what extent the analytical model of Doron et al. [12] may apply to the present physical parameters, with solids of much higher specific mass and even higher relative diameter.

In the original work of Doron et al. [12], the values of the parameters are the following: $\eta = 0.3$, $\tan\varphi = 0.6$ and $C_b = 0.52$. The packing concentration C_b has first been experimentally measured by weighting a tube of same diameter and capacity two liters filled with dry beads and with beads and water. A dozen of measurements have been performed for each type of bead. The concentration is found to be 0.52 ± 0.01. The determination of the solid friction coefficient for an immersed granular bed is a very difficult problem [20], and the friction coefficient itself can strongly vary with the beads roughness [21]. We thus choose to vary η and to present the results that better match the experimental data in the vicinity of the critical velocity. The angle φ is set to $\varphi = \pi/2$ which corresponds to neglecting the contribution of the normal stress transmitted into the bottom layer by the shear at the interface. This assumption is validated *a posteriori* by evaluation of its relative contribution.

The results for the hydraulic gradient are presented in Fig. 10. The final value of the friction coefficient is $\eta = 0.25$. The predictions of the model for the two small beads of different specific mass and relative diameter 5% are in relatively good accordance with the experiments. For the largest beads, the trend of the reduction of the hydraulic gradient is reproduced but the model is not satisfactory: it matches the data point only very close to the critical velocity.

The model also predicts the height of the lower layer and the velocities of the two layers. Some pictures taken for the Glass beads at $C = 5\%$ are presented in Fig. 11 at different velocities. The right column corresponds to the difference between two successive images and allows to better identify the different flow regimes and the velocity gradient in the bed. At $V = 1.0$ m s^{-1}, one can clearly identify a static bottom layer and a packed layer of 3–4 beads that are transported with almost no vertical gradient. The height of the static bed is roughly 42 mm while the value predicted by the model is 40 mm. At $V = 1.9$ m s^{-1}, the bottom layer is moving slowly with almost no vertical gradient of velocity. The

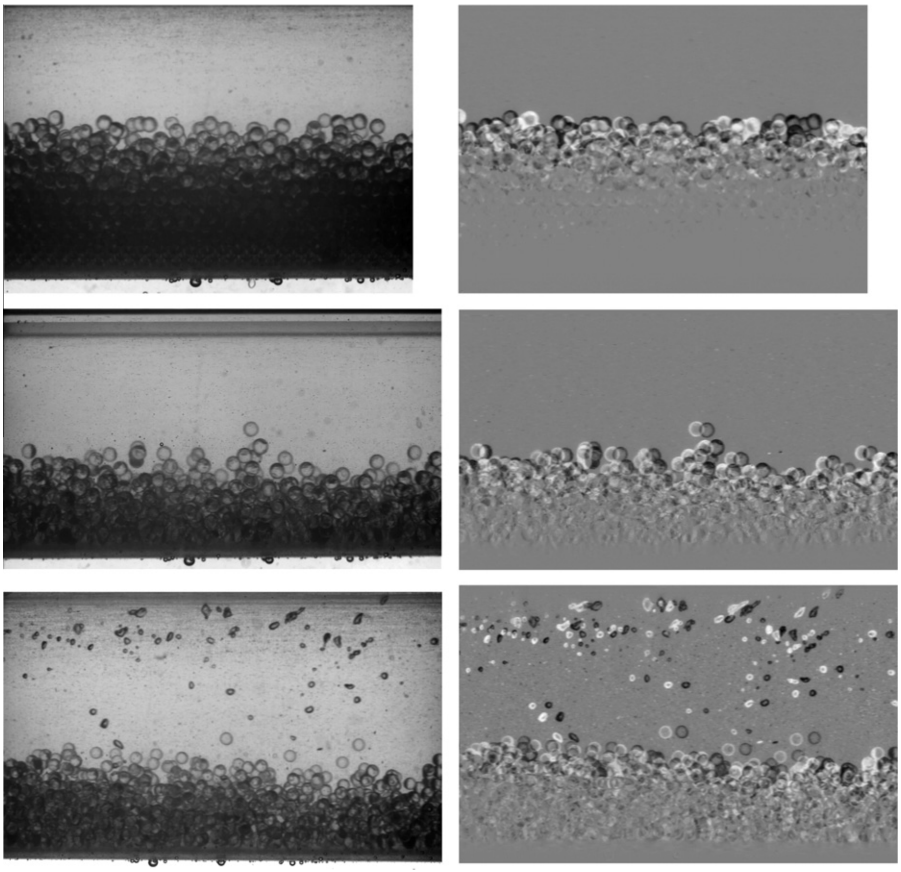

Fig. 11. Pictures taken in the horizontal pipe of Glass beads of diameter 5 mm at $C = 5\%$. Left column: rough picture. Right column: difference between two successive images taken at the frame rate f. From top to bottom: $V = 1.0$ m s^{-1} and $f = 50$ Hz, $V = 1.9$ m s^{-1} and $f = 500$ Hz, and $V = 3.9$ m s^{-1} and $f = 630$ Hz.

height of the moving packed bed is roughly 25 mm while the value predicted by the model is 22 mm. Above this moving bed, an unpacked layer of suspended beads is observed. And finally, at $V = 3.9$ m s^{-1}, one can still distinguish two layers of solids, with a bottom layer that is moving more rapidly. The height of this static bed is roughly 22 mm while the value predicted by the model is 15 mm. The velocities that are evaluated with the movies give similar accordance.

In conclusion, this two-layer model, originally validated only on small specific mass particles, is promising and predicts well the global and few local features of the two-phase flow for larger specific masses. It seems however limited to not too large particles. One question is the validity of the advection–diffusion equation that is used to determine the concentration in the upper layer for particles that become larger than the turbulent eddies.

5. Conclusion

The hydraulic gradient as a function of mixture velocity has thus been measured for calibrated beads of two specific masses (2500 kg m^{-3} and 3650 kg m^{-3}), with large particle to pipe diameter ratios of 5%, 10% and up to 15%, as well as for mixtures of calibrated beads and for real stones of similar physical properties. The tests have been conducted in an horizontal pipe. The main results are the following:

- The increase of friction in an horizontal pipe is quite large at velocities of the order of the terminal velocity of a settling particle. This increase of the hydraulic gradient is however lower than that which would be observed because of the hydrostatic contribution in an ascending vertical pipe. On the other hand, the critical velocities that are a key parameter with respect to plugging for the design of a complex industrial application are greater.
- For a given specific mass and delivered concentration, the hydraulic gradient decreases with the increase of the particle size in an horizontal pipe, contrary to what is observed in vertical pipes.
- The empirical correlations that are available in the Literature give satisfactory results but the classical constants that are recommended clearly do not correspond to the present case of very large particles. Further studies with even larger beads are necessary to better model the variation of these constants with the particle size.
- The mixtures and real stones could be modeled with mono-dispersed beads of equivalent specific mass and size. However, at low velocities, strong segregation mechanisms are present and would make the modelisation harder.
- Analytical models based on more physical arguments are of great interest. They however show their limits for the largest beads.

This last point may be linked to the fact that for large beads the modelisation of the solids using a continuous medium even with the help of granular theory becomes very untrustworthy. The number of particles that can be put in the pipe cross-section is too small to be treated with statistical methods. For instance, numerical methods with Eulerian–Eulerian formulation such as the one presented in Ref. [22] is unappropriate to our case and even give unpresentable results. Full Lagrangian methods would also be very expensive owing to the nevertheless large number of particles. We are now developing two alternate methods: one is based on Lagrangian dynamics for the solids, the forces being prescribed with the help of a two-layer global model for the fluid. The idea is to detect the position of the compact bed and to compute the concentration in the upper layer, and then to apply some bed-load sediment transport equations [19] for the momentum balance in the bed. The second is to develop a Navier–Stokes code that uses volume penalization [23] that seem very promising to cope with the solids.

Further experiments are scheduled in the S-shape part, and in inclined pipes.

Acknowledgement

We would like to thank the Technip company for financial support, especially J. Denegre, P. Espinasse and T. Parenteau. F.R. thanks Colette Gauthier for fruitful discussion. We are particularly indebted to M. Joulin from the DynFluid laboratory of Arts et Metiers ParisTech, as well as to the students J.-R. De Céa and C. Valet for their assistance in the design and development of the experiment. The main part of the experiments have been carried out with the help of A. Lemaire.

References

[1] P.E. Baha Abulnaga, Slurry Systems Handbook, McGraw-Hill, 2002.
[2] K.C. Wilson, G.R. Addie, A. Sellgren, R. Clift, Slurry Transport Using Centrifugal Pumps, Springer, 2006.
[3] V. Matousek, Predictive model for frictional pressure drop in settling-slurry pipe with stationary deposit, Powder Technology 192 (2009) 367–374.
[4] D.M. Newitt, J.F. Richardson, M. Abbott, R.B. Turtle, Hydraulic conveying of solids in horizontal pipes, Transactions of the Institution of Chemical Engineers 33 (1955) 93–110.
[5] H.E. Engelmann, Vertical hydraulic lifting of large-size particles – a contribution to marine mining, in: 10th Offshore Technology Conference, 1978, pp. 731–740.
[6] K. Pougatch, M. Salcudean, Numerical modeling of deep sea air-lift, Ocean Engineering 35 (2008) 1173.
[7] D.M. Newitt, J.F. Richardson, B.J. Gliddon, Hydraulic conveying of solids in vertical pipes, Transactions of the Institution of Chemical Engineers 39 (1961) 93–100.
[8] J.F. Richardson, W.N. Zaki, Sedimentation and fluidisation, Transactions of the Institution of Chemical Engineers 32 (1957) 35–53.
[9] J.X. Xia, J.R. Ni, C. Mendoza, Hydraulic lifting of manganese nodules through a riser, Journal of Offshore Mechanics and Arctic Engineering 126 (2004) 72.
[10] S. Hong, J. Choi, C.K. Yan, Experimental study on solid–water slurry flow in vertical pipe by using ptv method, in: Proceedings of the 12th International Offshore and Polar Engineering Conference, 2002, pp. 462–466.
[11] C.H. Yoon, J.S. Kang, Y.C. Park, Y.J. Kim, J.M. Park, S.K. Kwon, Solid–liquid flow experiment with real and artificial manganese nodules in flexible hoses, in: Proceedings of the 18th International Offshore and Polar Engineering Conference, 2008, pp. 68–72.
[12] P. Doron, D. Granica, D. Barnea, Slurry flow in horizontal pipes – experimental and modeling, International Journal of Multiphase Flow 13 (1987) 535–547.
[13] P. Doron, M. Simkhis, D. Barnea, Flow of solid–liquid mixtures in inclined pipes, International Journal of Multiphase Flow 23 (1997) 313–323.
[14] R. Durand, E. Condolios, Experimental investigation of the transport of solids in pipes, in: Deuxième Journée de lhydraulique, Societé Hydrotechnique de France, 1952.
[15] R. Durand, Basic relationship of the transportation of solids in pipes—experimental research, in: Proceedings of Minnesota International Hydraulics Conference, 1953, pp. 89–103.
[16] V. Matousek, Pressure drops and flow patterns in sand–mixture pipes, Experimental Thermal and Fluid Science 26 (2002) 693–702.
[17] H. Yamaguchi, X.-D. Niu, S. Nagaoka, F. de Vuyst, Solid–liquid two-phase flow measurement using an electromagnetically induced signal measurement method, Journal of Fluids Engineering 133 (2011) 041302.
[18] M. Van de Velden, J. Baeyens, K. Smolders, Solids mixing in the riser of a circulating fluidized bed, Chemical Engineering Science 62 (2007) 2139–2153.
[19] R.A. Bagnold, The flow of cohesionless grains in fluids, Philosophical Transactions of the Royal Society of London, Series A, Mathematical and Physical Sciences 249 (1956) 235–297.
[20] T. Divoux, J.-C. Géminard, Friction and dilatancy in immersed granular matter, Physical Review Letters 99 (2007) 258301.
[21] N.A. Pohlman, B.L. Severson, J.M. Ottino, R.M. Lueptow, Surface roughness effects in granular matter: influence on angle of repose and the absence of segregation, Physical Review E 73 (2006) 031304.
[22] J. Ling, P.V. Skudarnov, C.X. Lin, M.A. Ebadian, Numerical investigations of liquid–solid slurry flows in a fully developed turbulent flow region, International Journal of Heat and Fluid Flow 24 (2003) 389–398.
[23] D. Kolomenskiy, K. Schneider, A fourier spectral method for the Navier–Stokes equations with volume penalization for moving solid obstacles, Journal of Computational Physics 228 (2009) 5687–5709.